N° d'ordre : 00000 ANNÉE 2014

UNIVERSITÉ DE RENNES 1

THÈSE / UNIVERSITÉ DE RENNES 1
sous le sceau de l'Université Européenne de Bretagne

pour le grade de

DOCTEUR DE L'UNIVERSITÉ DE RENNES 1

Mention : Traitement du Signal et Télécommunications

École doctorale Matisse

présentée par

Xuan-Quy DAO

préparée à l'unité de recherche INRIA
Centre INRIA Rennes - Bretagne Atlantique
Université Rennes 1

Fluid flow control by visual servoing

Thèse soutenue à Rennes le 30/09/2014

devant le jury composé de :

M. Edouard LAROCHE
Professeur, Université de Strasbourg / *Rapporteur*

M. Guillermo ARTANA
Professeur, Université de Buenos Aires / *Rapporteur*

M. Azeddine KOURTA
Professeur, Université d'Orléans / *Examinateur*

M. François CHAUMETTE
Directeur de recherche, INRIA Rennes / *Examinateur*

M. Étienne MÉMIN
Directeur de recherche, INRIA Rennes / *Examinateur*

M. Christophe COLLEWET
Chargé de recherche, INRIA Rennes / *Directeur de thèse*

For their love and support,
this thesis is dedicated to my Mother and Father.

Abstract

The visual servoing control approach is formulated for the flow control of the plane Poiseuille flow. Generally, the flow control can lead the flow from its current state to a desired state. In transition to turbulence, the growth of kinetic energy density can lead the flow to turbulence. Moreover, the drag reduction is a potential application in the engineering applications. Therefore, this thesis aims to minimize the kinetic energy density and the skin friction drag.

The governing equations of the plane Poiseuille flow are modeled to a standard form in the automatic control. More precisely, the partial differential equations of the plane Poiseuille flow are transformed to a state space representation by using the spectral method. The streamwise and spanwise directions are discretized based on the Fourier series while the wall-normal direction is discretized based on the Chebyshev polynomials. The state vector involves the wall-normal velocity and vorticity. The control signals depend on the inhomogeneous Dirichlet boundary conditions which correspond to blowing/suction boundary control. The number of independent control signals is called the number of the degree of freedom. Moreover, the skin-friction drag and the kinetic energy density are modeled as a function of the state vector. The goal is to minimize both the skin-friction drag and the kinetic energy density by appropriate methods.

The linear feedback control, in general, is designed for the plane Poiseuille flow based on its linearized model.

The dimension of linearized plane Poiseuille flow is large, therefore, we need to reduce the order of controller. We demonstrate that the control law based on a mode reduction can be applied for the full system. Moreover, the kinetic energy density almost will monotonically decreases in time even using two degrees of freedom when the visual servoing control is designed based on the model order reduction.

Key words: flow control, visual servoing control, optimal control, model order reduction, Navier-Stokes equation, plane Poiseuille flow, spectral method.

Résumé

Cette thèse a pour but l'étude de la mise en œuvre de commandes par asservissement visuel pour le contrôle actif d'un écoulement de Poiseuille. D'un point de vue général, le contrôle d'écoulements vise à modifier ou à maintenir l'état de l'écoulement, malgré une éventuelle perturbation extérieure. Une des situations d'intérêt concerne par exemple la transition vers la turbulence où l'écoulement peut devenir turbulent avec la croissance de sa densité d'énergie cinétique. La réduction de la traînée est également une application potentielle dans des problèmes d'ingénierie. Un des buts applicatifs de cette thèse cherchera ainsi à minimiser à la fois la densité d'énergie cinétique et la traînée.

Des modèles numériques peuvent être utilisés pour générer un modèle d'état des équations aux dérivées partielles d'un écoulement de Poiseuille. Le modèle d'état considéré dans cette thèse s'appuie sur une représentation spectrale afin de transformer les équations aux dérivées partielles originelles en un système d'équations différentielles ordinaires. Le vecteur d'état rassemble dans notre cas la vitesse et la vorticité. Les signaux de commande dépendent eux de conditions aux limites de type Dirichlet non homogènes qui correspondent à des actions de soufflage/aspiration. Le nombre de degrés de liberté commandé du problème correspond à la dimension du signal de commande. La densité d'énergie cinétique et la traînée sont modélisées en fonction du vecteur d'état et du signal de commande.

Dans cette thèse nous avons plus particulièrement considéré un asservissement visuel partitionné. Celui-ci est appliqué au modèle d'état de l'écoulement avec deux degrés de liberté afin de minimiser simultanément la densité d'énergie cinétique et la traînée. La trainée, contrairement à l'énergie cinétique, diminue de façon monotone en fonction du temps. Une augmentation du nombre de degrés de liberté permet d'améliorer la décroissance de la densité d'énergie cinétique. Lorsque le nombre de degré de liberté correspond à la dimension du vecteur d'état, et en s'appuyant sur une commande par asservissement visuel, nous montrons que la densité d'énergie cinétique décroit de façon monotone au cours du temps.

Le modèle d'état de l'écoulement de Poiseuille vit dans un espace de très grande dimension. Par conséquent, il est nécessaire d'un point de vue pratique de réduire la dimension du contrôleur. Nous démontrons que la loi de commande s'appuyant sur un modèle réduit peut être appliquée au système complet. Dans ce cas la densité d'énergie cinétique décroit presque de façon monotone au cours du temps en utilisant une commande par asservissement visuel à deux degrés de liberté.

Mots clés : contrôle des écoulements, asservissement visuel, commande optimale, modèle réduit, équations de Navier-Stokes, écoulement de Poiseuille, méthode spectrale.

Acknowledgements

I would like to acknowledge many people who have helped me along the way to this milestone. The first and foremost, I sincerely thank my advisor, Christophe COLLEWET for continuous support to my research, and for patient teacher of my work. I would not have been able to complete this thesis without his guidance. Besides, I would like to thank Edouard LAROCHE, Guillermo ARTANA, Azeddine KOURTA, François CHAUMETTE, and Étienne MÉMIN for accepting to be part of my thesis committee and for their insightful comments on my pre-defense.

I would like to thank Étienne MÉMIN and Tudor Bogdan AIRIMITOAIE for their helpful during my work. I would also like to thank Huguette BÉCHU and Ioana BARBU for their helpful and kindness. And there are many people in Fluminance team I would like to thank.

I wish to thank my friends, especially Vietnamese friends in Rennes city for sharing both good and bad times.

Last but most importantly, I would like to express my love to my parents, my brother and my sister who have always been there for me, encouraging me and helping me to be who I am. This thesis would not have been possible without the love and affection that they have provided.

Résumé de la thèse en français

La commande par l'asservissement visuel est utilisée pour le problème du contrôle actif de l'écoulement de Poiseuille. Nous avons développé des contrôleurs qui obtiennent la stabilité de l'écoulement de Poiseuille basée sur l'information visuelle.

Ce résumé est architecturé comme suit. Tout d'abord, nous présentons le contrôle des écoulement et l'asservissement visuel. Ensuit, nous donnons l'état de l'art où nous considérons les travaux précédents et l'objectives. Et puis, nous modélisons l'écoulement de Poiseuille où le problématique existe. Après, toutes les contributions de cette thèse sont montrées: commande par asservissement visuel partitionné, commande par asservissement visuel, modèle d'ordre réduit de commande par asservissement visuel et commande robuste. Enfin, la conclusion est donnée pour terminer ce résumé.

Contrôle des écoulements et Asservissement visuel

Contrôle des écoulements

Le contrôle des écoulements permet de changer l'état actuel à un autre état ou maintenir son état actuel, quelque soit la perturbation extérieure. Nous pouvons agir partout à l'intérieur de l'écoulement ou uniquement aux frontières. Les applications potentiels du contrôle des écoulements sont la réduction de la traînée, l'augmentation de la portance, la réduction de bruit, etc.

Le contrôle des écoulements peut être effectué de manière passive ou active. Le contrôle passif consiste à agir de manière constante sur le système. Le plus souvent il s'agit en fait d'optimiser des formes ou d'utiliser certains revêtements de surface particuliers. Par contre, la contrôle actif, quant à lui, nécessite un apport d'énergie extérieur pour agir sur l'écoulement. Par exemple, le contrôle actif d'écoulement de Poiseuille est par les techniques de soufflage et d'aspiration [Joshi, 1996].

Asservissement visuel

L'asservissement visuel, une approche de contrôle en comité robotique, permet de contrôler les mouvements d'un robot à l'aide des données fournies par un capteur de vision [Chaumette and Hutchinson, 2006]. Pour réaliser une tâche d'asservissement visuel, un ensemble d'informations visuelles $\mathbf{s}(t)$ est choisi à partir de l'image de la scène visualisée par un dispositif optique. Une loi de commande est ensuite élaborée de telle sorte que le vecteur d'informations visuelles $\mathbf{s}(t)$ atteigne la consigne $\mathbf{s}^*$ correspondante à l'ensemble désiré d'informations visuelles et donc à un état désiré du système dynamique. Généralement une partie de l'image est utilisée pour définir un difféomorphisme entre la scène observée et l'ensemble d'informations visuelles $\mathbf{s}(t)$. Le principe de la commande est donc de réguler le vecteur d'erreur $\mathbf{e}(t) = \mathbf{s}(t) - \mathbf{s}^*$ à zéro. La dynamique du vecteur erreur est alors donnée par

$$\dot{\mathbf{e}}(t) = \frac{\partial \mathbf{e}(t)}{\partial t} + \mathbf{L}_\mathbf{e}(t)\mathbf{u}(t), \tag{1}$$

où $\mathbf{u}(t)$ est vecteur d'entrées de commande du système, $\mathbf{L_e}(t)$ est la matrice jacobienne qui définit la variation des informations visuelles par rapport à la variation de la commande [Espiau et al., 1992], et $\partial\mathbf{e}(t)/\partial t$ exprime la variation propre des informations visuelles.

Si nous souhaitions, par exemple, d'assurer une décroissance exponentielle du vecteur erreur

$$\dot{\mathbf{e}}(t) = -\lambda\mathbf{e}(t). \tag{2}$$

Nous obtenons

$$\mathbf{u}(t) = -\lambda\mathbf{L}_\mathbf{e}^+(t)\mathbf{e}(t) - \mathbf{L}_\mathbf{e}^+(t)\frac{\partial\mathbf{e}(t)}{\partial t}, \tag{3}$$

où $\mathbf{L}_\mathbf{e}^+$ est la matrice pseudo inverse de Moore Penrose $\mathbf{L_e}$. La commande est donnée par

$$\mathbf{u}(t) = -\lambda\mathbf{L}_\mathbf{e}^{-\mathbf{1}}(t)\mathbf{e}(t) - \mathbf{L}_\mathbf{e}^{-\mathbf{1}}(t)\frac{\partial\mathbf{e}(t)}{\partial t}. \tag{4}$$

Notons que la matrice $\mathbf{L_e}$ peut être non-carré mais de plein rang. Donc, la matrice pseudo inverse de Moore Penrose est $\mathbf{L}_\mathbf{e}^+$.

En appliquant les techniques d'asservissement visuel au contrôle actif des écoulements, $\mathbf{s}(t)$ peut être égale à la densité d'énergie cinétique ou la traînée ou le vecteur d'état. Une commande sera conçue pour obtenir les objectifs de commande en assurant le forme $\dot{\mathbf{e}}(t) = -\lambda\mathbf{e}(t)$.

État de l'art

Description du problème

Quelques écoulements sont étudiés, e.g. l'écoulement de cavité, profils d'ailles, l'écoulements autour des cylindres bidimensionels, vectorisation de jet, l'écoulement de canal. Nous choisissions d'étudier l'écoulement de Poiseuille parce que

- Il est plus adapté à la théorie du contrôle que les autres écoulements
- Il contient des propriétaires fondamentaux des écoulements
- Il illustre un grand nombre des problèmes importants non résolus du contrôle des écoulements
- Cet écoulement est un bon exemple de l'application de l'asservissement visuel au contrôle des écoulements

Ensuite, nous présentons l'équation dynamique de l'écoulement de Poiseuille. Les équations de Navier-Stokes sont données par

$$\begin{cases} \nabla.\mathbf{V} & = 0 \\ \dfrac{\partial\mathbf{V}}{\partial t} + (\mathbf{V}.\nabla)\mathbf{V} & = -\nabla P + \dfrac{1}{R}\Delta\mathbf{V}. \end{cases} \tag{5}$$

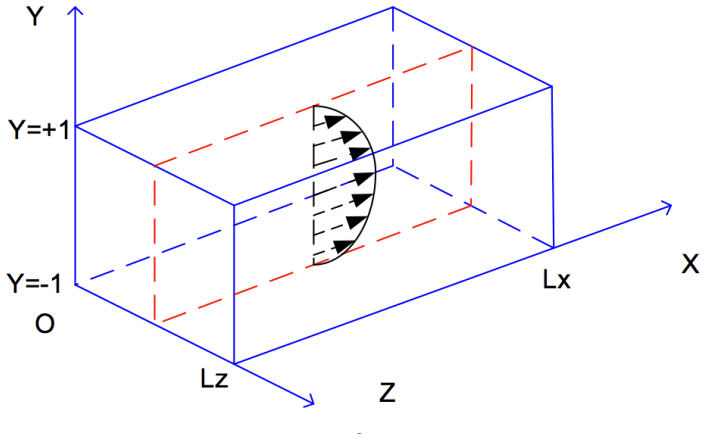

Figure 1: Écoulement de Poiseuille

où $\mathbf{V}$ est la vitesse, P est la pressure et R le nombre de Reynolds, ∇ est le gradient et Δ est le laplacien. Son profile est donné par la figure 1.

Pour déterminer l'état de l'écoulement et sa stabilité, la densité d'énergie cinétique est définie par [Bewley and Liu, 1998]

$$\varepsilon(t) = \frac{1}{\mathbf{V}_o} \int_{\mathbf{V}_o} \mathbf{v^2 dV_o}, \tag{6}$$

où $\mathbf{v} = (u, v, w) = \mathbf{V} - \mathbf{V}_e$ est la perturbation entre la vitesse $\mathbf{V}$ et la solution stable $\mathbf{V}_e$ et $\mathbf{V}_o$ est le volume. **Si $\dot{\varepsilon}(t) \leq 0$, alors la solution $\mathbf{V}$ de l'équation (5) est dite monotone stable** [Schmid and Henningson, 2001].

En plus, la traînée est définie par [Aamo et al., 2003]

$$\mathbf{d}(t) = \int_{x=0}^{L_x} \left(\frac{\partial u(y=+1)}{\partial y} - \frac{\partial u(y=-1)}{\partial y}\right) dx \tag{7}$$

L'écoulement de Poiseuille devient turbulent si le nombre de Reynolds est grand ($R > 5772$) et/ou la croissance de la densité d'énergie cinétique (1000<R<5772). Donc, nous avons besoin d'une commande qui obtient la stabilité de l'écoulement. À notre connaissance, dans la littérature scientifique, le problème du contrôle de l'écoulement en boucle fermée existe déjà

- Il existe dans la littérature une commande nonlinéaire [Balogh et al., 2001] et [Aamo et al., 2003] qui permet de garantir $\dot{\varepsilon}(t) \leq 0$ mais cette commande est conçue pour le nombre de Reynolds $R < 1/4$; toutefois nous n'avons pas besoin de commander si $R < 49.6$. Aucune autre commande garantit $\dot{\varepsilon}(t) \leq 0$ dans les travaux précédents.
- Aucune commande garantit $\dot{\mathbf{d}}(t) \leq 0$.
- La commande basée sur un modèle linéaire suffit pour stabiliser l'écoulement.

- **L'idée de cette thèse est de donner une approche de commande basée sur le modèle linéaire qui garantit $\dot{\varepsilon}(t) \leq 0$ et/ou $\dot{\mathbf{d}}(t) \leq 0$. En plus, cette commande peut appliquer pour tout le nombre de Reynolds. Par conséquent, l'écoulement devient monotone stable.**

Solution proposée

Le contrôle de l'asservissement visuel va être appliqué au contrôle actif des écoulements. Basé sur le contexte du contrôle de l'asservissement visuel, nous allons concevoir une approche de commande qui garantit

$$\begin{cases} \dot{\varepsilon}(t) & = -2\lambda\varepsilon(t) \\ \dot{\mathbf{d}}(t) & = -\lambda\mathbf{d}(t) \end{cases} \tag{8}$$

Modélisation de l'écoulement de Poiseuille

Les méthodes numériques peuvent être utilisées pour générer un modèle d'état des équations aux dérivées partielles (EDP). Un modèle linéaire a été développé en utilisant une méthode spectrale qui pourrait transformer EDP dans un ensemble des équations différentielles ordinaire (EDO).

Obtention d'un modèle d'état

L'approche classique consiste à linéariser les équations de Navier-Stokes autour de l'écoulement en régime établi. Il est alors possible d'obtenir une formulation en vitesse-vorticité [Butler and Farrell, 1992] :

$$\frac{\partial(\Delta v)}{\partial t} + U\frac{\partial(\Delta v)}{\partial x} - \frac{d^2U}{dy^2}\frac{\partial v}{\partial x} - \frac{1}{R}\Delta^2 v = 0 \tag{9}$$

$$\frac{\partial \eta}{\partial t} + U\frac{\partial \eta}{\partial x} - \frac{1}{R}\Delta\eta = -\frac{dU}{dy}\frac{\partial v}{\partial z}, \tag{10}$$

dans lesquelles v est la composante normale de la vitesse de la perturbation $v(x, y, z, t)$ définie comme étant la différence entre la vitesse courante $\mathbf{V}(x, y, z, t)$ et la vitesse en régime établi $\mathbf{V}_b = (1-y^2, 0, 0)$. η est la composante normale de la vorticité. $U = 1-y^2$ est la composante suivant x de $\mathbf{V}_b$, x étant la direction d'écoulement, y la direction normale aux parois et z la direction perpendiculaire à la direction d'écoulement et aux parois. R est le nombre de Reynolds.

En cherchant des solutions complexes (v_c, η_c) aux equations (9-10) sous la forme d'une série de Fourier tronquée dans les directions x et z conformément au modèle conceptuel proposé par [Joshi et al., 1997] et en ne considérant qu'un seul couple de nombre d'onde (n_{st}, n_{sp}) (où $n_{st} = 0 \cdots N_{st}$ et $n_{sp} = 0 \cdots N_{sp}$), il vient :

$$v_c(x, y, z, t) = \tilde{v}(y, t)e^{j(\alpha x+\beta y)},\ \eta_c(x, y, z, t) = \tilde{\eta}(y, t)e^{j(\alpha x+\beta y)}, \tag{11}$$

où $\alpha = \frac{2\pi n_{st}}{L_x}$ et $\beta = \frac{2\pi n_{sp}}{L_z}$ avec L_x la période dans la directions x, et L_z celle dans la direction z.

En injectant (11) dans (9-10), une approximation à (9-10) est obtenue en résolvant (12-13) (avec $k^2 = \alpha^2 + \beta^2$, voir le Chapitre 5 en anglais pour plus amples details) :

$$\begin{aligned}(-k^2U - \frac{d^2U}{dy^2} - \frac{k^4}{jR\alpha})\tilde{v} + (U + \frac{2k^2}{jR\alpha})\frac{\partial^2\tilde{v}}{\partial y^2} - \frac{1}{jR\alpha}\frac{\partial^4\tilde{v}}{\partial y^4} &= \frac{j}{\alpha}(\frac{\partial^3\tilde{v}}{\partial y^2\partial t} - k^2\frac{\partial\tilde{v}}{\partial t}) \quad (12)\\ (j\alpha U + \frac{k^2}{R})\tilde{\eta} - \frac{1}{R}\frac{\partial^2\tilde{\eta}}{\partial y^2} + j\beta\frac{dU}{dy}\tilde{v} &= -\frac{\partial\tilde{\eta}}{\partial t}. \quad (13)\end{aligned}$$

Dans le cas de l'écoulement de Poiseuille, une commande aux frontières est possible. Cette façon de faire conduit aux conditions de Dirichlet non homogènes de $\tilde{v}(y = \pm 1, t)$ et $\tilde{\eta}(y = \pm 1, t)$ suivantes :

$$\begin{cases} \tilde{v}(+1,t) &= \tilde{q}_{v,u}(t) \\ \tilde{v}(-1,t) &= \tilde{q}_{v,l}(t) \\ \tilde{\eta}(+1,t) &= \tilde{q}_{\eta,u}(t) \\ \tilde{\eta}(-1,t) &= \tilde{q}_{\eta,l}(t) \end{cases} \quad (14)$$

les conditions de Neumann restant homogènes aux frontières. Nous pouvons noter

$$\tilde{\phi}(y = \pm 1, t) = \tilde{q}_{\phi,\psi}(t) \quad (15)$$

où ϕ est v ou η et ψ est u ou l. Néanmoins, comme proposé dans [Boyd, 2001], le changement de variables suivant permet de rétablir des conditions de Dirichlet homogènes :

$$\begin{cases} \tilde{v}(y,t) = \tilde{v}_h(y,t) + \mathbf{F}_v(y)\mathbf{q}_v(t) \\ \tilde{\eta}(y,t) = \tilde{\eta}_h(y,t) + \mathbf{F}_\eta(y)\mathbf{q}_\eta(t), \end{cases} \quad (16)$$

dans lesquelles nous avons introduit les vecteurs $\mathbf{F}_v(y) = \begin{bmatrix} f_{v,u}(y) & f_{v,l}(y) \end{bmatrix}$, $\mathbf{q}_v(t) = \begin{bmatrix} \tilde{q}_{v,u}(t) \\ \tilde{q}_{v,l}(t) \end{bmatrix}$, $\mathbf{F}_\eta(y) = \begin{bmatrix} f_{\eta,u}(y) & f_{\eta,l}(y) \end{bmatrix}$, et $\mathbf{q}_\eta(t) = \begin{bmatrix} \tilde{q}_{\eta,u}(t) \\ \tilde{q}_{\eta,l}(t) \end{bmatrix}$, où les conditions suivantes doivent être vérifiées :

$$\begin{cases} f_{v,u}(+1) = f_{v,l}(-1) = 1, \quad f_{v,u}(-1) = f_{v,l}(+1) = 0, \quad f'_{v,u}(\pm 1) = f'_{v,l}(\pm 1) = 0 \\ f_{\eta,u}(+1) = f_{\eta,l}(-1) = 1, \quad f_{\eta,u}(-1) = f_{\eta,l}(+1) = 0, \end{cases} \quad (17)$$

ainsi que $\tilde{v}_h(\pm 1, t) = \tilde{v}'_h(\pm 1, t) = \tilde{\eta}_h(\pm 1, t) = 0$ (les conditions de Dirichlet et Neumann homogènes). Nous pouvons noter $f_{\phi,\psi}(y)$.

L'obtention du modèle de l'état reverché s'obtient alors par le bais de la discrétisation suivante :

$$\tilde{v}_h(y,t) = \sum_{n=0}^{N} a_{v,n}(t)\Xi_n(y), \;\; \tilde{\eta}_h(y,t) = \sum_{n=0}^{N} a_{\eta,n}(t)\Theta_n(y), \quad (18)$$

où les polynômes $\Xi_n(y)$ et $\Theta_n(y)$ vérifient à la fois les conditions de Dirichlet et Neumann (voir le Chapitre 5 en anglais pour plus amples détails). Dans la suite, en utilisant (18) dans (16) et en injectant le résultat dans (12-13) nous obtenons un système d'équations

ordinaires qui, une fois évalué en $N+1$ points de Gauss-Lobatto $y_i = cos(i\pi/(N+1))), 0 \leq i \leq N$ conduit à la représentation recherchée :

$$\mathbf{L}\dot{\mathbf{x}}(t) = \mathbf{A}\mathbf{x}(t) + \mathbf{B}\mathbf{u}(t) + \mathbf{E}\dot{\mathbf{u}}(t), \tag{19}$$

où $\mathbf{x}(t)$ est le vecteur d'état: $\mathbf{x}(t) = \begin{bmatrix} a_{v,0}(t) & \cdots & a_{v,N}(t) & a_{\eta,0}(t) & \cdots & a_{\eta,N}(t) \end{bmatrix}^\top$, $\mathbf{u}(t)$ est le signal de commande: $\mathbf{u}(t) = \begin{bmatrix} \mathbf{q}_v^\top(t) & \mathbf{q}_\eta^\top(t) \end{bmatrix}^\top$. Les matrices $\mathbf{L}$, $\mathbf{A}$, $\mathbf{B}$ et $\mathbf{E}$ s'expriment de façon complexe. Toutefois, il est important de noter dès à présent que les matrices $\mathbf{B}$ et $\mathbf{E}$ dépendent fortement des vecteurs $\mathbf{F}_v(y_i)$ et $\mathbf{F}_\eta(y_i)$ ainsi que de leurs dérivées suivant y jusqu'à l'ordre 4 au plus.

Le nombre de degré de liberté (DDL) est le nombre du signal de commande. Nous utilisons $\mathbf{u}(t) = \begin{bmatrix} \mathbf{q}_v^\top(t) & \mathbf{q}_\eta^\top(t) \end{bmatrix}^\top$, nous avons 4 **DDL**. Si nous prendrons $\mathbf{u}(t) = \mathbf{q}_v(t)$, nous ne considérons que 2 **DDL**.

En effet, la trainée $\mathbf{d}(t)$ s'exprime de la façon suivante :

$$\mathbf{d}(t) = \mathbf{D}_1\mathbf{x}(t) + \mathbf{D}_2\mathbf{u}(t), \tag{20}$$

où la matrice $\mathbf{D}_1$ est calculée par les polynômes $\Xi_n(y)$ et $\Theta_n(y)$ et la matrice $\mathbf{D}_2$ est calculée par les vecteurs $\mathbf{F}_v(y_i)$ et $\mathbf{F}_\eta(y_i)$. L'énergie cinétique $\varepsilon(t)$ s'écrit quant à elle de la façon suivante :

$$\varepsilon(t) = \mathbf{x}^\top(t)\mathbf{Q}_{11}\mathbf{x}(t) + \mathbf{x}^\top(t)\mathbf{Q}_{12}\mathbf{u}(t) + \mathbf{u}^\top(t)\mathbf{Q}_{21}\mathbf{x}(t) + \mathbf{u}^\top(t)\mathbf{Q}_{22}\mathbf{u}(t), \tag{21}$$

où la matrice $\mathbf{Q}_{11}$ est calculée par les polynômes $\Xi_n(y)$ et $\Theta_n(y)$ tandis que les matrices $\mathbf{Q}_{12}$, $\mathbf{Q}_{21}$ et $\mathbf{Q}_{22}$ sont aussi calculées par les polynômes $\Xi_n(y)$ et $\Theta_n(y)$ et les vecteurs $\mathbf{F}_v(y_i)$ et $\mathbf{F}_\eta(y_i)$.

Introduisons tout d'abord les grandeurs intéressantes. L'énergie synchronique $\varepsilon_s(t)$ est définie comme l'énergie cinétique maximum à l'instant t pour la pire condition initiale sur l'état telle que $\varepsilon(0) = 1$, soit

$$\varepsilon_s(t) = \max_{\varepsilon(0)=1} \varepsilon(t) \tag{22}$$

L'énergie diachronique ε_d est définie comme le maximum de l'énergie synchronique

$$\varepsilon_d = \max_{t\geq 0} \varepsilon_s(t) \tag{23}$$

De plus, pour une condition initiale, l'énergie maximale $\varepsilon_{\max}$ est définie comme le maximum de l'énergie cinétique

$$\varepsilon_{\max} = \max_{t\geq 0} \varepsilon(t) \tag{24}$$

Comportement du système en boucle ouverte

On considère le système en boucle ouverte ou noté l'équation de Orr-Sommerfeld. Si la matrice $\mathbf{L}$ est invertible, l'équation (19) devient

$$\dot{\mathbf{x}}(t) = \mathbf{L}^{-1}\mathbf{A}\mathbf{x}(t), \tag{25}$$

ensuite, le comportement du vecteur d'état et de la densité d'énergie cinétique décrit le problème du contrôle des écoulements.

Comportement du vecteur d'état

Notons que les écoulements 2D et 3D de Poiseuille contiennent les valeurs propres instables. Afin d'enquêter sur les valeurs propres instables, nous avons seulement besoin de considérer l'écoulement 2D de Poiseuille.

Tout d'abord, nous considérons l'écoulement 2D de Poiseuille avec $L_x = 4\pi$. Tous les multiples entiers de nombre d'onde fondamentale (α_0) existent dans cet écoulement

$$\alpha = n_{st}\alpha_0 = n_{st}\frac{2\pi}{L_x} = 0.5n_{st} \text{ avec } n_{st} = 0 \dots N_{st}. \tag{26}$$

Sur la base du diagramme de Orzag dans la figure 2(a) (obtenu à partir de l'équation de Orr-Sommerfeld), nous trouvons que la valeur propre instable de l'écoulement de Poiseuille est une fonction du nombre de Reynolds R et le nombre d'onde α. Certains modes sont des modes instables. Dans ce cas, seul le nombre d'onde $\alpha_1 = 2\alpha_0 = 1$ est le nombre d'onde instable (sa partie réelle est positive), alors que $\alpha_0 = 0.5$ et $\alpha = 1.5 \cdots +\infty$ sont des nombres d'onde stable. En particulière, dans le cas $\alpha = 1$, $\beta = 0$ et $R = 10\ 000$, les modes instables sont $\lambda = 0.003739670622977 \pm 0.237526488820464i$ [Orszag, 1971]. La densité d'énergie cinétique tend vers l'infini dans la figure 2(b).

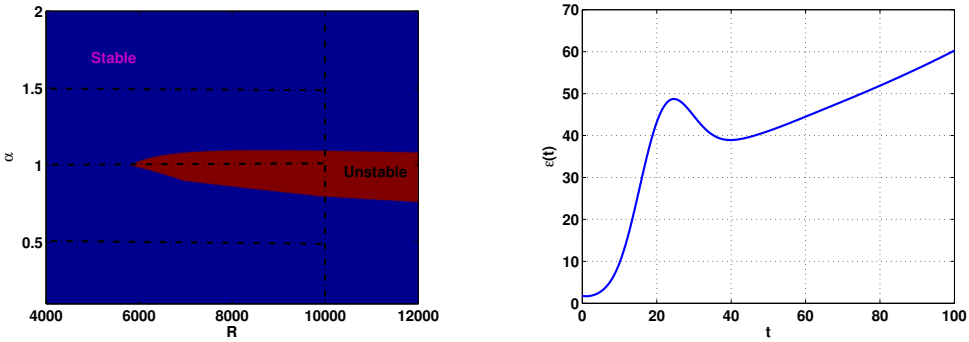

(a) modes instables en fonction de α et R (b) $\varepsilon(t)$ en fonction du temps

Figure 2: Comportement du vecteur d'état.

Comportement de la densité d'énergie cinétique

Dans [Orszag, 1971], le modèle linéaire contient les modes instables lorsque le nombre de Reynolds $R > 5\ 772$. Le fait que le modèle linéaire n'a pas de modes instables au nombre de Reynolds $1\ 000 < R < 5\ 772$, l'écoulement est encore turbulent. Plus précisément, la croissance de la densité d'énergie cinétique rend l'écoulement turbulent. Par exemple, l'écoulement est turbulent au nombre de Reynolds $R \approx 1\ 000$ à partir des études expérimentales [Patel and Head, 1969]. Notons qu'il n'y a pas de croissance de la densité d'énergie cinétique si le nombre de Reynolds est inférieur à $R = 49.6$, comme indiqué dans [Joseph and Carmi, 1969] par les méthodes de l'énergie.

Dans l'écoulement 3D de Poiseuille [Butler and Farrell, 1992], [Bewley and Liu, 1998], [McKernan et al., 2007], la densité d'énergie cinétique est souvent étudiée au nombre de Reynolds $R = 5\ 000$ et au nombres d'ondes $\alpha = 0$ et $\beta = 2.044$, la valeur pour laquelle nous obtenons la valeur maximale de l'énergie diachronique ε_d, vue dans la figure 3. L'énergie diachronique ε_d est la fonction des nombres d'onde α et β, donnée dans la figure 3(a). Sa valeur maximale est à $\alpha = 0$ et $\beta = 2.044$. L'énergie synchronique $\varepsilon_s(t)$ et l'énergie diachronique ε_d sont données dans la figure 3(b).

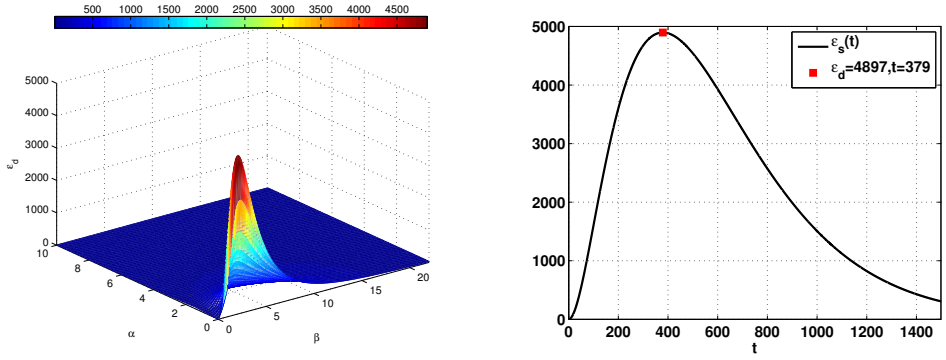

(a) ε_d en fonction de α et β (b) $\varepsilon_s(t)$ en fonction du temps

Figure 3: Comportement de la densité d'énergie cinétique ($R = 5\ 000$).

Remarques

Bien que le modèle linéaire de l'écoulement de Poiseuille contient toutes les valeurs propres négatives, le vecteur d'état diminue de façon monotone dans le temps, mais l'écoulement devient encore turbulent. Afin de déterminer l'état de l'écoulement et sa stabilité, nous nous concentrons sur le comportement de la densité d'énergie cinétique.

À partir des éléments théoriques décrits ci-dessus, nous allons concevoir les contrôleurs qui garantissent

$$\begin{cases} \dot{\varepsilon}(t) & = -2\lambda\varepsilon(t) \\ \dot{\mathbf{d}}(t) & = -\lambda\mathbf{d}(t), \end{cases} \tag{27}$$

autrement dit, si $\dot{\varepsilon}(t) = -2\lambda\varepsilon(t)$, l'écoulement est toujours monotone stable. Dans les sections suivantes, nous allons présenter des approches de commandes qui représentent les contributions de cette thèse.

Commande par asservissement visuel partitionné

Objectif

Lorsque le nombre de **DDL** est 2. Nous utilisons l'asservissement visuel partitionné (**AVS**) comme suit

- Un **DDL** est utilisé afin d'obtenir $\dot{\mathbf{d}}(t) = -\lambda\mathbf{d}(t)$

- Un **DDL** est utilisé pour minimiser $\varepsilon(t)$

Conception de la commande

On considère le système suivant

$$\begin{cases} \mathbf{L}\dot{\mathbf{x}}(t) &= \mathbf{A}\mathbf{x}(t) + \mathbf{B}\mathbf{u}(t) + \mathbf{E}\dot{\mathbf{u}}(t), \\ \mathbf{d}(t) &= \mathbf{D}_1\mathbf{x}(t) + \mathbf{D}_2\mathbf{u}(t), \end{cases} \tag{28}$$

pour 2 **DDL**. Si nous utilisons la commande $\mathbf{u}(t) = \mathbf{K}\mathbf{x}(t)$, la traînée est donnée par $\mathbf{d}(t) = (\mathbf{D}_1 + \mathbf{D}_2\mathbf{K})\mathbf{x}(t)$. Nous voulons $\dot{\mathbf{d}}(t) = -\lambda\mathbf{d}(t)$, c'est-à-dire

$$(\mathbf{D}_1 + \mathbf{D}_2\mathbf{K})\dot{\mathbf{x}}(t) = -\lambda(\mathbf{D}_1 + \mathbf{D}_2\mathbf{K})\mathbf{x}(t) \Rightarrow \dot{\mathbf{x}}(t) = -\lambda\mathbf{x}(t) \tag{29}$$

Avec 2 **DDL**, nous ne pouvons pas d'obtenir $\dot{\mathbf{x}}(t) = -\lambda\mathbf{x}(t)$. Dans la section suivante, nous montrons une façon d'obtenir $\dot{\mathbf{x}}(t) = -\lambda\mathbf{x}(t)$ quand la dimension du vecteur d'état est égal au nombre de **DDL**.

Nous utilisons la commande $\mathcal{U}(t) = \dot{\mathbf{u}}(t)$, (voir [Aamo, 2002], [Bewley and Liu, 1998], [Joshi, 1996], [McKernan, 2006]), le système (28) est décrit

$$\begin{bmatrix} \dot{\mathbf{x}}(t) \\ \dot{\mathbf{u}}(t) \end{bmatrix} = \begin{bmatrix} \mathbf{L}^{-1}\mathbf{A} & \mathbf{L}^{-1}\mathbf{B} \\ 0 & 0 \end{bmatrix} \begin{bmatrix} \mathbf{x}(t) \\ \mathbf{u}(t) \end{bmatrix} + \begin{bmatrix} \mathbf{L}^{-1}\mathbf{E} \\ \mathbf{I} \end{bmatrix} \dot{\mathbf{u}}(t), \tag{30}$$

ou nous proposons

$$\dot{\mathcal{X}}(t) = \mathcal{A}\mathcal{X}(t) + \mathcal{B}\mathcal{U}(t), \tag{31}$$

où le vecteur d'état est $\mathcal{X}(t) = \begin{bmatrix} \mathbf{x}(t) \\ \mathbf{u}(t) \end{bmatrix}$. Les matrices $\mathcal{A}$ et $\mathcal{B}$ sont définies

$$\mathcal{A} = \begin{bmatrix} \mathbf{L}^{-1}\mathbf{A} & \mathbf{L}^{-1}\mathbf{B} \\ 0 & 0 \end{bmatrix}, \quad \mathcal{B} = \begin{bmatrix} \mathbf{L}^{-1}\mathbf{E} \\ \mathbf{I} \end{bmatrix}. \tag{32}$$

Donc, la densité d'énergie cinétique est réécrite en fonction de $\mathcal{X}(t)$

$$\begin{aligned} \varepsilon(t) &= \mathbf{x}^\top(t)\mathbf{Q}_{11}\mathbf{x}(t) + \mathbf{x}^\top(t)\mathbf{Q}_{12}\mathbf{u}(t) + \mathbf{u}^\top(t)\mathbf{Q}_{21}\mathbf{x}(t) + \mathbf{u}^\top(t)\mathbf{Q}_{22}\mathbf{u}(t) \\ &= \begin{bmatrix} \mathbf{x}^\top(t) & \mathbf{u}^\top(t) \end{bmatrix} \begin{bmatrix} \mathbf{Q}_{11} & \mathbf{Q}_{12} \\ \mathbf{Q}_{21} & \mathbf{Q}_{22} \end{bmatrix} \begin{bmatrix} \mathbf{x}(t) \\ \mathbf{u}(t) \end{bmatrix} \\ &= \mathcal{X}^\top(t)\mathcal{Q}\mathcal{X}(t), \end{aligned} \tag{33}$$

où la matrice $\mathcal{Q}$ est définie par

$$\mathcal{Q} = \begin{bmatrix} \mathbf{Q}_{11} & \mathbf{Q}_{12} \\ \mathbf{Q}_{21} & \mathbf{Q}_{22} \end{bmatrix}. \tag{34}$$

De la même manière, la traînée est également réécrite par

$$\mathbf{d}(t) = \mathbf{D}_1\mathbf{x}(t) + \mathbf{D}_2\mathbf{u}(t) = \mathcal{D}\mathcal{X}(t), \tag{35}$$

où $\mathcal{D} = \begin{bmatrix} \mathbf{D}_1 & \mathbf{D}_2 \end{bmatrix}$. Par conséquent, le modèle linéaire de l'écoulement de Poiseuille est donné par

$$\begin{cases} \dot{\mathcal{X}}(t) & = \mathcal{A}\mathcal{X}(t) + \mathcal{B}\mathcal{U}(t) \\ \varepsilon(t) & = \mathcal{X}^\top(t)\mathcal{Q}\mathcal{X}(t) \\ \mathbf{d}(t) & = \mathcal{D}\mathcal{X}(t) \end{cases} \tag{36}$$

En utilisant la commande par asservissement visuel partitionné [Espiau et al., 1992], nous avons besoin de la dynamique de la traînée

$$\dot{\mathbf{d}}(t) = \frac{\partial \mathbf{d}(t)}{\partial t} + \mathbf{L}_d \mathcal{U}(t), \tag{37}$$

où $\dfrac{\partial \mathbf{d}(t)}{\partial t}$ exprime la variation propre de la traînée et $\mathbf{L}_d$ définit la variation de la traînée par rapport à la variation de la commande.

À partir de l'équation (36), nous obtenons

$$\dot{\mathbf{d}}(t) = \mathcal{D}\dot{\mathcal{X}}(t) = \mathcal{D}\left(\mathcal{A}\mathcal{X}(t) + \mathcal{B}\mathcal{U}(t)\right). \tag{38}$$

Donc, grâce à (37) et (38), nous obtenons

$$\begin{cases} \mathbf{L}_d & = \mathcal{D}\mathcal{B} \\ \dfrac{\partial \mathbf{d}(t)}{\partial t} & = \mathcal{D}\mathcal{A}\mathcal{X}(t) \end{cases} \tag{39}$$

Introduisons à présent les composantes de la matrice d'interaction relative aux composantes du signal de commande (2 **DDL**)

$$\mathbf{L}_d = \begin{bmatrix} \mathbf{L}_{du} & \mathbf{L}_{dl} \end{bmatrix} = \begin{bmatrix} \mathbf{D}_1 & \mathbf{D}_2 \end{bmatrix} \begin{bmatrix} \mathbf{L}^{-1}\mathbf{E} \\ \mathbf{I} \end{bmatrix}. \tag{40}$$

L'asservissement visuel partitionné repose sur une formulation partitionnée de la matrice d'interaction. Grâce à (40), la variation temporelle de la traînée (38) devient

$$\dot{\mathbf{d}}(t) = \mathbf{L}_{du}\mathcal{U}_u(t) + \mathbf{L}_{dl}\mathcal{U}_l(t) + \frac{\partial \mathbf{d}(t)}{\partial t}, \tag{41}$$

où $\mathcal{U}(t) = \begin{bmatrix} \mathcal{U}_u(t) & \mathcal{U}_l(t) \end{bmatrix}^\top$. Il est tout à fait possible d'imposer une décroissance souhaitée de la traînée. Imposons par exemple une décroissance exponentielle

$$\dot{\mathbf{d}}(t) = -\lambda \mathbf{d}(t) \tag{42}$$

où λ est un gain positif permettant d'ajuster la vitesse de décroissance. Par suite, de (41) et (42), nous avons

$$-\lambda \mathbf{d}(t) = \mathbf{L}_{du}\mathcal{U}_u(t) + \mathbf{L}_{dl}\mathcal{U}_l(t) + \frac{\partial \mathbf{d}(t)}{\partial t}. \tag{43}$$

À ce stade, l'une ou l'autre des composantes de $\mathcal{U}(t)$ peut être utilisée pour réduire la traînée, choisissons arbitrairement $\mathcal{U}_l(t)$. Il vient alors

$$\mathcal{U}_l(t) = -\frac{1}{\mathbf{L}_{dl}}\left(\lambda \mathbf{d}(t) + \mathbf{L}_{du}\mathcal{U}_u(t) + \frac{\partial \mathbf{d}(t)}{\partial t}\right). \tag{44}$$

Cette grandeur sera effectivement connue si le signal de commande $\mathcal{U}_u(t)$ est connu aussi. La phase suivante consiste donc à en trouver une expression.

Pour ce faire, nous considérons classiquement une commande **LQR** sur un horizon infini afin de minimiser la densité d'énergie cinétique (36) et l'énergie nécessaire à sa minimisation. Le critère à minimiser s'écrit comme suit

$$J = \int_0^\infty \left(\mathcal{X}^\top(t)\mathcal{Q}\mathcal{X}(t) + \gamma^2 \mathcal{U}_u^2(t)\right) \mathrm{d}t. \tag{45}$$

Cela peut être fait en exprimant la variation temporelle de l'état en fonction du signal de commande $\mathcal{U}_u(t)$. Pour ce faire, réécrivons (44) grâce à (36)

$$\mathcal{U}_l(t) = -\frac{1}{\mathbf{L}_{dl}}\left(\left(\lambda\mathcal{D} + \mathcal{D}\mathcal{A}\right)\mathcal{X}(t) + \mathbf{L}_{du}\mathcal{U}_u(t)\right), \tag{46}$$

que nous injectons dans (36) pour obtenir

$$\dot{\mathcal{X}}(t) = \mathcal{A}_1\mathcal{X}(t) + \mathcal{B}_1\mathcal{U}_u(t), \tag{47}$$

où les matrices suivantes ont été introduites: $\mathcal{A}_1 = \mathcal{A} - \dfrac{\mathcal{B}_l}{\mathbf{L}_{dl}}(\lambda\mathcal{D} + \mathcal{D}\mathcal{A})$ et $\mathcal{B}_1 = \mathcal{B}_u - \dfrac{\mathbf{L}_{du}}{\mathbf{L}_{dl}}\mathcal{B}_l$ avec $\mathcal{B} = \begin{bmatrix} \mathcal{B}_u & \mathcal{B}_l \end{bmatrix}$.

Il devient alors très aisé de calculer le gain $\mathcal{K}$ impliqué dans la commande optimale $\mathcal{U}_u(t) = \mathcal{K}\mathcal{X}(t)$ en considérant (47) et en résolvant l'équation algébrique de Ricatti. Ce gain est donné par

$$\mathcal{K} = -\frac{1}{\gamma^2}\mathcal{B}_1^\top\mathcal{P}, \tag{48}$$

où $\mathcal{P}$ est la solution de l'équations algébrique de Ricatti

$$\mathcal{A}_1^\top\mathcal{P} + \mathcal{P}\mathcal{A}_1 + \mathcal{Q} - \frac{1}{\gamma^2}\mathcal{P}\mathcal{B}_1\mathcal{B}_1^\top\mathcal{P} = 0. \tag{49}$$

Il est important de noter que, à notre connaissance, contrairement aux travaux rencontrés dans la littérature de la commande des écoulements fluides, nous exploitons ici pleinement les **DDL**.

Résultat de Simulation

Nous comparons à présent notre approche avec les approches les plus pertinentes de la littérature, il s'agit des travaux relatés dans [Joshi et al., 1997], [McKernan et al., 2007], [Cortelezzi and Speyer, 1998]. Nous notons respectivement ces approches **P**, **LQR**$_1$,

LQR$_2$, et notons **AVP** la nôtre. Rappelons brièvement ces travaux. Dans le travail de [Joshi et al., 1997], un retour proportionnel à la mesure du frottement pariétal est utilisé conduisant à la réduction de la traînée. Dans ce travail la réduction de la densité d'énergie cinétique n'est pas considérée. Dans le travail de [McKernan et al., 2007] la densité d'énergie cinétique est minimisée via une commande **LQR**. Notons qu'il s'agit là d'une façon indirecte de minimiser la traînée. En effet, la traînée due à la perturbation s'annule si la densité d'énergie cinétique est nulle aussi. Finalement, dans [Cortelezzi and Speyer, 1998], le frottement pariétal est minimisé également par une approche **LQR**.

Nous testons le cas où $\alpha = 1$, $\beta = 0$ et $R = 10\,000$. La figure 4 décrit la comparaison entre notre approche et les autres. Seulement notre approche a donnée un bon résultat.

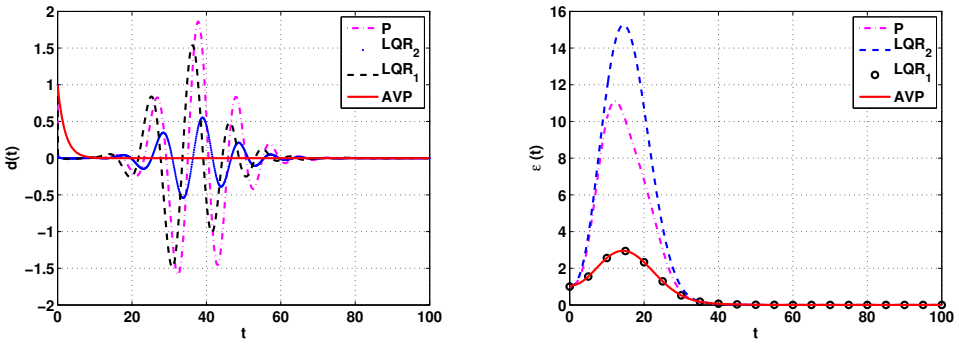

(a) $\mathbf{d}(t)$ (b) $\varepsilon(t)$

Figure 4: Comportement de la traînée et de l'énergie cinétique en fonction du temps.

Remarques

Quelques remarques sont donnés. Si **DDL** est 2

- **AVP** obtient $\dot{\mathbf{d}}(t) = -\lambda \mathbf{d}(t)$
- **AVP** ne peut pas garantir $\dot{\varepsilon}(t) \leq 0$. Nous avons besoin de plus de nombres de **DDL**. Dans la section suivante, nous allons chercher une solution à ce problème.

Augmenter le nombre de dégrée de liberté

Pourquoi et comment d'augmenter le nombre de dégrée de liberté ?

Pourquoi ?

Dans cette section, nous allons donner une condition nécessaire pour obtenir la stabilité monotone. On considère le système suivant

$$\dot{\mathbf{z}}(t) = \mathbf{A}_z \mathbf{z}(t) + \mathbf{B}_z \mathbf{u}(t) \tag{50}$$

aver la commande $\mathbf{u}(t) = \mathbf{K}\mathbf{z}(t)$. L'énergie cinétique est définie par

$$\varepsilon_z(t) = \mathbf{z}^\top(t)\mathbf{Q}_z\mathbf{z}(t), \tag{51}$$

où $\mathbf{Q}_z$ est une matrice Hermitienne. Dans [Whidborne and McKernan, 2007], la condition nécessaire pour garantir $\dot{\varepsilon}_z(t) \leq 0$ est donnée par

$$(\mathbf{A}_z + \mathbf{B}_z\mathbf{K})^\top\mathbf{Q}_z + \mathbf{Q}_z(\mathbf{A}_z + \mathbf{B}_z\mathbf{K}) \leq 0 \tag{52}$$

Pour que cette inégalité ait une solution $\mathbf{K}$, nous avons besoin de $\mathbf{B}_z\mathbf{B}_z^\top > 0$. Par conséquent, la matrice $\mathbf{B}_z$ doit être une matrice de plein rang. Cette cause explique pourquoi nous voulons augmenter le nombre de **DDL** dans le système en boucle fermée du des écoulements.

Comment ?

Si nous utilisons $f_{\phi,\psi,m}(y)$ (voir la façon d'utiliser $f_{\phi,\psi}(y)$), nous obtenons l'équation de l'état

$$\mathbf{L}\dot{\mathbf{x}}(t) = \mathbf{A}\mathbf{x}(t) + \mathbf{B}_m\mathbf{u}_m(t) + \mathbf{E}_m\dot{\mathbf{u}}_m(t) \tag{53}$$

Quand nous utilisons $f_{\phi,\psi,m}(y)$ où $m = 1 \cdots M$, de même façon, nous obtenons

$$\begin{array}{rl} \mathbf{L}\dot{\mathbf{x}}(t) & = \mathbf{A}\mathbf{x}(t) + \mathbf{B}_1\mathbf{u}_1(t) + \mathbf{E}_1\dot{\mathbf{u}}_1(t) \\ \mathbf{L}\dot{\mathbf{x}}(t) & = \mathbf{A}\mathbf{x}(t) + \mathbf{B}_2\mathbf{u}_2(t) + \mathbf{E}_2\dot{\mathbf{u}}_2(t) \\ \vdots & \vdots \\ \mathbf{L}\dot{\mathbf{x}}(t) & = \mathbf{A}\mathbf{x}(t) + \mathbf{B}_M\mathbf{u}_M(t) + \mathbf{E}_M\dot{\mathbf{u}}_M(t) \end{array} \tag{54}$$

C'est facile de voir que nous pouvons obtenir

$$\begin{aligned} \mathbf{L}\dot{\mathbf{x}}(t) &= \mathbf{A}\mathbf{x}(t) + \sum_{m=1}^{M}\mathbf{B}_m\mathbf{u}_m(t) + \sum_{m=1}^{M}\mathbf{E}_m\dot{\mathbf{u}}_m(t) \\ &= \mathbf{A}\mathbf{x}(t) + \begin{bmatrix}\mathbf{B}_1 & \cdots & \mathbf{B}_M\end{bmatrix}\begin{bmatrix}\mathbf{u}_1(t) \\ \cdots \\ \mathbf{u}_M(t)\end{bmatrix} + \begin{bmatrix}\mathbf{E}_1 & \cdots & \mathbf{E}_M\end{bmatrix}\begin{bmatrix}\dot{\mathbf{u}}_1(t) \\ \cdots \\ \dot{\mathbf{u}}_M(t)\end{bmatrix} \end{aligned} \tag{55}$$

Si $f_{\phi,\psi,1}(y)$, $f_{\phi,\psi,2}(y)$, $\cdots$, $f_{\phi,\psi,M}(y)$ sont indépendant, nous pouvons augmenter **DDL**, montré dans [Joshi, 1996]. Donc, nous supposons qu'il existe une façon de faire conduit aux conditions de Dirichlet non homogènes de $\tilde{\phi}(y = \pm 1, t)$ suivante:

$$\tilde{\phi}(y = \pm 1, t) = \sum_{m=1}^{M}\tilde{q}_{\phi,\psi,m}(t) \tag{56}$$

les conditions de Neumann restant homogènes aux frontières. L'équation (16) devient

$$\tilde{\phi}(y, t) = \tilde{\phi}_h(y, t) + \sum_{m=1}^{M}\mathbf{F}_{\phi,m}(y)\mathbf{q}_{\phi,m}(t) \tag{57}$$

dans lesquelles nous avons introduit les vecteurs $\mathbf{F}_{\phi,m}(y) = \left[\begin{array}{cc} f_{\phi,u,m}(y) & f_{\phi,l,m}(y)) \end{array} \right]$, $\mathbf{q}_{\phi,m}(t) = \left[\begin{array}{c} \tilde{q}_{\phi,u,m}(t) \\ \tilde{q}_{\phi,l,m}(t) \end{array} \right]$ où les conditions suivantes doivent être vérifiées :

$$\left\{ \begin{array}{ll} f_{v,u,m}(+1) = f_{v,l,m}(-1) = 1, & f_{v,u,m}(-1) = f_{v,l,m}(+1) = 0, \\ f_{\eta,u,m}(+1) = f_{\eta,l,m}(-1) = 1, & f_{\eta,u,m}(-1) = f_{\eta,l,m}(+1) = 0, \\ f^{'}_{v,u,m}(\pm 1) = f^{'}_{v,l,m}(\pm 1) = 0 & \end{array} \right. \tag{58}$$

Comme le cas précédent, l'équation (19) est modifiée

$$\mathbf{L}\dot{\mathbf{x}}(t) = \mathbf{A}\mathbf{x}(t) + \mathbf{B}\mathbf{u}(t) + \mathbf{E}\dot{\mathbf{u}}(t), \tag{59}$$

où $\mathbf{u}(t) = \left[\begin{array}{cccc} \mathbf{q}^{\top}_{v,1}(t) & \cdots & \mathbf{q}^{\top}_{v,M}(t) & \mathbf{q}^{\top}_{\eta,1}(t) \quad \cdots \quad \mathbf{q}^{\top}_{\eta,M}(t)) \end{array} \right]^{\top}$ est le nouveau signal de commande. Toutes les matrices $\mathbf{B}$, $\mathbf{E}$, $\mathbf{Q}_{12}$, $\mathbf{Q}_{21}$, $\mathbf{Q}_{22}$ et $\mathbf{D}_2$ sont modifiées.

Avantages d'augmenter le nombre de dégrée de liberté

Nous montrons les avantages obtenus en augmentant le nombre **DDL** dans le cas où $\alpha = 0$, $\beta = 2.044$ et $R = 5\ 000$ (les résultats dans le cas $\alpha = 1$, $\beta = 0$ et $R = 10\ 000$ sont le même). La figure 5(a) rapporte le comportement des énergies synchronique et diachronique en boucle ouverte. Comme on s'y attendait, l'énergie cinétique présente un pic responsable d'une transition potentielle vers la turbulence. La figure 5(a) montre qu'une commande **LQR** avec 2 **DDL** permet de diminuer la valeur de l'énergie diachronique sans toutefois éviter le pic d'énergie. La figure 5(b) montre clairement le bénéfice d'augmenter le nombre **DDL**.

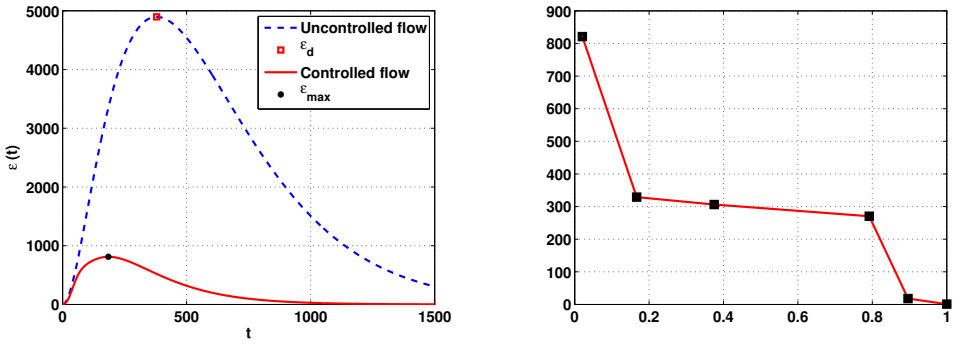

(a) $\varepsilon(t)$ en fonction du temps (b) ε_{max} en fonction de **DDL**

Figure 5: Bénéfice d'augmenter le nombre de dégrée de libertés.

Remarque

Malgré le fait d'avoir démontré lorsque le nombre de **DDL** est augmenté, le bénéfice est décrit par la commande **LQR**, nous avons aussi besoin d'une commande qui garantit $\dot{\varepsilon}(t) \leq 0$.

Commande par asservissement visuel

Objectif

Lorsque le nombre de **DDL** est augmenté, nous proposons une approche de commande qui satisfait $\dot{\varepsilon}(t) = -2\lambda\varepsilon(t)$, $\dot{\mathbf{d}}(t) = -\lambda\mathbf{d}(t)$ et $\dot{\mathbf{u}}(t) = -\lambda\mathbf{u}(t)$.

Conception de la commande

Considérons le système suivant

$$\left\{\begin{array}{ll} \mathbf{L}\dot{\mathbf{x}}(t) & = \mathbf{A}\mathbf{x}(t) + \mathbf{B}\mathbf{u}(t) + \mathbf{E}\dot{\mathbf{u}}(t), \\ \varepsilon(t) & = \mathbf{x}^\top(t)\mathbf{Q}_{11}\mathbf{x}(t) + \mathbf{x}^\top(t)\mathbf{Q}_{12}\mathbf{u}(t) + \mathbf{u}^\top(t)\mathbf{Q}_{21}\mathbf{x}(t) + \mathbf{u}^\top(t)\mathbf{Q}_{22}\mathbf{u}(t) \\ \mathbf{d}(t) & = \mathbf{D}_1\mathbf{x}(t) + \mathbf{D}_2\mathbf{u}(t), \end{array}\right. \tag{60}$$

Le système (60) n'est pas à la formulaire standard. Nous pouvons réécrire l'équation (60) par le changement des variables $\mathbf{x}(t) = \mathbf{z}(t) + \mathbf{L}^{-1}\mathbf{E}\mathbf{u}(t)$, dans [Cortelezzi and Speyer, 1998], [Cortelezzi et al., 1998a], [Cortelezzi et al., 1998b]. Nous obtenons

$$\dot{\mathbf{z}}(t) = \mathbf{A}_z\mathbf{z}(t) + \mathbf{B}_z\mathbf{u}(t), \tag{61}$$

où les matrices sont définies

$$\left\{\begin{array}{ll} \mathbf{A}_z & = \mathbf{L}^{-1}\mathbf{A} \\ \mathbf{B}_z & = \mathbf{L}^{-1}\mathbf{B} + \mathbf{L}^{-1}\mathbf{A}\mathbf{L}^{-1}\mathbf{E}, \end{array}\right. \tag{62}$$

La densité de l'énergie cinétique est réécrite par

$$\begin{array}{ll} \varepsilon(t) & = \mathbf{x}^\top(t)\mathbf{Q}_{11}\mathbf{x}(t) + \mathbf{x}^\top(t)\mathbf{Q}_{12}\mathbf{u}(t) + \mathbf{u}^\top(t)\mathbf{Q}_{21}\mathbf{x}(t) + \mathbf{u}^\top(t)\mathbf{Q}_{22}\mathbf{u}(t) \\ & = (\mathbf{z}(t) + \mathbf{L}^{-1}\mathbf{E}\mathbf{u}(t))^\top\mathbf{Q}_{11}(\mathbf{z}(t) + \mathbf{L}^{-1}\mathbf{E}\mathbf{u}(t)) + (\mathbf{z}(t) + \mathbf{L}^{-1}\mathbf{E}\mathbf{u}(t))^\top\mathbf{Q}_{12}\mathbf{u}(t) \\ & \quad + \mathbf{u}^\top(t)\mathbf{Q}_{21}(\mathbf{z}(t) + \mathbf{L}^{-1}\mathbf{E}\mathbf{u}(t)) + \mathbf{u}^\top(t)\mathbf{Q}_{22}\mathbf{u}(t) \end{array} \tag{63}$$

ou plus simplement

$$\varepsilon(t) = \mathbf{z}^\top(t)\mathbf{Q}_z\mathbf{z}(t) + \mathbf{z}^\top(t)\mathbf{N}_{zu}\mathbf{u}(t) + \mathbf{u}^\top(t)\mathbf{N}_{uz}\mathbf{z}(t) + \mathbf{u}^\top(t)\mathbf{R}_z\mathbf{u}(t), \tag{64}$$

où les matrices $\mathbf{N}_{zu}$, $\mathbf{N}_{uz}$ et $\mathbf{R}_z$ sont définies

$$\left\{\begin{array}{ll} \mathbf{Q}_z & = \mathbf{Q}_{11} \\ \mathbf{N}_{zu} & = \mathbf{Q}_{12} + \mathbf{Q}_{11}\mathbf{L}^{-1}\mathbf{E} \\ \mathbf{N}_{uz} & = \mathbf{Q}_{21} + (\mathbf{L}^{-1}\mathbf{E})^\top\mathbf{Q}_{11} \\ \mathbf{R}_z & = \mathbf{Q}_{22} + (\mathbf{L}^{-1}\mathbf{E})^\top\mathbf{Q}_{12} + \mathbf{Q}_{21}\mathbf{L}^{-1}\mathbf{E} + (\mathbf{L}^{-1}\mathbf{E})^\top\mathbf{Q}_{11}\mathbf{L}^{-1}\mathbf{E}. \end{array}\right. \tag{65}$$

De même façon, la traînée est réécrite par

$$\mathbf{d}(t) = \mathbf{D}_1\mathbf{x}(t) + \mathbf{D}_2\mathbf{u}(t) = \mathbf{D}_1\mathbf{z}(t) + (\mathbf{D}_1\mathbf{L}^{-1}\mathbf{E} + \mathbf{D}_2)\mathbf{u}(t), \tag{66}$$

ou plus simplement

$$\mathbf{d}(t) = \mathbf{D}_{z1}\mathbf{z}(t) + \mathbf{D}_{z2}\mathbf{u}(t), \tag{67}$$

où les matrices $\mathbf{D}_{z1}$ and $\mathbf{D}_{z2}$ sont définies

$$\begin{cases} \mathbf{D}_{z1} & = \mathbf{D}_1 \\ \mathbf{D}_{z2} & = \mathbf{D}_1\mathbf{L}^{-1}\mathbf{E} + \mathbf{D}_2. \end{cases} \tag{68}$$

Nous obtenons le système

$$\begin{cases} \dot{\mathbf{z}}(t) & = \mathbf{A}_z\mathbf{z}(t) + \mathbf{B}_z\mathbf{u}(t) \\ \varepsilon(t) & = \mathbf{z}^\top(t)\mathbf{Q}_z\mathbf{z}(t) + \mathbf{z}^\top(t)\mathbf{N}_{zu}\mathbf{u}(t) + \mathbf{u}^\top(t)\mathbf{N}_{uz}\mathbf{z}(t) + \mathbf{u}^\top(t)\mathbf{R}_z\mathbf{u}(t) \\ \mathbf{d}(t) & = \mathbf{D}_{z1}\mathbf{z}(t) + \mathbf{D}_{z2}\mathbf{u}(t) \\ \mathbf{z}(0) & = \mathbf{z}_0 \end{cases} \tag{69}$$

Par conséquent, en supposant une commande par retour d'état $\mathbf{u}(t) = \mathbf{K}\mathbf{z}(t)$ et en supposant qu'il soit possible de calculer une matrice $\mathbf{K}$ assurant une décroissance exponentielle du vecteur d'état $\dot{\mathbf{z}}(t) = -\lambda\mathbf{z}(t)$, il est aisé d'établir les relations suivantes: $\dot{\mathbf{u}}(t) = -\lambda\mathbf{u}(t)$, $\dot{\mathbf{d}}(t) = -\lambda\mathbf{d}(t)$ et $\dot{\varepsilon}(t) = -2\lambda\varepsilon(t)$. Cette façon de faire assuré le comportement recherché.

Dans l'asservissement visuel, la dynamique du vecteur erreur est alors donnée par

$$\dot{\mathbf{e}}(t) = \frac{\partial \mathbf{e}(t)}{\partial t} + \mathbf{L}_\mathbf{e}(t)\mathbf{u}(t) \tag{70}$$

Nous voulons stabiliser le vecteur d'état $\mathbf{z}(t)$ par une décroissance exponentielle. Donc, le vecteur d'état est choisie à être l'ensemble d'informations visuelles $\mathbf{z}(t) = \mathbf{s}(t)$. Grâce à (69), nous obtenons

$$\begin{cases} \mathbf{L}_\mathbf{e}(t) & = \mathbf{B}_z \\ \dfrac{\partial \mathbf{e}(t)}{\partial t} & = \mathbf{A}_z\mathbf{z}(t). \end{cases} \tag{71}$$

Nous souhaitions d'assurer une décroissance exponentielle du vecteur erreur

$$\dot{\mathbf{e}}(t) = -\lambda\mathbf{e}(t). \tag{72}$$

Nous obtenons

$$\mathbf{u}(t) = -\lambda\mathbf{L}_\mathbf{e}^{-1}(t)\mathbf{e}(t) - \mathbf{L}_\mathbf{e}^{-1}(t)\frac{\partial \mathbf{e}(t)}{\partial t}. \tag{73}$$

Dans ce cas, la commande peut être réécrite par $\mathbf{u}(t) = \mathbf{K}\mathbf{z}(t)$ où

$$\mathbf{K} = -\mathbf{L}_\mathbf{e}^{-1}(t)(\lambda\mathbf{I} + \mathbf{A}_z) \tag{74}$$

Résultat de Simulation

Les résultats suivants concernent la loi de commande que nous proposons. Nous avons fixé $\lambda = 0.25$. Les figures 6(a) et 7(a) montrent que notre loi de commande permet effectivement de découpler les composantes du vecteur d'état. Par suite, la commande (figures 6(b) et 7(b)), l'énergie cinétique (figures 6(c) et 7(c)) et la traînée (figures 6(d) et 6(d)) sont bien des exponentielles décroissantes comme il était attendu. Ce résultat est de toute importance car il garantit que les grandeurs physiques observées ne peuvent que décroitre.

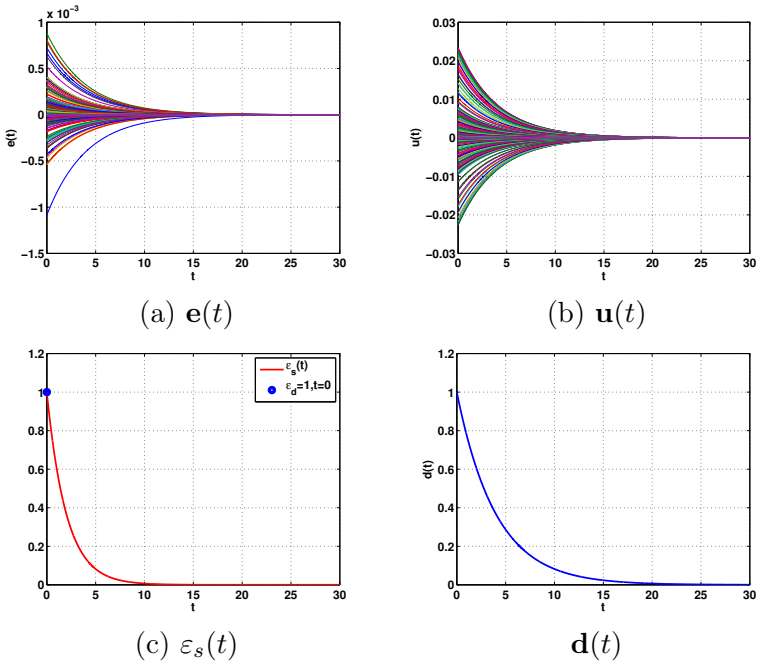

(a) $\mathbf{e}(t)$ (b) $\mathbf{u}(t)$

(c) $\varepsilon_s(t)$ $\mathbf{d}(t)$

Figure 6: Comportement de l'écoulement 2D de Poiseuille en boucle fermée en fonction du temps.

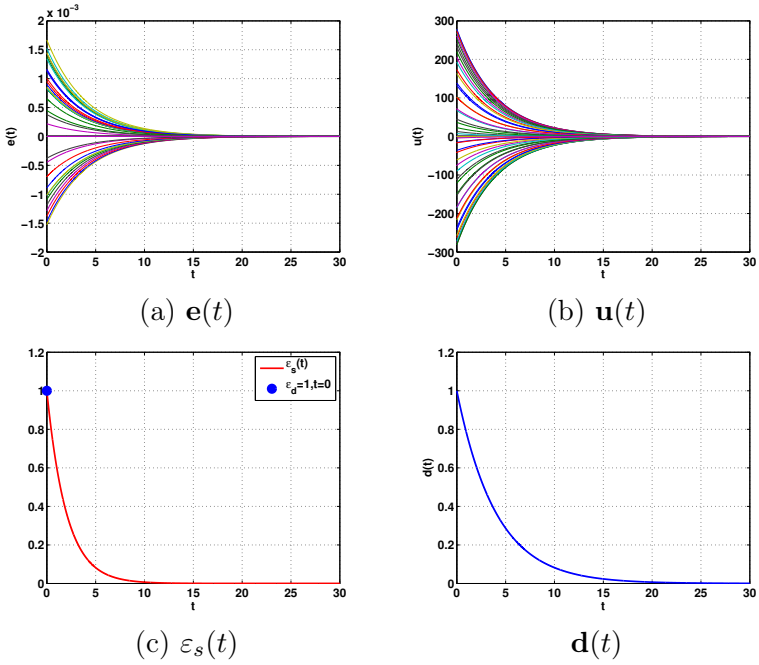

(a) $\mathbf{e}(t)$ (b) $\mathbf{u}(t)$

(c) $\varepsilon_s(t)$ $\mathbf{d}(t)$

Figure 7: Comportement de l'écoulement 3D de Poiseuille en boucle fermée en fonction du temps.

Remarques

- Commande par asservissement visuel obtient $\dot{\mathbf{z}}(t) = -\lambda \mathbf{z}(t)$, par conséquent nous obtenons $\dot{\varepsilon}(t) = -2\lambda\varepsilon(t)$, $\dot{\mathbf{d}}(t) = -\lambda \mathbf{d}(t)$ et $\dot{\mathbf{u}}(t) = -\lambda \mathbf{u}(t)$. Ces résultats sont les résultats souhaités en boucle fermée du contrôle des écoulements.
- **DDL** est égale au nombre du vecteur d'état. Et il s'agit des conditions très fortes. Nous devons réduire cette condition car le nombre du vecteur d'état peut être trop grand.

Modèle d'ordre réduit

Objectif

Objectif de cette section est de chercher une approche de commande qui garantit $\dot{\varepsilon}(t) \approx -2\lambda\varepsilon(t)$ et $\dot{\mathbf{u}}(t) = -\lambda \mathbf{u}(t)$ alors même que nous utilisons 2 **DDL**.

Conception de la commande

Considérons le système suivant

$$\left\{ \begin{array}{ll} \dot{\mathbf{z}}(t) & = \mathbf{A}_z \mathbf{z}(t) + \mathbf{B}_z \mathbf{u}(t) \\ \varepsilon(t) & = \mathbf{z}^\top(t)\mathbf{Q}_z \mathbf{z}(t) + \mathbf{z}^\top(t)\mathbf{N}_{zu}\mathbf{u}(t) + \mathbf{u}^\top(t)\mathbf{N}_{uz}\mathbf{z}(t) + \mathbf{u}^\top(t)\mathbf{R}_z\mathbf{u}(t) \end{array} \right. \tag{75}$$

Lorsque le nombre de **DDL** est inférieur au nombre du vecteur d'état. Nous ne pouvons pas de utiliser la commande par asservissement visuel pour le système (75). Afin de garantir $\dot{\varepsilon}(t) \approx -2\lambda\varepsilon(t)$, nous cherchons une approche de commande qui assure

- $\dot{\mathbf{u}}(t) = -\lambda \mathbf{u}(t)$
- $\dot{\mathbf{z}}_r(t) = -\lambda \mathbf{z}_r(t)$ où $\mathbf{z}(t) = \mathbf{V}_z \begin{bmatrix} \mathbf{z}_r(t) \\ \mathbf{z}_{n-r}(t) \end{bmatrix}$, r est le nombre de **DDL**.

Basé sur les résultats dans [Cortelezzi and Speyer, 1998], [Cortelezzi et al., 1998a], et [Cortelezzi et al., 1998b], nous utilisons le forme canonique de Jordan. (75) devient

$$\begin{bmatrix} \dot{\mathbf{z}}_r(t) \\ \dot{\mathbf{z}}_{n-r}(t) \end{bmatrix} = \begin{bmatrix} \Lambda_r & 0 \\ 0 & \Lambda_{n-r} \end{bmatrix} \begin{bmatrix} \mathbf{z}_r(t) \\ \mathbf{z}_{n-r}(t) \end{bmatrix} + \begin{bmatrix} \mathbf{B}_{r,m} \\ \mathbf{B}_{n-r,m} \end{bmatrix} \mathbf{u}(t) \tag{76}$$

où les matrices sont

$$\mathbf{B}_z = \mathbf{V}_z \begin{bmatrix} \mathbf{B}_{r,m} \\ \mathbf{B}_{n-r,m} \end{bmatrix}, \mathbf{A}_z = \mathbf{V}_z \begin{bmatrix} \Lambda_r & 0 \\ 0 & \Lambda_{n-r} \end{bmatrix} \mathbf{V}_z^{-1} \tag{77}$$

et $\mathbf{V}_z$ est la matrice des vecteurs propres qui transforme $\mathbf{A}_z$ en forme canonique de Jordan. Notons que Λ_r contient toutes les valeurs propres positives si elles existent. L'idée est de déterminer $\dot{\mathbf{z}}_r(t) = -\lambda \mathbf{z}_r(t)$. Nous pouvons facilement trouver une commande

$$\mathbf{u}(t) = -\mathbf{B}_{r,m}^{-1}(\lambda \mathbf{I}_r + \Lambda_r)\mathbf{z}_r(t) \tag{78}$$

Donc, la commande est ensuite donnée par

$$\mathbf{u}(t) = -\mathbf{B}_{r,m}^{-1}(\lambda \mathbf{I}_r + \Lambda_r) \begin{bmatrix} \mathbf{I}_r & [0]_{r,n-r} \end{bmatrix} \mathbf{V}_z^{-1} \mathbf{z}(t) \tag{79}$$

qui garantit $\dot{\mathbf{u}}(t) = -\lambda \mathbf{u}(t)$.

Résultat de Simulation

Nous ne considérons que 2 **DDL**. Quand **DDL** est assez grand, nous assurons $\dot{\varepsilon}(t) \approx -2\lambda\varepsilon(t)$. Si **DDL** est 2, nous trouvons que nous pouvons assurer $\dot{\varepsilon}(t) \approx -2\lambda\varepsilon(t)$ si nous cherchons λ pour assurer $\varepsilon(t) \approx \mathbf{u}^\top(t)\mathbf{R}_z\mathbf{u}(t)$.

Pour le cas où $\alpha = 1$, $\beta = 0$ et $R = 10\ 000$, par exemple, les fonctions $f_{\phi,\psi}(y)$ sont choisies

$$f_{v,l}(y) = \frac{y^3 - 3y + 2}{4}, \quad f_{v,u}(y) = \frac{-y^3 + 3y + 2}{4} \tag{80}$$

Les résultats sont donnés dans la figure 8. Malgré 2 **DDL** sont utilisé avec $\varepsilon(t) \approx \mathbf{u}^\top(t)\mathbf{R}_z\mathbf{u}(t)$, l'énergie cinétique est une approximation de la décroissance exponentielle (où $\lambda = 0.25$). Ces résultats valident l'approche proposée.

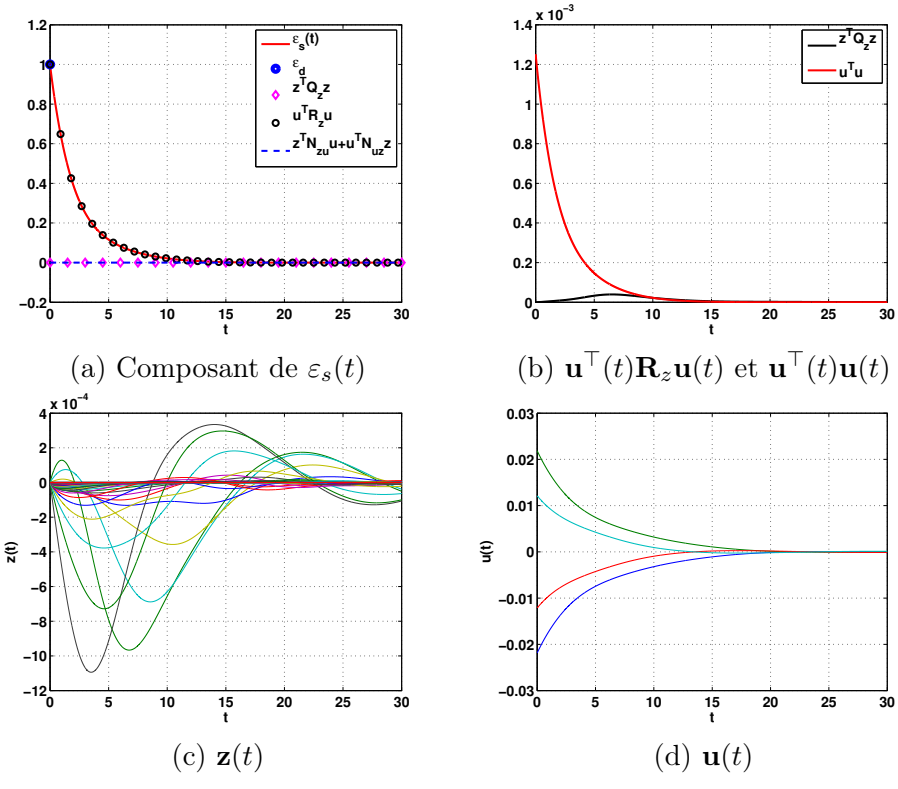

(a) Composant de $\varepsilon_s(t)$

(b) $\mathbf{u}^\top(t)\mathbf{R}_z\mathbf{u}(t)$ et $\mathbf{u}^\top(t)\mathbf{u}(t)$

(c) $\mathbf{z}(t)$

(d) $\mathbf{u}(t)$

Figure 8: Comportement de l'écoulement 2D de Poiseuille en boucle fermée en fonction du temps.

Pour le cas où $\alpha = 0$, $\beta = 2.044$ et $R = 5\ 000$. L'énergie cinétique est une approximation de la décroissance exponentielle, illustrée dans la figure 9 (où $\lambda = 250$).

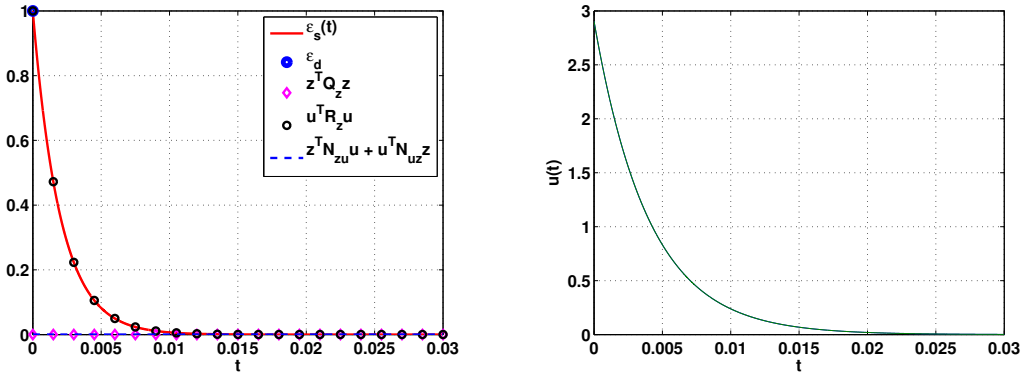

(a) Composant de $\varepsilon(t)$ (b) $\mathbf{u}(t)$

Figure 9: Comportement de l'écoulement 3D de Poiseuille en boucle fermée en fonction du temps.

Remarques

La commande par asservissement visuel est d'assurer $\dot{\varepsilon}(t) \approx -2\lambda\varepsilon(t)$ pour tout **DDL**, si l'énergie de régulation est admissible.

Notre travail ouvre les perspectives pour le futur. S'il existe une commande pour assurer $\dot{\varepsilon}(t) \leq 0$ pour tout **DDL**, nous avons la condition

$$\begin{aligned}&(\mathbf{A}_z + \mathbf{B}_z\mathbf{K})^\top(\mathbf{Q}_z + \mathbf{K}^\top\mathbf{N}_{uz} + \mathbf{N}_{zu}\mathbf{K} + \mathbf{K}^\top\mathbf{R}_z\mathbf{K})\\ &+(\mathbf{Q}_z + \mathbf{K}^\top\mathbf{N}_{uz} + \mathbf{N}_{zu}\mathbf{K} + \mathbf{K}^\top\mathbf{R}_z\mathbf{K})(\mathbf{A}_z + \mathbf{B}_z\mathbf{K}) \leq 0\end{aligned} \tag{81}$$

où les paramètres $\mathbf{R}_z$, $\mathbf{N}_{uz}$ et $\mathbf{N}_{zu}$ sont variés. Mais l'inégalité est trop difficile à trouver. Notons que l'inégalité

$$(\mathbf{A}_z + \mathbf{B}_z\mathbf{K})^\top\mathbf{Q}_z + \mathbf{Q}_z(\mathbf{A}_z + \mathbf{B}_z\mathbf{K}) < 0 \tag{82}$$

a une solution $\mathbf{K}$ si $\mathbf{B}_z$ est une matrice de plein rang. Il s'agit de notre "challenge".

Conclusion

Dans cette thèse, nous avons appliqué l'asservissement visuel au contrôle actif des écoulements. L'énergie cinétique est minimisée par une décroissance exponentielle qui assure la stabilité des écoulements.

Contents

List of Figures

List of Tables

Notation and Acronyms

Mathematical Notation

$\mathbf{x}$	a vector $\mathbf{x}$
$\mathbf{x}^\top$	transpose of a vector $\mathbf{x}$
$\widehat{\mathbf{x}}$	estimation of a vector $\mathbf{x}$
x_k	the k-th element of vector $\mathbf{x}$
x_c	complex number x_c
$\mathfrak{R}(x_c)$	real part of complex number x_c
$\mathfrak{I}(x_c)$	image part of complex number x_c
$\mathbf{A}$	a matrix $\mathbf{A}$
$\mathbf{A}^\top$	transpose of a matrix $\mathbf{A}$

Roman Symbols

P	pressure
P^*	pressure in dimension (N/m^2)
R	Reynold number
$\mathbf{V}$	velocity
$\mathbf{V}^*$	velocity in dimension (m/s)
$\mathbf{V}_o$	volume
U, V, W	steady base fluid velocity in x, y, z directions
x, y, z	streamwise, wall-normal, spanwise directions
u, v, w	fluid velocity perturbation in x, y, z directions
$\tilde{u}, \tilde{v}, \tilde{w}$	u, v, w Fourier coefficients at wavenumber pair α, β
$a_{v,n}$	discretization $\tilde{v}$ at point y_n
$a_{\eta,n}$	discretization $\tilde{\eta}$ at point y_n
$q_{v,l}$	control signal on wall normal velocity at lower wall
$q_{v,u}$	control signal on wall normal velocity at upper wall
$q_{v,l}$	control signal on wall normal vorticity at lower wall
$q_{v,l}$	control signal on wall normal vorticity at upper wall

$q_{v,l,m}$ mth control signal on wall normal velocity at lower wall
$q_{v,u,m}$ mth control signal on wall normal velocity at upper wall
$q_{v,l,m}$ mth control signal on wall normal vorticity at lower wall
$q_{v,l,m}$ mth control signal on wall normal vorticity at upper wall

$\tilde{q}_{v,l}$ $q_{v,l}$ Fourier coefficient
$\tilde{q}_{v,u}$ $q_{v,u}$ Fourier coefficient
$\tilde{q}_{\eta,l}$ $q_{\eta,l}$ Fourier coefficient
$\tilde{q}_{\eta,l}$ $q_{\eta,l}$ Fourier coefficient

$\tilde{q}_{v,l,m}$ $q_{v,l,m}$ Fourier coefficient
$\tilde{q}_{v,u,m}$ $q_{v,u,m}$ Fourier coefficient
$\tilde{q}_{\eta,l,m}$ $q_{\eta,l,m}$ Fourier coefficient
$\tilde{q}_{\eta,l,m}$ $q_{\eta,l,m}$ Fourier coefficient

$$\mathbf{q}_v = \begin{bmatrix} \tilde{q}_{v,u} \\ \tilde{q}_{v,l} \end{bmatrix}$$
$$\mathbf{q}_\eta = \begin{bmatrix} \tilde{q}_{\eta,u} \\ \tilde{q}_{\eta,l} \end{bmatrix}$$
$$\mathbf{q}_{v,m} = \begin{bmatrix} \tilde{q}_{v,u,m} \\ \tilde{q}_{v,l,m} \end{bmatrix}$$
$$\mathbf{q}_{\eta,m} = \begin{bmatrix} \tilde{q}_{\eta,u,m} \\ \tilde{q}_{\eta,l,m} \end{bmatrix}$$

$f_{v,l}$ inhomogeneous function at lower wall
$f_{v,u}$ inhomogeneous function at upper wall

$f_{v,l,m}$ mth inhomogeneous function at lower wall
$f_{v,u,m}$ mth inhomogeneous function at upper wall

$$\mathbf{F}_v = \begin{bmatrix} f_{v,u} & f_{v,l} \end{bmatrix}$$
$$\mathbf{F}_\eta = \begin{bmatrix} f_{\eta,u} & f_{\eta,l} \end{bmatrix}$$

$$\mathbf{F}_{v,m} = \begin{bmatrix} f_{v,u,m} & f_{v,l,m} \end{bmatrix}$$
$$\mathbf{F}_{\eta,m} = \begin{bmatrix} f_{\eta,u,m} & f_{\eta,l,m} \end{bmatrix}$$

$\mathbf{I}$ identity matrix
k $k = \sqrt{\alpha^2 + \beta^2}$
j $j = \sqrt{-1}$

Roman Symbols

$\mathbf{D}n$	matrix of n^{th} derivative of Chebyshev polynomials, $n = 0, 1, 2, 3, 4$
$\mathbf{D}n_D$	modified $\mathbf{D}n$ with Dirichlet boundary conditions
$\mathbf{D}n_{DN}$	modified $\mathbf{D}n$ with Dirichlet and Neumann boundary conditions
$\mathbf{d}(t)$	skin friction drag
$\mathbf{x}(t)$	state vector
$\mathbf{z}(t)$	state vector
$\mathbf{y}(t)$	the output signal
$\mathbf{u}(t)$	control signal
$\mathbf{A}$	state matrix
$\mathbf{L}$	state matrix
$\mathbf{B}$	input matrix
$\mathbf{E}$	input matrix
$\mathbf{A}_z$	state matrix, $\mathbf{A}_z = \mathbf{L}^{-1}\mathbf{A}$
$\mathbf{B}_z$	input matrix, $\mathbf{B}_z = \mathbf{L}^{-1}\mathbf{B} + \mathbf{L}^{-1}\mathbf{A}\mathbf{L}^{-1}\mathbf{E}$
$\mathbf{C}$	output matrix
$\mathbf{D}$	feedforward matrix
$\mathbf{D}_1$	transfer matrix from the state vector $\mathbf{x}(t)$ to the skin friction drag $\mathbf{d}(t)$
$\mathbf{D}_{z1}$	transfer matrix from the state vector $\mathbf{z}(t)$ to the skin friction drag $\mathbf{d}(t)$
$\mathbf{D}_2$	transfer matrix from the control signal $\mathbf{u}(t)$ to the skin friction drag $\mathbf{d}(t)$
$\mathbf{D}_{z2}$	transfer matrix from the control signal $\mathbf{x}(t)$ to the skin friction drag $\mathbf{d}(t)$
$\mathbf{K}$	gain of control law
$\mathbf{K}_o$	gain of observer
$\mathbf{K}_{lqr}$	gain of **LQR** control
$\mathbf{K}_r$	gain of control law based on the model reduction
$\mathbf{L}_\mathbf{e}$	interaction matrix
$\mathbf{L}_{\mathbf{e}_r}$	interaction matrix
$[\tilde{v}_n(t)]$	$[\tilde{v}_n(t)] = [\tilde{v}(y_0, t) \dots \tilde{v}(y_N, t)]^\top$
$[\tilde{\eta}_n(t)]$	$[\tilde{\eta}_n(t)] = [\tilde{\eta}(y_0, t) \dots \tilde{\eta}(y_N, t)]^\top$
$\mathbf{T}_{a_v}$	transfer matrix from the state vector $\mathbf{x}(t)$ to velocity $[\tilde{v}_n(t)]$
$\mathbf{T}_{a_\eta}$	transfer matrix from the state vector $\mathbf{x}(t)$ to vorticity $[\tilde{\eta}_n(t)]$
$\mathbf{T}_{q_v}$	transfer matrix from the control singal $\mathbf{u}(t)$ to velocity $[\tilde{v}_n(t)]$
$\mathbf{T}_{q_\eta}$	transfer matrix from the control signal $\mathbf{u}(t)$ to vorticity $[\tilde{\eta}_n(t)]$

Roman Symbols

$\mathbf{Q}$	quadrature weight
$\mathbf{Q}_{11}$	$\mathbf{Q}_{11} = \frac{1}{8k^2}(\mathbf{T}_{a_v}^\top \mathbf{Q}\mathbf{T}_{a_v} + (\partial \mathbf{T}_{a_v}/\partial y)^\top \mathbf{Q}(\partial \mathbf{T}_{a_v}/\partial y) + \mathbf{T}_{a_\eta}^\top \mathbf{Q}\mathbf{T}_{a_\eta})$
$\mathbf{Q}_{12}$	$\mathbf{Q}_{12} = \frac{1}{8k^2}(\mathbf{T}_{a_v}^\top \mathbf{Q}\mathbf{T}_{q_v} + (\partial \mathbf{T}_{a_v}/\partial y)^\top \mathbf{Q}(\partial \mathbf{T}_{q_v}/\partial y) + \mathbf{T}_{a_\eta}^\top \mathbf{Q}\mathbf{T}_{q_\eta})$
$\mathbf{Q}_{21}$	$\mathbf{Q}_{21} = \frac{1}{8k^2}(\mathbf{T}_{q_v}^\top \mathbf{Q}\mathbf{T}_{a_v} + (\partial \mathbf{T}_{q_v}/\partial y)^\top \mathbf{Q}(\partial \mathbf{T}_{a_v}/\partial y) + \mathbf{T}_{q_\eta}^\top \mathbf{Q}\mathbf{T}_{a_\eta})$
$\mathbf{Q}_{22}$	$\mathbf{Q}_{22} = \frac{1}{8k^2}(\mathbf{T}_{q_v}^\top \mathbf{Q}\mathbf{T}_{q_v} + (\partial \mathbf{T}_{q_v}/\partial y)^\top \mathbf{Q}(\partial \mathbf{T}_{q_v}/\partial y) + \mathbf{T}_{q_\eta}^\top \mathbf{Q}\mathbf{T}_{q_\eta})$
$\mathbf{Q}_z$	$\mathbf{Q}_z = \mathbf{Q}_{11}$
$\mathbf{N}_{zu}$	$\mathbf{N}_{zu} = \mathbf{Q}_{12} + \mathbf{Q}_{11}\mathbf{L}^{-1}\mathbf{E}$
$\mathbf{N}_{uz}$	$\mathbf{N}_{uz} = \mathbf{Q}_{21} + (\mathbf{L}^{-1}\mathbf{E})^\top \mathbf{Q}_{11}$
$\mathbf{R}_z$	$\mathbf{R}_z = \mathbf{Q}_{22} + (\mathbf{L}^{-1}\mathbf{E})^\top \mathbf{Q}_{12} + \mathbf{Q}_{21}\mathbf{L}^{-1}\mathbf{E} + (\mathbf{L}^{-1}\mathbf{E})^\top \mathbf{Q}_{11}\mathbf{L}^{-1}\mathbf{E}$

Greek Symbols

∇	Gradient operator, $\nabla = (\frac{\partial}{\partial x}, \frac{\partial}{\partial y}, \frac{\partial}{\partial z})$
Δ	Laplacian operator, $\Delta = (\frac{\partial^2}{\partial x^2}, \frac{\partial^2}{\partial y^2}, \frac{\partial^2}{\partial z^2})$
Γ	Chebyshev polynomial
Ξ	modified Chebyshev polynomial
Θ	modified Chebyshev polynomial
ρ	density
τ	shear stress or response time
μ	viscosity
ν	dynamic viscosity
η	vorticity
α, β	pair wavenumber ($\alpha = \frac{2\pi n_{st}}{L_x}$ and $\beta = \frac{2\pi n_{sp}}{L_z}$)
γ	control weight of **LQR** control
ε	kinetic energy density
ε_z	kinetic energy density
ε_x	kinetic energy density
ε_{max}	maximum kinetic energy density
ε_s	synchronic transient energy
ε_d	diachronic transient energy

Calligraphic Symbols

$\mathcal{X}(t)$	state vector, $\mathcal{X}(t) = \begin{bmatrix} \mathbf{x}(t) \\ \mathbf{u}(t) \end{bmatrix}$
$\mathcal{U}(t)$	control signal, $\mathcal{U}(t) = \dot{\mathbf{u}}(t)$
$\mathcal{A}$	state matrix, $\mathcal{A} = \begin{bmatrix} \mathbf{L}^{-1}\mathbf{A} & \mathbf{L}^{-1}\mathbf{B} \\ 0 & 0 \end{bmatrix}$
$\mathcal{B}$	input matrix, $\mathcal{B} = \begin{bmatrix} \mathbf{L}^{-1}\mathbf{E} \\ \mathbf{I} \end{bmatrix}$
$\mathcal{D}$	output matrix, $\mathcal{D} = \begin{bmatrix} \mathbf{D}_1 & \mathbf{D}_2 \end{bmatrix}$
$\mathcal{Q}$	$\mathcal{Q} = \begin{bmatrix} \mathbf{Q}_{11} & \mathbf{Q}_{12} \\ \mathbf{Q}_{21} & \mathbf{Q}_{22} \end{bmatrix}$
$\mathcal{K}$	gain of control law

Acronyms

CFD	Computational Fluid Dynamics
DNS	Direct Numerical Simulation
LED	Large Eddy Simulation
NSE	Navier Stokes Equations
PDE	Partial differential Equations
ODE	Ordinary Differential Equations
PID	Proportional Integral Derivative
LQG	Linear Quadratic Gaussian
LQR	Linear Quadratic Regulator
LQE	Linear Quadratic Estimator
LMI	Linear Matrix Inequality
PVS	Partitioned Visual Servo
VS	Visual Servoing
MIMO	Multiple Inputs Multiple Outputs
MOR	Model Order Reduction
TMOR	Truncation Model Order Reduction
POD	Proper Orthogonal Decomposition
BPOD	Balanced Proper Orthogonal Decomposition
DOF	Degree Of Freedom
CCD	Charge Coupled Device
MEMS	Micro-Electro-Mechanical-Systems

Acronyms

A/D	Analog to Digital converter
D/A	Digital to Analog converter
DSP	Digital Signal Processor
ASP	Analog Signal Processing

Chapter 1

Introduction

1.1 Why flow control

The flow control has many applications in aerospace (improve lift, reduce drag and noise). We consider the motion of an aircraft in the air. The aircraft can fly due to four forces in Figure 1.1: weight, drag, lift and thrust. The weight is a force due to the gravity of the earth and is always toward the center of the earth. The drag, an aerodynamic force, is the resistance force generated by the motion of the aircraft in the air. The lift, an another aerodynamic force to overcome the weight, is generated by the aircraft's wing. And the thrust is a force created by a power source which gives the aircraft forward motion. In the level flight at constant speed, the thrust exactly

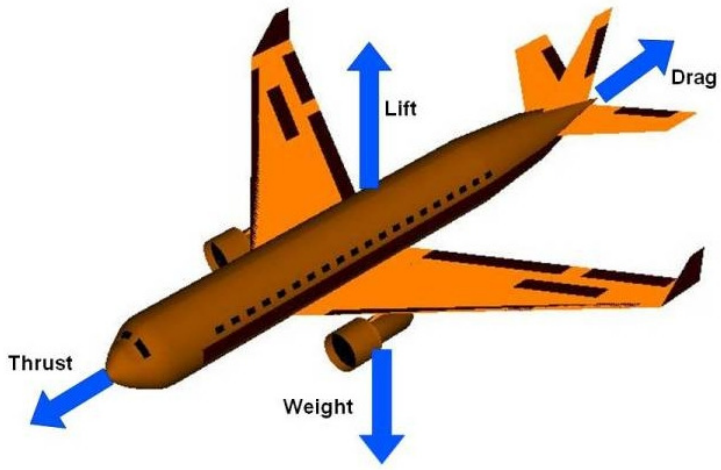

Figure 1.1: Four forces on an aircraft.

equals the drag and the lifts exactly equals the weight. In order to economize the power source, we want to reduce the drag and enhance the lift. In all cases, there are many research in the drag reduction and lift enhancement.

For instance, Airbus expects in 2020 to decrease by 50% the CO2 emissions compared to a standard aircraft in 2000, and 20% of this decrease being expected from the airframe by diminishing the fuel consumption of their aircrafts through aerodynamic drag reduction and structural weight savings [Flaig, 2008]. In the aerospace drag reduction, the flow control such as laminar flow control and turbulence & separation may achieve 15% of the drag reduction as shown in Figure 1.2 (taken from [Schrauf and Golling, 2006]). The main question is how to reduce the drag and enhance the lift in the motion of air-

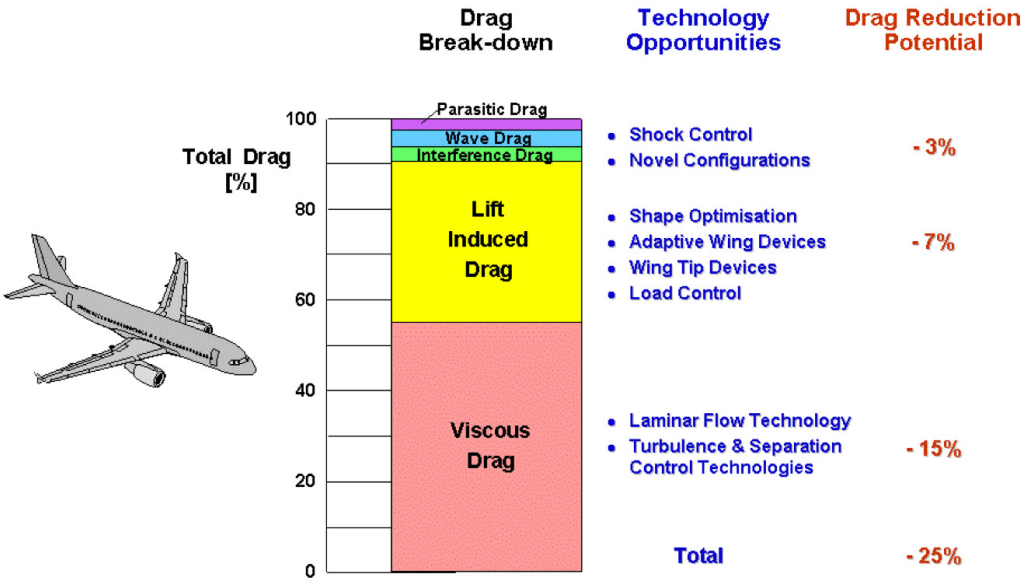

Figure 1.2: Drag reduction potential.

craft or vehicle ? In order to reduce the drag and enhance the lift, we must know when the fluid flow has the minimum value of the drag and the maximum value of the lift. Therefore, the objective is minimizing the drag and enhancing the lift. More precisely, we need to control the fluid flow from its current state to a desired state.

In the next section, we present the visual servoing control which will be applied to the flow control.

1.2 Visual servoing control

The visual servoing or visual servo control aims to control the motions of a robot by using data provided by a vision sensor [Chaumette and Hutchinson, 2006]. It is now a well established technique in the robotics community. More precisely, to achieve a visual servoing task, a set of visual features $\mathbf{s}(t)$ is selected from the image of the scene being observed. A control law is then designed so that this set of visual features $\mathbf{s}(t)$ reaches a desired value $\mathbf{s}^*$ corresponding to a desired state of the system. The dynamic

of the error vector $\mathbf{e}(t) = \mathbf{s}(t) - \mathbf{s}^*$ is then given by

$$\dot{\mathbf{e}}(t) = \frac{\partial \mathbf{e}(t)}{\partial t} + \mathbf{L_e}(t)\mathbf{u}(t), \tag{1.1}$$

where $\mathbf{u}(t)$ is the system control inputs assumed to be velocities, $\mathbf{L_e}(t)$ is the so-called interaction matrix, see previous works in [Espiau et al., 1992] or the image Jacobian that links the time variation of the visual features to the variation of the control signal acting on the system and $\partial \mathbf{e}(t)/\partial t$ expresses the variation of the error vector due to the free motion of the visual features. The control goal is of course to regulate the error vector $\mathbf{e}$ to zero. The control law is built from (1.1) using the knowledge or an approximation of the interaction matrix and an approximation of the free motion of the visual features. Visual servoing has shown impressive results in numerous complex contexts such as underwater, medical and aerial (helicopters, blimps) robotic as shown in [Bonin-Font et al., 2008].

If we would like for instance to try to ensure an exponential decoupled decrease of the error

$$\dot{\mathbf{e}}(t) = -\lambda \mathbf{e}(t). \tag{1.2}$$

We now obtain

$$\mathbf{u}(t) = -\lambda \mathbf{L_e^+}(t)\mathbf{e}(t) - \mathbf{L_e^+}(t)\frac{\partial \mathbf{e}(t)}{\partial t}, \tag{1.3}$$

where $\mathbf{L_e^+}$ is the Moore Penrose pseudo-inverse matrix of $\mathbf{L_e}$. If $\mathbf{L_e}$ were a square and invertible matrix, the control law could be

$$\mathbf{u}(t) = -\lambda \mathbf{L_e^{-1}}(t)\mathbf{e}(t) - \mathbf{L_e^{-1}}(t)\frac{\partial \mathbf{e}(t)}{\partial t}. \tag{1.4}$$

Note that the interaction matrix $\mathbf{L_e}$ may be not a square matrix but must be full rank matrix, therefore we use the Moore Penrose pseudo-inverse matrix $\mathbf{L_e^+}$.

We shall apply this technique to control the fluid flow. The visual feature $\mathbf{s}(t)$ may be equal to the velocity, the skin friction drag and the kinetic energy density.

1.3 Plane Poiseuille flow

The plane Poiseuille flow is chosen to study in this thesis because this flow is more adapted to the control theory than the other flows, contains a fundamental character of the flow control and illustrates many of the important unsolved issue of the flow control.

The active control, more precisely the visual servoing control in the closed loop system of the plane Poiseuille flow is proposed to obtain the stability of this flow. Since the governing equations of the plane Poiseuille flow are the Navier-stokes Equations, a popular partial differential equation in fluid dynamics, we use spectral method to convert the partial differential equations of Navier-Stokes Equations to a set of ordinary differential equations. A standard formulation in automatic control is presented for the plane Poiseuille flow where the control inputs are the boundary conditions, more precisely the velocity at the walls. The visual servoing control is applied on the standard formation in automatic control to achieve the stability of the flow.

In the next section, we present the outline of the thesis.

1.4 Outline of the thesis

This thesis aims to study the implementation of the visual servoing control for the active control of the plane Poiseuille flow. Transition to turbulence is one of interests where the flow becomes turbulent with the growth of its kinetic energy density. The reduction of the skin friction drag is also a potential application in engineering problems. The goal of this thesis is to minimise both the kinetic energy density and the skin friction drag. By using the visual servoing control, we show in this thesis that the kinetic energy density and the skin friction drag are monotonically decreasing over time to ensure the stability of the flow.

The outline of this thesis is as follows.

Chapter 2 presents some fundamentals of flow control. The basic definitions of the fluid flow are given such as the density, the viscosity, the Reynolds number, the kinetic energy density. Indeed, the kinetic energy density is a physical quantity to study the stability of the fluid flow. Therefore, we want to minimize the kinetic energy density.

Chapter 3 introduces some fundamentals of automatic control. This chapter allows us to understand the process of control system based on simple examples. The control theory of linear and nonlinear systems is derived. The stability and stabilization of systems are also discussed in detail.

Chapter 4 presents previous works and the objectives of this thesis. Here we introduce the problem of flow control and propose the solutions. The goal of this thesis is to use the visual servoing control to apply to the plane Poiseuille flow in order to improve the stability of flow control and reduce the skin-friction drag.

Chapter 5 gives a modeling of the plane Poiseuille flow where the Navier-Stokes equations are modeled to a standard model in the automatic control. We control the plane Poiseuille flow by using the blowing/suction boundary control. The number of degrees of freedom is the number of independent control signals.

The originalcontribution is in Chapter 6 where the partitioned visual servoing control is applied to obtain an exponential decrease of the skin-friction drag. The next contributions concern how to obtain an exponential decrease of the kinetic energy density in the controlled flow. Since the minimization of the kinetic energy density relates the degrees of freedom, Chapter 7 shows how to increase the number of degree of freedom. The minimization of kinetic energy density is improved as the function of increasing the number of degrees of freedom. In particular, Chapter 8 presents a design of the visual servoing control in order to obtain an exponential decrease of the kinetic energy density. Chapter 9 introduces a reduced order controller where an approximation of the exponential decrease of the kinetic energy density is obtained even using two degrees of freedom.

Finally, Chapter 10 gives conclusions from the work described in this thesis and suggests possible directions for future work.

Chapter 2

Fundamentals of Flow Control

This chapter is fundamentals of flow control. The fluid mechanics is briefly presented. Some definitions and some physical quantities are considered in the fluid mechanics such as the viscosity, the Reynolds number, laminar and turbulence. As well known, the Navier Stokes equations are the governing equations of the flow. The kinetic energy density is introduced as a physical quantity which is necessary used to study the stability of flow. The general flow control is given in the end of this chapter where the first views of the flow control are brought out.

2.1 Fluid mechanics

In this section, the fluid mechanics and its basic quantities are presented. The viscosity, the Reynolds number, laminar and turbulent flows are focused. This summary is taken from previous works, especially [Schlichting and Gersten, 2000]. It must be noted that the flow can be change its state, laminar or turbulent state. Therefore, the ideal of this thesis is to control the flow from its current state to a desired state.

2.1.1 Introduction

The fluid mechanics is the science of the study of fluids and the forces on it such as the friction forces, the inertial forces and the gravitational forces. It is a branch of physics which studies the statics and dynamics of liquids and gases. It contains two main sub-branches:

- Fluid statics studies fluids at rest.
- Fluid dynamics studies fluids in motion.

The fluid dynamics is distinguished by two sub-branches: aerodynamics and hydrodynamics. Aerodynamics studies the motion of air and gases while hydrodynamics studies the motions of liquids. But it is very difficult to distinguish the aerodynamics and the hydrodynamics when the liquids can change its state from liquid state to gases state due to the temperature.

The fluid mechanics, especially the fluid dynamics, is an active field of research with many unsolved or partly solved problems. The analysis of the behavior of fluids is based on the fundamental laws of physics that relate the conservation of mass, momentum and energy. With the help of computer, the fluid mechanics can be solved by numerical methods where the computational fluid dynamics (**CFD**) is an approach to solving the fluid mechanics problem. The direct numerical simulation (**DNS**) and the large eddy simulation (**LED**) are two of many tools of **CFD** which are usually used to study the fluid mechanics problems. In engineering applications, the fluid mechanics has many applications in various fields such as marine engineering, aeronautics, meteorology, climatology and oceanography.

2.1.2 Types of fluid

The fluids may also be classified into two families by their relative viscosity. The viscosity is one of their physical chemical characteristic that is defined later in the next section. The two large families are:

- Newtonian fluid, a fluid whose stress at each point is linearly proportional to its strain rate at that point, such as water, air and most of gases.
- Non-Newtonian fluid is a fluid whose flow properties differ in any way from those of Newtonian fluids, such as the blood, gels, sludges, pastes, suspensions, emulsions.

Note that in physics, the shear stress is a physical quantity that expresses the internal forces. In a solid, the shear stress is a function of strain. Nut in a fluid, the shear stress is a function of strain rate. In this thesis, only the Newtonian fluid is considered and classified by

- Ideal fluid is a fluid whose movement can be described without taking into account the effects of friction.
- Real fluid is a fluid whose movement are taking into account the effects of friction.
- Compressible fluid is a fluid whose volume is a function of variation of pressure. Gases are considered as a compressible fluids, such as the air, hydrogen, methane in the gaseous state.
- Incompressible fluid is a fluid whose volume is not changed by a variation of pressure. Liquids can be considered as an incompressible fluids, such as water, oil.

2.1.3 Physical characteristics

2.1.3.1 Density

The density is defined as an objects mass par unit volume. The density is calculated by

$$\rho = \frac{m}{\mathbf{V}_o}, \tag{2.1}$$

where ρ is density (kg/m^3), m is the mass (kg) and $\mathbf{V}_o$ is the volume (m^3). We give some examples of density, for the benzene $\rho = 0.88\ 10^3 kg/m^3$, water $\rho = 10^3 kg/m^3$, air $\rho = 0.001205\ 10^3 kg/m^3$ and methane $\rho = 0.00717\ 10^3 kg/m^3$.

2.1.3.2 Viscosity

The viscosity is a quantity that characterizes the internal friction of the fluid. In other word, the viscosity is a measure of a fluid's resistance to flow, e.g. molasses is highly viscous, water is medium viscous and gases are low viscous. In order to give a form of viscosity, the flow between two parallel plane plates is studied, see Figure 2.1 (taken from [Schlichting and Gersten, 2000]). The shear stress τ is the force per unit surface

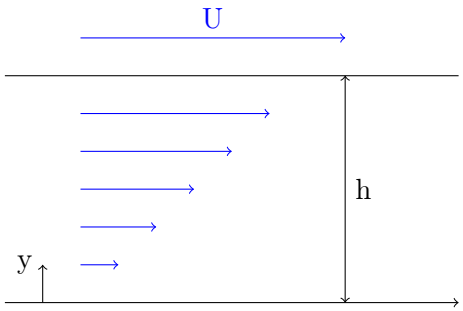

Figure 2.1: Velocity distribution in a viscous fluid between two parallel plane plates, plane Couette flow. U is the maximum velocity, the velocity u at y is calculated by $u = yU/h$.

area of the plates

$$\tau = \mu \frac{du}{dy}, \tag{2.2}$$

this equation is Newton's law of friction and can be interpreted as the defining equation of the viscosity. Note that the dynamic viscosity is in general a function of the temperature and the pressure, e.g. for water $\mu = 1.787\ 10^{-3} Pa.s$ at 0^oC, $\mu = 1.002\ 10^{-3} Pa.s$ at 20^oC and $\mu = 0.2818\ 10^{-3} Pa.s$ at 100^oC. The kinematic viscosity is the ratio of dynamic viscosity to density and is given by

$$\nu = \frac{\mu}{\rho}. \tag{2.3}$$

It must be noted that if the relation between the shear stress τ and the velocity gradient du/dy is nonlinear, the the fluids will be called non-Newtonian fluids.

2.1.4 Reynolds number

The Reynolds number is one of fundamental important numbers in the fluid dynamics. This number helps us to distinguish a laminar or turbulent state of the flow. In order to give a form of the Reynolds number, we consider the forces on a volume element in the fluid, as shown in Figure 2.2 (taken from [Schlichting and Gersten, 2000]). The

following forces generally act on a volume: friction forces (proportional to the viscosity μ), inertial forces (proportional to the density ρ), pressure forces and volumes forces (e.g. gravitational force) but we only consider the ratio of the inertial forces to the friction forces. This ratio allows us to give a definition of the Reynolds number.

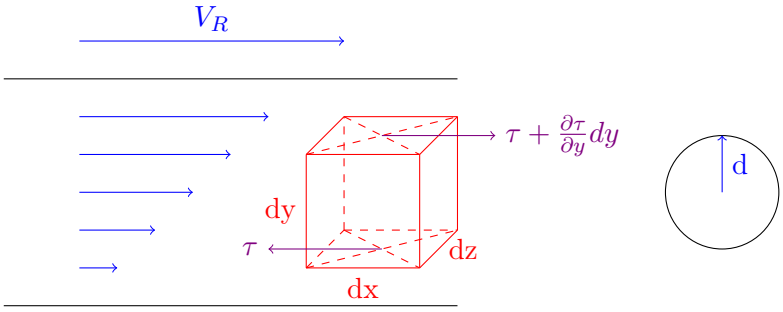

Figure 2.2: Friction forces acting on a fluid particle.

For motion which is mainly in the x directions, the inertial force per unit volume is $\rho du/dt$ where u is the velocity component in the x direction. Therefore, we can give the inertial force (see [Schlichting and Gersten, 2000], p.13)

$$F_i = \rho \frac{du}{dt} = \rho \frac{\partial u}{\partial x} \frac{dx}{dt} = \rho u \frac{\partial u}{\partial x}. \tag{2.4}$$

While the shear force is given from (2.2) by the following expression

$$(\tau + \frac{\partial \tau}{\partial y} dy) dx dz - \tau dx dz = \frac{\partial \tau}{\partial y} dx dy dz. \tag{2.5}$$

Consequently, the friction force per unit volume is thus given by

$$F_f = \frac{\partial \tau}{\partial y} = \rho \frac{\partial^2 u}{\partial y^2}. \tag{2.6}$$

Indeed, the ratio of inertial to friction forces is given by

$$\frac{\text{inertial force}}{\text{friction force}} = \frac{\rho u \partial u/\partial x}{\mu \partial^2 u/\partial y^2}. \tag{2.7}$$

When we consider the sphere in the flow illustrated in Figure 2.2. It is now necessary to investigate how these forces are changed when the magnitudes which determined the flow are varied. The latter includes the density ρ, the viscosity μ, a respectively velocity, e.g. the free stream velocity V_R, and a characteristic linear dimension of the body, e.g. the diameter d of the sphere. The velocity u at some points in the velocity field is proportional to the maximum velocity V_R, the velocity gradient $\partial u/\partial x$ is proportional to V_R/d, and similarly $\partial^2 u/\partial y^2$ is proportional to V_R/d^2. Therefore, we get

$$\frac{\text{inertial force}}{\text{friction force}} = \frac{\rho u \partial u/\partial x}{\mu \partial^2 u/\partial y^2} = \frac{\rho V_R^2 d}{\mu V_R d^2} = \frac{\rho V_R}{\mu d}. \tag{2.8}$$

The Reynolds number is a dimensionless number and expresses the ratio of inertial force to friction force as calculated by

$$R = \frac{V_R d}{\upsilon}. \tag{2.9}$$

And the critical Reynolds number is the Reynolds number where the flow can change its state, from laminar to turbulent state. In the next section, the laminar and turbulent flows are presented.

2.1.5 Laminar and turbulent flows

The process by which turbulent flow develops and replaces laminar flow is known as transition. This process is emphasized in Figure 2.3 (taken from [Durst, 2008]). It is noted that the laminar flow is characterized by the layers moving parallel to others while the fluid motion in the turbulent flow is highly random and unpredictable. The transitional flow is a process between the laminar and turbulence, this flow contains both laminar and turbulent characteristics.

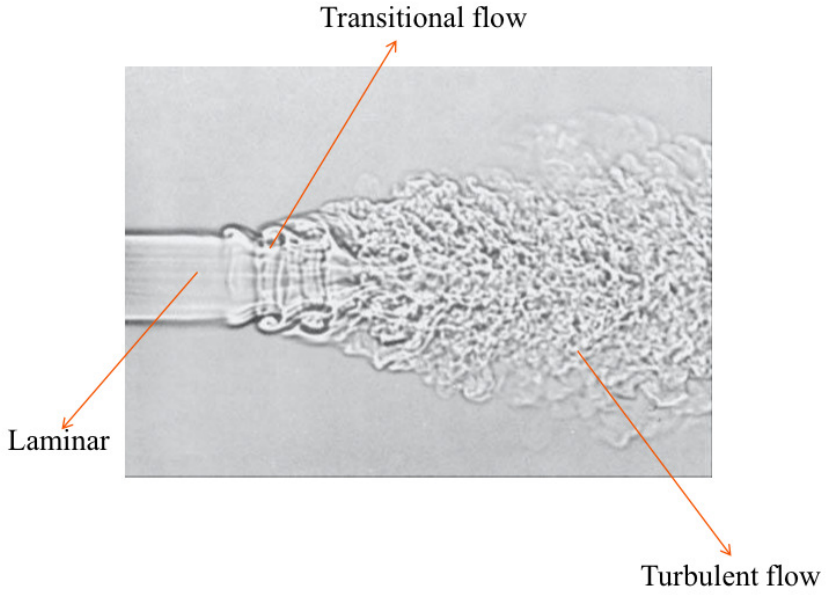

Figure 2.3: Subsonic open jet with areas of laminar, transitional and turbulent flow.

Since laminar to turbulent transition is specified based on the critical Reynolds number, we must be determined this number. Fortunately, in linear theory, the critical Reynolds number is given based on the stability theory as linear stability analysis and energy methods. An example of linear stability analysis or energy methods is found in [Orszag, 1971] or [Trefethen et al., 1993], [Butler and Farrell, 1992], respectively.

The idea of this thesis is to control the flow in order to change its state from the current state to a desired state to satisfy our goals, e.g. the flow is controlled from the

turbulent flow to the laminar flow due to the potential application of laminar flow. To do that, both the passive and active controls will be presented in the next sections and the following of this thesis. The subject of this thesis is precisely in the next chapters, especially in the state of the art.

The basic physical quantities have been presented in the fluid dynamics, and the laminar and turbulent flows have been focused. In the next section, the governing equations of the fluid flow are the conservation of mass and momentum.

2.2 Governing Navier-Stokes Equations

The governing equations of the fluid flow are introduced. Note that only the important equations of Navier-Stokes equations are recalled (see [Bird et al., 1960] for more details).

Consider the behavior of a fluid in 3D cartesian coordinates illustrated in Figure 2.4. The velocity field is denoted $\mathbf{V} = (U(x,y,z,t), V(x,y,z,t), W(x,y,z,t))$ where $(U(x,y,z,t)$, $V(x,y,z,t)$, $W(x,y,z,t))$ are the velocity components in the x, y and z directions. We recall the works of Aamo [Aamo, 2002].

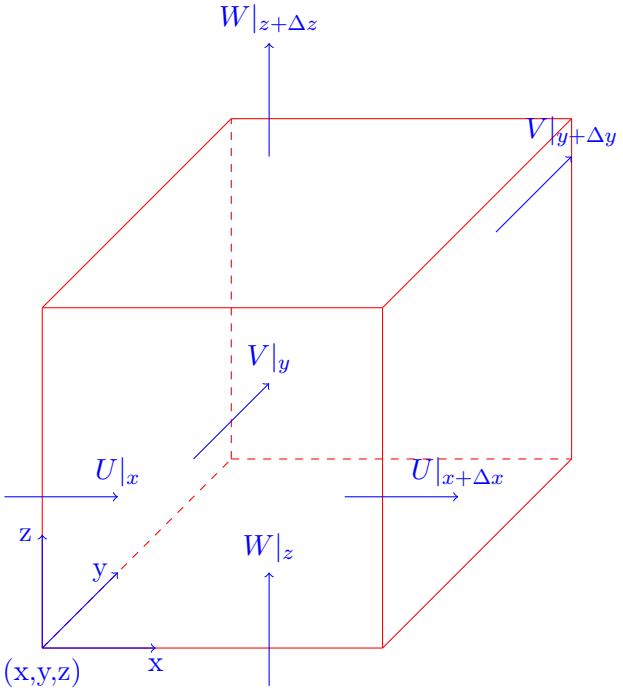

Figure 2.4: Control volume for derivation of the governing equations.

2.2.1 Conservation of mass

We use a mass balance over the volume in Figure 2.4. The equation of conservation of mass is given

$$\text{rate of mass accumulation} = \text{rate of mass in - rate of mass out}, \tag{2.10}$$

where

$$\begin{aligned} \text{rate of mass in} &= (\rho U)|_x \Delta y \Delta z + (\rho V)|_y \Delta x \Delta z + (\rho W)|_z \Delta x \Delta y \\ \text{rate of mass out} &= (\rho U)|_{x+\Delta x} \Delta y \Delta z + (\rho V)|_{y+\Delta y} \Delta x \Delta z + (\rho W)|_{z+\Delta z} \Delta x \Delta y \end{aligned} \tag{2.11}$$

Therefore, we obtain

$$\begin{aligned} \frac{\partial \rho}{\partial t} \Delta x \Delta y \Delta z &= [(\rho U)|_x - (\rho U)|_{x+\Delta x}] \Delta y \Delta z + [(\rho V)|_y - (\rho V)|_{y+\Delta y}] \Delta x \Delta z \\ &\quad + [(\rho W)|_z - (\rho W)|_{z+\Delta z}] \Delta x \Delta y \end{aligned} \tag{2.12}$$

or we can rewrite the above equation by dividing the volume $\Delta x \Delta y \Delta z$

$$\frac{\partial \rho}{\partial t} = \frac{[(\rho U)|_x)) - (\rho U)|_{x+\Delta x}]}{\Delta x} + \frac{[(\rho V)|_y - (\rho V)|_{y+\Delta y}]}{\Delta y} + \frac{[(\rho W)|_z - (\rho W)|_{z+\Delta z}]}{\Delta z} \tag{2.13}$$

When $\Delta x \to 0$, $\Delta y \to 0$ and $\Delta z \to 0$, we get

$$\frac{\partial \rho}{\partial t} = -\frac{\partial (\rho U)}{\partial x} - \frac{\partial (\rho V)}{\partial y} - \frac{\partial (\rho W)}{\partial z} \tag{2.14}$$

We can have a compact form of the equation of conservation of mass

$$\frac{\partial \rho}{\partial t} + \nabla . (\rho \mathbf{V}) = 0, \tag{2.15}$$

where $\mathbf{V}$ is the velocity, ρ is the fluid density, and the gradient operator is given by $\nabla = (\frac{\partial}{\partial x}, \frac{\partial}{\partial y}, \frac{\partial}{\partial z})$. If an incompressible flow is considered, the fluid density ρ is a constant, the equation of conservation of mass will become the equation of continuity

$$\nabla . \mathbf{V} = 0. \tag{2.16}$$

2.2.2 Conservation of momentum

The equation of conservation of momentum is given

$$\begin{aligned} \text{rate of momentum accumulation} &= \text{rate of momentum in - rate of momentum out} \\ &+ \text{sum of force acting on system.} \end{aligned} \tag{2.17}$$

We calculate the momentum in the x-direction

$$\begin{aligned} \text{rate of momentum in} &= (\rho U^2)|_x \Delta y \Delta z + (\rho UV)|_y \Delta x \Delta z + (\rho UW)|_z \Delta x \Delta y \\ \text{rate of momentum out} &= (\rho U^2)|_{x+\Delta x} \Delta y \Delta z + (\rho UV)|_{y+\Delta y} \Delta x \Delta z + (\rho UW)|_{z+\Delta z} \Delta x \Delta y \end{aligned} \tag{2.18}$$

And we calculate the sum of forces acting on system

$$\begin{aligned}\text{sum of forces acting on system} &= (\tau_{xx}|_x - \tau_{xx}|_{x+\Delta x})\Delta y\Delta z + (\tau_{yx}|_y - \tau_{yx}|_{y+\Delta y})\Delta x\Delta z \\ &+(\tau_{zx}|_z - \tau_{zx}|_{z+\Delta z})\Delta x\Delta y + (P|_x - P|_{x+\Delta x})\Delta y\Delta z\end{aligned} \tag{2.19}$$

where τ_{ij} denotes the viscous force acting in the direction of f on a face normal to the i-direction. Therefore, we obtain

$$\begin{aligned}\frac{\partial(\rho U)}{\partial t}\Delta x\Delta y\Delta z &= [(\rho U^2)|_x - (\rho U^2)|_{x+\Delta x}]\Delta y\Delta z + [(\rho UV)|_y - (\rho UV)|_{y+\Delta y}]\Delta x\Delta z \\ &+[(\rho UW)|_z - (\rho UW)|_{z+\Delta z}]\Delta x\Delta y + (\tau_{xx}|_x - \tau_{xx}|_{x+\Delta x})\Delta y\Delta z \\ &+(\tau_{yx}|_y - \tau_{yx}|_{y+\Delta y})\Delta x\Delta z + (\tau_{zx}|_z - \tau_{zx}|_{z+\Delta z})\Delta x\Delta y \\ &+(P|_x - P|_{x+\Delta x})\Delta y\Delta z\end{aligned} \tag{2.20}$$

We can rewrite the above equation by dividing the volume $\Delta x\Delta y\Delta z$ and letting $\Delta x \to 0$, $\Delta y \to 0$ and $\Delta z \to 0$, we get

$$\frac{\partial(\rho U)}{\partial t} + \frac{\partial(\rho U^2)}{\partial x} + \frac{\partial(\rho UV)}{\partial y} + \frac{\partial(\rho UW)}{\partial z} = -\frac{\partial P}{\partial x} - \frac{\partial \tau_{xx}}{\partial x} - \frac{\partial \tau_{yx}}{\partial y} - \frac{\partial \tau_{zx}}{\partial z} \tag{2.21}$$

When $\rho = constant$, we have

$$\begin{aligned}\rho\frac{\partial U}{\partial t} &+\rho(U\frac{\partial U}{\partial x} + V\frac{\partial U}{\partial y} + W\frac{\partial U}{\partial z}) + \rho U(\frac{\partial U}{\partial x} + \frac{\partial V}{\partial y} + \frac{\partial W}{\partial z}) \\ &= -\frac{\partial P}{\partial x} - \frac{\partial \tau_{xx}}{\partial x} - \frac{\partial \tau_{yx}}{\partial y} - \frac{\partial \tau_{zx}}{\partial z}\end{aligned} \tag{2.22}$$

Using (2.16), it means $\dfrac{\partial U}{\partial x} + \dfrac{\partial V}{\partial y} + \dfrac{\partial W}{\partial z} = 0$, we get

$$\rho\frac{\partial U}{\partial t} + \rho(U\frac{\partial U}{\partial x} + V\frac{\partial U}{\partial y} + W\frac{\partial U}{\partial z}) = -\frac{\partial P}{\partial x} - \frac{\partial \tau_{xx}}{\partial x} - \frac{\partial \tau_{yx}}{\partial y} - \frac{\partial \tau_{zx}}{\partial z} \tag{2.23}$$

Therefore, by using the similar way for the momentum in the y and z directions, we get the complete set of equations

$$\rho\frac{\partial U}{\partial t} + \rho(U\frac{\partial U}{\partial x} + V\frac{\partial U}{\partial y} + W\frac{\partial U}{\partial z}) = -\frac{\partial P}{\partial x} - \frac{\partial \tau_{xx}}{\partial x} - \frac{\partial \tau_{yx}}{\partial y} - \frac{\partial \tau_{zx}}{\partial z} \tag{2.24}$$

$$\rho\frac{\partial V}{\partial t} + \rho(U\frac{\partial V}{\partial x} + V\frac{\partial V}{\partial y} + W\frac{\partial V}{\partial z}) = -\frac{\partial P}{\partial y} - \frac{\partial \tau_{xy}}{\partial x} - \frac{\partial \tau_{yy}}{\partial y} - \frac{\partial \tau_{zy}}{\partial z} \tag{2.25}$$

$$\rho\frac{\partial W}{\partial t} + \rho(U\frac{\partial W}{\partial x} + V\frac{\partial W}{\partial y} + W\frac{\partial W}{\partial z}) = -\frac{\partial P}{\partial z} - \frac{\partial \tau_{xz}}{\partial x} - \frac{\partial \tau_{yz}}{\partial y} - \frac{\partial \tau_{zz}}{\partial z} \tag{2.26}$$

The viscous forces τ_{ij} is a function of the fluid motion $\mathbf{V} = (U, V, W)$. We consider the Newtonian fluids, we have

$$\tau_{xx} = -2\mu\frac{\partial U}{\partial x}, \tau_{yy} = -2\mu\frac{\partial V}{\partial y}, \tau_{zz} = -2\mu\frac{\partial W}{\partial z} \tag{2.27}$$

$$\tau_{xy} = \tau_{yx} = -\mu(\frac{\partial U}{\partial y} + \frac{\partial V}{\partial x}) \tag{2.28}$$

$$\tau_{yz} = \tau_{zy} = -\mu(\frac{\partial V}{\partial z} + \frac{\partial W}{\partial y}) \tag{2.29}$$

$$\tau_{xz} = \tau_{zx} = -\mu(\frac{\partial U}{\partial z} + \frac{\partial W}{\partial x}) \tag{2.30}$$

Substituting ((2.27)-(2.30)) into ((2.24)-(2.26)), we get

$$\rho\frac{\partial U}{\partial t} + \rho(U\frac{\partial U}{\partial x} + V\frac{\partial U}{\partial y} + W\frac{\partial U}{\partial z}) = \tag{2.31}$$

$$-\frac{\partial P}{\partial x} - \mu(\frac{\partial^2 U}{\partial x^2} + \frac{\partial^2 U}{\partial y^2} + \frac{\partial^2 U}{\partial z^2}) + \mu\frac{\partial}{\partial x}(\frac{\partial U}{\partial x} + \frac{\partial V}{\partial y} + \frac{\partial W}{\partial z}) \tag{2.32}$$

$$\rho\frac{\partial V}{\partial t} + \rho(U\frac{\partial V}{\partial x} + V\frac{\partial V}{\partial y} + W\frac{\partial V}{\partial z}) = \tag{2.33}$$

$$-\frac{\partial P}{\partial y} - \mu(\frac{\partial^2 V}{\partial x^2} + \frac{\partial^2 V}{\partial y^2} + \frac{\partial^2 V}{\partial z^2}) + \mu\frac{\partial}{\partial y}(\frac{\partial U}{\partial x} + \frac{\partial V}{\partial y} + \frac{\partial W}{\partial z}) \tag{2.34}$$

$$\rho\frac{\partial W}{\partial t} + \rho(U\frac{\partial W}{\partial x} + V\frac{\partial W}{\partial y} + W\frac{\partial W}{\partial z}) = \tag{2.35}$$

$$-\frac{\partial P}{\partial z} - \mu(\frac{\partial^2 W}{\partial x^2} + \frac{\partial^2 W}{\partial y^2} + \frac{\partial^2 W}{\partial z^2}) + \mu\frac{\partial}{\partial z}(\frac{\partial U}{\partial x} + \frac{\partial V}{\partial y} + \frac{\partial W}{\partial z}) \tag{2.36}$$

Using $\frac{\partial U}{\partial x} + \frac{\partial V}{\partial y} + \frac{\partial W}{\partial z} = 0$, the Navier-Stokes equation of motion is given by

$$\rho\frac{\partial U}{\partial t} + \rho(U\frac{\partial U}{\partial x} + V\frac{\partial U}{\partial y} + W\frac{\partial U}{\partial z}) = -\frac{\partial P}{\partial x} - \mu(\frac{\partial^2 U}{\partial x^2} + \frac{\partial^2 U}{\partial y^2} + \frac{\partial^2 U}{\partial z^2}) \tag{2.37}$$

$$\rho\frac{\partial V}{\partial t} + \rho(U\frac{\partial V}{\partial x} + V\frac{\partial V}{\partial y} + W\frac{\partial V}{\partial z}) = -\frac{\partial P}{\partial y} - \mu(\frac{\partial^2 V}{\partial x^2} + \frac{\partial^2 V}{\partial y^2} + \frac{\partial^2 V}{\partial z^2}) \tag{2.38}$$

$$\rho\frac{\partial W}{\partial t} + \rho(U\frac{\partial W}{\partial x} + V\frac{\partial W}{\partial y} + W\frac{\partial W}{\partial z}) = -\frac{\partial P}{\partial z} - \mu(\frac{\partial^2 W}{\partial x^2} + \frac{\partial^2 W}{\partial y^2} + \frac{\partial^2 W}{\partial z^2}) \tag{2.39}$$

We can get a compact form

$$\frac{\partial \mathbf{V}}{\partial t} + (\mathbf{V}.\nabla)\mathbf{V} = -\frac{1}{\rho}\nabla P + \frac{\mu}{\rho}\Delta\mathbf{V}, \tag{2.40}$$

where $\mu = \rho\upsilon$ is the dynamic viscosity, and and the Laplacian operator is given by $\Delta = \frac{\partial^2}{\partial x^2} + \frac{\partial^2}{\partial y^2} + \frac{\partial^2}{\partial z^2}$.

2.2.3 The Dimensionless Navier Stokes Equations

The Navier-Stokes equations can be written in dimensionless. We can rewrite the Navier Stokes in dimensionless form by introducing a characteristic length d and the characteristic velocity V_R. The new variables are dimensionless

$$\mathbf{V}^* = (U^*, V^*, W^*) = \frac{\mathbf{V}}{V_R} = (\frac{U}{V_R}, \frac{V}{V_R}, \frac{W}{V_R}) \tag{2.41}$$

$$P^* = \frac{P}{\rho V_R^2}, x^* = \frac{x}{d}, y^* = \frac{y}{d}, z^* = \frac{z}{d}, t^* = \frac{V_R}{d}t \tag{2.42}$$

Therefore, we get a change of variable

$$\frac{\partial U}{\partial t} = V_R \frac{\partial U^*}{\partial t^*}\frac{\partial t^*}{\partial t} = \frac{V_R^2}{d}\frac{\partial U^*}{\partial t^*} \tag{2.43}$$

$$\frac{\partial U}{\partial x} = V_R \frac{\partial U^*}{\partial x^*}\frac{\partial x^*}{\partial x} = \frac{V_R}{d}\frac{\partial U^*}{\partial x^*} \tag{2.44}$$

$$\frac{\partial P}{\partial x} = \rho V_R^2 \frac{\partial P^*}{\partial x^*}\frac{\partial x^*}{\partial x} = \frac{\rho V_R^2}{d}\frac{\partial P^*}{\partial x^*} \tag{2.45}$$

$$\frac{\partial^2 U}{\partial x^2} = \frac{\partial}{\partial x^*}(\frac{\partial U^*}{\partial x^*})\frac{\partial x^*}{\partial x} = \frac{V_R}{d^2}\frac{\partial^2 U^*}{\partial x^{*2}} \tag{2.46}$$

Using the new variables, we have

$$\begin{aligned}
\frac{\partial U^*}{\partial x^*} + \frac{\partial V^*}{\partial y^*} + \frac{\partial W^*}{\partial z^*} &= 0 \\
\frac{\partial U^*}{\partial t^*} + (U^*\frac{\partial U^*}{\partial x^*} + V^*\frac{\partial U^*}{\partial y^*} + W^*\frac{\partial U^*}{\partial z^*}) &= -\frac{\partial P^*}{\partial x^*} - \frac{1}{R}(\frac{\partial^2 U^*}{\partial x^{*2}} + \frac{\partial^2 U^*}{\partial y^{*2}} + \frac{\partial^2 U^*}{\partial z^{*2}}) \\
\frac{\partial V^*}{\partial t^*} + (U^*\frac{\partial V^*}{\partial x^*} + V^*\frac{\partial V^*}{\partial y^*} + W^*\frac{\partial V^*}{\partial z^*}) &= -\frac{\partial P^*}{\partial y^*} - \frac{1}{R}(\frac{\partial^2 V^*}{\partial x^{*2}} + \frac{\partial^2 V^*}{\partial y^{*2}} + \frac{\partial^2 V^*}{\partial z^{*2}}) \\
\frac{\partial W^*}{\partial t^*} + (U^*\frac{\partial W^*}{\partial x^*} + V^*\frac{\partial W^*}{\partial y^*} + W^*\frac{\partial W^*}{\partial z}) &= -\frac{\partial P^*}{\partial z^*} - \frac{1}{R}(\frac{\partial^2 W^*}{\partial x^{*2}} + \frac{\partial^2 W^*}{\partial y^{*2}} + \frac{\partial^2 W^*}{\partial z^{*2}})
\end{aligned}$$

where the Reynolds number $R = \rho d V_R/\mu$. We skip the superscript * for notational convenience, we get

$$\frac{\partial U}{\partial x} + \frac{\partial V}{\partial y} + \frac{\partial W}{\partial z} = 0 \tag{2.47}$$

$$\frac{\partial U}{\partial t} + (U\frac{\partial U}{\partial x} + V\frac{\partial U}{\partial y} + W\frac{\partial U}{\partial z}) = -\frac{\partial P}{\partial x} - \frac{1}{R}(\frac{\partial^2 U}{\partial x^2} + \frac{\partial^2 U}{\partial y^2} + \frac{\partial^2 U}{\partial z^2}) \tag{2.48}$$

$$\frac{\partial V}{\partial t} + (U\frac{\partial V}{\partial x} + V\frac{\partial V}{\partial y} + W\frac{\partial V}{\partial z}) = -\frac{\partial P}{\partial y} - \frac{1}{R}(\frac{\partial^2 V}{\partial x^2} + \frac{\partial^2 V}{\partial y^2} + \frac{\partial^2 V}{\partial z^2}) \tag{2.49}$$

$$\frac{\partial W}{\partial t} + (U\frac{\partial W}{\partial x} + V\frac{\partial W}{\partial y} + W\frac{\partial W}{\partial z}) = -\frac{\partial P}{\partial z} - \frac{1}{R}(\frac{\partial^2 W}{\partial x^2} + \frac{\partial^2 W}{\partial y^2} + \frac{\partial^2 W}{\partial z^2}) \tag{2.50}$$

Finally, the Navier-Stokes equations for an incompressible fluid flow are

$$\left\{ \begin{array}{ll} \nabla.\mathbf{V} & = 0 \\ \frac{\partial \mathbf{V}}{\partial t} + (\mathbf{V}.\nabla)\mathbf{V} & = -\nabla P + \frac{1}{R}\Delta\mathbf{V}. \end{array} \right. \tag{2.51}$$

2.3 Kinetic energy density

In order to determine the state flow and its stability, we have to give a quantity which is to capture the change of the state flow. The kinetic energy density of an object will be the energy if it possesses due to its motions. Indeed, this quantity can capture the stability of the flow. In the fluid dynamics, the kinetic energy density is given by

$$\varepsilon(t) = \frac{1}{\mathbf{V}_o} \int_{\mathbf{V}_o} \mathbf{v}^2 d\mathbf{V}_o, \tag{2.52}$$

where $\mathbf{v} = \mathbf{V} - \mathbf{V}_e$ is the perturbation between the velocity $\mathbf{V}$ and the steady solution $\mathbf{V}_e$, $\mathbf{V}_o$ is volume. On the other hand, the kinetic energy density is a physically interesting measure of perturbation magnitude.

In the hydrodynamics, the stability theory is used to investigate the behavior of the fluid flow. Note that the kinetic energy density has a similar role with respect to the Lyapunov function in control theory. This function will be defined later in the next chapter. Therefore, the kinetic energy density is not only a measure of the stability of the dynamic system but also is the actual energy of the flow.

The transient energy growth is the growth of the kinetic energy density in time. In previous works, the transient energy growth is a function of the Reynolds number. In [Butler and Farrell, 1992], [Reddy and Henningson, 1993], the transient energy growth could grow up to $O(R^2)$ in the transient time period, which is proportional to $O(R)$ in the transient time period (see section E.1 for more detail). In [Bamieh and Dahleh, 1999], [Bamieh and Dahleh, 2001], if the streamwise wavenumber is constant, the transient energy growth could grow up to $O(R^3)$ in the transient time period. The transient energy growth gives the informations when the Reynolds number becomes the critical Reynolds number which specifies laminar and turbulent flows.

The definitions of stability and the critical Reynolds numbers are presented in the following, these results are taken from [Schmid and Henningson, 2001]. It is noted that $\mathbf{V}$ is the velocity of the Navier Stokes equations (2.51).

Definition 2.3.1 *Stability*
A solution $\mathbf{V}$ *to the Navier-Stokes equations* (2.51) *is stable to perturbation if the perturbation energy satisfies*

$$lim_{t\to\infty} \frac{\varepsilon(t)}{\varepsilon(0)} \to 0. \tag{2.53}$$

Definition 2.3.2 *Conditional stability*
If there exists a threshold energy $\delta > 0$ *such that* $\mathbf{V}$ *is stable when* $\varepsilon(0) < \delta$ *then solution* $\mathbf{V}$ *is said to be conditionally stable.*

Definition 2.3.3 *Global stability*
If the threshold energy is infinite, i.e. $\delta \to \infty$*, the solution is said to be globally stable.*

Definition 2.3.4 *Monotonically stable*
If

$$\frac{d\varepsilon(t)}{dt} = \dot{\varepsilon}(t) \leq 0, \tag{2.54}$$

then the solution is said to be monotonically stable.

Based on the definitions of stability, it is appropriate to introduce the following critical Reynolds numbers

Definition 2.3.5 *For $R < R_E$ the flow is monotonically stable*

Definition 2.3.6 *For $R < R_G$ the flow is globally stable*

Definition 2.3.7 *For $R < R_T$ the flow will relaminearize*

Definition 2.3.8 *For $R > R_L$ the flow is linearly unstable or not conditionally stable*

The critical Reynolds number is given for the plane Poiseuille and Couette flows in Table 2.1 (taken from [Joshep, 1976], [Drazin and Reid, 1981]), see Figure 2.5 for its profile.

Flow	R_E	R_G	R_T	R_L
Plane Poseuille	49.6	-	1000	5772
Plane Couette	20.7	125	360	∞

Table 2.1: Critical Reynolds numbers from the literature.

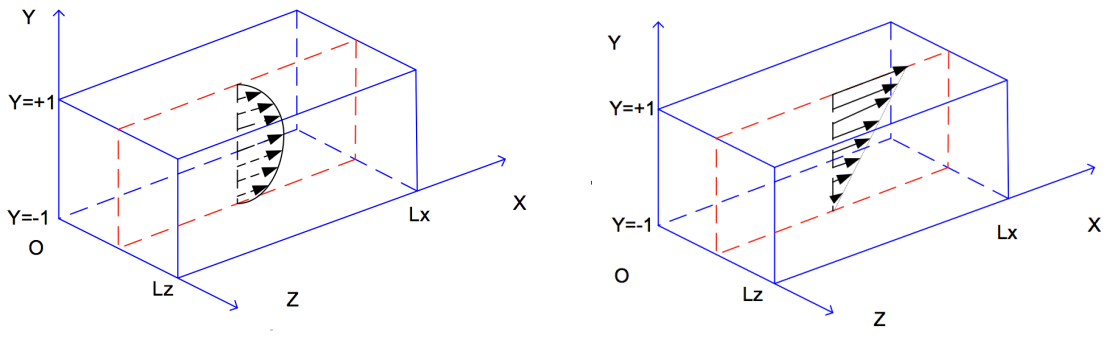

(a) plane Poiseuille flow (b) plane Couette flow

Figure 2.5: Plane Poiseuille and Couette flows and its profile.

Based on the kinetic energy density, the path of transition to turbulence will be briefly presented in the next section.

2.4 Path of transition to turbulence

This section briefly presents the path of transition to turbulence. Indeed, it must be noted that it is very difficult to explain the path of transition to turbulence and it is

not the subject of this thesis. Therefore, our goal is to demonstrate that it exists some paths of transition to turbulence. Consequently, the path of transition to turbulence is generally classified in Figure 2.6 (taken from [Morkovin et al., 1994]). Some definitions must be given before considering the details of the paths.

The process of a laminar flow becoming turbulent is known as laminar-turbulent transition (or called transition to turbulence). This is an extraordinary complicated process which at present is not fully understood.

Note that the stability theory is used to investigate the behavior of the fluid flow and the numerical methods are used to give a solution. The flow is modeled to a model by numerical methods such as a spectral method and a finite element method. An approximation solution is derived. The Navier Stokes equations are transformed to the Orr-Sommerfeld and Squire equations. In order to determine the stability of the flow, we study the eigenmodes and eigenfunctions of the Orr-Sommerfeld and Squire operators. We will present these operators in the next chapters. The behavior of approximation solution is based on considering the eigenmodes which are considered as the eigenfunction of a system. The eigenmode will be presented in the next chapter. The role of eigenfunction of operator is considered as the eigenvector of a matrix, the eigenmode growth corresponds to the eigenfunction with the positive eigenvalue. The problem of transient energy growth is called as the non-normality problem, the transient energy growth appears even though the negative eigenvalues. These problems will be precisely in the next chapters.

Tollmien-Schlichting mechanic is the streamwise instability, more precisely if we consider the 2D flow, the approximation model contains positive eigenvalues. Therefore, the transient energy growth is infinity. Therefore, we only need to consider the positive eigenvalues. The eigenmode growth is called in this case.

We consider the transition to turbulence. The five paths of transition to turbulence are clarified in [Morkovin et al., 1994], [Reshotko, 2001], [Reshotko et al., 2006], from path A to path E, as shown in Figure 2.6.

Definition 2.4.1 *Path of transition to turbulence (taken from [Reshotko, 2001])*

- *Path A corresponds to the situation where transient growth is insignificant and transition is due to traditional Tollmien-Schlichting or Gortler mechanisms.*
- *Path B indicates some transient growth providing a higher amplitude to the eigenmode growth upon crossing into an exponentially unstable region.*
- *Path C is the case where eigenmode growth is absent or else that the transient growth is large enough to directly excite secondary instabilities and mode interactions.*
- *In Path D, the result of the transient growth is that the spectrum of disturbances is full it looks like a turbulent spectrum.*
- *Path E represents the case of very large amplitude forcing where there is no linear regime.*

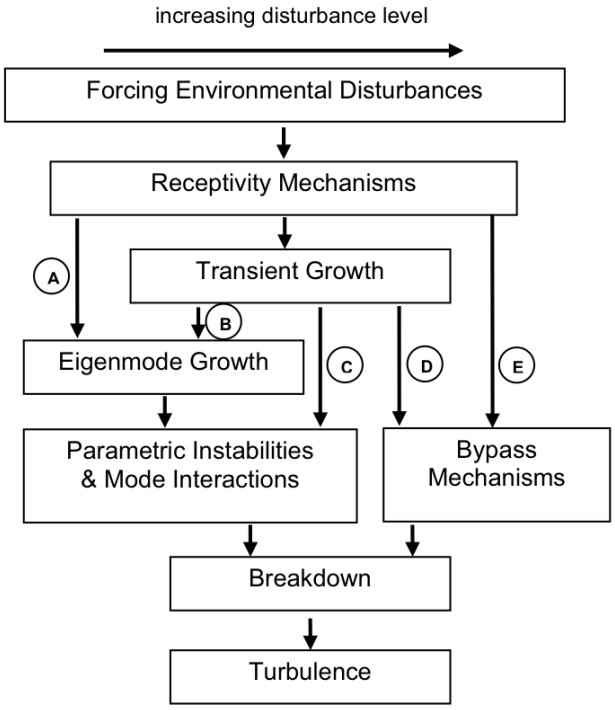

Figure 2.6: Path from receptivity to laminar-turbulent transition.

Some special cases where the path of transition to turbulence correspond to the critical Reynolds number are given. The path A corresponds to the Reynolds number $R > R_L$ (e.g. $R > 5772$ for the plane Poiseuille flow) while the path C corresponds to the Reynolds number $R_G < R < R_L$ (e.g. $49.6 < R < 5772$ for the plane Poiseuille flow).

2.5 General flow control

The flow control techniques allow to modify a current state of a flow to another state or maintain its current state whatever external disturbance. We can act everywhere inside the flow or only at the walls (by modifying the boundary conditions). The potential benefits of the flow control are in engineering applications, e.g. in transportation domain (aircraft and vehicle water), environment domain (combustion, bioengineering) and chemical industry: drag reduction, lift enhancement in aerospace, aerodynamic noises reduction, enhance mixing etc.

The flow control is based on the boundary layer theory, transitional and turbulent shear flow theory. And the flow control may be passive or active such as natural laminar flow, laminar flow control, polymer drag reduction, chaos control and networks control. The passive or active strategy can be considered to control a flow with common control objectives [Gad-el Hak, 2000]: delaying or advancing transition from laminar to tur-

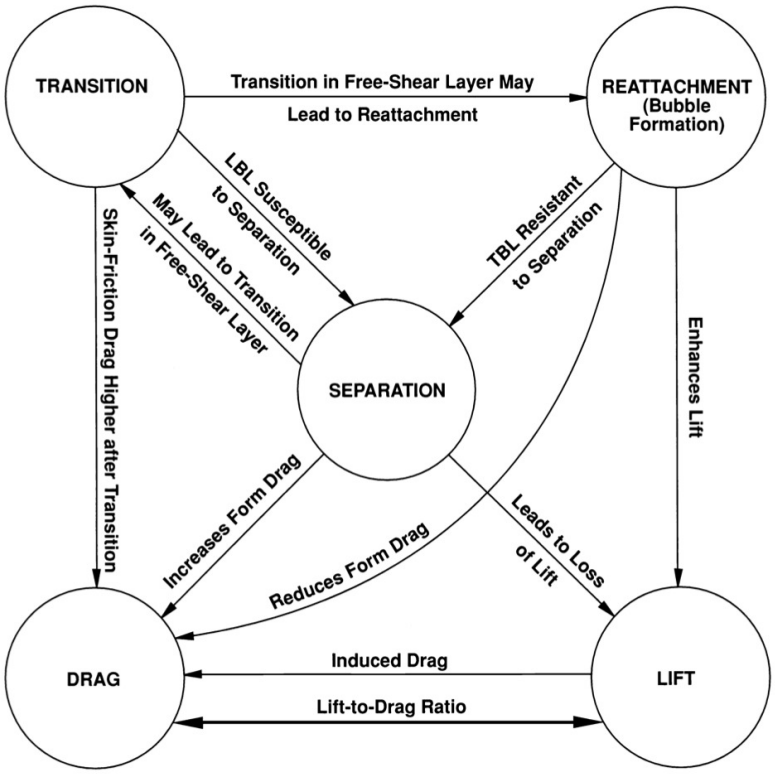

Figure 2.7: Interrelation between flow control goals.

bulent flow, suppressing or enhancing turbulence, preventing or provoking separation. And their goals are: reducing the drag, enhancing the lift, augmenting the mixing of mass, momentum or energy, suppressing the flow induced noise and a combination of all above. The interrelation of flow control goals is shown in Figure 2.7 (taken from [Gad-el Hak, 2000]). The most control applications are found in the scientific literature such as control of jets, transition control, separation control, wake vortex control and drag reduction.

In this thesis, a feedback control is focused on the flow control. This technique is based on the frontier of flow, or more precisely the boundary conditions, as the technique blowing and suction [Wygnanski, 1997], when the sensors and actuators are available. An example of this technique is applied to the airfoil [Schlichting and Gersten, 2000]. Bewley [Bewley, 1999], [Bewley, 2001] has discussed the future of feedback flow control and the need for a renaissance approach. Therefore, we must understand the fundamental flow physics and the requirements and limitations of control algorithms to achieve a feedback control schemes. The flow control is a combination of fluid mechanics, mathematics and control theory.

In this chapter, some basic definitions about the fluid flow have been given. In the next chapter, the detail of feedback control for a dynamic system will be presented, especially a linear feedback control for the nonlinear dynamic system.

Chapter 3

Fundamentals of Automatic Control

Automatic control is a science at the intersection of engineering and applied mathematics. Its aim is to control a dynamic system and consider the evolution of the dynamic system in time. In the controlled system, the action is required to achieve a desired state $\mathbf{x}^*$ from any initial state and maintain the desired state with any external disturbances to the system. The fundamental concepts in automatic control will be introduced: stability, controllability, observability and stabilization.

3.1 Definition of open-loop control, forcing and closed-loop control

The difference between the open-loop system and the closed-loop system is introduced through a simple example.

3.1.1 Problem description

In this example, our goal is to regulate the temperature of a room from a radiator. A boiler provides the hot water in the radiator, the flow of the radiator is controlled by a valve. We want to act on this valve to achieve the desired temperature whatever the external disturbances: the presence or absence of sunlight, the opening of a window and the change of shape of radiator or valve.

3.1.2 Open-loop control

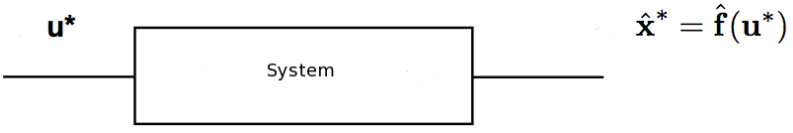

Figure 3.1: Open loop control case.

This approach is based on a complete modeling of the real system. It leads to a relationship (usually very complex) between the flow of hot water volume and the room temperature. Note that this relationship depends on many parameters, such as building materials of the room and the radiator, the shape of the valve which controls the flow of hot water volume, the surface of windows. This model is very complex. An open-loop approach is proposed to write this model, and we must calculate the flow of hot water volume via the valve to obtain the desired temperature in the room. Assuming that such as a model can be obtained, the reader suspect that it will be robust to a variation of one of the component parameters. Indeed, this approach is only done if everything has been properly modeled. It seems illusory in practice, it will be very difficult for example to take into account the consequence of the opening of the window or the appearance of the sunlight or any other provision of unmodeled temperature. Therefore, this approach is systematically avoided in automatic control.

3.1.3 Closed-loop control

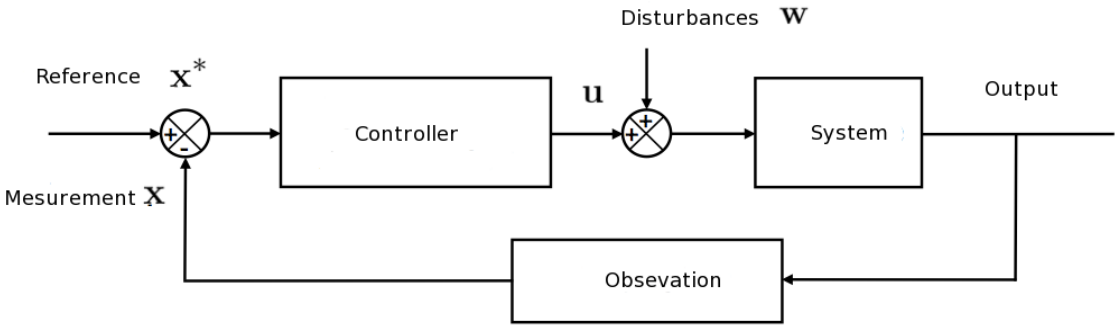

Figure 3.2: Closed loop control case.

This approach is completely different from the open-loop control. This approach is always based on a model linking the actuator to the quantity to be controlled but this model is now very rough. It may be for example sufficient to say that the room temperature will be an increasing function of the opening of the valve. This approach requires a measurement of the ambient temperature. A device will compare the ambient temperature and the desired temperature, then actuates the opening of the valve. Such a device could be for example a proportional control where the action will be proportional to the difference between two temperatures. This approach will depend on less external disturbances: the opening of the window or the presence or absence of the sunlight.

3.2 Benefits of using closed-loop control

In the following section, we clearly prove the benefits of using a closed-loop approach through simple examples.

3.2.1 First example: water tank

In this example, we provide a way of closed loop control for a dynamic system. Moreover, we demonstrate some advantages of the closed loop control with respect to the open loop control

3.2.1.1 Problem description

We want to regulate the depth water h to the desired depth water h^* in a water tank as described in Figure 3.3. The water tank is filled by the flow in q_i while the flow out is q_o. And the surface is denoted S.

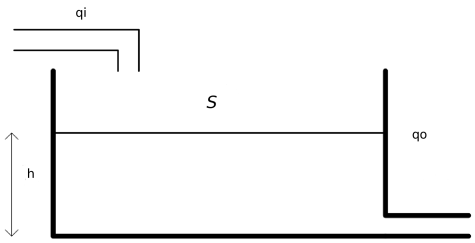

Figure 3.3: Open loop control in the water tank.

The dynamic equation of the water tank is the equation of the volume variation

$$\text{volume variation} = \text{flow in - flow out}, \tag{3.1}$$

that is

$$S\frac{dh(t)}{dt} = q_i(t) - q_o(t), \tag{3.2}$$

where $q_o(t) = \alpha h(t)$ where α is unknown parameter, however this parameter depends on the geometry of the water tank and the way of the flow out. Therefore, we get the dynamic equation of the depth water

$$S\frac{dh(t)}{dt} = q_i(t) - \alpha h(t) \tag{3.3}$$

Providing the flow in $q_i(t)$ in order to achieve the desired depth water, we give two approaches to do it in the next section.

3.2.1.2 Behavior of the system in the open loop control case

This approach does not use any measurement and the flow in $q_i(t)$ is proposed to be constant

$$q_i(t) = q_i^* = \alpha h^*. \tag{3.4}$$

Note that in practice, it is difficult to regulate $q_i(t)$ to the exact value because $q_i(t)$ depends on the unknown parameter α. We have

$$S\frac{dh(t)}{dt} = q_i^* - \alpha h(t) \Rightarrow \frac{dh(t)}{dt} = \frac{q_i^*}{S} - \frac{\alpha}{S}h(t) \Rightarrow h(t) = \frac{q_i^*}{\alpha}(1 - e^{-\frac{\alpha t}{S}}) \tag{3.5}$$

We denote $h_\infty = \frac{q_i^*}{\alpha}$ and $\tau = \frac{S}{\alpha}$. We get

$$h(t) = h_\infty(1 - e^{-\frac{\alpha t}{S}}) \tag{3.6}$$

It is clear that the system is stable without the control signal. It means that the depth water h tends toward the desired value $h(t) \to h_\infty$, in theory after an infinite time and in practice a time $t = 3\tau$ (the error between the depth water and its desired value is 5%). However, we cannot give the exact time $t = 3\tau$ because the parameter τ depends on the surface S and the unknown parameter α.

We consider the behavior of the system when the measurement error occurs. When the surface occurs an error $S^{'}$ and the response time depends on the parameter $\tau^{'}$

$$\tau^{'} = \frac{S^{'}}{\alpha} = \frac{S^{'}}{S}\tau, \tag{3.7}$$

therefore we cannot give the exact value of response time. And when the flow in occurs an error $q_i^{'}$, the depth water is given

$$h^{'*} = \frac{q_i^{'}}{\alpha} = \frac{q_i^{'}}{q_i^*}h^* \Rightarrow \frac{h^* - h^{'*}}{h^*} = 1 - \frac{q_i^{'}}{q_i^*}, \tag{3.8}$$

we have an error on the desired value of the depth water. Another case, when the unknown parameter α occurs an error $\alpha^{'}$. The response time has an error

$$\tau^{'} = \frac{S}{\alpha^{'}} = \frac{\alpha}{\alpha^{'}}\tau, \tag{3.9}$$

and the desired value of the depth water has an error

$$h^{'*} = \frac{q_i^*}{\alpha^{'}} = \frac{\alpha}{\alpha^{'}}h^* \Rightarrow \frac{h^* - h^{'*}}{h^*} = 1 - \frac{\alpha}{\alpha^{'}} \tag{3.10}$$

Conclusion, the above results allow us to ensure that the system behavior is not robust to the measurement error when the open loop control case is used. Furthermore, the behavior of the system depends on the system parameters. Therefore, we need an approach which is robust to the measurement error and leads the system behavior to be independently on the system parameters.

3.2.1.3 Behavior of the system in the closed loop control case

In this section, we consider the system behavior when we use the closed loop control case as described in Figure 3.4. To do it, we use a sensor to capture the depth water $h(t)$ and regulate the flow in $q_i(t)$ to achieve the desired value h^*. A feedback control law is proposed as a function of $h(t)$

$$q_i(t) = K_p(h_p - h(t)) - K_d\dot{h}(t), \tag{3.11}$$

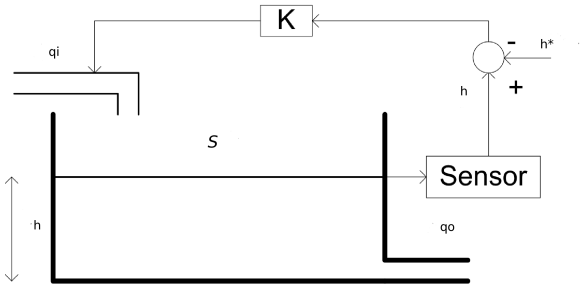

Figure 3.4: Closed loop control in a water tank.

where K_p and K_d are the gain of control law while h_p is a fixed parameter. We have the closed loop of dynamic equation

$$\begin{aligned} S\dot{h}(t) &= q_i(t) - \alpha h(t) = K_p(h_p - h(t)) - K_d\dot{h}(t) - \alpha h(t) && (3.12)\\ (1+\frac{K_d}{S})\dot{h}(t) &= \frac{K_p}{S}h_p - \frac{K_p+\alpha}{S}h(t) && (3.13)\\ \dot{h}(t) &= \frac{K_p}{K_d+S}h_p - \frac{K_p+\alpha}{K_d+S}h(t) && (3.14)\\ h(t) &= \frac{K_p}{K_p+\alpha}h_p(1-e^{-\frac{K_p+\alpha}{K_d+S}t}) && (3.15) \end{aligned}$$

Solving the dynamic equation, we obtain $h(t)$, we must find h_p to achieve the desired value $h(t) = h^*$ at the infinite time. We propose the depth water

$$h(t) = h^*(1 - e^{-\frac{t}{\tau}}) \tag{3.16}$$

therefore, we get

$$\begin{cases} h^* &= \dfrac{K_p}{K_p+\alpha}h_p \Rightarrow h_p = \dfrac{K_p+\alpha}{K_p}h^* \\ \tau &= \dfrac{K_d+S}{K_p+\alpha} \end{cases} \tag{3.17}$$

Consequently, the control signal is given by

$$q_i(t) = K_p(h_p - h(t)) - K_d\dot{h}(t) = K_p(h_p - \frac{K_p}{K_p+\alpha}h_p(1-e^{-\frac{K_p+\alpha}{K_d+S}t})) + \frac{K_p}{K_d+S}h_p e^{-\frac{K_p+\alpha}{K_d+S}t} \tag{3.18}$$

and we get

$$\begin{aligned} q_i(t) &= \alpha h^* + h^*\frac{K_p\tau - K_d}{\tau}e^{-\frac{t}{\tau}} && (3.19)\\ q_i(0) &= \frac{K_p+\alpha}{K_d+S}Sh^* && (3.20)\\ q_i(\infty) &= \alpha h^* && (3.21)\\ \frac{q_i(0)}{q_i(\infty)} &= \frac{K_p+\alpha}{K_d+S}Sh^*\frac{1}{\alpha h^*} = \frac{K_p+\alpha}{K_d+S}\frac{S}{\alpha} = \frac{\tau_{ol}}{\tau_{cl}} && (3.22) \end{aligned}$$

where $\tau_{cl} = \frac{K_d+S}{K_p+\alpha}$ and $\tau_{ol} = \frac{S}{\alpha}$. Indeed, we can adjust the response time to achieve the reference through τ_{cl}. Note that this time only does not depend on any more the system's parameter. Furthermore, we can also dispense the precise knowledge of the surface S and α when we impose $K_p >> \alpha$ and $K_d >> S$, therefore we get

$$\begin{cases} \tau_a &= \dfrac{K_d}{K_p} \approx \dfrac{K_d+S}{K_p+\alpha} = \tau_{cl} \\ h_{pa} &= h^* \approx \frac{K_p+\alpha}{K_p} h^* = h_p \end{cases} \tag{3.23}$$

Indeed, the behavior of the system in the closed loop case does not depend on the system's parameter and we can set the response time τ. Furthermore, we can write the control input

$$q_i(t) = \alpha h^* + h^* \frac{K_p\tau - K_d}{\tau} e^{-\frac{t}{\tau}} = \alpha h^* - \alpha h^* K_p \frac{\frac{K_d}{K_p} - \frac{S}{\alpha}}{K_d+S} e^{-\frac{t}{\tau}} = \frac{K_p}{K_p+\alpha} h_p(\alpha - \beta e^{-\frac{t}{\tau_{cl}}}) \tag{3.24}$$

where

$$\begin{cases} \tau_{cl} &= \dfrac{\alpha\tau_{ol} + K_p\tau_a}{\alpha + K_p} \\ \beta &= \alpha K_p \dfrac{\tau_a - \tau_{ol}}{K_p\tau_a + \alpha\tau_{ol}} \end{cases} \tag{3.25}$$

If we can set $\tau_a = \tau_{ol}$ by imposing $\frac{K_d}{K_p} = \frac{S}{\alpha}$ or obtain a constant flow $\beta = 0$ and $\tau_{cl} = \tau_{ol} = \tau_a$, we obtain $q_i(t) = \alpha h^*$ as the open loop case does. Note that when $K_p >> \alpha$ and $K_d >> S$, the behavior of the system is robust to the system's parameter. The results allow us to emphasize the advantages of the closed loop control case with respect to the open loop control case.

In the following section, we introduce another important issue in automatic control: the stability of the controlled system, still through a simple example

3.2.2 Second example: pendulum

3.2.2.1 Problem description

We want to regulate the position $\theta(t)$ of a pendulum, as described in Figure 3.5. More precisely, we want to act on the torque $\Gamma(t)$ to achieve the desired position θ^*. The length and mass of pendulum are denoted by l and m, respectively while the gravitational acceleration is denote by g. The dynamic equation of this pendulum is given by

$$\ddot{\theta}(t) + \frac{k}{ml^2}\dot{\theta}(t) + \frac{g}{l} sin(\theta) = \Gamma(t). \tag{3.26}$$

By using the change of variable, $\mathbf{x}_1(t) = \theta(t)$ and $\mathbf{x}_2(t) = \dot{\theta}(t) = \dot{\mathbf{x}}_1(t)$, $2\lambda = \dfrac{k}{ml^2}$, $\omega_0^2 = \dfrac{g}{l}$ and $\mathbf{u}(t) = \Gamma(t)$. Therefore, the nonlinear pendulum (3.26) becomes

$$\begin{cases} \dot{\mathbf{x}}_1(t) = \mathbf{x}_2(t) \\ \dot{\mathbf{x}}_2(t) = -\omega_0^2 sin(\mathbf{x}_1(t)) - 2\lambda\mathbf{x}_2(t) + \mathbf{u}(t) \end{cases} \tag{3.27}$$

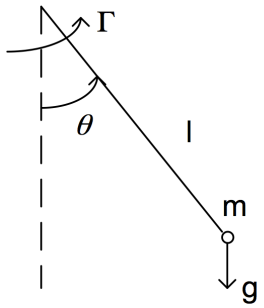

Figure 3.5: Model of pendulum.

Note that since $sin(\theta(t)) \approx \theta(t)$ when $-\pi/9 \leq \theta(t) \leq +\pi/9$, we obtain an approximation model

$$\begin{cases} \dot{\mathbf{x}}_1(t) = \mathbf{x}_2(t) \\ \dot{\mathbf{x}}_2(t) = -\omega_0^2 \mathbf{x}_1(t) - 2\lambda \mathbf{x}_2(t) + \mathbf{u}(t) \end{cases} \tag{3.28}$$

And we can rewrite (3.28) by

$$\begin{cases} \dot{\mathbf{x}}(t) &= \mathbf{A}\mathbf{x}(t) + \mathbf{B}\mathbf{u}(t) \\ \mathbf{y}(t) &= \mathbf{C}\mathbf{x}(t) \end{cases} \tag{3.29}$$

where $\mathbf{x}(t) = \begin{bmatrix} \mathbf{x}_1(t) \\ \mathbf{x}_2(t) \end{bmatrix}$, $\mathbf{y}(t) = \theta(t)$ and the matrices are defined by

$$\mathbf{A} = \begin{bmatrix} 0 & 1 \\ -\omega_0^2 & -2\lambda \end{bmatrix}, \mathbf{B} = \begin{bmatrix} 0 \\ 1 \end{bmatrix}, \mathbf{C} = \begin{bmatrix} 1 & 0 \end{bmatrix}$$

3.2.2.2 Behavior of the system in the closed loop control case

We propose a proportioned and derive control law $\mathbf{u}(t) = q - \mathbf{K}\mathbf{x}(t) = q - k_1\mathbf{x}_1(t) - k_2\mathbf{x}_2(t)$ for the nonlinear pendulum (3.27), where q is a precompensator and k_1, k_2 are given based on studying the behavior of the system (3.28). The pendulum is not only considered around $\theta^* = 0$, therefore we consider the precompensator. Note that the precompensator is calculated from the desired position, $q = H\mathbf{y}^*$ with $\mathbf{y}^* = \theta^*$. We give the way where H is calculated. The closed loop of the system (3.27) becomes

$$\begin{cases} \dot{\mathbf{x}}_1(t) = \mathbf{x}_2(t) \\ \dot{\mathbf{x}}_2(t) = -\omega_0^2 sin(\mathbf{x}_1(t)) - 2\lambda \mathbf{x}_2(t) + q - k_1\mathbf{x}_1(t) - k_2\mathbf{x}_2(t) \end{cases} \tag{3.30}$$

Therefore, the closed-loop system of (3.26) becomes

$$\ddot{\theta}(t) + \frac{k}{ml^2}\dot{\theta}(t) + \frac{g}{l}sin(\theta) = q - k_1\theta(t) - k_2\dot{\theta}(t). \tag{3.31}$$

When the pendulum is at the equilibrium point, we have $\ddot{\theta}(t) = \dot{\theta}(t) = 0$ and $\theta(t) = \theta^*$. From (3.31), it is easy to see that

$$H = \frac{\omega_0^2 sin(\theta^*) + k_1\theta^*}{\theta^*} \tag{3.32}$$

Therefore, the control law is control law $\mathbf{u}(t) = \omega_0^2 sin(\theta^*) + k_1\theta^* - k_1\mathbf{x}_1(t) - k_2\mathbf{x}_2(t)$

In the approximation model, the closed-loop system (3.28) becomes

$$\begin{cases} \dot{\mathbf{x}}_1(t) = \mathbf{x}_2(t) \\ \dot{\mathbf{x}}_2(t) = -\omega_0^2\mathbf{x}_1(t) - 2\lambda\mathbf{x}_2(t) + \omega_0^2\theta^* + k_1\theta^* - k_1\mathbf{x}_1(t) - k_2\mathbf{x}_2(t) \end{cases} \tag{3.33}$$

We use $\omega_0 = 4$, $\lambda = 1$ and $k_1 = -14$, $k_2 = 0$, the closed-loop system (3.33) becomes

$$\begin{cases} \dot{\mathbf{x}}_1(t) = \mathbf{x}_2(t) \\ \dot{\mathbf{x}}_2(t) = -2\mathbf{x}_1(t) + 2\theta^* \end{cases} \tag{3.34}$$

The solution of (3.34) is given by

$$\begin{cases} \mathbf{x}_1(t) = \theta^* + [(x_{10} - \theta^*)cos(t) + (x_{10} + x_{20} - \theta^*)sin(t)]e^{-t} \\ \mathbf{x}_2(t) = [x_{20}cos(t) + (-2x_{10} - x_{20} + 2\theta^*)sin(t)]e^{-t} \end{cases} \tag{3.35}$$

where x_{10} and x_{20} are the initial conditions of $\mathbf{x}_1(t)$ and $\mathbf{x}_2(t)$, respectively. When the time is large enough, the position $\theta(t)$ becomes the desired position θ^*. We must emphasize that k_1 and k_2 are calculated based on the analysis of the behavior of the system (3.28). However, we do not give the way to calculate k_1 and k_2, we give this way in the next sections.

Indeed, the most important problem is to know the behavior of the true system, that is where the control law is injected in (3.26). The close-loop true system is

$$\ddot{\theta}(t) + (2\lambda + k_2)\dot{\theta}(t) + k_1\theta(t) + \omega_0^2 sin(\theta) = \omega_0^2 sin(\theta^*) + k_1\theta^*. \tag{3.36}$$

The behavior of the system (3.36) is depicted in Figure (3.6). The green area corresponds to the initial conditions $(\theta, \dot{\theta})$ where the system (3.36) effectively reaches the desired value $(\theta^*, 0)$ in contrast to the red area where the system (3.36) is not able to reach it. Two blue lines corresponds to the interval $[-\pi/9, \pi/9]$ where the approximation $sin(\theta) = \theta$ is considered to be true. Firstly, we can see that the system converges for a large domain outside the validity domain for which the control law has been designed. It also shows that even in the domain for which the assumption is validated the control law does not systematically converge. Four trajectories have been pointed out to illustrate this result.

The goal of automatic control is to design the simplest control law that will ensure that largest convergence area of the control law. This domain is called the stability domain. It is recovered though a stability analysis as will be detailed in section 3.4.2.

3.3 Representation of a dynamic system

A natural choice to represent a dynamic system consists in describing the link between the action and its consequence on the system to control, that is between the input signal and the output one provided from measurements. In the example of the control water depth a model could be given by the relation (3.2). On other hand, in the case of the pendulum the relation (3.26) could be also a model. This kind of representation is

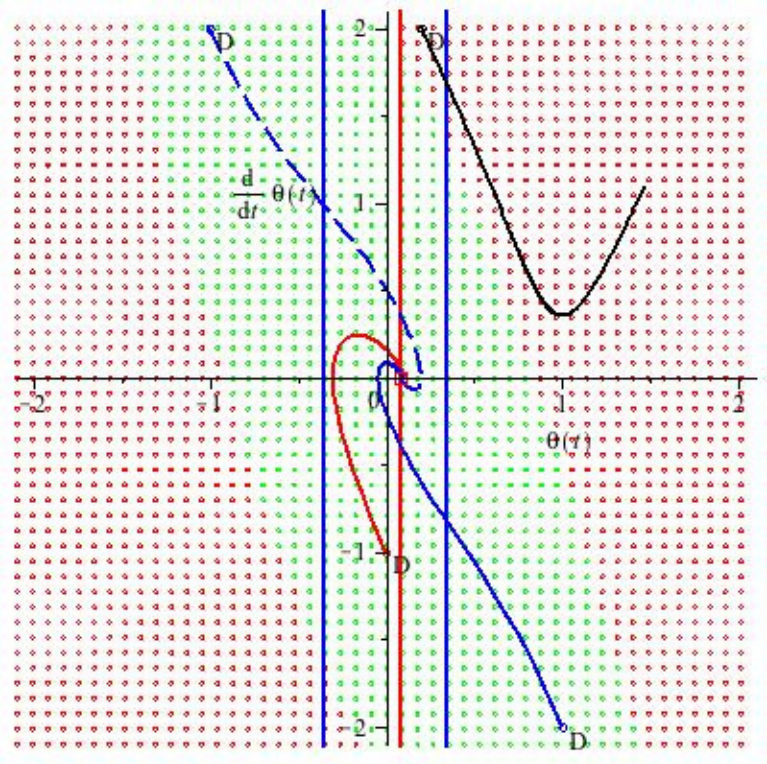

Figure 3.6: Behavior of the pendulum.

known in automatic control as an internal representation. An external representation also exists, in this case, the goal is to emphasize the relevance of other variables that are not input or outputs while taking into account the whole dynamics of the system. The state space representation is the most popular one.

3.3.1 State space representation

A state space representation is a mathematical model of a physical system as a set of input, output and state variables related by first-order differential equations. We shall give the definitions of state, state variable, state space.

Definition 3.3.1 *State, state variable, state vector, state space*

- *State: the state of a dynamic system is the smallest possible subset of system variables or quantities such as knowledge of the set at time $t = t_0$, as well as the input signal for $t \geq t_0$, is sufficient completely to determine the behavior of the system for $t \geq t_0$.*

- *State variables: these are variables or quantities that constitute the state of the system.*

- *State vector: more mathematical, it represents the state of system by a concatenation of all the state variables in a vector, a priori real dimension n, which is denoted by* $\mathbf{x}(t) = \begin{bmatrix} \mathbf{x}_1(t) & \mathbf{x}_2(t) & \dots & \mathbf{x}_n(t) \end{bmatrix}^\top$.
- *State space: this is simply the vector space in which the state vector* $\mathbf{x}$ *is likely to change every instance of* $\mathbf{x}$ *is associated with a point in this space. This space is* $\mathbb{R}^n$.

Therefore, a dynamic system can be represented by a state space representation

$$\begin{cases} \dot{\mathbf{x}}(t) & = \begin{bmatrix} \dot{\mathbf{x}}_1(t) \\ \dot{\mathbf{x}}_2(t) \\ \vdots \\ \dot{\mathbf{x}}_n(t) \end{bmatrix} = f(\mathbf{x}(t), \mathbf{u}(t), t) = \begin{bmatrix} f_1(\mathbf{x}(t), \mathbf{u}(t), t) \\ f_2(\mathbf{x}(t), \mathbf{u}(t), t) \\ \vdots \\ f_n(\mathbf{x}(t), \mathbf{u}(t), t) \end{bmatrix} \\ \mathbf{y}(t) & = g(\mathbf{x}(t), \mathbf{u}(t), t) \end{cases} \tag{3.37}$$

where $\mathbf{x}(t)$, $\mathbf{y}(t)$ and $\mathbf{u}(t)$ are the state vector, the output vector and the input (or control) vector, respectively. The dimension of the state vector, the output vector and the input vector are n, m and p, respectively that we can denote $\mathbf{x}(t) \in \mathbb{R}^n$, $\mathbf{y}(t) \in \mathbb{R}^m$ and $\mathbf{u}(t) \in \mathbb{R}^p$. The functions f and g are linear or nonlinear functions.

Therefore, we can give the state space representation of the nonlinear pendulum (3.26) by

$$\begin{cases} \dot{\mathbf{x}}_1(t) = \mathbf{x}_2(t) \\ \dot{\mathbf{x}}_2(t) = -\omega_0^2 sin(\mathbf{x}_1(t)) - 2\lambda \mathbf{x}_2(t) + \mathbf{u}(t) \\ \mathbf{y}(t) = \mathbf{x}_1(t) \end{cases} \tag{3.38}$$

However, note that the specific physical quantities that define the state are not unique, although their number is unique. We can use $\mathbf{x}_1(t) = \theta(t)$ and $\mathbf{x}_2(t) = \dot{\theta}(t) = \dot{\mathbf{x}}_1(t)$ or $\mathbf{x}_1(t) = \theta(t) + \pi$ and $\mathbf{x}_2(t) = \dot{\theta}(t) = \dot{\mathbf{x}}_1(t)$ but the dimension of the state vector is always two.

3.3.2 Stability of dynamic systems

Stability of a system is a fundamental issue. Indeed, an unstable system could be dangerous to use in practice since its behavior is not fully predictable. However, providing a precise definition is not so simple. We give here some basic definitions.

3.3.2.1 BIBO stability

This definition is the most intuitive one.

Definition 3.3.2 *BIBO (Bounded Input Bounded Output) stability*

- *A system is defined to be BIBO stable if and only if, for all the initial state* $\mathbf{x}_0 = \mathbf{x}(0)$*, every input* $\mathbf{u}(t)$ *is bounded, the output* $\mathbf{y}(t)$ *is also.*

- *Another definition of BIBO stability, more mathematical and " philosophically " somewhat different, may be given: noting* $\mathbf{y}^*(t)$ *the impulse response of the model, it is BIBO stable if and only if, there exists a scalar* k *satisfying* $0 < k < \infty$ *and*

$$\int_0^\infty \mid \mathbf{y}^*(\tau) \mid d\tau \leq k \tag{3.39}$$

A BIBO-stable model can be interpeted in this second definition as a model whose impulse response is of finite energy signal. It is not easy to directly exploit this last formulation. However, the study of stability of a system is through the concept of stability of equilibrium states, especially in the state space.

In the next section the stability is defined through the state representation leading to an "internal" definition of the stability [Sastry and Bodson, 1989].

3.3.2.2 Stability of an equilibrium state

We first have to define what is an equilibrium state. To do it, we consider the system

$$\begin{cases} \dot{\mathbf{x}}(t) & = f(\mathbf{x}(t), t) \\ \mathbf{x}(t_0) & = \mathbf{x}_0 \end{cases} \tag{3.40}$$

Definition 3.3.3 *A system is said to be in equilibrium state if its state is not modified when the system is not controlled. That is if* $f(\mathbf{x}(t), t) = 0$ *for all* $t \geq 0$.

By translating the origin to an equilibrium point $\mathbf{x}_0$, we can make the origin 0 an equilibrium point. This is of great notational help, and we shall assume henceforth 0 is an equilibrium point of (3.40).

3.3.2.3 Stability definitions

Informally, $\mathbf{x} = 0$ is a stable equilibrium point, if the trajectory $\mathbf{x}(t)$ remains close to 0 if the initial condition $\mathbf{x}_0$ is close to 0. More precisely, we say

Definition 3.3.4 *Stability in the Sense of Lyapunov*
$\mathbf{x} = 0$ *is called a stable equilibrium point of (3.40), if, for all* $t_0 \geq$ *and* $\epsilon > 0$, *there exists* $\delta(t_0, \epsilon)$ *such that*

$$\mid \mathbf{x}_0 \mid < \delta(t_0, \epsilon) \Rightarrow \mid \mathbf{x}(t) \mid < \epsilon \text{ for all } t \geq t_0 \tag{3.41}$$

where $\mathbf{x}(t)$ *is the solution of (3.40), starting from* $\mathbf{x}_0$ *at* t_0.

Definition 3.3.5 *Asymptotic stability*
$\mathbf{x} = 0$ *is called an asymptotically stable equilibrium point of (3.40), if,*

- $\mathbf{x} = 0$ *is a stable equilibrium point of (3.40),*

- $\mathbf{x} = 0$ *is attractive, that is, for all* $t_0 \geq 0$*, there exists* $\delta(t_0)$*, such that*

$$| \mathbf{x}_0 | < \delta(t_0, \epsilon) \Rightarrow \lim_{t \to \infty} | \mathbf{x}(t) | = 0 \tag{3.42}$$

Definition 3.3.6 *Global asymptotic stability*
$\mathbf{x} = 0$ *is called a globally asymptotically stable equilibrium point of (3.40), if it is asymptotically stable and* $\lim_{t\to\infty} | \mathbf{x}(t) | = 0$ *for all* $\mathbf{x}_0 \in \mathbb{R}^n$.

Global uniform asymptotic stability is defined likewise. Note that the speed of convergence is not quantified in the definitions of asymptotic stability. In the following definition, the convergence to zero is required to be at least exponential.

Definition 3.3.7 *Exponential stability, rate of convergence*
$\mathbf{x} = 0$ *is called an exponetially stable equilibrium point of (3.40), if there exists* m, $\alpha > 0$ *such that the solution* $\mathbf{x}(t)$ *satisfies*

$$| \mathbf{x}(t) | \leq m e^{-\alpha(t-t_0)} | \mathbf{x}_0 | \tag{3.43}$$

for all $\mathbf{x}_0 \in \mathbb{R}^n$, $t \geq t_0 \geq 0$. *The constant* α *is called the rate of convergence.*

The main problem in automatic control is to synthetize a control law that ensures that the closed loop system is stable. To analyze the stability of a dynamic system a powerful tools is used : the Lyapunov Stability Theory.

3.3.2.4 Lyapunov stability theory

The so-called Lyapunov second method enables one to determine the nature of stability of an equilibrium point of (3.40) without explicitly integrating the differential equation. This approach is based on the use of a so-called Lyapunov candidate function.

Definition 3.3.8 *Lyapunov function*
A Lyapunov function is a Lyapunov candidate function, denoted $V(\mathbf{x})$ *such that*

$$V(\mathbf{x}) > 0 \ \forall \mathbf{x} \neq 0, \ V(0) = 0, \tag{3.44}$$

and

$$\dot{V}(\mathbf{x}) \leq 0 \ \forall \mathbf{x} \neq 0, \ \dot{V}(\mathbf{x}) = 0 \ \mathbf{x} = 0, \tag{3.45}$$

We present the theorem of the local stability based on the analysis of the Lyapunov function. The local stability is concerned around the equilibrium point. We present the following theorems which give the stability of a system based on the analysis of the Lyapunov function.

Theorem 3.3.1 *If there exists* $\Omega \in \mathbb{R}^n$ *such that*

- $V(\mathbf{x}) > 0 \ \forall \mathbf{x} \neq 0 \in \Omega, V(0) = 0$

- $\dot{V}(\mathbf{x}) \leq 0 \ \forall \mathbf{x} \in \Omega$

then the equilibrium point $\mathbf{x} = 0$ *is stable. In addition, if* $\dot{V}(\mathbf{x}) < 0 \ \forall \mathbf{x} \neq 0$*, then* $\mathbf{x} = 0$ *is asymptotically stable.*

Theorem 3.3.2 *So that we can ensure that the Lyapunov theorem can conclude the global stability of a system, it is necessary that all the hypotheses of this theorem are satisfied, but it also requires that the radial boundedness condition exists, that is to say*

$$\|\mathbf{x}\| \to \infty \Rightarrow V(\mathbf{x}) \to \infty \tag{3.46}$$

The following theorem summarizes the conditions

Theorem 3.3.3 *If there exists a function* V *such that*

- $V(\mathbf{x}) > 0 \ \forall \mathbf{x} \neq 0, V(0) = 0$
- $\|\mathbf{x}\| \to \infty \Rightarrow V(\mathbf{x}) \to \infty$
- $\dot{V}(\mathbf{x}) < 0 \ \forall \mathbf{x} \neq 0$

then $\mathbf{x} = 0$ *is globally asymptotically stable.*

3.3.3 Observability and controllability

Even if stability issues are very important, observability and controllability issues are also very important.

Definition 3.3.9 *Controllability*
A system is controllable if for any $\mathbf{x}_0$ *and* $\mathbf{x}_1$*, there exists an input signal* $\mathbf{u}(t)$ *(finite energy) that allows the system pass from the state* $\mathbf{x}_0$ *to the state* $\mathbf{x}_1$ *in a finite times.*

Definition 3.3.10 *Observability*
A system is observable if, for any time t_0*, there exists a finite time interval* $[t_0, t_1]$ *such that the state* $\mathbf{x}(t_0)$ *can be determined using the input signal* $\mathbf{u}(t)$ *and the output signal* $\mathbf{y}(t)$*.*

3.4 Linearized and linear systems

Of course, dealing with nonlinear equations is rarely a simple task. Thus, very often a linearization around an equilibrium point is considered. The first observation is often annoying that the differential algebraic equations are not linear in terms of the involved quantities and their successive derivatives. Or, the nonlinear models are inherently difficult to handle. This means in practice that these nonlinear equations make difficult the analysis of system behavior and, more importantly, the control law. Therefore, even if it is a violation of the principle of accurate description of the system dynamics, we often decide to work in a range value of quantities around a central value constituting

what is agreed call a function point. When the system is considered to be not too far from the function point, we can approach the nonlinear equation by an approximation but certainly linear equations. Without repeating the known concepts which can be used to obtain this approximation, the nonlinear system is usually approximated by using limited development or first order Taylor development of some mathematical functions. So, we call the nonlinear system and its "linearized tangent" which is linearized. As the previously example, the results in Figure 3.6 allows us to ensure that we have no problem when we use the linear model to give a control law.

3.4.1 Representation of linear or linearized systems

As in the case of nonlinear system, we can define a state space representation. However, as we shall show in section 3.4.1.2, another powerful representation exists

3.4.1.1 State space representation

We shall give the state space representation of the nonlinear system around its equilibrium point. Therefore, we calculate the equilibrium point of the nonlinear system (3.37)

$$\begin{cases} f(\mathbf{x}_e(t), \mathbf{u}_e(t), t) &= 0 \\ \mathbf{y}_e(t) &= g(\mathbf{x}_e(t), \mathbf{u}_e(t), t). \end{cases} \tag{3.47}$$

The linearization of the nonlinear system (3.37) around the equilibrium point $(\mathbf{x}_e(t), \mathbf{u}_e(t))$ is given by

$$\begin{cases} \dot{\tilde{\mathbf{x}}}(t) &= \mathbf{A}(t)\tilde{\mathbf{x}}(t) + \mathbf{B}(t)\tilde{\mathbf{u}}(t) \\ \tilde{\mathbf{y}}(t) &= \mathbf{C}(t)\tilde{\mathbf{x}}(t) + \mathbf{D}(t)\tilde{\mathbf{u}}(t) \end{cases} \tag{3.48}$$

where $\tilde{\mathbf{x}}(t) = \mathbf{x}(t) - \mathbf{x}_e(t)$, $\tilde{\mathbf{u}}(t) = \mathbf{u}(t) - \mathbf{u}_e(t)$, $\tilde{\mathbf{y}}(t) = \mathbf{y}(t) - \mathbf{y}_e(t)$. $\mathbf{A}(t)$ is the state matrix, $\mathbf{B}(t)$ is the input matrix, $\mathbf{C}(t)$ is the output matrix and $\mathbf{D}(t)$ is the feedforward matrix. These matrices are defined by

$$\begin{cases} \mathbf{A}(t) &= \begin{bmatrix} \frac{\partial f_1}{\partial \mathbf{x}_1}(\mathbf{x}_e(t), \mathbf{u}_e(t), t) & \dots & \frac{\partial f_1}{\partial \mathbf{x}_n}(\mathbf{x}_e(t), \mathbf{u}_e(t), t) \\ \vdots & \ddots & \vdots \\ \frac{\partial f_n}{\partial \mathbf{x}_1}(\mathbf{x}_e(t), \mathbf{u}_e(t), t) & \dots & \frac{\partial f_n}{\partial \mathbf{x}_n}(\mathbf{x}_e(t), \mathbf{u}_e(t), t) \end{bmatrix} \\ \mathbf{B}(t) &= \begin{bmatrix} \frac{\partial f_1}{\partial \mathbf{u}}(\mathbf{x}_e(t), \mathbf{u}_e(t), t) \\ \vdots \\ \frac{\partial f_n}{\partial \mathbf{u}}(\mathbf{x}_e(t), \mathbf{u}_e(t), t) \end{bmatrix} \\ \mathbf{C}(t) &= \begin{bmatrix} \frac{\partial g}{\partial \mathbf{x}_1}(\mathbf{x}_e(t), \mathbf{u}_e(t), t) & \dots & \frac{\partial g}{\partial \mathbf{x}_n}(\mathbf{x}_e(t), \mathbf{u}_e(t), t) \end{bmatrix} \\ \mathbf{D}(t) &= \frac{\partial g}{\partial \mathbf{u}}(\mathbf{x}_e(t), \mathbf{u}_e(t), t). \end{cases} \tag{3.49}$$

For simplicity and without loss of generality, it is assumed that $\mathbf{x}_e(t) = \mathbf{u}_e(t) = \mathbf{y}_e(t) = 0$, the linearization of the nonlinear system (3.37) is simplified

$$\begin{cases} \dot{\mathbf{x}}(t) &= \mathbf{A}(t)\mathbf{x}(t) + \mathbf{B}(t)\mathbf{u}(t) \\ \mathbf{y}(t) &= \mathbf{C}(t)\mathbf{x}(t) + \mathbf{D}(t)\mathbf{u}(t). \end{cases} \tag{3.50}$$

If the system matrices are independent on time, a linear time invariant system will be given by

$$\begin{cases} \dot{\mathbf{x}}(t) &= \mathbf{A}\mathbf{x}(t) + \mathbf{B}\mathbf{u}(t) \\ \mathbf{y}(t) &= \mathbf{C}\mathbf{x}(t) + \mathbf{D}\mathbf{u}(t). \end{cases} \tag{3.51}$$

We can distinguish between the linear system and the linearized system by considering the matrices $\mathbf{A}$, $\mathbf{B}$, $\mathbf{C}$ and $\mathbf{D}$. The system matrices of the linear system are always constant and independent on time while the system matrices of the linearized system may contain the time t and is always considered around an equilibrium point.

3.4.1.2 Transfer matrix

As the previously figures 3.1 and 3.2, a dynamic system can be represented by an external representation which concerns an input/output representation. The input/output relation is called a transfer function. At this step, we have some benefits of using the Laplace transform. We have some ways to get the transfer function but there exists one based on the state space representation. From (3.51), we get

$$\begin{cases} pX(p) &= \mathbf{A}X(p) + \mathbf{B}U(p) \Leftrightarrow X(p) = (p\mathbf{I} - \mathbf{A})^{-1}\mathbf{B}U(p) \\ Y(p) &= \mathbf{C}X(p) + \mathbf{D}U(p), \end{cases} \tag{3.52}$$

where p is the Laplace operator and $X(p)$, $Y(p)$, $U(p)$ are the Laplace transform of $\mathbf{x}(t)$, $\mathbf{y}(t)$, $\mathbf{u}(t)$, respectively. Note that we are not taking into account the initial condition in the transfer function $G(p)$. We get the relation between the input signal and the output signal

$$G(p) = \frac{Y(p)}{U(p)} = \mathbf{C}(p\mathbf{I} - \mathbf{A})^{-1}\mathbf{B} + \mathbf{D} \tag{3.53}$$

The transfer function $D(p)$ is used to investigate the system behavior and provides a basic for determining important system respones characteristics without solving the complete differential equation. This function is usually used in SISO system (single input single output system). The transfer function $G(p)$ can be decomposed by the denominator $D(p)$ and the numerator $N(p)$

$$G(p) = \frac{N(p)}{D(p)} = \frac{b_m p^m + b_{m-1}p^{m-1} + \ldots + b_1 p + b_0}{a_n p^n + a_{n-1}p^{n-1} + \ldots + a_1 p + a_0} \tag{3.54}$$

Definition 3.4.1 *Pokes and zeros*

- *Roots of the transfer function denominator $D(p)$ are called poles of the system*

- *Roots of the transfer function numerator $N(p)$ are called zeros of the system*

The influence of zeros to the system behavior is difficult to estimate, however the influence of poles to system behavior is easy to recognize, especially the stability. Therefore, the denominator $D(p)$ of the transfer function is characteristic function. It is very easy to see that $D(p)$ is calculated by

$$D(p) = det(p\mathbf{I} - \mathbf{A}) \tag{3.55}$$

Note that the roots of the denominator, it means the poles of the system, are the eigenvalues of the state matrix $\mathbf{A}$.

We recall that $G(p) = \mathbf{C}(p\mathbf{I} - \mathbf{A})^{-1}\mathbf{B} + \mathbf{D}$, such matrices are called a realization for $G(p)$. Any restricted realizationn to the controllable and observable part of system is called minimal. It must be clear to the reader's mind that a transfer function whose roots of the denominator are strictly negative real part may suggest that the described system is asymptotically stable, whereas it contains an unstable mode which is uncontrollable and unobservable. Such a mode appears in the state space representation.

3.4.2 Stability analysis

Firstly, let us consider an autonomous system

$$\dot{\mathbf{x}}(t) = \mathbf{A}\mathbf{x}(t) \tag{3.56}$$

In this case, to recover the equilibrium points we have to solve the following equation :

$$\mathbf{A}\mathbf{x}(t) = 0, \tag{3.57}$$

from this equation, we have one or some equilibrium points that depends on the rank of the state matrix $\mathbf{A}$. In the case of $rank(\mathbf{A}) = n \Leftrightarrow det(\mathbf{A}) \neq 0$ (it means that $\mathbf{A}$ has not zero eigenvalue), only one equilibrium point $\mathbf{x}_e = 0$ exists. Other case, $rank(\mathbf{A}) < n \Leftrightarrow det(\mathbf{A}) = 0$ ($\mathbf{A}$ has at least one zero eigenvalue), there exists infinite equilibrium points.

The stability of (3.56) depends on the eigenvalues λ_j of the state matrix $\mathbf{A}$. We give some cases of the system behavior.

In the case of $rank(\mathbf{A}) = n$, the system (3.56) has one equilibrium point, we have

- $\mathcal{R}(\lambda_i) < 0,\ \forall i$ the system is asymptotically stable
- $\exists j \mid \mathcal{R}(\lambda_j) > 0$ the system is unstable
- $\exists j \mid \mathcal{R}(\lambda_j) = 0$ and $\mathcal{R}(\lambda_i) \leq 0,\ \forall i$
  - $\lambda_j = 0$ we cannot conclude
  - $\lambda_{j,I} = \pm j\omega$ the system is stable

In the case of $rank(\mathbf{A}) < n$, the system (3.56) has infinite equilibrium points, we have at least one zero eigenvalue of the state matrix $\mathbf{A}$, the asymptotical stability is impossible. Note that any matrix $\mathbf{A}$ can be transformed into Jordan form with the eigenvalues λ_i of $\mathbf{A}$. The Jordan block is given by

$$\mathbf{J}_k(\lambda_i) = \begin{bmatrix} \lambda_i & 1 & & & 0 \\ 0 & \lambda_i & 1 & & \\ & & \ddots & \ddots & \\ & & & \ddots & 1 \\ 0 & & & & \lambda_i \end{bmatrix} \tag{3.58}$$

Therefore, the Jordan matrix is given in the form

$$\begin{bmatrix} \mathbf{J}_{k1}(\lambda_1) & 0 & & 0 \\ 0 & \mathbf{J}_{k2}(\lambda_2) & & \\ & & \ddots & \\ 0 & & & \mathbf{J}_{kn}(\lambda_n) \end{bmatrix} \tag{3.59}$$

For an eigenvalue λ_i, its algebraic multiplicity is the multiplicity of λ_i as a root of the characteristic polynomial. Its geometric multiplicity is the maximal number of linearly independent eigenvectors corresponding to it. The algebraic multiplicity is larger or equal than the geometric multiplicity. We have

- $\exists j \mid \mathcal{R}(\lambda_j) > 0$ the system is unstable
- $\nexists j \mid \mathcal{R}(\lambda_j) > 0$
  - the Jordan blocks corresponding to each eigenvalue with zero real part are scalar blocks (the geometric multiplicity of these eigenvalues equals its algebraic multiplicity), the system is stable
  - there exists a Jordan block corresponding to eigenvalue with zero real part which is not scalar (the geometric multiplicity of these eigenvalues is strictly lower than its algebraic multiplicity), the system is unstable.

For example, we consider the matrix

$$\mathbf{A} = \begin{bmatrix} -5 & 1 & 2 & 10 \\ 0 & 0 & -1 & -1 \\ -1 & -1 & 0 & 0 \\ 1 & 1 & 0 & 0 \end{bmatrix} \tag{3.60}$$

And the Jordan block and the Jordan matrix are given by

$$\mathbf{J} = \begin{bmatrix} \mathbf{J}_2(0) & 0 & 0 \\ 0 & \mathbf{J}_1(-\frac{5}{2} - \frac{1}{2}\sqrt{57}) & 0 \\ 0 & 0 & \mathbf{J}_1(-\frac{5}{2} + \frac{1}{2}\sqrt{57}) \end{bmatrix} = \begin{bmatrix} 0 & 1 & 0 & 0 \\ 0 & 0 & 0 & 1 \\ 0 & 0 & -\frac{5}{2} - \frac{1}{2}\sqrt{17} & 0 \\ 0 & 0 & 0 & -\frac{5}{2} + \frac{1}{2}\sqrt{17} \end{bmatrix} \tag{3.61}$$

Due to $\lambda = -\frac{5}{2} + \frac{1}{2}\sqrt{57} > 0$ and $\mathbf{J}_2(0) = \begin{bmatrix} 0 & 1 \\ 0 & 0 \end{bmatrix}$ is not a scalar, therefore $\mathbf{A}$ is unstable. Note that

$$det(\lambda\mathbf{I} - \mathbf{A}) = \lambda^2(\lambda + \frac{5}{2} + \frac{1}{2}\sqrt{17})(\lambda + \frac{5}{2} - \frac{1}{2}\sqrt{17}) \tag{3.62}$$

the algebraic multiplicity of $\lambda = 0$ is 2 while the geometric multiplicity is 1.

In conclusion, we have

- $\exists j \mid \mathcal{R}(\lambda_j) > 0$ the system is unstable
- $\nexists j \mid \mathcal{R}(\lambda_j) > 0$
  - $\mathcal{R}(\lambda_i) < 0, \ \forall i$ the system is asymptotically stable
  - the geometric multiplicity of zero eigenvalues equals its algebraic multiplicity, the system is stable
  - the geometric multiplicity of one zero eigenvalue is strictly lower than its algebraic multiplicity, the system is unstable.

We recall that the poles of the transfer function correspond to the eigenvalues of the state matrix $\mathbf{A}$, therefore, the stability of the system is investigated based on the eigenvalues of the state matrix $\mathbf{A}$.

To conclude on the stability of a linear system, the Lyapunov theory can also be used (see section 3.3.2.4). The system (3.56) is asymptotically stable if and only if, there exists a Lyapunov function $V(x) = \mathbf{x}^\top\mathbf{P}\mathbf{x} > 0 (\leftrightarrow \mathbf{P} = \mathbf{P}^\top > 0)$ such that

$$\begin{aligned} & \dot{V}(\mathbf{x}) < 0, \forall \mathbf{x} \neq 0 \\ \Leftrightarrow \quad & \mathbf{x}^\top(\mathbf{A}^\top\mathbf{P} + \mathbf{P}\mathbf{A})\mathbf{x} < 0, \forall \mathbf{x} \in \mathbb{R}^n, \mathbf{x} \neq 0 \\ \Leftrightarrow \quad & \mathbf{A}^\top\mathbf{P} + \mathbf{P}\mathbf{A} < 0 \\ \Leftrightarrow \quad & \exists \mathbf{Q} = \mathbf{Q}^\top < 0, \mathbf{P} = \mathbf{P}^\top > 0 \mid \mathbf{A}^\top\mathbf{P} + \mathbf{P}\mathbf{A} = \mathbf{Q} \end{aligned} \tag{3.63}$$

Therefore, the system (3.56) is asymptotically stable if and only if there exists any symmetric negative definite matrix $\mathbf{Q}$, the unique solution of the equation

$$\mathbf{A}^\top\mathbf{P} + \mathbf{P}\mathbf{A} = \mathbf{Q} \tag{3.64}$$

is definite-positive matrix.

When the system (3.56) is the linearized tangent of a nonlinear system, the result allows us to ensure that the nonlinear system is asymptotically stable in a neighborhood around the function point (the equilibrium point of the linear system is the function point of the nonlinear system). Indeed, without detailing these concepts, when the linearized tangent has $rank(\mathbf{A}) = n$, so the function point is hyperbolic equilibrium point. We have a topological equivalence between the linearized tangent and the nonlinear system. Therefore, the stability of linearized tangent is of the nonlinear system in the neighborhood of the function point. The nonlinear system will be asymptotically stable in neighborhood of the function point if its linearized system is asymptotically stable.

Or all linear system asymptotically stable corresponds to a hyperbolic equilibrium point that the nonlinear system is also asymptotically stable in neighborhood of the function point.

Because we do not have an unique realization, we must consider the influence of minimal realization on the stability. A minimal realization can be presented based on the system matrices. For the system (3.51), $\mathbf{A}$, $\mathbf{B}$, $\mathbf{C}$, $\mathbf{D}$ is minimal if and only if $\mathbf{A}$, $\mathbf{B}$ is controllable and $\mathbf{A}$, $\mathbf{C}$ is observable. For a system, we have infinite realization but only one transfer function. It means that we have another realization $\mathbf{A}'$, $\mathbf{B}'$, $\mathbf{C}'$, $\mathbf{D}'$ of the system (3.51), we always have

$$G(p) = \mathbf{C}(p\mathbf{I} - \mathbf{A})^{-1}\mathbf{B} + \mathbf{D} = \mathbf{C}'(p\mathbf{I} - \mathbf{A}')^{-1}\mathbf{B}' + \mathbf{D}' \tag{3.65}$$

even if the dimension of $\mathbf{A}$ and $\mathbf{A}'$ is different. Therefore, the stability of $\mathbf{A}$ and $\mathbf{A}'$ may be different. If the realization $\mathbf{A}$, $\mathbf{B}$, $\mathbf{C}$, $\mathbf{D}$ is minimal, the stability of $\mathbf{A}$ is equivalent to the stability of $\mathbf{A}'$ if and only if the realization $\mathbf{A}'$, $\mathbf{B}'$, $\mathbf{C}'$, $\mathbf{D}'$ is minimal. In conclusion, the asymptotically stability of a realization is equivalent to the BIBO stability of associated system if and only if the realization is minimal.

3.5 Observers

Consider the dynamic system

$$\begin{cases} \dot{\mathbf{x}}(t) &= \mathbf{A}\mathbf{x}(t) + \mathbf{B}\mathbf{u}(t) + \mathbf{M}w_d \\ \mathbf{y}(t) &= \mathbf{C}\mathbf{x}(t) + \mathbf{D}\mathbf{u}(t) + w_n \end{cases} \tag{3.66}$$

where w_d and w_n are the disturbance (process noise) and measurement noise inputs respectively, which are usually assumed to be uncorrelated zero-mean Gaussian stochastic processes with constant covariance matrices $\mathbf{W}_d$ and $\mathbf{V}_n$ respectively. w_d and w_n are white noise processes with covariances

$$\begin{cases} E\{w_d(t)w_d^\top(\tau)\} &= \mathbf{W}_d\delta(t-\tau) \\ E\{w_n(t)w_n^\top(\tau)\} &= \mathbf{W}_n\delta(t-\tau) \\ E\{w_d(t)w_n^\top(\tau)\} &= E\{w_n(t)w_d^\top(\tau)\} = 0, \end{cases} \tag{3.67}$$

where E is the expectation operator and $\delta(t-\tau)$ is a delta function.

In practice, recovering the state of a system is not a simple task since we only have access to the input $\mathbf{u}(t)$ and the output of the system $\mathbf{y}(t)$. The problem is thus to construct a dynamic system to be able to provide an estimate $\widehat{\mathbf{x}}(t)$ of the true state $\mathbf{x}(t)$. The final goal is to act on the system from its estimate state. In the linear case, an observer writes as follows:

$$\dot{\widehat{\mathbf{x}}}(t) = (\mathbf{A}\widehat{\mathbf{x}}(t) + \mathbf{B}\mathbf{u}(t)) + \mathbf{K}_o(\mathbf{y}(t) - \mathbf{C}\widehat{\mathbf{x}}(t) - \mathbf{D}\mathbf{u}(t)), \tag{3.68}$$

where $\mathbf{K}_o$ is the gain of filter. We recognize in the first term of the second member of this equation, the term $\mathbf{A}\widehat{\mathbf{x}}(t) + \mathbf{B}\mathbf{u}(t)$ is used to prediction of the evolution of the state vector of system from the current state vector $\widehat{\mathbf{x}}(t)$. Indeed, this prediction

is actually an online simulation of the model of system. If the model is wrong, this prediction is readjusted a function of the error between the measurement $\mathbf{y}(t)$ and the predict measurement $\widehat{\mathbf{y}}(t) = \mathbf{C}\widehat{\mathbf{x}}(t) + \mathbf{D}\mathbf{u}(t)$ and of the gain of filter $\mathbf{K}_o$. The output error signal $\mathbf{y}(t) - \widehat{\mathbf{y}}(t)$ is also called the innovation. The diagram corresponding to the estimator (in the case $\mathbf{D} = 0$) is represented in Figure 3.7. This structure ensures that the estimator is unbiased whatever the system matrices $\mathbf{A}$, $\mathbf{B}$, $\mathbf{C}$, $\mathbf{D}$ and the gain $\mathbf{K}_o$ such that $\mathbf{A} - \mathbf{K}_o\mathbf{C}$ is stable (note that the presence of unstable and unobservable modes does not allow to find the gain $\mathbf{K}_o$ and construct the unbiased estimator).

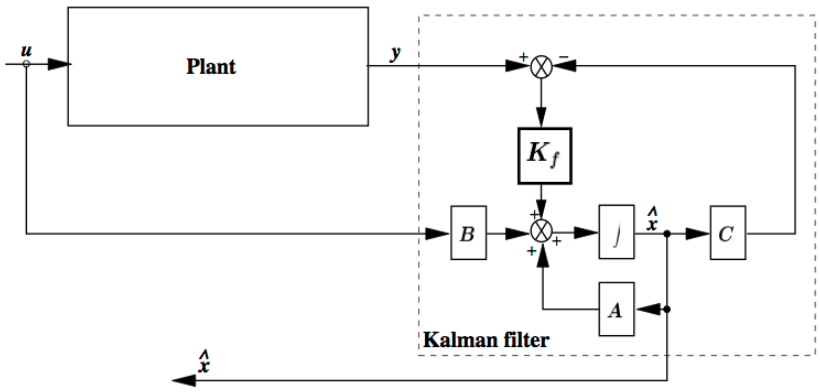

Figure 3.7: Kalman filter diagram

Basically, two main approaches exist. We recall them in the next sections.

3.5.1 Luenberger observer

Either we simply minimize the estimation error, that is $\epsilon(t) = \mathbf{x}(t) - \widehat{\mathbf{x}}(t)$ such that the observer is stable. In that case, we simply ensure:

$$\lim_{t\to\infty} \epsilon(t) = 0 \tag{3.69}$$

The classic structure of observers is given

$$\begin{cases} \dot{\widehat{\mathbf{x}}}(t) &= \mathbf{A}\widehat{\mathbf{x}}(t) + \mathbf{B}\mathbf{u}(t) + \mathbf{K}_o(\mathbf{y}(t) - \widehat{\mathbf{y}}(t)) \\ \widehat{\mathbf{y}}(t) &= \mathbf{C}\widehat{\mathbf{x}}(t) + \mathbf{D}\mathbf{u}(t) \end{cases} \tag{3.70}$$

The observer error satisfies the equation

$$\dot{\epsilon}(t) = (\mathbf{A} - \mathbf{K}_o\mathbf{C})\epsilon(t) \tag{3.71}$$

The observer gain $\mathbf{K}_o$ is chosen such that $\mathbf{A} - \mathbf{K}_o\mathbf{C}$ is stable, it can made Hurwitz, so the observer error $\epsilon(t) \to 0$ when $t \to \infty$. Note that we can choose the observer gain $\mathbf{K}_o$ when the pair $\mathbf{A}$, $\mathbf{C}$ is observable.

3.5.2 Kalman observer

As in the previous case, we also want to ensure that the observer is stable but also: we desire that the observer is unbiased, it means that

- whatever the input signal $\mathbf{u}(\tau)$ applied to $\tau \in [t_0, t]$,
- whatever the initial condition $\widehat{\mathbf{x}}(t_0)$

we desire that the average error of estimator tends toward to 0 when t tends toward to infinite.

The noises w_d and w_n are centered, we can write

$$\begin{aligned} E[\dot{\epsilon}(t)] &= E[\dot{\mathbf{x}}(t) - \dot{\widehat{\mathbf{x}}}(t)] = E[\mathbf{A}\mathbf{x}(t) + \mathbf{B}\mathbf{u}(t) + w_d(t) - \mathbf{A}\widehat{\mathbf{x}}(t) - \mathbf{B}\mathbf{u}(t) \\ &\quad -\mathbf{K}_o(\mathbf{C}\mathbf{x}(t) + \mathbf{D}\mathbf{u}(t) + w_n(t) - \mathbf{C}\widehat{\mathbf{x}}(t) - \mathbf{D}\mathbf{u}(t))] \\ &= E[\mathbf{A}\mathbf{x}(t) - \mathbf{A}\widehat{\mathbf{x}}(t)] + E[\mathbf{M}w_d(t)] - E[\mathbf{K}_o(\mathbf{C}\mathbf{x}(t) - \mathbf{C}\widehat{\mathbf{x}}(t))] - E[\mathbf{K}_o w_n(t)] \\ &= (\mathbf{A} - \mathbf{K}_o\mathbf{C})E[\epsilon(t)] \end{aligned} \tag{3.72}$$

Therefore, we have

$$E[\epsilon(t)] = e^{(\mathbf{A}-\mathbf{K}_o\mathbf{C})(t-t_0)}\epsilon(t_0) \tag{3.73}$$

and $\lim_{t\to\infty} E[\epsilon(t)] = 0$ when $\mathbf{A} - \mathbf{K}_o\mathbf{C}$ is stable. The observer gain $\mathbf{K}_o$ is calculated by a function of confidence in the model (expressed by the spectral density $\mathbf{W}_d$) with regard to in the measurement (expressed by the spectral density $\mathbf{W}_n$). If the model is very good ($\mathbf{W}_d$ is very small) and the measurement is very noise ($\mathbf{W}_n$ very large), the observer gain $\mathbf{K}_o$ is very small, among all gains $\mathbf{K}_o$ satisfying that $\mathbf{A}-\mathbf{K}_o\mathbf{C}$ is stable, we shall choose the gain $\mathbf{K}_o$ that minimizes the variance of the estimation error $\epsilon(t), \forall t$. We recall that $\epsilon(t)$ is a centered Gaussian random vector. The Gaussian character of this variable allows that the variance of estimation error is effectively minimized, therefore $\widehat{\mathbf{x}}(t)$ is the best estimate of $\mathbf{x}(t)$.

We find $\mathbf{K}_o$ that minimizes the cost function

$$\begin{aligned} J(t) = \textstyle\sum_{i=1}^{n} E[\epsilon_i^2(t)] &= E[\epsilon^\top(t)\epsilon(t)] \\ &= traceE[\epsilon(t)\epsilon^\top(t)] \\ &= traceP(t) \end{aligned} \tag{3.74}$$

where $\mathbf{P}(t) = E[(\mathbf{x}(t) - \widehat{\mathbf{x}}(t))(\mathbf{x}(t) - \widehat{\mathbf{x}}(t))^\top]$ is the covariance matrix of the estimation error. We recall the dynamic equation of estimation error

$$\begin{aligned} \dot{\epsilon}(t) &= \mathbf{A}\mathbf{x}(t) - \mathbf{A}\widehat{\mathbf{x}}(t) + \mathbf{M}w_d(t) - \mathbf{K}_o(\mathbf{C}\mathbf{x}(t) - \mathbf{C}\widehat{\mathbf{x}}(t)) - \mathbf{K}_o w_n(t) \\ &= (\mathbf{A} - \mathbf{K}_o\mathbf{C})\epsilon(t) + \begin{bmatrix} \mathbf{M} & -\mathbf{K}_o \end{bmatrix} \begin{bmatrix} w_d(t) \\ w_n(t) \end{bmatrix} \end{aligned} \tag{3.75}$$

The differential equation of the covariance matrix of the estimation error is given by

$$\dot{\mathbf{P}}(t) = (\mathbf{A} - \mathbf{K}_o\mathbf{C})\mathbf{P}(t) + \mathbf{P}(t)(\mathbf{A} - \mathbf{K}_o\mathbf{C})^\top + \mathbf{M}\mathbf{W}_d\mathbf{M}^\top + \mathbf{K}_o\mathbf{W}_n\mathbf{K}_o^\top \tag{3.76}$$

In order to minimize $trace\mathbf{P}(t)$, it is simple to minimize $trace\dot{\mathbf{P}}(t)$

$$\begin{array}{ll} \frac{\partial(trace\dot{\mathbf{P}}(t))}{\partial\mathbf{K}_o} & = -\mathbf{P}(t)\mathbf{C}^\top - \mathbf{P}(t)\mathbf{C}^\top + 2\mathbf{K}_o\mathbf{W}_n \\ \Rightarrow \mathbf{K}_o(t) & = \mathbf{P}(t)\mathbf{C}^\top\mathbf{W}_n^{-1} \end{array} \tag{3.77}$$

Substituting (3.77) into (3.76), we obtain the Riccati differential equation

$$\dot{\mathbf{P}}(t) = \mathbf{A}\mathbf{P}(t) + \mathbf{P}(t)\mathbf{A}^\top - \mathbf{P}(t)\mathbf{C}^\top\mathbf{W}_n^{-1}\mathbf{C}\mathbf{P}(t) + \mathbf{M}\mathbf{W}_d\mathbf{M}^\top \tag{3.78}$$

In order to obtain a solution of the Riccati differential equation, we must consider the initial condition

$$\mathbf{P}(t_0) = E[(\mathbf{x}(t_0) - \widehat{\mathbf{x}}(t_0))(\mathbf{x}(t_0) - \widehat{\mathbf{x}}(t_0))^\top] \tag{3.79}$$

The Kalman filter is usually used in the **LQG** control described in the next section to determine the estimate of the state vector.

3.6 Closed-loop control

In control theory, the most accepted approach used to the synthesis of multivariable control law is an approach known as "state feedback control". The idea of this approach is to act on the controlled system based on its measured state. It is different to the open loop control, we use the sensor to give the feedback information of controlled variable in the closed-loop control. In this section, we focus on various important aspects of this approach. To do it, we first focus on linear systems then non-linear systems

3.6.1 Linear systems

The goal of design of control law is to determine the gain of control law which stabilizes the system. The stabilization can place the eigenvalue and the eigenvector of system or generally reconstruct the structure of system with our aims. In control theory, we use the proportional integral derivative control, the optimal control, the robust control, etc.

Let us consider the dynamic system

$$\left\{ \begin{array}{ll} \dot{\mathbf{x}}(t) & = \mathbf{A}\mathbf{x}(t) + \mathbf{B}\mathbf{u}(t) \\ \mathbf{y}(t) & = \mathbf{C}\mathbf{x}(t) + \mathbf{D}\mathbf{u}(t), \end{array} \right. \tag{3.80}$$

and the control law is proposed as

$$\mathbf{u}(t) = \mathbf{H}\mathbf{y}_{ref}(t) + \mathbf{K}\mathbf{x}(t), \tag{3.81}$$

which leads to the output reference $\mathbf{y}_{ref}(t)$.

3.6.1.1 Pole assignment

This technique is presented based on the result in [Kautsky et al., 1985]. The problem description of pole assignment can be given such as: we have the real matrices $(\mathbf{A}, \mathbf{B})$, of orders $(n \times n, n \times m)$, respectively, and a set of n complex numbers , $\mathcal{L} = \{\lambda_1, \lambda_2, \ldots, \lambda_n\}$, closed under complex conjugation, our problem is to find a real matrix $\mathbf{K}$ such that the eigenvalues of $\mathbf{A} - \mathbf{BK}$ are λ_j.

We consider the first condition to determine $\mathbf{K}$. Indeed, we find the real matrix $\mathbf{K}$ for every set $\mathcal{L}$ of self-conjugate complex numbers if and only if the pair $(\mathbf{A}, \mathbf{B})$ is controllable.

In the pole assignment design, we have mn components of $\mathbf{K}$ (m degrees of freedom (**DOF**)), n components of $\mathbf{K}$ must be used to place the eigenvalues. Therefore, we still have $n(m-1)$ components of $\mathbf{K}$ to reconstruct the eigenstructure. It is properly to exploit and identify these **DOF**.

To determine the real matrix $\mathbf{K}$, we consider the characteristic polynomial of closed loop system described by

$$P(p) = \prod_{i=1}^{n}(p - \lambda_i) = p^n + \beta_{n-1}p^{n-1} + \ldots + \beta_1 p + \beta_0, \tag{3.82}$$

and therefore, the real matrix $\mathbf{K}$ is given by solving the equation

$$det(p\mathbf{I} - \mathbf{A} + \mathbf{BK}) = P(p) = p^n + \beta_{n-1}p^{n-1} + \ldots + \beta_1 p + \beta_0. \tag{3.83}$$

For more detail, the numerical solution of this equation is detailed in [Kautsky et al., 1985].

3.6.1.2 Eigenstructure assignment

For the system (3.80), we recall that the problem of eigenstructure assignment consist to determine the gain control $\mathbf{K}$ in (3.81) such that $\mathbf{A}_c = \mathbf{A} - \mathbf{BK}$ coincides with a set of desired specified value.

In the case of the system is single input, it means that the matrix $\mathbf{K}$ contains n components and we want to place n poles. Therefore, we do not have anymore components of $\mathbf{K}$ and the solution of $\mathbf{K}$ is unique. However, in the case of the system is multiple inputs, the matrix $\mathbf{K}$ contains mn components and therefore, we still have $n(m-1)$ additional components of $\mathbf{K}$. Indeed, these additional **DOF** can be used to reconstruct the eigenstructure.

3.6.1.3 Optimal control

LQR control The approaches in section 3.5.1 and section 3.5.2 allow us to stabilize the closed loop system with the presence of disturbance. These approaches are very interesting when we want to specially eliminate the influence of disturbance.

While the optimal control technique consists to a differential problem, this technique is to find a control law which minimizes a certain criterion J reflecting a desired behavior. For example, in order to determine the control law which moves the closed loop system

from state A to state B in minimum time or minimizes the energy actuators. We first restrict to the case of **LQ** (also called **LQR** for linear quadratic regulator) in order to introduce **LQG** control. Indeed, we shall see section (4.3.2.4), **LQG** control is extremely popular in flow control.

The general problem of optimal control is given as follows: determine the control law $\mathbf{u}(t)$ which makes the minimal criterion J tacking account the initial and final conditions and the constraint defined by the state equation.

In the case of **LQ** control, a linear system is considered, the criterion J is quadratic and aims to minimize the error between the current state and the desired state while minimizing the energy actuators. This problem is thus formalized: the quadratic cost function is defined as

$$J(t) = \int_0^\infty (\mathbf{x}^\top(t)\mathbf{Q}\mathbf{x}(t) + \mathbf{u}^\top(t)\mathbf{R}\mathbf{x}(t)), \tag{3.84}$$

where the matrices $\mathbf{Q}$ and $\mathbf{R}$ are positive definite and positive-semidefinite, respectively. Note that we shall see section (6.4), the term $\mathbf{x}^\top(t)\mathbf{Q}\mathbf{x}(t)$ is defines as the kinetic energy of perturbation in flow control while the term $\mathbf{u}^\top(t)\mathbf{R}\mathbf{x}(t)$ is the energy actuators. The control law is given by $\mathbf{u}(t) = \mathbf{K}_{lqr}\mathbf{x}(t)$ where $\mathbf{K}_{lqr}$ is given by ([Skogestad and Postlenthwaite, 2007])

$$\mathbf{K}_{lqr} = -\mathbf{R}^{-1}\mathbf{B}^\top\mathbf{X}_r, \tag{3.85}$$

and $\mathbf{X}_r$ is found by solving the continuous time Riccati differential equation

$$\mathbf{A}^\top\mathbf{X}_r + \mathbf{X}_r\mathbf{A} - \mathbf{X}_r\mathbf{B}\mathbf{R}^{-1}\mathbf{B}^\top\mathbf{X}_r + \mathbf{Q} = 0. \tag{3.86}$$

In order to find the gain control, the pair $(\mathbf{A}, \mathbf{B})$ must be stabilizable. By using the decomposition $\mathbf{Q} = \mathbf{N}_r^\top\mathbf{N}_r$ and $\mathbf{B}\mathbf{R}^{-1}\mathbf{B}^\top = \mathbf{M}_r\mathbf{M}_n^\top$, when the pair $(\mathbf{A}, \mathbf{M}_r)$ is controllable and the pair $(\mathbf{A}, \mathbf{N}_r)$ is observable, the positive definite solution of the Riccati differential equation always exists and is always unique. Moreover, $\mathbf{A} - \mathbf{B}\mathbf{R}^{-1}\mathbf{B}^\top\mathbf{X}_r$ always has negative eigenvalues.

One of the advantages of **LQ** control is to ensure a good robustness toward the error of the gains on the inputs channels. However, it is not possible to imposer a priori dynamic of closed loop system corresponding to the optimality of the quadratic criterion.

LQG control Like the **LQR** problem itself, the **LQG** problem is one of the most fundamental problems in control theory. In practice, the state vector is not most often known so that the **LQR** control cannot be used. In that case, an observer has to be used. Therefore, the control law is given by $\mathbf{u}(t) = \mathbf{K}_{lqr}\widehat{\mathbf{x}}(t)$ where $\widehat{\mathbf{x}}(t)$ is the estimate of $\mathbf{x}(t)$ from using the Kalman filter. We recall the system (3.66)

$$\begin{cases} \dot{\mathbf{x}}(t) &= \mathbf{A}\mathbf{x}(t) + \mathbf{B}\mathbf{u}(t) + \mathbf{M}w_d \\ \mathbf{y}(t) &= \mathbf{C}\mathbf{x}(t) + \mathbf{D}\mathbf{u}(t) + w_n \end{cases} \tag{3.87}$$

Indeed, the **LQG** control is designed based on two steps. First step is determine an optimal control $\mathbf{u}(t) = \mathbf{K}_{lqr}\mathbf{x}(t)$, **LQR** problem (see the above results to determine $\mathbf{K}_{lqr}$). And the second step is to find an optimal estimate $\widehat{\mathbf{x}}(t)$ of the state $\mathbf{x}(t)$, Kalman filter problem, so that $E\{[\mathbf{x}(t) - \widehat{\mathbf{x}}(t)]^\top[\mathbf{x}(t) - \widehat{\mathbf{x}}(t)]\}$ is minimized (see section 3.5.2). The diagram of the **LQG** control shown in Figure 3.8 (taken from [Skogestad and Postlenthwaite, 2007] in the case $\mathbf{D} = 0$).

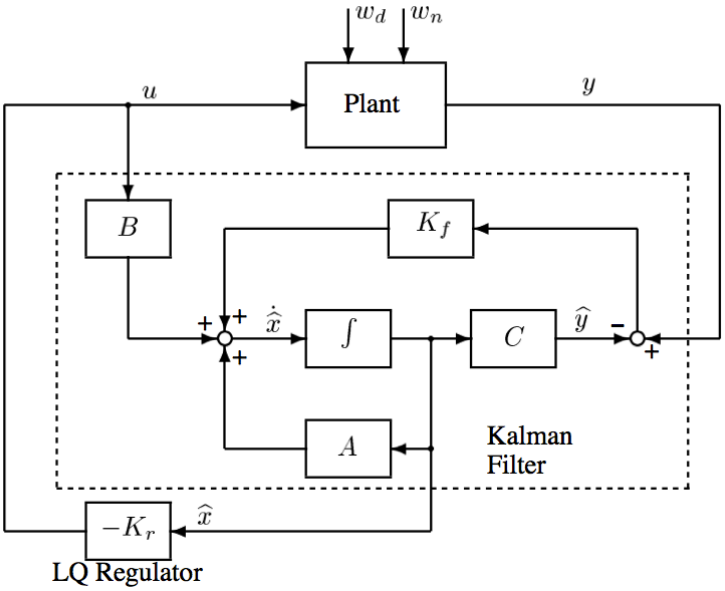

Figure 3.8: LQG controller and noise plant.

In practice, the control law $\mathbf{u}(t) = \mathbf{K}_{lqr}\mathbf{x}(t)$ is changed by $\mathbf{u}(t) = \mathbf{K}_{lqr}\widehat{\mathbf{x}}(t)$ where $\widehat{\mathbf{x}}(t)$ is an estimate of the state vector $\mathbf{x}(t)$. We recall the dynamic system of estimator or observer given by

$$\dot{\widehat{\mathbf{x}}}(t) = \mathbf{A}\widehat{\mathbf{x}}(t) + \mathbf{B}\mathbf{u}(t) + \mathbf{K}_o(\mathbf{y}(t) - \mathbf{C}\widehat{\mathbf{x}}(t) - \mathbf{D}\mathbf{u}(t)). \tag{3.88}$$

If $(\mathbf{A}, \mathbf{C})$ is detectable, the optimal choice of $\mathbf{K}_o$, which minimizes $E\{[\mathbf{x}(t)-\widehat{\mathbf{x}}(t)]^\top[\mathbf{x}(t)-\widehat{\mathbf{x}}(t)]\}$, is given by

$$\mathbf{K}_o = \mathbf{P}\mathbf{C}^\top\mathbf{W}_n^{-1}, \tag{3.89}$$

When the linear system is considered and often convergence of the state covariance matrix $\mathbf{P}$, we have $\dot{\mathbf{P}}(t) = 0$, the solution of (3.78), the unique positive-semidefinite solution of the algebraic Riccati differential equation $\mathbf{P} = \mathbf{P}^\top \geq 0$ is

$$\mathbf{P}\mathbf{A}^\top + \mathbf{A}\mathbf{P} - \mathbf{P}\mathbf{C}^\top\mathbf{W}_n^{-1}\mathbf{C}\mathbf{P} + \mathbf{M}\mathbf{W}_d\mathbf{M}^\top = 0. \tag{3.90}$$

The closed loop system is given by

$$\begin{cases} \dot{\mathbf{x}}(t) &= \mathbf{A}\mathbf{x}(t) + \mathbf{B}\mathbf{u}(t) + \mathbf{M}w_d \\ \dot{\widehat{\mathbf{x}}}(t) &= \mathbf{A}\widehat{\mathbf{x}}(t) + \mathbf{B}\mathbf{u}(t) + \mathbf{K}_o(\mathbf{y}(t) - \mathbf{C}\widehat{\mathbf{x}}(t) - \mathbf{D}\mathbf{u}(t)) \\ \mathbf{u}(t) &= \mathbf{K}_{lqr}\widehat{\mathbf{x}}(t) \\ \mathbf{y}(t) &= \mathbf{C}\mathbf{x}(t) + \mathbf{D}\mathbf{u}(t) + w_n. \end{cases} \tag{3.91}$$

Therefore, the **LQG** control is the combination of the optimal state estimation and the optimal state feedback control

$$\begin{bmatrix} \dot{\widehat{\mathbf{x}}}(t) \\ \mathbf{u}(t) \end{bmatrix} = \left[\begin{array}{c|c} \mathbf{A} + \mathbf{B}\mathbf{K}_{lqr} - \mathbf{K}_o\mathbf{C} - \mathbf{K}_o\mathbf{D}\mathbf{K}_{lqr} & \mathbf{K}_o \\ \hline \mathbf{K}_{lqr} & 0 \end{array}\right] \begin{bmatrix} \widehat{\mathbf{x}}(t) \\ \mathbf{y}(t) \end{bmatrix}. \tag{3.92}$$

3.6.2 Nonlinear systems

Some methods can be used for the nonlinear system, but we choose the Lyapunov synthesis to illustrate the concept of the design of nonlinear system.

3.6.2.1 Direct Lyapunov analysis

This method is simple to determine the control law which guarantees the stability of the closed loop system. The following example illustrates this method.

Let us to consider the system

$$\dot{\mathbf{x}}(t) = \mathbf{x}^2(t) + \mathbf{u}(t) \tag{3.93}$$

The problem is to regulate the state vector $\mathbf{x}(t)$ around the reference $\mathbf{x}_c(t)$. By using the change of variable $\mathbf{z}(t) = \mathbf{x}(t) - \mathbf{x}_c(t)$, we have the dynamic error

$$\dot{\mathbf{z}}(t) = \mathbf{x}_c^2(t) + 2\mathbf{x}_c(t)\mathbf{z}(t) + \mathbf{z}^2(t) + \mathbf{u}(t) \tag{3.94}$$

The Lyapunov function is $V = \frac{1}{2}\mathbf{z}^2(t)\mathbf{z}(t)$, we have

$$\dot{V} = \mathbf{z}(t)\dot{\mathbf{z}}(t) = \mathbf{z}(t)(\mathbf{x}_c^2(t) + 2\mathbf{x}_c(t)\mathbf{z} + \mathbf{z}^2(t) + \mathbf{u}(t)) \tag{3.95}$$

A control law which guarantees the stability of the closed loop system is

$$\mathbf{u}(t) = -\mathbf{x}_c^2(t) - 2\mathbf{x}_c(t)\mathbf{z}(t) - \mathbf{z}^2(t) - c\mathbf{z}(t) \tag{3.96}$$

where $c > 0$. Therefore, the dynamic error is final given by

$$\dot{\mathbf{z}}(t) = -c\mathbf{z}(t) \tag{3.97}$$

which is linear and exponential stable.

In the next section, we present the integrator Backstepping.

3.6.2.2 Integrator Backstepping

Integrator Backstepping was develop by Petar V. Kokotovic [Kokotovic, 1992], this method becomes popular method in the control theory. Consider the system

$$\begin{cases} \dot{\mathbf{x}}(t) &= f(\mathbf{x}(t)) + h(\mathbf{x}(t))\xi(t) \\ \dot{\xi}(t) &= \mathbf{u}(t) \end{cases} \tag{3.98}$$

We suppose that it exists a control law $\xi(t) = \phi(\mathbf{x}(t))$ ($\phi(0) = 0$) that can asymptotically stabilize the system. This implies that the system

$$\dot{\mathbf{x}}(t) = f(\mathbf{x}(t)) + h(\mathbf{x}(t))\phi(\mathbf{x}(t)) \tag{3.99}$$

is asymptotically stable. Furthermore, we can suppose that we know a Lyapunov function $V(\mathbf{x}(t))$ that satisfies the inequality

$$\frac{\partial V}{\partial \mathbf{x}}[f(\mathbf{x}(t)) + h(\mathbf{x}(t))\phi(\mathbf{x}(t))] \leq -W(\mathbf{x}(t)) \tag{3.100}$$

where $W(\mathbf{x}(t))$ is positive definite. By adding and subtracting the term $h(\mathbf{x}(t))\phi(\mathbf{x}(t))$, we obtain

$$\begin{cases} \dot{\mathbf{x}}(t) &= f(\mathbf{x}(t)) + h(\mathbf{x})\xi(t) = [f(\mathbf{x}(t)) + h(\mathbf{x}(t))\phi(\mathbf{x}(t))] + h(\mathbf{x}(t))[\xi(t) - \phi(\mathbf{x}(t))] \\ \dot{\xi}(t) &= \mathbf{u}(t) \end{cases} \tag{3.101}$$

By using the change of variables, $\mathbf{z}(t) = \xi(t) - \phi(\mathbf{x}(t))$, which generates the following system

$$\begin{cases} \dot{\mathbf{x}}(t) &= f(\mathbf{x}(t)) + h(\mathbf{x})\xi(t) = [f(\mathbf{x}(t)) + h(\mathbf{x}(t))\phi(\mathbf{x}(t))] + h(\mathbf{x}(t))\mathbf{z}(t) \\ \dot{\mathbf{z}}(t) &= \mathbf{u}(t) - \dot{\phi}(\mathbf{x}(t)) \end{cases} \tag{3.102}$$

Since f, h and ϕ are known, the derivative can be written as

$$\dot{\phi}(\mathbf{x}(t)) = \frac{\partial \phi}{\partial \mathbf{x}}[f(\mathbf{x}(t)) + h(\mathbf{x}(t))\phi(\mathbf{x}(t)) + h(\mathbf{x}(t))\mathbf{z}(t)] \tag{3.103}$$

Let's us to use $\mathbf{v}(t) = \mathbf{u}(t) - \dot{\phi}(\mathbf{x}(t))$ which reduces our system to

$$\begin{cases} \dot{\mathbf{x}}(t) &= f(\mathbf{x}(t)) + h(\mathbf{x})\xi(t) = [f(\mathbf{x}(t)) + h(\mathbf{x}(t))\phi(\mathbf{x}(t))] + h(\mathbf{x}(t))\mathbf{z}(t) \\ \dot{\mathbf{z}}(t) &= \mathbf{v}(t) \end{cases} \tag{3.104}$$

This modular property of backstopping will be exploited to stabilize the overall system with the control law $\mathbf{v}(t)$. This is done by considering the Lyapunov function

$$V_c(\mathbf{x}(t), \xi(t)) = V(\mathbf{x}(t)) + \frac{1}{2}\mathbf{z}^2(t) = V(\mathbf{x}(t)) + \frac{1}{2}(\xi(t) - \phi(\mathbf{x}(t)))^2 \tag{3.105}$$

The derivate of V_c is

$$\begin{aligned} \dot{V}_c(\mathbf{x}(t), \xi(t)) &= \frac{\partial V}{\partial \mathbf{x}}[f(\mathbf{x}(t)) + h(\mathbf{x}(t))\phi(\mathbf{x}(t))] + \frac{\partial V}{\partial \mathbf{x}}h(\mathbf{x}(t))\mathbf{z}(t) + \mathbf{z}(t)\mathbf{v}(t) \\ &\leq -W(\mathbf{x}(t)) + \frac{\partial V}{\partial \mathbf{x}}h(\mathbf{x}(t))\mathbf{z}(t) + \mathbf{z}(t)\mathbf{v}(t) \end{aligned} \tag{3.106}$$

We can choose

$$\mathbf{v}(t) = -\frac{\partial V}{\partial \mathbf{x}}h(\mathbf{x}(t)) - c\mathbf{z}(t) \tag{3.107}$$

where $c > 0$. This implies that

$$\dot{V}_c(\mathbf{x}(t), \xi(t)) \leq -W(\mathbf{x}(t)) - c\mathbf{z}^2(t) \tag{3.108}$$

which implies the closed loop system is asymptotically stable. Finally, the control law $\mathbf{u}(t)$ is given by

$$\mathbf{u}(t) = -\frac{\partial \phi}{\partial \mathbf{x}}[f(\mathbf{x}(t)) + h(\mathbf{x}(t))\xi(t)] - \frac{\partial V}{\partial \mathbf{x}}h(\mathbf{x}(t)) - c[\xi(t) - \phi(\mathbf{x}(t))] \tag{3.109}$$

We can conclude that the closed loop system is asymptotically stable.

Lemma 3.6.1 *Backstepping lemma*
Consider the system

$$\dot{\mathbf{x}}(t) = f(\mathbf{x}(t)) + h(\mathbf{x}(t))\xi(t) \tag{3.110}$$
$$\dot{\xi}(t) = \mathbf{u}(t) \tag{3.111}$$

Let $\phi(\mathbf{x}(t))$ be a stabilizing stable feedback law for the system (3.110) where $\phi(0) = 0$. Let $V(\mathbf{x}(t))$ be a Lyapunov functions such that

$$\frac{\partial V}{\partial \mathbf{x}}[f(\mathbf{x}(t)) + h(\mathbf{x}(t))\phi(\mathbf{x}(t))] \leq -W(\mathbf{x}(t)) \tag{3.112}$$

for some positive definite $W(\mathbf{x}(t))$. Then the feedback law

$$\mathbf{u}(t) = -\frac{\partial \phi}{\partial \mathbf{x}}[f(\mathbf{x}(t)) + h(\mathbf{x}(t))\xi(t)] - \frac{\partial V}{\partial \mathbf{x}}h(\mathbf{x}(t)) - c[\xi(t) - \phi(\mathbf{x}(t))] \tag{3.113}$$

for $c > 0$ stabilize the origin with the Lyapunov function

$$V(\mathbf{x}(t)) = \frac{1}{2}[\xi(t) - \phi(\mathbf{x}(t))]^2 \tag{3.114}$$

In order to illustrate this method, we consider a simple example. Consider the following system

$$\dot{\mathbf{x}}(t) = \mathbf{x}^2(t)) + \mathbf{x}^3(t)) + \xi(t) \tag{3.115}$$
$$\dot{\xi}(t) = \mathbf{u}(t) \tag{3.116}$$

Firstly, consider the system

$$\dot{\mathbf{x}}(t) = \mathbf{x}^2(t)) + \mathbf{x}^3(t)) + \xi(t) \tag{3.117}$$

with the control law $\xi(t)$. The Lyapunov function $V(\mathbf{x}(t))$ can be chosen

$$V(\mathbf{x}(t)) = \frac{1}{2}\mathbf{x}^2(t) \rightarrow \dot{V}(\mathbf{x}(t)) = \mathbf{x}(t)\dot{\mathbf{x}}(t) = \mathbf{x}(t)[\mathbf{x}^2(t)) + \mathbf{x}^3(t)) + \xi(t)] \tag{3.118}$$

Therefore, the control law is chosen by

$$\xi(t) = \phi(\mathbf{x}(t)) = -\mathbf{x}(t) - \mathbf{x}^2(t) - 2\mathbf{x}^3(t) \tag{3.119}$$

The Lyapunov function $V(\mathbf{x}(t))$ satisfies

$$V(\mathbf{x}(t)) = -\mathbf{x}^2(t)) - \mathbf{x}^4(t)) \leq -\mathbf{x}^2(t) \tag{3.120}$$

which implies that $\mathbf{x}(t) = 0$ is asymptotically stable. Now we use the backstopping change of variables,

$$\mathbf{z}(t) = \xi(t) - \phi(\mathbf{x}(t)) = \xi(t) + \mathbf{x}(t) + \mathbf{x}^2(t) + 2\mathbf{x}^3(t) \tag{3.121}$$

to transform our system to

$$\begin{aligned} \dot{\mathbf{x}}(t) &= -\mathbf{x}(t) - \mathbf{x}^3(t) + \mathbf{z}(t) && (3.122)\\ \dot{\mathbf{z}}(t) &= \mathbf{u}(t) - (1 + 2\mathbf{x}(t) + 6\mathbf{x}^2(t))(-\mathbf{x}(t) - \mathbf{x}^3(t) + \mathbf{z}(t)) && (3.123) \end{aligned}$$

and let

$$V_c(\mathbf{x}(t), \xi(t)) = V(\mathbf{x}(t)) + \frac{1}{2}\mathbf{z}^2(t) = \frac{1}{2}\mathbf{x}^2(t) + \frac{1}{2}\mathbf{z}^2(t) \tag{3.124}$$

Therefore, the derivate of $V_c(\mathbf{x}(t), \xi(t))$ is

$$\begin{aligned} \dot{V}_c &= \mathbf{x}(t)(-\mathbf{x}(t) - \mathbf{x}^3(t) + \mathbf{z}(t)) \\ &\quad +\mathbf{z}(t)[\mathbf{u}(t) - (1 + 2\mathbf{x}(t) + 6\mathbf{x}^2(t))(-\mathbf{x}(t) - \mathbf{x}^3(t) + \mathbf{z}(t))] \\ &= -\mathbf{x}^2(t) - \mathbf{x}^4(t) + \mathbf{z}(t)[\mathbf{u}(t) + \mathbf{x}(t) - (1 + 2\mathbf{x}(t) + 6\mathbf{x}^2(t))(-\mathbf{x}(t) - \mathbf{x}^3(t) + \mathbf{z}(t))] \end{aligned} \tag{3.125}$$

and choose

$$\mathbf{u}(t) = -\mathbf{x}(t) - (1 + 2\mathbf{x}(t) + 6\mathbf{x}^2(t))(-\mathbf{x}(t) - \mathbf{x}^3(t) + \mathbf{z}(t)) - \mathbf{z}(t) \tag{3.126}$$

This implies that

$$\dot{V}_c(\mathbf{x}(t), \xi(t)) = -\mathbf{x}^2(t) - \mathbf{x}^4(t) - \mathbf{z}^2(t) \tag{3.127}$$

guarantees the closed loop system to be asymptotically stable.

The actual control is given

$$\begin{aligned} \mathbf{u}(t) &= -\mathbf{x}(t) - (1 + 2\mathbf{x}(t) + 6\mathbf{x}^2(t))(-\mathbf{x}(t) - \mathbf{x}^3(t) + \xi(t) + \mathbf{x}(t) + \mathbf{x}^2(t) + 2\mathbf{x}^3(t)) \\ &\quad -\xi(t) - \mathbf{x}(t) - \mathbf{x}^2(t) - 2\mathbf{x}^3(t) \\ &= -\mathbf{x}(t) - (1 + 2\mathbf{x}(t) + 6\mathbf{x}^2(t))(\xi(t) + \mathbf{x}^2(t) + \mathbf{x}^3(t)) - \xi(t) - \mathbf{x}(t) - \mathbf{x}^2(t) - 2\mathbf{x}^3(t) \end{aligned} \tag{3.128}$$

3.7 Conclusion

Since the fluid flow is infinite dimension and nonlinear model. The results in the control theory allow us to ensure that the controller based on the linearization and model reduction can be applied to the fluid flow. In the next chapters, we shall apply the control theory to the flow control.

Chapter 4

State of the art

In this chapter, a review of previous works is presented where the active flow control is particularly emphasized. The case study considered in this thesis is the plane Poiseuille flow. This will be introduced in Section 4.3 and discussed in more detail in the next chapter. Section 4.4 will present the objectives of our works.

4.1 Classification of flow control

The flow control is classified by energy expenditure and control loop system, as shown in Figure 4.1 (taken from [Gad-el Hak, 2000]).

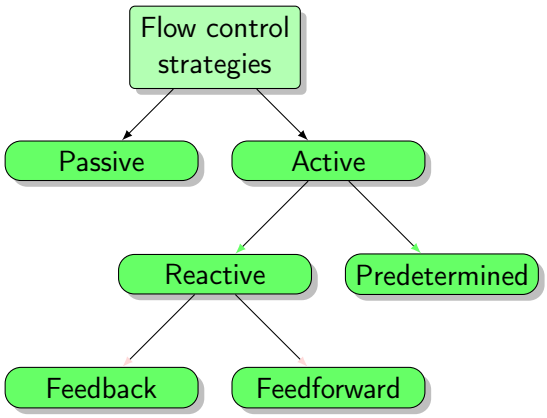

Figure 4.1: Classification of flow control strategies.

The passive control, see the reviews in [Bushnell and Hef, 1990], [Gad-el Hak, 2000], [Gad-el Hak et al., 1998], is affected without requiring an energy expenditure and no control loop. The devices of passive control are usually such as vortex generators, riblets, and steady suction or blowing. The passive techniques usually include a geometric shaping to manipulate a pressure gradient, a use of fixed mechanical vortex generators for separation control, a placement of riblets on a surface to reduce the drag. An example of the passive control, the wing of aircraft is designed to decrease the drag and

enhance the lift [Chatto, 2006]. For more examples, the design of riblets for the drag reduction is found in [Choi et al., 1993a], [Garcia-Mayoral and Jimenez, 2011]. Indeed, the majority of the passive control is the shape optimization.

In contrast to the passive control, the active control requires an energy expenditure. The recent reviews of the active flow control were described in [Moin and Bewley, 1994], [Gad-el Hak, 1996], [Gad-el Hak, 2000], [Bewley, 2001], [Collis et al., 2004]. The active flow control contains both predetermined and reactive controls. The energy expenditure may be a power of the actuator which provides a force to act the flow.

The passive flow control is simple, less expensive to design and manufacture, and easier to maintain than the active flow control. Thus, the passive flow control is usually used in real-world applications, especially in aircraft. However, the passive flow control is only applied to simple flows and is limited since the most engineering flows contain complex unsteady motions (instabilities, turbulence). This reason makes the active flow control more attention than the passive flow control in the currently.

The detail of the active control will be presented in the next section.

4.2 Active flow control

The active flow control triad contains the phenomena, the actuators-sensors and the control method. These problems are shown in Figure 4.2 (taken from [Kral, 2000]). As a result, the flow phenomena is listed along with the actuators, the sensors and the methods of control.

4.2.1 Sensors

The sensors are an equipment which provides a feedback information to help us to control the flow. In the fluid flow, the measured variables are usually pressure and velocity. The sensors are a conventional sensor or a Micro-Electro-Mechanical-System(**MEMS**) sensor or an optical sensor. For the conventional and **MEMS** sensors, the measured variable is the wall pressure and/or skin friction such as floating element sensors, hot films and shear stress crystals while the optical sensors measure all field of velocity such as Charge-Coupled Device (**CCD**) camera. The optical sensors are very useful in the image processing where the velocity is directly obtained from the **CCD** camera. The recent reviews of hot film sensors are found in [Comte-Bellot, 1976] and the sensor techniques are presented in [Monsma et al., 1995].

4.2.2 Actuators

The actuators are an equipment to controlling the flow. There are many types of actuators which are listed in Figure 4.2, e.g. piezoelectric, synthetic jets, electromagnetic and **MEMS** actuators, specifically **MEMS** actuators. The recent reviews of actuators for the flow control were in [Cattafesta III and Sheplak, 2011], which clearly illustrate the advantages and inconveniences of each actuator. Two actuators: synthetic jet and **MEMS** are emphasized for instance in the following.

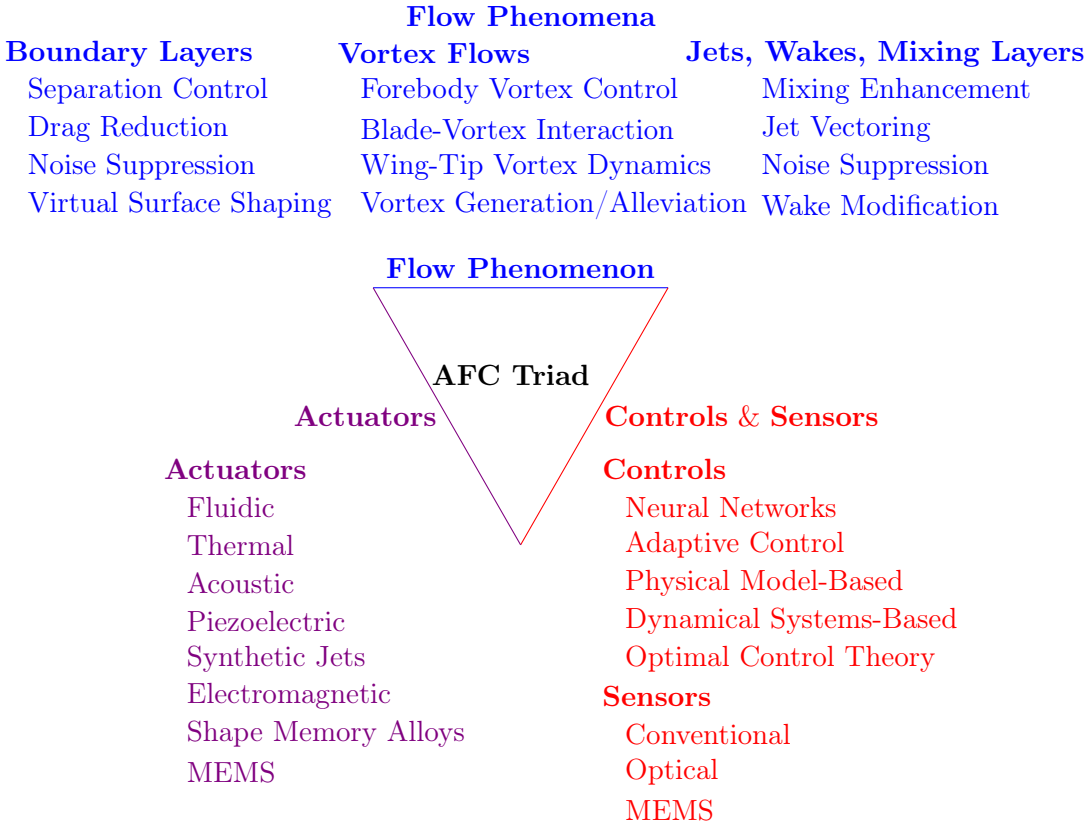

Figure 4.2: Active flow control (AFC) triad.

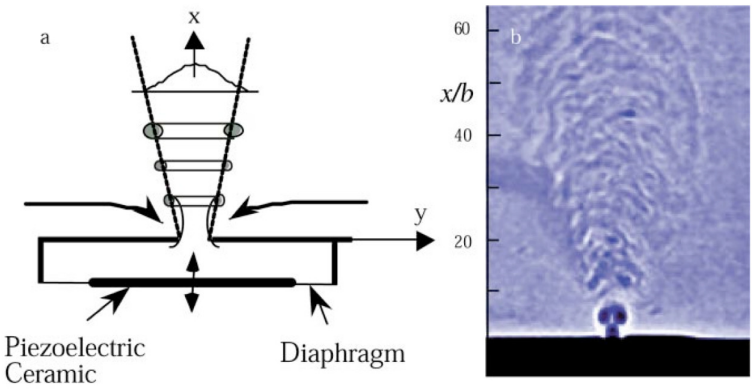

Figure 4.3: Synthetic jet actuator and flow patterns: (a) schematic and (b) schlieren flow visualization.

The synthetic jet actuator was developed at Georgia Institute of Technology. A schematic of this actuator was described in [Smith and Glezer, 1998], as shown in Figure 4.3 (Courtesy B. L. Smith and A. Glezer, Georgia Tech Research Institute, taken

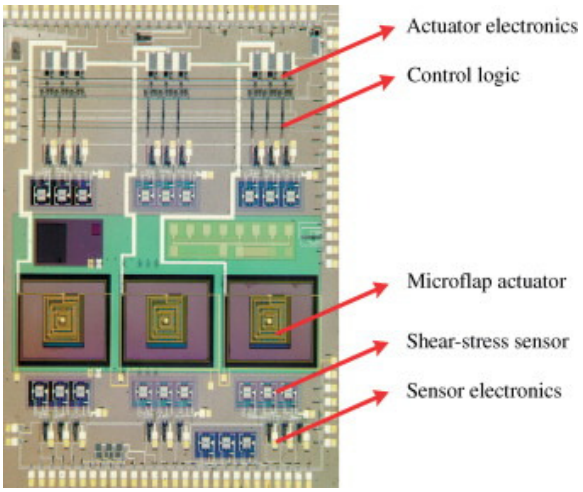

Figure 4.4: A **MEMS** tile integrating sensors, actuators and control logic for distributed flow control application, developed by Prof. Chih-Ming Ho (UCLA) and Yu-Chong Tai (Caltech).

from [Glezer and Amitay, 2002]). This actuator is applied to thrust-vectoring, mixing enhancement, separation control and virtual surface shaping, for more details of its applications, see previous works in [Amitay et al., 1997], [Smith and Glezer, 1998], [Amitay et al., 1999], [Amitay et al., 2001]. The recent reviews of synthetic jet actuator and its applications were given in [Glezer and Amitay, 2002].

The **MEMS** actuators are largely used in the active flow control, [Ho and Tai, 1996], [Ho and Tai, 1998]. A concept of **MEMS** arrays of sensors and actuators is shown in Figure 4.4 (taken from [Bewley, 2001]). Note that **MEMS** sensors measure the shear stress and **MEMS** actuators are blowing/suction actuators. For more technology of **MEMS**, the recent **MEMS** handbook was presented in [Gad-el Hak, 2010a], [Gad-el Hak, 2010b].

Both the sensors and the actuators have been presented, we next discuss about the methods of reactive flow control.

4.2.3 Methods of reactive flow control

In [Moin and Bewley, 1994], the reactive feedback control strategies were categorized by four categories: adaptive, physical model-based, dynamical systems-based, optimal control, as shown in Figure 4.5.

First strategy is adaptive flow control technique which concerns models and controllers without regarding to the detail of the flow physics. Note that a model for the adaptive control is identified independently of the Navier-Stokes equations. The adaptive schemes are based on the feedback control theory such as linear and nonlinear control theories, neural networks control. An example, the nonlinear adaptive control technique has been successfully applied to control the transition process in turbulent

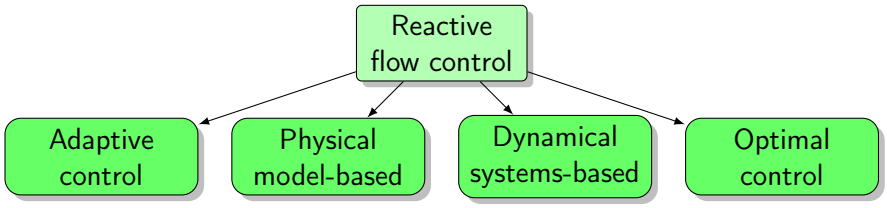

Figure 4.5: Methods of reactive flow control.

boundary layers [Fan et al., 1993] while the neural networks technique was used in turbulence control for the drag reduction.

Second strategy is physical model-based, this technique is used when the dominant physics are well understood. An example of this strategy is to reduce the drag by mitigating the effect of near wall vortices in [Gad-el Hak and Blackwelder, 1989], [Choi et al., 1994]. Although this strategy can be applied to the flow, it is limited to simple flows.

Third strategy is dynamical systems-based which supposes that the flow is controlled based on a reduced model. The nonlinear dynamical system theory allows turbulence to be decomposed into a reduced model where the control theory is applied. An example of this strategy is Proper Orthogonal Decomposition (**POD**) method which gives a model reduction based on the analysis of turbulent flows, in [Berkooz et al., 1993]. A Balanced Model Reduction is usually used in **POD** method, as shown in [Willcox and Peraire, 2002], [Rowley, 2005].

Finally, the optimal control theory is used to apply directly the Navier-Stokes equations to minimize a cost function. The controller is designed based on the Navier-Stokes equations such as sub-optimal control [Choi et al., 1993b] or linear feedback control: **PID** control [Joshi et al., 1997], **LQR** control [Joshi et al., 1999]. This strategy is the ideal of controller in this thesis.

In the next section, we consider some types of flow in the closed loop control.

4.2.4 Types of flow

Some types of flow are often studied in the flow control such as: the cavity flow, flow around a cylinder and plane channel flow.

The flow over a cavity, as shown in Figure 4.6, mainly produces acoustic waves which contain many problematic sources in aircraft. The recent reviews of the cavity flow were given in [Cattafesta et al., 2003], [Rowley and Williams, 2006]. An example of the active closed loop control of the cavity flow has been studied and developed at the Ohio State University. A shallow cavity flow is as shown in Figure 4.7 (taken from [Samimy et al., 2007]). The shallow cavity flow was studied at low Mach number. In previous works such as [Yan et al., 2004], [Yuan et al., 2005], [Yan et al., 2006], [Samimy et al., 2007], the linear feedback controls such as $\mathbf{H}_\infty$, **PID**, and Smith predictor based on controllers were designed and tested. **POD** technique and synthetic jet actuators were used to obtain a model reduction and control the flow, respectively.

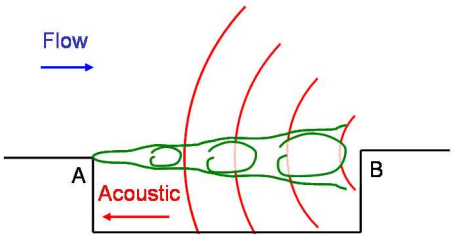

Figure 4.6: Cavity flow is an acoustic sources.

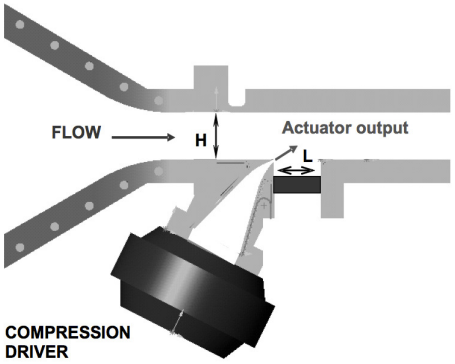

Figure 4.7: Scaled drawing of the experimental set up showing the test section with the cavity and the actuator.

More studies about the cavity flow are found [Caraballo et al., 2008], [Kim et al., 2008], [Kim et al., 2009].

The flow around a cylinder is classical active flow control. The configuration of flow around a cylinder is shown in Figure 4.8 for both laminar and turbulent flows. In

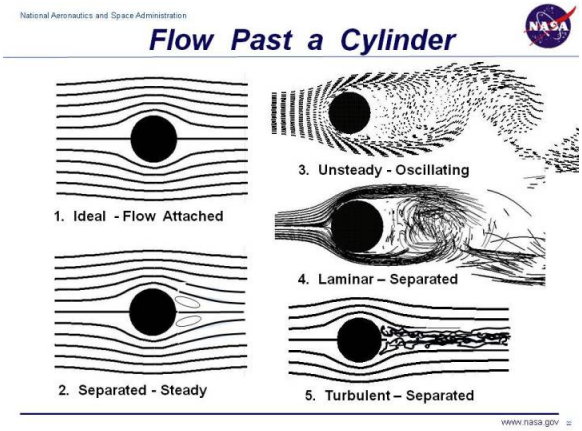

Figure 4.8: Flow around a cylinder and the phenomenas.

[Min and Choi, 1999], a suboptimal feedback control was studied and applied to the flow behind a circular cylinder. The sensors and actuators are located on the cylinder, as shown in Figure 4.9 (taken from [Min and Choi, 1999]). The control signal is blowing/suction and the feedback control is developed based on minimizing the cost functions to reduce the drag and vortex shedding. The recent reviews of this flow were described in [Choi et al., 2008] for the problem of 3D forcing, the active feedback control, the control based on local and global instability, and the control with synthetic jet actuators. More examples of this flow are found in [Lauga and Bewley, 2002], [Bergmann and Brancher, 2005].

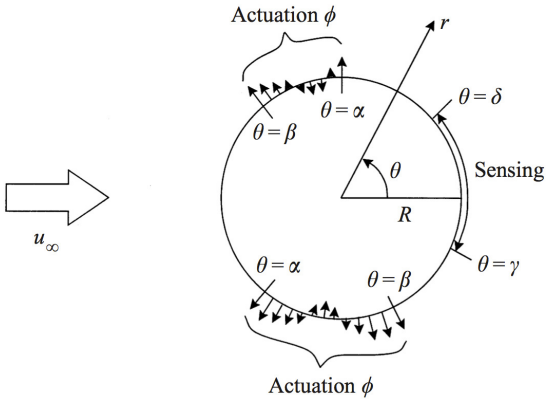

Figure 4.9: Schematic of the sensing and actuation for vortex shedding.

The plane Poiseuille flow, as shown in Figure 4.10 (taken from [Joshi et al., 1997]), is easier to consider in the context of classical control theory than the others. Joshi was

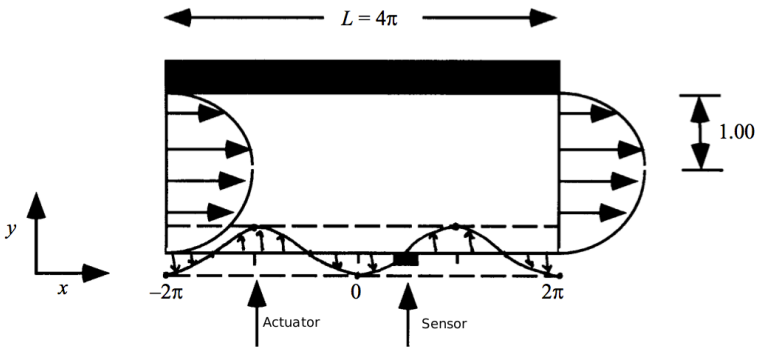

Figure 4.10: Plane Poiseuille flow.

the first person who designed a linear feedback control based on the linear model for the full nonlinear process. A simple **PID** control was used to stabilize the plane Poiseuille flow. Since the success of Joshi's work [Joshi et al., 1997], a **LQG** control was developed for the 2D plane Poiseuille flow in [Joshi, 1996], [Joshi et al., 1999], it contains a **LQR** regulator and a **LQE** estimator. In order to reduce the order of the controller,

in [Cortelezzi and Speyer, 1998], [Cortelezzi et al., 1998a], [Cortelezzi et al., 1998b], a **LQR** control was applied to a reduced model. The control of the 3D plane Poiseuille flow was extensively studied and developed in [Kang et al., 1999], [Bewley and Liu, 1998]. When the 3D plane Poiseuille flow was considered, the transient energy growth was focused. Therefore, in [Bewley and Liu, 1998], $\mathbf{H}_2/\mathbf{H}_\infty$ controls were used to stabilize the 3D plane Poiseuille flow and minimize the kinetic energy density. The recent reviews of linear feedback control for the plane Poiseuille flow were introduced in [Kim and Bewley, 2007]. On the other hand, a feedback control based on the analysis of Lyapunov function stabilized the 2D plane Poiseuillel flow in [Balogh et al., 1999], [Balogh et al., 2000], [Balogh et al., 2001], [Aamo et al., 2003].

The subject of this thesis in the next section is studying the problem of the plane Poiseuille flow.

4.3 Plane Poiseuille flow

The plane Poiseuille flow is chosen as academic case study in this thesis due to the fact that it is traight torward to obtain a model to be used for controller design. A list of control approaches includes: opposition control, adjoint-based suboptimal control, neural networks control, linear control and also nonlinear control. In particular, we can model the plane Poiseuille flow to a state space representation, whose control approach is easy to be designed. Furthermore, it contains fundamental difficulties encountered in all flow control applications such as the problem of distributed sensor and actuators. In addition, many important unsolved issues of flow control can be studied, for instance, drag reduction and kinetic energy minimization. Finally, in our opinion, this flow is a good example of the application of the visual servoing control in the context of flow control.

4.3.1 Problem description

The governing equations of the plane Poiseuille flow are the Navier-Stokes Equations. In order to study the behavior of this flow, we use numerical methods to convert **PDE** of small perturbation to a set of **ODE**. The linearized Navier-Stokes equations are converted to a state-space representation

$$\dot{\mathbf{x}}(t) = \mathbf{L}^{-1}\mathbf{A}\mathbf{x}(t), \tag{4.1}$$

where the vector $\mathbf{x}(t)$ involves the velocity. And the operator $\mathbf{L}^{-1}\mathbf{A}$ is given by

$$\mathbf{L}^{-1}\mathbf{A} = \begin{bmatrix} \mathbf{L_{OS}} & 0 \\ \mathbf{L_C} & \mathbf{L_{Sq}} \end{bmatrix}, \tag{4.2}$$

where the operators $\mathbf{L_{OS}}, \mathbf{L_{Sq}}, \mathbf{L_C}$ are Orr-Sommerfeld, Squire, and coupling operators, respectively or we simply call Orr-Sommerfeld operators. Note that these operators are defined later.

From previous works in the scientific literature, we can classify the active control of plane Poiseuille flow into several important problems which are: stabilization, kinetic energy density minimization and drag reduction. We illustrate these problems through a simple example in order to explain these concepts more clearly. Considering the following systems

$$\dot{\mathbf{x}}_1(t) = \begin{bmatrix} 0.1 & 0 \\ 0.5 & -0.11 \end{bmatrix} \mathbf{x}_1(t) \tag{4.3}$$

$$\dot{\mathbf{x}}_2(t) = \begin{bmatrix} -0.1 & 0 \\ 0.5 & -0.11 \end{bmatrix} \mathbf{x}_2(t) \tag{4.4}$$

$$\dot{\mathbf{x}}_3(t) = \begin{bmatrix} -0.1 & 0 \\ 0 & -0.1 \end{bmatrix} \mathbf{x}_3(t). \tag{4.5}$$

The behavior of uncontrolled plane Poiseuille flow is equivalent to the systems $\mathbf{x}_1(t)$ and $\mathbf{x}_2(t)$. The kinetic energy density of three systems can be denoted $\varepsilon_1(t) = \mathbf{x}_1^\top(t)\mathbf{x}_1(t)$, $\varepsilon_2(t) = \mathbf{x}_2^\top(t)\mathbf{x}_2(t)$ and $\varepsilon_3(t) = \mathbf{x}_3^\top(t)\mathbf{x}_3(t)$, respectively. As a result, the behavior of the three systems are shown in Figure 4.11 with the initial condition $\mathbf{x}_{10} = \mathbf{x}_{20} = \mathbf{x}_{30} = (1, 1)$. In this example, the system $\mathbf{x}_1(t)$ has an unstable eigenvalue (positive

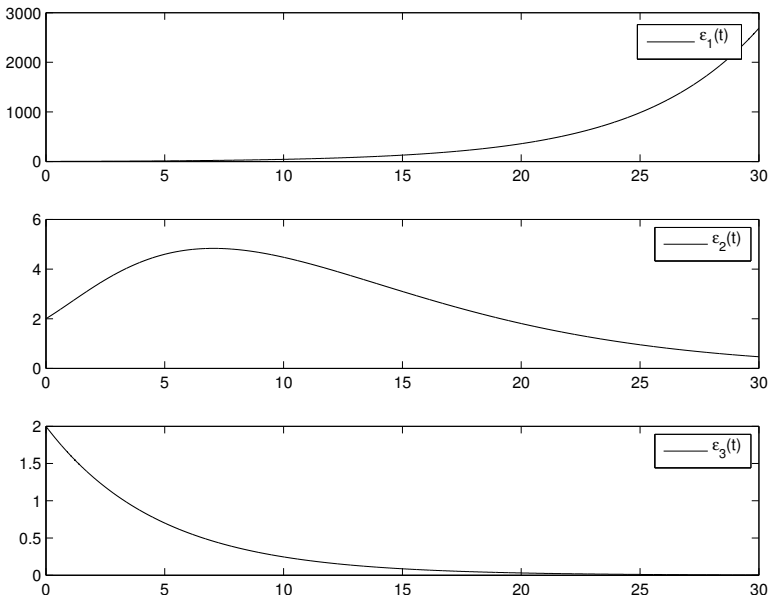

Figure 4.11: Behavior of the kinetic energy density versus time.

eigenvalue), therefore the kinetic energy density is infinite and insignificant. Hence, the system $\mathbf{x}_1(t)$ must be stabilized. For the system $\mathbf{x}_2(t)$, although all eigenvalues are stable (negative eigenvalue) but the eigenvectors are nonorthogonal, therefore the kinetic energy density increases and obtains the maximum value before decreasing and tending toward to zero, this problem is called a non-normality problem. Note that the plane Poiseuille flow becomes turbulent when the kinetic energy density increases,

for this reason, the maximum kinetic energy density must be reduced. In brief, this example illustrates the behavior of the plane Poiseuille flow because the form of the Orr-Sommerfeld operators is similar to the systems $\mathbf{x}_1(t)$ and $\mathbf{x}_2(t)$. In contrast to the systems $\mathbf{x}_1(t)$ and $\mathbf{x}_2(t)$, the system $\mathbf{x}_3(t)$ contains all stable eigenvalues and its eigenvectors are orthogonal. The kinetic energy density has an exponential decrease. For this reason, the main aim of this thesis is to obtain the closed loop system of the plane Poiseuille flow as the system $\mathbf{x}_3(t)$.

On the other hand, the problems of the plane Poiseuille flow can be distinguished based on the Reynolds number (see section 2.3). More precisely, the plane Poiseuille flow contains the unstable modes at the high Reynolds number $R > R_L = 5772$, which means we have a problem of stabilization. In addition, this flow has the non-normality at the Reynolds number $R_G = 49.6 < R < R_L$, we have a problem of kinetic energy density minimization. Note that when the flow is laminar, the drag reduction is significant, therefore the drag reduction is investigated at the low Reynolds number $R < R_T = 1000$. Previous works on the control of the plane Poiseuille flow will be presented in the following.

4.3.2 Previous works

4.3.2.1 Stabilization

A linear model of the plane Poiseuille flow was first proposed by Joshi [Joshi, 1996]. He used the Galerkin method to form a linear model system from the linearized 2D plane Poiseuille flow. The linear model contains unstable modes [Orszag, 1971], [Joshi, 1996], [Joshi et al., 1997] ($R > R_L = 5772$) which lead the flow to turbulence. Therefore, a simple controller as a **PID** control was used to stabilize the unstable modes [Joshi, 1996], [Joshi et al., 1997]. Another way to stabilize the unstable modes was to use a **LQR** control in [Joshi, 1996], [Joshi et al., 1999] where the shear stress energy was chosen as the cost function of the **LQR** criteria. The **LQR** control is a state feedback control which needs an estimation of the state vector. Therefore, a **LQG** control was used in [Joshi, 1996], [Joshi et al., 1999] to provide the estimation of the state vector from the measurement of the shear stress. **In the Joshi's work, he demonstrated that the linear feedback control based on the linear model could be applied to the full nonlinear plane Poiseuille flow. Hence, these results are the fundamental result for the channel flow control based on a linear model.**

Although the controller was designed based on the linear model, the order of controller was still large because numerical method needs a large dimension. In order to reduce the order of controller, the dimension of linear model was reduced to a reduced order model by using a Jordan Canonical Form. This technique was studied in [Cortelezzi and Speyer, 1998], [Cortelezzi et al., 1998a], [Cortelezzi et al., 1998b] and the **LQR** control like in [Joshi et al., 1999] was applied to the reduced order model. Hence, Cortelezzi and co-workers have given a very good drag reduction in their nonlinear simulation. Once again, these results demonstrated that the linear control based on the linearized plane Poiseuille flow could give a good result for the nonlinear plane

Poiseuille flow.

Since the 2D plane Poiseuille flow does not fully represent turbulence, the 3D plane Poiseuille flow was extensively developed in [Bewley and Liu, 1998], [Lee et al., 2001]. Although the linear model contains all stable modes, the flow may become turbulent due to the appearance of the transient energy growth ($R_E = 49.6 < R < R_L = 5772$), see the experiments in [Patel and Head, 1969] and [Lundbladh and Johansson, 1991]. This problem is called the non-normality problem of the flow. So that, the transient energy growth of the flow must be minimized.

4.3.2.2 Kinetic energy density minimization

The operators or matrices are said to be normal if their condition numbers equal one [Kato, 1976], [Trefethen, 1992], they have a set of orthogonal eigenfunctions or orthogonal eigenvectors which can be diagonalized by an unitary similarity transformation [Trefethen and Embree, 2005]. In numerical methods, the non-normality of operators or matrices may be investigated based on methods such as matrix exponential, resolvent (or $\varepsilon-$pseudospectra), numerical abscissa, transfer function norm in component form, and the impulse response (see recent reviews in [Schmid, 2007]).

In the fluid flow, the non-normality problem occurs due to the non-normality of the Orr-Sommerfeld operators. In fact, linear terms of Navier Stokes equations maintain turbulence [Kim and Lim, 2000], [Kim, 2003], and [Kim, 2011] while nonlinear terms only redistribute the energy [Högberg and Bewley, 2000]. **Therefore, Orr-Sommerfeld operators are sufficient enough for investigating the transient energy growth**.

Previous works in the scientific literature showed that the plane Poiseuille flow becomes turbulent even though their linear model contains all stable modes. More precisely, the eigenfunctions are nonorthogonal, the transient energy growth occurs [Butler and Farrell, 1992], [Henningson et al., 1993], [Reddy and Henningson, 1993] and [Trefethen et al., 1993], [Henningson, 1991], [Gustavsson, 1991]. When the transient energy growth is large enough, the flow becomes turbulent. Note that the small perturbations to the smooth flow may be amplified by a factors on the order of 10^5 by a linear mechanism even though all the states of the linear model monotonically decay [Trefethen et al., 1993].

The eigenvalues and eigenfunctions of an operator are still defined as a matrix [Trefethen and Embree, 2005]. Indeed, the eigenvalue problems for the matrices often come out through the discretizations of linear operators [Lanczos, 1950]. Therefore, the nonorthogonal eigenfunctions become the nonorthogonal eigenvectors [Reddy et al., 1993], [Reddy and Henningson, 1993]. In the plane Poiseuille flow, the non-normality problem of Orr-Sommerfeld operators becomes the nonorthogonality of the eigenvectors in [Bewley and Liu, 1998]. With the purpose of limitation of the transient energy growth, Bewley used optimal ($\mathbf{H}_2$) and robust ($\mathbf{H}_\infty$) controls to achieve a closed loop system whose nonorthogonality of eigenvectors are reduced. The $\mathbf{H}_2$ and $\mathbf{H}_\infty$ controls modify all of the eigenvectors, and thus these controls reduce the nonortohognality but the eigenvectors of the closed loop system are still nonorthogonal. Of course, the transient

energy growth is only reduced. In the same way, a **PID** control was used but provided less performance than the $\mathbf{H}_2$ and $\mathbf{H}_\infty$ controls.

The cause of the nonorthogonality of eigenvectors is due to the nearly identical pairs of eigenvalues [Bewley and Liu, 1998]. Indeed, this cause comes from the coupling term of Orr-Sommerfelds operators [Kim and Lim, 2000]. Motivated by these results, a **LQR** control was designed to minimize this coupling term [Lim, 2003]. An interesting result is that the **LQR** control could reduce the coupling term but could not completely eliminate it, in contrast to the virtual flow, where the coupling term was artificially removed and a better result obtained from the nonlinear simulations [Kim and Lim, 2000], [Kim, 2003]. In addition, the similar **LQR** control was also developed in [Högberg and Bewley, 2000], [Högberg et al., 2001], [Högberg et al., 2003], [Högberg and Henningson, 2002] to reduce the nonorthogonality.

On the other hand, a **LMI** approach [Whidborne and McKernan, 2007] was also applied to the plane Poiseuille flow [McKernan, 2006], [Whidborne et al., 2008] in order to find the minimum value of the transient energy growth. Although this approach could reduce the energy bound to the minimum value in their model but it is the same thing as with above control approaches ($\mathbf{H}_2$, $\mathbf{H}_\infty$ and **LQR**). This control approach was just verified in the lineari and nonlinear models of the plane Poiseuille flow [Martinelli et al., 2009], [Martinelli et al., 2011]. And again, a linear control is a good choice for the nonlinear plane Poiseuille flow.

Using the nonlinear theory, [Balogh et al., 2001], [Aamo, 2002], [Aamo et al., 2003], the standard Lyapunov-based approach was applied to the 2D plane Poiseuille flow. The energy of perturbation could decay exponentially in time, therefore we have no problem of non-normality any more but this control approach depends on the low Reynolds number (in this case $R < 1/4$, note that $R < R_E = 49.6$, the flow is always monotonically stable). Although the author gave the good simulation results at $R = 7500$, however this problem must be extended to the 3D plane Poiseuille flow and the control law does not depend on the Reynolds number since the Reynolds number may be an uncertain number.

The plane Poiseuille flow is different to general nonlinear systems, the flow still becomes turbulent even if its linearization contains all negative eigenvalue. Therefore, we must minimize the kinetic energy density ($\varepsilon(t)$) which captures the stability of the flow. Our core aim of this thesis is trying to guarantee $\dot{\varepsilon}(t) \leq 0$ in the closed loop system of the plane Poiseuille flow.

4.3.2.3 Drag reduction

General reviews of the drag reduction were recently reported in [Kim, 2011]. When the Reynolds number is low, we do not have the problem of transient energy growth, the drag reduction becomes important.

The controllers for drag reduction are opposition control, neural networks control, adjoint-based suboptimal control and linear control which are based on a linear model as **PID** and **LQR** controls, see [Kim, 2003].

In [Choi et al., 1994], [Hammond et al., 1998], the drag reduction was obtained by

using opposition control, an interesting result with $25\% - 30\%$ drag reduction. However, this technique used blowing/ suction at the wall $y^+ = 10$, therefore this technique is not available in practice.

A neural networks control [Fan et al., 1993], [Lee et al., 1997] was applied to a turbulent channel flow at low Reynolds number, 20% drag reduction.

An adjoint-based suboptimal control approach has been proposed in previous works [Bewley et al., 1993], a drag reduction, approximately 17%, have been obtained. However, this way of process leads to a very high computation cost, not compatible with in a real time control scheme. Moreover, it is not possible to implement this approach in practice.

A **PID** control was used to suppress the wall shear stress (**WSS**) leading consequently to a drag reduction. While in [Cortelezzi et al., 1998a], [Cortelezzi et al., 1998b], [Cortelezzi and Speyer, 1998], a **LQR** control was used in which the cost function to minimize includes the drag reduction, the reported result of drag reduction to 50% below the laminar level.

A Lorentz force actuator was used to reduce skin friction drag, 40% drag reduction at the low Reynolds number $R = 100$. This actuator was also applied to high Reynolds number $R = 200$ and $R = 400$.

In drag reduction, some control approaches are opposition control, neural networks control, adjoint-based suboptimal control and linear control but only the linear control is significant in practice due to the limitation of the other approaches [Kim, 2003]. The linear control approaches in previous works are **PID**, **LQR** and **LMI** controls, however, these control approaches do not minimize directly the skin-friction drag, therefore we need a control approach which can minimize directly the skin-friction drag.

4.3.2.4 Measurement of flow

How can we determine the state flow. In [Bewley and Protas, 2004], the measurement of **WSS** and pressure are sufficient to determine the state of turbulent flow while the **WSS** alone is sufficient to determine the state of linearized flow. In [Hoepffner et al., 2005], [Chevalier et al., 2006], an estimation of the state flow was designed based on the Kalman filter, the linearized Navier-Stokes equations were used.

We use the active control, more precisely a feedback control. To do it, we must determine the state vector estimation (when a state feedback control is used, e.g. a **LQR** control in [Joshi et al., 1999])) or the output estimation (when output feedback control is used, a proportional control [Joshi et al., 1997]) from the output information. From the information of **WSS**, the **LQG** control is used to construct the state vector estimation, see previous works in [Joshi et al., 1997], [Bewley and Liu, 1998], [Högberg et al., 2003], [Hoepffner et al., 2005] and [Chevalier et al., 2006].

In the fluid flow, **WSS** is often measured by using sensors such as **MEMS** sensors in [Ho and Tai, 1996] and [Xu et al., 2003]. This technique is limited due to the limited surface of the sensing element, thus limiting the applicability of these devices in physic relevant geometries.

Another way can be used to estimate the state vector, the velocity map is directly

measured by using Charge Coupled Device (**CCD**) camera in [Heitz et al., 2010]. We use a **CCD** camera to estimate the state vector, of course a great advantage with respect to a sensor at the walls, see [Tatsambon Fomena and Collewet, 2011b]. The optical sensor was used, the state vector can be directly calculated from the velocity. Concerning the visual servoing control, the optical flow technique is used to estimate the state vector from the visual measurement that is shown in Figure 4.12.

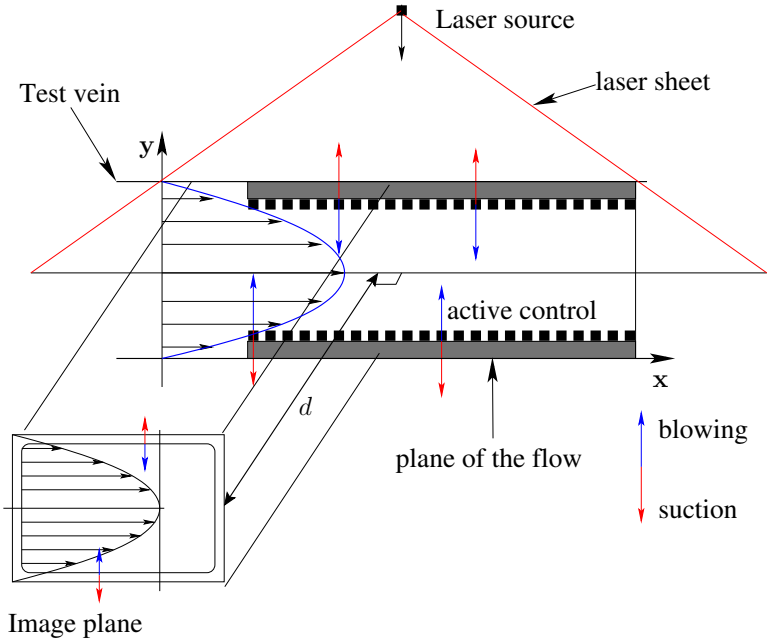

Figure 4.12: Fronto-parallel visualization of a 2D flow using laser sheet which role is to enlighten the particles seeded in the fluid.

A laser sheet is used to enlighten the particles for which the velocities are computed, see Figure 4.12. As a result, from this visualization process, it is possible to compute the dense flow which can be defined as the apparent velocity vector field representing the motion of photometric pattern (pixels brightness) in successive image sequences in [Heitz et al., 2010] in three steps ([Tatsambon Fomena and Collewet, 2011b]):

- Perspective projection of a flow particle
- Estimation of the flow velocity particle from its image
- Estimation of the state vector

4.3.2.5 Validation of linear feedback control on nonlinear simulation

In order to answer to the question: can a feedback control based on the linear model be applied to the full nonlinear flow. In previous works, the feedback controller based on the linear model was tested on the full flow. **DNS** toolbox was used to simulate

the result for the full nonlinear flow. A first **DNS** was developed in [Kim et al., 1987] and the recent reviews of **DNS** tool is found in [Moin and Mahesh, 1998]. Some feedback controllers based on the linear model were applied to **DNS** toolbox such as the **PID** control in [Joshi, 1996], [Joshi et al., 1997], the **LQR** control in [Lim, 2003], [Kim, 2003], [Högberg et al., 2003], [McKernan et al., 2007] and the **LMI** control in [Martinelli et al., 2011]. Indeed, a linear feedback controller based on linear model can be applied to the full nonlinear flow. This is why a linear feedback control is chosen to obtain the stability of the flow.

4.4 Objectives

In this thesis, we denote the kinetic energy density $\varepsilon(t)$ and the skin-friction drag $\mathbf{d}(t)$. Our objectives concern both the kinetic energy density and the skin-friction drag to be minimized.

In previous works, **PID**, $\mathbf{H}_2/\mathbf{H}_\infty$, **LQR**, and **LMI** controls make the set eigenvectors more orthogonal through minimizing the shear stress or the kinetic energy density but these control approaches cannot directly eliminate the nonorthogonality. Hence, the limitation of these control approaches are due to the number of the degree of freedom (**DOF**) (the independent control signals). The number of **DOF** is one for the linear model in [Joshi et al., 1997], two for the linear model in [Aamo, 2002], [Bewley and Liu, 1998], [Högberg et al., 2003], [McKernan, 2006]. Therefore, the non-normality still exists with these control schemes, more precisely, the transient energy growth still occurs and the flow becomes turbulent. Thus, some control schemes always achieve an exponential decrease of kinetic energy density must be proposed. It means that the non-normality or the problem of nonorthogonality of eigenfunctions of the Orr-Sommerfeld operators is completely solved.

We recall previous important works. A controller was designed to ensure $\dot{\varepsilon}(t) \leq 0$ in [Balogh et al., 2001], [Aamo, 2002], [Aamo et al., 2003] but these control approaches depend on the Reynolds number and are only applied when $R < 1/4$. To our knowledge, the previous controllers have never been able to ensure $\dot{\varepsilon}(t) \leq 0$ and $\dot{\mathbf{d}}(t) \leq 0$ for all the Reynolds number.

Our main aim of this thesis is to design a controller which is capable to ensure $\dot{\varepsilon}(t) \leq 0$ or/and $\dot{\mathbf{d}}(t) \leq 0$ in the closed loop system of the plane Poiseuille flow and our approach can be applied for all the Reynolds number. In the context of the visual servoing control, the kinetic energy density and the skin-friction drag achieve:

$$\begin{cases} \dot{\varepsilon}(t) & = -\lambda\varepsilon(t) \\ \dot{\mathbf{d}}(t) & = -\lambda\mathbf{d}(t), \end{cases} \tag{4.6}$$

it means that the kinetic energy density and skin friction drag monotonically decrease in time. Based on the above points of view, the objectives of this thesis are contributions as follows

- The first objective is to demonstrate the benefits of the partitioned visual servoing control to the plane Poiseuille flow for drag reduction. The partitioned visual servoing control exploits two **DOF** to simultaneously minimize the skin friction drag and the kinetic energy density. The skin-friction drag monotonically decreases in time but the behavior of the kinetic energy density does not monotonically decrease in time.

- The next objective is to obtain multiple inputs multiple outputs (**MIMO**) model of the plane Poiseuille flow. The number of **DOF** increase and is very large than the exist models in the scientific literature. The behavior of the kinetic energy density in the closed system is improved since increasing the number of **DOF**.

- A further objective is to design a feedback control which leads the state vector to monotonically decrease in time. Certainly, the kinetic energy density, the skin friction drag and the velocity component also monotonically decrease in time. The visual servoing control is used when the number of **DOF** is equal to the number of the state vector. The non-normality of the plane Poiseuille flow is solved, and the result allows us to ensure that the flow always remains laminar state.

- Another objective is to design a controller based on a reduced model when the dimension of the linearized plane Poiseuille flow is large. Indeed, we use the model reduction to design a controller which leads the kinetic energy density to almost monotonically decrease. We demonstrate that the kinetic energy density will almost monotonically decrease in time even using two **DOF**.

- The final objective is to show the robustness of the controller to measurement noise. Since the optical flow is used to estimate the state vector, our control approach is robust to measurement noise.

4.5 Achievements

The following paper have been written to disseminate the results of the research described in this thesis:

Dao13a : X-Q. Dao, C. Collewet. Minimisation de l'énergie cinétique transitoire dans l'écoulement 3D plan de Poiseuille commandé. In 21ème **Congrès français de Mécanique**, Bordeau, France, August 2013.

Dao12a : X-Q. Dao, C. Collewet. Drag Reduction of the Plane Poiseuille Flow by Partitioned Visual Servo Control. In **American Control Conference**, Pages 4084-4089, Montréal, Canada, June 2012.

Dao12b : X-Q. Dao, C. Collewet. Simultaneous Drag Reduction and Kinetic Energy Density of the Plane Poiseuille Flow. In 6th **AIAA Flow Control Conference**, Pages 2807-2817, New Orleans, Louisiana, USA, June 2012.

Dao12c : X-Q. Dao, C. Collewet. Réduction de la traïnée de l'écoulement de Poiseuille 2D par asservissement visuel partitionné. In 7ème **Conférence Internationale Francophone d'Automatique**, Pages 449-454, Grenoble, France, July 2012.

Dao11a : X-Q. Dao, C. Collewet. La commande basée vision : une nouvelle approche pour la commande en boucle fermée des écoulements fluides. In **GdR: Contrôle des décollements**, 2011.

Chapter 5

Modeling of Plane Poiseuille Flow

In this chapter, a linear model is proposed for the plane Poiseuille flow. We first present a steady solution of the Navier Stokes equations, then the "wall-normal velocity vorticity" desired formulation is chosen to use in this thesis. We are interested in the control principle which is based on the distributed actuation. The plane Poiseuille flow is solved by using the spectral method based on the Fourier series and the Chebyshev polynomials leading to the linear model, a state-space representation. We describe a linear model of the plane Poiseuille flow based on previous works in [Joshi, 1996], [Bewley and Liu, 1998], [Aamo et al., 2003] and [McKernan, 2006].

5.1 Formulation of plane Poiseuille flow

5.1.1 Navier Stokes equations for incompressible, viscous flow

The Navier-Stokes equations for an incompressible fluid flow are

$$\left\{ \begin{array}{ll} \nabla.\mathbf{V} & = 0 \\ \dfrac{\partial \mathbf{V}}{\partial t} + (\mathbf{V}.\nabla)\mathbf{V} & = -\nabla P + \dfrac{1}{R}\Delta \mathbf{V}. \end{array} \right. \tag{5.1}$$

where P and $\mathbf{V}$ are pressure and velocity, respectively. The gradient operator is given by $\nabla = (\dfrac{\partial}{\partial x}, \dfrac{\partial}{\partial y}, \dfrac{\partial}{\partial z})$ and the Laplacian operator is given by $\Delta = \dfrac{\partial^2}{\partial x^2} + \dfrac{\partial^2}{\partial y^2} + \dfrac{\partial^2}{\partial z^2}$. The Reynolds number is denoted R. The Navier-Stokes equations are rewritten in Cartesian coordinates where the velocity is denoted by $\mathbf{V} = (U, V, W)$, the equations (5.1) are rewritten by

$$\left\{ \begin{array}{ll} \dfrac{\partial U}{\partial x} + \dfrac{\partial V}{\partial y} + \dfrac{\partial W}{\partial z} & = 0 \\ \dfrac{\partial U}{\partial t} + U\dfrac{\partial U}{\partial x} + V\dfrac{\partial U}{\partial y} + W\dfrac{\partial U}{\partial z} & = -\dfrac{\partial P}{\partial x} + \dfrac{1}{R}(\dfrac{\partial^2 U}{\partial x^2} + \dfrac{\partial^2 U}{\partial y^2} + \dfrac{\partial^2 U}{\partial z^2}) \\ \dfrac{\partial V}{\partial t} + U\dfrac{\partial V}{\partial x} + V\dfrac{\partial V}{\partial y} + W\dfrac{\partial V}{\partial z} & = -\dfrac{\partial P}{\partial y} + \dfrac{1}{R}(\dfrac{\partial^2 V}{\partial x^2} + \dfrac{\partial^2 V}{\partial y^2} + \dfrac{\partial^2 V}{\partial z^2}) \\ \dfrac{\partial W}{\partial t} + U\dfrac{\partial W}{\partial x} + V\dfrac{\partial U}{\partial y} + W\dfrac{\partial W}{\partial z} & = -\dfrac{\partial P}{\partial z} + \dfrac{1}{R}(\dfrac{\partial^2 W}{\partial x^2} + \dfrac{\partial^2 W}{\partial y^2} + \dfrac{\partial^2 W}{\partial z^2}). \end{array} \right. \tag{5.2}$$

5.1.2 Steady solution of Navier-Stokes equations

The steady solution is given by

$$(\frac{\partial U}{\partial t}, \frac{\partial V}{\partial t}, \frac{\partial W}{\partial t}, \frac{\partial P}{\partial t}) = (0, 0, 0, 0), \tag{5.3}$$

therefore, substituting (5.3) into (5.2), we get

$$\begin{cases} \frac{\partial U}{\partial x} + \frac{\partial V}{\partial y} + \frac{\partial W}{\partial z} & = 0 \\ U\frac{\partial U}{\partial x} + V\frac{\partial U}{\partial y} + W\frac{\partial U}{\partial z} & = -\frac{\partial P}{\partial x} + \frac{1}{R}(\frac{\partial^2 U}{\partial x^2} + \frac{\partial^2 U}{\partial y^2} + \frac{\partial^2 U}{\partial z^2}) \\ U\frac{\partial V}{\partial x} + V\frac{\partial V}{\partial y} + W\frac{\partial V}{\partial z} & = -\frac{\partial P}{\partial y} + \frac{1}{R}(\frac{\partial^2 V}{\partial x^2} + \frac{\partial^2 V}{\partial y^2} + \frac{\partial^2 V}{\partial z^2}) \\ U\frac{\partial W}{\partial x} + V\frac{\partial U}{\partial y} + W\frac{\partial W}{\partial z} & = -\frac{\partial P}{\partial z} + \frac{1}{R}(\frac{\partial^2 W}{\partial x^2} + \frac{\partial^2 W}{\partial y^2} + \frac{\partial^2 W}{\partial z^2}). \end{cases} \tag{5.4}$$

Now, a steady solution of Navier-Stokes equations is solved for the plane Poiseuille

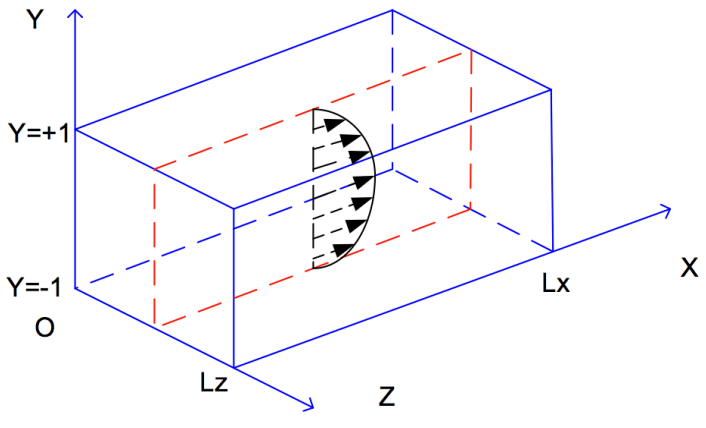

Figure 5.1: Steady solution of the plane Poiseuille flow and its profile.

flow where its profile is as shown in Figure 5.1. The domain of this flow is given by $\Omega = \{(x, y, z) \in [0, L_x) \times [-1, +1] \times [0, L_z)\}$ and the boundary conditions are assumed as $(U, V, W) = (0, 0, 0)$ at the walls $y = \pm 1$.

It is assumed that the velocity is independent on the streamwise and spanwise directions, the steady solution is $(U, V, W = U(y), V(y), W(y))$. The steady solution of

Navier-Stokes equations in (5.4) becomes

$$\begin{cases} \dfrac{\partial V}{\partial y} & = 0 \\ V\dfrac{\partial U}{\partial y} & = -\dfrac{\partial P}{\partial x} + \dfrac{1}{R}\dfrac{\partial^2 U}{\partial y^2} \\ V\dfrac{\partial V}{\partial y} & = -\dfrac{\partial P}{\partial y} + \dfrac{1}{R}\dfrac{\partial^2 V}{\partial y^2} \\ V\dfrac{\partial W}{\partial y} & = -\dfrac{\partial P}{\partial z} + \dfrac{1}{R}\dfrac{\partial^2 W}{\partial y^2}. \end{cases} \tag{5.5}$$

From $\dfrac{\partial V}{\partial y} = 0$, it is easy to see that $V(y) = constant$, since $V(y = \pm 1) = 0$ leads to $V(y) = 0$. Finding (U, W, P) is the next step, therefore, (5.5) becomes

$$\begin{cases} \dfrac{\partial P}{\partial x} & = \dfrac{1}{R}\dfrac{\partial^2 U}{\partial y^2} \\ \dfrac{\partial P}{\partial y} & = 0 \\ \dfrac{\partial P}{\partial z} & = \dfrac{1}{R}\dfrac{\partial^2 W}{\partial y^2}, \end{cases} \tag{5.6}$$

this equation leads to $P = P(x, z)$. It is assumed that the order of $U(y)$ and $W(y)$ is maximal two, (5.6) becomes

$$\begin{cases} \dfrac{\partial P}{\partial x} & = c_1 = \dfrac{1}{R}\dfrac{\partial^2 U}{\partial y^2} \\ \dfrac{\partial P}{\partial z} & = c_2 = \dfrac{1}{R}\dfrac{\partial^2 W}{\partial y^2}, \end{cases} \tag{5.7}$$

where c_1 and c_2 are constant. Therefore, (5.7) becomes

$$\begin{cases} P & = c_1 x + c_2 z + c_3 \\ U & = \dfrac{c_1 R}{2} y^2 + c_4 y + c_5 \\ W & = \dfrac{c_2 R}{2} y^2 + c_6 y + c_7, \end{cases} \tag{5.8}$$

where c_3, c_4, c_5, c_6, c_7 are constant. Note that c_3 may be arbitrarily chosen, so $c_3 = 0$. The other coefficients are given based on the boundary conditions at the walls.

For the plane Poiseuille flow, the boundary conditions at the walls $(y = \pm 1)$ are given by $(U(y = \pm 1) = 0, W(y = \pm 1) = 0)$, we get

$$\begin{cases} \dfrac{c_1 R}{2} + c_4 + c_5 = 0, & \dfrac{c_1 R}{2} - c_4 + c_5 = 0 \\ \dfrac{c_2 R}{2} + c_6 + c_7 = 0, & \dfrac{c_2 R}{2} - c_6 + c_7 = 0, \end{cases} \tag{5.9}$$

so that

$$c_4 = c_6 = 0, \quad c_1 = -\frac{2c_5}{R}, \quad c_2 = -\frac{2c_7}{R}. \tag{5.10}$$

We assume that $U(y=0)=1, W(y=0)=0$, we have $c_5=1, c_7=0$, therefore we obtain $c_1=-\frac{2}{R}, c_2=0$. The steady solution of Navier-Stokes equations in the plane Poiseuille flow is $(U,V,W,P_e=1-y^2,0,0,-\frac{2}{R}x)$.

5.1.3 Linearized Navier-Stokes equations

The linearized Navier-Stoke equations of small perturbation will be given. By using the change of variables $(\mathbf{V},P)=(u+U,v+V,w+W,p+P_e)$ where (U,V,W,P_e) are the steady solution and (u,v,w,p) are the perturbation. The equations (5.1) become

$$\begin{cases} \dfrac{\partial(u+U)}{\partial x}+\dfrac{\partial(v+V)}{\partial y}+\dfrac{\partial(w+W)}{\partial z}=0 \\ \dfrac{\partial(u+U)}{\partial t}+(u+U)\dfrac{\partial(u+U)}{\partial x}+(v+V)\dfrac{\partial(u+U)}{\partial y}+(w+W)\dfrac{\partial u}{\partial z} \\ \quad =-\dfrac{\partial(p+P_e)}{\partial x}+\dfrac{1}{R}(\dfrac{\partial^2(u+U)}{\partial x^2}+\dfrac{\partial^2(u+U)}{\partial y^2}+\dfrac{\partial^2(u+U)}{\partial z^2}) \\ \dfrac{\partial(v+V)}{\partial t}+(u+U)\dfrac{\partial(v+V)}{\partial x}+(v+V)\dfrac{\partial(v+V)}{\partial y}+(w+W)\dfrac{\partial(v+V)}{\partial z} \\ \quad =-\dfrac{\partial(p+P_e)}{\partial y}+\dfrac{1}{R}(\dfrac{\partial^2(v+V)}{\partial x^2}+\dfrac{\partial^2(v+V)}{\partial y^2}+\dfrac{\partial^2(v+V)}{\partial z^2}) \\ \dfrac{\partial(w+W)}{\partial t}+(u+U)\dfrac{\partial(w+W)}{\partial x}+(v+V)\dfrac{\partial(u+U)}{\partial y}+(w+W)\dfrac{\partial(w+W)}{\partial z} \\ \quad =-\dfrac{\partial(p+P_e)}{\partial z}+\dfrac{1}{R}(\dfrac{\partial^2(w+W)}{\partial x^2}+\dfrac{\partial^2(w+W)}{\partial y^2}+\dfrac{\partial^2(w+W)}{\partial z^2}). \end{cases} \tag{5.11}$$

By using (5.3) and (5.4), the perturbation equations become

$$\begin{cases} \dfrac{\partial u}{\partial x}+\dfrac{\partial v}{\partial y}+\dfrac{\partial w}{\partial z}=0 \\ \dfrac{\partial u}{\partial t}+u\dfrac{\partial u}{\partial x}+u\dfrac{\partial U}{\partial x}+U\dfrac{\partial u}{\partial x}+v\dfrac{\partial u}{\partial y}+v\dfrac{\partial U}{\partial y}+V\dfrac{\partial u}{\partial y}+w\dfrac{\partial u}{\partial z}+w\dfrac{\partial U}{\partial z}+W\dfrac{\partial u}{\partial z} \\ \quad =-\dfrac{\partial p}{\partial x}+\dfrac{1}{R}(\dfrac{\partial^2 u}{\partial x^2}+\dfrac{\partial^2 u}{\partial y^2}+\dfrac{\partial^2 u}{\partial z^2}) \\ \dfrac{\partial v}{\partial t}+u\dfrac{\partial v}{\partial x}+u\dfrac{\partial V}{\partial x}+U\dfrac{\partial v}{\partial x}+v\dfrac{\partial v}{\partial y}+v\dfrac{\partial V}{\partial y}+V\dfrac{\partial v}{\partial y}+w\dfrac{\partial v}{\partial z}+w\dfrac{\partial V}{\partial z}+W\dfrac{\partial v}{\partial z} \\ \quad =-\dfrac{\partial p}{\partial y}+\dfrac{1}{R}(\dfrac{\partial^2 v}{\partial x^2}+\dfrac{\partial^2 v}{\partial y^2}+\dfrac{\partial^2 v}{\partial z^2}) \\ \dfrac{\partial w}{\partial t}+u\dfrac{\partial w}{\partial x}+u\dfrac{\partial W}{\partial x}+U\dfrac{\partial w}{\partial x}+v\dfrac{\partial w}{\partial y}+v\dfrac{\partial W}{\partial y}+V\dfrac{\partial w}{\partial y}+w\dfrac{\partial w}{\partial z}+w\dfrac{\partial W}{\partial z}+W\dfrac{\partial w}{\partial z} \\ \quad =-\dfrac{\partial p}{\partial z}+\dfrac{1}{R}(\dfrac{\partial^2 w}{\partial x^2}+\dfrac{\partial^2 w}{\partial y^2}+\dfrac{\partial^2 w}{\partial z^2}). \end{cases} \tag{5.12}$$

The linearized equations are now obtained by omitting the second order terms in the perturbation equations

$$\begin{cases} \dfrac{\partial u}{\partial x}+\dfrac{\partial v}{\partial y}+\dfrac{\partial w}{\partial z} & =0 \\ \dfrac{\partial u}{\partial t}+u\dfrac{\partial U}{\partial x}+U\dfrac{\partial u}{\partial x}+v\dfrac{\partial U}{\partial y}+V\dfrac{\partial u}{\partial y}+w\dfrac{\partial U}{\partial z}+W\dfrac{\partial u}{\partial z} & =-\dfrac{\partial p}{\partial x}+\dfrac{1}{R}(\dfrac{\partial^2 u}{\partial x^2}+\dfrac{\partial^2 u}{\partial y^2}+\dfrac{\partial^2 u}{\partial z^2}) \\ \dfrac{\partial v}{\partial t}+u\dfrac{\partial V}{\partial x}+U\dfrac{\partial v}{\partial x}+v\dfrac{\partial V}{\partial y}+V\dfrac{\partial v}{\partial y}+w\dfrac{\partial V}{\partial z}+W\dfrac{\partial v}{\partial z} & =-\dfrac{\partial p}{\partial y}+\dfrac{1}{R}(\dfrac{\partial^2 v}{\partial x^2}+\dfrac{\partial^2 v}{\partial y^2}+\dfrac{\partial^2 v}{\partial z^2}) \\ \dfrac{\partial w}{\partial t}+u\dfrac{\partial W}{\partial x}+U\dfrac{\partial w}{\partial x}+v\dfrac{\partial W}{\partial y}+V\dfrac{\partial w}{\partial y}+w\dfrac{\partial W}{\partial z}+W\dfrac{\partial w}{\partial z} & =-\dfrac{\partial p}{\partial z}+\dfrac{1}{R}(\dfrac{\partial^2 w}{\partial x^2}+\dfrac{\partial^2 w}{\partial y^2}+\dfrac{\partial^2 w}{\partial z^2}). \end{cases} \tag{5.13}$$

The linearized equations (note that $(U,V,W)=U(y),0,0)$ are given by

$$\begin{cases} \dfrac{\partial u}{\partial x}+\dfrac{\partial v}{\partial y}+\dfrac{\partial w}{\partial z} & =0 \\ \dfrac{\partial u}{\partial t}+U\dfrac{\partial u}{\partial x}+v\dfrac{dU}{dy} & =-\dfrac{\partial p}{\partial x}+\dfrac{1}{R}(\dfrac{\partial^2 u}{\partial x^2}+\dfrac{\partial^2 u}{\partial y^2}+\dfrac{\partial^2 u}{\partial z^2}) \\ \dfrac{\partial v}{\partial t}+U\dfrac{\partial v}{\partial x} & =-\dfrac{\partial p}{\partial y}+\dfrac{1}{R}(\dfrac{\partial^2 v}{\partial x^2}+\dfrac{\partial^2 v}{\partial y^2}+\dfrac{\partial^2 v}{\partial z^2}) \\ \dfrac{\partial w}{\partial t}+U\dfrac{\partial w}{\partial x} & =-\dfrac{\partial p}{\partial z}+\dfrac{1}{R}(\dfrac{\partial^2 w}{\partial x^2}+\dfrac{\partial^2 w}{\partial y^2}+\dfrac{\partial^2 w}{\partial z^2}). \end{cases} \tag{5.14}$$

These equations are the linearized equations of the plane Poiseuille flow. These results will be used in the next section to convert **PDE** to **ODE**.

5.1.4 Wall-normal velocity vorticity formulation

We can rewrite (5.14) by the velocity pressure formulation

$$\frac{\partial u}{\partial x}+\frac{\partial v}{\partial y}+\frac{\partial w}{\partial z} = 0 \tag{5.15}$$

$$\frac{\partial u}{\partial t}+U\frac{\partial u}{\partial x}+\frac{dU}{dy}v = -\frac{\partial p}{\partial x}+\frac{1}{R}\Delta u \tag{5.16}$$

$$\frac{\partial v}{\partial t}+U\frac{\partial v}{\partial x} = -\frac{\partial p}{\partial y}+\frac{1}{R}\Delta v \tag{5.17}$$

$$\frac{\partial w}{\partial t}+U\frac{\partial w}{\partial x} = -\frac{\partial p}{\partial z}+\frac{1}{R}\Delta w. \tag{5.18}$$

The no-slip condition for viscous fluid is imposed at a solid surface as a boundary condition, the fluid flow has a zero velocity relative to the boundary

$$\begin{cases} v(x,\pm 1,z,t) & =0 \\ \dfrac{\partial v(x,\pm 1,z,t)}{\partial y} & =0. \end{cases} \tag{5.19}$$

Taking the derivative of (5.16-5.18) and using (5.15) yields an equation for the pressure

$$\Delta p=-2\frac{dU}{dy}\frac{\partial v}{\partial x}. \tag{5.20}$$

Next, (5.20) is used with (5.17) to eliminate the pressure p, the wall-normal velocity is given by

$$\frac{\partial(\Delta v)}{\partial t} + U\frac{\partial(\Delta v)}{\partial x} - \frac{d^2U}{dy^2}\frac{\partial v}{\partial x} - \frac{1}{R}\Delta^2 v = 0. \tag{5.21}$$

To describe the complete three-dimensional flow field, we need to use a second equation with the most conveniently wall-normal vorticity

$$\eta = \frac{\partial u}{\partial z} - \frac{\partial w}{\partial x}, \tag{5.22}$$

where η satisfies

$$\frac{\partial \eta}{\partial t} + U\frac{\partial \eta}{\partial x} - \frac{1}{R}\Delta\eta = -\frac{dU}{dy}\frac{\partial v}{\partial z}. \tag{5.23}$$

The wall-normal velocity vorticity formulation is

$$\frac{\partial(\Delta v)}{\partial t} + U\frac{\partial(\Delta v)}{\partial x} - \frac{d^2U}{dy^2}\frac{\partial v}{\partial x} - \frac{1}{R}\Delta^2 v = 0 \tag{5.24}$$

$$\frac{\partial \eta}{\partial t} + U\frac{\partial \eta}{\partial x} - \frac{1}{R}\Delta\eta = -\frac{dU}{dy}\frac{\partial v}{\partial z}. \tag{5.25}$$

These equations are also called the Orr-Sommerfeld and Squire equations. Note that (5.24) can be solved independently on (5.25). Therefore, (5.24) is first solved, plugging then $v(x, y, z, t)$ into (5.25), we can solve for $\eta(x, y, z, t)$. The no-slip boundary conditions concern the wall-normal velocity and the vorticity, they are given as

$$\begin{cases} v(x, y = \pm 1, z, t) & = 0 \\ \eta(x, y = \pm 1, z, t) & = 0 \\ \dfrac{\partial v(x, y = \pm 1, z, t)}{\partial y} & = 0, \end{cases} \tag{5.26}$$

An homogeneous Dirichlet boundary condition is imposed on the vorticity $\eta(x, y = \pm 1, z, t) = 0$ while for the wall-normal velocity simultaneous homogeneous Dirichlet and Neumann boundary conditions, $v(x, y = \pm 1, z, t) = 0$ and $\dfrac{\partial v(x, y = \pm 1, z, t)}{\partial y} = 0$ are respectively. The wall normal velocity vorticity formulation was used in previous works [Bewley and Liu, 1998], [Kang et al., 1999], [Högberg and Bewley, 2000], [Schmid and Henningson, 2001], [Chughtai and Werner, 2010], [McKernan, 2006] and [Aamo, 2002], [Tatsambon Fomena and Collewet, 2011a] for both 2D and 3D cases of the plane Poiseuille flow, for the plane Couette flow in [Schmid and Henningson, 2001] and [Butler and Farrell, 1992].

Note that we have another formulation: vorticity stream function. However, this formulation is only used in the 2D case in [Joshi et al., 1995], [Cortelezzi and Speyer, 1998].

5.1.5 Control principle

5.1.5.1 Boundary control

PDE are controlled by modifying the boundary conditions. The plane Poiseuille flow can be controlled via boundary control at the walls. Hence, the boundary control

consists in modifying the upper ($y = +1$) and lower ($y = -1$) boundary conditions [Joshi et al., 1995], [Joshi, 1996].

Using the wall-normal velocity vorticity formulation, in the controlled flow, an inhomogeneous Dirichlet boundary condition is on the wall-normal velocity and the vorticity. Based on the previous results in [Joshi et al., 1997], [McKernan, 2006] and [Martinelli et al., 2011], the boundary conditions on $v(x, y, z, t)$ and $\eta(x, y, z, t)$ are given by

$$\begin{cases} v(x, y = +1, z, t) & = q_{v,u}(x, z, t), \ v(x, y = -1, z, t) = q_{v,l}(x, z, t) \\ \eta(x, y = +1, z, t) & = q_{\eta,u}(x, z, t), \ \eta(x, y = -1, z, t) = q_{\eta,l}(x, z, t) \\ \dfrac{\partial v(x, y = \pm 1, t)}{\partial y} & = 0. \end{cases} \tag{5.27}$$

where $q_{v,u}(x, z, t)$, $q_{v,l}(x, z, t)$, $q_{\eta,u}(x, z, t)$ and $q_{\eta,l}(x, z, t)$ are the control signals.

The control law is a feedback control in Fourier space. The control principle is given in Figure 5.2 by some steps

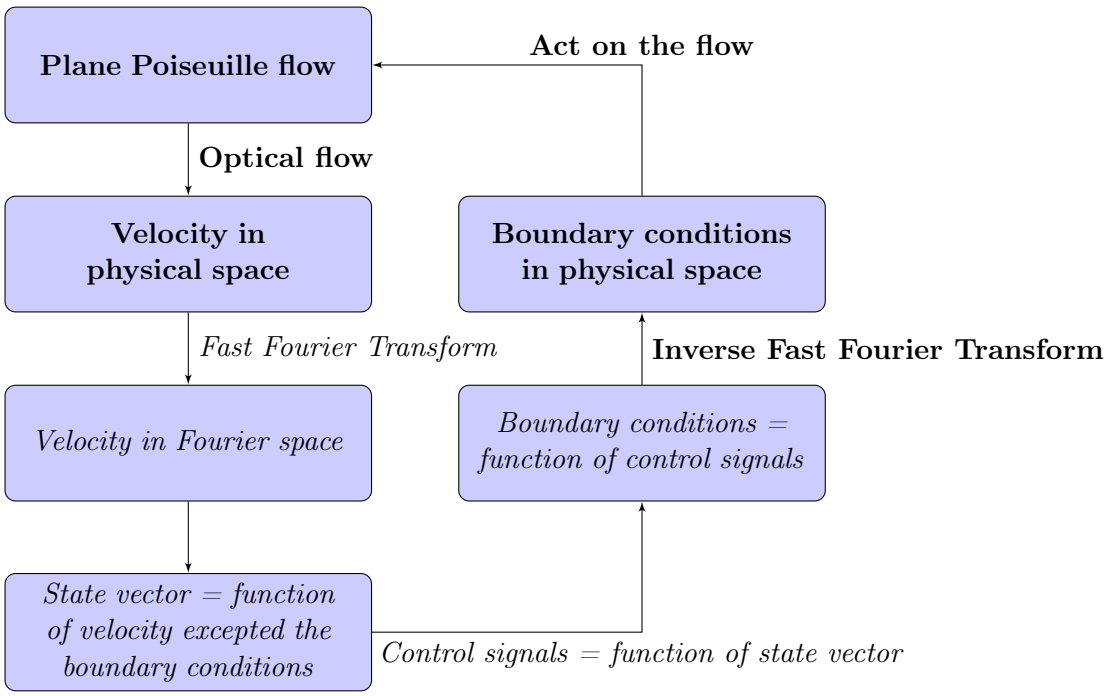

Figure 5.2: Boundary control schema: .

- First step, the velocity is calculated in physical space by using the optical flow
- Second step, the velocity is obtained in Fourier space by using Fast Fourier Transform
- Third step, the state vector is a function of the velocity in Fourier space excepted the boundary conditions

- Fourth step, the control signals are a function of the state vector
- Fifth step, the boundary conditions in Fourier space are function of the control signals
- Sixth step, the boundary conditions in Fourier space are transformed to the boundary conditions in physical space
- Final step, the control signals in physical space are acted on the flow

At the moment, we have introduced the control principle but we need to present the actuators used to physically modify the flow state. This problem is presented in the next section.

5.1.5.2 Actuators

In this study, we shall use **MEMS** as in [Ho and Tai, 1996], [Tsao et al., 1997] and [Ho and Tai, 1998] which have demonstrated that spatially distributed actuation possible. One way to implement **MEMS** based control schemes, we use online Fast Fourier Transform (**FFT**) and its inverse along the streamwise and spanwise directions as previous works in [Bewley and Liu, 1998], [Joshi et al., 1997], [Aamo, 2002], [Högberg et al., 2003], [McKernan, 2006]. It means that the Navier Stokes equations in physical space are transformed to a linear model in Fourier space by using **FFT**. We design a controller based on the linear model in Fourier space. And the control signals in Fourier space are then transformed into physical space by using Inverse Fast Fourier Transform (**IFFT**). An algorithm of implementation of controller into **DNS** code is presented in Appendix A.

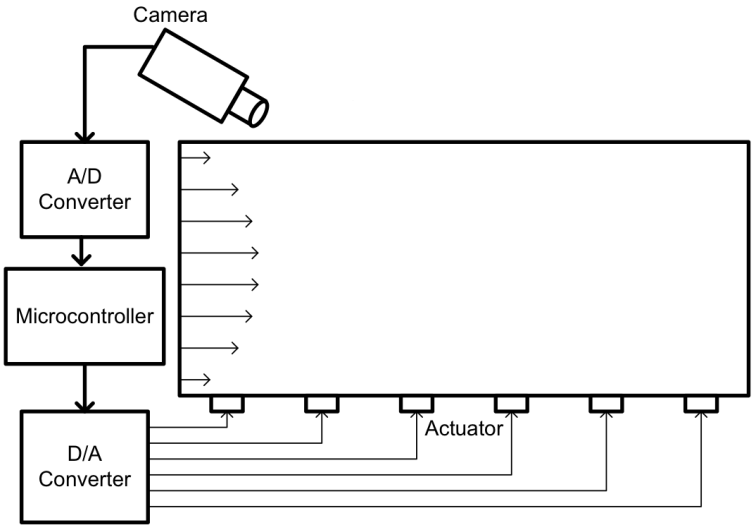

Figure 5.3: Controller architecture using camera

We extend the controller architecture presented in [Cortelezzi et al., 1998b] and [Lee et al., 2001] which also provided the basic architecture for the implementation of the controller in practical engineering applications. We use a **CCD** camera to estimate the state vector instead of using the sensors at the walls. More importantly, the camera is used to estimate the state vector, we do not need to use the **LQE** control because the state vector is estimated by the motion measurement technique. Analog to digital converters (**A/D**), digital signal processors (**DSP**), analog signal processing (**ASP**) and digital to analog converter (**D/A**) are necessary hardware to convert from the analog signal to the digital signal and inverse.

Figure 5.3 provides the architecture for the implementation of the present controller in engineering applications. The camera provides the velocity maps which is computed from the optical flow techniques. From the velocity map, the estimation of the state vector is given. Finally, the necessary hardware is provided. A simple procedure is

- Use the camera to compute the velocity map which gives the estimation value of the state vector. The state vector estimation is converted from the analog signal to the digital signal by the **A/D** and **DSP**.
- Compute the control law in a microprocessor
- From control signal, the **ASP** and **D/A** produce the actuating signal on blowing/suction actuators.

In the next section, we motivate the use of a linear model of controlled flow.

5.2 Linear model

In order to convert from the system of **PDE** to the system of **ODE**, several methods of spatial discretization can be used, e.g. spectral, finite difference, finite element, and finite volume methods. We use the spectral collocation discretization method similar to that used by McKernan [McKernan, 2006] where the weight residual from evaluating **PDE** using an approximate solution is set to zero.

5.2.1 Homogeneous formulation

5.2.1.1 Streamwise and spanwise discretizations

The solution in the streamwise and spanwise directions is assumed to be periodic and approximated by the terms from a truncated Fourier series. The streamwise direction is periodic in $[0, L_x]$, we have

$$\frac{\partial^n u(x=0,y,z,t)}{\partial x^n} = \frac{\partial^n u(x=L_x,y,z,t)}{\partial x^n}, n = 1, 2, 3, \ldots \tag{5.28}$$

The complex solutions of the wall-normal velocity and the vorticity are denoted v_c and η_c, respectively, therefore the real solutions v and η are given by

$$\begin{cases} v(x,y,z,t) &= \Re(v_c(x,y,z,t)) \\ \eta(x,y,z,t) &= \Re(\eta_c(x,y,z,t)). \end{cases} \tag{5.29}$$

Thus the complex solutions of the wall-normal velocity and the vorticity are approximated by

$$\begin{cases} v_c(x,y,z,t) &= \sum_{n_{st}=0}^{N_{st}} \sum_{n_{sp}=0}^{N_{sp}} \tilde{v}(y,t,n_{st},n_{sp}) e^{2\pi j(\frac{n_{st}x}{L_x}+\frac{n_{sp}z}{L_z})} \\ \eta_c(x,y,z,t) &= \sum_{n_{st}=0}^{N_{st}} \sum_{n_{sp}=0}^{N_{sp}} \tilde{\eta}(y,t,n_{st},n_{sp}) e^{2\pi j(\frac{n_{st}x}{L_x}+\frac{n_{sp}z}{L_z})}, \end{cases} \tag{5.30}$$

where n_{st} and n_{sp} are the streamwise harmonic number and spanwise harmonic number, respectively. L_x and L_z are a fundamental wavelenghts in the streamwise and spanwise directions. N_{st} and N_{sp} are finite and represent the truncation of the series.

The linearized equations can be decoupled by wavenumber pairs and thus it is possible to treat each wavenumber pairs separately, therefore the single wavenumber pair system is considered. The velocity and vorticity are approximated at each wavenumber pair by

$$\begin{cases} v_c(x,y,z,t) &= \tilde{v}(y,t) e^{j(\alpha x+\beta z)} \\ \eta_c(x,y,z,t) &= \tilde{\eta}(y,t) e^{j(\alpha x+\beta z)}, \end{cases} \tag{5.31}$$

where $\alpha = \frac{2\pi n_{st}}{L_x}$ and $\beta = \frac{2\pi n_{sp}}{L_z}$. $\tilde{v}(y,t)$ and $\tilde{\eta}(y,t)$ are the wall-normal velocity and the vorticity perturbation Fourier coefficients which are calculated by

$$\begin{cases} \tilde{v}(y,t) &= \frac{1}{L_x}\frac{1}{L_z}\int_0^{L_x}\int_0^{L_z} v_c(x,y,z,t) e^{-j(\alpha x+\beta z)} dz dx \\ \tilde{\eta}(y,t) &= \frac{1}{L_x}\frac{1}{L_z}\int_0^{L_x}\int_0^{L_z} \eta_c(x,y,z,t) e^{-j(\alpha x+\beta z)} dz dx. \end{cases} \tag{5.32}$$

Substituting the assumed solution of velocity and vorticity (5.31) into (5.24-5.25), the wall-normal velocity and vorticity perturbation Fourier coefficients in $\tilde{v}(y,t)$ and $\tilde{\eta}(y,t)$, are respectively

$$\begin{cases} (-k^2 U - \frac{d^2U}{dy^2} - \frac{k^4}{jR\alpha})\tilde{v} + (U + \frac{2k^2}{jR\alpha})\frac{\partial^2\tilde{v}}{\partial y^2} - \frac{1}{jR\alpha}\frac{\partial^4\tilde{v}}{\partial y^4} &= \frac{j}{\alpha}(\frac{\partial^3\tilde{v}}{\partial y^2 \partial t} - k^2\frac{\partial\tilde{v}}{\partial t}) \\ (j\alpha U + \frac{k^2}{R})\tilde{\eta} - \frac{1}{R}\frac{\partial^2\tilde{\eta}}{\partial y^2} + j\beta\frac{dU}{dy}\tilde{v} &= -\frac{\partial\tilde{\eta}}{\partial t}, \end{cases} \tag{5.33}$$

where $k^2 = \alpha^2 + \beta^2$. The no-slip boundary conditions are

$$\begin{cases} \tilde{v}(x, y=\pm 1, z, t) &= 0 \\ \tilde{\eta}(x, y=\pm 1, z, t) &= 0 \\ \dfrac{\partial\tilde{v}(x, y=\pm 1, z, t)}{\partial y} &= 0. \end{cases} \tag{5.34}$$

By the same way, the assumed solution of streamwise and spanwise velocities are given

$$\begin{cases} u(x,y,z,t) &= \Re(u_c(x,y,z,t)) = \Re(\tilde{u}(y,t)e^{j(\alpha x+\beta z)}) \\ w(x,y,z,t) &= \Re(w_c(x,y,z,t)) = \Re(\tilde{w}(y,t)e^{j(\alpha x+\beta z)}). \end{cases} \tag{5.35}$$

Substituting the assumed solution of streamwise and spanwise velocities (5.35) into the continuity equation

$$\frac{\partial u}{\partial x} + \frac{\partial v}{\partial y} + \frac{\partial w}{\partial z} = 0, \tag{5.36}$$

yields

$$j\alpha\tilde{u} + \frac{\partial \tilde{v}}{\partial y} + j\beta\tilde{w} = 0, \tag{5.37}$$

and into the vorticity $\eta = \frac{\partial u}{\partial z} - \frac{\partial w}{\partial x}$, yields

$$\tilde{\eta} = j\beta\tilde{u} - j\alpha\tilde{w}. \tag{5.38}$$

Therefore, the streamwise and spanwise velocity components are calculated from

$$\begin{cases} \tilde{u} &= \frac{j}{k^2}(\alpha\frac{\partial \tilde{v}}{\partial y} - \beta\tilde{\eta}) \\ \tilde{w} &= \frac{j}{k^2}(\beta\frac{\partial \tilde{v}}{\partial y} + \alpha\tilde{\eta}). \end{cases} \tag{5.39}$$

5.2.1.2 Wall-normal discretization

Discretization in the wall-normal direction is based on the Chebyshev polynomial series at Gauss-Lobatto collocation points $y_k = \cos(k\pi/N), 0 \leq k \leq N$. Using the Chebyshev polynomial series to discretize in the wall-normal direction, the wall-normal velocity $\tilde{v}(y,t)$ and the vorticity $\tilde{\eta}(y,t)$ are given by

$$\begin{cases} \tilde{v}(y,t) &= \sum_{n=0}^{N} a_{v,n}(t)\Gamma_n(y_k), 0 \leq k \leq N \\ \tilde{\eta}(y,t) &= \sum_{n=0}^{N} a_{\eta,n}(t)\Gamma_n(y_k), 0 \leq k \leq N, \end{cases} \tag{5.40}$$

The Chebyshev polynomials $\Gamma(y)$ are definite as $\Gamma_n(y) = cos(n\ arcos(y))$, where $-1 \leq y \leq +1$.

5.2.1.3 State-space representation

When the wall-normal discretization is used, the solution of (5.33) can be written (as in [Schmid and Henningson, 2001], p.488)

$$\begin{aligned} &(-k^2U - \frac{d^2U}{dy^2} - \frac{k^4}{jR\alpha})\sum_{i=0}^{N} a_{v,n}(t)\Gamma_n(y) + (U + \frac{2k^2}{jR\alpha})\sum_{i=0}^{N} a_{v,n}(t)\Gamma_n''(y) \\ &-\frac{1}{jR\alpha}\sum_{i=0}^{N} a_{v,n}(t)\Gamma_n''''(y) = \frac{j}{\alpha}\left[\sum_{i=0}^{N} \dot{a}_{v,n}(t)\Gamma_n''(y) - k^2\sum_{i=0}^{N} \dot{a}_{v,n}(t)\Gamma_n(y)\right], \end{aligned} \tag{5.41}$$

and

$$\begin{aligned}&(j\alpha U+\frac{k^2}{R})\sum_{i=0}^{N}a_{\eta,n}(t)\Gamma_n(y)-\frac{1}{R}\sum_{i=0}^{N}a_{\eta,n}(t)\Gamma_n''(y)\\&+j\beta\frac{dU}{dy}\sum_{i=0}^{N}a_{v,n}(t)\Gamma_n(y)=-\sum_{i=0}^{N}\dot{a}_{\eta,n}(t)\Gamma_n(y).\end{aligned}\tag{5.42}$$

After the evaluation of (5.41) and (5.42) at each of the collocation points y_k, we obtain a system as following

$$\mathbf{L}\dot{\mathbf{x}}(t)=\mathbf{A}\mathbf{x}(t),\tag{5.43}$$

where the state vector $\mathbf{x}(t)=\left[\begin{array}{cccccc}a_{v,0}(t)&\cdots&a_{v,N}(t)&a_{\eta,0}(t)&\cdots&a_{\eta,N}(t)\end{array}\right]^\top$. The state matrices are given as

$$\mathbf{L}=\left[\begin{array}{cc}\mathbf{L}_{11}&\mathbf{L}_{12}\\\mathbf{L}_{21}&\mathbf{L}_{22}\end{array}\right],\quad\mathbf{A}=\left[\begin{array}{cc}\mathbf{A}_{11}&\mathbf{A}_{12}\\\mathbf{A}_{21}&\mathbf{A}_{22}\end{array}\right]\tag{5.44}$$

where

$$\begin{cases}\mathbf{L}_{11}&=j(-k^2\mathbf{D}0(\Gamma)+\mathbf{D}2(\Gamma)),\ \mathbf{L}_{12}=[0],\ \mathbf{L}_{21}=[0],\ \mathbf{L}_{22}=j\mathbf{D}0(\Gamma)\\\mathbf{A}_{11}&=(-\alpha\overline{U}k^2-\alpha\overline{U}''-\frac{k^4\mathbf{I}}{jR})\mathbf{D}0(\Gamma)+(\alpha\overline{U}+\frac{2k^2\mathbf{I}}{jR})\mathbf{D}2(\Gamma)-\frac{1}{jR}\mathbf{D}4(\Gamma)\\\mathbf{A}_{12}&=[0],\ \mathbf{A}_{21}=\beta\overline{U}'\mathbf{D}0(\Gamma),\ \mathbf{A}_{22}=(\alpha\overline{U}+\frac{k^2\mathbf{I}}{jR})\mathbf{D}0(\Gamma)-\frac{1}{jR}\mathbf{D}2(\Gamma).\end{cases}\tag{5.45}$$

or we can simplify to

$$\mathbf{L}=\left[\begin{array}{cc}\mathbf{L}_{11}&0\\0&\mathbf{L}_{22}\end{array}\right],\quad\mathbf{A}=\left[\begin{array}{cc}\mathbf{A}_{11}&0\\\mathbf{A}_{21}&\mathbf{A}_{22}\end{array}\right]\tag{5.46}$$

The element of derivative matrices is calculated from

$$\mathbf{D}0(\Gamma)_{kn}=\Gamma_n(y_k)\quad\mathbf{D}2(\Gamma)_{kn}=\Gamma_n''(y_k)\quad\mathbf{D}4(\Gamma)_{kn}=\Gamma_n''''(y_k)\tag{5.47}$$

where $n=0\ldots N$ and $k=0\ldots N$. And the diagonal base flow matrices $\overline{U}$, $\overline{U}'$, $\overline{U}''$ are $diag(1-y_k^2)$, $diag(-2y_k)$ and $diag(-2)$, respectively. The dimension of the matrices $\mathbf{L}$ and $\mathbf{A}$, the state vector $\mathbf{x}(t)$ are $(N+1)\times(N+1)$, $(N+1)\times(N+1)$ and $(N+1)\times 1$, respectively.

If $\mathbf{L}^{-1}$ exists, (5.43) could be given in the canonical form

$$\dot{\mathbf{x}}(t)=\mathbf{L}^{-1}\mathbf{A}\mathbf{x}(t),\tag{5.48}$$

where the Orr-Sommerfeld, Squire, and coupling matrices are give as follows

$$\begin{cases}\mathbf{L_{OS}}&=\mathbf{L}_{11}^{-1}\mathbf{A}_{11}\\\mathbf{L_C}&=\mathbf{L}_{21}^{-1}\mathbf{A}_{21}\\\mathbf{L_{Sq}}&=\mathbf{L}_{22}^{-1}\mathbf{A}_{22}.\end{cases}\tag{5.49}$$

5.2.2 Inhomogeneous formulation with boundary control

5.2.2.1 Boundary control

Boundary control consists in modifying the upper and lower boundary conditions. We know that in the uncontrolled flow, the homogeneous Dirichlet and Neumann boundary conditions on the wall-normal velocity $\tilde{v}(y=\pm 1,t)=0$ and $\tilde{v}'(y=\pm 1,t)=0$, respectively. But in the controlled case, the inhomogeneous Dirichlet boundary condition and the homogeneous Neumann boundary condition on the wall-normal velocity applies

$$\begin{cases} \tilde{v}(y=+1,t) & = \tilde{q}_{v,u}(t) \\ \tilde{v}(y=-1,t) & = \tilde{q}_{v,l}(t) \\ \tilde{v}'(y=\pm 1,t) & = 0. \end{cases} \tag{5.50}$$

where $\tilde{q}_{v,u}(t)$ and $\tilde{q}_{v,l}(t)$ are the Fourier coefficients of the upper and lower control signals on the wall-normal velocity ($q_{v,u}(x,z,t)$ and $q_{v,l}(x,z,t)$ at pair wavenumbers (α, β)).

And based on previous works in [Martinelli et al., 2011], the inhomogeneous Dirichlet boundary condition on the vorticity is proposed

$$\begin{cases} \tilde{\eta}(y=+1,t) & = \tilde{q}_{\eta,u}(t) \\ \tilde{\eta}(y=-1,t) & = \tilde{q}_{\eta,l}(t). \end{cases} \tag{5.51}$$

where $\tilde{q}_{\eta,u}(t)$ and $\tilde{q}_{\eta,u}(t)$ are the Fourier coefficients of the upper and lower control signals on the vorticity ($q_{\eta,u}(x,z,t)$ and $q_{\eta,l}(x,z,t)$ at pair wavenumbers (α, β)).

In order to convert from the inhomogeneous formulation to the homogeneous formulation, the change of variable described in [Boyd, 2001] can be used. The inhomogeneous solution $(\tilde{v}(y,t),\tilde{\eta}(y,t))$ is combined with the homogeneous solution $(\tilde{v}_h(y,t),\tilde{\eta}_h(y,t))$ and the particular solution $(\tilde{v}_p(y,t),\tilde{\eta}_p(y,t))$. A new variable of wall-normal velocity vorticity formulation are proposed

$$\begin{cases} \tilde{v}(y,t) & = \tilde{v}_h(y,t)+\tilde{v}_p(y,t) \\ \tilde{\eta}(y,t) & = \tilde{\eta}_h(y,t)+\tilde{\eta}_p(t,t), \end{cases} \tag{5.52}$$

where the wall-normal velocity and vorticity perturbation Fourier coefficients for the homogeneous solution are

$$\begin{cases} \tilde{v}_h(y,t) & = \sum_{n=0}^{N} a_{v,n}(t)\Gamma_n(y) \\ \tilde{\eta}_h(y,t) & = \sum_{n=0}^{N} a_{\eta,n}(t)\Gamma_n(y). \end{cases} \tag{5.53}$$

The wall-normal velocity and vorticity boundary Fourier coefficients for the particular solution are

$$\begin{cases} \tilde{v}_p(y,t) & = f_{v,u}(y)\tilde{q}_{v,u}(t)+f_{v,l}(y)\tilde{q}_{v,l}(t) \\ \tilde{\eta}_p(y,t) & = f_{\eta,u}(y)\tilde{q}_{\eta,u}(t)+f_{\eta,l}(y)\tilde{q}_{\eta,l}(t), \end{cases} \tag{5.54}$$

where the functions $f_{v,u}(y)$, $f_{v,l}(y)$, $f_{\eta,u}(y)$ and $f_{\eta,l}(y)$ satisfy the conditions

$$\begin{cases} f_{v,u}(y=+1) & = f_{v,l}(y=-1) = 1 \\ f_{v,u}(y=-1) & = f_{v,l}(y=+1) = 0 \\ f'_{v,u}(y=\pm 1) & = f'_{v,l}(y=\pm 1) = 0 \\ f_{\eta,u,}(y=+1) & = f_{\eta,l}(y=-1) = 1 \\ f_{\eta,u}(y=-1) & = f_{\eta,l}(y=+1) = 0. \end{cases} \tag{5.55}$$

The wall-normal velocity and the vorticity can be rewritten in a more compact form by

$$\begin{cases} \tilde{v}(y,t) & = \tilde{v}_h(y,t) + \mathbf{F}_v(y)\mathbf{q}_v(t) \\ \tilde{\eta}(y,t) & = \tilde{\eta}_h(y,t) + \mathbf{F}_\eta(y)\mathbf{q}_\eta(t), \end{cases} \tag{5.56}$$

where we denote

$$\mathbf{q}_v(t) = \begin{bmatrix} \tilde{q}_{v,u}(t) \\ \tilde{q}_{v,l}(t) \end{bmatrix}, \mathbf{q}_\eta(t) = \begin{bmatrix} \tilde{q}_{\eta,u}(t) \\ \tilde{q}_{\eta,l}(t) \end{bmatrix} \tag{5.57}$$

and

$$\mathbf{F}_\eta(y) = \begin{bmatrix} f_{\eta,u}(y) & f_{\eta,l}(y) \end{bmatrix}, \mathbf{F}_v(y) = \begin{bmatrix} f_{v,u}(y) & f_{v,l}(y) \end{bmatrix} \tag{5.58}$$

5.2.2.2 State-space representation

By plugging (5.56) into (5.41) and (5.42), the system of **ODE** is given by

$$\begin{aligned} &(-k^2U - \frac{d^2U}{dy^2} - \frac{k^4}{jR\alpha})\sum_{n=0}^{N} a_{v,n}(t)\Gamma_n(y) + (U + \frac{2k^2}{jR\alpha})\sum_{n=0}^{N} a_{v,n}(t)\Gamma''_n(y) - \frac{1}{jR\alpha}\sum_{n=0}^{N} a_{v,n}(t)\Gamma''''_n(y) \\ &+(-k^2U - \frac{d^2U}{dy^2} - \frac{k^4}{jR\alpha})\mathbf{F}_v(y)\mathbf{q}_v(t) + (U + \frac{2k^2}{jR\alpha})\mathbf{F}''_v(y)\mathbf{q}_v(t) - \frac{1}{jR\alpha}\mathbf{F}''''_v(y)\mathbf{q}_v(t) \\ &= \frac{j}{\alpha}\left[\sum_{n=0}^{N} \dot{a}_{v,n}(t)\Gamma''_n(y) - k^2\sum_{n=0}^{N} \dot{a}_{v,n}(t)\Gamma_n(y)\right] + \frac{j}{\alpha}\left[\mathbf{F}''_v(y)\dot{\mathbf{q}}_v(t) - k^2\mathbf{F}_v(y)\dot{\mathbf{q}}_v(t)\right], \end{aligned} \tag{5.59}$$

and

$$\begin{aligned} &(j\alpha U + \frac{k^2}{R})\sum_{n=0}^{N} a_{\eta,n}(t)\Gamma_n(y) - \frac{1}{R}\sum_{n=0}^{N} a_{\eta,n}(t)\Gamma''_n(y) + j\beta\frac{dU}{dy}\sum_{n=0}^{N} a_{v,n}(t)\Gamma_n(y) \\ &+(j\alpha U + \frac{k^2}{R})\mathbf{F}_\eta(y)\mathbf{q}_\eta(t) - \frac{1}{R}\mathbf{F}''_\eta(y)\mathbf{q}_\eta(t) + j\beta\frac{dU}{dy}\mathbf{F}_v(y)\mathbf{q}_v(t) \\ &= -\sum_{n=0}^{N} \dot{a}_{\eta,n}(t)\Gamma_n(y) - \mathbf{F}_\eta(y)\dot{\mathbf{q}}_\eta(t). \end{aligned} \tag{5.60}$$

After the evaluation of (5.59) and (5.60) at each of the collocations points y_k, a system with control signals is obtained

$$\mathbf{L}\dot{\mathbf{x}}(t) = \mathbf{A}\mathbf{x}(t) + \mathbf{B}\mathbf{u}(t) + \mathbf{E}\dot{\mathbf{u}}(t), \tag{5.61}$$

where the control signals are $\mathbf{u}(t) = \left[\begin{array}{cccc} \tilde{q}_{v,u}(t) & \tilde{q}_{v,l}(t) & \tilde{q}_{\eta,u}(t) & \tilde{q}_{\eta,l}(t) \end{array} \right]^{\top}$. And the input matrices are

$$\mathbf{E} = \left[\begin{array}{cc} \mathbf{E}_{11} & \mathbf{E}_{12} \\ \mathbf{E}_{21} & \mathbf{E}_{22} \end{array} \right], \quad \mathbf{B} = \left[\begin{array}{cc} \mathbf{B}_{11} & \mathbf{B}_{12} \\ \mathbf{B}_{21} & \mathbf{B}_{22} \end{array} \right] \tag{5.62}$$

where

$$\begin{cases} \mathbf{E}_{11} & = j(k^2\mathbf{D}0(\mathbf{F}_v) - \mathbf{D}2(\mathbf{F}_v)), \ \mathbf{E}_{12} = [0], \ \mathbf{E}_{21} = [0], \ \mathbf{E}_{22} = -j\mathbf{D}0(\mathbf{F}_\eta) \\ \mathbf{B}_{11} & = (-\alpha\overline{U}k^2 - \alpha\overline{U}^{''} - \dfrac{k^4\mathbf{I}}{jR})\mathbf{D}0(\mathbf{F}_v) + (\alpha\overline{U} + \dfrac{2k^2\mathbf{I}}{jR})\mathbf{D}2(\mathbf{F}_v) - \dfrac{1}{jR}\mathbf{D}4(\mathbf{F}_v) \\ \mathbf{B}_{12} & = [0], \ \mathbf{B}_{21} = \beta\overline{U}^{'}\mathbf{D}0(\mathbf{F}_v), \ \mathbf{B}_{22} = (\alpha\overline{U} + \dfrac{k^2\mathbf{I}}{jR})D0(\mathbf{F}_\eta) - \dfrac{1}{jR}\mathbf{D}2(\mathbf{F}_\eta). \end{cases} \tag{5.63}$$

or we can simplify to

$$\mathbf{E} = \left[\begin{array}{cc} \mathbf{E}_{11} & 0 \\ 0 & \mathbf{E}_{22} \end{array} \right], \quad \mathbf{B} = \left[\begin{array}{cc} \mathbf{B}_{11} & 0 \\ \mathbf{B}_{21} & \mathbf{B}_{22} \end{array} \right] \tag{5.64}$$

The element of derivative matrices is calculated from

$$\begin{array}{lll} \mathbf{D}0(\mathbf{F}_v)_k = \mathbf{F}_v(y_k) & \mathbf{D}2(\mathbf{F}_v)_k = \mathbf{F}_v^{''}(y_k) & \mathbf{D}4(\mathbf{F}_v)_k = \mathbf{F}_v^{''''}(y_k) \\ \mathbf{D}0(\mathbf{F}_\eta)_k = \mathbf{F}_\eta(y_k) & \mathbf{D}2(\mathbf{F}_\eta)_k = \mathbf{F}_\eta^{''}(y_k), & \end{array} \tag{5.65}$$

where $k = 0 \ldots N$. The dimension of the matrices $\mathbf{E}$ and $\mathbf{B}$ are $(N+1) \times 4$, $(N+1) \times 4$, respectively. Note that the matrices $\mathbf{L}$ and $\mathbf{A}$ have been given in (5.43).

5.3 Modification of the Chebyshev polynomials

The homogeneous Dirichlet and Neaumann boundary conditions without the control signals are

$$\begin{cases} \tilde{v}(y=-1,t) & = \displaystyle\sum_{n=0}^{N} a_{v,n}(t)\Gamma_n(y_0) = \tilde{v}(y=+1,t) = \sum_{n=0}^{N} a_{v,n}(t)\Gamma_n(y_N) = 0 \\ \tilde{\eta}(y=-1,t) & = \displaystyle\sum_{n=0}^{N} a_{\eta,n}(t)\Gamma_n(y_0) = \tilde{\eta}(y=+1,t) = \sum_{n=0}^{N} a_{\eta,n}(t)\Gamma_n(y_N) = 0 \\ \tilde{v}^{'}(y=-1,t) & = \displaystyle\sum_{n=0}^{N} a_{v,n}(t)\Gamma_n^{'}(y_0) = \tilde{v}^{'}(y=+1,t) = \sum_{n=0}^{N} a_{v,n}(t)\Gamma_n^{'}(y_N) = 0 \end{cases} \tag{5.66}$$

or these conditions become

$$\begin{cases} \Gamma_n(y_0) & = \Gamma_n(y_N) = 0 \\ \Gamma_n^{'}(y_0) & = \Gamma_n^{'}(y_N) = 0. \end{cases} \tag{5.67}$$

However, some Chebyshev polynomials and their first derivatives are given

$$\begin{array}{llll} \Gamma_0(y) = 1 & \Gamma_1(y) = y & \Gamma_2(y) = 2y^2 - 1 & \Gamma_3(y) = 4y^3 - 3y \\ \Gamma_0^{'}(y) = 0 & \Gamma_1^{'}(y) = 1 & \Gamma_2^{'}(y) = 4y & \Gamma_3^{'}(y) = 12y^2 - 3. \end{array} \tag{5.68}$$

It is easy to see that the Chebyshev polynomials do not satisfy the homogeneous Dirichlet and Neumann boundary conditions. Therefore, we must modify the Chebyshev polynomials to satisfy the homogeneous Dirichlet and Neumann boundary conditions.

In this section, we describe the modification of the Chebyshev polynomials proposed by McKernan in [McKernan, 2006] that allows satisfying directly the homogeneous Dirichlet and Neumann boundary conditions.

5.3.1 Discretization on wall-normal direction

In the spectral collocation polynomial function method, the wall-normal velocity and vorticity perturbation Fourier coefficients, $\tilde{v}(y,t)$ and $\tilde{\eta}(y,t)$ are approximated by

$$\begin{cases} \tilde{v}(y_k,t) & = \sum_{n=0}^{N} a_{v,n}(t)\Gamma_n(y_k) \\ \tilde{\eta}(y_k,t) & = \sum_{n=0}^{N} a_{\eta,n}(t)\Gamma_n(y_k), \end{cases} \tag{5.69}$$

at Gauss-Lobatto collocation points $y_k = \cos(k\pi/N),\ 0 \le k \le N$.

By evaluating $\tilde{v}(y,t)$ at the collocation points y_k, the discretized form of $\tilde{v}(y,t)$ is the values at the collocation points

$$\begin{bmatrix} \tilde{v}(y_0,t) \\ \vdots \\ \tilde{v}(y_N,t) \end{bmatrix} = \begin{bmatrix} \Gamma_0(y_0) & \dots & \Gamma_N(y_0) \\ \vdots & \ddots & \vdots \\ \Gamma_0(y_N) & \dots & \Gamma_N(y_N) \end{bmatrix} \begin{bmatrix} a_{v,0}(t) \\ \vdots \\ a_{v,N}(t) \end{bmatrix} = \mathbf{D}0(\Gamma)\mathbf{a}_v(t) \tag{5.70}$$

and by evaluating $\tilde{\eta}(y,t)$ at the collocation points, the discretized form $\tilde{\eta}(y,t)$ is the values at the collocation points

$$\begin{bmatrix} \tilde{\eta}(y_0,t) \\ \vdots \\ \tilde{\eta}(y_N,t) \end{bmatrix} = \begin{bmatrix} \Gamma_0(y_0) & \dots & \Gamma_N(y_0) \\ \vdots & \ddots & \vdots \\ \Gamma_0(y_N) & \dots & \Gamma_N(y_N) \end{bmatrix} \begin{bmatrix} a_{\eta,0}(t) \\ \vdots \\ a_{\eta,N}(t) \end{bmatrix} = \mathbf{D}0(\Gamma)\mathbf{a}_\eta(t). \tag{5.71}$$

We have defined $\mathbf{D}0(\Gamma)$, therefore $\mathbf{D}2(\Gamma)$ and $\mathbf{D}4(\Gamma)$ are defined by the same way. The linear model of the plane Poiseuille flow (5.61) is rewritten as

$$\begin{cases} j\left(-k^2\mathbf{D}0(\Gamma) + \mathbf{D}2(\Gamma)\right)\dot{\mathbf{a}}_v & = \left(c_1\mathbf{D}0(\Gamma) + c_2\mathbf{D}2(\Gamma) + c_3\mathbf{D}4(\Gamma)\right)\mathbf{a}_v \\ j\mathbf{D}0(\Gamma)\dot{\mathbf{a}}_\eta & = (c_4\mathbf{D}0(\Gamma) + c_3\mathbf{D}2(\Gamma))\mathbf{a}_\eta + c_5\mathbf{D}0(\Gamma)\mathbf{a}_v, \end{cases} \tag{5.72}$$

where the coefficients are given by

$$\begin{cases} c_1 & = (-\alpha\overline{U}k^2 - \alpha\overline{U}'' - \dfrac{k^4\mathbf{I}}{jR}),\ c_2 = (\alpha\overline{U} + \dfrac{2k^2\mathbf{I}}{jR}) \\ c_3 & = -\dfrac{1}{jR},\ c_4 = \alpha\bar{U} + \dfrac{k^2\mathbf{I}}{jR}),\ c_5 = \beta\overline{U}'. \end{cases} \tag{5.73}$$

It is well known that this model is not a canonical form. However, some control approaches design a controller based on the canonical form, therefore it must be transferred to a canonical form

$$\begin{cases} \dot{\mathbf{a}}_v &= -j\left(-k^2\mathbf{D}0(\Gamma)+\mathbf{D}2(\Gamma)\right)^{-1}\left(c_1\mathbf{D}0(\Gamma)+c_2\mathbf{D}2(\Gamma)+c_3\mathbf{D}4(\Gamma)\right)\mathbf{a}_v \\ \dot{\mathbf{a}}_\eta &= -j\mathbf{D}0^{-1}(\Gamma)(c_4\mathbf{D}0(\Gamma)+c_3\mathbf{D}2(\Gamma))\mathbf{a}_\eta - jc_5\mathbf{a}_v. \end{cases} \tag{5.74}$$

Therefore, $\left(-k^2\mathbf{D}0(\Gamma)+\mathbf{D}2(\Gamma)\right)$ and $\mathbf{D}0(\Gamma)$ are invertible and have a good condition number. Note that $\left(-k^2\mathbf{D}0(\Gamma)+\mathbf{D}2(\Gamma)\right)$ has the column 1 being $\Gamma_0(y)-\Gamma''_0(y)=1$ for $k=1$ therefore $\left(-k^2\mathbf{D}0(\Gamma)+\mathbf{D}2(\Gamma)\right)$ is singular matrix, as in the previous work [Bewley, 2001]. We have $det(\mathbf{L})=0$, therefore we have no change to invert this matrix to obtain a canonical form.

We must modify the Chebyshev polynomials to ensure the homogeneous Dirichlet and Neumann boundary conditions and the good condition number of the state matrix $\mathbf{L}$.

5.3.2 Boundary conditions and basis modification

$\Xi(y)$ and $\Theta(y)$ are modified Chebyshev polynomials and are chosen to satisfy the homogeneous Dirichlet and Neumann boundary conditions. Therefore (5.72) may be modified to

$$\begin{cases} j(-k^2\mathbf{D}0_{DN}(\Xi)+\mathbf{D}2_{DN}(\Xi))\dot{\mathbf{a}}_v &= (c_1\mathbf{D}0_{DN}(\Xi)+c_2\mathbf{D}2_{DN}(\Xi)+c_3\mathbf{D}4_{DN}(\Xi))\mathbf{a}_v \\ j\mathbf{D}0_D(\Theta)\dot{\mathbf{a}}_\eta &= (c_4\mathbf{D}0_D(\Theta)+c_3\mathbf{D}2_D(\Theta))\mathbf{a}_\eta + c_5\mathbf{D}0_{DN}(\Xi)\mathbf{a}_v \end{cases} \tag{5.75}$$

where $_D$ and $_N$ show matrices where the Dirichlet and Neumann boundary conditions are required respectively.

We must determine the conditions on $\Xi(y)$ and $\Theta(y)$. For the vorticity, the homogeneous Dirichlet boundary conditions are

$$\begin{bmatrix} \tilde{\eta}(y_0,t)=0 \\ \tilde{\eta}(y_1,t) \\ \vdots \\ \tilde{\eta}(y_{N-1},t) \\ \tilde{\eta}(y_N,t)=0 \end{bmatrix} = \begin{bmatrix} \Theta_0(y_0) & \dots & \Theta_N(y_0) \\ \Theta_1(y_2) & \dots & \Theta_N(y_1) \\ \vdots & \ddots & \vdots \\ \Theta_0(y_{N-1}) & \dots & \Theta_N(y_{N-1}) \\ \Theta_0(y_N) & \dots & \Theta_N(y_N) \end{bmatrix} \begin{bmatrix} a_{\eta,0}(t) \\ a_{\eta,1}(t) \\ \vdots \\ a_{\eta,N-1}(t) \\ a_{\eta,N}(t) \end{bmatrix}. \tag{5.76}$$

whereas for the wall-normal velocity, the homogeneous Dirichlet boundary conditions are

$$\begin{bmatrix} \tilde{v}(y_0,t)=0 \\ \tilde{v}(y_1,t) \\ \vdots \\ \tilde{v}(y_{N-1},t) \\ \tilde{v}(y_N,t)=0 \end{bmatrix} = \begin{bmatrix} \Xi_0(y_0) & \dots & \Xi_N(y_0) \\ \Xi_0(y_1) & \dots & \Xi_N(y_1) \\ \vdots & \ddots & \vdots \\ \Xi_0(y_{N-1}) & \dots & \Xi_N(y_{N-1}) \\ \Xi_0(y_N) & \dots & \Xi_N(y_N) \end{bmatrix} \begin{bmatrix} a_{v,0}(t) \\ a_{v,1}(t) \\ \vdots \\ a_{v,N-1}(t) \\ a_{v,N}(t) \end{bmatrix}, \tag{5.77}$$

and the homogeneous Neumann boundary conditions are

$$\begin{bmatrix} \tilde{v}'(y_0,t)=0 \\ \tilde{v}'(y_1,t) \\ \vdots \\ \tilde{v}'(y_{N-1},t) \\ \tilde{v}'(y_N,t)=0 \end{bmatrix} = \begin{bmatrix} \Xi_0'(y_0) & \dots & \Xi_N'(y_0) \\ \Xi_0'(y_1) & \dots & \Xi_N'(y_1) \\ \vdots & \ddots & \vdots \\ \Xi_0'(y_{N-1}) & \dots & \Xi_N'(y_{N-1}) \\ \Xi_0'(y_N) & \dots & \Xi_N'(y_N) \end{bmatrix} \begin{bmatrix} a_{v,1}(t) \\ a_{v,2}(t) \\ \vdots \\ a_{v,M-1}(t) \\ a_{v,M}(t) \end{bmatrix}. \tag{5.78}$$

Therefore, we have the conditions on $\Xi(y)$ and $\Theta(y)$

$$\begin{cases} \Theta_0(y_0) = \dots = \Theta_N(y_0) = \Theta_0(y_N) = \dots = \Theta_N(y_N) = 0 \\ \Xi_0(y_0) = \dots = \Xi_N(y_0) = \Xi_0(y_N) = \dots = \Xi_N(y_N) = 0 \\ \Xi_0'(y_0) = \dots = \Xi_N'(y_0) = \Xi_0'(y_N) = \dots = \Xi_N'(y_N) = 0 \end{cases} \tag{5.79}$$

In order to respect such constraints, one solution is find to a Chebyshev polynomials basis modification $\Xi(y)$ and $\Theta(y)$ that enables satisfying directly the requirement of homogeneous Dirichlet and Neumann boundary conditions.

5.3.3 Methods of basis modifications

Two different methods have been proposed by McKernan ([McKernan, 2006], pp.73-106) to modify the Chebyshev polynomials, we accessibly present both of them. Note that McKernan's method has solved problem of the "spurious" modes with respect to Bewley's model [Bewley and Liu, 1998]. The "spurious" eigenvalues (unwanted eigenvalues) move significantly when N is modified slightly, this is a way to determine the "spurious" modes.

The simplest method to ensure that Chebyshev polynomials respect the homogeneous Dirichlet and Neumann boundary conditions was proposed by Heirichs, as described in [Heinrichs, 1989] and [Heinrichs, 1991]. The modified Chebyshev polynomials $\Xi_n(y)$ and $\Theta_n(y)$ satisfying those conditions are given by

$$\begin{cases} \Xi_n(y) &= (1-y^2)^2\Gamma_n(y) \\ \Theta_n(y) &= (1-y^2)\Gamma_n(y). \end{cases} \tag{5.80}$$

Another method was proposed by Joshi [Joshi, 1996]

$$\Xi_n(y) = a\Gamma_n(y) + b\Gamma_{n+1}(y) + c\Gamma_{n+3}(y) + \Gamma_{n+4}(y), \tag{5.81}$$

where the coefficients a, b, c and d are determined to satisfy the simultaneous homogeneous Dirichlet and Neumann boundary conditions.

Although Heinrichs's method and Joshi's method gave both modified Chebyshev polynomials which satisfy the homogeneous Dirichlet and Neumann boundary conditions, the condition number of the state matrix $\mathbf{L}$ is not good enough (see section 5.3.3.3). To alleviate those deficiency McKernan ([McKernan, 2006], pp.73-106) proposed a novel method. We now briefly summarize McKernan's method to modify the Chebyshev polynomials.

McKernan's methods are proposed to satisfy the homogeneous boundary conditions and have a good condition number of the state matrix $\mathbf{L}$. We first present these methods, then discussing the advantages of each methods in section 5.3.3.3. We choose the modified Chebyshev polynomials $\Xi(y)$ and $\Theta(y)$ which satisfy (5.79), we obtain $\tilde{v}(y_0,t) = \tilde{v}(y_N,t) = \tilde{\eta}(y_0,t) = \tilde{\eta}(y_N,t) = 0$.

5.3.3.1 Combined method 1

We use the Combined method 1, as described in Figure 5.4, we only consider the collocation points from y_2 to y_{N-2} for the velocity $\tilde{v}(y)$ and from y_1 to y_{N-1} for the vorticity $\tilde{\eta}(y)$. Note that we do not mention $\tilde{v}(y_1)$ and $\tilde{v}(y_{N-1})$ while $\tilde{v}(y_0)$, $\tilde{v}(y_N)$, $\tilde{\eta}(y_0)$ and $\tilde{\eta}(y_N)$ are the control signals in the controlled flow.

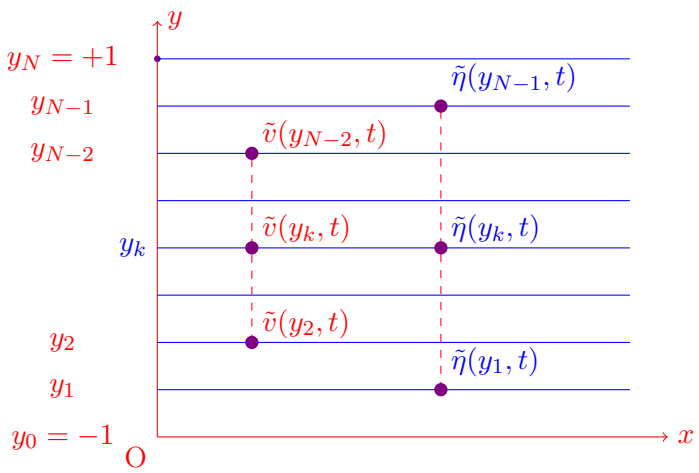

Figure 5.4: Combined method 1: collocation points in y-discretization (y_k).

The modified Chebyshev polynomials $\Xi(y)$ and $\Theta(y)$ are given by

$$\begin{cases} \Theta_0(y) & = 1,\ \Theta_1(y) = y \\ \Theta_{n\geq 2,odd}(y) & = \Gamma_n(y) - \Gamma_0(y) \\ \Theta_{n\geq 2,even}(y) & = \Gamma_n(y) - \Gamma_1(y) \\ \Gamma_n(y) & = cos(n\ arcos(y)), \end{cases} \tag{5.82}$$

and

$$\begin{cases} \Xi_0(y) & = \Gamma_0(y) \\ \Xi_1(y) & = \Gamma_1(y) \\ \Xi_2(y) & = \Gamma_2(y) - \Gamma_0(y) \\ \Xi_3(y) & = \Gamma_3(y) - \Gamma_0(y) \\ \Xi_{n\geq 4,odd}(y) & = \Gamma_n(y) - \Gamma_0(y) - \dfrac{n^2}{(n-2)^2}(\Gamma_{n-1}(y) - \Gamma_0(y)) \\ \Xi_{n\geq 4,even}(y) & = \Gamma_n(y) - \Gamma_1(y) - \dfrac{n^2-1}{(n-2)^2-1}(\Gamma_{n-1}(y) - \Gamma_0(y)). \end{cases} \tag{5.83}$$

Note that $\Xi_{n\geq 4}(y)$ and $\Theta_{n\geq 2}(y)$ satisfy

$$\begin{cases} \Theta_2(y_0) = \ldots = \Theta_N(y_0) = \Theta_2(y_N) = \ldots = \Theta_N(y_N) = 0 \\ \Xi_4(y_0) = \ldots = \Xi_N(y_0) = \Xi_4(y_N) = \ldots = \Xi_N(y_N) = 0 \\ \Xi_4^{'}(y_0) = \ldots = \Xi_N^{'}(y_0) = \Xi_4^{'}(y_N) = \ldots = \Xi_N^{'}(y_N) = 0 \end{cases} \tag{5.84}$$

In addition, $\Xi_{n\geq 4}(y_1) \approx \Xi_{n\geq 4}(y_{N-1}) \approx 0$, we do not mention $\tilde{v}(y_1)$ and $\tilde{v}(y_{N-1})$. Therefore, the wall-normal velocity $\tilde{v}(y,t)$ and the vorticity $\tilde{\eta}(y,t)$ are given by

$$\begin{cases} \tilde{v}(y_k,t) & = \sum_{n=4}^{N} a_{v,n}(t)\Xi_n(y_k), 2 \leq k \leq N-2 \\ \tilde{\eta}(y_k,t) & = \sum_{n=2}^{N} a_{\eta,n}(t)\Theta_n(y_k), 1 \leq k \leq N-1. \end{cases} \tag{5.85}$$

Consequently, the discretized form $\tilde{v}(y_k,t)$ is given by the values at the collocation points

$$\begin{bmatrix} \tilde{v}(y_2,t) \\ \vdots \\ \tilde{v}(y_{N-2},t) \end{bmatrix} = \begin{bmatrix} \Xi_4(y_2) & \ldots & \Xi_N(y_2) \\ \vdots & \ddots & \vdots \\ \Xi_4(y_{N-2}) & \ldots & \Xi_N(y_{N-2}) \end{bmatrix} \begin{bmatrix} a_{v,4}(t) \\ \vdots \\ a_{v,N}(t) \end{bmatrix} = \mathbf{D0}_{DN}(\Xi)\mathbf{a}_v(t), \tag{5.86}$$

and the discretized form $\tilde{\eta}(y,t)$ is given by the values at the collocation points

$$\begin{bmatrix} \tilde{\eta}(y_1,t) \\ \vdots \\ \tilde{\eta}(y_{N-1},t) \end{bmatrix} = \begin{bmatrix} \Theta_2(y_1) & \ldots & \Theta_N(y_1) \\ \vdots & \ddots & \vdots \\ \Theta_2(y_{N-1}) & \ldots & \Theta_N(y_{N-1}) \end{bmatrix} \begin{bmatrix} a_{\eta,2}(t) \\ \vdots \\ a_{\eta,N}(t) \end{bmatrix} = \mathbf{D0}_D(\Theta)\mathbf{a}_\eta(t). \tag{5.87}$$

5.3.3.2 Combined method 2

In the Combined method 2, as described in Figure 5.5, we consider the collocation points from y_1 to y_{N-1} for the velocity $\tilde{v}(y)$ and from y_1 to y_{N-1} for the vorticity $\tilde{\eta}(y)$

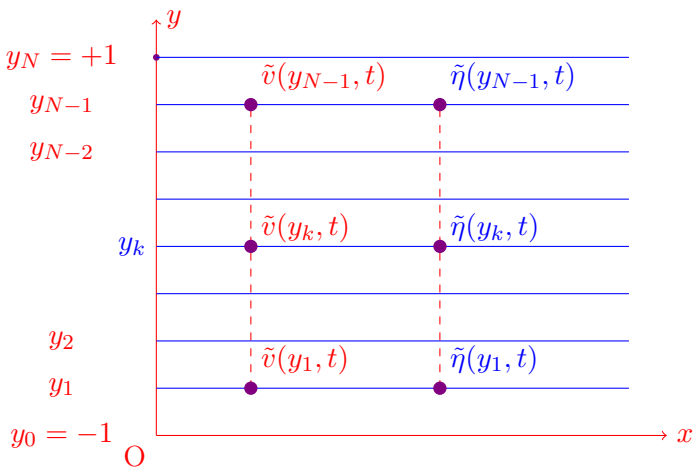

Figure 5.5: Combined method 2: collocation points in y-discretization (y_k).

A second method has been proposed, the modified Chebyshev polynomials $\Xi(y)$ and $\Theta(y)$ are given by

$$\begin{cases} \Theta_0(y) & = 1 \\ \Theta_1(y) & = y \\ \Theta_{n\geq 2,odd}(y) & = \Gamma_n(y) - \Gamma_0(y) \\ \Theta_{n\geq 2,even}(y) & = \Gamma_n(y) - \Gamma_1(y) \\ \Xi_n(y) & = (1-y^2)\Theta_n(y) \\ \Gamma_n(y) & = cos((n\ arcos(y)). \end{cases} \tag{5.88}$$

Note that $\Xi_{n\geq 2}(y)$ and $\Theta_{n\geq 2}(y)$ satisfy

$$\begin{cases} \Theta_2(y_0) = \ldots = \Theta_N(y_0) = \Theta_2(y_N) = \ldots = \Theta_N(y_N) = 0 \\ \Xi_2(y_0) = \ldots = \Xi_N(y_0) = \Xi_2(y_N) = \ldots = \Xi_N(y_N) = 0 \\ \Xi_2'(y_0) = \ldots = \Xi_N'(y_0) = \Xi_2'(y_N) = \ldots = \Xi_N'(y_N) = 0 \end{cases} \tag{5.89}$$

The wall-normal velocity $\tilde{v}(y,t)$ and vorticity $\tilde{\eta}(y,t)$ are given by

$$\begin{cases} \tilde{v}(y_k,t) & = \sum_{n=2}^{N} a_{v,n}(t)\Xi_n(y_k), 1 \leq k \leq N-1 \\ \tilde{\eta}(y_k,t) & = \sum_{n=2}^{N} a_{\eta,n}(t)\Theta_n(y_k), 1 \leq k \leq N-1, \end{cases} \tag{5.90}$$

Therefore, the discretized form $\tilde{v}(y,t)$ is given by the values at the collocation points

$$\begin{bmatrix} \tilde{v}(y_1,t) \\ \vdots \\ \tilde{v}(y_{N-1},t) \end{bmatrix} = \begin{bmatrix} \Xi_2(y_1) & \ldots & \Xi_N(y_1) \\ \vdots & \ddots & \vdots \\ \Xi_2(y_{N-1}) & \ldots & \Xi_N(y_{N-1}) \end{bmatrix} \begin{bmatrix} a_{v,2}(t) \\ \vdots \\ a_{v,N}(t) \end{bmatrix} = \mathbf{D}0_{DN}(\Xi)\mathbf{a}_v(t), \tag{5.91}$$

and the discretized form $\tilde{\eta}(y,t)$ is given by the values at the collocation points

$$\begin{bmatrix} \tilde{\eta}(y_1,t) \\ \vdots \\ \tilde{\eta}(y_{N-1},t) \end{bmatrix} = \begin{bmatrix} \Theta_2(y_1) & \dots & \Theta_N(y_1) \\ \vdots & \ddots & \vdots \\ \Theta_2(y_{N-1}) & \dots & \Theta_N(y_{N-1}) \end{bmatrix} \begin{bmatrix} a_{\eta,2}(t) \\ \vdots \\ a_{\eta,N}(t) \end{bmatrix} = \mathbf{D}0_D(\Theta)\mathbf{a}_\eta(t). \tag{5.92}$$

We have defined $\mathbf{D}0_{DN}(\Xi)$ and $\mathbf{D}0_D(\Theta)$, therefore $\mathbf{D}2_{DN}(\Xi)$, $\mathbf{D}4_{DN}(\Xi)$ and $\mathbf{D}2_D(\Theta)$ may be given by the same way.

5.3.3.3 Condition number of the state matrix

In order to convert to the canonical form, we must invert the matrices $(-k^2\mathbf{D}0_{DN}(\Xi) + \mathbf{D}2_{DN}(\Xi))$ and $\mathbf{D}0_D(\Theta)$. The condition number helps us to estimate how numerically difficult will invert a matrix. The condition number is given as the ratio of the maximum and minimum singular values

$$Cond(\mathbf{L}) = \frac{\sigma_1(\mathbf{L})}{\sigma_{N_o}(\mathbf{L})}, \tag{5.93}$$

where $\mathbf{L}$ is a square matrix of dimension N_o and $\sigma_1(\mathbf{L})$, $\sigma_{N_o}(\mathbf{L})$ are the maximum and minimum singular values, respectively.

The condition number of the state matrix $\mathbf{L}$ is of particular interest, we can determine it through the condition number of the matrices $(-k^2\mathbf{D}0_{DN}(\Xi) + \mathbf{D}2_{DN}(\Xi))$ and $\mathbf{D}0_D(\Theta)$. Therefore, we need to determine the condition number of the matrices $\mathbf{D}0_{DN}(\Xi)$, $\mathbf{D}2_{DN}(\Xi)$ and $\mathbf{D}0_D(\Theta)$. The comparison of the condition number between McKernan's methods [McKernan, 2006] and Heirichs's method [Heinrichs, 1989] is given in Table 5.1 where N is the order of Chebyshev polynomials (see Table 3.2, Table 3.3, p.97 and Table 3.5, p.99 in [McKernan, 2006]). Note that the result provided Joshi's method [Joshi, 1996] is the midst of the others, see [McKernan, 2006].

Table 5.1: Condition number of element matrices

Method	$\mathbf{D}0_D$	$\mathbf{D}0_{DN}$	$\mathbf{D}0_{DN} - \mathbf{D}2_{DN}$
Heinrichs	$0.14 \times N^{2.1}$	$0.011 \times N^{4.1}$	$0.026 \times N^{3.8}$
Combined method 1	$1 \times N^{0.5}$	$0.25 \times N^{1.1}$	$0.0077 \times N^{3}$
Combined method 2	$1 \times N^{0.5}$	$0.042 \times N^{2.6}$	$0.18 \times N^{1.9}$

For the condition number of the matrix $\mathbf{D}0_D(\Theta)$, both Method 1 and Method 2 have a good result and the identical result. As can be observed, the Method 1 has the lowest conditioning for $\mathbf{D}0_{DN}(\Xi)$ while the Method 2 has the lowest conditioning for $\mathbf{D}0_{DN}(\Xi) - \mathbf{D}2_{DN}(\Xi)$. It is very difficult to give the best method since $-k^2\mathbf{D}0_{DN}(\Xi) + \mathbf{D}2_{DN}(\Xi)$ depends on $k^2 = \alpha^2 + \beta^2$. We choose McKernan's method which provided a better results than other ones.

5.3.4 Modification of the linear model

When we use the modified Chebyshev polynomials $\Xi(y)$ and $\Theta(y)$, all elements of the derivative matrices are modified to

$$\begin{array}{lll} \mathbf{D}0_{DN,km}(\Xi) = \Xi_m(y_k) & \mathbf{D}2_{DN,km}(\Xi) = \Xi_m''(y_k) & \mathbf{D}4_{DN,km}(\Xi) = \Xi_m''''(y_k) \\ \mathbf{D}0_{D,hn}(\Theta) = \Theta_n(y_h) & \mathbf{D}2_{D,hn}(\Theta) = \Theta_n''(y_h) & \end{array} \tag{5.94}$$

and

$$\begin{array}{lll} \mathbf{D}0_{DN,k}(\mathbf{F}_v) = \mathbf{F}_v(y_k) & \mathbf{D}2_{DN,k}(\mathbf{F}_v) = \mathbf{F}_v''(y_k) & \mathbf{D}4_{DN,k}(\mathbf{F}_v) = \mathbf{F}_v''''(y_k) \\ \mathbf{D}0_{D,h}(\mathbf{F}_\eta) = \mathbf{F}_\eta(y_h) & \mathbf{D}2_{D,h}(\mathbf{F}_\eta) = \mathbf{F}_\eta''(y_h), & \end{array} \tag{5.95}$$

where $m = p_o \ldots N,\ n = 2 \ldots N,\ k = q_o \ldots N - q_o$ and $h = 1 \ldots N - 1$. We have $(p_o = 4,\ q_o = 2)$ for the Method 1 and $(p_o = 2,\ q_o = 1)$ for the Method 2. The linear model is modified by

$$\mathbf{L}\dot{\mathbf{x}}(t) = \mathbf{A}\mathbf{x}(t) + \mathbf{B}\mathbf{u}(t) + \mathbf{E}\dot{\mathbf{u}}(t), \tag{5.96}$$

where the state vector is $\mathbf{x}(t) = \left[\ a_{v,p_o}(t) \quad \cdots \quad a_{v,N}(t) \quad a_{\eta,2}(t) \quad \cdots \quad a_{\eta,N}(t)\ \right]^\top$ and the control signals are $\mathbf{u}(t) = \left[\ \tilde{q}_{v,u}(t) \quad \tilde{q}_{v,l}(t) \quad \tilde{q}_{\eta,u}(t) \quad \tilde{q}_{\eta,l}(t)\ \right]^\top$. The state and input matrices are

$$\begin{cases} \mathbf{L}_{11} & = j(-k^2\mathbf{D}0_{DN}(\Xi) + \mathbf{D}2_{DN}(\Xi)),\ \mathbf{L}_{12} = [0],\ \mathbf{L}_{21} = [0],\ \mathbf{L}_{22} = j\mathbf{D}0_D(\Theta) \\ \mathbf{A}_{11} & = (-\alpha\overline{U}k^2 - \alpha\overline{U}'' - \dfrac{k^4\mathbf{I}}{jR})\mathbf{D}0_{DN}(\Xi) + (\alpha\overline{U} + \dfrac{2k^2\mathbf{I}}{jR})\mathbf{D}2_{DN}(\Xi) - \dfrac{1}{jR}\mathbf{D}4_{DN}(\Xi) \\ \mathbf{A}_{12} & = [0],\ \mathbf{A}_{21} = \beta\overline{U}'\mathbf{D}0_{DN}(\Xi),\ \mathbf{A}_{22} = (\alpha\bar{U} + \dfrac{k^2\mathbf{I}}{jR})\mathbf{D}0_D(\Theta) - \dfrac{1}{jR}\mathbf{D}2_D(\Theta). \end{cases} \tag{5.97}$$

and

$$\begin{cases} \mathbf{E}_{11} & = j(k^2\mathbf{D}0_{DN}(\mathbf{F}_v) - \mathbf{D}2_{DN}(\mathbf{F}_v)),\ \mathbf{E}_{12} = [0],\ \mathbf{E}_{21} = [0],\ \mathbf{E}_{22} = -j\mathbf{D}0_D(\mathbf{F}_\eta) \\ \mathbf{B}_{11} & = (-\alpha\overline{U}k^2 - \alpha\overline{U}'' - \dfrac{k^4\mathbf{I}}{jR})\mathbf{D}0_{DN}(\mathbf{F}_v) + (\alpha\overline{U} + \dfrac{2k^2\mathbf{I}}{jR})\mathbf{D}2_{DN}(\mathbf{F}_v) - \dfrac{1}{jR}\mathbf{D}4_{DN}(\mathbf{F}_v) \\ \mathbf{B}_{12} & = [0],\ \mathbf{B}_{21} = \beta\overline{U}'\mathbf{D}0_{DN}(\mathbf{F}_v),\ \mathbf{B}_{22} = (\alpha\overline{U} + \dfrac{k^2\mathbf{I}}{jR})\mathbf{D}0_D(F_\eta) - \dfrac{1}{jR}\mathbf{D}2_D(\mathbf{F}_\eta). \end{cases} \tag{5.98}$$

However, if we consider the 2D plane Poiseuille flow, the state vector becomes $\mathbf{x}(t) = \left[\ a_{v,p_o}(t) \quad \cdots \quad a_{v,N}(t)\ \right]^\top$ and the control signals become $\mathbf{u}(t) = \left[\ \tilde{q}_{v,u}(t) \quad \tilde{q}_{v,l}(t)\ \right]^\top$. The state and input matrices become

$$\begin{cases} \mathbf{L} & = j(-\alpha^2\mathbf{D}0_{DN}(\Xi) + \mathbf{D}2_{DN}(\Xi)) \\ \mathbf{A} & = (-\alpha^3\overline{U} - \alpha\overline{U}'' - \dfrac{\alpha^4\mathbf{I}}{jR})\mathbf{D}0_{DN}(\Xi) + (\alpha\overline{U} + \dfrac{2\alpha^2\mathbf{I}}{jR})\mathbf{D}2_{DN}(\Xi) - \dfrac{1}{jR}\mathbf{D}4_{DN}(\Xi), \end{cases} \tag{5.99}$$

and

$$\begin{cases} \mathbf{E} & = j(\alpha^2\mathbf{D}0_{DN}(\mathbf{F}_v) - \mathbf{D}2_{DN}(\mathbf{F}_v)) \\ \mathbf{B} & = (-\alpha^3\overline{U} - \alpha\overline{U}'' - \dfrac{\alpha^4\mathbf{I}}{jR})\mathbf{D}0_{DN}(\mathbf{F}_v) + (\alpha\overline{U} + \dfrac{2\alpha^2\mathbf{I}}{jR})\mathbf{D}2_{DN}(\mathbf{F}_v) - \dfrac{1}{jR}\mathbf{D}4_{DN}(\mathbf{F}_v). \end{cases} \tag{5.100}$$

5.4 Modeling of the kinetic energy density

The kinetic energy density of flow perturbation was given by [Bewley and Liu, 1998]

$$\varepsilon(t) = \frac{1}{\mathbf{V}_0}\int_{\mathbf{V}_0}\frac{\|\mathbf{V}(x,y,z,t)\|^2}{2}d\mathbf{V}_0, \tag{5.101}$$

where $\mathbf{V}_0$ is the volume of a period of the domain under consideration. We expand (5.101) at pair wavenumbers (α, β)

$$\varepsilon(t) = \frac{\alpha\beta}{8\pi^2}\int_{y=-1}^{y=+1}\int_{z=0}^{2\pi/\beta}\int_{x=0}^{2\pi/\alpha}\frac{u^2+v^2+w^2}{2}dxdzdy, \tag{5.102}$$

where $\mathbf{V}_0 = 8\pi^2/(\alpha\beta)$. From the complex velocity components are

$$\begin{cases} u &= \Re(\tilde{u}(y,t)e^{j(\alpha x+\beta z)}) \\ v &= \Re(\tilde{v}(y,t)e^{j(\alpha x+\beta z)}) \\ w &= \Re(\tilde{w}(y,t)e^{j(\alpha x+\beta z)}) \end{cases} \tag{5.103}$$

we have ([McKernan, 2006], pp. 110)

$$\begin{cases} u^2 &= \dfrac{2\tilde{u}(y,t)\tilde{u}^\top(y,t)+\tilde{u}(y,t)\tilde{u}(y,t)e^{2j(\alpha x+\beta z)})+\tilde{u}^\top(y,t)\tilde{u}^\top(y,t)e^{-2j(\alpha x+\beta z)})}{4} \\ v^2 &= \dfrac{2\tilde{v}(y,t)\tilde{v}^\top(y,t)+\tilde{v}(y,t)\tilde{v}(y,t)e^{2j(\alpha x+\beta z)})+\tilde{v}^\top(y,t)\tilde{v}^\top(y,t)e^{-2j(\alpha x+\beta z)})}{4} \\ w^2 &= \dfrac{2\tilde{w}(y,t)\tilde{v}^\top(y,t)+\tilde{w}(y,t)\tilde{v}(y,t)e^{2j(\alpha x+\beta z)})+\tilde{w}^\top(y,t)\tilde{w}^\top(y,t)e^{-2j(\alpha x+\beta z)})}{4} \end{cases} \tag{5.104}$$

and

$$\begin{cases} \displaystyle\int_{z=0}^{2\pi/\beta}\int_{x=0}^{2\pi/\alpha}\frac{u^2}{2}dxdz = \frac{\pi^2\tilde{u}(y,t)\tilde{u}^\top(y,t)}{\alpha\beta} \\ \displaystyle\int_{z=0}^{2\pi/\beta}\int_{x=0}^{2\pi/\alpha}\frac{v^2}{2}dxdz = \frac{\pi^2\tilde{v}(y,t)\tilde{v}^\top(y,t)}{\alpha\beta} \\ \displaystyle\int_{z=0}^{2\pi/\beta}\int_{x=0}^{2\pi/\alpha}\frac{w^2}{2}dxdz = \frac{\pi^2\tilde{w}(y,t)\tilde{w}^\top(y,t)}{\alpha\beta} \end{cases} \tag{5.105}$$

So, the kinetic energy density $\varepsilon(t)$ becomes

$$\varepsilon(t) = \frac{\alpha\beta}{8\pi^2}\int_{y=-1}^{y=+1}\frac{\pi^2(\tilde{u}(y,t)\tilde{u}^\top(y,t)+\tilde{v}(y,t)\tilde{v}^\top(y,t)+\tilde{w}(y,t)\tilde{w}^\top(y,t))}{\alpha\beta}dy \tag{5.106}$$

or

$$\varepsilon(t) = \frac{1}{8}\int_{y=-1}^{y=+1}\left(\tilde{u}(y,t)\tilde{u}^\top(y,t)+\tilde{v}(y,t)\tilde{v}^\top(y,t)+\tilde{w}(y,t)\tilde{w}^\top(y,t)\right)dy \tag{5.107}$$

By using

$$\begin{cases} \tilde{u}(y,t) &= \dfrac{j}{k^2}(\alpha\dfrac{\partial\tilde{v}(y,t)}{\partial y}-\beta\tilde{\eta}(y,t)) \\ \tilde{w}(y,t) &= \dfrac{j}{k^2}(\beta\dfrac{\partial\tilde{v}(y,t)}{\partial y}+\alpha\tilde{\eta}(y,t)). \end{cases} \tag{5.108}$$

we get

$$\tilde{u}(y,t)\tilde{u}^{\top}(y,t)+\tilde{w}(y,t)\tilde{w}^{\top}(y,t)=\frac{1}{\alpha^2+\beta^2}\left(\frac{\partial\tilde{v}^{\top}(y,t)}{\partial y}\frac{\partial\tilde{v}(y,t)}{\partial y}+\tilde{\eta}^{\top}(y,t)\tilde{\eta}(y,t)\right) \tag{5.109}$$

Therefore, the kinetic energy density $\varepsilon(t)$ is given by

$$\varepsilon(t)=\frac{1}{8k^2}\int_{y=-1}^{y=+1}\left(\tilde{v}(y,t)\tilde{v}^{\top}(y,t)+\frac{\partial\tilde{v}^{\top}(y,t)}{\partial y}\frac{\partial\tilde{v}(y,t)}{\partial y}+\tilde{\eta}^{\top}(y,t)\tilde{\eta}(y,t)\right)dy \tag{5.110}$$

where $k^2=\alpha^2+\beta^2$. In [Boyd, 2001], [McKernan, 2006], Curtis-Clenshaw quadrature was used for approximate evaluation of the integral

$$\int_{y=-1}^{y=+1}\tilde{v}(y,t)\tilde{v}^{\top}(y,t)dy\approx\sum_{0}^{N}\tilde{v}(y_n,t)\tilde{v}^{\top}(y_n,t)\omega_n \tag{5.111}$$

where the weights ω_n are

$$\omega_n=\frac{2}{N}\sqrt{1-y_n^2}\sum_{m=1}^{N-1}\frac{1}{m}sin(\frac{m\pi n}{N})(1-cos(m\pi)),n=1\cdots N \tag{5.112}$$

Therefore, in discretized form $\varepsilon(t)$ is rewritten by

$$\varepsilon(t)=\frac{[\tilde{v}_n(t)]^{\top}\mathbf{Q}[\tilde{v}_n(t)]+(\partial[\tilde{v}_n(t)]/\partial y)^{\top}\mathbf{Q}(\partial[\tilde{v}_n(t)]/\partial y)+[\tilde{\eta}_n(t)]^{\top}\mathbf{Q}[\tilde{\eta}_n(t)]}{8k^2}, \tag{5.113}$$

where the vectors $[\tilde{v}_n(t)]=[\tilde{v}(y_0,t)\dots\tilde{v}(y_N,t)]^{\top}$, $[\tilde{\eta}_n(t)]=[\tilde{\eta}(y_0,t)\dots\tilde{\eta}(y_N,t)]^{\top}$ and $\mathbf{Q}$ contains the quadrature weights (see eq.(4.20), pp.111 in [McKernan, 2006])

$$\mathbf{Q}=\begin{bmatrix}\omega_0 & & 0\\ & \ddots & \\ 0 & & \omega_N\end{bmatrix}. \tag{5.114}$$

The kinetic energy density is modeled by a function of the state vector $\mathbf{x}(t)$ and the control signal $\mathbf{u}(t)$. Since the kinetic energy density is a function of the velocity, therefore the velocity is first calculated by a function of the state vector $\mathbf{x}(t)$ and the control signal $\mathbf{u}(t)$. From (5.56), the velocity and the vorticity may be recovered from the state variables via

$$\begin{bmatrix}\tilde{v}(y_{k_1},t)\\ \tilde{\eta}(y_{k_2},t)\end{bmatrix}=\begin{bmatrix}\Xi_{n_1}(y_{k_1}) & 0\\ 0 & \Theta_{n_2}(y_{k_2})\end{bmatrix}\begin{bmatrix}a_{v,n_1}(t)\\ a_{\eta,n_2}(t)\end{bmatrix}+\begin{bmatrix}\mathbf{F}_v(y_{k_1}) & 0\\ 0 & \mathbf{F}_\eta(y_{k_2})\end{bmatrix}\begin{bmatrix}\mathbf{q}_v(t)\\ \mathbf{q}_\eta(t)\end{bmatrix}, \tag{5.115}$$

where $k_1=0\dots N$, $k_2=0\dots N$, $n_1=p_0\dots N$, $n_2=2\dots N$ (see eq.(2.105), p.36 in [McKernan, 2006]). Therefore, the velocity and the vorticity are rewritten as

$$\begin{cases}[\tilde{v}_n(t)] &= \mathbf{T}_{a_v}\mathbf{x}(t)+\mathbf{T}_{q_v}\mathbf{u}(t)\\ [\tilde{\eta}_n(t)] &= \mathbf{T}_{a_\eta}\mathbf{x}(t)+\mathbf{T}_{q_\eta}\mathbf{u}(t)\end{cases} \tag{5.116}$$

where the transfer matrices are defined by

$$\mathbf{T}_{a_v} = \left[\begin{array}{cc} [\Xi_n(y_{k_1})] & [0] \end{array} \right], \mathbf{T}_{a_\eta} = \left[\begin{array}{cc} [0] & [\Theta_n(y_{k_2})] \end{array} \right] \tag{5.117}$$

and

$$\mathbf{T}_{q_v} = \left[\begin{array}{cc} \mathbf{F}_v(y_{k_1}) & [0] \end{array} \right], \mathbf{T}_{q_\eta} = \left[\begin{array}{cc} [0] & \mathbf{F}_\eta(y_{k_2}) \end{array} \right]. \tag{5.118}$$

The dimension of matrices $\mathbf{T}_{a_v}$ and $\mathbf{T}_{a_\eta}$ are $(N+1) \times (2N - p_0)$ while the dimension of matrices $\mathbf{T}_{q_v}$ and $\mathbf{T}_{q_\eta}$ are $(N+1) \times 4$.

Therefore, from (5.116), the kinetic energy density becomes

$$\begin{aligned} \varepsilon(t) = & \frac{1}{8k^2}\mathbf{x}^\top(t)(\mathbf{T}_{a_v}^\top \mathbf{Q}\mathbf{T}_{a_v} + (\partial \mathbf{T}_{a_v}/\partial y)^\top \mathbf{Q}(\partial \mathbf{T}_{a_v}/\partial y) + \mathbf{T}_{a_\eta}^\top \mathbf{Q}\mathbf{T}_{a_\eta})\mathbf{x}(t) \\ & + \frac{1}{8k^2}\mathbf{x}^\top(t)(\mathbf{T}_{a_v}^\top \mathbf{Q}\mathbf{T}_{q_v} + (\partial \mathbf{T}_{a_v}/\partial y)^\top \mathbf{Q}(\partial \mathbf{T}_{q_v}/\partial y) + \mathbf{T}_{a_\eta}^\top \mathbf{Q}\mathbf{T}_{q_\eta})\mathbf{u}(t) \\ & + \frac{1}{8k^2}\mathbf{u}^\top(t)(\mathbf{T}_{\mathbf{F}_v}^\top \mathbf{Q}\mathbf{T}_{a_v} + (\partial \mathbf{T}_{q_v}/\partial y)^\top \mathbf{Q}(\partial \mathbf{T}_{a_v}/\partial y) + \mathbf{T}_{q_\eta}^\top \mathbf{Q}\mathbf{T}_{a_\eta})\mathbf{x}(t) \\ & + \frac{1}{8k^2}\mathbf{u}^\top(t)(\mathbf{T}_{q_v}^\top \mathbf{Q}\mathbf{T}_{q_v} + (\partial \mathbf{T}_{q_v}/\partial y)^\top \mathbf{Q}(\partial \mathbf{T}_{q_v}/\partial y) + \mathbf{T}_{q_\eta}^\top \mathbf{Q}\mathbf{T}_{q_\eta})\mathbf{u}(t) \end{aligned} \tag{5.119}$$

We define the matrices $\mathbf{Q}_{11}$, $\mathbf{Q}_{12}$, $\mathbf{Q}_{21}$ and $\mathbf{Q}_{22}$

$$\left\{ \begin{array}{ll} \mathbf{Q_{11}} & = \frac{1}{8k^2}(\mathbf{T}_{a_v}^\top \mathbf{Q}\mathbf{T}_{a_v} + (\partial \mathbf{T}_{a_v}/\partial y)^\top \mathbf{Q}(\partial \mathbf{T}_{a_v}/\partial y) + \mathbf{T}_{a_\eta}^\top \mathbf{Q}\mathbf{T}_{a_\eta}) \\ \mathbf{Q_{12}} & = \frac{1}{8k^2}(\mathbf{T}_{a_v}^\top \mathbf{Q}\mathbf{T}_{q_v} + (\partial \mathbf{T}_{a_v}/\partial y)^\top \mathbf{Q}(\partial \mathbf{T}_{q_v}/\partial y) + \mathbf{T}_{a_\eta}^\top \mathbf{Q}\mathbf{T}_{q_\eta}) \\ \mathbf{Q_{21}} & = \frac{1}{8k^2}(\mathbf{T}_{q_v}^\top \mathbf{Q}\mathbf{T}_{a_v} + (\partial \mathbf{T}_{q_v}/\partial y)^\top \mathbf{Q}(\partial \mathbf{T}_{a_v}/\partial y) + \mathbf{T}_{q_\eta}^\top \mathbf{Q}\mathbf{T}_{a_\eta}) \\ \mathbf{Q_{22}} & = \frac{1}{8k^2}(\mathbf{T}_{q_v}^\top \mathbf{Q}\mathbf{T}_{q_v} + (\partial \mathbf{T}_{q_v}/\partial y)^\top \mathbf{Q}(\partial \mathbf{T}_{q_v}/\partial y) + \mathbf{T}_{q_\eta}^\top \mathbf{Q}\mathbf{T}_{q_\eta}). \end{array} \right. \tag{5.120}$$

Therefore, the kinetic energy density is calculated from the state vector $\mathbf{x}(t)$ and the control signal $\mathbf{u}(t)$

$$\varepsilon(t) = \mathbf{x}^\top(t)\mathbf{Q_{11}}\mathbf{x}(t) + \mathbf{x}^\top(t)\mathbf{Q_{12}}\mathbf{u}(t) + \mathbf{u}^\top(t)\mathbf{Q_{21}}\mathbf{x}(t) + \mathbf{u}^\top(t)\mathbf{Q_{22}}\mathbf{u}(t) \tag{5.121}$$

The synchronic transient energy bound at a given time t is defined as the maximum value of the kinetic energy at time t:

$$\varepsilon_s(t) = \max_{\varepsilon(0)=1} \varepsilon(t). \tag{5.122}$$

The diachronic transient energy bound or the maximum transient energy growth is the maximum value of the synchronic transient energy bound over all time, thus it is defined by

$$\varepsilon_d = \max_{t \geq 0} \varepsilon_s(t). \tag{5.123}$$

5.5 Modeling of the skin friction drag

The skin friction drag $\mathbf{d}(t)$ due to the perturbation is given by (see [Aamo et al., 2003])

$$\mathbf{d}(t) = \int_{x=0}^{L_x} (-\frac{\partial u(x,+1,z,t)}{\partial y} + \frac{\partial u(x,-1,z,t)}{\partial y}) dx \tag{5.124}$$

where $u(x,+1,z,t)$ and $u(x,-1,z,t)$ are the streamwise components of the perturbation velocity $\mathbf{V}(x,y,z,t)$ at the walls. Note that $\partial u(x,-1,z,t)/\partial y$ and $\partial u(x,+1,z,t)/\partial y$ are the components of the wall shear stress $\mathbf{s}(t)$ due to the perturbation:

$$\mathbf{s}(t) = \frac{1}{R} \left[\begin{array}{cccc} \frac{\partial u(x,+1,z,t)}{\partial y} & \frac{\partial u(x,-1,z,t)}{\partial y} & \frac{\partial w(x,+1,z,t)}{\partial y} & \frac{\partial w(x,-1,z,t)}{\partial y} \end{array} \right]^\top. \tag{5.125}$$

We expand the skin friction drag by

$$\begin{aligned} \mathbf{d}(t) &= \int_{x=0}^{L_x} \Re(-\frac{\partial \tilde{u}(x,+1,z,t) e^{j(\alpha x+\beta z)}}{\partial y} + \frac{\partial \tilde{u}(x,-1,z,t) e^{j(\alpha x+\beta z)}}{\partial y}) dx \\ &= \int_{x=0}^{L_x} (-\frac{\partial \tilde{u}(x,+1,z,t)}{\partial y} + \frac{\partial \tilde{u}(x,-1,z,t)}{\partial y}) e^{j(\alpha x+\beta z)} dx \end{aligned} \tag{5.126}$$

Therefore, the skin friction drag at pair wavenumbers (α, β) can be considered

$$\mathbf{d}(t) = -\frac{\partial \tilde{u}(y=+1,t)}{\partial y} + \frac{\partial \tilde{u}(y=-1,t)}{\partial y} \tag{5.127}$$

Note that the wall shear stress in the streamwise and spanwise discretizations are

$$\tilde{\mathbf{s}}(t) = \frac{1}{R} \left[\begin{array}{cccc} \frac{\partial \tilde{u}(+1,t)}{\partial y} & \frac{\partial \tilde{u}(-1,t)}{\partial y} & \frac{\partial \tilde{w}(+1,t)}{\partial y} & \frac{\partial \tilde{w}(-1,t)}{\partial y} \end{array} \right]^\top. \tag{5.128}$$

We recall that $\tilde{u} = \frac{j}{k^2}(\alpha \frac{\partial \tilde{v}}{\partial y} - \beta \tilde{\eta})$ and $\tilde{w} = \frac{j}{k^2}(\beta \frac{\partial \tilde{v}}{\partial y} + \alpha \tilde{\eta})$. Therefore, $\tilde{\mathbf{s}}(t)$ becomes

$$\tilde{\mathbf{s}}(t) = \frac{j}{k^2 R} \left[\begin{array}{c} \alpha \frac{\partial^2 \tilde{v}}{\partial y^2} - \beta \frac{\partial \tilde{\eta}}{\partial y}|_{y=+1} \\ \alpha \frac{\partial^2 \tilde{v}}{\partial y^2} - \beta \frac{\partial \tilde{\eta}}{\partial y}|_{y=-1} \\ \beta \frac{\partial^2 \tilde{v}}{\partial y^2} + \alpha \frac{\partial \tilde{\eta}}{\partial y}|_{y=+1} \\ \beta \frac{\partial^2 \tilde{v}}{\partial y^2} + \alpha \frac{\partial \tilde{\eta}}{\partial y}|_{y=-1} \end{array} \right]. \tag{5.129}$$

The wall-normal discretization is used by the Chebyshev polynomials, we have

$$\begin{cases} \tilde{v}(y=+1,t) &= \sum_{n=p_0}^{N} a_{v,n}(t)\Xi_n(y=+1) \\ \tilde{v}(y=-1,t) &= \sum_{n=p_0}^{N} a_{v,n}(t)\Xi_n(y=-1) \\ \tilde{\eta}(y=+1,t) &= \sum_{n=2}^{N} a_{\eta,n}(t)\Theta_n(y=+1) \\ \tilde{\eta}(y=-1,t) &= \sum_{n=2}^{N} a_{\eta,n}(t)\Theta_n(y=-1) \end{cases} \tag{5.130}$$

Therefore, $\tilde{\mathbf{s}}(t)$ becomes

$$\tilde{\mathbf{s}}(t) = \frac{j}{k^2 R} \begin{bmatrix} \alpha \sum_{n=p_0}^{N} a_{v,n}(t)\Xi_n^{''}(y=+1) - \beta \sum_{n=p_0}^{N} \Theta_n^{'} a_{\eta,n}(t)(y=+1) \\ \alpha \sum_{n=p_0}^{N} a_{v,n}(t)\Xi_n^{''}(y=-1) - \beta \sum_{n=p_0}^{N} \Theta_n^{'} a_{\eta,n}(t)(y=-1) \\ \beta \sum_{n=2}^{N} a_{v,n}(t)\Xi_n^{''}(y=+1) + \alpha \sum_{n=2}^{N} \Theta_n^{'} a_{\eta,n}(t)(y=+1) \\ \beta \sum_{n=2}^{N} a_{v,n}(t)\Xi_n^{''}(y=-1) + \alpha \sum_{n=2}^{N} \Theta_n^{'} a_{\eta,n}(t)(y=-1) \end{bmatrix}, \tag{5.131}$$

and can be given by

$$\tilde{\mathbf{s}}(t) = \mathbf{S}_1 \mathbf{x}(t), \tag{5.132}$$

where the matrix $\mathbf{S}_1$ is given by

$$\begin{cases} \mathbf{S}_{1,11} &= +\frac{j\alpha}{k^2 R} \begin{bmatrix} \Xi_{p_0}^{''}(y=+1) & \dots & \Xi_N^{''}(y=+1) \\ \Xi_{p_0}^{''}(y=-1) & \dots & \Xi_N^{''}(y=-1) \end{bmatrix} \\ \mathbf{S}_{1,21} &= +\frac{j\beta}{k^2 R} \begin{bmatrix} \Xi_{p_0}^{''}(y=+1) & \dots & \Xi_N^{''}(y=+1) \\ \Xi_{p_0}^{''}(y=-1) & \dots & \Xi_N^{''}(y=-1) \end{bmatrix} \\ \mathbf{S}_{1,12} &= -\frac{j\beta}{k^2 R} \begin{bmatrix} \Theta_2^{'}(y=+1) & \dots & \Theta_N^{'}(y=+1) \\ \Theta_2^{'}(y=-1) & \dots & \Theta_N^{'}(y=-1) \end{bmatrix} \\ \mathbf{S}_{1,22} &= +\frac{j\alpha}{k^2 R} \begin{bmatrix} \Theta_2^{'}(y=+1) & \dots & \Theta_N^{'}(y=+1) \\ \Theta_2^{'}(y=-1) & \dots & \Theta_N^{'}(y=-1) \end{bmatrix}. \end{cases} \tag{5.133}$$

The skin friction drag is modeled by

$$\mathbf{d}(t) = \mathbf{D}_1 \mathbf{x}(t), \tag{5.134}$$

where $\mathbf{D}_1 = R\left[\begin{array}{cccc} -1 & +1 & 0 & 0 \end{array}\right]\mathbf{S}_1$. In the controlled flow, the velocity and vorticity are

$$\begin{cases} \tilde{v}(y=+1,t) &= \sum_{n=p_0}^{N} a_{v,n}(t)\Xi_n(y=+1) + \mathbf{F}_v(y=+1)\mathbf{q}_v(t) \\ \tilde{v}(y=-1,t) &= \sum_{n=p_0}^{N} a_{v,n}(t)\Xi_n(y=-1) + \mathbf{F}_v(y=-1)\mathbf{q}_v(t) \\ \tilde{\eta}(y=+1,t) &= \sum_{n=2}^{N} a_{\eta,n}(t)\Theta_n(y=+1) + \mathbf{F}_\eta(y=+1)\mathbf{q}_\eta(t) \\ \tilde{\eta}(y=-1,t) &= \sum_{n=2}^{N} a_{\eta,n}(t)\Theta_n(y=-1) + \mathbf{F}_\eta(y=-1)\mathbf{q}_\eta(t) \end{cases} \tag{5.135}$$

Therefore, the shear stress is calculated by

$$\tilde{\mathbf{s}}(t) = \mathbf{S}_1\mathbf{x}(t) + \mathbf{S}_2\mathbf{u}(t), \tag{5.136}$$

where

$$\begin{cases} \mathbf{S}_{2,11} = +\dfrac{j\alpha}{k^2R}\begin{bmatrix} \mathbf{F}_v''(y=+1) \\ \mathbf{F}_v''(y=-1) \end{bmatrix}, & \mathbf{S}_{2,21} = +\dfrac{j\beta}{k^2R}\begin{bmatrix} \mathbf{F}_v''(y=+1) \\ \mathbf{F}_v''(y=-1) \end{bmatrix} \\ \mathbf{S}_{2,12} = -\dfrac{j\beta}{k^2R}\begin{bmatrix} \mathbf{F}_\eta'(y=+1) \\ \mathbf{F}_\eta'(y=-1) \end{bmatrix}, & \mathbf{S}_{2,22} = +\dfrac{j\alpha}{k^2R}\begin{bmatrix} \mathbf{F}_\eta'(y=+1) \\ \mathbf{F}_\eta'(y=-1) \end{bmatrix}. \end{cases} \tag{5.137}$$

Therefore, the skin friction drag is modeled by

$$\mathbf{d}(t) = \mathbf{D}_1\mathbf{x}(t) + \mathbf{D}_2\mathbf{u}(t), \tag{5.138}$$

where $\mathbf{D}_2 = R\left[\begin{array}{cccc} -1 & +1 & 0 & 0 \end{array}\right]\mathbf{S}_2$.

5.6 Behavior of the open-loop system

5.6.1 Behavior of the state vector

The open-loop system is

$$\mathbf{L}\dot{\mathbf{x}}(t) = \mathbf{A}\mathbf{x}(t), \tag{5.139}$$

where the state matrix $\mathbf{A}$ for all wavenumber pairs is given by (see [Joshi et al., 1997], p.167, eq.(4.2))

$$\mathbf{A} = \begin{bmatrix} \mathbf{A}_{n_{st}=0,n_{sp}=0} & 0 & \cdots & 0 \\ 0 & \mathbf{A}_{n_{st}=1,n_{sp}=0} & 0 & 0 \\ \vdots & 0 & \ddots & \vdots \\ 0 & 0 & 0 & \mathbf{A}_{N_{st},N_{sp}} \end{bmatrix}. \tag{5.140}$$

We recall that the linear model can be decoupled by wavenumber pairs and thus it is possible to treat each wavenumber pair separately as can be seen from the matrix

A. Therefore, we see that the eigenvalues and eigenvectors of the entire matrix **A** are simply the eigenvalues and eigenvectors of each sub-matrix block $\mathbf{A}_{n_{st},n_{sp}}$. As a result, we only consider the open-loop system with one wavenumber pair. We determine the wavenumber pairs where the open-loop system contains the unstable eigenvalues.

Note that both the 2D and 3D plane Poiseuille flows contain unstable eigenvalues but in order to investigate the unstable eigenvalues, we only need the 2D plane Poiseuille flow.

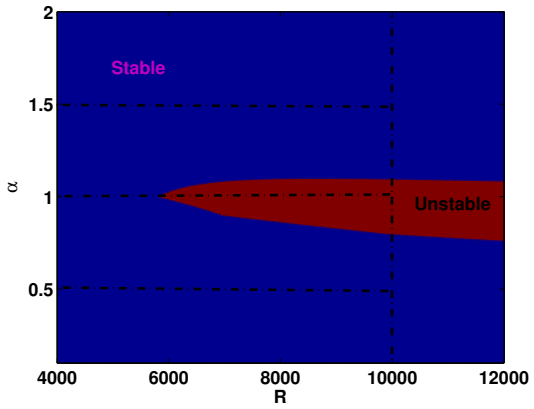

Figure 5.6: Channel model: $R = 10\ 000$ and $L_x = 4\pi$. The fundamental wavenumber $\frac{2\pi}{L_x} = \frac{1}{2}$. All integral numbers of this fundamental wavenumber exist in the channel. Only $2\alpha_0 = 1$ leads to unstable mode.

Firstly, we consider the 2D plane Poiseuille flow with $L_x = 4\pi$, all integral multiples of the fundamental wavenumber exist in the plane Poiseuille flow

$$\alpha = n_{st}\alpha_0 = n_{st}\frac{2\pi}{L} = 0.5n_{st} \text{ with } n_{st} = 0 \ldots N_{st}. \tag{5.141}$$

Based on the curve obtained from the Orr-Sommerfeld equation and is denoted Orzag's diagram, as shown in Figure 5.6, we see that the unstable mode of the plane Poiseuille flow is a function of the Reynolds number R and the wavenumber α. Only some modes are unstable modes. In this case, only wavenumber $\alpha_1 = 2\alpha_0 = 1$ is unstable wavenumber, while both $\alpha_0 = 0.5$ and $\alpha = 1.5 \cdots + \infty$ are stable wavenumber. In the case $\alpha = 1$, $\beta = 0$ and $R = 10\ 000$, the unstable modes are $\lambda = 0.003739670622977 \pm 0.237526488820464i$ [Orszag, 1971].

5.6.2 Behavior of the kinetic energy density

In [Orszag, 1971], the linear model contains unstable modes when the Reynolds number $R > 5\ 772$. And the linear model has no unstable modes at the Reynolds number $1\ 000 < R < 5\ 772$ but the flow may be turbulent. More precisely, the appearance of transient energy growth leads the flow to turbulent, as shown at the Reynolds number $R \approx 1000$ from the experimental studies [Patel and Head, 1969]. Note that there is no

transient energy growth if the Reynolds number is less than $R = 49.6$, as shown in [Joseph and Carmi, 1969] by the energy methods. Indeed, the unstable modes do not fully represent turbulence, therefore we need to investigate the transient energy growth of the flow (see section 2.3).

We recall that the problem of transient energy growth is the problem of non-orthogonality of the eigenvectors of the linear model (see section 4.3.2.2). In the 3D plane Poiseuille flow, the transient energy growth was investigated at the Reynolds number $R = 5\ 000$ and the wavenumbers $\alpha = 0$, $\beta = 2.044$ where ε_d is the highest value [Butler and Farrell, 1992], as shown in Figure 5.7. The behavior of the kinetic energy

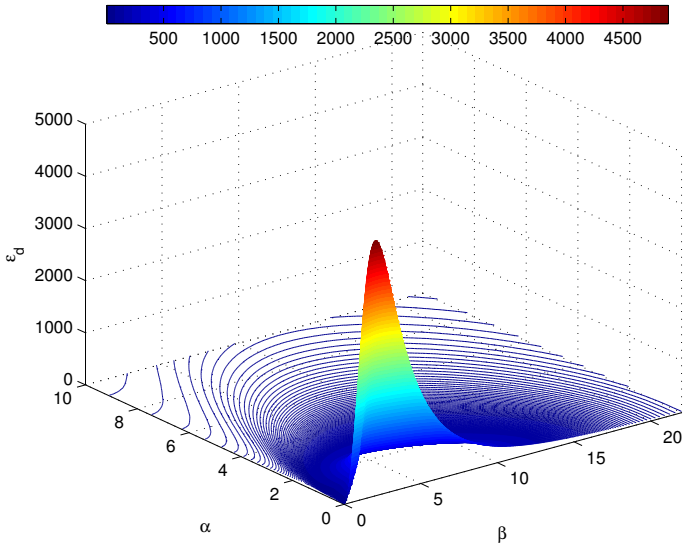

Figure 5.7: Behavior of the diachronic transient energy growth ε_d versus α and β ($R = 5\ 000$).

density is as shown in Figure 5.8. The diachronic transient energy growth is $\varepsilon_d = 4897$.

Although the linearization of the model of the plane Poiseuille flow contains all negative eigenvalues, all state vector monotonically decreases in time but the flow still becomes turbulent. In order to determine the state of the flow and its stability, we are interested in the behavior of the kinetic energy density.

5.7 Conclusion

In this chapter, we have presented a linear model of the plane Poiseuille flow with the boundary control, given by blowing/suction boundary. The skin friction drag and the kinetic energy density are modeled as a function of the state vector. Since the linear model of the plane Poiseuille flow is reached, a control scheme is next step. A Matlab code used for flow simulation which is developed based on the code and the result

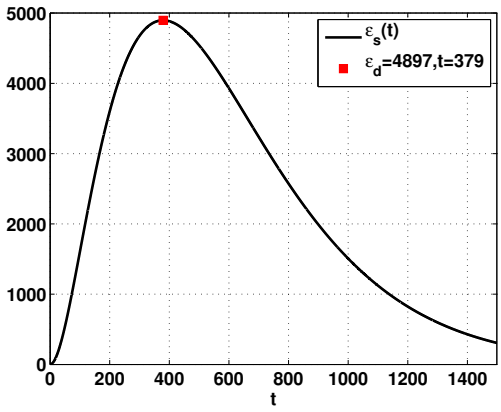

Figure 5.8: Behavior of the synchronic transient energy versus time ($R = 5\ 000$, $\alpha = 0$, $\beta = 2.044$).

provided by McKernan [McKernan, 2006], Bewley [Bewley and Liu, 1998] and Schmid [Schmid and Henningson, 2001].

In the next chapter, we use the partitioned visual servoing control to simultaneously minimize the skin friction drag and the kinetic energy density.

Chapter 6

Partitioned Visual Servoing Control

The goal of this chapter is to obtain the behavior of the skin friction drag $\mathbf{d}(t) = e^{-\lambda t}\mathbf{d}_0$ in the closed loop system of the plane Poiseuille flow. However, this chapter only considers two degrees of freedom (**DOF**) and it demonstrates what can be obtained with them. The idea is to fully exploit two **DOF** to minimize, simultaneously, the skin friction drag and the kinetic energy density. Although there exist methods such as **PID** control, **LQR** control, $\mathbf{H}_2/\mathbf{H}_\infty$ control and **LMI** control to minimize the skin friction drag in the literature but these are indirectly. It means that the skin friction drag was usually minimized by minimization of the shear stress or the state vector.

6.1 State space representation

In the chapter, we only consider two **DOF** on the wall-normal velocity, it means

$$\begin{cases} v(x, y = +1, z, t) & = q_{v,u}(t) \\ v(x, y = -1, z, t) & = q_{v,l}(t) \\ \eta(x, y = \pm 1, z, t) & = 0 \end{cases} \tag{6.1}$$

therefore, the input matrices $\mathbf{B}$ and $\mathbf{E}$ become

$$\begin{cases} \mathbf{E}_{11} & = j(k^2\mathbf{D}0_{DN}(\mathbf{F}_v) - \mathbf{D}2_{DN}(\mathbf{F}_v)),\ \mathbf{E}_{12} = [0],\ \mathbf{E}_{21} = [0],\ \mathbf{E}_{22} = 0 \\ \mathbf{B}_{11} & = (-\alpha\overline{U}k^2 - \alpha\overline{U}'' - \dfrac{k^4\mathbf{I}}{jR})\mathbf{D}0_{DN}(\mathbf{F}_v) + (\alpha\overline{U} + \dfrac{2k^2\mathbf{I}}{jR})\mathbf{D}2_{DN}(\mathbf{F}_v) - \dfrac{1}{jR}\mathbf{D}4_{DN}(F_v) \\ \mathbf{B}_{12} & = [0],\ \mathbf{B}_{21} = \beta\overline{U}'\mathbf{D}0_{DN}(\mathbf{F}_v),\ \mathbf{B}_{22} = 0. \end{cases} \tag{6.2}$$

When the state matrix $\mathbf{L}$ is invertible, $\mathbf{L}^{-1}$ exists and (5.96) is rewritten under the following form

$$\begin{cases} \dot{\mathbf{x}}(t) & = \mathbf{L}^{-1}\mathbf{A}\mathbf{x}(t) + \mathbf{L}^{-1}\mathbf{B}\mathbf{u}(t) + \mathbf{L}^{-1}\mathbf{E}\dot{\mathbf{u}}(t) \\ \varepsilon(t) & = \mathbf{x}^\top(t)\mathbf{Q_{11}}\mathbf{x}(t) + \mathbf{x}^\top(t)\mathbf{Q_{12}}\mathbf{u}(t) + \mathbf{u}^\top(t)\mathbf{Q_{21}}\mathbf{x}(t) + \mathbf{u}^\top(t)\mathbf{Q_{22}}\mathbf{u}(t) \\ \mathbf{d}(t) & = \mathbf{D}_1\mathbf{x}(t) + \mathbf{D}_2\mathbf{u}(t). \end{cases} \tag{6.3}$$

If we use the control law $\mathbf{u}(t) = \mathbf{K}\mathbf{x}(t)$, the skin friction drag will be calculated by

$$\mathbf{d}(t) = (\mathbf{D}_1 + \mathbf{D}_2\mathbf{K})\mathbf{x}(t), \tag{6.4}$$

Therefore, the derivate of skin friction drag is given by

$$\dot{\mathbf{d}}(t) = (\mathbf{D}_1 + \mathbf{D}_2\mathbf{K})\dot{\mathbf{x}}(t), \tag{6.5}$$

In order to ensure $\dot{\mathbf{d}}(t) = -\lambda\mathbf{d}(t)$, this implies that

$$(\mathbf{D}_1 + \mathbf{D}_2\mathbf{K})\dot{\mathbf{x}}(t) = -\lambda(\mathbf{D}_1 + \mathbf{D}_2\mathbf{K})\mathbf{x}(t) \Rightarrow \dot{\mathbf{x}}(t) = -\lambda\mathbf{x}(t) \tag{6.6}$$

Indeed, we do not have a chance to obtain $\dot{\mathbf{x}}(t) = -\lambda\mathbf{x}(t)$ with two **DOF**. Thus, we only obtain $\dot{\mathbf{x}}(t) = -\lambda\mathbf{x}(t)$ when the number of **DOF** must be equal to the dimension of the state vector (see B).

In order to exploit two **DOF** and ensure $\dot{\mathbf{d}}(t) = -\lambda\mathbf{d}(t)$, we use the control signal $\mathcal{U}(t) = \dot{\mathbf{u}}(t)$ as in [Aamo, 2002], [Bewley and Liu, 1998], [Joshi, 1996], [McKernan, 2006]. It is easy to show that the system (6.3) becomes

$$\begin{bmatrix} \dot{\mathbf{x}}(t) \\ \dot{\mathbf{u}}(t) \end{bmatrix} = \begin{bmatrix} \mathbf{L}^{-1}\mathbf{A} & \mathbf{L}^{-1}\mathbf{B} \\ 0 & 0 \end{bmatrix} \begin{bmatrix} \mathbf{x}(t) \\ \mathbf{u}(t) \end{bmatrix} + \begin{bmatrix} \mathbf{L}^{-1}\mathbf{E} \\ \mathbf{I} \end{bmatrix} \dot{\mathbf{u}}(t), \tag{6.7}$$

and is rewritten by

$$\dot{\mathcal{X}}(t) = \mathcal{A}\mathcal{X}(t) + \mathcal{B}\mathcal{U}(t), \tag{6.8}$$

where the state vector is $\mathcal{X}(t) = \begin{bmatrix} \mathbf{x}(t) \\ \mathbf{u}(t) \end{bmatrix}$. The state matrix $\mathcal{A}$ and the input matrix $\mathcal{B}$ are given by

$$\mathcal{A} = \begin{bmatrix} \mathbf{L}^{-1}\mathbf{A} & \mathbf{L}^{-1}\mathbf{B} \\ 0 & 0 \end{bmatrix}, \quad \mathcal{B} = \begin{bmatrix} \mathbf{L}^{-1}\mathbf{E} \\ \mathbf{I} \end{bmatrix}. \tag{6.9}$$

According to the state vector $\mathcal{X}(t)$, the kinetic energy density is rewritten

$$\begin{aligned} \varepsilon(t) &= \mathbf{x}^\top(t)\mathbf{Q}_{11}\mathbf{x}(t) + \mathbf{x}^\top(t)\mathbf{Q}_{12}\mathbf{u}(t) + \mathbf{u}^\top(t)\mathbf{Q}_{21}\mathbf{x}(t) + \mathbf{u}^\top(t)\mathbf{Q}_{22}\mathbf{u}(t) \\ &= \begin{bmatrix} \mathbf{x}^\top(t) & \mathbf{u}^\top(t) \end{bmatrix} \begin{bmatrix} \mathbf{Q}_{11} & \mathbf{Q}_{12} \\ \mathbf{Q}_{21} & \mathbf{Q}_{22} \end{bmatrix} \begin{bmatrix} \mathbf{x}(t) \\ \mathbf{u}(t) \end{bmatrix} \\ &= \mathcal{X}^\top(t)\mathcal{Q}\mathcal{X}(t), \end{aligned} \tag{6.10}$$

where the matrix $\mathcal{Q}$ is given by

$$\mathcal{Q} = \begin{bmatrix} \mathbf{Q}_{11} & \mathbf{Q}_{12} \\ \mathbf{Q}_{21} & \mathbf{Q}_{22} \end{bmatrix}. \tag{6.11}$$

In the same way, the skin friction drag is also is given by

$$\mathbf{d}(t) = \mathbf{D}_1\mathbf{x}(t) + \mathbf{D}_2\mathbf{u}(t) = \mathcal{D}\mathcal{X}(t), \tag{6.12}$$

where $\mathcal{D} = \begin{bmatrix} \mathbf{D}_1 & \mathbf{D}_2 \end{bmatrix}$. Therefore, the linear model of the plane Poiseuille flow is given by

$$\begin{cases} \dot{\mathcal{X}}(t) &= \mathcal{A}\mathcal{X}(t) + \mathcal{B}\mathcal{U}(t) \\ \varepsilon(t) &= \mathcal{X}^\top(t)\mathcal{Q}\mathcal{X}(t) \\ \mathbf{d}(t) &= \mathcal{D}\mathcal{X}(t) \\ \mathcal{X}(0) &= \mathcal{X}_0. \end{cases} \tag{6.13}$$

6.2 Our goal of the control law

Considering here a state feedback control

$$\mathcal{U}(t) = \mathcal{K}\mathcal{X}(t), \tag{6.14}$$

and suppose that this control is able to achieve an exponential decrease of the skin friction drag

$$\dot{\mathbf{d}}(t) = -\lambda \mathbf{d}(t), \tag{6.15}$$

and simultaneously minimize the kinetic energy density

$$\varepsilon(t) = \mathcal{X}^{\top}(t)\mathcal{Q}\mathcal{X}(t). \tag{6.16}$$

Note that this chapter only considers two **DOF**. Due to the limitation of the number of **DOF**, the partitioned visual servoing control is chosen to simultaneously minimize the skin friction drag and the kinetic energy density. This approach is a well known approach in the robotics community used to decouple the rotational motions from the translational ones. To do that, it needs to compute the interaction matrix $\mathbf{L}_d$ related to the skin friction drag.

6.3 Computation of the interaction matrix related to the drag

Indeed, according to the definition of the interaction matrix [Espiau et al., 1992], this approach needs to express the total time variation of the skin friction drag

$$\dot{\mathbf{d}}(t) = \mathbf{L}_d \mathcal{U}(t) + \frac{\partial \mathbf{d}(t)}{\partial t}. \tag{6.17}$$

$\mathbf{L}_d$ encodes the variation of the skin friction drag due to the actions, while $\partial \mathbf{d}(t)/\partial t$ expresses the variation of the skin friction drag due to the flow itself.

This computation can be done by deviating the skin friction drag in (6.13) and using the equation of the state space representation, therefore we obtain

$$\dot{\mathbf{d}}(t) = \mathcal{D}\dot{\mathcal{X}}(t) = \mathcal{D}\left(\mathcal{A}\mathcal{X}(t) + \mathcal{B}\mathcal{U}(t)\right). \tag{6.18}$$

Therefore, by comparing (6.17) and (6.18), we get

$$\begin{cases} \mathbf{L}_d &= \mathcal{D}\mathcal{B} \\ \dfrac{\partial \mathbf{d}(t)}{\partial t} &= \mathcal{D}\mathcal{A}\mathcal{X}(t). \end{cases} \tag{6.19}$$

Let us introduce the components of the interaction matrix related to the components of the control signals $\mathcal{U}(t)$

$$\mathbf{L}_d = \begin{bmatrix} \mathbf{L}_{du} & \mathbf{L}_{dl} \end{bmatrix} = \begin{bmatrix} \mathbf{D}_1 & \mathbf{D}_2 \end{bmatrix} \begin{bmatrix} \mathbf{L}^{-1}\mathbf{E} \\ \mathbf{I} \end{bmatrix}. \tag{6.20}$$

This expression will be useful in the next section to introduce the partitioned visual servo control.

6.4 Design of the control law

The partitioned visual servoing control relies on the partition of the interaction matrix. From (6.20), the time variation of the skin friction drag (6.17) becomes

$$\dot{\mathbf{d}}(t) = \mathbf{L}_{du}\mathcal{U}_u(t) + \mathbf{L}_{dl}\mathcal{U}_l(t) + \frac{\partial \mathbf{d}(t)}{\partial t}. \tag{6.21}$$

where $\mathcal{U}(t) = \begin{bmatrix} \mathcal{U}_u(t) & \mathcal{U}_l(t) \end{bmatrix}^\top$. Since a decrease of the drag is desired, a particular behavior is chosen for the drag. An exponential decrease is imposed

$$\dot{\mathbf{d}}(t) = -\lambda \mathbf{d}(t) \tag{6.22}$$

where λ is a positive gain able to tune the decrease rate. Thereafter, from (6.21) and (6.22), we have

$$-\lambda \mathbf{d}(t) = \mathbf{L}_{du}\mathcal{U}_u(t) + \mathbf{L}_{dl}\mathcal{U}_l(t) + \frac{\partial \mathbf{d}(t)}{\partial t}. \tag{6.23}$$

Any of the two components of $\mathcal{U}(t)$ can be used to reduce the skin friction drag, we arbitrarily choose $\mathcal{U}_l(t)$. We thus have

$$\mathcal{U}_l(t) = -\frac{1}{\mathbf{L}_{dl}}\left(\lambda \mathbf{d}(t) + \mathbf{L}_{du}\mathcal{U}_u(t) + \frac{\partial \mathbf{d}(t)}{\partial t}\right). \tag{6.24}$$

Since the lower boundary control law $\mathcal{U}_l(t)$ is known if the upper boundary control law $\mathcal{U}_u(t)$ is known, the next step is to express $\mathcal{U}_u(t)$.

In order to minimize the kinetic energy density (6.13) and the energy consumption of actuators, a **LQR** control scheme over an infinite time horizon is used by considering the following cost function

$$J = \int_0^\infty \left(\mathcal{X}^\top(t)\mathcal{Q}\mathcal{X}(t) + \gamma^2 \mathcal{U}_u^2(t)\right) \mathrm{d}t. \tag{6.25}$$

This can be done by expressing the time variation of the state vector with respect to the control signal $\mathcal{U}_u(t)$. To do that, we first rewrite (6.24) from (6.19) to exhibit the state vector

$$\mathcal{U}_l(t) = -\frac{1}{\mathbf{L}_{dl}}\left((\lambda\mathcal{D} + \mathcal{D}\mathcal{A})\,\mathcal{X}(t) + \mathbf{L}_{du}\mathcal{U}_u(t)\right), \tag{6.26}$$

that we have to plug in (6.13) leading to

$$\dot{\mathcal{X}}(t) = \mathcal{A}_1\mathcal{X}(t) + \mathcal{B}_1\mathcal{U}_u(t), \tag{6.27}$$

with the matrices $\mathcal{A}_1 = \mathcal{A} - \frac{\mathcal{B}_l}{\mathbf{L}_{dl}}(\lambda\mathcal{D} + \mathcal{D}\mathcal{A})$ and $\mathcal{B}_1 = \mathcal{B}_u - \frac{\mathbf{L}_{du}}{\mathbf{L}_{dl}}\mathcal{B}_l$ with $\mathcal{B} = \begin{bmatrix} \mathcal{B}_u & \mathcal{B}_l \end{bmatrix}$. Note that $\mathbf{L}_{dl}$ is always non null in the case $\alpha \neq 0$.

Thereafter, the **LQR** gain $\mathcal{K}$ involved in the optimal control $\mathcal{U}_u(t) = \mathcal{K}\mathcal{X}(t)$ is computed by considering (6.27) and solving the Algebraic Ricatti Equation (see **LQR**

control for more details, we only use $\mathcal{K} = -lqr(\mathcal{A}, \mathcal{B}, \mathcal{Q}, \gamma^2\mathcal{I})$ in Matlab). The gain $\mathcal{K}$ is given by

$$\mathcal{K} = -\frac{1}{\gamma^2}\mathcal{B}_1^\top \mathcal{P}, \tag{6.28}$$

where $\mathcal{P}$ is the solution of the Algebraic Ricatti Equation

$$\mathcal{A}_1^\top \mathcal{P} + \mathcal{P}\mathcal{A}_1 + \mathcal{Q} - \frac{1}{\gamma^2}\mathcal{P}\mathcal{B}_1\mathcal{B}_1^\top \mathcal{P} = 0. \tag{6.29}$$

Note that here, contrary to previous works involved in flow control, this approach has fully exploited two **DOF** of control signal.

Due to the fact that the linear model of the plane Poiseuille flow is used, it must consider the behavior of the nonlinear system. The next section is dedicated to the stability analysis of the exponential decrease of skin friction drag since the skin friction drag is a nonlinear system.

6.5 Stability analysis

The stability of skin friction drag is discussed. It is assumed that a nonlinear model of the skin friction drag can be obtained in a certain domain of variation of $\mathcal{X}(t)$ and $\mathcal{U}(t)$:

$$\dot{\mathbf{d}}(t) = f(\mathcal{X}(t), \mathcal{U}(t)). \tag{6.30}$$

According to (6.22), it is clear that $\mathbf{d} = \mathbf{0}$ is an exponentially stable equilibrium point for the linearized system (6.17) and for the control law derived in section 6.4. Therefore, $\mathbf{d} = \mathbf{0}$ is also an exponentially stable equilibrium point for the nonlinear system (6.30).

The next section is dedicated to the study of the behavior of the closed loop system when the measurement noise is considered.

6.6 Robustness to measurement noise

Of course, when measurement noise occurs, the main problem is the stability analysis of (6.27). In that case, the upper control signal becomes

$$\widehat{\mathcal{U}}_u = \mathcal{K}\widehat{\mathcal{X}}(t). \tag{6.31}$$

According to previous work [Tatsambon Fomena and Collewet, 2011a], we also use here a vision-based approach to estimate $\mathbf{x}(t)$. This is done concretely through the computation of the optical flow, as proposed in [Heitz et al., 2010] for example. A visualization system, like a **CCD** camera, is thus required. In that case, we have (see [Tatsambon Fomena and Collewet, 2011a])

$$\widehat{\mathcal{X}}(t) = \mathcal{X}(t) + \frac{1}{N_x}\mathbf{e}_x(t), \tag{6.32}$$

where N_x is the number of pixels of the camera in the streamwise direction of the flow and $\mathbf{e}_x(t)$ is related to the measurement noise ([Tatsambon Fomena and Collewet, 2011a] for more details). It is clear from (6.32), that the larger the value of N_x the closer $\widehat{\mathcal{X}}(t)$ is to $\mathcal{X}(t)$. Consequently, plugging (6.31) and (6.32) into (6.27), it is very easy to show that (6.27) becomes

$$\dot{\mathcal{X}}(t) = (\mathcal{A}_1 + \mathcal{B}_1\mathcal{K})\mathcal{X}(t) + \mathcal{B}_1\mathcal{K}\frac{1}{N_x}\mathbf{e}_x(t). \tag{6.33}$$

When N_x is large enough (it is always the case in practice), the estimation error tends toward 0, and, consequently the closed loop system (6.33) is written as

$$\dot{\mathcal{X}}(t) \approx (\mathcal{A}_1 + \mathcal{B}_1\mathcal{K})\mathcal{X}(t), \tag{6.34}$$

which is stable. The state vector is robust to measurement noise.

The other issue concerns the skin friction drag. Indeed, we have to verify that it is still a decreasing function. To do that, we examine (6.21) by considering $\widehat{\mathcal{U}}_u$, $\widehat{\mathcal{U}}_l$ and $\partial\widehat{\mathbf{d}}(t)/\partial t$. From (6.26), we have

$$\widehat{\mathcal{U}}_l(t) = -\frac{1}{\mathbf{L}_{dl}}\left((\lambda\mathcal{D} + \mathcal{D}\mathcal{A})\,\widehat{\mathcal{X}}(t) + \mathbf{L}_{du}\widehat{\mathcal{U}}_u(t)\right) \tag{6.35}$$

that is written in function of $\mathcal{X}(t)$ by considering (6.31) and (6.32)

$$\widehat{\mathcal{U}}_l(t) = -\frac{1}{\mathbf{L}_{dl}}\left(\lambda\mathcal{D} + \mathcal{D}\mathcal{A} - \mathbf{L}_{du}\mathcal{K}\right)\left(\mathcal{X}(t) + \frac{1}{N_x}\mathbf{e}_x(t)\right). \tag{6.36}$$

The last step is the computation of $\partial\widehat{\mathbf{d}}(t)/\partial t$, it can easily be done from (6.19) and (6.32). All computations done, (6.21) becomes

$$\dot{\mathbf{d}}(t) = -\lambda\mathbf{d}(t) - \frac{\lambda\mathcal{D} + \mathcal{D}\mathcal{A}}{N_x}\mathbf{e}_x(t). \tag{6.37}$$

leading to

$$\dot{\mathbf{d}}(t) \approx -\lambda\mathbf{d}(t). \tag{6.38}$$

Here again, since N_x is a large value, the skin friction drag follows the desired behavior $\dot{\mathbf{d}}(t) = -\lambda\mathbf{d}(t)$. The simulation result is given in the next section for validation of the proposed approach.

6.7 Simulation Results

In the following **P** is the proportional control [Joshi et al., 1997], $\mathbf{LQR}_2$ is the **LQR** control in [Cortelezzi and Speyer, 1998], $\mathbf{LQR}_1$ is the **LQR** control in [McKernan et al., 2007] and **PVS** is the partitioned visual serving control [Dao and Collewet, 2012], the proposed approach. Note that we cannot exactly compare the proposed approach with the other mentioned results since none of them simultaneously minimizes the skin friction drag and the kinetic energy density. The simulation results are given based on a Matlab code.

6.7.1 Initial condition:

It is well known that the highest transient energy growth is unbounded for an unstable system but for a stable system, it exists a method for computing the highest transient energy growth. The worst initial condition is the initial condition to achieve the highest diachronic transient energy growth. Hence, the initial conditions are chosen the worst initial condition which generate the diachronic transient energy density as given in [Bewley and Liu, 1998], [McKernan, 2006].

In the uncontrolled flow, the synchronic transient energy growth corresponding to this initial condition is given by

$$\varepsilon_s(t) = \bar{\sigma}^2(e^{\mathbf{Q}_{11}^{1/2}\mathbf{L}^{-1}\mathbf{A}\mathbf{Q}_{11}^{-1/2}t}), \tag{6.39}$$

The worst initial condition is defined as

$$\mathbf{x}_0 = \mathbf{x}_{worst,\varepsilon_0=1}(t=0), \tag{6.40}$$

since the transient energy growth is the synchronic transient energy growth

$$\varepsilon_s(t) = \varepsilon(t) \tag{6.41}$$

and the diachronic transient energy growth at time $t = \tau$

$$\varepsilon_d = \max_{\varepsilon_0=1} \varepsilon_s(t=\tau). \tag{6.42}$$

The worst initial condition of the uncontrolled flow is $\mathbf{x}_0 = \mathbf{x}_{worst,\varepsilon_0=1}$, the initial value of the uncontrolled kinetic energy density is

$$\varepsilon_0 = \mathbf{x}_{worst,\varepsilon_0=1}^{\top}\mathbf{Q}_{11}\mathbf{x}_{worst,\varepsilon_0=1} = 1. \tag{6.43}$$

However, the initial value of the controlled kinetic energy density is

$$\varepsilon_{0,c} = \mathbf{x}_{worst,\varepsilon_0=1}^{\top}\mathbf{Q}_{11}\mathbf{x}_{worst,\varepsilon_0=1} + \mathbf{x}_{worst,\varepsilon_0=1}^{\top}\mathbf{Q}_{12}\mathbf{u}_0 + \mathbf{u}\top_0\mathbf{Q}_{21}\mathbf{x}_{worst,\varepsilon_0=1} + \mathbf{u}_0^{\top}\mathbf{Q}_{22}\mathbf{u}_0, \tag{6.44}$$

this value may be different to $\varepsilon_0 = 1$. This is very important thing, the initial condition $\mathbf{x}_0 = \mathbf{x}_{worst,\varepsilon_0=1}$ is the worst initial condition of the uncontrolled flow but is not the worst initial condition of the controlled flow.

The maximum kinetic energy density is defined as the maximum value of the kinetic energy density over time, thus it is defined by

$$\varepsilon_{max} = \max_{t\geq 0} \varepsilon(t), \tag{6.45}$$

this value at time $t = \tau$ and we do not need to impose the condition $\varepsilon_0 = 1$. Note that since $\varepsilon(t) = \varepsilon_s(t)$, then $\varepsilon_d = \varepsilon_{max}$. An example is given in Figure 6.1, we have one diachronic transient energy growth corresponding to one synchronic transient energy growth.

Due to the variety of the approaches, we have four worst initial conditions for each corresponding control approach. We set the same condition for all four control approaches. Therefore, the initial condition is chosen as the worst initial condition of the uncontrolled flow, $\mathcal{X}_0 = \begin{bmatrix} \mathbf{x}_{worst,\varepsilon_0=1}^{\top} & 0 & 0 \end{bmatrix}^{\top}$, in order to facilitate the comparison of the results.

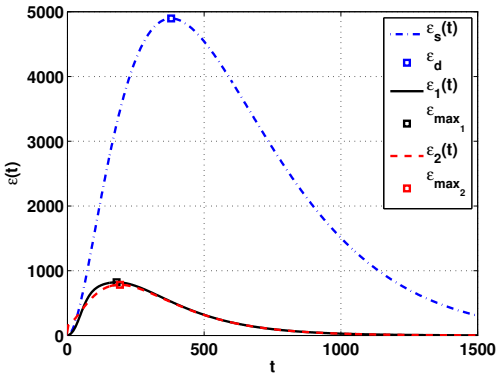

Figure 6.1: Behavior of the kinetic energy density versus time. ε_s is the synchronic transient energy growth, ε_d is the diachronic transient energy growth, ε_{max} is the maximum of the kinetic energy density.

6.7.2 Case I: 2D plane Poiseuille flow

6.7.2.1 Behavior of the 2D uncontrolled plane Poiseuille flow

We set $\alpha = 1$, $\beta = 0$ and $R = 10\ 000$ (see section 5.6) which presents an unstable mode as proven by the solutions of the classical Orr-Sommerfeld equation [Orszag, 1971]. We set $N = 100$ for the simulation results. The instability can be seen through the poles of the state matrix $\mathbf{L^{-1}A}$, obtained by selecting the linear model of plane Poiseuille flow with $\alpha = 1$, $\beta = 0$ and $R = 10\ 000$. The Table 6.1 gives the detail of the eigenvalues of matrix $\mathbf{L^{-1}A}$. And it contains the unstable eigenvalues $\lambda = 0.00373967 \pm i0.23752649$.

Table 6.1: Eigenvalues λ, $R = 10\ 000$, $\alpha = 1$, $\beta = 0$

Mode i	Eigenvalue λ
1	0.003739670622977 - 0.237526488820464i
2	-0.035167277631026 - 0.964630915450592i
3	-0.035186583792445 - 0.964642510039284i
4	-0.050898727256974 - 0.277204343808815i
5	-0.063201495839922 - 0.936316535881319i
6	-0.063251569074270 - 0.936351781164718i
7	-0.091222735433638 - 0.907983054629456i
8	-0.091312861779036 - 0.908056334492060i
9	-0.119232852619757 - 0.879627292207361i
10	-0.119370731008601 - 0.879755695814655i
7	⋮

The eigenvalues are depicted in Figure 6.2(a) which shows three branches: the center, upper (mode 1 and mode 4) and lower branches (modes 2, 3 and modes 5, 6). We can know the unstable eigenvalues based on the results in this figure, but we do not know

the controllability of each eigenvalues. Therefore, we consider the velocity eigenvector.

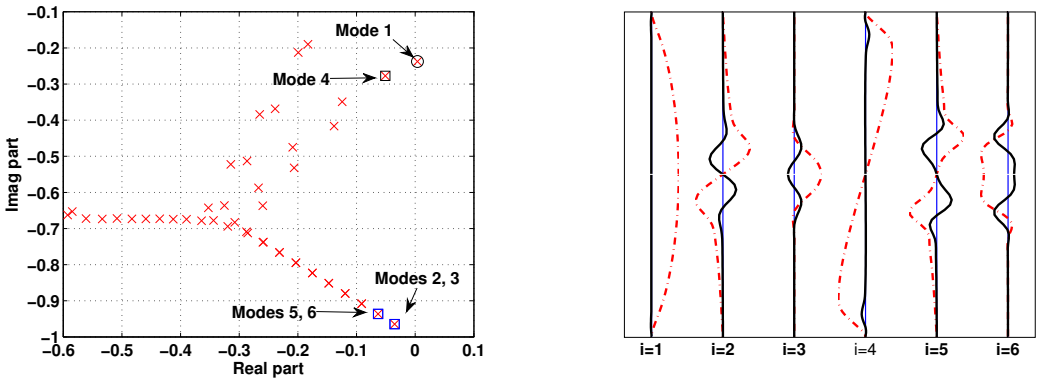

(a) eigenvalues (b) eigenvectors

Figure 6.2: Eigenvalues and eigenvectors of velocity component (real part (dashed line), imaginary part (solid line)). The wal-normal velocity eigenvectors are plotted as a function of y from $y = -1$ to $y = +1$ (vertical axis) and corresponding to the modes $i = 1, 2, 3, \ldots$ (horizontal axis).

The wall-normal velocity eigenvectors corresponding to the modes in Table 6.1 are shown in Figure 6.2(b) (Bewley and Liu [Bewley and Liu, 1998] and McKernan [McKernan, 2006]). Note that the profile of velocity is calculated by

$$\text{velocity } (t) = \sum i\text{th velocity eigenvector} \times e^{i\text{th eigenvalue } t}. \tag{6.46}$$

Therefore, based on the velocity eigenvector, we can predict the velocity profile. This is the cause we do not use the eigenvectors of $\mathbf{L^{-1}A}$. The real (dashed line) and imaginary (solid line) parts of the wall-normal velocity eigenvectors are plotted as a function of y from the lower wall to the upper wall. Note that mode 1 is the unstable mode, and thus it should be stabilized to stable mode. The result shown in Figure 6.2(b), the modes corresponding to the lower branch of Figure 6.2(a) (modes 2, 3 and 5, 6) are various in the center of the flow while the modes corresponding to the upper branch of Figure 6.2(a) (modes 1 and 4) which are various at the boundary of the flow. Therefore, in the case of using the boundary control at $y = \pm 1$, the lower branch of eigenvalues is less controllable than the upper branch of eigenvalues, the similar result as reported by Bewley and Liu [Bewley and Liu, 1998].

We depict the streamwise and wall-normal velocity components, the kinetic energy density and the velocity field of the flow in Figure 6.3. As can be seen in Figure 6.3(a) (similar results for (b)-(d)), at the left subfigure is the kinetic energy density and the velocity component at the point O($x = 0$ and $y = 0$), the left upper subfigure is the kinetic energy density and the left lower subfigure is the velocity component with the streamwise velocity component (dashed line) as compared with the wall-normal velocity component (solid line). The velocity field is shown at the right subfigure. Fom Figure 6.3(a) to Figure 6.3(d), the evolution of the uncontrolled flow is versus time. The kinetic

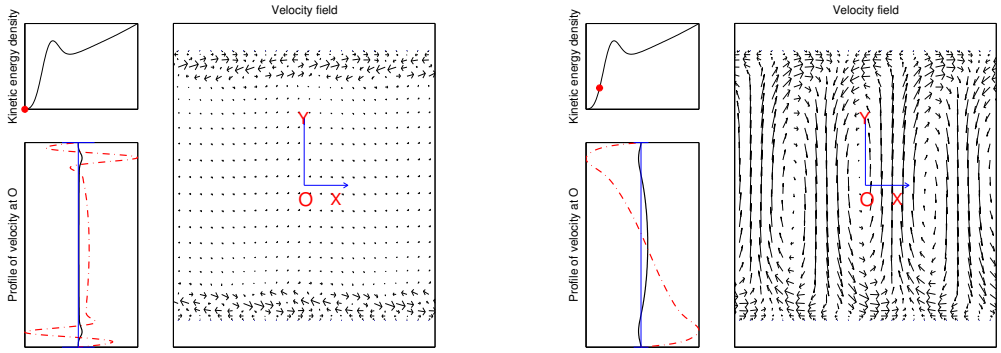

(a) t=0

(b) $t = \tau/2$

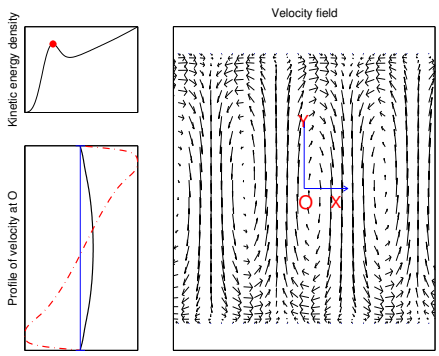

(c) $t = \tau$

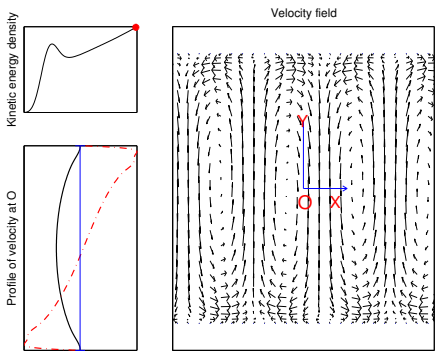

(d) $t \approx 4\tau$

Figure 6.3: Shape of the flow perturbation in the uncontrolled flow versus time, $\tau \approx 25$. We give the result at the times $t = 0$, $t = \tau/2$, $t = \tau$ and $t = 4\tau$.

energy density of the uncontrolled flow is unbounded. The flow becomes turbulent due to the unstable mode.

6.7.2.2 Behavior of the 2D controlled plane Poiseuille flow

The eigenvalues of the open loop system are depicted in Figure 6.4(a) which shows three branches: the center, upper (1, 2, 3 and 6) and lower (modes 4, 5) branches and the corresponding velocity eigenvectors are depicted in Figure 6.4(b). We have two novel modes (modes 2, 3) with respect to the uncontrolled flow. Mode 1 is the unstable mode while modes (2, 3) are associated with the integrators in (6.13), each representing steady-state transpiration from the upper and lower walls respectively, as shown by the non-zero wall velocities reported in [McKernan, 2006].

Comparison of the eigenvalues between the open loop system and the closed loop system in Figure 6.5(a), the unstable mode of the open loop system is relocated by the stable mode. And the result allows us to ensure that the modes corresponding to the

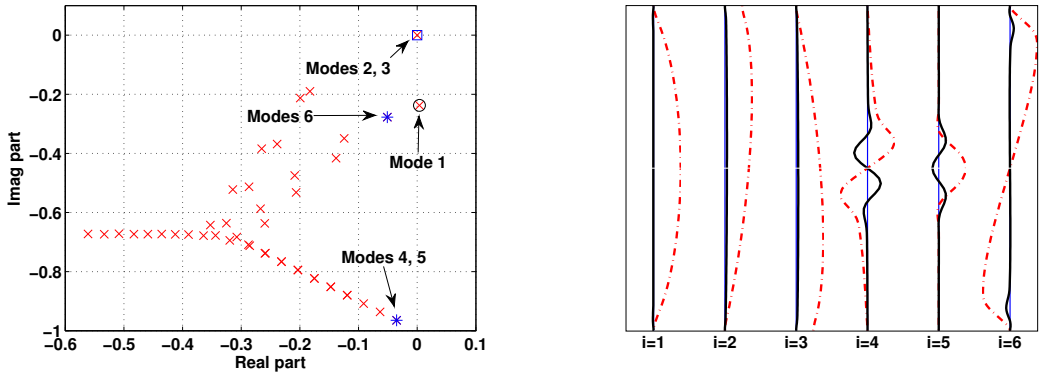

(a) eigenvalues (b) eigenvectors

Figure 6.4: Eigenvalues and eigenvectors of velocity component (real part (dashed line), imaginary part (solid line)). The wal-normal velocity eigenvectors are plotted as a function of y from $y = -1$ to $y = +1$ (vertical axis) and corresponding to the modes $i = 1, 2, 3, \ldots$ (horizontal axis).

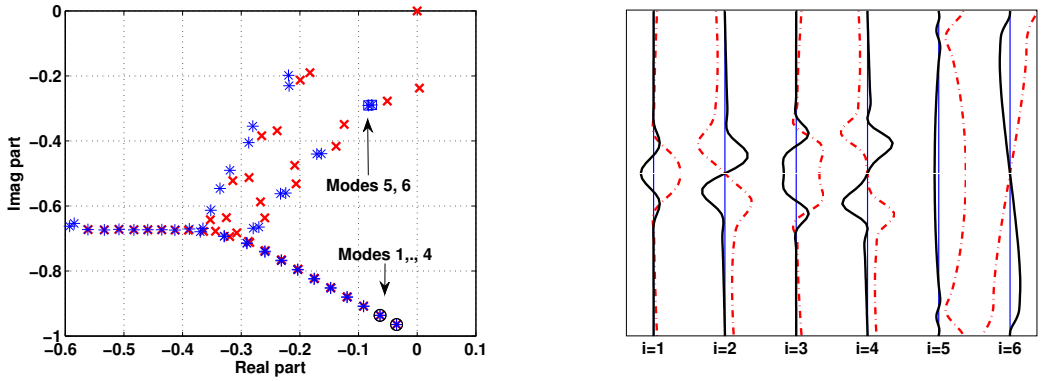

(a) eigenvalues (b) eigenvectors

Figure 6.5: Eigenvalues (open loop system ($\times$), closed loop system ($*$)) and eigenvectors of velocity component (real part (dashed line), imaginary part (solid line)). The wal-normal velocity eigenvectors are plotted as a function of y from $y = -1$ to $y = +1$ (vertical axis) and corresponding to the modes $i = 1, 2, 3, \ldots$ (horizontal axis).

center and lower branches of Figure 6.5(a) are less controllable than the upper branch of Figure 6.5(a) due to the modes corresponding to the center and lower branches of Figure 6.5(a) are remained while the modes corresponding to the upper branch of Figure 6.5(a) are relocated.

The kinetic energy density, the velocity component and the velocity field are given in Figure 6.6. As can be seen in Figure 6.6(a) (similar results for (b)-(d)), at the right subfigure the vertical arrows at the upper and lower boundaries are the control signal.

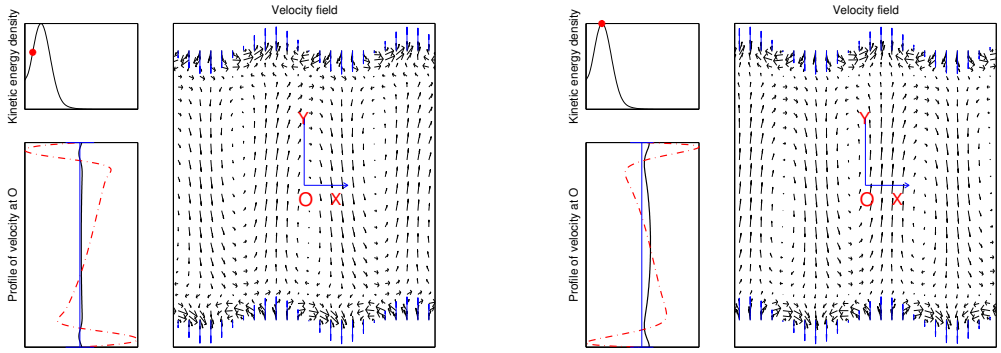

(a) $t = 0$ (b) $t = \tau$

(c) $t = 2\tau$ (d) $t \approx 6.67\tau$

Figure 6.6: Shape of the flow perturbation in the controlled flow versus time, $\tau = 16$.

From Figure 6.6(a) to Figure 6.6(d), the evolution of controlled the flow is versus time. By applying the boundary control, the kinetic energy density is minimized and tends toward zero, the velocity component tends toward the steady solution $(1 - y^2, 0)$. The flow becomes the laminar flow from turbulence .

6.7.2.3 PVS control for the 2D plane Poiseuille flow

The variation of maximum kinetic energy density with control weights k_p (the proportional control) or γ (the **LQR** and **PVS** controls) is shown in Figure 6.7 (the similar result for the $\mathbf{LQR}_1$ was given by McKernan [McKernan, 2006], p.130, Figure 4.9). We set $k_p = \gamma^2$ to be able to illustrate all results on the same axis. Let's look first at the proportional control, the maximum kinetic energy density for the **P** control is minimum value at $\mathbf{k}_p \approx 16$. In contrast to the proportional control, the **LQR** and **PVS** controls, the maximum kinetic energy density obtains the minimum value at the smallest value of γ. As can be seen in Figure 6.7, $\gamma \leq 0.25$ (the best case of parameter $\gamma = 0.25$ in [McKernan et al., 2007]), both the $\mathbf{LQR}_1$ and **PVS** controls provide an almost constant of maximum kinetic energy density.

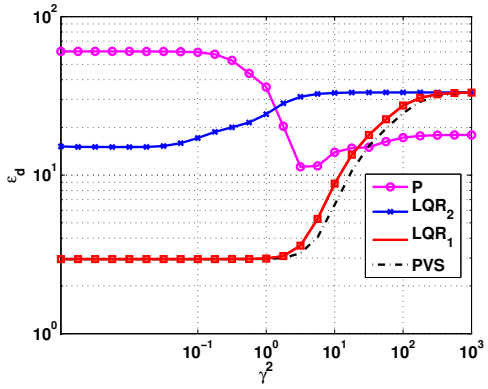

Figure 6.7: Maximum kinetic energy density versus the control weight γ.

Next, we consider the behavior of the closed loop system. We set $k_p = 16$ for the **P** control, $\gamma = 0.25$ for the $\mathbf{LQR}_1$ and **PVS** controls and $\gamma = 0.01$ for the $\mathbf{LQR}_2$ control. And we set $\lambda = 0.5$ for the **PVS** control.

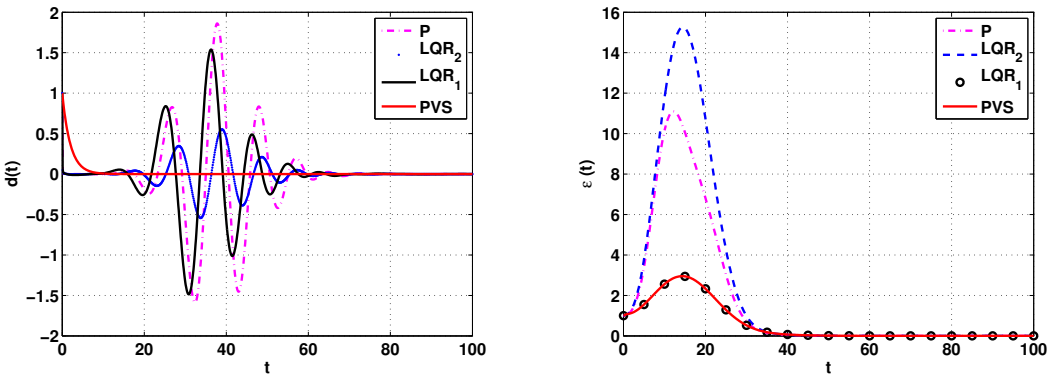

(a) $\mathbf{d}(t)$ versus time (b) $\varepsilon(t)$ versus time

Figure 6.8: Behavior of the closed loop system.

As expected, our approach provides better results than the other approaches. A nice decrease of the skin friction drag and the kinetic energy density are observed. The skin friction drag is shown in Figure 6.8(a) and only our approach obtains a nice decrease of skin friction drag.

The $\mathbf{LQR}_1$ control leads also to a nice minimization of the kinetic energy density but the (indirect) minimization of the skin friction drag is not satisfactory. Both methods based on the minimization of the shear stress (the **P** and $\mathbf{LQR}_2$ controls) lead to a worse behavior than the $\mathbf{LQR}_1$ and **PVS** controls as shown in Figure 6.8(b). The maximum kinetic energy density for four control approaches are given $\varepsilon_{max,PVS} = 2.9537$, $\varepsilon_{max,LQR_1} = 2.9544$, $\varepsilon_{max,P} = 11.0916$ and $\varepsilon_{max,LQR_2} = 15.2652$.

Next, we discuss the influence of parameter λ of the **PVS** control. In the **PVS**

control, λ decides the convergence velocity of skin friction drag. As shown as, only our approach is able to control directly the convergence velocity of skin friction drag in Figure 6.9(a). The other ones (the **P** and **LQR** controls) can only control indirectly the convergence velocity through the convergence of shear stress or the kinetic energy density.

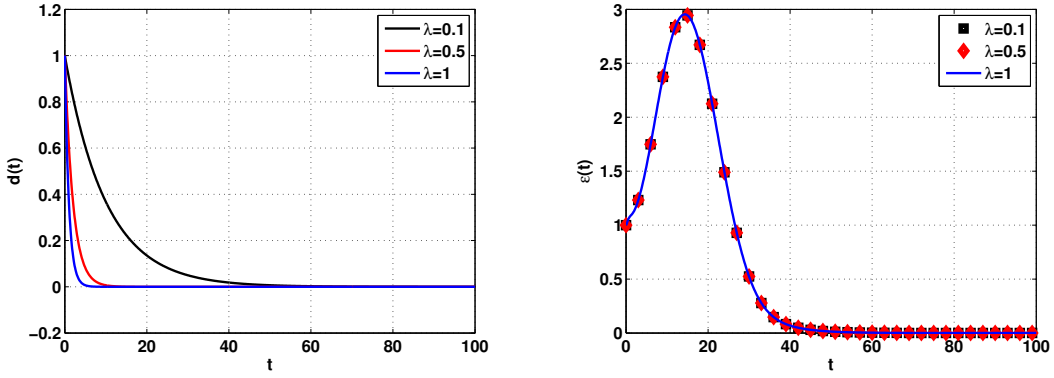

(a) $\mathbf{d}(t)$ versus time (b) $\varepsilon(t)$ versus time

Figure 6.9: Behavior of the closed loop system versus time with various choices of λ.

Figure 6.9(b) describes the variation of kinetic energy density for various choices of λ, as can be seen in this figure, this kinetic energy density almost has a small dependence on this value. It means that the way the skin friction drag is reduced does not influence the way the kinetic energy density is reduced in this case.

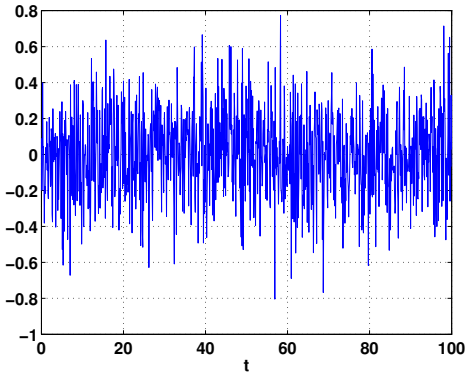

Figure 6.10: White Gaussian noise versus time.

The next simulation concerns the behavior of the closed loop system when measurement noise is considered. The measurement noise is depicted in Figure 6.10 where $\sigma = 0.3$ is chosen. We set $N_x = 2048$ the number of pixels of camera. As can be seen in this figure, a good result is obtained in Figures 6.11 where the results with and without measurement noise are depicted to compare the sensitivity due to noisy measurement.

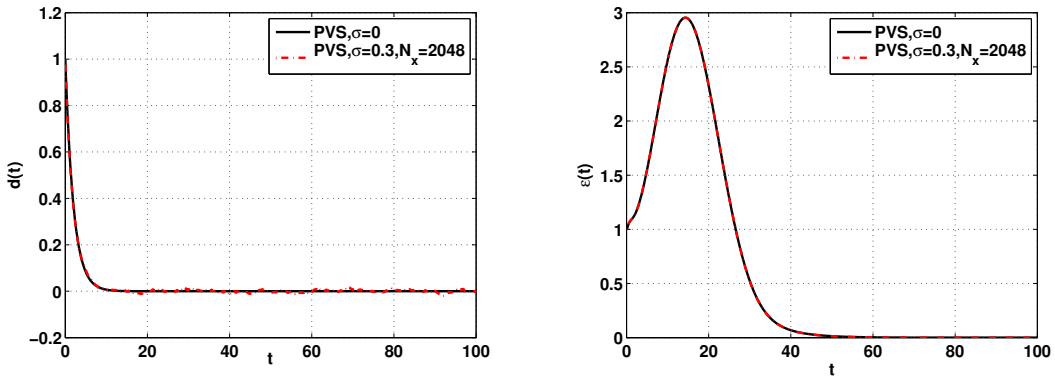

(a) $\mathbf{d}(t)$ versus time (b) $\varepsilon(t)$ versus time

Figure 6.11: Behavior of the closed loop system with measurement noise.

In this case, our approach provides a better result than the other approaches. Both the skin friction drag and the kinetic energy density are reduced and we obtain better transitory behavior. The minimization of the skin friction drag is improved and directly controlled. This is an impressive result. Note that a similar result was presented in [Dao and Collewet, 2012].

6.7.3 Case II: 3D plane Poiseuille flow

6.7.3.1 Behavior of the 3D uncontrolled plane Poiseuille flow

We set $\alpha = 0$, $\beta = 2.044$ and $R = 5\ 000$ (see section 5.6) which was shown to have the highest value of the transient energy growth in [Farrell and Ioannou, 1993]. We set $N = 50$ for the simulation results. The flow becomes turbulent due to the transient energy growth occurs, this problem is an interesting problem of uncontroleded flow and flow control. Due to the non-orthogonality of eigenvector, the kinetic energy density increases in time and the transient energy growth occurs.

In [Bewley and Liu, 1998], the authors gave the cause of transient energy growth is due to the similar value of eigenvalue pairs, the eigenvectors are parallel, therefore the transient energy growth occurs. We consider the eigenvalues in Table 6.2 and plotted in Figure 6.12(a), we have the similar value of eigenvalue pairs, i.e modes (10 and 11), (12 and 13), the eigenvectors are parallel shown in Figure 6.12(b). As can be seen in Figure 6.12(b), the imaginary (solid line) part of the vorticity eigenvectors and the real (dashed line) part of the wall-normal velocity eigenvectors (scaled by 1/550 between solid and dashed curves) are plotted as a function of y from the lower wall to the upper wall.

We consider the behavior of the uncontrolled flow with the worst initial condition, like the above case, we depict the streamwise, wall-normal and spanwise velocity components, the kinetic energy density and the velocity field of the flow in Figure 6.13. As can be seen in 6.13(a) (similar results for (b)-(d)), at the left subfigure is the kinetic

Table 6.2: Eigenvalues λ, $\alpha = 0$, $\beta = 2.044$.

Modes (i_{odd},i_{even})	λ_{odd}	λ_{even}	$\lambda_{odd} - \lambda_{even}$
(1)	-0.001329067420059		
(3,2)	-0.002809508080207	-0.002051722077213	-0.000757786002994
(5,4)	-0.005276909180495	-0.004449707797102	-0.000827201383394
(7,6)	-0.008731270720869	-0.007947340738985	-0.000783929981884
(9,8)	-0.013172592701346	-0.012333250161689	-0.000839342539656
(11,10)	-0.018600875121961	-0.017813122399373	-0.000787752722589
(13,12)	-0.025016117982696	-0.024173705097527	-0.000842412885169
(15,14)	-0.032418321283488	-0.031629292169515	-0.000789029113972
(17,16)	-0.040807485024363	-0.039963840723070	-0.000843644301293
⋮	⋮	⋮	⋮

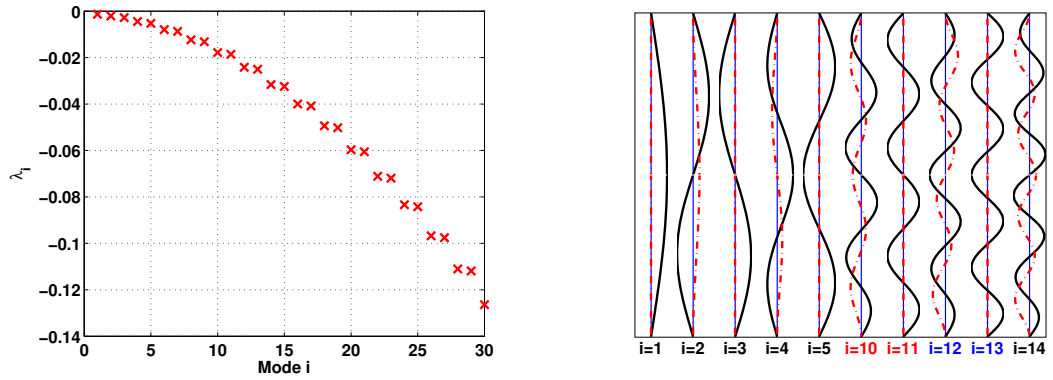

(a) eigenvalues (b) eigenvectors

Figure 6.12: Eigenvalues and eigenvectors of velocity and vorticity components (real wall-normal velocity (dashed-line), imaginary vorticity (solid line), solid line scaled by 1/550).

energy density and the velocity component at the point O($x = 0$, $y = 0$ and $z = 0$), the left upper subfigure is the kinetic energy density and the left lower subfigure is the velocity component with the streamwise velocity component (dashed line) as compared with the spanwise velocity component (dashed-dot line), the wall-normal velocity component (solid line) (dashed line scaled by 1/50). The cross-flow velocity is shown in the right subfigure at $x = 0$. The contours are the streamwise velocity. The arrows are the velocity field of the spanwise and wall-normal velocities. As can be seen from Figure 6.13(a) to 6.13(d), the evolution of the uncontrolled flow is versus time. At $t = 0$, the kinetic energy density is 1 and the contours are from 0.1 to 1. The diachronic transient energy growth $\varepsilon_d = 4897$ is at $\tau = 379$. At the peak magnitude of kinetic energy den-

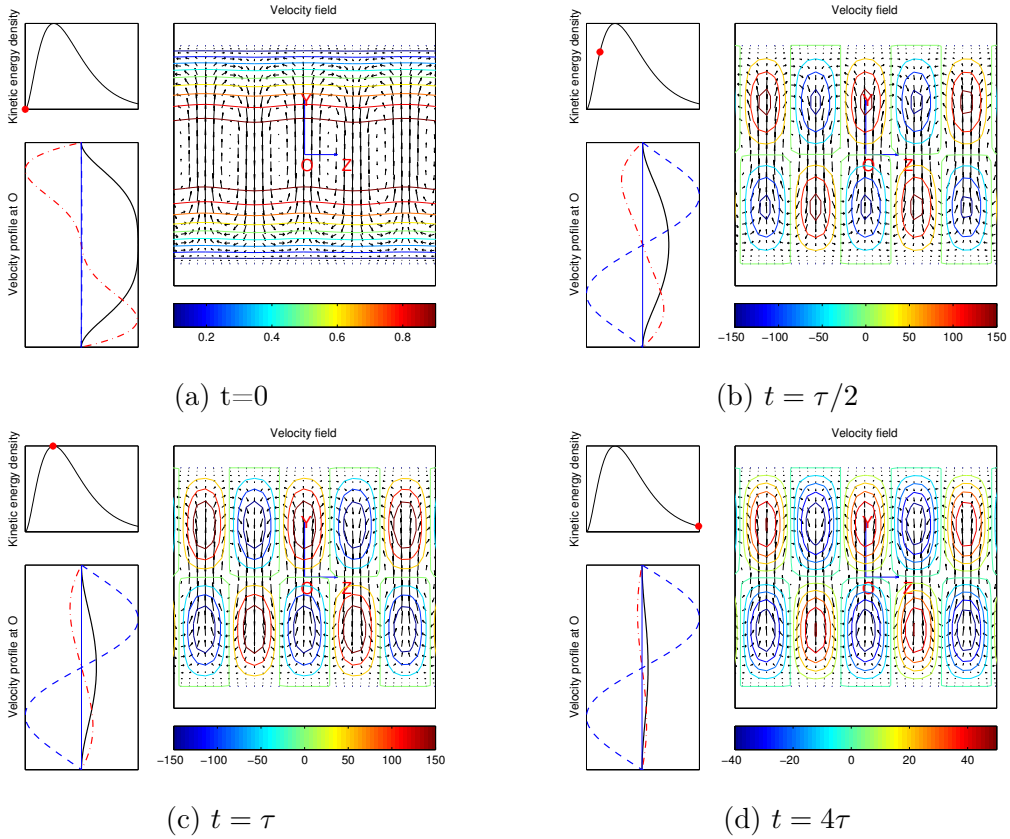

(a) t=0 (b) $t = \tau/2$

(c) $t = \tau$ (d) $t = 4\tau$

Figure 6.13: Shape of the flow perturbation in the uncontrolled flow versus time, $\tau = 379$.

sity, the contours of the streamwise velocity obtain the maximum value, the contours are from -150 to $+150$. The flow is very high turbulent.

6.7.3.2 Behavior of the 3D controlled plane Poiseuille flow

The eigenvalues of the open loop system are depicted in Figure 6.14(a) and the velocity and vorticity eigenvectors are depicted in Figure 6.14(b). The first and second modes are associated with the integrators in (6.13).

Comparison of the eigenvalues between the open loop system and the closed loop system are given in Figure 6.15(a), as can be seen in this figure the eigenvalues (nearly pairs) of the open loop system are relocated by the different value, is not similar pair value. The wall-normal velocity and vorticity eigenvectors are depicted in Figure 6.15(b), the orthogonality of these eigenvectors is improved.

The kinetic energy density, the velocity component and the cross velocity are depicted in Figure 6.16. As can be seen in Figure 6.16(a) (similar results for (b)-(d)), at the right subfigure the vertical arrows at the upper and lower boundaries are the con-

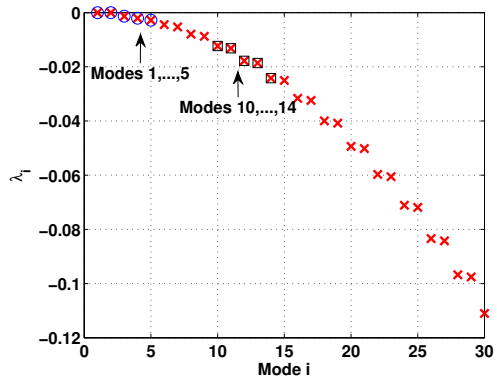

(a) eigenvalues

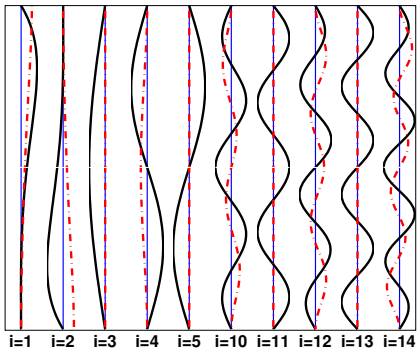

(b) eigenvectors

Figure 6.14: Eigenvalues and eigenvectors of velocity and vorticity components (real wall-normal velocity, dashed-line; imaginary vorticity, solid line, scaled by 1/550).

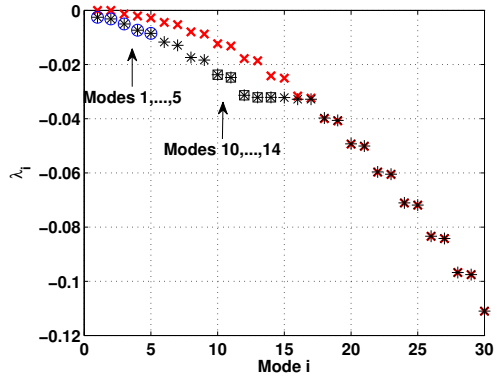

(a) eigenvalues

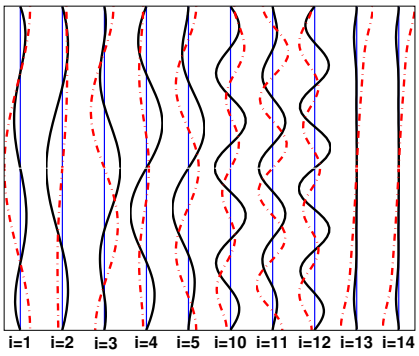

(b) eigenvectors, modes $i = 1 \cdots 5, 10 \cdots 14$

Figure 6.15: Eigenvalues (open loop system (x), closed loop system (*)) and eigenvectors of velocity and vorticity components (real wall-normal velocity (dashed-line), imaginary vorticity (solid line), scaled by 1/550).

trol signals. From Figure 6.16(a) to Figure 6.16(d), the evolution of the flow is versus times. At the left upper subfigure is the kinetic energy density of closed loop system. At the peak magnitude of kinetic energy density, the countours are from -80 to $+80$ with respect to -150 and $+150$ of uncontrolled flow. The flow becomes laminar and the velocity component becomes the steady solution $(1 - y^2, 0, 0)$.

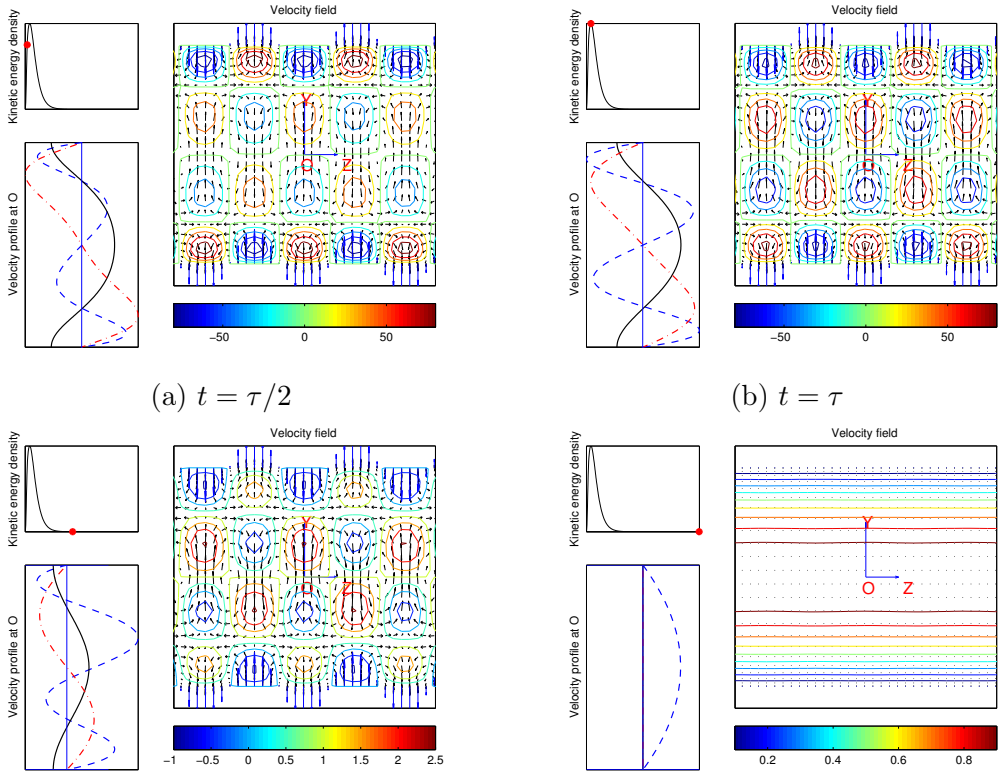

(a) $t = \tau/2$ (b) $t = \tau$

(c) $t = 10\tau$ (d) $t = 25\tau$

Figure 6.16: Shape of the flow perturbation in the controlled flow versus time, $\tau = 180$. Velocity profile at O, dashed line scaled by 1/50.

6.7.3.3 PVS control for the 3D plane Poiseuille flow

In this case, we only compare our approach and the $\mathbf{LQR}_1$ control because this was shown to have better results than the $\mathbf{P}$ control and the $\mathbf{LQR}_2$ control.

- We set $\alpha = 1$, $\beta = 1$ and $R = 5\ 000$, the oblique wave.

The variation of maximum kinetic energy density is in Figure 6.17. The maximum kinetic energy density obtains the minimum value at $\gamma \approx 1$ for the $\mathbf{LQR}_1$ control and at $\gamma \approx 1.4125$ for the **PVS** control. We set $\gamma = 1$ for the $\mathbf{LQR}_1$ control and $\gamma = 1.4125$ for the **PVS** control. Again, a nice decrease of skin friction drag is only obtained in our approach in Figure 6.18(a). Both the $\mathbf{LQR}_1$ control and our control are able to limit the kinetic energy density as compared to the open-loop system see Figure 6.18(b). The diachronic transient energy growth for uncontrolled flow is $\varepsilon_d = 187.379$, is very large with respect to the maximum kinetic energy density for the controlled flow $\varepsilon_{max,LQR_1} = 14.9991$ and $\varepsilon_{max,PVS} = 14.9993$.

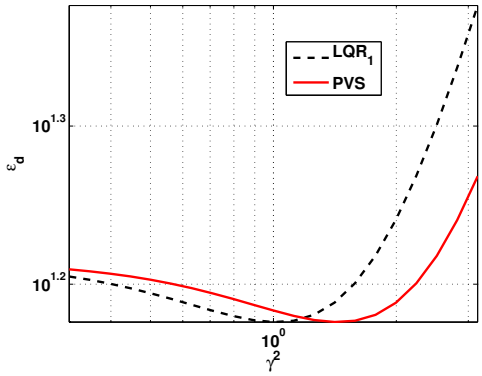

Figure 6.17: Maximum kinetic energy density versus control weight γ.

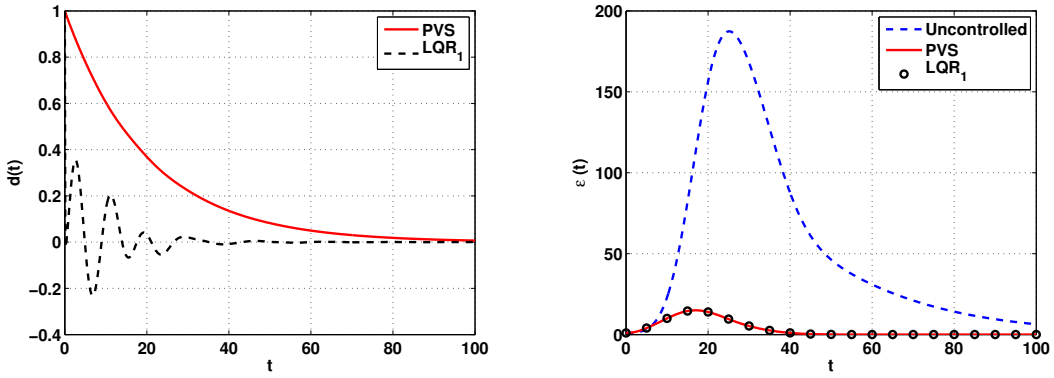

(a) $\mathbf{d}(t)$ versus time (b) $\varepsilon(t)$ versus time

Figure 6.18: Behavior of the closed loop system.

- We set $\alpha = 0$, $\beta = 2.044$ and $R = 5\ 000$, the streamwise vortex.

In the case of $\alpha = 0$ and using the boundary control on the wall normal velocity, we see $\mathbf{L}_{dl} = 0$. Note that we shall ensure $\mathbf{L}_{dl} \neq 0$ if we use the boundary control on the wall normal vorticity. In order to have $\mathbf{L}_{dl} \neq 0$ and use the boundary control on the wall normal velocity, the skin friction drag $\mathbf{d}(t)$ is modified and considered as

$$\mathbf{d}(t) = -\frac{\partial w(x,+1,z,t)}{\partial y} + \frac{\partial w(x,-1,z,t)}{\partial y}. \tag{6.47}$$

The variation of maximum kinetic energy density is in Figure 6.19 (similar result for the $\mathbf{LQR}_1$ was given by McKernan [McKernan, 2006], p.131, Figure 4.11). As can be seen in this figure, $\gamma \leq 128$, the maximum kinetic energy density is almost constant versus γ.

We set $\gamma = 128$ for the $\mathbf{LQR}_1$ control (the best value of parameter γ in previous works [McKernan et al., 2007]) and the **PVS** control, as shown in Figure 6.19, the same maximum kinetic energy density is given.

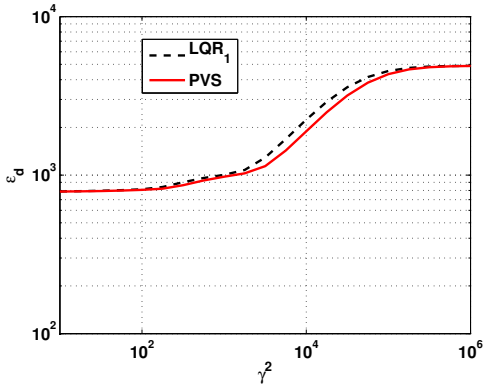

Figure 6.19: Maximum kinetic energy density versus control weight γ.

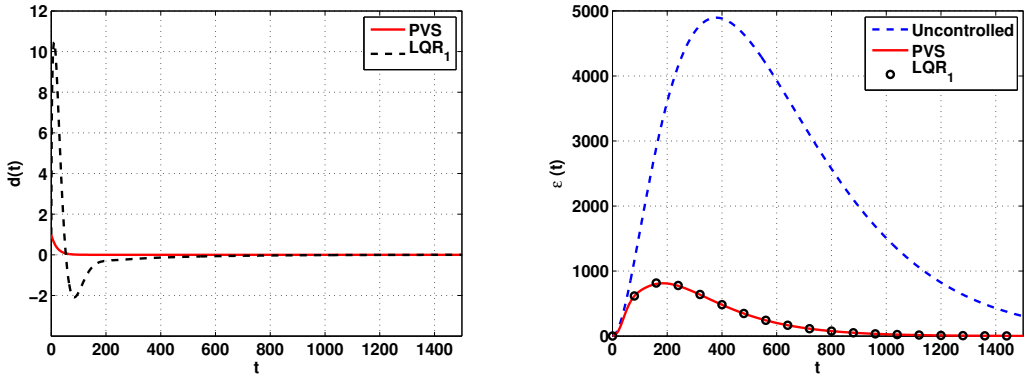

(a) $\mathbf{d}(t)$ versus time (b) $\varepsilon(t)$ versus time

Figure 6.20: Behavior of the closed loop system.

As expected, our approach provides a nice result, see Figure 6.20. This is similar result to the result of the previous case. A nice decrease of skin friction drag is only obtained in our approach, see Figure 6.20(a). Once again, both the $\mathbf{LQR}_1$ control and our control are able to limit the kinetic energy density as compared to the open-loop system in Figure 6.20(b). As the above result, the diachronic transient energy growth for the uncontrolled flow $\varepsilon_d = 4897$ is very large with respect to the maximum kinetic energy density for the controlled flow $\varepsilon_{max,LQR_1} = 821.6032$ and $\varepsilon_{max,PVS} = 811.7179$.

6.8 Conclusion

In this chapter, the partitioned visual servoing control has been exploited for the plane Poiseuille flow. This technique allows us to minimize, simultaneously, the skin friction drag and the kinetic energy density. As expected, the **PVS** approach provides the better results than the existing ones (**PID** and **LQR** controls), the skin friction drag being minimized and controlled. This approach only needs one **DOF** to minimize directly the

skin friction drag. Furthermore, the **PVS** approach not only obtains an exponential decrease of the skin friction drag in time but also decides the convergence velocity of the skin friction drag.

Because the number of **DOF** is limited (two in this model), the transient energy growth still occurs when we use the partitioned visual servoing control. Therefore, we need to increase the number of **DOF** to improve the behavior of the kinetic energy density in the closed loop system. In the next chapters, we shall present how to increase the number of **DOF**. And we shall also show how to achieve a monotonic decrease of kinetic energy density in time ($\varepsilon(t) = e^{-2\lambda t}\varepsilon_0$).

Chapter 7

Increase the number of Degrees of Freedom

This chapter shows how to increase the number of degree of freedom (**DOF**). In the previous chapter, with two **DOF**, the positive results for the skin friction drag minimization ($\mathbf{d}(t) = e^{-\lambda t}\mathbf{d}_0$) have been obtained by the application of the partitioned visual servoing control. However, the behavior of the kinetic energy density in the closed loop system must be improved because we do not ensure $\dot{\varepsilon}(t) \leq 0$. Note that this problem $\dot{\varepsilon}(t) \nleq 0$ can lead the flow to turbulence. In order to improve the behavior of the kinetic energy density, we give the way how to increase the number of **DOF** increases. Noted that we only increase the number of **DOF** in the Fourier space. As expected, the behavior of the kinetic energy density is improved as a function of increasing the number of **DOF**.

7.1 Why to increase the number of DOF in a general system

7.1.1 Improve the stability

Firstly, we consider the simple example

$$\left\{ \begin{array}{ll} \dot{\mathbf{x}}_1(t) & = \mathbf{x}_1(t) + 2\mathbf{x}_2(t) \\ \dot{\mathbf{x}}_2(t) & = \mathbf{x}_1^2(t) + \mathbf{x}_2(t) + \mathbf{u}(t) \end{array} \right. \tag{7.1}$$

Then we calculate the equilibrium point for the nonlinear system (7.1) with $\mathbf{u}_e(t) = 0$

$$\left\{ \begin{array}{ll} \dot{\mathbf{x}}_{1e}(t) & = 0 \\ \dot{\mathbf{x}}_{2e}(t) & = 0 \end{array} \right. \rightarrow \left\{ \begin{array}{ll} \mathbf{x}_{1e}(t) + 2\mathbf{x}_{2e}(t) & = 0 \\ \mathbf{x}_{1e}^2(t) + \mathbf{x}_2(t) + \mathbf{u}_e(t) & = 0 \end{array} \right. \tag{7.2}$$

We have two equilibrium points ($\mathbf{x}_{1e}(t) = 0, \mathbf{x}_{2e}(t) = 0$) and ($\mathbf{x}_{1e}(t) = 0.5, \mathbf{x}_{1e}(t) = -0.25$). However, we only consider the linearization of the nonlinear system (7.1) around the equilibrium point ($\mathbf{x}_1 = 0, \mathbf{x}_2 = 0$). We have the linear model

$$\left\{ \begin{array}{ll} \dot{\mathbf{x}}_1(t) & = \mathbf{x}_1(t) + 2\mathbf{x}_2(t) \\ \dot{\mathbf{x}}_2(t) & = \mathbf{x}_2(t) + \mathbf{u}(t) \end{array} \right. \tag{7.3}$$

We use a feedback control to the nonlinear system. It means that we use the linear control $\mathbf{u}(t) = \mathbf{K}\mathbf{x}(t) = -k_1\mathbf{x}_1(t) - k_2\mathbf{x}_2(t)$ for the nonlinear system (7.1) where the gain of control law $\mathbf{K}$ is designed based on its linearization (7.3). Therefore, the linear model of the closed loop system of (7.3) is given by

$$\begin{cases} \dot{\mathbf{x}}_1(t) &= \mathbf{x}_1(t) + 2\mathbf{x}_2(t) \\ \dot{\mathbf{x}}_2(t) &= -k_1\mathbf{x}_1(t) + (1-k_2)\mathbf{x}_2(t) \end{cases} \tag{7.4}$$

Note that k_1 and k_2 are designed based on the stability of the system (7.4) and we use **LQR** control to give the control law. The nonlinear model of the closed loop system of (7.1) is given by

$$\begin{cases} \dot{\mathbf{x}}_1(t) &= \mathbf{x}_1(t) + 2\mathbf{x}_2(t) \\ \dot{\mathbf{x}}_2(t) &= -k_1\mathbf{x}_1(t) + \mathbf{x}_1^2(t) + (1-k_2)\mathbf{x}_2(t) \end{cases} \tag{7.5}$$

We compare the behavior of the closed loop systems (7.4) and (7.5) with various values of the initial conditions. We choose three initial conditions $\mathbf{x}_{10,1} = 0.5$, $\mathbf{x}_{20,1} = 0.5$; $\mathbf{x}_{10,2} = 1$, $\mathbf{x}_{20,2} = 0.01$ and $\mathbf{x}_{10,3} = -1$, $\mathbf{x}_{20,3} = -1$. From the **LQR** control ($\mathbf{Q} = \mathbf{I}_2$, $\mathbf{R} = \mathbf{I}$), we have $k_1 = 3.1300$ and $k_2 = 4.8105$. We give the results in the $\mathbf{x}_1 - \mathbf{x}_2$ plane.

Based on the phase portraits in Figure 7.1, the closed loop system of the linear model (7.4) is asymptotically stable, all the trajectories tend toward to the equilibrium point $(0, 0)$. However, we only obtain the local stability for the nonlinear system (7.5) as shown in Figure 7.1(b). Note that Figure 7.1(b) distinguishes two areas, $(*)$ pink area is stable and another area is unstable. Two initial conditions $(\mathbf{x}_{10,1}, \mathbf{x}_{20,1})$ and $(\mathbf{x}_{10,3}, \mathbf{x}_{20,3})$ are in the $(*)$ pink area, the blue solid line and the black dashed dot line

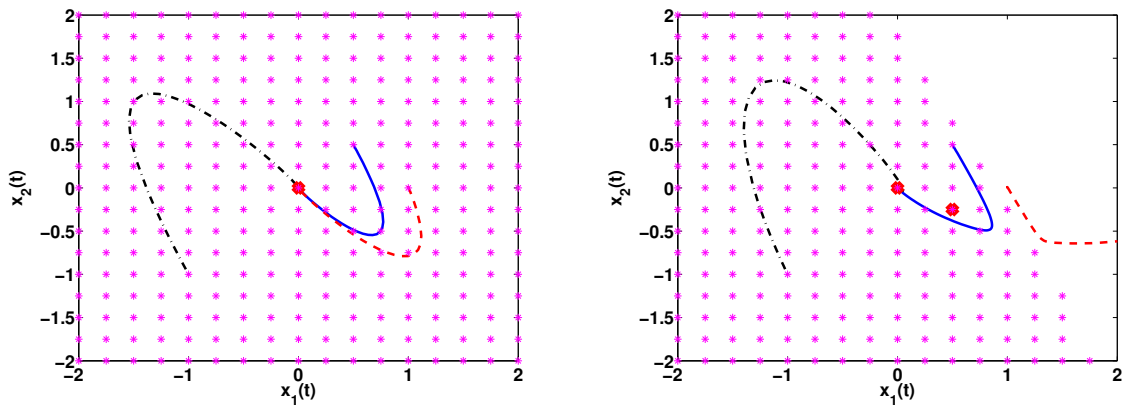

(a) linear model (b) nonlinear model

Figure 7.1: Behavior of the phase portraits. Blue solid line is the trajectory of $\mathbf{x}_{10,1} = 0.5$, $\mathbf{x}_{20,1} = 0.5$, red dashed line is the trajectory of $\mathbf{x}_{10,2} = 1$, $\mathbf{x}_{20,2} = 0.01$ and black dashed dot line is the trajectory of $\mathbf{x}_{10,3} = -1$, $\mathbf{x}_{20,3} = -1$.

tend toward to the equilibrium point $(0, 0)$ while the red dashed line does not tend toward to the equilibrium point and tends toward to the infinity.

With one **DOF**, we only obtain the local stability. How to improve the stability, we can improve the stability by increasing the number of **DOF**. To do it, we consider the modified nonlinear system

$$\begin{cases} \dot{\mathbf{x}}_1(t) &= \mathbf{x}_1(t) + 2\mathbf{x}_2(t) + \mathbf{u}_1(t) \\ \dot{\mathbf{x}}_2(t) &= \mathbf{x}_1^2(t) + \mathbf{x}_2(t) + \mathbf{u}_2(t) \end{cases} \tag{7.6}$$

and its linearization around the equilibrium point $(\mathbf{x}_1 = 0, \mathbf{x}_2 = 0)$ is

$$\begin{cases} \dot{\mathbf{x}}_1(t) &= \mathbf{x}_1(t) + 2\mathbf{x}_2(t) + \mathbf{u}_1(t) \\ \dot{\mathbf{x}}_2(t) &= \mathbf{x}_2(t) + \mathbf{u}_2(t) \end{cases} \tag{7.7}$$

As the previous case, the feedback control is $\mathbf{u}(t) = \mathbf{K}\mathbf{x}(t)$ with $\mathbf{u}_1(t) = -k_{11}\mathbf{x}_1(t) - k_{12}\mathbf{x}_2(t)$ and $\mathbf{u}_2(t) = -k_{21}\mathbf{x}_1(t) - k_{22}\mathbf{x}_2(t)$. Therefore, the closed loop system of (7.7) is given by

$$\begin{cases} \dot{\mathbf{x}}_1(t) &= (1 - k_{11})\mathbf{x}_1(t) + (2 - k_{12})\mathbf{x}_2(t) \\ \dot{\mathbf{x}}_2(t) &= -k_{21}\mathbf{x}_1(t) + (1 - k_{22})\mathbf{x}_2(t) \end{cases} \tag{7.8}$$

And the closed loop system of (7.6) is given by

$$\begin{cases} \dot{\mathbf{x}}_1(t) &= (1 - k_{11})\mathbf{x}_1(t) + (2 - k_{12})\mathbf{x}_2(t) \\ \dot{\mathbf{x}}_2(t) &= -k_{21}\mathbf{x}_1(t) + \mathbf{x}_1^2(t) + (1 - k_{22})\mathbf{x}_2(t) \end{cases} \tag{7.9}$$

In comparison to the results in Figure 7.1, from the **LQR** control ($\mathbf{Q} = \mathbf{I}_2$, $\mathbf{R} = \mathbf{I}_2$), we have $k_{11} = 1.8058$ $k_{12} = 1.1622$ $k_{21} = 1.1622$ and $k_{22} = 3.3018$. The stability in Figure 7.2 for the nonlinear model is improved, we do not have unstable area. The closed loop system of the nonlinear model is asymptotically stable. This example demonstrates the benefits of increasing the number of **DOF**.

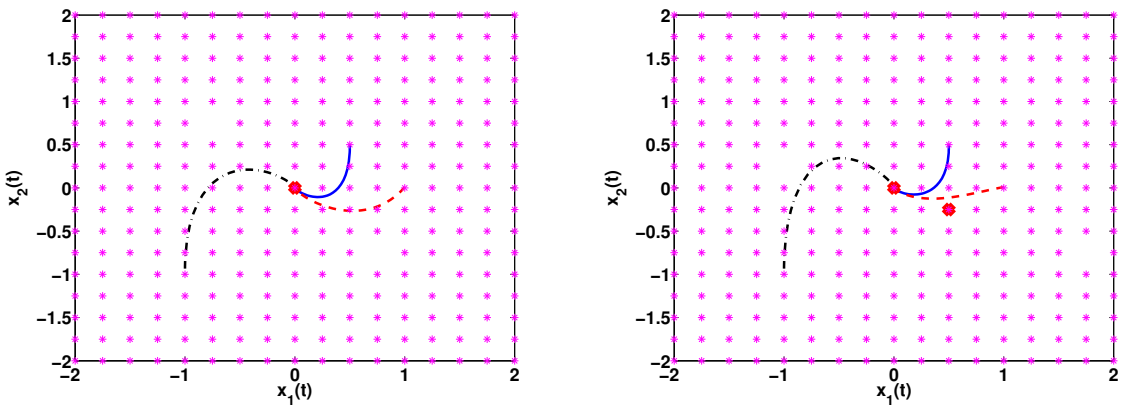

(a) linear model (b) nonlinear model

Figure 7.2: Behavior of the phase portraits. Blue solid line is the trajectory of $\mathbf{x}_{10,1} = 0.5$, $\mathbf{x}_{20,1} = 0.5$, red dashed line is the trajectory of $\mathbf{x}_{10,2} = 1$, $\mathbf{x}_{20,2} = 0.01$ and black dashed dot line is the trajectory of $\mathbf{x}_{10,3} = -1$, $\mathbf{x}_{20,3} = -1$.

7.1.2 Kinetic energy density is monotonically decreased in time

In this section, we give the necessary condition of the input matrix to ensure the monotonic stability of the kinetic energy density. We consider the linear system

$$\dot{\mathbf{z}}(t) = \mathbf{A}_z\mathbf{z}(t) + \mathbf{B}_z\mathbf{u}(t) \tag{7.10}$$

with the control law $\mathbf{u}(t) = \mathbf{K}\mathbf{z}(t)$ and the kinetic energy density is defined by

$$\varepsilon_z(t) = \mathbf{z}^\top(t)\mathbf{Q}_z\mathbf{z}(t), \tag{7.11}$$

where $\mathbf{Q}_z$ is a Hermitian matrix. In previous works [Whidborne and McKernan, 2007], the necessary condition to ensure $\dot{\varepsilon}_z(t) \leq 0$ is

$$(\mathbf{A}_z + \mathbf{B}_z\mathbf{K})^\top\mathbf{Q}_z + \mathbf{Q}_z(\mathbf{A}_z + \mathbf{B}_z\mathbf{K}) < 0 \tag{7.12}$$

and this inequality has a solution $\mathbf{K}$, we need $\mathbf{B}_z\mathbf{B}_z^\top > 0$. Hence, the matrix $\mathbf{B}_z$ must be a full rank matrix. This cause explains why we want to increase the number of **DOF** in the closed loop system of the plane Poiseuille flow.

7.2 How to increase the number of DOF

In order to improve the stability or the kinetic energy density minimization, it means that we want to ensure $\dot{\varepsilon}(t) \leq 0$, we increase the number of **DOF**. Based the results in [Joshi, 1996] about the multiple inputs multiple outputs system, we assume that we have M independent control signals in the Fourier space. It must be noted that we only increase the number of **DOF** of control signal in the Fourier space, we do not increase the number of **DOF** of control signal in the physical space. Therefore, we always increase the number of **DOF** of control signal in the Fourier space. If we have the M independent boundary conditions $\tilde{v}_m(y=-1,t)$, $\tilde{v}_m(y=+1,t)$, $\tilde{\eta}_m(y=+1,t)$ and $\tilde{\eta}_m(y=-1,t)$, the control signals will be chosen by

$$\begin{cases} \tilde{v}_m(y=+1,t) = \tilde{q}_{v,u,m}(t) & \tilde{v}_m(y=-1,t) = \tilde{q}_{v,l,m}(t) \\ \tilde{\eta}_m(y=+1,t) = \tilde{q}_{\eta,u,m}(t) & \tilde{\eta}_m(y=-1,t) = \tilde{q}_{\eta,l,m}(t), \end{cases} \tag{7.13}$$

where $m = 1 \ldots M$. Note that for each $\tilde{v}_m(y=-1,t)$, $\tilde{v}_m(y=+1,t)$, $\tilde{\eta}_m(y=+1,t)$ and $\tilde{\eta}_m(y=-1,t)$, as previous results in Chapter 5, the plane Poiseuille flow is modeled by

$$\mathbf{L}\dot{\mathbf{x}}(t) = \mathbf{A}\mathbf{x}(t) + \mathbf{B}_m\mathbf{u}_m(t) + \mathbf{E}_m\dot{\mathbf{u}}_m(t), \tag{7.14}$$

where $\mathbf{B}_m$ and $\mathbf{E}_m$ are given by the same way in Chapter 5. More precisely, $\mathbf{B}_m$ and $\mathbf{E}_m$ are calculated from $f_{v,l,m}(y)$, $f_{v,u,m}(y)$, $f_{\eta,l,m}(y)$ and $f_{\eta,u,m}(y)$. Therefore, if we consider M **DOF**, we shall have

$$\begin{aligned} \mathbf{L}\dot{\mathbf{x}}(t) &= \mathbf{A}\mathbf{x}(t) + \sum_{m=1}^{M}(\mathbf{B}_m\mathbf{u}_m(t) + \mathbf{E}_m\dot{\mathbf{u}}_m(t)) \\ &= \mathbf{A}\mathbf{x}(t) + \mathbf{B}\mathbf{u}(t) + \mathbf{E}\dot{\mathbf{u}}(t)) \end{aligned} \tag{7.15}$$

where the input matrices are $\mathbf{B} = \begin{bmatrix} \mathbf{B}_1 & \mathbf{B}_2 & \dots & \mathbf{B}_M \end{bmatrix}$, $\mathbf{E} = \begin{bmatrix} \mathbf{E}_1 & \mathbf{E}_2 & \dots & \mathbf{E}_M \end{bmatrix}$ and the control signals are $\mathbf{u}(t) = \begin{bmatrix} \mathbf{u}_1^\top(t) & \mathbf{u}_2^\top(t) & \dots & \mathbf{u}_M^\top(t) \end{bmatrix}^\top$.

In order to give the input matrices $\mathbf{B}$ and $\mathbf{E}$, when we use M **DOF**, the wall-normal velocity and vorticity boundary Fourier coefficients for the particular solution in (5.54) are

$$\begin{cases} \tilde{v}_p(y,t) &= \sum_{m=1}^{M} f_{v,u,m}(y)\tilde{q}_{v,u,m}(t) + \sum_{m=1}^{M} f_{v,l,m}(y)\tilde{q}_{v,l,m}(t) \\ \tilde{\eta}_p(y,t) &= \sum_{m=1}^{M} f_{\eta,u,m}(y)\tilde{q}_{\eta,u,m}(t) + \sum_{m=1}^{M} f_{\eta,l,m}(y)\tilde{q}_{\eta,l,m}(t), \end{cases} \tag{7.16}$$

where the functions $f_{v,u,m}(y)$, $f_{v,l,m}(y)$, $f_{\eta,u,m}(y)$ and $f_{\eta,l,m}(y)$ satisfy the conditions

$$\begin{cases} f_{v,u,m}(y=+1) = f_{v,l,m}(y=-1) = f_{\eta,u,m}(y=+1) = f_{\eta,l,m}(y=-1) = 1 \\ f_{v,u,m}(y=-1) = f_{v,l,m}(y=+1) = f_{\eta,u,m}(y=-1) = f_{\eta,l,m}(y=+1) = 0 \\ f'_{v,u,m}(y=\pm 1) = f'_{v,l,m}(y=\pm 1) = 0. \end{cases} \tag{7.17}$$

The wall-normal velocity and the vorticity is rewritten in a more compact form by

$$\begin{cases} \tilde{v}(y,t) &= \tilde{v}_h(y,t) + \sum_{m=1}^{M} \mathbf{F}_{v,m}(y)\mathbf{q}_{v,m}(t) \\ \tilde{\eta}(y,t) &= \tilde{\eta}_h(y,t) + \sum_{m=1}^{M} \mathbf{F}_{\eta,m}(y)\mathbf{q}_{\eta,m}(t), \end{cases} \tag{7.18}$$

where we denote

$$\mathbf{q}_{v,m}(t) = \begin{bmatrix} \tilde{q}_{v,u,m}(t) \\ \tilde{q}_{v,l,m}(t) \end{bmatrix}, \mathbf{q}_{\eta,m}(t) = \begin{bmatrix} \tilde{q}_{\eta,u,m}(t) \\ \tilde{q}_{\eta,l,m}(t) \end{bmatrix} \tag{7.19}$$

and

$$\mathbf{F}_{\eta,m}(y) = \begin{bmatrix} f_{\eta,u,m}(y) & f_{\eta,l,m}(y) \end{bmatrix}, \mathbf{F}_{v,m}(y) = \begin{bmatrix} f_{v,u,m}(y) & f_{v,l,m}(y) \end{bmatrix} \tag{7.20}$$

By plugging (7.18) into (5.41) and (5.42), the system of **ODE** is given by

$$\begin{aligned} &(-k^2U - \frac{d^2U}{dy^2} - \frac{k^4}{jR\alpha})\sum_{n=0}^{N} a_{v,n}(t)\Gamma_n(y) + (U + \frac{2k^2}{jR\alpha})\sum_{n=0}^{N} a_{v,n}(t)\Gamma''_n(y) \\ &-\frac{1}{jR\alpha}\sum_{n=0}^{N} a_{v,n}(t)\Gamma''''_n(y) + (-k^2U - \frac{d^2U}{dy^2} - \frac{k^4}{jR\alpha})\sum_{m=1}^{M} \mathbf{F}_{v,m}(y)\mathbf{q}_{v,m}(t) \\ &+(U + \frac{2k^2\mathbf{I}}{jR\alpha})\sum_{m=1}^{M} \mathbf{F}''_{v,m}(y)\mathbf{q}_{v,m}(t) - \frac{1}{jR\alpha}\sum_{m=1}^{M} \mathbf{F}''''_{v,m}(y)\mathbf{q}_{v,m}(t) \\ &= \frac{j}{\alpha}\left[\sum_{n=0}^{N} \dot{a}_{v,n}(t)\Gamma''_n(y) - k^2\sum_{n=0}^{N} \dot{a}_{v,n}(t)\Gamma_n(y)\right] \\ &+\frac{j}{\alpha}\left[\sum_{m=1}^{M} \mathbf{F}''_{v,m}(y)\dot{\mathbf{q}}_{v,m}(t) - k^2\sum_{m=1}^{M} \mathbf{F}_{v,m}(y)\dot{\mathbf{q}}_{v,m}(t)\right], \end{aligned} \tag{7.21}$$

and

$$
\begin{aligned}
&(j\alpha U + \frac{k^2}{R})\sum_{n=0}^{N} a_{\eta,n}(t)\Gamma_n(y) - \frac{1}{R}\sum_{n=0}^{N} a_{\eta,n}(t)\Gamma_n''(y) + j\beta\frac{dU}{dy}\sum_{n=0}^{N} a_{v,n}(t)\Gamma_n(y) \\
&+(j\alpha U + \frac{k^2}{R})\sum_{m=1}^{M} \mathbf{F}_{\eta,m}(y)\mathbf{q}_{\eta,m}(t) - \frac{1}{R}\sum_{m=1}^{M} \mathbf{F}''_{\eta,m}(y)\mathbf{q}_{\eta,m}(t) + j\beta\frac{dU}{dy}\sum_{m=1}^{M} \mathbf{F}_{v,m}(y)\mathbf{q}_{v,m}(t) \\
&= -\sum_{n=0}^{N} \dot{a}_{\eta,n}(t)\Gamma_n(y) - \sum_{m=1}^{M} \mathbf{F}_{\eta,m}(y)\dot{\mathbf{q}}_{\eta,m}(t).
\end{aligned}
\tag{7.22}
$$

After the evaluation of (7.21) and (7.22) at each of the collocations points y_k, a system with control signal is obtained

$$
\mathbf{L}\dot{\mathbf{x}}(t) = \mathbf{A}\mathbf{x}(t) + \mathbf{B}\mathbf{u}(t) + \mathbf{E}\dot{\mathbf{u}}(t), \tag{7.23}
$$

where the control signal is $\mathbf{u}(t) = \begin{bmatrix} \mathbf{q}_{v,1}^{\top}(t) & \cdots & \mathbf{q}_{v,M}^{\top}(t) & \mathbf{q}_{\eta,1}^{\top}(t) & \cdots & \mathbf{q}_{\eta,M}^{\top}(t) \end{bmatrix}^{\top}$ and the input matrices are

$$
\begin{cases}
\mathbf{E}_{11} = j(k^2\mathbf{D}0(\mathbf{F}_v) - \mathbf{D}2(\mathbf{F}_v)),\ \mathbf{E}_{12} = [0],\ \mathbf{E}_{21} = [0],\ \mathbf{E}_{22} = -j\mathbf{D}0(\mathbf{F}_\eta) \\
\mathbf{B}_{11} = (-\alpha\overline{U}k^2 - \alpha\overline{U}'' - \dfrac{k^4\mathbf{I}}{jR})\mathbf{D}0(\mathbf{F}_v) + (\alpha\overline{U} + \dfrac{2k^2\mathbf{I}}{jR})\mathbf{D}2(\mathbf{F}_v) - \dfrac{1}{jR}\mathbf{D}4(\mathbf{F}_v) \\
\mathbf{B}_{12} = [0],\ \mathbf{B}_{21} = \beta\overline{U}'\,\mathbf{D}0(\mathbf{F}_v),\ \mathbf{B}_{22} = (\alpha\overline{U} + \dfrac{k^2\mathbf{I}}{jR})\mathbf{D}0(\mathbf{F}_\eta) - \dfrac{1}{jR}\mathbf{D}2(\mathbf{F}_\eta).
\end{cases}
\tag{7.24}
$$

The element of derivative matrices is calculated from

$$
\begin{array}{lll}
\mathbf{D}0(\mathbf{F}_v)_{km} = \mathbf{F}_{v,m}(y_k) & \mathbf{D}2(\mathbf{F}_v)_{km} = \mathbf{F}''_{v,m}(y_k) & \mathbf{D}4(\mathbf{F}_v)_{km} = \mathbf{F}''''_{v,m}(y_k) \\
\mathbf{D}0(\mathbf{F}_\eta)_{km} = \mathbf{F}_{\eta,m}(y_k) & \mathbf{D}2(\mathbf{F}_\eta)_{km} = \mathbf{F}''_{\eta,m}(y_k), &
\end{array}
\tag{7.25}
$$

where $m = 1 \ldots M$ and $k = 0 \ldots N$. Note that the model is modified from $k = 0 \ldots N$ to $k = 2 \ldots N-2$ (Combined method 1) or $k = 1 \ldots N-1$ (Combined method 2) (see section 5.3). We have shown how the number of **DOF** increased. In the next section, the benefit of this procedure is emphasized.

7.3 Benefits of increasing the number of DOF

In this section, we answer for the question why do we want to increase the number of **DOF** in the plane Poiseuille flow. The answer of this question is increasing the number of **DOF**, the behavior of state vector is improved and consequently the behavior of the kinetic energy density will be improved.

7.3.1 Design of the control law

Note that, **LQR** control can apply to one or any **DOF**. Therefore, we choose the **LQR** control approach because we can use it with any M **DOF**. Taking into account that

the kinetic energy density depends on $\mathbf{u}(t) = q(t)$ but does not depend on $\mathcal{U}(t) = \dot{q}(t)$, therefore we use the control signal $\mathcal{U}(t)$, so it is very easy to compare the behavior of the kinetic energy density with various values of M.

The system (7.23) is rewritten

$$\begin{bmatrix} \dot{\mathbf{x}}(t) \\ \dot{\mathbf{u}}(t) \end{bmatrix} = \begin{bmatrix} \mathbf{L}^{-1}\mathbf{A} & \mathbf{L}^{-1}\mathbf{B} \\ 0 & 0 \end{bmatrix} \begin{bmatrix} \mathbf{x}(t) \\ \mathbf{u}(t) \end{bmatrix} + \begin{bmatrix} \mathbf{L}^{-1}\mathbf{E} \\ \mathbf{I} \end{bmatrix} \dot{\mathbf{u}}(t), \tag{7.26}$$

It must be noted that the dimension of the input matrices $\mathbf{B}$ and $\mathbf{E}$ change. We use the state vector $\mathcal{X}(t) = \begin{bmatrix} \mathbf{x}(t) \\ \mathbf{u}(t) \end{bmatrix}$. The state matrix $\mathcal{A}$ and the input matrix $\mathcal{B}$ are given by

$$\mathcal{A} = \begin{bmatrix} \mathbf{L}^{-1}\mathbf{A} & \mathbf{L}^{-1}\mathbf{B} \\ 0 & 0 \end{bmatrix}, \quad \mathcal{B} = \begin{bmatrix} \mathbf{L}^{-1}\mathbf{E} \\ \mathbf{I} \end{bmatrix}. \tag{7.27}$$

Therefore, we consider the following system

$$\begin{cases} \dot{\mathcal{X}}(t) & = \mathcal{A}\mathcal{X}(t) + \mathcal{B}\mathcal{U}(t) \\ \varepsilon(t) & = \mathcal{X}(t)^T \mathcal{Q} \mathcal{X}(t) \\ \mathcal{X}(0) & = \mathcal{X}_0 \end{cases} \tag{7.28}$$

We consider here a state feedback control law

$$\mathcal{U}(t) = \mathcal{K}\mathcal{X}(t). \tag{7.29}$$

In order to minimize the kinetic energy density and the energy combustion of actuators, a **LQR** control scheme over an infinite time horizon is used by considering the following cost function

$$J = \int_0^\infty (\mathcal{X}(t)^\top \mathcal{Q} \mathcal{X}(t) + \gamma^2 \mathcal{U}(t)^\top \mathcal{U}(t)) dt. \tag{7.30}$$

Thereafter, the LQR gain $\mathcal{K}$ involved in the optimal control $\mathcal{U}(t) = \mathcal{K}\mathcal{X}(t)$ is computed taking into account (7.28) and solving the Algebraic Ricatti Equation (see **LQR** control for more details, we only use $\mathcal{K} = -lqr(\mathcal{A}, \mathcal{B}, \mathcal{Q}, \gamma^2 \mathcal{I})$ in Matlab). The gain $\mathcal{K}$ is given by

$$\mathcal{K} = -\frac{1}{\gamma^2} \mathcal{B}^\top \mathcal{P}, \tag{7.31}$$

where $\mathcal{P}$ is the solution of the Algebraic Ricatti Equation

$$\mathcal{A}^\top \mathcal{P} + \mathcal{P}\mathcal{A} + \mathcal{Q} - \frac{1}{\gamma^2} \mathcal{P}\mathcal{B}\mathcal{B}^\top \mathcal{P} = 0. \tag{7.32}$$

Because the control matrix $\mathcal{B}$ is not full rank, we do not ensure $\dot{\varepsilon}(t) \leq 0$ with the control signal $\mathcal{U}(t)$. It must be note that **LQR** control cannot guarantee $\dot{\varepsilon}(t) \leq 0$.

In the next section, the simulation result will validate our proposed approach.

7.3.2 Simulation results

We give an example about choosing the functions $f_{v,u,m}(y)$, $f_{v,l,m}(y)$, $f_{\eta,u,m}(y)$ and $f_{\eta,l,m}(y)$. With one **DOF**, only the lower boundary condition was used, Joshi proposed the polynomials $f_v(y)$ at the lower wall (see [Joshi, 1996], p.15)

$$f_v(y) = \frac{2y^4 + 3y - 4y^2 - 3y + 4}{4}, \tag{7.33}$$

And for two **DOF**, the simultaneous upper and lower boundary conditions were used, McKernan proposed the polynomials $f_{v,l}(y)$ and $f_{v,u}(y)$ (see [McKernan, 2006], p.32)

$$\begin{aligned} f_{v,l}(y) &= \frac{y^3 - 3y + 2}{4} \\ f_{v,u}(y) &= \frac{-y^3 + 3y + 2}{4} \end{aligned} \tag{7.34}$$

In order to increase the number of **DOF**, we have to find the independent polynomials $f_{v,l,m}(y)$, $f_{v,u,m}(y)$ which satisfy the simultaneous inhomogeneous Dirichlet and homogeneous Neumann boundary conditions, and $f_{\eta,l,m}(y)$, $f_{\eta,u,m}(y)$ which satisfy the inhomogeneous Dirichlet boundary condition.

We see that the polynomials proposed by McKernan satisfy the inhomogeneous Dirichlet and homogeneous Neumann boundary conditions but we only have two independent functions. Therefore, we may propose the polynomials $\mathbf{F}_{v,m}(y)$ and $\mathbf{F}_{\eta,m}(y)$ as

$$\begin{aligned} f_{v,l,m}(y) &= (1-y^2)^{h_v}\Xi_m(y) + \frac{y^3 - 3y + 2}{4} \\ f_{v,u,m}(y) &= (1-y^2)^{h_v}\Xi_m(y) + \frac{-y^3 + 3y + 2}{4} \\ f_{\eta,l,m}(y) &= (1-y^2)^{k_\eta}\Theta_m(y) + \frac{-y+1}{2} \\ f_{\eta,u,m}(y) &= (1-y^2)^{k_\eta}\Theta_m(y) + \frac{y+1}{2}, \end{aligned} \tag{7.35}$$

where $h_v \geq 1$ and $k_\eta \geq 1$ are entire number. These polynomials satisfy the inhomogeneous Dirichlet and homogeneous Neumann boundary conditions (the conditions (7.17)). It must be noted that we have given an example of the polynomials $\mathbf{F}_{v,m}(y)$ and $\mathbf{F}_{\eta,m}(y)$. However, there exist other methods too, e.g. we shall use the Hermite interpolating polynomials in the Appendix C.

When we use the various values of M, the dimension of the state vector $\mathcal{X}(t)$ is changed. Indeed, we only want to compare the kinetic energy density minimization when M varies. In order to compare the minimizing of the kinetic energy density, we need to set the same initial condition of $\varepsilon(t)$. Therefore, we use the same initial conditions $\mathbf{x}_0$ and ε_0. The initial condition is chosen as $\mathcal{X}_0 = \begin{pmatrix} \mathbf{x}_0^\top & 0 & \cdots & 0 \end{pmatrix}^\top$ where $\mathbf{x}_0 = \mathbf{x}_{worst,\varepsilon_0=1}(t=0)$ is the worst initial condition of the uncontrolled flow. Note that in this case, the initial condition is not the worst initial condition $\mathcal{X}_0 \neq \mathcal{X}_{worst,\varepsilon_0=1}(t=0)$ of the controlled flow.

7.3.2.1 Case I: 2D plane Poiseuille flow

The case of $\alpha = 1$, $\beta = 0$ and $R = 10\ 000$ is considered (see section 5.6). We fix the value of N and use the various values of M. For **LQR** control, we set $\gamma = 0.25$ as in [McKernan, 2006], [McKernan et al., 2007]. We set $f_{v,l,m}(y) = (1-y^2)^2\Xi_m(y) + \frac{y^3-3y+2}{4}$. We use the Combined method 1 (see section 5.3.3 for more detail), the dimension of the state matrix $\mathbf{A}$ and the input matrix $\mathbf{B}$ are $(N-3)\times(N-3)$ and $(N-3)\times M$, respectively. Therefore the dimension of the state matrix $\mathcal{A}$ and the input matrix $\mathcal{B}$ are $(N+M-3)\times(N+M-3)$ and $(N+M-3)\times(M)$, respectively. We set $N = 100$.

In order to study the behavior of the closed loop system, we first consider the eigenvalues of the closed loop system which are depicted in Figure 7.3. Indeed, it can be observed in this figure that we have more the number of **DOF**, we have more the number of relocated poles. A comparison between the open loop system and the closed loop system, the number of relocated poles is increased versus the ratio of $M/(N-3)$, as can be seen in Figure 7.3, shown from Figure 7.3(a) to Figure 7.3(d).

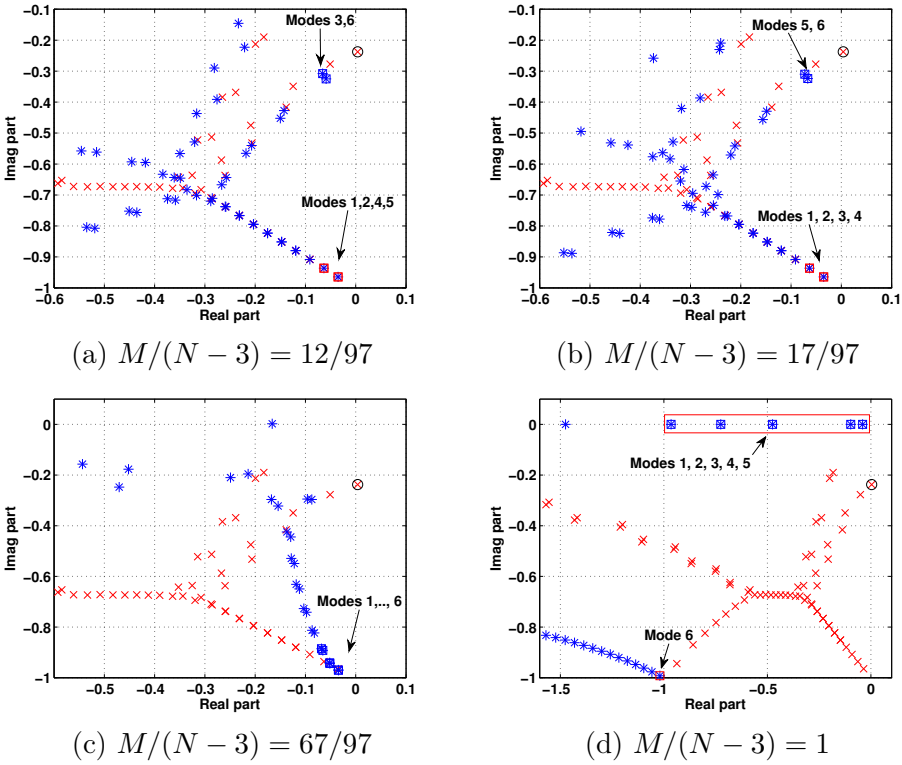

(a) $M/(N-3) = 12/97$ (b) $M/(N-3) = 17/97$

(c) $M/(N-3) = 67/97$ (d) $M/(N-3) = 1$

Figure 7.3: Eigenvalues of the open loop system ($\times$) and closed loop system ($*$). $\square$ is the sixth eigenvalues of the closed loop system.

In addition, the maximum kinetic energy density ε_{max} versus the ratio of $M/(N-3)$ is depicted in Figure 7.4. The result shows that increasing of the number of **DOF** is of

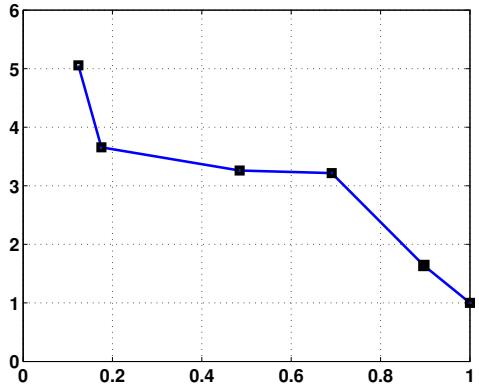

Figure 7.4: Behavior of the maximum kinetic energy density versus the ratio of $M/(N-3)$. y-axis is the maximum kinetic energy density and x-axis is the ratio of the number of **DOF** and the number of states.

great interest since the maximum kinetic energy density ε_{max} is a decreasing function of M.

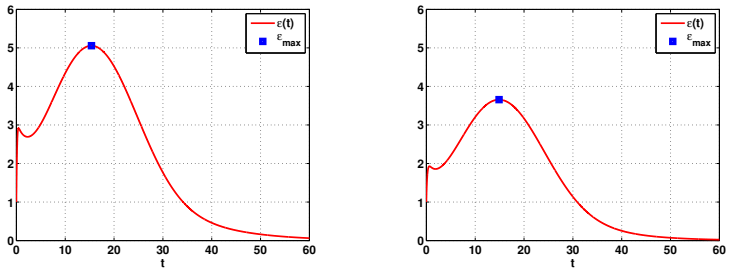

(a) $M/(N-3) = 12/97$ (b) $M/(N-3) = 17/97$

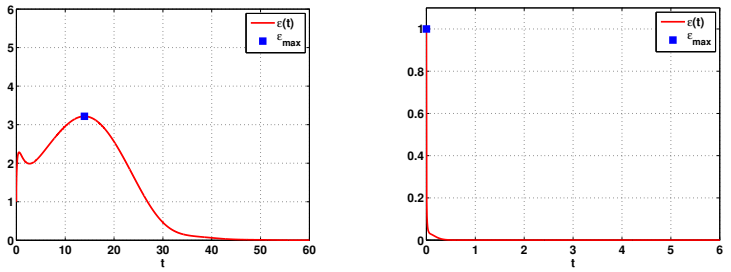

(c) $M/(N-3) = 67/97$ (d) $M/(N-3) = 1$

Figure 7.5: Behavior of the kinetic energy density versus time.

More detail, the behavior of kinetic energy density is shown in Figure 7.5. As can be seen in this figure, the kinetic energy density minimization is improved versus the ratio of $M/(N-3)$. In Figure 7.5(d), the nice configuration is obtained where the kinetic

energy density minimization is monotonically decreasing.

7.3.2.2 Case II: 3D plane Poiseuille flow

We consider the case of $\alpha = 0$, $\beta = 2.044$ and $R = 5\ 000$ (see section 5.6). For **LQR** control, we set $\gamma = 128$ as in [McKernan, 2006], [McKernan et al., 2007]. We set $f_{v,l,m}(y) = f_{\eta,l,m}(y) = (1-y^2)^2\Xi_m(y) + \frac{y^3-3y+2}{4}$. We use the Combined method 1 (see section 5.3.3 for more detail), the dimension of the state matrix $\mathbf{A}$ and the input matrix $\mathbf{B}$ are $(2N-4)\times(2N-4)$ and $(2N-4)\times(2M)$, respectively. Therefore, the dimension of the state matrix $\mathcal{A}$ and the input matrix $\mathcal{B}$ are $(2N+2M-4)\times(2N+2M-4)$ and $(2N+2M-4)\times(2M)$, respectively. We set $N = 50$.

As the previous case, the eigenvalues of the closed loop system are depicted in Figure 7.6, only the real part is shown (all real part of eigenvalues are negative, we do not need to consider the image part of eigenvelue), the imaginary part of being negligible. We obtain the same results in the previous case, the number of relocated poles is improved versus the ratio of $M/(N-2)$. When we use two **DOF** ($M/(N-2) = 2/96$), just a few eigenvalues are relocated. As before, we have more **DOF**, we have more the number of relocated eigenvalues.

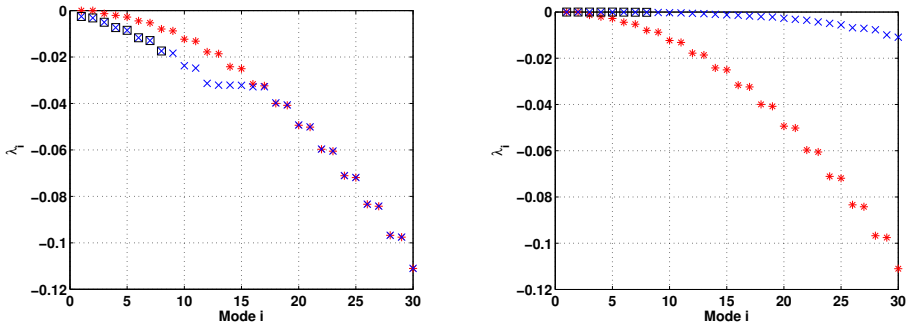

(a) $M/(N-2) = 2/96$ (b) $M/(N-2) = 56/96$

(c) $M/(N-2) = 86/96$ (d) $M/(N-2) = 1$

Figure 7.6: Eigenvalues of the open loop system ($\times$) and closed loop system ($*$). $\square$ is the eighth eigenvalues of the closed loop system.

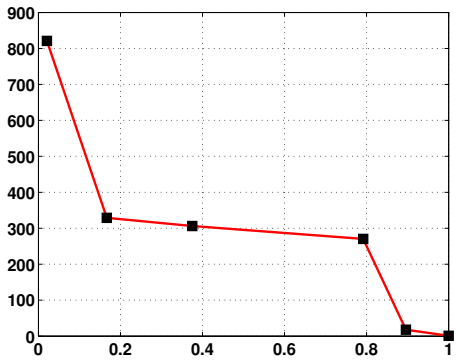

Figure 7.7: Behavior of the maximum kinetic energy density versus the ratio of $M/(N-2)$. y-axis is the maximum kinetic energy density and x-axis is the ratio of the number of **DOF** and the number of states.

Considering the kinetic energy density minimization, the maximum kinetic energy density ε_{max} versus the ratio of $M/(N-2)$ is depicted in Figure 7.7. Once again we note that increasing the number of **DOF** proves to be desirable since the maximum kinetic energy density ε_{max} is a decreasing function of $M/(N-2)$.

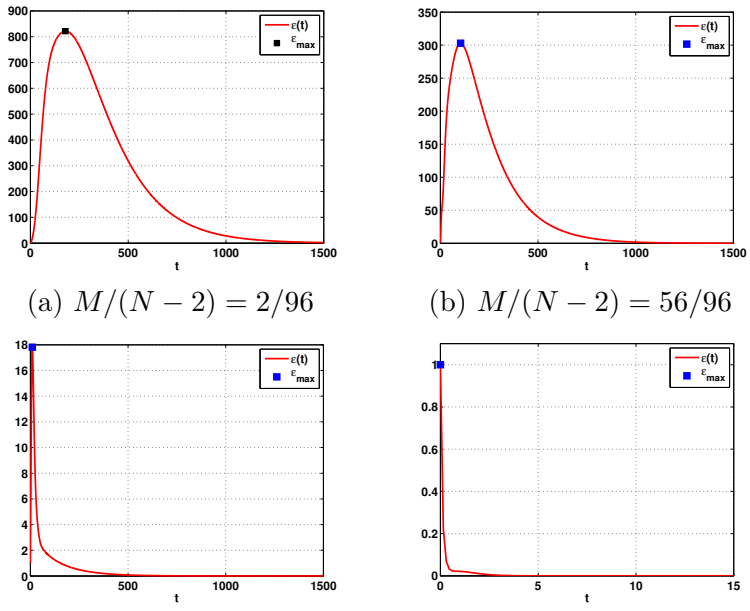

(a) $M/(N-2) = 2/96$ (b) $M/(N-2) = 56/96$

(c) $M/(N-2) = 86/96$ (d) $M/(N-2) = 1$

Figure 7.8: Behavior of the kinetic energy density versus time.

As before, the behavior of kinetic energy density is depicted in Figure 7.8 versus the

ratio of $M/(N-2)$. A very strong decrease of kinetic energy density is versus the ratio of $M/(N-2)$. The case $M/(N-2)=1$ shows the nice behavior of the kinetic energy density.

7.4 Conclusion

When we increase the number of **DOF**, the behavior of the closed loop system is in general improved. Based on this result, we propose the way where the number of **DOF** increases in the plane Poiseuille flow. Our goal is to improve the behavior of the kinetic energy density in the closed loop system which concerns the stability of the flow control.

When the number of **DOF** increases, with the **LQR** control, the number of relocated poles is increased, so the behavior of the state vector is improved. As a result, the behavior of the kinetic energy density is improved since increasing the number of **DOF**. An interesting result of kinetic energy density minimization is obtained when the number of states $\mathbf{x}(t)$ is equal to the number of **DOF**. However, we still do not ensure that the kinetic energy density always decreases ($\dot{\varepsilon}(t) \leq 0$) in time because the fact that the **LQR** control can minimize the kinetic energy density but does not ensure the strict monotonic decrease of kinetic energy density. Therefore, in the next chapter, we shall propose a control approach which can achieve an exponential decrease of kinetic energy density.

Chapter 8

Visual Servoing Control

The goal of this chapter is to ensure the nice behavior of kinetic energy density, skin friction drag and control signals in the closed loop system of the plane Poiseuille flow such as $\varepsilon(t) = e^{-2\lambda t}\varepsilon_0$, $\mathbf{d}(t) = e^{-\lambda t}\mathbf{d}_0$ and $\mathbf{u}(t) = e^{-\lambda t}\mathbf{u}_0$, respectively.

As shown in previous chapters, in the context of **LQR** control, increasing the number of the degree of freedom (**DOF**) of control signals is of great interest since the behavior of the kinetic energy density is a decreasing function of **DOF**. Unfortunately, the **LQR** control approach does not ensure that the kinetic energy density monotonically decreases in time. Therefore, we need to find a control approach to ensure that the kinetic energy density monotonically decreases in time, $\dot{\varepsilon}(t) \leq 0$. This problem becomes easier when the state vector has an exponential decoupled decrease (see Appendix B). More precisely, we use the visual servoing control to obtain an exponential decoupled decrease of the state vector for the linearized plane Poiseuille flow.

8.1 State space representation

When the state matrix $\mathbf{L}$ is invertible, (7.23) is rewritten under the following form

$$\dot{\mathbf{x}}(t) = \mathbf{L}^{-1}\mathbf{A}\mathbf{x}(t) + \mathbf{L}^{-1}\mathbf{B}\mathbf{u}(t) + \mathbf{L}^{-1}\mathbf{E}\dot{\mathbf{u}}(t), \tag{8.1}$$

and by the change of variable $\mathbf{z}(t) = \mathbf{x}(t) - \mathbf{L}^{-1}\mathbf{E}\mathbf{u}(t)$ in [Cortelezzi and Speyer, 1998, Cortelezzi et al., 1998a, Cortelezzi et al., 1998b, Kang et al., 1999, Lee et al., 2001], it is easy to show that (8.1) becomes

$$\dot{\mathbf{z}}(t) = \mathbf{A}_z\mathbf{z}(t) + \mathbf{B}_z\mathbf{u}(t), \tag{8.2}$$

where the state and input matrices are presented

$$\begin{cases} \mathbf{A}_z &= \mathbf{L}^{-1}\mathbf{A} \\ \mathbf{B}_z &= \mathbf{L}^{-1}\mathbf{B} + \mathbf{L}^{-1}\mathbf{A}\mathbf{L}^{-1}\mathbf{E}. \end{cases} \tag{8.3}$$

The kinetic energy density is rewritten as a function of $\mathbf{z}(t)$

$$\begin{aligned}\varepsilon(t) &= \mathbf{x}^\top(t)\mathbf{Q}_{11}\mathbf{x}(t) + \mathbf{x}^\top(t)\mathbf{Q}_{12}\mathbf{u}(t) + \mathbf{u}^\top(t)\mathbf{Q}_{21}\mathbf{x}(t) + \mathbf{u}^\top(t)\mathbf{Q}_{22}\mathbf{u}(t)\\ &= (\mathbf{z}(t) + \mathbf{L}^{-1}\mathbf{E}\mathbf{u}(t))^\top\mathbf{Q}_{11}(\mathbf{z}(t) + \mathbf{L}^{-1}\mathbf{E}\mathbf{u}(t)) + (\mathbf{z}(t) + \mathbf{L}^{-1}\mathbf{E}\mathbf{u}(t))^\top\mathbf{Q}_{12}\mathbf{u}(t)\\ &+\mathbf{u}^\top(t)\mathbf{Q}_{21}(\mathbf{z}(t) + \mathbf{L}^{-1}\mathbf{E}\mathbf{u}(t)) + \mathbf{u}^\top(t)\mathbf{Q}_{22}\mathbf{u}(t)\\ &= \mathbf{z}^\top(t)\mathbf{Q}_z\mathbf{z}(t) + \mathbf{z}^\top(t)\mathbf{N}_{zu}\mathbf{u}(t) + \mathbf{u}^\top(t)\mathbf{N}_{uz}\mathbf{z}(t) + \mathbf{u}^\top(t)\mathbf{R}_z\mathbf{u}(t),\end{aligned} \tag{8.4}$$

where the matrices $\mathbf{N}_{zu}$, $\mathbf{N}_{uz}$ and $\mathbf{R}_z$ are given by

$$\begin{cases}\mathbf{Q}_z &= \mathbf{Q}_{11}\\ \mathbf{N}_{zu} &= \mathbf{Q}_{12} + \mathbf{Q}_{11}\mathbf{L}^{-1}\mathbf{E}\\ \mathbf{N}_{uz} &= \mathbf{Q}_{21} + (\mathbf{L}^{-1}\mathbf{E})^\top\mathbf{Q}_{11}\\ \mathbf{R}_z &= \mathbf{Q}_{22} + (\mathbf{L}^{-1}\mathbf{E})^\top\mathbf{Q}_{12} + \mathbf{Q}_{21}\mathbf{L}^{-1}\mathbf{E} + (\mathbf{L}^{-1}\mathbf{E})^\top\mathbf{Q}_{11}\mathbf{L}^{-1}\mathbf{E}.\end{cases} \tag{8.5}$$

The corresponding skin friction drag is also given by

$$\mathbf{d}(t) = \mathbf{D}_1\mathbf{x}(t) + \mathbf{D}_2\mathbf{u}(t) = \mathbf{D}_1\mathbf{z}(t) + (\mathbf{D}_1\mathbf{L}^{-1}\mathbf{E} + \mathbf{D}_2)\mathbf{u}(t), \tag{8.6}$$

and is rewritten by

$$\mathbf{d}(t) = \mathbf{D}_{z1}\mathbf{z}(t) + \mathbf{D}_{z2}\mathbf{u}(t), \tag{8.7}$$

where the matrices $\mathbf{D}_{z1}$ and $\mathbf{D}_{z2}$ are given by

$$\begin{cases}\mathbf{D}_{z1} &= \mathbf{D}_1\\ \mathbf{D}_{z2} &= \mathbf{D}_1\mathbf{L}^{-1}\mathbf{E} + \mathbf{D}_2.\end{cases} \tag{8.8}$$

Therefore, the linearized plane Poiseuille flow is given by

$$\begin{cases}\dot{\mathbf{z}}(t) &= \mathbf{A}_z\mathbf{z}(t) + \mathbf{B}_z\mathbf{u}(t)\\ \varepsilon(t) &= \mathbf{z}^\top(t)\mathbf{Q}_z\mathbf{z}(t) + \mathbf{z}^\top(t)\mathbf{N}_{zu}\mathbf{u}(t) + \mathbf{u}^\top(t)\mathbf{N}_{uz}\mathbf{z}(t) + \mathbf{u}^\top(t)\mathbf{R}_z\mathbf{u}(t)\\ \mathbf{d}(t) &= \mathbf{D}_{z1}\mathbf{z}(t) + \mathbf{D}_{z2}\mathbf{u}(t)\\ \mathbf{z}(0) &= \mathbf{z}_0\end{cases} \tag{8.9}$$

8.2 Our goal of the control law

We consider here a state feedback control law

$$\mathbf{u}(t) = \mathbf{K}\mathbf{z}(t), \tag{8.10}$$

and suppose that this control is able to achieve an exponential decoupled decrease of the state vector

$$\dot{\mathbf{z}}(t) = -\lambda\mathbf{z}(t). \tag{8.11}$$

The derivative of kinetic energy density and skin friction drag are calculated from (8.9) as

$$\begin{cases}\dot{\varepsilon}(t) &= 2\mathbf{z}^\top(t)\mathbf{Q}_z\dot{\mathbf{z}}(t) + \dot{\mathbf{z}}^\top(t)\mathbf{N}_{zu}\mathbf{u}(t) + \mathbf{z}^\top(t)\mathbf{N}_{zu}\dot{\mathbf{u}}(t)\\ &+\dot{\mathbf{u}}^\top(t)\mathbf{N}_{uz}\mathbf{z}(t) + \mathbf{u}^\top(t)\mathbf{N}_{uz}\dot{\mathbf{z}}(t) + 2\mathbf{u}^\top(t)\mathbf{R}_z\dot{\mathbf{u}}(t)\\ \dot{\mathbf{d}}(t) &= \mathbf{D}_{z1}\dot{\mathbf{z}}(t) + \mathbf{D}_{z2}\dot{\mathbf{u}}(t)\end{cases} \tag{8.12}$$

And taking into account (8.10) and (8.11), it is very easy to show that we have

$$\begin{cases} \dot{\mathbf{u}}(t) &= -\lambda \mathbf{u}(t) \\ \dot{\mathbf{d}}(t) &= -\lambda \mathbf{d}(t) \\ \dot{\varepsilon}(t) &= -2\lambda \varepsilon(t). \end{cases} \tag{8.13}$$

Finally, looking at the temporal evolution of closed loop system, we obtain

$$\begin{cases} \mathbf{z}(t) &= e^{-\lambda t}\mathbf{z}_0 \\ \mathbf{u}(t) &= e^{-\lambda t}\mathbf{u}_0 \\ \mathbf{d}(t) &= e^{-\lambda t}\mathbf{d}_0 \\ \varepsilon(t) &= e^{-2\lambda t}\varepsilon_0, \end{cases} \tag{8.14}$$

where $\mathbf{z}_0$, $\mathbf{u}_0$, $\mathbf{d}_0$ and ε_0 are the initial conditions. It is of course a very interesting result. This result shows that the initial condition does not influence to the behavior of the closed loop system, whose kinetic energy density becomes exponentially decreasing which is a highly desired result in linear control theory.

The velocity and vorticity are calculated as a function of the state vector and the control signals

$$\begin{bmatrix} [\tilde{v}_n(t)] \\ [\tilde{\eta}_n(t)] \end{bmatrix} = \begin{bmatrix} \mathbf{T}_{a_v} \\ \mathbf{T}_{a_\eta} \end{bmatrix} \mathbf{x}(t) + \begin{bmatrix} \mathbf{T}_{q_v} \\ \mathbf{T}_{a_\eta} \end{bmatrix} \mathbf{u}(t), \tag{8.15}$$

where $[\tilde{v}_n(t)] = [\tilde{v}(y_0,t)\dots\tilde{v}(y_N,t)]^\top$, $[\tilde{\eta}_n(t)] = [\tilde{\eta}(y_0,t)\dots\tilde{\eta}(y_N,t)]^\top$. The derivatives of velocity and vorticity are given by

$$\begin{aligned} \begin{bmatrix} [\dot{\tilde{v}}_n(t)] \\ [\dot{\tilde{\eta}}_n(t)] \end{bmatrix} &= \begin{bmatrix} \mathbf{T}_{a_v} \\ \mathbf{T}_{a_\eta} \end{bmatrix} \dot{\mathbf{x}}(t) + \begin{bmatrix} \mathbf{T}_{q_v} \\ \mathbf{T}_{q_\eta} \end{bmatrix} \dot{\mathbf{u}}(t) \\ &= \begin{bmatrix} \mathbf{T}_{a_v} \\ \mathbf{T}_{a_\eta} \end{bmatrix} \dot{\mathbf{z}}(t) + \left(\begin{bmatrix} \mathbf{T}_{a_v} \\ \mathbf{T}_{a_\eta} \end{bmatrix} \mathbf{L}^{-1}\mathbf{E} + \begin{bmatrix} \mathbf{T}_{q_v} \\ \mathbf{T}_{q_\eta} \end{bmatrix} \right) \dot{\mathbf{u}}(t), \end{aligned} \tag{8.16}$$

Using (8.11) and (8.13), it is easy to show that the we have:

$$\begin{cases} [\dot{\tilde{v}}_n(t)] = -\lambda [\tilde{v}_n(t)] \\ [\dot{\tilde{\eta}}_n(t)] = -\lambda [\tilde{\eta}_n(t)], \end{cases} \tag{8.17}$$

leading to an exponential decoupled decrease of the velocity component. When the state vector has an exponential decrease, the velocity also has an exponential decoupled decrease. This is a new result in the context of our work.

In the next section, we use the visual servoing control to obtain an exponential decoupled decrease of the state vector.

8.3 Design of the control law

In the visual servoing control, the dynamic equation of the error is given by

$$\dot{\mathbf{e}}(t) = \frac{\partial \mathbf{e}(t)}{\partial t} + \mathbf{L}_\mathbf{e}(t)\mathbf{u}(t) \tag{8.18}$$

In order to stabilize the state vector by an exponential decrease, the state vector is chosen to be the visual feature $\mathbf{z}(t) = \mathbf{s}(t)$. By comparing (8.9) and (8.18), we obtain

$$\begin{cases} \mathbf{L_e}(t) & = \mathbf{B}_z \\ \dfrac{\partial \mathbf{e}(t)}{\partial t} & = \mathbf{A}_z \mathbf{z}(t). \end{cases} \tag{8.19}$$

If we would like for instance to try to ensure an exponential decoupled decrease of the error

$$\dot{\mathbf{e}}(t) = -\lambda \mathbf{e}(t). \tag{8.20}$$

We now obtain

$$\mathbf{u}(t) = -\lambda \mathbf{L_e}^{+}(t)\mathbf{e}(t) - \mathbf{L_e}^{+}(t)\frac{\partial \mathbf{e}(t)}{\partial t}, \tag{8.21}$$

where $\mathbf{L_e}^{+}$ is the Moore Penrose pseudo-inverse matrix of $\mathbf{L_e}$. Note that the interaction matrix $\mathbf{L_e}$ may not be a square matrix but must be full rank matrix, therefore we use the Moore Penrose pseudo-inverse matrix $\mathbf{L_e}^{+}$. If $\mathbf{L_e}$ were a square and invertible matrix, the control law could be

$$\mathbf{u}(t) = -\lambda \mathbf{L_e^{-1}}(t)\mathbf{e}(t) - \mathbf{L_e^{-1}}(t)\frac{\partial \mathbf{e}(t)}{\partial t}. \tag{8.22}$$

In this case, the control law can be rewritten by $\mathbf{u}(t) = \mathbf{K}\mathbf{z}(t)$ where

$$\mathbf{K} = -\mathbf{L_e^{-1}}(t)(\lambda \mathbf{I} + \mathbf{A}_z) \tag{8.23}$$

The control law $\mathbf{K} = -{\mathbf{L_e}}^{-1}(t)(\lambda \mathbf{I} + \mathbf{A}_z)$ is based on the inverse of the interaction matrix $\mathbf{L_e}$. Therefore, we shall study the condition number of the interaction matrix $\mathbf{L_e}$ which gives the ability of inverting a matrix in the next section.

8.4 Condition number of the interaction matrix

A matrix is said to be an invertible matrix, the necessary and sufficient conditions are that it must be a square matrix and has full rank. However, the result will be not good enough if the condition number is very high. So, the condition number of $\mathbf{L_e}$ is an interesting problem.

We give the form of the interaction matrix $\mathbf{L_e}$. From the system in sections 5.3.4 and 7.2, the state space representation is rewritten by

$$\begin{cases} \dot{\mathbf{a}}_v & = \mathbf{L}_{11}^{-1}\mathbf{A}_{11}\mathbf{a}_v + \mathbf{L}_{11}^{-1}\mathbf{B}_{11}\mathbf{q}_v + \mathbf{L}_{11}^{-1}\mathbf{E}_{11}\dot{\mathbf{q}}_v \\ \dot{\mathbf{a}}_\eta & = \mathbf{L}_{22}^{-1}\mathbf{A}_{22}\mathbf{a}_\eta + \mathbf{L}_{22}^{-1}\mathbf{A}_{21}\mathbf{a}_v + \mathbf{L}_{22}^{-1}\mathbf{B}_{22}\mathbf{q}_\eta + \mathbf{L}_{22}^{-1}\mathbf{B}_{21}\mathbf{q}_v + \mathbf{L}_{22}^{-1}\mathbf{E}_{22}\dot{\mathbf{q}}_\eta, \end{cases} \tag{8.24}$$

where $\mathbf{x}(t) = \begin{bmatrix} \mathbf{a}_v^\top(t) & \mathbf{a}_\eta^\top(t) \end{bmatrix}^\top$ and $\mathbf{u}(t) = \begin{bmatrix} \mathbf{q}_v^\top(t) & \mathbf{q}_\eta^\top(t) \end{bmatrix}^\top$. The element matrices have been given in previous sections 5.3.4 and 7.2. By the change of variable

$$\begin{cases} \mathbf{a}_{v,z} & = \mathbf{a}_v - \mathbf{L}_{11}^{-1}\mathbf{E}_{11}\mathbf{q}_v \\ \mathbf{a}_{\eta,z} & = \mathbf{a}_\eta - \mathbf{L}_{22}^{-1}\mathbf{E}_{22}\mathbf{q}_\eta, \end{cases} \tag{8.25}$$

(8.24) becomes

$$\left\{\begin{array}{ll}\dot{\mathbf{a}}_{v,z} & = \mathbf{L}_{11}^{-1}\mathbf{A}_{11}\mathbf{a}_{v,z} + (\mathbf{L}_{11}^{-1}\mathbf{B}_{11} + \mathbf{L}_{11}^{-1}\mathbf{A}_{11}\mathbf{L}_{11}^{-1}\mathbf{E}_{11})\mathbf{q}_v \\ \dot{\mathbf{a}}_{\eta,z} & = \mathbf{L}_{22}^{-1}\mathbf{A}_{22}\mathbf{a}_{\eta,z} + \mathbf{L}_{22}^{-1}\mathbf{A}_{21}\mathbf{a}_{v,z} \\ & +(\mathbf{L}_{22}^{-1}\mathbf{B}_{22} + \mathbf{L}_{22}^{-1}\mathbf{A}_{22}\mathbf{L}_{22}^{-1}\mathbf{E}_{22})\mathbf{q}_\eta + (\mathbf{L}_{22}^{-1}\mathbf{B}_{21} + \mathbf{L}_{22}^{-1}\mathbf{A}_{21}\mathbf{L}_{11}^{-1}\mathbf{E}_{11})\mathbf{q}_v\end{array}\right. \tag{8.26}$$

It is very easy to see that the form of the interaction matrix $\mathbf{L_e}$ is given by

$$\mathbf{L_e} = \left[\begin{array}{cc}\mathbf{L}_{11}^{-1}(\mathbf{B}_{11} + \mathbf{A}_{11}\mathbf{L}_{11}^{-1}\mathbf{E}_{11}) & 0 \\ \mathbf{L}_{22}^{-1}(\mathbf{B}_{21} + \mathbf{A}_{21}\mathbf{L}_{11}^{-1}\mathbf{E}_{11}) & \mathbf{L}_{22}^{-1}(\mathbf{B}_{22} + \mathbf{A}_{22}\mathbf{L}_{22}^{-1}\mathbf{E}_{22})\end{array}\right], \tag{8.27}$$

which is rewritten by

$$\mathbf{L_e} = \left[\begin{array}{cc}\mathbf{L}_{\mathbf{e},11} & 0 \\ \mathbf{L}_{\mathbf{e},21} & \mathbf{L}_{\mathbf{e},22}\end{array}\right], \tag{8.28}$$

where the element matrices $\mathbf{L}_{\mathbf{e},11}$, $\mathbf{L}_{\mathbf{e},21}$ and $\mathbf{L}_{\mathbf{e},22}$ are given by

$$\left\{\begin{array}{ll}\mathbf{L}_{\mathbf{e},11} & = \mathbf{L}_{11}^{-1}(\mathbf{B}_{11} + \mathbf{A}_{11}\mathbf{L}_{11}^{-1}\mathbf{E}_{11}) \\ \mathbf{L}_{\mathbf{e},21} & = \mathbf{L}_{22}^{-1}(\mathbf{B}_{21} + \mathbf{A}_{21}\mathbf{L}_{11}^{-1}\mathbf{E}_{11}) \\ \mathbf{L}_{\mathbf{e},22} & = \mathbf{L}_{22}^{-1}(\mathbf{B}_{22} + \mathbf{A}_{22}\mathbf{L}_{22}^{-1}\mathbf{E}_{22}).\end{array}\right. \tag{8.29}$$

Therefore, the inverse of the interaction matrix $\mathbf{L_e}$ is given by

$$\mathbf{L_e}^{-1} = \left[\begin{array}{cc}\mathbf{L}_{\mathbf{e},11}^{-1} & 0 \\ \mathbf{L}_{\mathbf{e},22}^{-1}\mathbf{L}_{\mathbf{e},21}\mathbf{L}_{\mathbf{e},11}^{-1} & \mathbf{L}_{\mathbf{e},22}^{-1}\end{array}\right], \tag{8.30}$$

where the element matrices $\mathbf{L}_{\mathbf{e},11}^{-1}$ and $\mathbf{L}_{\mathbf{e},22}^{-1}$ are given by

$$\left\{\begin{array}{ll}\mathbf{L}_{\mathbf{e},11}^{-1} & = (\mathbf{B}_{11} + \mathbf{A}_{11}\mathbf{L}_{11}^{-1}\mathbf{E}_{11})^{-1}\mathbf{L}_{11} \\ \mathbf{L}_{\mathbf{e},22}^{-1} & = (\mathbf{B}_{22} + \mathbf{A}_{22}\mathbf{L}_{22}^{-1}\mathbf{E}_{22})^{-1}\mathbf{L}_{22}.\end{array}\right. \tag{8.31}$$

The condition number of the matrices $\mathbf{L}_{11} = j(-k^2\mathbf{D}0_{DN}(\Xi) + \mathbf{D}2_{DN}(\Xi))$ and $\mathbf{L}_{22} = \mathbf{D}0_D(\Theta)$ are discussed in section 5.3.3.3. Although the interaction matrix $\mathbf{L_e}$ is very complex in order to know its condition number, it is necessary and sufficient to consider the condition number of two matrices $\mathbf{L}_{11}\mathbf{L}_{\mathbf{e},11} = (\mathbf{B}_{11} + \mathbf{A}_{11}\mathbf{L}_{11}^{-1}\mathbf{E}_{11})$ and $\mathbf{L}_{22}\mathbf{L}_{\mathbf{e},22} = (\mathbf{B}_{22} + \mathbf{A}_{22}\mathbf{L}_{22}^{-1}\mathbf{E}_{22})$. Therefore, we have

$$\left\{\begin{array}{ll}\mathbf{L}_{11}\mathbf{L}_{\mathbf{e},11} & = (c_1\mathbf{D}0_{DN}(\mathbf{F}_v) + c_2\mathbf{D}2_{DN}(\mathbf{F}_v) + c_3\mathbf{D}4_{DN}(\mathbf{F}_v)) \\ & -(c_1\mathbf{D}0_{DN}(\Xi) + c_2\mathbf{D}2_{DN}(\Xi) + c_3\mathbf{D}4_{DN}(\Xi))(k^2\mathbf{D}0_{DN}(\Xi) - \mathbf{D}2_{DN}(\Xi))^{-1} \\ & (k^2\mathbf{D}0_{DN}(\mathbf{F}_v) - \mathbf{D}2_{DN}(\mathbf{F}_v)) \\ \mathbf{L}_{22}\mathbf{L}_{\mathbf{e},22} & = (c_4\mathbf{D}0_D(\mathbf{F}_\eta) + c_3\mathbf{D}2_D(\mathbf{F}_\eta)) \\ & -(c_4\mathbf{D}0_D(\Theta) + c_3\mathbf{D}2_D(\Theta))(\mathbf{D}0_D(\Theta))^{-1}\mathbf{D}0_D(\mathbf{F}_\eta).\end{array}\right. \tag{8.32}$$

where c_1, c_2, c_3 and c_4 were defined in section 5.3.1. The condition number of the interaction matrix $\mathbf{L_e}$ is simplified by considering the condition number of two smaller matrices $(\mathbf{B}_{11} + \mathbf{A}_{11}\mathbf{L}_{11}^{-1}\mathbf{E}_{11})$ and $(\mathbf{B}_{22} + \mathbf{A}_{22}\mathbf{L}_{22}^{-1}\mathbf{E}_{22})$, however, it is still very complex to compute.

Once again, we use the linear model of the plane Poiseuille flow, it must be consider the behavior of the nonlinear system. The next section introduces the stability analysis of the exponential decrease of error since the dynamic of error is a nonlinear system.

8.5 Stability analysis

We analyze the stability of the closed loop nonlinear system. We first assume that a nonlinear model can be obtained in a certain domain of variation of $\mathbf{e}$ and $\mathbf{u}$:

$$\dot{\mathbf{e}}(t) = f(\mathbf{e}(t), \mathbf{u}(t)). \tag{8.33}$$

According to (8.20), it is clear that $\mathbf{e} = \mathbf{0}$ is an exponentially stable equilibrium point for the linearized system (8.18) and for the control law (8.22). Therefore, $\mathbf{e} = \mathbf{0}$ is also an exponentially stable equilibrium point for the nonlinear system (8.33).

8.6 Robustness to measurement noise

Recall that in our case, the state vector is directly obtained from the computation of the optical flow through a visualization system (see [Tatsambon Fomena and Collewet, 2011a]). More precisely, the optical flow is the apparent velocity vector field representing the motion of photometric pattern (pixels luminance) in successive image sequences. Optical flow techniques can be used to estimate instantaneous velocities of a fluid flow from any image sequences as detailed in [Heitz et al., 2010]. In practice, the control law is calculated by

$$\mathbf{u}(t) = -\lambda \widehat{\mathbf{L}_\mathbf{e}}^{+}(t)\widehat{\mathbf{e}}(t) - \widehat{\mathbf{L}_\mathbf{e}}^{+}(t)\frac{\partial \widehat{\mathbf{e}}(t)}{\partial t}, \tag{8.34}$$

where $\widehat{\mathbf{L}_\mathbf{e}}^{+}(t)$ and $\dfrac{\partial \widehat{\mathbf{e}}(t)}{\partial t}$ are an estimation or an approximation of $\mathbf{L_e}^{+}(t)$ and $\dfrac{\partial \mathbf{e}(t)}{\partial t}$, respectively (see [Chaumette and Hutchinson, 2006]). In this case, we use the linear model, thus we can choose $\widehat{\mathbf{L}_\mathbf{e}}^{+}(t) = \mathbf{L_e}^{+}(t)$. In [Tatsambon Fomena and Collewet, 2011a] it has been shown that in our vision-based approach the state estimation writes as

$$\widehat{\mathbf{z}}(t) = \mathbf{z}(t) + \frac{1}{N_x}\mathbf{e}_x(t), \tag{8.35}$$

where N_x is the number of pixels of the camera in the stream wise direction of the flow and $\mathbf{e}_x(t)$ is related to the measurements noise ([Tatsambon Fomena and Collewet, 2011a] for more detail). Thus the estimation of $\dfrac{\partial \widehat{\mathbf{e}}(t)}{\partial t}$ can be given by

$$\frac{\partial \widehat{\mathbf{e}}(t)}{\partial t} = \frac{\partial \mathbf{e}(t)}{\partial t} + \frac{\mathbf{A}_z}{N_x}\mathbf{e}_x(t). \tag{8.36}$$

The closed loop system of error is written as

$$\dot{\mathbf{e}}(t) = -\lambda \mathbf{e}(t) - (\lambda \mathbf{I} + \mathbf{A}_z)\frac{1}{N_x}\mathbf{e}_x(t), \tag{8.37}$$

leading to

$$\dot{\mathbf{e}}(t) \approx -\lambda \mathbf{e}(t), \tag{8.38}$$

when N_x is large enough (it is always the case in practice), the estimation error tends toward 0, and, consequently the error has the desired decreasing profile.

In the next section, we shall present simulation results and the related condition numbers of the interaction matrices.

8.7 Simulation results

Due to the fact that the kinetic energy density depends on the control signals $\mathbf{u}(t)$, the initial value of the kinetic energy density is calculated by

$$\varepsilon_0 = \mathbf{z}_0^\top [\mathbf{Q}_z + \mathbf{N}_{zu}\mathbf{K} + \mathbf{K}^\top \mathbf{N}_{uz} + \mathbf{K}^\top \mathbf{R}_z \mathbf{K}]\mathbf{z}_0. \tag{8.39}$$

where $\mathbf{K} = -{\mathbf{L_e}}^{-1}(\lambda \mathbf{I} + \mathbf{A}_z)$. The initial condition $\mathbf{z}_0$ is chosen as the worst initial condition for the normalized initial value of the kinetic energy density $\varepsilon_0 = 1$ with $\mathbf{z}_0 = \mathbf{z}_{worst,\varepsilon_0=1}(t=0)$.

8.7.1 Case I: 2D plane Poiseuille flow

We set $R = 10\ 000$, $\alpha = 1$, $\beta = 0$ and $f_{v,l,m}(y) = (1-y^2)^2 \Xi_m(y) + \dfrac{y^3 - 3y + 2}{4}$.

The condition numbers of the state matrix $\mathbf{L}$ (see section 5.3.3.3) and the interaction matrix $\mathbf{L_e}$ are given in Table 8.1. The comparison between the condition numbers of the state matrix $\mathbf{L}$ and the interaction matrix $\mathbf{L_e}$ is given in Figure 8.1. This result shows that the interaction matrix has a high condition number, $Cond(\mathbf{L}_e) \approx 10^3 Cond(\mathbf{L})$. It is noted that we only give an example of functions $f_{v,l,m}(y)$ but another choice.

Table 8.1: Condition numbers of the state matrix $\mathbf{L}$ and the interaction matrix $\mathbf{L_e}$

N	50	100	150	200	250	300
$\mathbf{L}$	914.9901	$7.1238\ 10^3$	$2.3836\ 10^4$	$5.6260\ 10^4$	$1.0960\ 10^5$	$1.8908\ 10^5$
$\mathbf{L_e}$	$5.2396\ 10^5$	$1.4987\ 10^7$	$9.7477\ 10^7$	$4.1557\ 10^7$	$1.2898\ 10^9$	$3.2405\ 10^9$

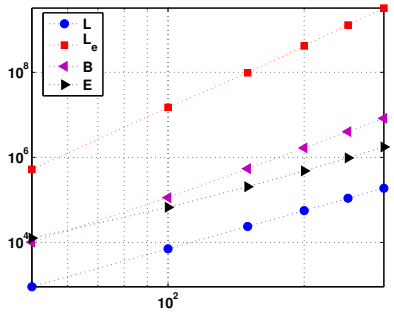

Figure 8.1: Variation of the condition numbers of $\mathbf{L}$, $\mathbf{B}$, $\mathbf{E}$ and $\mathbf{L_e}$ with respect to N.

For $N = 100$ and we set $\lambda = 0.25$ for the control law (8.22), we give the behavior of the closed loop system. The behavior of the error $\mathbf{e}(t)$ is given in Figure 8.2(a), an exponential decoupled decrease of error $\mathbf{e}(t)$ is obtained. Consequently the control signal, the kinetic energy density and the skin friction drag have also an exponential decoupled decrease as can be seen in Figures 8.2(b), 8.2(c) and 8.2(d), respectively.

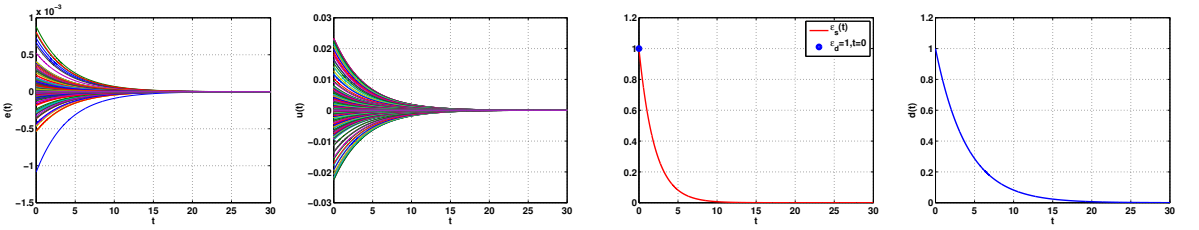

(a) $\mathbf{e}(t)$ versus time (b) $\mathbf{u}(t)$ versus time (c) $\varepsilon_s(t)$ versus time (d) $\mathbf{d}(t)$ versus time

Figure 8.2: Behavior of the closed loop system.

Figure 8.3 illustrates the behavior of the velocity components. All elements of the velocity components monotonically decrease in time. Indeed, the visual servoing control always ensure the exponential decrease of the velocity components when the interaction matrix is square and has full rank. Note that only our approach can do it, this result allows us to guarantee that the perturbation tends toward zero by the best way.

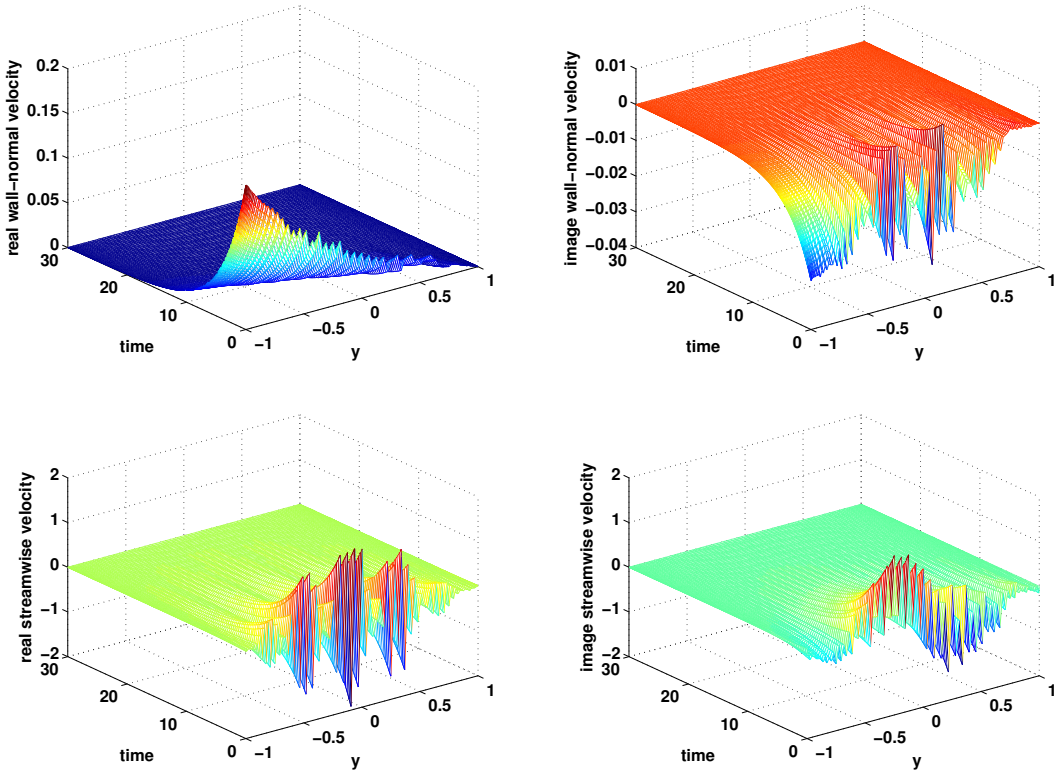

Figure 8.3: Behavior of the velocity components versus time and y direction.

The behavior of the kinetic energy density, the velocity profile and the velocity field are shown in Figure 8.4. The vertical arrows at the lower boundary is the control signal.

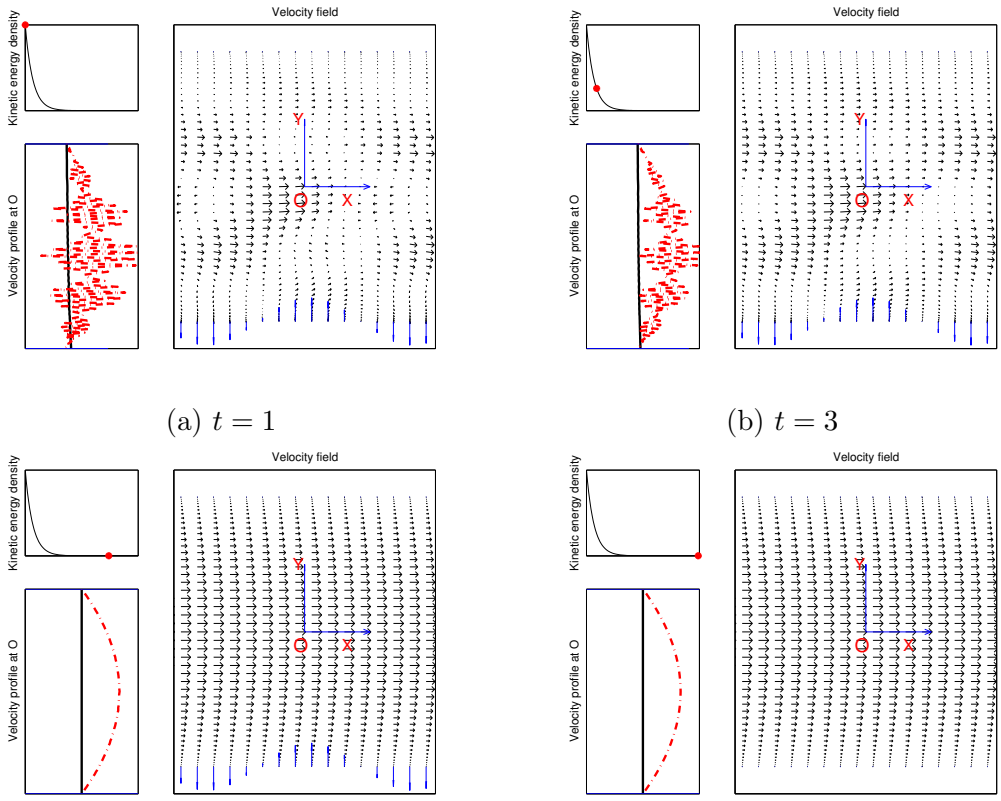

(a) $t = 1$ (b) $t = 3$

(c) $t = 22.5$ (d) $t = 30$

Figure 8.4: Shape of the flow perturbation in the controlled flow.

Although we only use the lower boundary condition but the control signal is assumed to be blowing/suction on the lower boundary. The proposed control law leads the velocity component to an exponential decoupled decrease. The velocity profile becomes the steady solution $(1 - y^2, 0)$. The flow becomes laminar.

In the presence of measurement noise appears and using the optical flow provided in [Tatsambon Fomena and Collewet, 2011a], the behavior of the error is very robust to

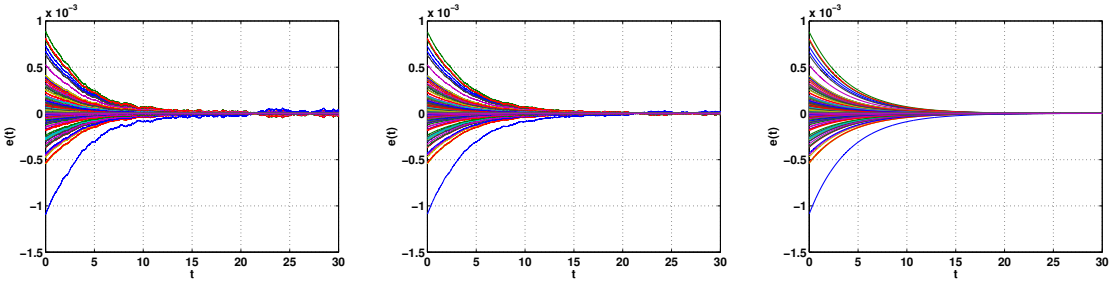

(a) $N_x = 2$ (b) $N_x = 4$ (c) $N_x = 256$

Figure 8.5: Behavior of the error versus time with measurement noise.

measurement noise as observed in Figure 8.5.

In the next section, we will present the result in the 3D plane Poiseuille flow.

8.7.2 Case II: 3D plane Poiseuille flow

We set $R = 5\,000$, $\alpha = 0$, $\beta = 2.044$ and $f_{v,l,m}(y) = f_{\eta,l,m} = (1-y^2)^2\Xi_i(y) + \dfrac{y^3 - 3y + 2}{4}$.

The condition numbers of the state matrix $\mathbf{L}$ and the interaction matrix $\mathbf{L_e}$ are given in Table 8.2 and depicted in Figure 8.6.

Table 8.2: Condition number of the state matrix $\mathbf{L}$ and the interaction matrix $\mathbf{L_e}$

N	50	100	150	200	250	300
$\mathbf{L}$	$1.9365\ 10^4$	$1.5066\ 10^5$	$5.0408\ 10^5$	$1.1898\ 10^6$	$2.3179\ 10^6$	$3.9985\ 10^6$
$\mathbf{L_e}$	$1.9039\ 10^9$	$1.2052\ 10^{10}$	$9.7056\ 10^{10}$	$5.4836\ 10^{11}$	$2.2376\ 10^{12}$	$7.0906\ 10^{12}$

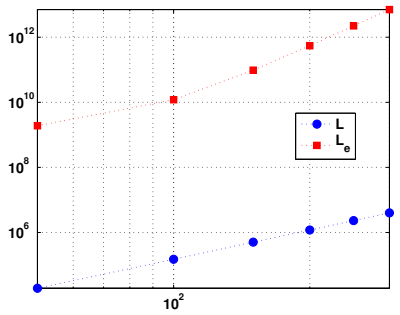

Figure 8.6: Variation of the condition numbers of $\mathbf{L}$ and $\mathbf{L_e}$ with respect to N.

We set $N = 50$ and $\lambda = 0.25$. As in the above case, the similar results are obtained. The behavior of the error vector, the control signal, the kinetic energy density and the skin friction drag are shown in Figure 8.7. Next, Figure 8.8 shows the behavior of the velocity components. Once again, we obtain an exponential decoupled decrease for the error vector, the control signal, the skin friction drag, the kinetic energy density and velocity components.

All observed physical quantities do not increase any more. Furthermore, the visual servoing control is easy to directly decide the convergence velocity of skin friction drag and kinetic energy density minimizations.

The behavior of the kinetic energy density, the velocity profile and the velocity field are illustrated in Figure 8.9. Once again, the velocity profile becomes the steady solution $(1 - y^2, 0, 0)$. The proposed control law ensures the way that the flow becomes laminar state.

As similar to the 2D plane Poiseuille flow, our approach is very robust to noise measurement as shown in Figure 8.10.

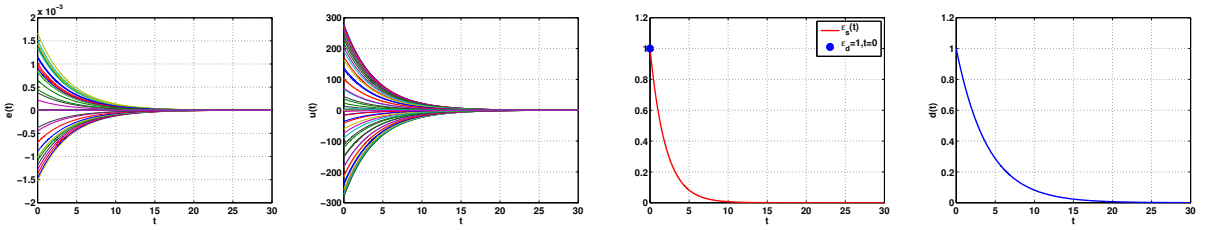

(a) $\mathbf{e}(t)$ versus time (b) $\mathbf{u}(t)$ versus time (c) $\varepsilon_s(t)$ versus time (d) $\mathbf{d}(t)$ versus time

Figure 8.7: Behavior of the closed loop system.

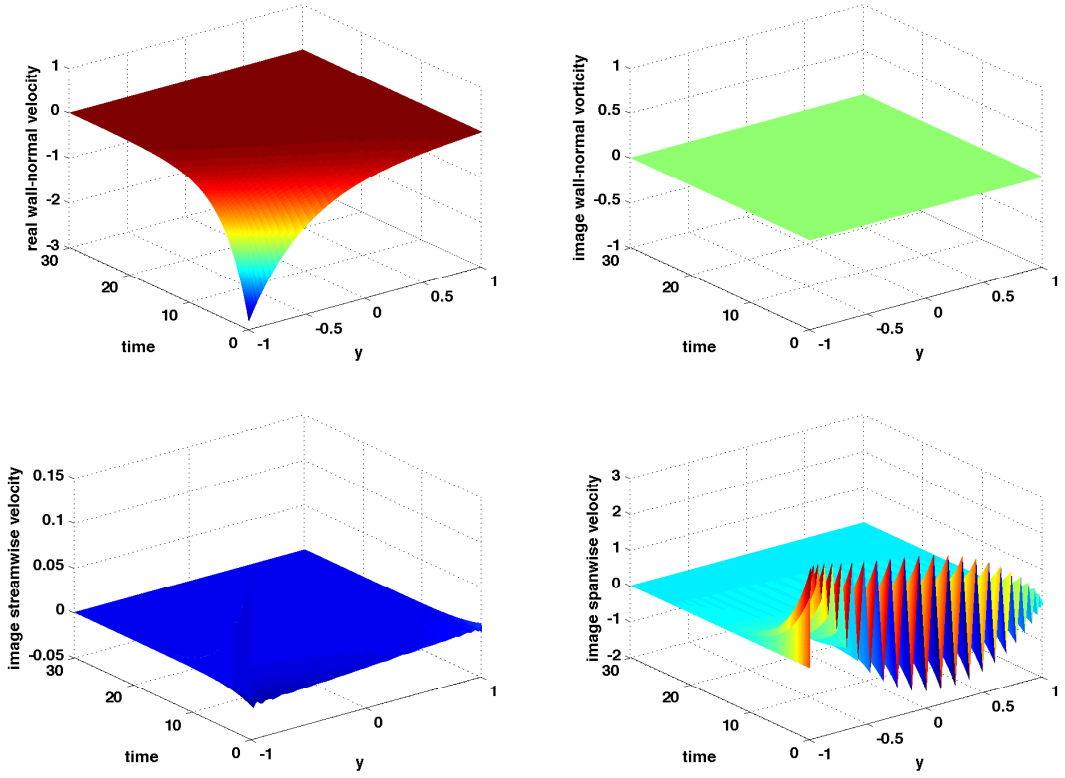

Figure 8.8: Behavior of the velocity components versus time and y direction.

We have given an example of functions $f_{v,l,m}(y)$ and $f_{\eta,l,m}(y)$. However, we can choose another functions $f_{v,l,m}(y)$ and $f_{\eta,l,m}(y)$. Another example is the Hermite interpolation which helps us to eliminate the problem of the condition number in the Appendix C.

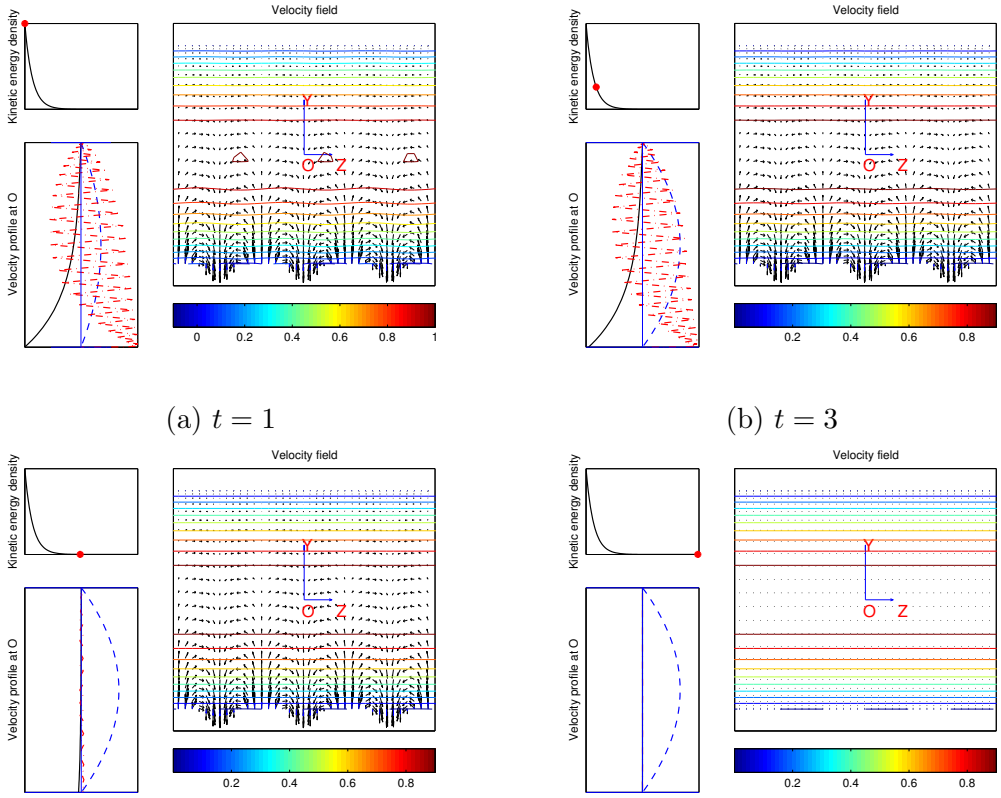

(a) $t = 1$ (b) $t = 3$

(c) $t = 15$ (d) $t = 30$

Figure 8.9: Shape of the flow perturbation in the controlled flow.

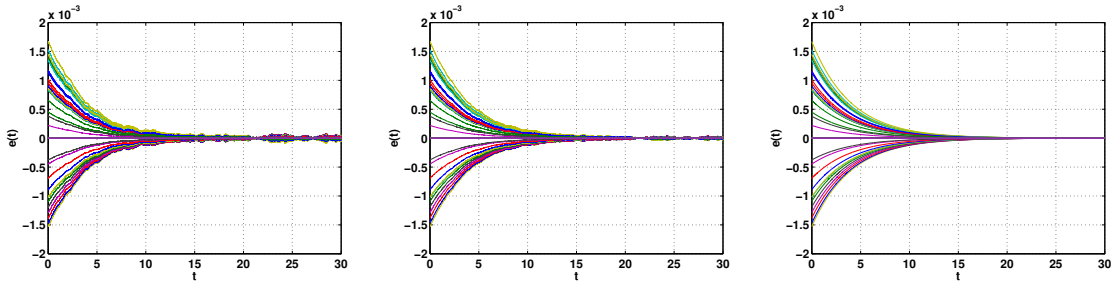

(a) $N_x = 2$ (b) $N_x = 4$ (c) $N_x = 256$

Figure 8.10: Behavior of the error versus time with measurement noise.

8.8 Conclusion

When the number of state vector is equal to the number of **DOF**, the interaction $\mathbf{L_e}$ may become a square and full rank matrix. Therefore, we can design a visual servoing

control to achieve an exponential decoupled decrease of the state vector. Through the state vector, the skin friction drag, the kinetic energy density and the velocity component have also an exponential decoupled decrease in time. The non-normality is solved, the kinetic energy density monotonically decreases in time. It emphasizes that the visual servoing control not only has an exponential decrease of skin-friction drag and kinetic energy density but also directly decides the convergence velocity of skin-friction drag and kinetic energy density minimizations. The visual servoing control gives better results than other control approaches in this case.

However, the order of controller in the flow control is always large because the dimension of linearized plane Poiseuille flow is very large (e.g. the order of the full system is 8000 in [Cortelezzi et al., 1998b]). Therefore, the order of controller need to be reduced. In the next chapter, we present a reduced model which is used to design a reduced controller for the closed loop system of the plane Poiseuille flow.

Chapter 9

Model Order Reduction

By using the spectral method, the dimension of the states is large (e.g. the dimension of states is 8000 in [Cortelezzi et al., 1998b]), the dimension of gain of the control law becomes large. Therefore, we want to reduce the order of controller. In addition, this goal in this chapter is to ensure that the kinetic energy density $\varepsilon(t) \approx e^{-2\lambda t}\varepsilon_0$ in the closed loop system of the plane Poiseuille flow even using two degrees of freedom (**DOF**).

Model order reduction is fundamental in control design, especially for systems with large dimension. In previous chapters, we have demonstrated the advantage of increasing the number of **DOF**. We also have obtained a good result for minimizing the kinetic energy density, $\varepsilon(t) = e^{-2\lambda t}\varepsilon_0$ due to $\mathbf{x}(t) = e^{-\lambda t}\mathbf{x}_0$ but the visual servoing control needs a strong condition on the number of **DOF**. It is very hard in the flow control when the dimension is infinite, therefore an idea of design of control law based on the reduced model is proposed. By using the visual servoing control based on the reduced model, we ensure that the control signal has an exponential decrease in time, $\mathbf{u}(t) = e^{-\lambda t}\mathbf{u}_0$. In particular, the kinetic energy density also has an approximation of the exponential decrease, $\varepsilon(t) \approx e^{-2\lambda t}\varepsilon_0$ due to $\mathbf{u}(t) = e^{-\lambda t}\mathbf{u}_0$, even using two **DOF**.

In the last years, many different reduced model methods have been developed in computational fluid dynamics and control design. Indeed, the reduced model methods are good enough when the behavior of reduced model is equivalent to the behavior of the full system. The Navier-Stokes equations in computational fluid dynamics and the Maxwell equations in electromagnetics are just few examples of reduced model.

In control theory, some methods of Model Order Reduction (**MOR**) are Truncated Balanced Realization (**TBR**) [Moore, 1981], Hankel-Norm Reduction (**HNR**) [Glover, 1984] and Proper Orthogonal Decomposition (**POD**) [Berkooz et al., 1993]. Especially in [Rowley, 2005], the analysis of the plane Poiseuille flow is studied by using Balanced Proper Orthogonal Decomposition (**BPOD**).

Why we use a reduced model instead of the full system. To answer this question, we begin by considering the advantage of reduced model in the next section.

9.1 General model order reduction

Let us consider the full nonlinear system

$$\begin{cases} \dot{\mathbf{x}}(t) &= f(\mathbf{x}(t), \mathbf{u}(t), t) \\ \mathbf{y}(t) &= g(\mathbf{x}(t), \mathbf{u}(t), t) \end{cases} \tag{9.1}$$

which is reduced to the reduced model (see references in [Chen, 1999])

$$\begin{cases} \dot{\mathbf{x}}_r(t) &= f_r(\mathbf{x}_r(t), \mathbf{u}(t), t) \\ \mathbf{y}(t) &= g_r(\mathbf{x}_r(t), \mathbf{u}(t), t) \end{cases} \tag{9.2}$$

where $\mathbf{x}_r(t)$ is a function of $\mathbf{x}(t)$: $\mathbf{x}_r(t) = h(\mathbf{x}(t))$.

In **MOR**, the behavior of the full system (9.1) is equivalent to the behavior of reduced reduction (9.2), it means $g(\mathbf{x}(t), \mathbf{u}(t), t) \approx g_r(\mathbf{x}_r(t), \mathbf{u}(t), t)$, the control design of reduced model is easier. It is noted that the dimension of $\mathbf{x}(t)$ is larger than the dimension of $\mathbf{x}_r(t)$. On the other hand, the control approach depends on the relationship between the number of states and the number of **DOF**. Some control approaches can apply to the reduced model but cannot be applied to the full system. For example, the full system has n states and the number of control signal are m ($m < n$). In the ideal case, the full system is reduced to a model with m states. When the number of control signal equals the number of the states, we can apply the visual servoing control to the reduced model. Another example, the number of **DOF** and the number of states also decide the pole assignment and the eigenstructure assignment. Moreover, the dimension of the full system may be infinite (the flow control case), it is better when we use the reduced model and increase **DOF** based on the reduced model.

We give the advantage of reduced model with respect to the full nonlinear system via a simple example. Let us consider the system

$$\begin{cases} \dot{\mathbf{x}}_1(t) &= \mathbf{x}_1(t) + \mathbf{x}_1^2(t) + \mathbf{x}_2(t) + \mathbf{u}(t) \\ \dot{\mathbf{x}}_2(t) &= \mathbf{x}_1(t) - 100\mathbf{x}_2(t) \\ \mathbf{y}(t) &= \mathbf{x}_1(t) + 10\mathbf{x}_2(t) \end{cases} \tag{9.3}$$

and we limit to consider the equilibrium point $\mathbf{x}_{1e} = \mathbf{x}_{2e} = 0$. Therefore, the linear model is given by

$$\begin{cases} \dot{\mathbf{x}}_1(t) &= \mathbf{x}_1(t) + \mathbf{x}_2(t) + \mathbf{u}(t) \\ \dot{\mathbf{x}}_2(t) &= \mathbf{x}_1(t) - 100\mathbf{x}_2(t) \\ \mathbf{y}(t) &= \mathbf{x}_1(t) + 10\mathbf{x}_2(t) \end{cases} \tag{9.4}$$

From the system (9.4), we see that the input matrix does not have full rank. Therefore, we cannot design a control law which satisfies $\dot{\mathbf{x}}_1(t) = -\lambda\mathbf{x}_1(t)$ and $\dot{\mathbf{x}}_2(t) = -\lambda\mathbf{x}_2(t)$. Therefore, we use a reduced model.

The eigenvalues of (9.4) are $\lambda_1 = 1.0099$ and $\lambda_2 = -100.0099$. It is very easy to see that the mode corresponding to the eigenvalue $\lambda_2 = -100.0099$ is a fast mode (high eigenvalue). Therefore, we can consider $\dot{\mathbf{x}}_2(t) = 0$, we get the reduced model

$$\begin{cases} \dot{\mathbf{x}}_1(t) &= \frac{101}{100}\mathbf{x}_1(t) + \mathbf{x}_1^2(t) + \mathbf{u}(t) \\ \mathbf{y}(t) &= 1.1\mathbf{x}_1(t) \end{cases} \tag{9.5}$$

and its linearization is

$$\left\{\begin{array}{ll}\dot{\mathbf{x}}_1(t) & = \frac{101}{100}\mathbf{x}_1(t) + \mathbf{u}(t) \\ \mathbf{y}(t) & = 1.1\mathbf{x}_1(t)\end{array}\right. \tag{9.6}$$

The control design aims at $\dot{\mathbf{x}}_1(t) = -\lambda\mathbf{x}_1(t)$, which is given by $\mathbf{u}(t) = -(\lambda + \frac{101}{100})\mathbf{x}_1(t)$. The behavior of the closed loop system of the reduced model is

$$\left\{\begin{array}{ll}\dot{\mathbf{x}}_1(t) & = -\lambda\mathbf{x}_1(t) + \mathbf{x}_1^2(t) \\ \mathbf{y}(t) & = 1.1\mathbf{x}_1(t)\end{array}\right. \Rightarrow \left\{\begin{array}{ll}\mathbf{x}_1(t) & = \dfrac{\lambda}{1 + \frac{\lambda - \mathbf{x}_{10}}{\mathbf{x}_{10}}e^{\lambda t}} \\ \mathbf{y}(t) & = \dfrac{1.1\lambda}{1 + \frac{\lambda - \mathbf{x}_{10}}{\mathbf{x}_{10}}e^{\lambda t}}\end{array}\right. \tag{9.7}$$

where $\mathbf{x}_{10}$ is the initial condition. When t is large enough and $\lambda >> \mathbf{x}_{10}$, we get the behavior of reduced model

$$\mathbf{x}_1(t) = \frac{\lambda}{1 + \frac{\lambda - \mathbf{x}_{10}}{\mathbf{x}_{10}}e^{\lambda t}} \approx \mathbf{x}_{10}e^{-\lambda t}, \quad \mathbf{y}(t) = \frac{1.1\lambda}{1 + \frac{\lambda - \mathbf{x}_{10}}{\mathbf{x}_{10}}e^{\lambda t}} \approx 1.1\mathbf{x}_{10}e^{-\lambda t} \tag{9.8}$$

Note that the behavior of the full system is

$$\left\{\begin{array}{ll}\dot{\mathbf{x}}_1(t) & = -(\lambda + \frac{1}{100})\mathbf{x}_1(t) + \mathbf{x}_1^2(t) + \mathbf{x}_2(t), \quad \dot{\mathbf{x}}_2(t) = \mathbf{x}_1(t) - 100\mathbf{x}_2(t) \\ \mathbf{y}(t) & = \mathbf{x}_1(t) + 10\mathbf{x}_2(t)\end{array}\right. \tag{9.9}$$

We first compare the behavior of the state vector $\mathbf{x}_1(t)$ of the reduced model (9.8) and the full nonlinear system (9.9) described in Figure 9.1. Although the control law

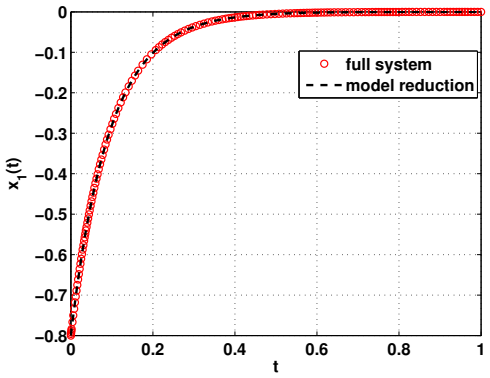

Figure 9.1: Comparison of full nonlinear system and reduced model: behavior of the closed loop system versus time.

$\mathbf{u}(t) = -(\lambda + \frac{101}{100})\mathbf{x}_1(t)$ is designed based on its linearization of the reduced model. We have a similar result for the behavior of the state vector $\mathbf{x}_1(t)$. Then, we compare the behavior of the output between the full nonlinear system and the reduced model as shown in Figure 9.2. When the time t is large enough, we do not see the difference between the reduced model and the full nonlinear system.

The advantage of reduced model has been emphasized. In the next section, we shall consider a reduced model of the plane Poiseuille flow.

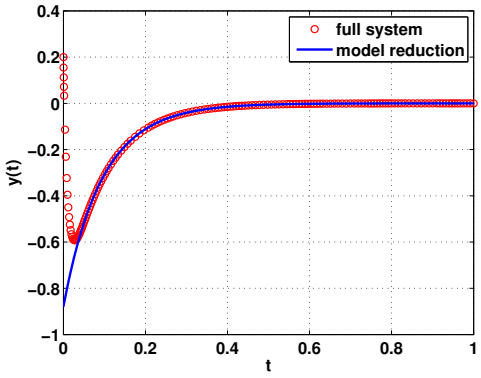

Figure 9.2: Comparison of full nonlinear system and reduced model: behavior of the closed loop system versus time. We have the same result in this case.

9.2 Reduced order of controller

The goal is to ensure

$$\begin{cases} \mathbf{u}(t) & = e^{-\lambda t}\mathbf{u}_0 \\ \varepsilon(t) & \approx e^{-2\lambda t}\varepsilon_0 \end{cases} \tag{9.10}$$

in the closed loop system of the plane Poiseuille flow. In the flow control, the system may be of infinite dimension while the number of **DOF** cannot be increased to infinite dimension. Therefore, the idea is to design a reduced model in which we can use the visual servoing control to obtain a good result of minimizing the kinetic energy density. In [Cortelezzi et al., 1998a], [Cortelezzi and Speyer, 1998], [Cortelezzi et al., 1998b], the Jordan Canonical Form was used to obtain a reduced model and the **LQR** control was applied to stabilize this reduced model. We also use the Truncated Model Order Reduction (**TMOR**) to demonstrate that the visual servoing control can be used for the reduced model.

9.2.1 Design of the reduced model

As shown in previous chapters, we consider the dynamic equation of linearized plane Poiseuille flow

$$\begin{cases} \dot{\mathbf{z}}(t) & = \mathbf{A}_z\mathbf{z}(t) + \mathbf{B}_z\mathbf{u}(t) \\ \varepsilon(t) & = \mathbf{z}^\top(t)\mathbf{Q}_z\mathbf{z}(t) + \mathbf{z}^\top(t)\mathbf{N}_{zu}\mathbf{u}(t) + \mathbf{u}^\top(t)\mathbf{N}_{uz}\mathbf{z}(t) + \mathbf{u}^\top(t)\mathbf{R}_z\mathbf{u}(t) \\ \mathbf{d}(t) & = \mathbf{D}_{z1}\mathbf{z}(t) + \mathbf{D}_{z2}\mathbf{u}(t) \\ \mathbf{z}(0) & = \mathbf{z}_0 \end{cases} \tag{9.11}$$

In order to obtain a reduced model, we only consider

$$\begin{cases} \dot{\mathbf{z}}(t) & = \mathbf{A}_z\mathbf{z}(t) + \mathbf{B}_z\mathbf{u}(t) \\ \varepsilon_z(t) & = \mathbf{z}^\top(t)\mathbf{Q}_z\mathbf{z}(t) \end{cases} \tag{9.12}$$

which is reduced to

$$\begin{cases} \dot{\mathbf{z}}_r(t) & = \mathbf{A}_r\mathbf{z}_r(t) + \mathbf{B}_r\mathbf{u}(t) \\ \varepsilon_r(t) & = \mathbf{z}_r^\top(t)\mathbf{Q}_r\mathbf{z}_r(t) \end{cases} \tag{9.13}$$

where $\mathbf{A}_r$, $\mathbf{B}_r$ and $\mathbf{Q}_r$ will be given in the next step. The system (9.12) is rewritten under the Jordan Canonical Form, it means that $\mathbf{A}_z = \mathbf{V}_z \Lambda \mathbf{V}_z^{-1}$. By using $\mathbf{w}(t) = \mathbf{V}_z^{-1}\mathbf{z}(t)$, the Jordan Canonical Form is given by

$$\dot{\mathbf{w}}(t) = \Lambda \mathbf{w}(t) + \mathbf{V}_z^{-1}\mathbf{B}_z \mathbf{u}(t) \tag{9.14}$$

We denote $\mathbf{w}(t) = \left[\begin{array}{cc} \mathbf{z}_r^\top(t) & \mathbf{z}_{n-r}^\top(t) \end{array} \right]^\top$ where $\mathbf{z}_r(t)$ is the state vector of the reduced model and $\mathbf{B}_{r,m}$ only contains r first rows of $\mathbf{V}_z^{-1}\mathbf{B}_z$ as following

$$\mathbf{V}_z^{-1}\mathbf{B}_z = \left[\begin{array}{c} \mathbf{B}_{r,m} \\ \mathbf{B}_{n-r,m} \end{array} \right] \tag{9.15}$$

Next, we define $\mathbf{Q}_{r,r}$ which only contains contains r first rows and columns of $\mathbf{V}_z^\top \mathbf{Q}_z \mathbf{V}_z$,

$$\mathbf{V}_z^\top \mathbf{Q}_z \mathbf{V}_z = \left[\begin{array}{cc} \mathbf{Q}_{r,r} & \mathbf{Q}_{n-r,r} \\ \mathbf{Q}_{n-r,r} & \mathbf{Q}_{n-r,n-r} \end{array} \right], \tag{9.16}$$

this matrix is need to design a **LQR** control. Therefore, (9.14) is rewritten by

$$\left\{ \begin{array}{ll} \left[\begin{array}{c} \dot{\mathbf{z}}_r(t) \\ \dot{\mathbf{z}}_{n-r}(t) \end{array} \right] & = \left[\begin{array}{cc} \Lambda_r & 0 \\ 0 & \Lambda_{n-r} \end{array} \right] \left[\begin{array}{c} \mathbf{z}_r(t) \\ \mathbf{z}_{n-r}(t) \end{array} \right] + \left[\begin{array}{c} \mathbf{B}_{r,m} \\ \mathbf{B}_{n-r,m} \end{array} \right] \mathbf{u}(t) \\ \varepsilon_z(t) & = \mathbf{z}_r^\top(t)\mathbf{Q}_{r,r}\mathbf{z}_r(t) + \mathbf{z}_r^\top(t)\mathbf{Q}_{r,n-r}\mathbf{z}_{n-r}(t) \\ & \quad + \mathbf{z}_{n-r}^\top(t)\mathbf{Q}_{n-r,r}\mathbf{z}_r(t) + \mathbf{z}_{n-r}^\top(t)\mathbf{Q}_{n-r,n-r}\mathbf{z}_{n-r}(t) \end{array} \right. \tag{9.17}$$

where Λ_{n-r} contains the reduced eigenvalues. Note that Λ_r must contain all positive eigenvalues. By using the **TMOR**, we obtain a reduced model

$$\left\{ \begin{array}{ll} \dot{\mathbf{z}}_r(t) & = \Lambda_r \mathbf{w}(t) + \mathbf{B}_{r,m}\mathbf{u}(t) \\ \varepsilon_r(t) & = \mathbf{z}_r^\top(t)\mathbf{Q}_{r,r}\mathbf{z}_r(t) \end{array} \right. \tag{9.18}$$

We design a control law $\mathbf{u}(t) = \mathbf{K}_r \mathbf{z}_r(t)$ based on the system (9.18) for the system (9.11). By comparing (9.13) and (9.18), we get $\mathbf{A}_r = \Lambda_r$, $\mathbf{B}_r = \mathbf{B}_{r,m}$ and $\mathbf{Q}_r = \mathbf{Q}_{r,r}$.

In order to ensure $\mathbf{u} = e^{-\lambda t}\mathbf{u}_0$, the visual servoing control will be used in the next section.

9.2.2 Desired performance

We consider here a state feedback control $\mathbf{u}(t) = \mathbf{K}_r \mathbf{z}_r(t)$, and suppose that this control law is able to achieve an exponential decoupled decrease of the state vector $\mathbf{z}_r(t)$, that is

$$\dot{\mathbf{z}}_r(t) = -\lambda \mathbf{z}_r(t) \tag{9.19}$$

Therefore, we have

$$\dot{\mathbf{u}}(t) = \mathbf{K}_r \dot{\mathbf{z}}_r(t) = -\lambda \mathbf{K}_r \mathbf{z}_r(t) = -\lambda \mathbf{u}(t) \tag{9.20}$$

9.2.3 Design of the control law

We recall the dynamic equation of the error given by

$$\dot{\mathbf{e}}_r(t) = \frac{\partial \mathbf{e}_r(t)}{\partial t} + \mathbf{L}_{\mathbf{e}_r}(t)\mathbf{u}(t) \tag{9.21}$$

In order to stabilize the state vector $\mathbf{z}_r(t)$ by an exponential decrease, the state vector is chosen to be the visual feature $\mathbf{z}_r(t) = \mathbf{s}(t)$. By comparing (9.18) and (9.21), we get

$$\begin{cases} \mathbf{L}_{\mathbf{e}_r}(t) & = \mathbf{B}_{r,m} \\ \dfrac{\partial \mathbf{e}_r(t)}{\partial t} & = \Lambda_r \mathbf{z}_r(t). \end{cases} \tag{9.22}$$

If we would like for instance to try to ensure an exponential decoupled decrease of the error

$$\dot{\mathbf{e}}_r(t) = -\lambda \mathbf{e}_r(t). \tag{9.23}$$

If $\mathbf{L}_{\mathbf{e}_r}$ were a square and invertible matrix, the control law could be

$$\mathbf{u}(t) = -\lambda \mathbf{L}_{\mathbf{e}_r}^{-1}(t)\mathbf{e}_r(t) - \mathbf{L}_{\mathbf{e}_r}^{-1}(t)\frac{\partial \mathbf{e}_r(t)}{\partial t}. \tag{9.24}$$

In this case, the control law can be rewritten by $\mathbf{u}(t) = \mathbf{K}_r \mathbf{z}_r(t)$ where

$$\mathbf{K}_r = -\mathbf{L}_{\mathbf{e}_r}^{-1}(t)(\lambda \mathbf{I}_r + \Lambda_r) \tag{9.25}$$

9.2.4 Behavior of the closed loop system

9.2.4.1 Stability analysis

However, our goal is to study the behavior of the closed loop system of (9.11) with the control gain $\mathbf{K}_r$ which is designed on the reduced model (9.18). The control law is $\mathbf{u}(t) = \mathbf{K}_r \begin{bmatrix} \mathbf{I}_r & [0]_{r,n-r} \end{bmatrix} \mathbf{V}_z^{-1}\mathbf{z}(t)$ and the closed loop system is given as following

$$\begin{cases} \begin{bmatrix} \dot{\mathbf{z}}_r(t) \\ \dot{\mathbf{z}}_{n-r}(t) \end{bmatrix} & = \begin{bmatrix} \Lambda_r + \mathbf{B}_{r,m}\mathbf{K}_r & 0 \\ \mathbf{B}_{n-r,m}\mathbf{K}_r & \Lambda_{n-r} \end{bmatrix} \begin{bmatrix} \mathbf{z}_r(t) \\ \mathbf{z}_{n-r}(t) \end{bmatrix} \\ \mathbf{K} & = \mathbf{K}_r \begin{bmatrix} \mathbf{I}_r & [0]_{r,n-r} \end{bmatrix} \mathbf{V}_z^{-1} \\ \varepsilon(t) & = \mathbf{z}^\top(t)(\mathbf{Q}_z + \mathbf{K}^\top \mathbf{N}_{uz} + \mathbf{N}_{zu}\mathbf{K} + \mathbf{K}^\top \mathbf{R}_z \mathbf{K})\mathbf{z}(t) \end{cases} \tag{9.26}$$

We must consider the stability of (9.26). To do this, we only need to consider the equation

$$\begin{bmatrix} \dot{\mathbf{z}}_r(t) \\ \dot{\mathbf{z}}_{n-r}(t) \end{bmatrix} = \begin{bmatrix} \Lambda_r + \mathbf{B}_{r,m}\mathbf{K}_r & 0 \\ \mathbf{B}_{n-r,m}\mathbf{K}_r & \Lambda_{n-r} \end{bmatrix} \begin{bmatrix} \mathbf{z}_r(t) \\ \mathbf{z}_{n-r}(t) \end{bmatrix} \tag{9.27}$$

We know that $\Lambda_r + \mathbf{B}_{r,m}\mathbf{K}_r$ and Λ_{n-r} are stable, therefore the system (9.26) also becomes stable. Although the control law is designed based on the reduced model but the full system is always stable. Indeed, the stability of (9.26) is always guaranteed.

The closed loop system of the plane Poiseuille flow is rewritten by

$$\begin{cases} \mathbf{K} & = \mathbf{K}_r \begin{bmatrix} \mathbf{I}_r & [0]_{r,n-r} \end{bmatrix} \mathbf{V}_z^{-1} \\ \mathbf{u}(t) & = \mathbf{K}\mathbf{z}(t) \\ \dot{\mathbf{z}}(t) & = \mathbf{A}_z \mathbf{z}(t) + \mathbf{B}_z \mathbf{u}(t) \\ \varepsilon(t) & = \mathbf{z}^\top(t)(\mathbf{Q}_z + \mathbf{K}^\top \mathbf{N}_{uz} + \mathbf{N}_{zu}\mathbf{K} + \mathbf{K}^\top \mathbf{R}_z \mathbf{K})\mathbf{z}(t) \end{cases} \tag{9.28}$$

9.2.4.2 Visual servoing control

Since $\mathbf{L}_{\mathbf{e}_r}^{-1}(t) = \mathbf{B}_{r,m}^{-1}$ exists ($\mathbf{B}_{r,m}$ has full rank), we use the visual servoing control based on the reduced model (9.18), we obtain the closed loop system

$$\begin{cases} \mathbf{K}_r & = -\mathbf{B}_{r,m}^{-1}(\lambda \mathbf{I}_r + \Lambda_r) \\ \dot{\mathbf{z}}_r(t) & = -\lambda \mathbf{z}_r(t) \\ \mathbf{u}(t) & = \mathbf{K}_r \mathbf{z}_r(t) \\ \dot{\mathbf{z}}_{n-r}(t) & = \mathbf{B}_{n-r,m}\mathbf{K}_r \mathbf{z}_r(t) + \Lambda_{n-r}\mathbf{z}_{n-r}(t) \end{cases} \tag{9.29}$$

And the behavior of the state vector is

$$\begin{cases} \mathbf{z}_r(t) & = e^{-\lambda t}\mathbf{z}_{r,0} \\ \mathbf{z}_{n-r}(t) & = -\dfrac{1}{\lambda}\mathbf{B}_{n-r,m}\mathbf{K}_r e^{-\lambda t}\mathbf{z}_{r,0} + e^{\Lambda_{n-r}t}\mathbf{z}_{n-r,0} \end{cases} \tag{9.30}$$

where $\mathbf{z}_{r,0}$ and $\mathbf{z}_{n-r,0}$ are the initial conditions of $\mathbf{z}_r(t)$ and $\mathbf{z}_{n-r}(t)$, respectively. It is very interesting that $\mathbf{z}_r(t)$ has an exponential decrease, the control signal $\mathbf{u}(t) = \mathbf{K}_r\mathbf{z}_r(t)$ also has an exponential decrease.

Moreover, the kinetic energy density and the skin friction drag are given by

$$\begin{cases} \mathbf{z}(t) & = \mathbf{V}_z \begin{bmatrix} \mathbf{z}_r(t) \\ \mathbf{z}_{n-r}(t) \end{bmatrix} \\ \mathbf{K} & = \mathbf{K}_r \begin{bmatrix} \mathbf{I}_r & [0]_{r,n-r} \end{bmatrix} \mathbf{V}_z^{-1} \\ \varepsilon(t) & = \mathbf{z}^\top(t)(\mathbf{Q}_z + \mathbf{K}^\top \mathbf{N}_{uz} + \mathbf{N}_{zu}\mathbf{K} + \mathbf{K}^\top \mathbf{R}_z \mathbf{K})\mathbf{z}(t) \\ \mathbf{d}(t) & = (\mathbf{D}_1 + \mathbf{D}_1\mathbf{L}^{-1}\mathbf{E}\mathbf{K} + \mathbf{D}_2\mathbf{K})\mathbf{z} \end{cases} \tag{9.31}$$

The behavior of the kinetic energy density is given by

$$\begin{aligned} \varepsilon(t) & = \mathbf{z}^\top(t)(\mathbf{Q}_z + \mathbf{K}^\top \mathbf{N}_{uz} + \mathbf{N}_{zu}\mathbf{K} + \mathbf{K}^\top \mathbf{R}_z \mathbf{K})\mathbf{z}(t) \\ & = \begin{bmatrix} \mathbf{z}_r(t) \\ \mathbf{z}_{n-r}(t) \end{bmatrix}^\top \mathbf{V}_z^\top \left(\mathbf{Q}_z + \mathbf{K}^\top \mathbf{N}_{uz} + \mathbf{N}_{zu}\mathbf{K} + \mathbf{K}^\top \mathbf{R}_z \mathbf{K}\right) \mathbf{V}_z \begin{bmatrix} \mathbf{z}_r(t) \\ \mathbf{z}_{n-r}(t) \end{bmatrix} \end{aligned} \tag{9.32}$$

We denote

$$\begin{bmatrix} \mathbf{P}_{r,r} & \mathbf{P}_{r,n-r} \\ \mathbf{P}_{n-r,r} & \mathbf{P}_{n-r,n-r} \end{bmatrix} = \mathbf{V}_z^\top(\mathbf{Q}_z + \mathbf{K}^\top \mathbf{N}_{uz} + \mathbf{N}_{zu}\mathbf{K} + \mathbf{K}^\top \mathbf{R}_z \mathbf{K})\mathbf{V}_z \tag{9.33}$$

Therefore, the behavior of the kinetic energy density is rewritten as

$$\begin{aligned} \varepsilon(t) & = \begin{bmatrix} \mathbf{z}_r(t) \\ \mathbf{z}_{n-r}(t) \end{bmatrix}^\top \begin{bmatrix} \mathbf{P}_{r,r} & \mathbf{P}_{r,n-r} \\ \mathbf{P}_{n-r,r} & \mathbf{P}_{n-r,n-r} \end{bmatrix} \begin{bmatrix} \mathbf{z}_r(t) \\ \mathbf{z}_{n-r}(t) \end{bmatrix} \\ & = \mathbf{z}_r^\top(t)\mathbf{P}_{r,r}\mathbf{z}_r(t) + \mathbf{z}_r^\top(t)\mathbf{P}_{r,n-r}\mathbf{z}_{n-r}(t) + \mathbf{z}_{n-r}^\top(t)\mathbf{P}_{n-r,r}\mathbf{z}_r(t) \\ & + \mathbf{z}_{n-r}^\top(t)\mathbf{P}_{n-r,n-r}\mathbf{z}_{n-r}(t) \\ & = \mathbf{z}_{r,0}^\top e^{-\lambda t}(\mathbf{P}_{r,r} - \frac{1}{\lambda}\mathbf{P}_{r,n-r}\mathbf{B}_{n-r,m}\mathbf{K}_r - \frac{1}{\lambda}\mathbf{K}_r^\top \mathbf{B}_{n-r,m}^\top \mathbf{P}_{n-r,r} \\ & + \frac{1}{\lambda^2}\mathbf{K}_r^\top \mathbf{B}_{n-r,m}^\top \mathbf{P}_{n-r,n-r}\mathbf{B}_{n-r,m}\mathbf{K}_r)e^{-\lambda t}\mathbf{z}_{r,0} \\ & + \mathbf{z}_{r,0}^\top e^{-\lambda t}(\mathbf{P}_{r,n-r} - \frac{1}{\lambda}\mathbf{K}_r^\top \mathbf{B}_{n-r,m}^\top \mathbf{P}_{n-r,n-r})e^{\Lambda_{n-r}t}\mathbf{z}_{n-r,0} \\ & + \mathbf{z}_{n-r,0}^\top e^{\Lambda_{n-r}t}(\mathbf{P}_{n-r,r} - \frac{1}{\lambda}\mathbf{P}_{n-r,n-r}\mathbf{B}_{n-r,m}\mathbf{K}_r)e^{-\lambda t}\mathbf{z}_{r,0} \\ & + \mathbf{z}_{n-r,0}^\top e^{\Lambda_{n-r}t}\mathbf{P}_{n-r,n-r}e^{\Lambda_{n-r}t}\mathbf{z}_{n-r,0} \end{aligned} \tag{9.34}$$

When r is large enough, we obtain

$$\begin{aligned}
&\mathbf{z}_{r,0}^{\top}e^{-\lambda t}(\mathbf{P}_{r,r}-\frac{1}{\lambda}\mathbf{P}_{r,n-r}\mathbf{B}_{n-r,m}\mathbf{K}_r-\frac{1}{\lambda}\mathbf{K}_r^{\top}\mathbf{B}_{n-r,m}^{\top}\mathbf{P}_{n-r,r}\\
&+\frac{1}{\lambda^2}\mathbf{K}_r^{\top}\mathbf{B}_{n-r,m}^{\top}\mathbf{P}_{n-r,n-r}\mathbf{B}_{n-r,m}\mathbf{K}_r)e^{-\lambda t}\mathbf{z}_{r,0}\\
&>>\mathbf{z}_{r,0}^{\top}e^{-\lambda t}(\mathbf{P}_{r,n-r}-\frac{1}{\lambda}\mathbf{K}_r^{\top}\mathbf{B}_{n-r,m}^{\top}\mathbf{P}_{n-r,n-r})e^{\Lambda_{n-r}t}\mathbf{z}_{n-r,0}\\
&+\mathbf{z}_{n-r,0}^{\top}e^{\Lambda_{n-r}t}(\mathbf{P}_{n-r,r}-\frac{1}{\lambda}\mathbf{P}_{n-r,n-r}\mathbf{B}_{n-r,m}\mathbf{K}_r)e^{-\lambda t}\mathbf{z}_{r,0}\\
&+\mathbf{z}_{n-r,0}^{\top}e^{\Lambda_{n-r}t}\mathbf{P}_{n-r,n-r}e^{\Lambda_{n-r}t}\mathbf{z}_{n-r,0}
\end{aligned}\tag{9.35}$$

The kinetic energy density is approximated by

$$\begin{aligned}
\varepsilon(t)\quad&\approx\mathbf{z}_{r,0}^{\top}e^{-\lambda t}(\mathbf{P}_{r,r}-\frac{1}{\lambda}\mathbf{P}_{r,n-r}\mathbf{B}_{n-r,m}\mathbf{K}_r-\frac{1}{\lambda}\mathbf{K}_r^{\top}\mathbf{B}_{n-r,m}^{\top}\mathbf{P}_{n-r,r}\\
&+\frac{1}{\lambda^2}\mathbf{K}_r^{\top}\mathbf{B}_{n-r,m}^{\top}\mathbf{P}_{n-r,n-r}\mathbf{B}_{n-r,m}\mathbf{K}_r)e^{-\lambda t}\mathbf{z}_{r,0}
\end{aligned}\tag{9.36}$$

Therefore, the kinetic energy density has an approximation of the exponential decrease

$$\varepsilon(t)\quad\approx e^{-2\lambda t}\varepsilon_0\tag{9.37}$$

where we denote

$$\begin{aligned}
\varepsilon_0\quad&=\mathbf{z}_{r,0}^{\top}(\mathbf{P}_{r,r}-\tfrac{1}{\lambda}\mathbf{P}_{r,n-r}\mathbf{B}_{n-r,m}\mathbf{K}_r-\tfrac{1}{\lambda}\mathbf{K}_r^{\top}\mathbf{B}_{n-r,m}^{\top}\mathbf{P}_{n-r,r}\\
&+\frac{1}{\lambda^2}\mathbf{K}_r^{\top}\mathbf{B}_{n-r,m}^{\top}\mathbf{P}_{n-r,n-r}\mathbf{B}_{n-r,m}\mathbf{K}_r)\mathbf{z}_{r,0}
\end{aligned}\tag{9.38}$$

Indeed, we obtain $\varepsilon(t)\approx e^{-2\lambda t}\varepsilon_0$ when r is large enough, the similar result for the skin friction drag. Generally, the kinetic energy density and the skin friction drag almost have an exponential decrease when r is large enough.

9.2.4.3 Influence of the control signal on the kinetic energy density

In the previous section, we showed that it is possible to minimises the kinetic energy density if r is large enough. We could still have a good result if r were small ? In order to assure that the kinetic energy density has an approximation of the exponential decrease when we use the visual servoing control. We shall study the influence of the control signal on the kinetic energy density in order to give a good choice of the functions $f_{v,l}(y)$, $f_{v,u}(y)$, $f_{\eta,u}(y)$ and $f_{\eta,l}(y)$ and the parameter λ.

As well known, the kinetic energy density is a combination of the state vector energy and the control energy

$$\varepsilon(t)=\mathbf{z}^{\top}(t)\mathbf{Q}_z\mathbf{z}(t)+\mathbf{z}^{\top}(t)\mathbf{N}_{zu}\mathbf{u}(t)+\mathbf{u}^{\top}(t)\mathbf{N}_{uz}\mathbf{z}(t)+\mathbf{u}^{\top}(t)\mathbf{R}_z\mathbf{u}(t)\tag{9.39}$$

where $\mathbf{N}_{uz}$, $\mathbf{N}_{zu}$ and $\mathbf{R}_z$ are constructed from the functions $f_{v,l}(y)$, $f_{v,u}(y)$, $f_{\eta,u}(y)$ and $f_{\eta,l}(y)$.

We recall that the flow is monotonically stable if

$$\dot{\varepsilon}(t)\leq 0\tag{9.40}$$

Generally, if $\varepsilon(t) \approx \mathbf{u}^\top(t)\mathbf{R}_z\mathbf{u}(t)$, it is easy to see that

$$\dot{\varepsilon}(t) \approx 2\mathbf{u}^\top(t)\mathbf{R}_z\dot{\mathbf{u}}(t) \tag{9.41}$$

By using the visual servoing control based on the reduced model, we can give

$$\dot{\varepsilon}(t) \approx 2\mathbf{u}^\top(t)\mathbf{R}_z\dot{\mathbf{u}}(t) = -2\lambda\mathbf{u}^\top(t)\mathbf{R}_z\mathbf{u}(t) \approx -2\lambda\varepsilon(t) \Rightarrow \varepsilon(t) \approx e^{-2\lambda t}\varepsilon_0 \tag{9.42}$$

We always obtain a nice result of $\varepsilon(t)$ if $\varepsilon(t) \approx \mathbf{u}^\top(t)\mathbf{R}_z\mathbf{u}(t)$ even for small r.

We conclude that the kinetic energy density has an approximation of the exponential decrease when r is large enough. If r is not large enough, we shall have $\varepsilon(t) \approx \mathbf{u}^\top(t)\mathbf{R}_z\mathbf{u}(t)$.

We shall give the simulation result to validate our proposed control approach in the next section.

9.3 Simulation Result

We use both **LQR** control and visual servoing control to validate our approach. We recall that the synchronic transient energy growth is the maximum value of the kinetic energy density over time. If the synchronic transient energy has an exponential decrease, all kinetic energy density will have an exponential decrease. We only consider small value of r (for large value of r, see Appendix D).

9.3.1 Reduced model

In this section, we consider the behavior of the uncontrolled flow. We compare between the reduced model $\varepsilon_r(t)$ and the full model $\varepsilon(t)$ ($\varepsilon(t) = \varepsilon_z(t)$ in this case).

9.3.1.1 2D plane Poiseuille flow

In the case of $\alpha = 1$, $\beta = 0$ and $R = 10\,000$, for $N = 50$, we have $n = 94$. The initial condition is the worst initial condition. Figures 9.3 shows the behavior of $\varepsilon_r(t)$ and $\varepsilon(t)$. Because we use **TMOR** method to obtain the reduced model, when the time is large enough ($t > 40$ for $r = 2, 3, 4$; $t > 6$ for $r = 37$; and $t \approx 0$ for $r > 45$), the behavior of reduced model is equivalent to the behavior of the full system. Moreover, **TMOR** method obtains a good reduced model with only $r = 2$. It means that the reduced model

$$\Lambda_2 = \begin{bmatrix} 0.00373 + j0.23752 & 0 \\ 0 & 0.00373 - j0.23752 \end{bmatrix} \tag{9.43}$$

can almost capture the kinetic energy density in the uncontrolled flow. Note that $\Lambda_1 = 0.00373 + j0.23752$ is not good enough because this reduced model does not contains all positive eigenvalues. In the 2D plane Poiseuille flow, we only need the reduced model Λ_2 which captures the behavior of unstable modes of the system.

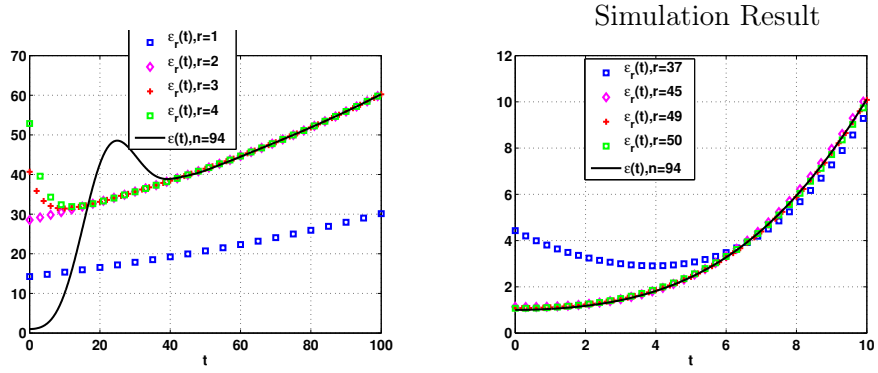

Figure 9.3: Comparison of the reduced model ($\varepsilon_r(t)$) with r states and the full model ($\varepsilon(t)$) with n states: behavior of the kinetic energy densitys $\varepsilon_r(t)$ and $\varepsilon(t)$ versus time.

9.3.1.2 3D plane Poiseuille flow

In the case of $\alpha = 0$, $\beta = 2.044$ and $R = 5\ 000$, for $N = 50$, we have $n = 96$. As the 2D plane Poiseuille flow, Figure 9.4 shows the behavior of $\varepsilon_r(t)$ and $\varepsilon(t)$. This result allows

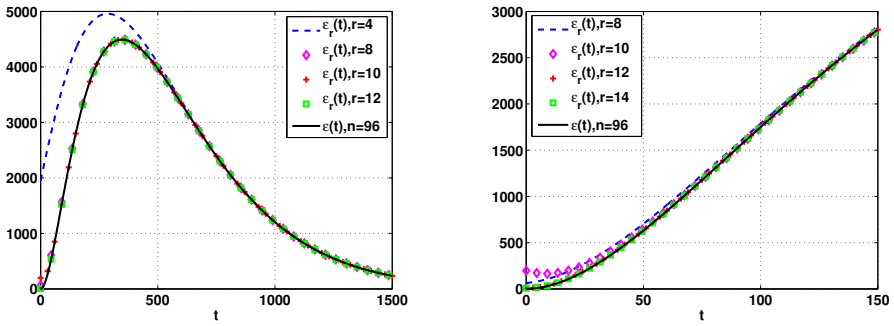

Figure 9.4: Comparison of the reduced model ($\varepsilon_r(t)$) with r states and the full model ($\varepsilon(t)$) with n states: behavior of the kinetic energy densitys $\varepsilon_r(t)$ and $\varepsilon(t)$ versus time.

us to ensure that we only need the reduced model Λ_8 which can capture the behavior of full system

$$\Lambda_8 = \begin{bmatrix} -0.0013 & 0 & \cdots & 0 \\ 0 & -0.0021 & & \vdots \\ \vdots & & \ddots & 0 \\ 0 & \cdots & 0 & -0.0123 \end{bmatrix} \tag{9.44}$$

The above reduced order models will be used for controller design. In the next section, results for **LQR** control are presented.

9.3.2 LQR control

In this section, we use **LQR** control to demonstrate that the control law can be designed based on the reduced model for the full system. Therefore, we consider here a state

feedback control law

$$\mathbf{u}(t) = \mathbf{K}_r \left[\begin{array}{cc} \mathbf{I}_r & [0]_{r,n-r} \end{array} \right] \mathbf{V}_z^{-1} \mathbf{z}(t) = \mathbf{K}_r \mathbf{z}_r(t). \tag{9.45}$$

In order to minimize the kinetic energy density $\varepsilon_r(t)$ and the energy combustion of actuators, a **LQR** control scheme over an infinite time horizon is used by considering the following cost function

$$J = \int_0^\infty (\mathbf{z}_r^\top(t)\mathbf{Q}_r\mathbf{z}_r(t) + \gamma^2 \mathbf{u}^\top(t)\mathbf{u}(t))dt. \tag{9.46}$$

Thereafter, the **LQR** gain $\mathbf{K}_r$ involved in the optimal control $\mathbf{u}(t) = \mathbf{K}_r\mathbf{z}_r(t)$ is computed taking into account (9.18) and solving the Algebraic Ricatti Equation (see **LQR** control for more details). The gain $\mathbf{K}_r$ is given by

$$\mathbf{K}_r = -\frac{1}{\gamma^2}\mathbf{B}_r^\top \mathbf{P}, \tag{9.47}$$

where $\mathbf{P}$ is the solution of the Algebraic Ricatti Equation

$$\mathbf{A}_r^\top \mathbf{P} + \mathbf{P}\mathbf{A}_r + \mathbf{Q}_r - \frac{1}{\gamma^2}\mathbf{P}\mathbf{B}_r\mathbf{B}_r^\top \mathbf{P} = 0. \tag{9.48}$$

In Matlab, we can use $\mathbf{K}_r = -lqr(\mathbf{A}_r, \mathbf{B}_r, \mathbf{Q}_r, \gamma^2\mathbf{I})$. Note that we can design a **LQR** control based on the system (9.12), which is $\mathbf{K}_f = -lqr(\mathbf{A}_z, \mathbf{B}_z, \mathbf{Q}_z, \gamma^2\mathbf{I})$. We will compare the behavior of the closed loop system (9.28) with the control law $\mathbf{K} = \mathbf{K}_r \left[\begin{array}{cc} \mathbf{I}_r & [0]_{r,n-r} \end{array} \right] \mathbf{V}_z^{-1}$ and the control law $\mathbf{K}_f$ in the case of **LQR** control.

9.3.2.1 2D plane Poiseuille flow

We use

$$\Lambda_2 = \left[\begin{array}{cc} 0.00373 + j0.23752 & 0 \\ 0 & 0.00373 - j0.23752 \end{array} \right] \tag{9.49}$$

and we only use one **DOF** with $f_{v,l}(y) = \dfrac{y^3 - 3y + 2}{4}$, more precisely, we only use lower boundary $\tilde{q}_{v,l}(t)$. The initial condition is the worst initial condition of the uncontrolled flow. It means that we set similar initial condition for simulation results for $\mathbf{K}_f$ and $\mathbf{K}$. The behavior of the closed loop system is illustrated in Figure 9.5, Figure 9.6 and Figure 9.7 for various choices of γ.

This result shows that we have similar results for both $\mathbf{K}$ and $\mathbf{K}_f$. Indeed, we can use the reduced model (9.18) to design a control law for the system (9.11). Note that, **TMOR** method is to reduce high eigenvalues, therefore the behavior of the system (9.28) is similar for $\mathbf{K}$ and $\mathbf{K}_f$ when t is large enough. When γ decreases, the behavior of the closed loop system (9.28) is improved as shown from Figure 9.5 to Figure 9.7. Although the behavior of the closed loop system is improved since decreasing of γ but the control energy also increases. Therefore, the initial value of kinetic energy density increases.

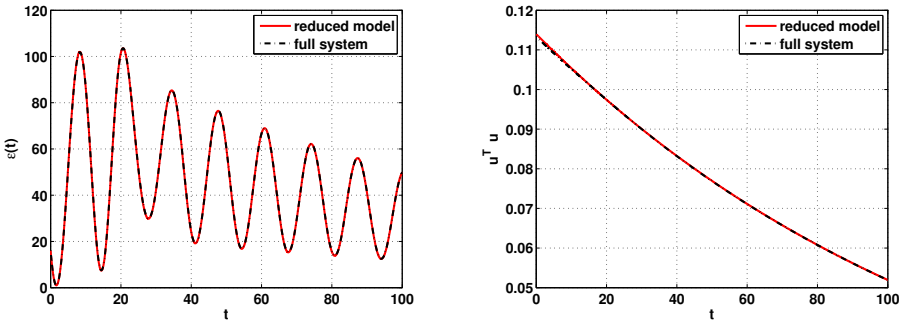

Figure 9.5: Behavior of the closed loop system versus time, $\gamma = 100$.

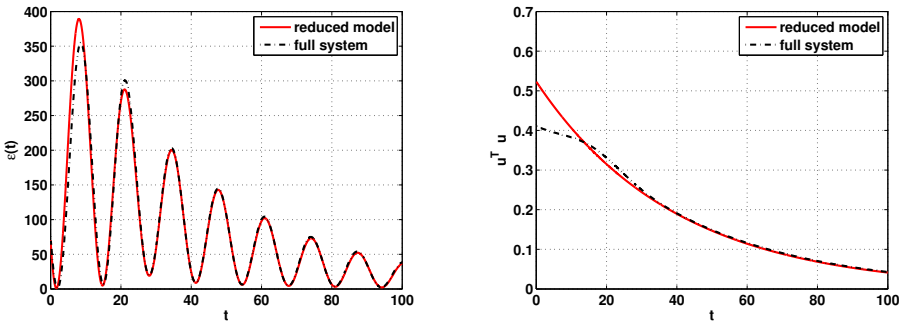

Figure 9.6: Behavior of the closed loop system versus time, $\gamma = 10$.

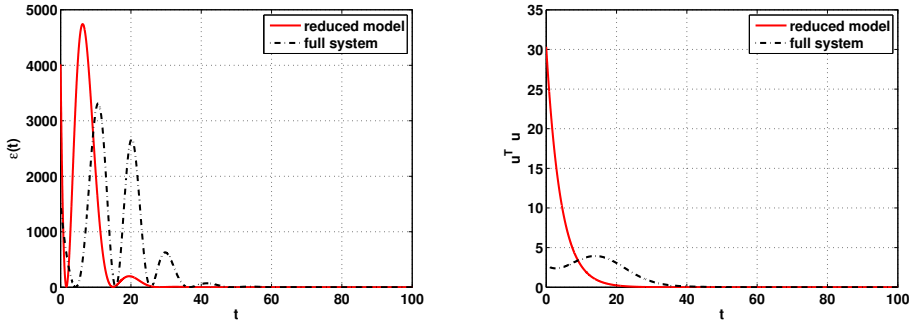

Figure 9.7: Behavior of the closed loop system versus time, $\gamma = 1$.

The kinetic energy density has an approximation of the exponential decrease if $\varepsilon(t) \approx \mathbf{u}^\top(t)\mathbf{R}_z\mathbf{u}(t)$ and $\mathbf{u}(t) = e^{-\lambda t}\mathbf{u}_0$. Therefore, we choose γ to ensure $\varepsilon(t) \approx \mathbf{u}^\top(t)\mathbf{R}_z\mathbf{u}(t)$. When $\gamma = 0.1$, the maximal value of kinetic energy density is the initial value, as shown in Figure 9.8. When $\gamma = 0.01$, the **LQR** control provides a nice result in Figure 9.9. Although $\mathbf{z}^\top(t)\mathbf{Q}_z\mathbf{z}(t)$ does not have an exponential decrease but $\varepsilon(t)$ always behaves like an exponential decrease.

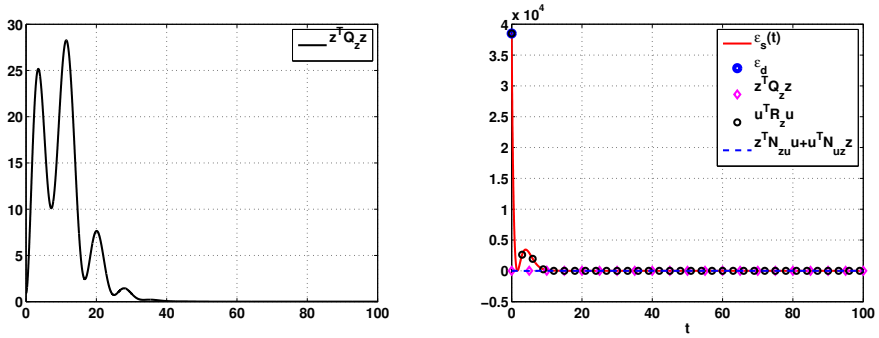

Figure 9.8: Behavior of the closed loop system versus time, $\gamma = 0.1$.

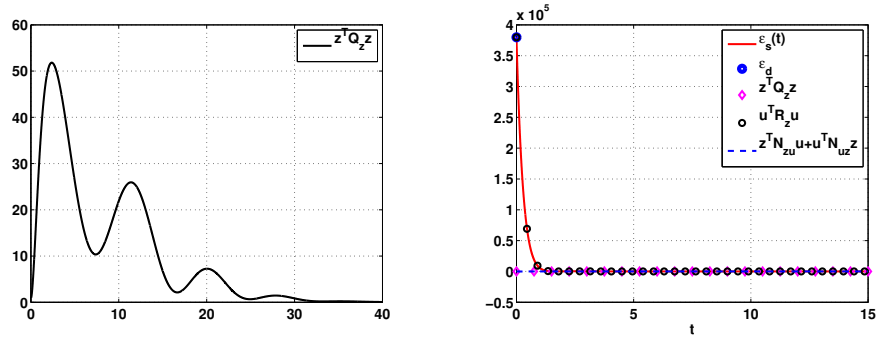

Figure 9.9: Behavior of the closed loop system versus time, $\gamma = 0.01$.

9.3.2.2 3D plane Poiseuille flow

We use two **DOF** in this case with $f_{v,l}(y) = \dfrac{y^3 - 3y + 2}{4}$ and $f_{v,u}(y) = \dfrac{-y^3 + 3y + 2}{4}$ As in the 2D plane Poiseuille flow, Figure 9.10, Figure 9.11 and Figure 9.12 provide a comparison between the control law based on the reduced model and the control law based on the full system. Once again, these results allow us to ensure that we can design a control law based on the reduced model instead of the full system.

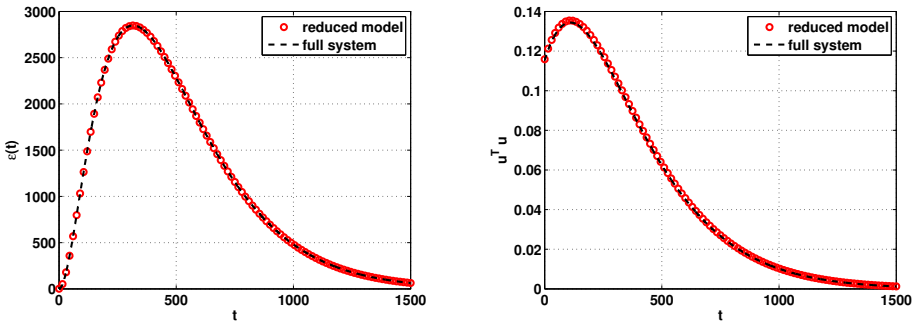

Figure 9.10: Behavior of the closed loop system versus time, $\gamma = 100$.

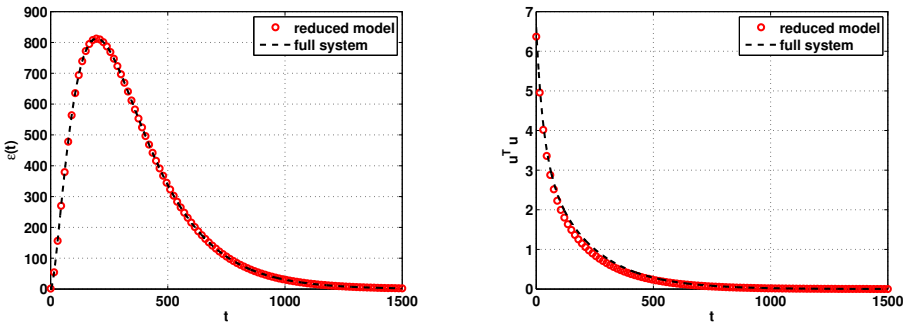

Figure 9.11: Behavior of the closed loop system versus time, $\gamma = 10$.

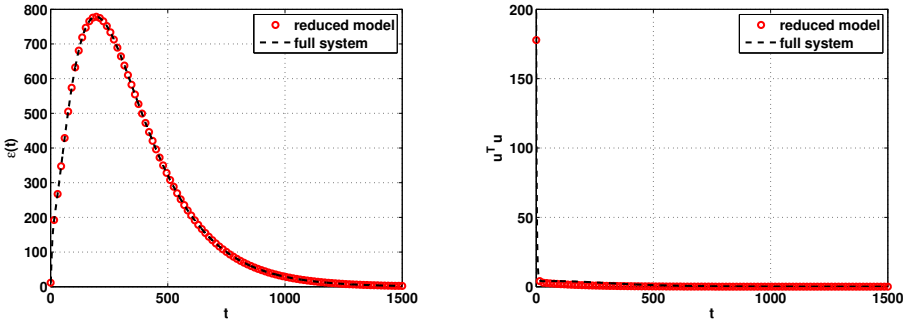

Figure 9.12: Behavior of the closed loop system versus time, $\gamma = 1$.

Note that when $\gamma = 10$, we have $\varepsilon_{max} = 812.4963$. We have a similar result in Chapter 6. And we can get better result in the case of $\gamma = 1$, $\varepsilon_{max} = 778.5630$. This result emphasizes the advantage of the reduced order controller.

We decrease γ to obtain the nice behavior of the kinetic energy density. As expected, Figure 9.13 and Figure 9.14 give a desired result.

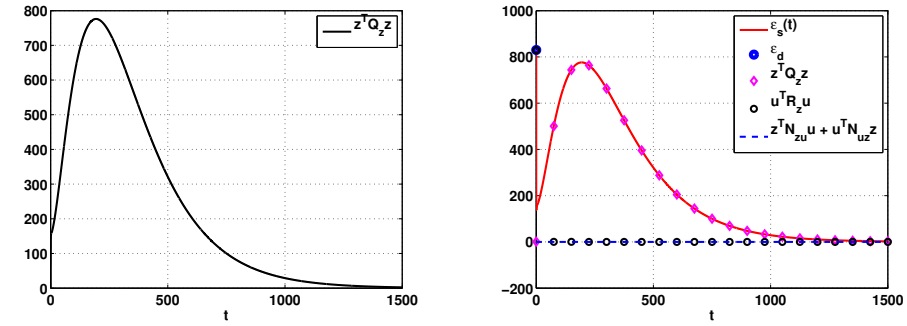

Figure 9.13: Behavior of the closed loop system versus time, $\gamma = 0.1$.

The fact **LQR** control can minimize $\mathbf{u}(t)$ but does not guarantee $\dot{\mathbf{u}}(t) = -\lambda \mathbf{u}(t)$. Therefore, we use the visual servo control in the next section.

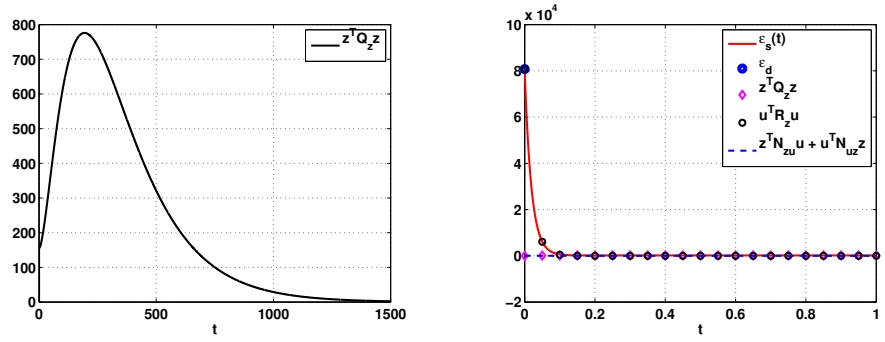

Figure 9.14: Behavior of the closed loop system versus time, $\gamma = 0.01$.

9.3.3 Visual servoing control

9.3.3.1 2D plane Poiseuille flow

One DOF We recall the test case of $\alpha = 1$, $\beta = 0$, $R = 10\ 000$ and $N = 50$. We compare the result between the visual servo control and the **LQR** control. We use $\lambda = 1$ for the visual servo control and the initial condition is the worst initial condition of the uncontrolled flow. Figure 9.15 provides $\varepsilon(t) \approx \mathbf{u}^\top(t)\mathbf{R}_z\mathbf{u}(t)$ and $\mathbf{u}(t) = e^{-\lambda t}\mathbf{u}_0$. As expected, this result is better than the result in Figure 9.9 ($\varepsilon_{max} \approx 5.10^4 < 4.10^5$).

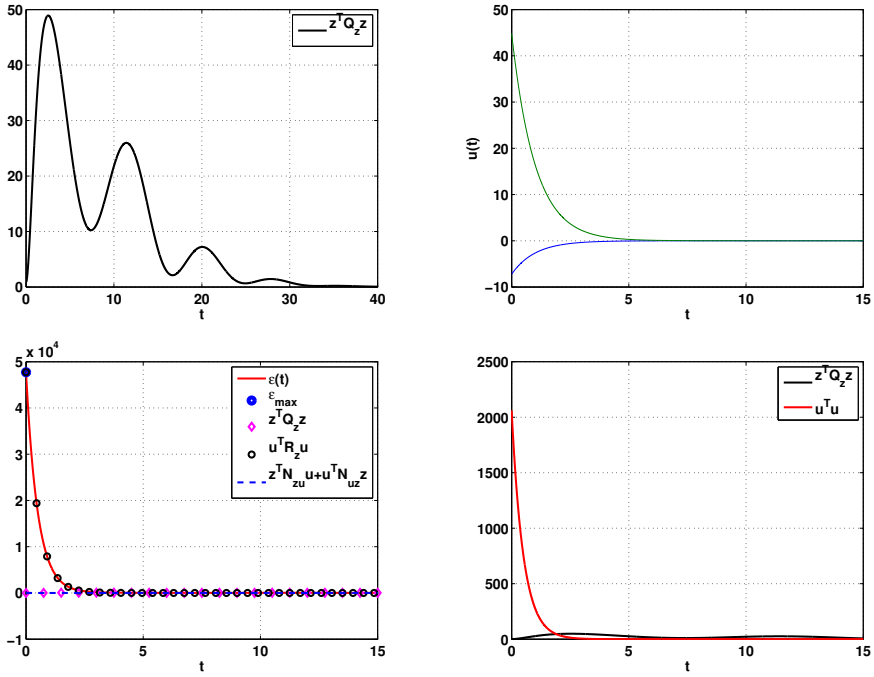

Figure 9.15: Behavior of the closed loop system.

We recall that if the synchronic transient energy has an exponential decrease, all kinetic energy density will have an exponential decrease. Therefore, the initial condition

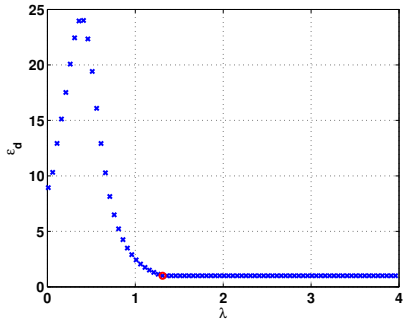

Figure 9.16: Variation of ε_d with respect to the parameter λ of the visual servoing control.

is next chosen as the worst initial condition of the controlled flow. Figure 9.16 shows the behavior of the diachronic transient energy with respect to λ ($\lambda = 0.05 : 0.05 : 4$). When $\lambda > 1.31$, we have $\varepsilon_d = 1$. The diachronic transient energy growth is the initial value of kinetic energy density. This condition is necessary to ensure that the kinetic energy density behaves like an exponential decrease. The behavior of synchronic transient

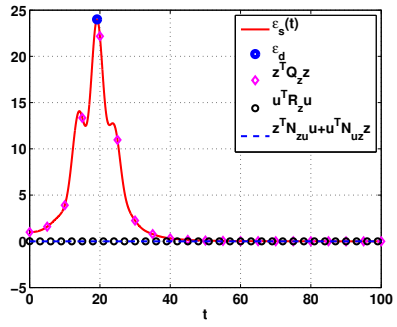

(a) $\lambda = 0.41$

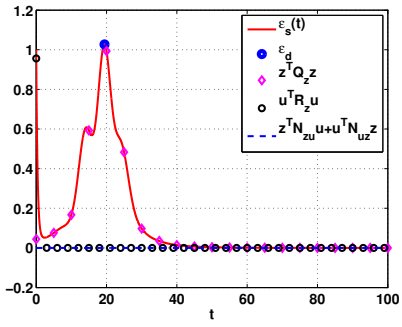

(b) $\lambda = 1.30$

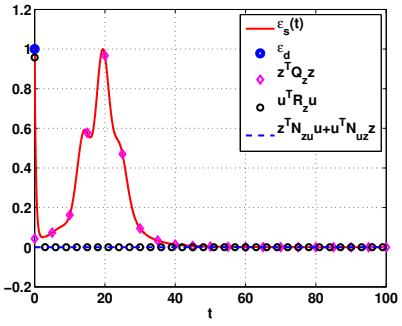

(c) $\lambda = 1.31$

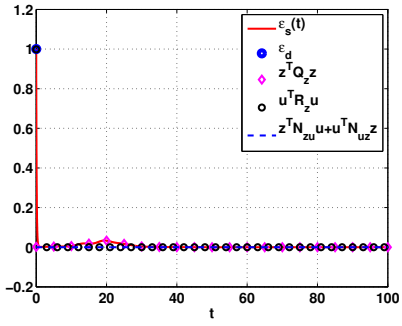

(d) $\lambda = 4$

Figure 9.17: Behavior of the synchronic transient energy versus time for variation of λ.

energy growth is illustrated in Figure 9.17. When $\lambda > 1.31$, we have nice result but we

do not ensure $\varepsilon(t) \approx \mathbf{u}^\top(t)\mathbf{R}_z\mathbf{u}(t)$ at $t = 20$. We use **TMOR**, Λ_4 is always better than Λ_2, therefore we use Λ_4 and two **DOF**.

Two DOF We use Λ_4

$$\Lambda_4 = \begin{bmatrix} 0.00373 + j0.23752 & 0 & 0 & \\ 0 & 0.00373 - j0.23752 & 0 & 0 \\ 0 & 0 & -0.1828 + 0.1901i & 0 \\ 0 & 0 & 0 & -0.1828 - 0.1901i \end{bmatrix} \tag{9.50}$$

and both upper and lower boundaries with

$$\begin{cases} f_{v,l}(y) &= \dfrac{y^3 - 3y + 2}{4} \\ f_{v,u}(y) &= \dfrac{-y^3 + 3y + 2}{4} \end{cases} \tag{9.51}$$

Figure 9.18 shows the behavior of the diachronic transient energy versus λ ($\lambda = 0.05 : 0.05 : 4$). We obtain $\varepsilon_d = 1$ for all λ.It is noted that the Again, we demonstrate the benefits of increasing the number of **DOF**.

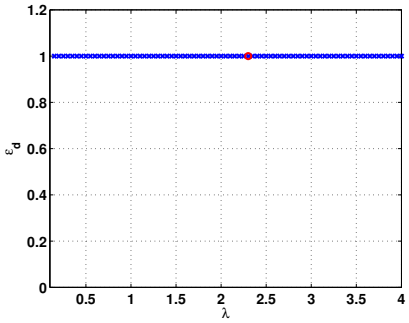

Figure 9.18: Variation of ε_d with respect to the parameter λ of the visual servoing control.

In the next result, we ensure $\varepsilon(t) \approx \mathbf{u}^\top(t)\mathbf{R}_z\mathbf{u}(t)$. We use $\lambda = 0.25$. As expected, Figure 9.19 shows $\varepsilon(t) \approx \mathbf{u}^\top(t)\mathbf{R}_z\mathbf{u}(t)$ and $\mathbf{z}^\top(t)\mathbf{Q}_z\mathbf{z}(t) << \mathbf{u}^\top(t)\mathbf{R}_z\mathbf{u}(t)$. Indeed, we have an interesting result $\mathbf{u}^\top(t)\mathbf{u}(t) << \mathbf{u}^\top(t)\mathbf{R}_z\mathbf{u}(t)$, it means that the influence of the control signal to the flow is larger than the needed control energy. We have desired result with two **DOF** in this case.

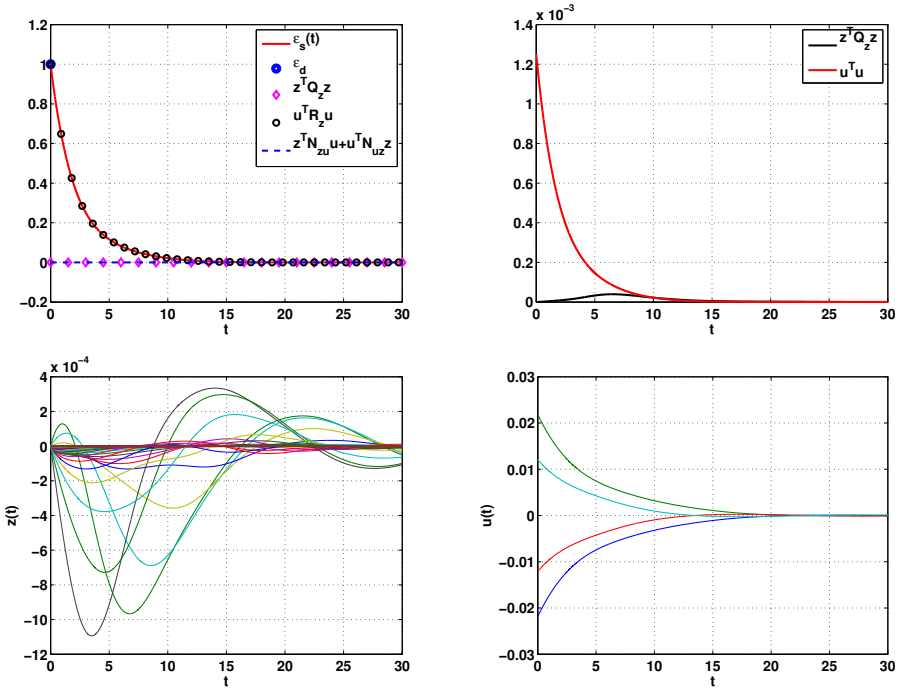

Figure 9.19: Behavior of the closed loop system versus time.

9.3.3.2 3D plane Poiseuille flow

We recall the test case of $\alpha = 0$, $\beta = 2.044$, $R = 5\ 000$ and $N = 50$. We use

$$\Lambda_2 = \begin{bmatrix} -0.0013 & 0 \\ 0 & -0.0021 \end{bmatrix} \tag{9.52}$$

and two **DOF**. As the 2D plane Poiseuille flow, we consider the diachronic transient energy versus the parameter λ in the visual servoing control, as shown in Figure 9.20. When $\lambda \geq 40.5$, we have $\varepsilon_d = 1$. The behavior of the synchronic transient energy is

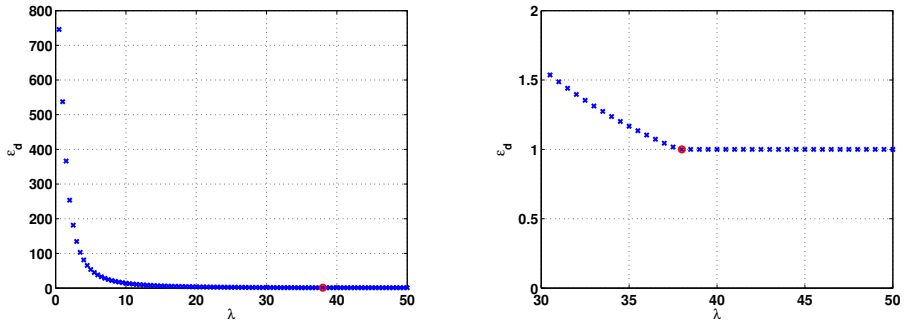

Figure 9.20: ε_d versus λ.

illustrated in Figure 9.21. It improves when we increase the parameter λ.

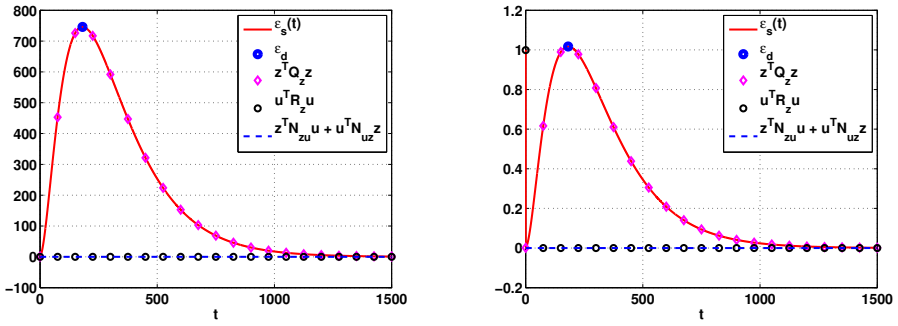

(a) $\lambda = 0.5$ (b) $\lambda = 37.5$

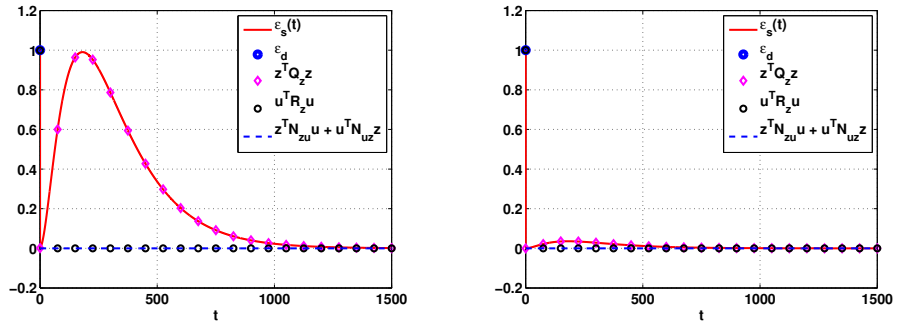

(c) $\lambda = 38$ (d) $\lambda = 200$

Figure 9.21: Behavior of the synchronic transient energy versus time for variation of λ.

We set $\lambda = 250$, the behavior of the closed loop system is given in Figure 9.22. As expected, we have a nice result as in the 2D plane Poiseuille flow.

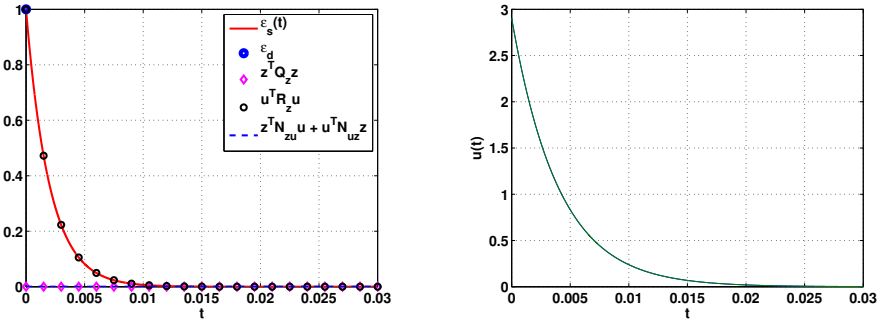

Figure 9.22: Behavior of the closed loop system versus time.

In this section, we have demonstrated that we almost obtain an approximation of the exponential decrease of the kinetic energy density even using two **DOF**, it means that the flow is almost monotonically stable. We recognize that we must give a lot of control energy. In practice, if the condition of control energy is satisfied, the flow could

be almost monotonically stable. However, we still have the problem of nonorthogonality of the plane Poiseuille flow in this case. It means that we do not ensure $\dot{\varepsilon}(t) \leq 0$ because we use the reduced model to design the control law.

9.4 Conclusion

Because the dimension of the linearized plane Poiseuille flow may be very large. Therefore, the problem of the flow control will become very easier when a control law is designed based on a reduced model instead of the full nonlinear system. The result of **LQR** control and visual servoing control allow us to ensure that the good result obtained even using the **TMOD**. Moreover, this chapter obtained a good result of the kinetic energy density when the visual servoing control is designed based on the reduced model. When the number of **DOF** is only equal to the number of the state vector of the reduced model. If the condition of control energy is satisfied, the kinetic energy density behaves like an exponential decrease by applying the visual servoing control even using two **DOF**.

Chapter 10

Conclusions and Future Work

This chapter describes the maiming findings from the work carried out in this thesis, and suggests future work that might be performed.

Conclusions

In this thesis, we have developed feedback controllers that assured the stability of the plane Poiseuille flow from visual information. Several conclusions about the flow control can be drawn.

Chapter 5

The numerical method is not used to generate a state-space model of **PDE**. A linear model is developed by using a spectral collocation method which could transform **PDE** to a set of **ODE**. More precisely, the spectral collocation method with the use of Fourier series in the streamwise and spanwise directions and the Chebyshev polynomials in the wall-normal direction could decouple the modeled system by wavenumber pairs. Therefore it is possible to treat each wavenumber pairs separately.

When the wall-normal velocity vorticity formulation is used, the state vector of the linear model involves the wall-normal velocity and vorticity. Moreover, the skin-friction drag and the kinetic energy density are modeled by a function of the state vector. The control approaches will be designed in order to minimize the skin-fricition drag and the kinetic energy density. Indeed, the skin-friction drag is a linear function of the state vector while the kinetic energy density always is a quadratic function of the state vector.

The plane Poiseuille flow is controlled by boundary conditions. In the controlled flow, the homogeneous Dirichlet boundary conditions become the inhomogeneous Dirichlet boundary conditions, therefore we must use the modified Chebyshev polynomials. We have used McKernan's method [McKernan, 2006] to modify the Chebyshev polynomials and we have obtained a linear model which has no "spurious" modes as Bewley's model [Bewley and Liu, 1998].

We also consider the two test cases. These test cases are usually used in previous works. The first test case is in the 2D plane Poiseuille flow with $\alpha = 1$, $\beta = 0$ and

$R = 10\ 000$, this case illustrates the unstable eigenvalues. While the second test case is in the 3D plane Poiseuille flow with $\alpha = 0$, $\beta = 2.044$ and $R = 5\ 000$, the diachronic transient energy growth reaches its highest value in this test case.

Chapter 6

When the number of the degree of freedom (**DOF**) is two, the partitioned visual servoing control shows a positive result for drag reduction. The skin friction drag has an exponential decrease with one **DOF**. In contrast to the existing controllers, this controller exploited two **DOF** to minimize, simultaneously, the skin friction drag and the kinetic energy density. Indeed, the partitioned visual servoing control only needs one **DOF** to minimize the skin friction drag but more than one **DOF** to minimize the kinetic energy density. This approach is compared to the other approaches: **PID** and **LQR** controls and obtains a better result than them. In contrast to the other approaches, the partitioned visual servoing control not only obtains an exponential decrease of skin friction drag minimization but also directly decides the convergence velocity of skin friction drag minimization.

Chapter 7

Although the kinetic energy density is minimized by the use of two **DOF**, the kinetic energy density does not monotonically decrease in time. Therefore, the stability of the controlled flow needs to be improved. Consequently, the number of **DOF** is increased to improve the stability.

Chapter 7 has shown the way of increasing of the **DOF** based on Joshi's result [Joshi, 1996]. For the 2D plane Poiseuille flow, we only use the wall-normal boundary condition but for the 3D plane Poiseuille flow, we use both the wall-normal boundary condition and the tangential (spanwise or streamwise direction) boundary condition.

When we have more **DOF**, we have more relocated eigenvalues. It means that the component of the state vector is improved, consequently the minimizing of kinetic energy density becomes better. It shows a significant decrease of kinetic energy density as **DOF** increase.

Chapter 8

Chapter 8 aims to answer the question how to obtain the monotonic decrease of kinetic energy density. The idea is to decouple the state vector, therefore the skin friction drag, the kinetic energy density and the components of the velocity have an exponential decoupled decrease. When the number of the state vector is equal to the number of **DOF** and the interaction matrix is a full rank matrix, we use the visual servoing control to obtain an exponential decrease of the state vector. All observed physical quantities also have an exponential decrease such as the components of the velocity, the skin friction drag, the kinetic energy density and the control signal. This result has not been obtained before by other approaches. Furthermore, the visual servoing control not only

obtains an exponential decoupled decrease of the state vector but also directly decides the convergence velocity of minimizing of the state vector.

Chapter 9

The dimension of linearized plane Poiseuille flow is large. Therefore, we usually use a model order reduction method to obtain a smaller dimension model of the linearized plane Poiseuille flow. The design of controller based on the model reduction becomes easier.

In this chapter, the visual servoing control is designed based on the model reduction. Hence, the visual servoing control can be applied to any **DOF** but always ensures the exponential decrease of the control signal. The important result is to demonstrate that if the control energy is satisfied, the behavior of the kinetic energy density in time will have an approximation of the exponential decrease. As a result, the flow may be monotonically stable even using only two **DOF**.

Future Work

In this section, we give future directions

Short Term Work

In Chapter 9, we want to ensure $\dot{\varepsilon}(t) \leq 0$ when the control matrix $\mathbf{B}_z$ is not full rank matrix. Indeed, we have the inequality

$$\begin{aligned}&(\mathbf{A}_z + \mathbf{B}_z\mathbf{K})^\top(\mathbf{Q}_z + \mathbf{K}^\top\mathbf{N}_{uz} + \mathbf{N}_{zu}\mathbf{K} + \mathbf{K}^\top\mathbf{R}_z\mathbf{K})\\ &+(\mathbf{Q}_z + \mathbf{K}^\top\mathbf{N}_{uz} + \mathbf{N}_{zu}\mathbf{K} + \mathbf{K}^\top\mathbf{R}_z\mathbf{K})(\mathbf{A}_z + \mathbf{B}_z\mathbf{K}) \leq 0\end{aligned} \tag{10.1}$$

and it is very difficult to solve this inequality. However, it is a new challenge in the future work. Could we have a solution if the control matrix $\mathbf{B}_z$ were not full rank matrix ? Although the inequality [Whidborne and McKernan, 2007]

$$(\mathbf{A}_z + \mathbf{B}_z\mathbf{K})^\top\mathbf{Q}_z + \mathbf{Q}_z(\mathbf{A}_z + \mathbf{B}_z\mathbf{K}) \leq 0 \tag{10.2}$$

has the solution $\mathbf{K}$, we need the control matrix $\mathbf{B}_z$ to be full rank matrix.

Medium Term Work

As **PID**, **LQR**, **LMI** controls, we shall validate our control approaches to **DNS**. Due to limitation of time and non availability of **DNS**, we have not given the nonlinear results yet. However, an algorithm is proposed to apply the controller in the **DNS**, see Apprendix A. In our case, we use the optical flow to estimate the state vector. Therefore, the state vector is directly calculated based on the velocity in our algorithm.

Long Term Work

The channel flow control is extended to the other flows as the magnetohydrodynamic channel flow ([Xu et al., 2008], [Vazquez et al., 2009]) or the plane channel flow with the temperature ([Pinarbasi and Liakopoulos, 1995]). In the magnetohydrodynamic channel flow, the governing equations of the plane channel flow are a combination of the Navier-Stokes equations and the Maxwell equation, we consider the influence of the magnetohydrodynamic field to the flow. While in the real flow, the motion of the flow depends on the conservation of energy, therefore the temperature needs to be studied. In these flows, the stability does not only depends on the Reynolds number but also depends on the other numbers such as Hartmann number for the magnetohydrodynamic channel flow or Prandtl number for the plane channel flow with heat transfer.

Appendix A

Implementing the Controller in the Navier-Stokes Solver

We can implement the controller in a Navier-Stokes Solver by considering the steps required in outline. The procedure is given in Figure A.1.

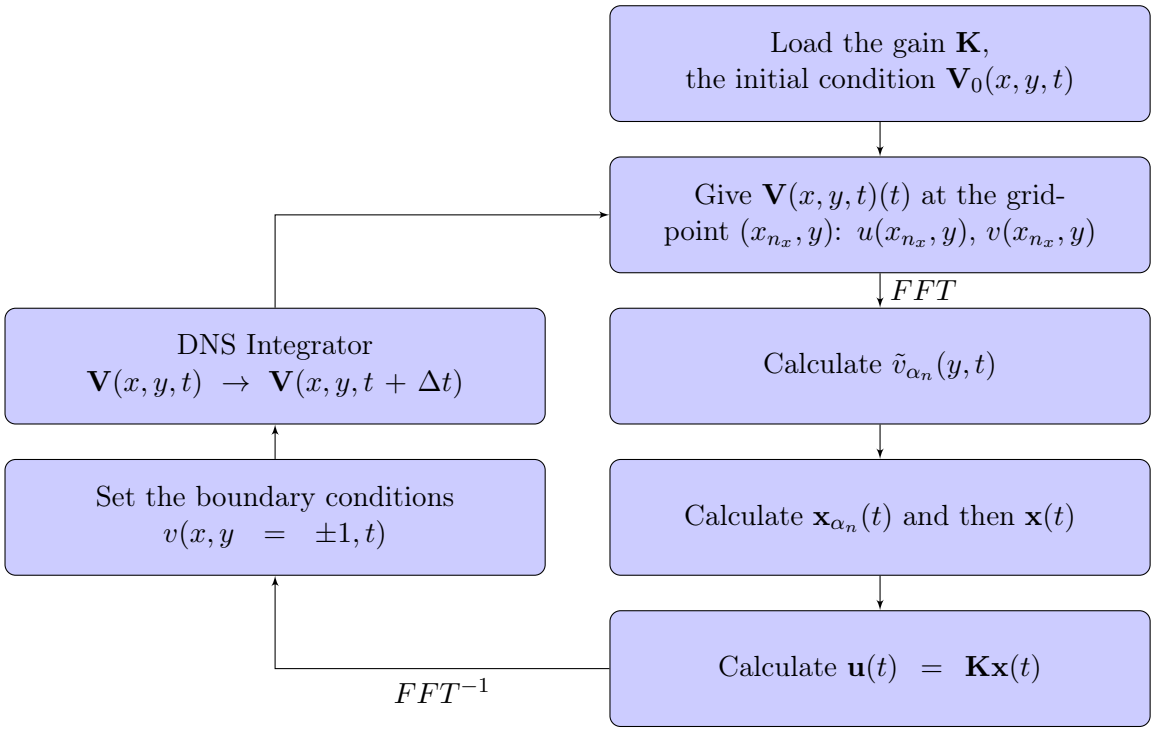

Figure A.1: Implement the controller in DNS solver. FFT is Fast Fourier Transform on x direction.

The steps are presented in the following:

A.1 Beforehan, off-line:

Make a linear model of the system, and generate matrices $\mathbf{L}$, $\mathbf{A}$, $\mathbf{B}$, $\mathbf{E}$, $\mathbf{D}_1$, $\mathbf{D}_2$, $\mathbf{Q}_{11}$, $\mathbf{Q}_{12}$, $\mathbf{Q}_{22}$. All system matrices contain all wavenumber pairs as follow

$$\mathbf{L} = \begin{bmatrix} \mathbf{L}_{\alpha_0} & 0 & 0 & \dots & 0 \\ 0 & \mathbf{L}_{\alpha_1} & 0 & \dots & 0 \\ 0 & 0 & \mathbf{L}_{\alpha_2} & \dots & 0 \\ \vdots & \vdots & \vdots & \ddots & \vdots \\ 0 & 0 & 0 & \dots & \mathbf{L}_{\alpha_{N_{st}/2}} \end{bmatrix} \tag{A.1}$$

We have $(N_{st}/2+1)$ sub-system $\mathbf{L}_{\alpha_n}$, the system with one wavenumber pair α_n. The other matrices $\mathbf{A}$, $\mathbf{B}$, $\mathbf{E}$, $\mathbf{D}_1$, $\mathbf{D}_2$, $\mathbf{Q}_{11}$, $\mathbf{Q}_{12}$, $\mathbf{Q}_{22}$ are given by the same way.

Synthesize the controller matrix $\mathbf{K}$, note that we also have

$$\mathbf{K} = \begin{bmatrix} \mathbf{K}_{\alpha_0} & 0 & 0 & \dots & 0 \\ 0 & \mathbf{K}_{\alpha_1} & 0 & \dots & 0 \\ 0 & 0 & \mathbf{K}_{\alpha_2} & \dots & 0 \\ \vdots & \vdots & \vdots & \ddots & \vdots \\ 0 & 0 & 0 & \dots & \mathbf{K}_{\alpha_{N_{st}/2}} \end{bmatrix} \tag{A.2}$$

where $\mathbf{K}_{\alpha_n}$ is the controller of system with one wavenumber pair α_n. Note that $\mathbf{K}_{\alpha_n}$ is calculated from the linearization (a feedback control law, e.g. **LQR**, **PID**, visual servoing control, partitioned visual servoing control, etc.).

Write the controller matrix $\mathbf{K}$ in a file.

Write $\mathbf{D}_{DN}(\Xi)$ and $\mathbf{D}_{DN}(\mathbf{F}_v)$ in a file.

A.2 On startup of the Navier-Stokes solver:

Read the matrices into the Navier-Stokes solver and store and then read the initial velocity field.

A.3 On each solver step-time:

A.3.1 Calculate the state variable $\mathbf{x}(t)$ from the velocity field $\mathbf{V}(x, y, t)$

Note that the state variable $\mathbf{x}(t)$ is given by

$$\mathbf{x}(t) = \begin{bmatrix} \mathbf{x}_{\alpha_0}(t) \\ \mathbf{x}_{\alpha_1}(t) \\ \vdots \\ \mathbf{x}_{\alpha_{N_{st}/2}}(t) \end{bmatrix} \tag{A.3}$$

where $\mathbf{x}_{\alpha_n}$ is the state variable of system with one wavenumber pair α_n. From the velocity $\mathbf{V}(x, y, t) = (u(x, y, t), v(x, y, t))$ where $u(x, y, t)$, $v(x, y, t)$, are the streamwise

(x-direction), wall normal (y-direction) velocity components. We use the Fast Fourier Transform to convert the physical space $v(x, y, t)$ to the Fourier space, $\tilde{v}_{\alpha_n}(y, t)$ and its inverse, see [Canuto et al., 2007] for more detail. By using the Chebyshev polynomials to discretize the y-direction, $\mathbf{x}_{\alpha_n}(t)$ depends on from $\tilde{v}_{\alpha_n}(y_2, t)$ to $\tilde{v}_{\alpha}(y_{N-2}, t)$.

A.3.1.1 x-direction

For the domain $x \in [0, L_x]$, the gridpoints and stepsizes are defined by $x_{n_x} = n_x \Delta x$; $\Delta x = L_x / N_{st}$. Fast Fourier Transform is illustrated in Figure A.2.

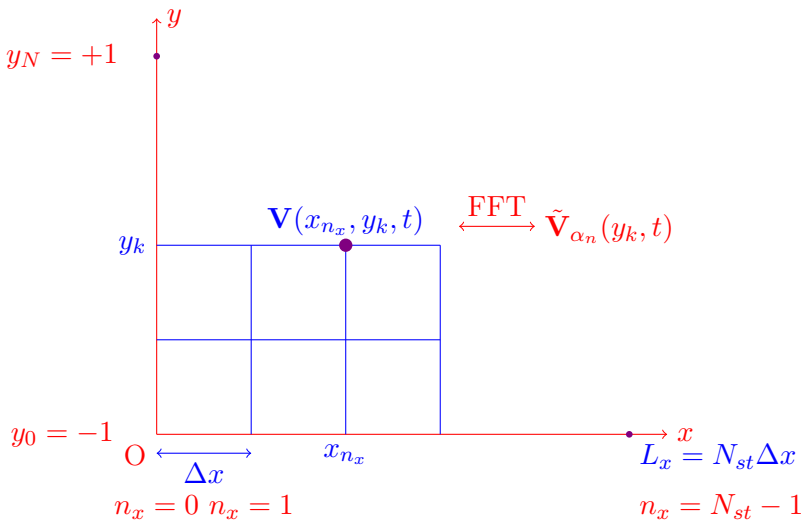

Figure A.2: Fast Fourier Transform at the gridpoint (x_{n_x}, y_k).

The velocity component $v(x_{n_x}, y, t)$ at the grid point (x_{n_x}, y) is calculated by

$$\begin{cases} v(x_{n_x}, y, t) & = \sum_{k_x=-N_{st}/2}^{N_{st}/2-1} \tilde{v}_{\alpha_n}(y, t) e^{2\pi j k_x n_x / N_{st}} \\ & = \sum_{k_x=0}^{N_{st}/2-1} \tilde{v}_{\alpha_n}(y, t) e^{2\pi j k_x n_x / N_{st}} + \sum_{k_x=-N_{st}/2}^{-1} \tilde{v}_{\alpha_n}(y, t) e^{2\pi j k_x n_x / N_{st}} \\ & = \sum_{k_x=0}^{N_{st}/2-1} \tilde{v}_{\alpha_n}(y, t) e^{2\pi j k_x n_x / N_{st}} + \sum_{k_x=1}^{N_{st}/2} \tilde{v}_{-\alpha_n}(y, t) e^{-2\pi j k_x n_x / N_{st}} \\ n_x & = 0 \dots N_{st} - 1 \end{cases} \tag{A.4}$$

where $\alpha_n = \frac{2\pi k_x}{L_x}$. Note that the wavenumbers are $(0, \pm 1, \pm 2, \cdots)\alpha_0$ where $\alpha_0 = \frac{2\pi}{L_x}$ is the fundamental wavenumber. We have N_{st} girdpoints $v(0, y, t), v(\Delta x, y, t), \dots, v(L_x, y, t)$. To calculate $v(x_{n_x}, y, t)$, we must have $\tilde{v}_{\alpha_n}(y, t)$ and $\tilde{v}_{-\alpha_n}(y, t)$. Because we only consider the positive value of α_n, we do not calculate $\tilde{v}_{-\alpha_n}(y, t)$. Therefore, we give the

way where $v(x_{n_x}, y, t)$ only depends on $\tilde{v}_{\alpha_n}(y,t)$ (α_n is positive). This way leads us to simplify calculations.

From the velocity $v(x_{n_x}, y, t)$, we calculate $\tilde{v}_{\alpha_n}(y,t)$ based on x-Fourier transform

$$\begin{cases} \tilde{v}_{\alpha_n}(y,t) & = \frac{1}{N_{st}} \sum_{n_x=0}^{N_{st}-1} v(x_{n_x}, y, t) e^{-2\pi j k_x n_x / N_{st}} \\ \alpha_n & = \frac{2\pi k_x}{L_x}, k_x = -N_{st}/2, \ldots, N_{st}/2 - 1 \end{cases} \tag{A.5}$$

We have N_{st} modes: $\tilde{v}_0(y,t), \tilde{v}_{\frac{2\pi}{L_x}}(y,t), \ldots, \tilde{v}_{\frac{2\pi(N_{st}/2-1)}{L_x}}(y,t), \tilde{v}_{-\frac{2\pi}{L_x}}(y,t), \ldots, \tilde{v}_{-\frac{2\pi N_{st}/2}{L_x}}(y,t)$. From (A.5), we have

$$\begin{cases} \tilde{v}_{\alpha_n}(y,t) & = \frac{1}{N_{st}} \sum_{n_x=0}^{N_{st}-1} v(x_{n_x}, y, t) e^{-2\pi j k_x n_x / N_{st}} \\ & = \frac{1}{N_{st}} \sum_{n_x=0}^{N_{st}-1} v(x_{n_x}, y, t) (cos(-2\pi j k_x n_x / N_{st}) + j sin(-2\pi j k_x n_x / N_{st})) \\ \tilde{v}_{-\alpha_n}(y,t) & = \frac{1}{N_{st}} \sum_{n_x=0}^{N_{st}-1} v(x_{n_x}, y, t) e^{-2\pi j (-k_x) n_x / N_{st}} \\ & = \frac{1}{N_{st}} \sum_{n_x=0}^{N_{st}-1} v(x_{n_x}, y, t) (cos(-2\pi j k_x n_x / N_{st}) - j sin(-2\pi j k_x n_x / N_{st})) \\ \alpha_n & = \frac{2\pi k_x}{L_x}, k_x = -N_{st}/2, \ldots, N_{st}/2 - 1 \end{cases} \tag{A.6}$$

Therefore, $\tilde{v}_{-\alpha_n}(y,t) = \tilde{v}^*_{\alpha_n}(y,t)$ where $\tilde{v}^*_{\alpha_n}(y,t)$ is the complex conjugate of $\tilde{v}_{\alpha_n}(y,t)$. Consequently, if we have $\tilde{v}_0(y,t), \tilde{v}_{\frac{2\pi}{L_x}}(y,t), \ldots, \tilde{v}_{\frac{2\pi(N_{st}/2-1)}{L_x}}(y,t)$, we can give the following equation

$$\begin{cases} \tilde{v}_{-\frac{2\pi}{L_x}}(y,t) & = \tilde{v}^*_{\frac{2\pi}{L_x}}(y,t) \\ \ldots & \\ \tilde{v}_{-\frac{2\pi(N_{st}/2-1)}{L_x}}(y,t) & = \tilde{v}^*_{\frac{2\pi(N_{st}-1)/2}{L_x}}(y,t) \end{cases} \tag{A.7}$$

And we have $\tilde{v}_{-\frac{2\pi N_{st}/2}{L_x}}(y,t) = \tilde{v}^*_{\frac{2\pi N_{st}/2}{L_x}}(y,t)$ or $\tilde{v}_{\frac{2\pi N_{st}/2}{L_x}}(y,t) = \tilde{v}^*_{-\frac{2\pi N_{st}/2}{L_x}}(y,t)$.

From N_{st} girdpoints: $v(0,y,t), v(\Delta x, y, t), \ldots, v(L_x, y, t)$, we change from the physical space to the Fourier space, $N_{st}/2+1$ modes: $\tilde{v}_0(y,t)$,$\tilde{v}_{\frac{2\pi}{L_x}}(y,t)$,..., $\tilde{v}_{\frac{2\pi(N_{st}/2-1)}{L_x}}(y,t)$ and $\tilde{v}_{\frac{2\pi(N_{st}/2)}{L_x}}(y,t)$. Its inverse may be given by

$$\begin{cases} v(x_{n_x}, y, t) & = \sum_{k_x=0}^{N_{st}/2-1} \tilde{v}_{\alpha_n}(y,t) e^{2\pi j k_x n_x / N_{st}} + \sum_{k_x=-N_{st}/2}^{-1} \tilde{v}_{\alpha_n}(y,t) e^{2\pi j k_x n_x / N_{st}} \\ & = \sum_{k_x=0}^{N_{st}/2-1} \tilde{v}_{\alpha_n}(y,t) e^{2\pi j k_x n_x / N_{st}} + \sum_{k_x=1}^{N_{st}/2} \tilde{v}^*_{\alpha_n}(y,t) e^{-2\pi j k_x n_x / N_{st}} \\ x_{n_x} & = n_x \Delta x, n_x = 0 \ldots N_{st} - 1 \end{cases} \tag{A.8}$$

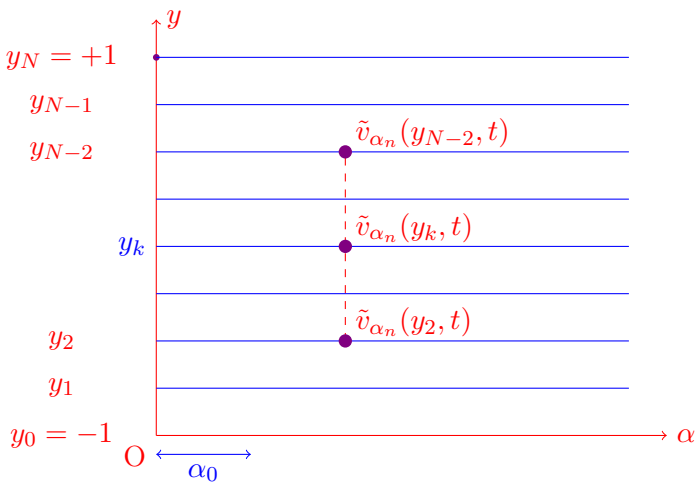

Figure A.3: y-discretization (α_n, y_k).

A.3.1.2 y-direction

By using Fast Fourier Transform, we obtain $\tilde{v}_{\alpha_n}(t)$, and then how can to obtain $\mathbf{x}_{\alpha_n}(t)$? We continue use the y-discretization, see Figure A.3, we use the **Chebyshev polynomials** for the y-discretization. We have $(N+1)$ points in y-direction from $\tilde{v}_{\alpha_n}(y_0)(t)$ to $\tilde{v}_{\alpha_n}(y_N)(t)$. Note that we use the Combined method 1 [McKernan, 2006], we discard the collocation points $\tilde{v}_{\alpha_n}(y_1)(t)$ and $\tilde{v}_{\alpha_n}(y_{N-1})(t)$, the state vector $\mathbf{x}_{\alpha_n}(t)$ depends on from $\tilde{v}_{\alpha_n}(y_2)(t)$ to $\tilde{v}_{\alpha_n}(y_{N-2})(t)$.

Note the velocity $\tilde{v}_{\alpha_n}(t)$ is calculated by (**we omit α_n in writing**)

$$\begin{bmatrix} \tilde{v}(y_0,t) \\ \vdots \\ \tilde{v}(y_N,t) \end{bmatrix} = \begin{bmatrix} \Xi_4(y_2) & \dots & \Xi_N(y_2) \\ \vdots & \ddots & \vdots \\ \Xi_4(y_{N-2}) & \dots & \Xi_N(y_{N-2}) \end{bmatrix} \begin{bmatrix} a_{v,4}(t) \\ \vdots \\ a_{v,N}(t) \end{bmatrix} + \begin{bmatrix} \mathbf{F}_{v,0}(y_0) & \dots & \mathbf{F}_{v,M}(y_0) \\ \vdots & \ddots & \vdots \\ \mathbf{F}_{v,0}(y_N) & \dots & \mathbf{F}_{v,M}(y_N) \end{bmatrix} \begin{bmatrix} \mathbf{q}_{v,0}(t) \\ \vdots \\ \mathbf{q}_{v,M}(t) \end{bmatrix}, \tag{A.9}$$

where $\mathbf{q}_{v,m}(t) = \begin{bmatrix} \tilde{q}_{v,l,m}(t) & \tilde{q}_{v,u,m}(t) \end{bmatrix}^\top$. We recall that $\tilde{q}_{v,l,m}(t)$ and $\tilde{q}_{v,u,m}(t)$ are the control signals or the boundary conditions. Or we can rewrite by using $\mathbf{x}(t)$ and $\mathbf{u}(t)$.

$$\begin{bmatrix} \tilde{v}(y_0,t) \\ \vdots \\ \tilde{v}(y_N,t) \end{bmatrix} = \begin{bmatrix} \Xi_4(y_2) & \dots & \Xi_N(y_2) \\ \vdots & \ddots & \vdots \\ \Xi_4(y_{N-2}) & \dots & \Xi_N(y_{N-2}) \end{bmatrix} \mathbf{x}(t) + \begin{bmatrix} \mathbf{F}_{v,0}(y_0) & \dots & \mathbf{F}_{v,M}(y_0) \\ \vdots & \ddots & \vdots \\ \mathbf{F}_{v,0}(y_N) & \dots & \mathbf{F}_{v,M}(y_N) \end{bmatrix} \mathbf{u}(t) \tag{A.10}$$

By using the combined method 1; and $\tilde{v}(y_0,t)$, $\tilde{v}(y_N,t)$ are the controlled signals. There-

fore, we only calculate

$$\begin{bmatrix} \tilde{v}(y_2,t) \\ \vdots \\ \tilde{v}(y_{N-2},t) \end{bmatrix} = \begin{bmatrix} \Xi_4(y_2) & \dots & \Xi_N(y_2) \\ \vdots & \ddots & \vdots \\ \Xi_4(y_{N-2}) & \dots & \Xi_N(y_{N-2}) \end{bmatrix} \mathbf{x}(t) + \begin{bmatrix} \mathbf{F}_{v,0}(y_2) & \dots & \mathbf{F}_{v,M}(y_2) \\ \vdots & \ddots & \vdots \\ \mathbf{F}_{v,0}(y_{N-2}) & \dots & \mathbf{F}_{v,M}(y_{N-2}) \end{bmatrix} \mathbf{u}(t) \tag{A.11}$$

or we can rewrite (note that $\mathbf{D}_{DN}(\Xi)$ is square and invertible, we use $\tilde{v}_{\alpha_n}(y_k,t)$ instead of $\tilde{v}(y_k,t)$)

$$\begin{aligned} \begin{bmatrix} \tilde{v}_{\alpha_n}(y_2,t) \\ \vdots \\ \tilde{v}_{\alpha_n}(y_{N-2},t) \end{bmatrix} &= \mathbf{D}_{DN}(\Xi)\mathbf{x}_{\alpha_n}(t) + \mathbf{D}_{DN}(\mathbf{F}_v)\mathbf{u}_{\alpha_n}(t) \\ &= \left[\mathbf{D}_{DN}(\Xi) + \mathbf{D}_{DN}(\mathbf{F}_v)\mathbf{K}_{\alpha_n}\right]\mathbf{x}_{\alpha_n}(t) \end{aligned} \tag{A.12}$$

The state variable is given by

$$\mathbf{x}_{\alpha_n}(t) = \left[\mathbf{D}_{DN}(\Xi) + \mathbf{D}_{DN}(\mathbf{F}_v)\mathbf{K}_{\alpha_n}\right]^{-1} \begin{bmatrix} \tilde{v}_{\alpha_n}(y_2,t) \\ \vdots \\ \tilde{v}_{\alpha_n}(y_{N-2},t) \end{bmatrix} \tag{A.13}$$

This formulation requires $[\mathbf{D}_{DN}(\Xi) + \mathbf{D}_{DN}(\mathbf{F}_v)\mathbf{K}_{\alpha_n}]^{-1}$. For approximation, note that we may calculate the state vector by

$$\mathbf{x}_{\alpha_n}(t) = \mathbf{D}_{DN}^{-1}(\Xi)\mathbf{D}_{DN}(\mathbf{F}_v)\mathbf{u}_{\alpha_n}(t-dt) + \mathbf{D}_{DN}^{-1}(\Xi) \begin{bmatrix} \tilde{v}_{\alpha_n}(y_2,t) \\ \vdots \\ \tilde{v}_{\alpha_n}(y_{N-2},t) \end{bmatrix} \tag{A.14}$$

Note that $\mathbf{u}_{\alpha_n}(t-dt)$ is the control signals in the previous step.

A.3.2 Calculate the actuation $\mathbf{u}(t) = \mathbf{K}\mathbf{x}(t)$ from $\mathbf{x}_{\alpha_n}(t)$ and $\mathbf{K}_{\alpha_n}$.

A.3.3 Set the boundary conditions for the next step using the actuation $\mathbf{u}(t)$

We set the boundary condition from the control signals $\mathbf{u}(t) = \mathbf{K}\mathbf{x}(t)$. For the one wavenumber α_n, we determine $\tilde{q}_{v,l,m,\alpha_n}(t)$ and $\tilde{q}_{v,u,m,\alpha_n}(t)$ by

$$\mathbf{u}_{\alpha_n}(t) = \begin{bmatrix} \mathbf{q}_{v,1,\alpha_n}(t) \\ \vdots \\ \mathbf{q}_{v,M,\alpha_n}(t) \end{bmatrix} = \begin{bmatrix} \begin{bmatrix} \tilde{q}_{v,l,1,\alpha_n}(t) \\ \tilde{q}_{v,u,1,\alpha_n}(t) \end{bmatrix} \\ \vdots \\ \begin{bmatrix} \tilde{q}_{v,l,M,\alpha_n}(t) \\ \tilde{q}_{v,u,M,\alpha_n}(t) \end{bmatrix} \end{bmatrix} \tag{A.15}$$

From $\tilde{q}_{v,l,m,\alpha_n}(t)$ and $\tilde{q}_{v,u,m,\alpha_n}(t)$, we calculate $\tilde{q}^*_{v,l,m,\alpha_n}(t)$ and $\tilde{q}^*_{v,u,m,\alpha_n}(t)$ (complex conjugate). The boundary conditions are updated by

$$\begin{cases} v(x_{n_x}, y=-1, t) & = \sum_{m=1}^{M} \sum_{k_x=0}^{N_{st}/2-1} \tilde{q}_{v,l,m,\alpha_n}(t) e^{2\pi j k_x n_x/N_{st}} + \sum_{m=1}^{M} \sum_{k_x=1}^{N_{st}/2} \tilde{q}^*_{v,l,m,\alpha_n}(t) e^{-2\pi j k_x n_x/N_{st}} \\ v(x_{n_x}, y=+1, t) & = \sum_{m=1}^{M} \sum_{k_x=0}^{N_{st}/2-1} \tilde{q}_{v,u,m,\alpha_n}(t) e^{2\pi j k_x n_x/N_{st}} + \sum_{m=1}^{M} \sum_{k_x=1}^{N_{st}/2} \tilde{q}^*_{v,u,m,\alpha_n}(t) e^{-2\pi j k_x n_x/N_{st}} \\ x_{n_x} & = n_x \Delta x, n_x = 0 \ldots N_{st}-1 \end{cases} \tag{A.16}$$

A.4 Implementation Code:

The algorithm is given by

- Fast Fourier Transform is used to convert from the physical space: N_{st} girdpoints $v(0,y,t), v(\Delta x, y, t), \ldots, v(L_x, y, t)$ to Fourier space $N_{st}/2+1$ modes: $\tilde{v}_0(y,t)$,$\tilde{v}_{\frac{2\pi}{L_x}}(y,t)$,..., $\tilde{v}_{\frac{2\pi(N_{st}/2-1)}{L_x}}(y,t)$ and $\tilde{v}_{\frac{2\pi(N_{st}/2)}{L_x}}(y,t)$ (this mode is calculated through $\tilde{v}_{\frac{2\pi(-N_{st}/2)}{L_x}}(y,t)$).
- A Matlab function gives the matrices: $\mathbf{K}_{\frac{2\pi k_x}{L_x}}$, $\mathbf{D}_{DN}(\Xi)$ and $\mathbf{D}_{DN}(\mathbf{F}_v)$. For simplicity in programming. The inputs are k_x, L_x, N.
- The state variable is calculated through

$$\mathbf{x}_{\frac{2\pi k_x}{L_x}}(t) = \mathbf{D}^{-1}_{DN}(\Xi)\mathbf{D}_{DN}(\mathbf{F}_v)\mathbf{u}_{\frac{2\pi k_x}{L_x}}(t-dt) + \mathbf{D}^{-1}_{DN}(\Xi) \begin{bmatrix} \tilde{v}_{\frac{2\pi k_x}{L_x}}(y_2, t) \\ \vdots \\ \tilde{v}_{\frac{2\pi k_x}{L_x}}(y_{N-2}, t) \end{bmatrix} \tag{A.17}$$

  where $k_x = 0 \ldots N_x/2$.

- The control signal is calculated $\mathbf{u}_{\frac{2\pi k_x}{L_x}}(t) = \begin{bmatrix} \begin{bmatrix} \tilde{q}_{v,l,1,\frac{2\pi k_x}{L_x}}(t) \\ \tilde{q}_{v,u,1,\frac{2\pi k_x}{L_x}}(t) \end{bmatrix} \\ \vdots \\ \begin{bmatrix} \tilde{q}_{v,l,M,\frac{2\pi k_x}{L_x}}(t) \\ \tilde{q}_{v,u,M,\frac{2\pi k_x}{L_x}}(t) \end{bmatrix} \end{bmatrix} = \mathbf{K}_{\frac{2\pi k_x}{L_x}} \mathbf{x}_{\frac{2\pi k_x}{L_x}}(t)$
- We calculate $\tilde{q}_{v,l,\frac{2\pi k_x}{L_x}}(t)$ and $\tilde{q}_{v,u,\frac{2\pi k_x}{L_x}}(t)$ by

$$\begin{cases} \tilde{q}_{v,l,\frac{2\pi k_x}{L_x}}(t) & = \sum_{m=1}^{M} \tilde{q}_{v,l,m,\frac{2\pi k_x}{L_x}}(t) \\ \tilde{q}_{v,u,\frac{2\pi k_x}{L_x}}(t) & = \sum_{m=1}^{M} \tilde{q}_{v,u,m,\frac{2\pi k_x}{L_x}}(t) \end{cases} \tag{A.18}$$

And we then update the boundary condition

$$\begin{cases} v(x_{n_x}, y=-1, t) & = \sum_{k_x=0}^{N_{st}/2-1} \tilde{q}_{v,l,\frac{2\pi k_x}{L_x}}(t) e^{2\pi j k_x n_x/N_{st}} + \sum_{k_x=1}^{N_{st}/2} \tilde{q}^*_{v,l,\frac{2\pi k_x}{L_x}}(t) e^{-2\pi j k_x n_x/N_{st}} \\ v(x_{n_x}, y=+1, t) & = \sum_{k_x=0}^{N_{st}/2-1} \tilde{q}_{v,u,\frac{2\pi k_x}{L_x}}(t) e^{2\pi j k_x n_x/N_{st}} + \sum_{k_x=1}^{N_{st}/2} \tilde{q}^*_{v,u,\frac{2\pi k_x}{L_x}}(t) e^{-2\pi j k_x n_x/N_{st}} \\ x_{n_x} & = n_x \Delta x, n_x = 0 \dots N_{st}-1 \end{cases} \tag{A.19}$$

- Update the time $t \to t + dt$

Appendix B

Reducing of Non-orthogonality

We want to determine the necessary condition to have no non-orthogonality. We assume that we design a feedback control $\mathbf{u}(t) = \mathbf{K}\mathbf{x}(t)$. Therefore, we have

$$\dot{\mathbf{x}}(t) = \mathbf{A}\mathbf{x}(t) + \mathbf{B}\mathbf{u}(t) = (\mathbf{A} + \mathbf{B}\mathbf{K})\mathbf{x}(t) = \mathbf{A}_{CL}\mathbf{x}(t), \tag{B.1}$$

where $\mathbf{A}_{CL} = \mathbf{A} + \mathbf{B}\mathbf{K}$. The kinetic energy density can be considered by

$$\varepsilon(t) = \mathbf{x}^{\top}(t)\mathbf{Q}_x\mathbf{x}(t), \tag{B.2}$$

where $\mathbf{Q}_x$ is a Hermitian matrix. The idea is to obtain the kinetic energy density to monotonically decrease in time.

In previous works [Whidborne and McKernan, 2007], the necessary condition to ensure $\dot{\varepsilon}(t) < 0$, the input matrix $\mathbf{B}$ must be a full rank matrix.

B.1 Kinetic energy density has an exponential decrease

We assume that the kinetic energy density has an exponential decrease. Therefore, it means

$$\begin{aligned}
\dot{\varepsilon}(t) &= -2\lambda\varepsilon(t) && \text{(B.3)}\\
\dot{\mathbf{x}}^{\top}(t)\mathbf{Q}_x\mathbf{x}(t) + \mathbf{x}^{\top}(t)\mathbf{Q}_x\dot{\mathbf{x}}(t) &= -2\lambda\mathbf{x}^{\top}(t)\mathbf{Q}_x\mathbf{x}(t) && \text{(B.4)}\\
2\mathbf{x}^{\top}(t)\mathbf{Q}_x\dot{\mathbf{x}}(t) &= -2\lambda\mathbf{x}^{\top}(t)\mathbf{Q}_x\mathbf{x}(t) && \text{(B.5)}\\
&\Rightarrow \begin{cases} \mathbf{x}(t) = 0 \text{ (is not considered)} \\ \dot{\mathbf{x}}(t) = -\lambda\mathbf{x}(t). \end{cases} && \text{(B.6)}
\end{aligned}$$

Therefore, the kinetic energy density has an exponential decrease if and only if the state vector has an exponential decrease. The gain $\mathbf{K}$ is given by

$$\begin{aligned}
\dot{\mathbf{x}}(t) &= -\lambda\mathbf{x}(t) && \text{(B.7)}\\
(\mathbf{A} + \mathbf{B}\mathbf{K})\mathbf{x}(t) &= -\lambda\mathbf{x}(t) && \text{(B.8)}\\
(\mathbf{A} + \mathbf{B}\mathbf{K}) &= -\lambda\mathbf{I} && \text{(B.9)}\\
\mathbf{K} &= -\mathbf{B}^{-1}(\lambda\mathbf{I} + \mathbf{A}) && \text{(B.10)}\\
& && \text{(B.11)}
\end{aligned}$$

this result shows that the input matrix $\mathbf{B}$ must be full rank.

B.2 Kinetic energy density monotonically decreases in time

We determine the necessary condition to satisfy that the kinetic energy density monotonically decreases in time. We can rewrite the kinetic energy density by

$$\varepsilon(t) = \mathbf{x}^\top(t)\mathbf{Q}_x\mathbf{x}(t) = \mathbf{x}^\top(t)\mathbf{C}^\top\mathbf{C}\mathbf{x}(t) = (\mathbf{C}\mathbf{x}(t))^\top(\mathbf{C}\mathbf{x}(t)) = \mathbf{y}^\top(t)\mathbf{y}(t), \tag{B.12}$$

where $\mathbf{y}(t) = \mathbf{C}\mathbf{x}(t)$ and $\mathbf{Q}_x = \mathbf{C}^\top\mathbf{C}$. Consequently, we obtain the system with the state vector $\mathbf{y}(t)$

$$\dot{\mathbf{y}}(t) = \mathbf{C}\mathbf{A}_{CL}\mathbf{C}^{-1}\mathbf{y}(t). \tag{B.13}$$

The evolution in time of the state vector $\mathbf{y}(t)$ is calculated by

$$\mathbf{y}(t) = \mathbf{V}_y e^{\Lambda t}\mathbf{V}_y^{-1}\mathbf{y}_0 \tag{B.14}$$

where the matrix $\mathbf{V}_y$ contain the eigenvectors and the matrix Λ is given by

$$\Lambda = \begin{bmatrix} \lambda_1 & 0 & \dots & 0 \\ 0 & \lambda_2 & \dots & 0 \\ \vdots & \vdots & \ddots & \vdots \\ 0 & 0 & \dots & \lambda_N \end{bmatrix} \tag{B.15}$$

where λ_k is the eigenvalue. If the eigenvectors of $\mathbf{C}\mathbf{A}_{CL}\mathbf{C}^{-1}$ are orthogonal and appropriately normalized, then $\mathbf{V}_y^{-1} = \mathbf{V}_y^\top$, and decomposing $\lambda_k = \lambda_{k,R} + i\lambda_{k,I}$ of the eigenvalues, it follows from $\mathbf{y}(t) = \mathbf{V}_y e^{\Lambda t}\mathbf{V}_y^{-1}\mathbf{y}_0$ that the kinetic energy density may be written

$$\begin{aligned} \varepsilon(t) &= \mathbf{y}^\top\mathbf{y} = [\mathbf{V}_y e^{\Lambda t}\mathbf{V}_y^{-1}\mathbf{y}_0]^\top\mathbf{V}_y e^{\Lambda t}\mathbf{V}_y^{-1}\mathbf{y}_0 && \text{(B.16)} \\ &= \mathbf{y}_0^\top(\mathbf{V}_y^{-1})^\top e^{\Lambda^\top t}\mathbf{V}_y^\top\mathbf{V}_y e^{\Lambda t}\mathbf{V}_y^{-1}\mathbf{x}_0 = \mathbf{y}_0^\top\mathbf{V}_y e^{\Lambda^\top t+\Lambda t}\mathbf{V}_y^\top\mathbf{y}_0. && \text{(B.17)} \end{aligned}$$

where

$$e^{\Lambda^\top t+\Lambda t} = \begin{bmatrix} e^{2t\lambda_{1,R}} & 0 & \dots & 0 \\ 0 & e^{2t\lambda_{2,R}} & \dots & 0 \\ \vdots & \vdots & \ddots & \vdots \\ 0 & 0 & \dots & e^{2t\lambda_{N,R}} \end{bmatrix}. \tag{B.18}$$

Defining $\mathbf{z}_0 = \mathbf{V}_y^\top\mathbf{y}_0$ and due to the orthogonal eigenvectors $\mathbf{V}_y$, it follows that

$$\varepsilon(t) = e^{2t\lambda_{1,R}}|\mathbf{z}_{10}|^2 + e^{2t\lambda_{2,R}}|\mathbf{z}_{20}|^2 + \cdots + e^{2t\lambda_{N,R}}|\mathbf{z}_{n0}|^2, \tag{B.19}$$

always decays in time. The kinetic energy density is not growth any more. Therefore, the control law is calculated by

$$\begin{cases} \mathbf{C}\mathbf{A}_{CL}\mathbf{C}^{-1} &= \mathbf{V}_y\Lambda\mathbf{V}_y^{-1} \\ \mathbf{V}_y\mathbf{V}_y^\top &= \mathbf{I}. \end{cases} \tag{B.20}$$

or by using $\mathbf{V} = \mathbf{C}^{-1}\mathbf{V}_y$, we can rewrite

$$\begin{cases} \mathbf{A}_{CL} & = \mathbf{C}^{-1}\mathbf{V}_y\Lambda\mathbf{V}_y^{-1}\mathbf{C} = (\mathbf{C}^{-1}\mathbf{V}_y\Lambda(\mathbf{C}^{-1}\mathbf{V}_y)^{-1} \\ \mathbf{V}\mathbf{V}^\top & = \mathbf{C}^{-1}\mathbf{V}_y\mathbf{V}_y^\top(\mathbf{C}^{-1})^\top = \mathbf{Q}^{-\mathbf{1}}. \end{cases} \tag{B.21}$$

The control law $\mathbf{u} = \mathbf{K}\mathbf{x}$ is based on

$$\begin{cases} \mathbf{B}\mathbf{K} & = \mathbf{V}\Lambda\mathbf{V}^{-1} - \mathbf{A} \\ \mathbf{V}\mathbf{V}^\top & = \mathbf{Q}^{-\mathbf{1}}. \end{cases} \tag{B.22}$$

Therefore, the gain of control law is

$$\mathbf{K} = -\mathbf{B}^{-1}(-\mathbf{V}\Lambda\mathbf{V}^{-1} + \mathbf{A}) \tag{B.23}$$

we find the same necessary condition for the input matrix $\mathbf{B}$ with respect to the above case.

Appendix C

Decoupling Feedback Control by Hermite Interpolation Polynomials

As discussed in the previous chapters, methods such as the proportional control, the **LQR** control (include the optimal control $\mathbf{H}_2/\mathbf{H}_\infty$), the partitioned visual servoing control and the visual servoing control make us of the inversion of the state matrix $\mathbf{L}$ (see section 5.3.3.3). Although in the literature there exists methods of improving the condition number of a matrix (e.g. in the plane Poiseuille flow the condition number of the state matrix $\mathbf{L}$ was improved in the works of Heincrichs [Heinrichs, 1989] and McKernan [McKernan, 2006]) but there are not still sufficient in practice. Therefore, we propose an alternate solution of control which is not sensible to the numerical issues raised by the inversion of matrices with bad condition numbers.

To avoid inverting the state matrix $\mathbf{L}$, we propose a control approach based on the model

$$\left\{\begin{array}{ll} \mathbf{L}\dot{\mathbf{x}}(t) & = \mathbf{A}\mathbf{x}(t) + \mathbf{B}\mathbf{u}(t) + \mathbf{E}\dot{\mathbf{u}}(t) \\ \varepsilon(t) & = \mathbf{x}^\top(t)\mathbf{Q}_{11}\mathbf{x}(t) + \mathbf{x}^\top(t)\mathbf{Q}_{12}\mathbf{u}(t) + \mathbf{u}^\top(t)\mathbf{Q}_{21}\mathbf{x}(t) + \mathbf{u}^\top(t)\mathbf{Q}_{22}\mathbf{u}(t) \\ \mathbf{d}(t) & = \mathbf{D}_1\mathbf{x}(t) + \mathbf{D}_2\mathbf{u}(t) \\ \mathbf{x}(0) & = \mathbf{x}_0. \end{array}\right. \tag{C.1}$$

Our control approach achieves an exponential decoupled decrease of the state vector. Consequently the skin friction drag, the kinetic energy density and the velocity component have also an exponential decoupled decrease.

C.1 Our goal of the control law

We consider here a state feedback control law

$$\mathbf{u}(t) = \mathbf{K}\mathbf{x}(t), \tag{C.2}$$

and suppose that this control law is able to achieve an exponential decoupled decrease of the state vector, that is

$$\dot{\mathbf{x}}(t) = -\lambda\mathbf{x}(t). \tag{C.3}$$

We calculate the derivative of kinetic energy density and skin friction drag from (C.1) by

$$\left\{\begin{array}{ll}\dot{\varepsilon}(t) & = 2\dot{\mathbf{x}}^{\top}(t)\mathbf{Q}_{11}\mathbf{x}(t) + \dot{\mathbf{x}}^{\top}(t)\mathbf{Q}_{12}\mathbf{u}(t) + \mathbf{x}^{\top}(t)\mathbf{Q}_{12}\dot{\mathbf{u}}(t) \\ & \quad + \dot{\mathbf{u}}^{\top}(t)\mathbf{Q}_{21}\mathbf{x}(t) + \mathbf{u}^{\top}(t)\mathbf{Q}_{21}\dot{\mathbf{x}}(t) + 2\mathbf{u}^{\top}(t)\mathbf{Q}_{22}\dot{\mathbf{u}}(t) \\ \dot{\mathbf{d}}(t) & = \mathbf{D}_1\dot{\mathbf{x}}(t) + \mathbf{D}_2\dot{\mathbf{u}}(t).\end{array}\right. \tag{C.4}$$

By plugging (C.2) and (C.3) into (C.4), it is easy to show that the we have

$$\left\{\begin{array}{l}\dot{\mathbf{u}}(t) = -\lambda\mathbf{u}(t) \\ \dot{\mathbf{d}}(t) = -\lambda\mathbf{d}(t) \\ \dot{\varepsilon}(t) = -2\lambda\varepsilon(t),\end{array}\right. \tag{C.5}$$

leading to an exponential decrease of the control signals, the skin friction drag and the kinetic energy.

The velocity and vorticity are calculated as a function of the state vector and the control signals

$$\left[\begin{array}{c}[\tilde{v}_n(t)] \\ [\tilde{\eta}_n(t)]\end{array}\right] = \left[\begin{array}{c}\mathbf{T}_{a_v} \\ \mathbf{T}_{a_\eta}\end{array}\right]\mathbf{x}(t) + \left[\begin{array}{c}\mathbf{T}_{q_v} \\ \mathbf{T}_{a_\eta}\end{array}\right]\mathbf{u}(t), \tag{C.6}$$

where $[\tilde{v}_n(t)] = [\tilde{v}(y_0,t)\dots\tilde{v}(y_N,t)]^{\top}$, $[\tilde{\eta}_n(t)] = [\tilde{\eta}(y_0,t)\dots\tilde{\eta}(y_N,t)]^{\top}$. Therefore it is very easy to show that the derivative of velocity and vorticity is given by

$$\left[\begin{array}{c}[\dot{\tilde{v}}_n(t)] \\ [\dot{\tilde{\eta}}_n(t)]\end{array}\right] = \left[\begin{array}{c}\mathbf{T}_{a_v} \\ \mathbf{T}_{a_\eta}\end{array}\right]\dot{\mathbf{x}}(t) + \left[\begin{array}{c}\mathbf{T}_{a_v} \\ \mathbf{T}_{a_\eta}\end{array}\right]\dot{\mathbf{u}}(t). \tag{C.7}$$

By plugging (C.3) and (C.5) into the derivative of velocity and vorticity (C.7), it is easy to show that the we have:

$$\left\{\begin{array}{l}[\dot{\tilde{v}}_n(t)] = -\lambda\,[\tilde{v}_n(t)] \\ [\dot{\tilde{\eta}}_n(t)] = -\lambda\,[\tilde{\eta}_n(t)]\,,\end{array}\right. \tag{C.8}$$

leading to an exponential decoupled decrease of the velocity component. It is of course a very interesting result.

Obtaining an exponential decoupled decrease of the state vector is the goal of the next section.

C.2 Design of the control law

In this section we want to express the matrix $\mathbf{K}$ involved in (C.2) such that (C.3) is verified. By plugging (C.2) and (C.3) into (C.1) we obtain

$$\begin{array}{rcl}-\lambda\mathbf{L}\mathbf{x}(t) & = & \mathbf{A}\mathbf{x}(t) + \mathbf{B}\mathbf{K}\mathbf{x}(t) - \lambda\mathbf{E}\mathbf{K}\mathbf{x}(t) \\ \mathbf{A} + \mathbf{B}\mathbf{K} - \lambda\mathbf{E}\mathbf{K} & = & -\lambda\mathbf{L} \\ (\mathbf{B} - \lambda\mathbf{E})\mathbf{K} & = & -(\lambda\mathbf{L} + \mathbf{A}).\end{array} \tag{C.9}$$

Since we are able to set the number of the controlled degrees of freedom (see Chapter 7), the number of **DOF** is imposed to equal the number of state vector. In that special case, $\mathbf{K}$ is simply obtained by inverting the square matrix $\mathbf{B} - \lambda\mathbf{E}$.

However, as shown in section 5.3.3.3, not only the matrices $\mathbf{L}$ and $\mathbf{A}$ are very bad conditioned but also the matrices $\mathbf{B}$, $\mathbf{E}$. In fact, it is not really a problem since these matrices depend on the vectors $\mathbf{F}_{v,n}(y_i)$ and $\mathbf{F}_{\eta,n}(y_i)$ for each n and y_i. Therefore, as will be shown in section C.4, by imposing suitable constraints on these vectors, the following equality can be obtained

$$\mathbf{B} - \lambda\mathbf{E} = -\mu(\lambda\mathbf{L} + \mathbf{A}), \tag{C.10}$$

leading simply to

$$\mathbf{K} = \frac{1}{\mu}\mathbf{I}, \tag{C.11}$$

where μ is a scalar that has to be set to limit the amplitude of the control signals at $t = 0$.

C.3 Robustness to measurement noise

Another important problem is the robustness of our control law with respect to the measurement noise. In that case, the control law becomes

$$\mathbf{u}(t) = \frac{1}{\mu}\widehat{\mathbf{x}}(t), \tag{C.12}$$

where $\widehat{\mathbf{x}}(t)$ is an approximation of the true state value.

The problem is to verify that $\mathbf{x} = \mathbf{0}$ is still an exponentially stable equilibrium point when the measurement noise appears.

From previous works [Tatsambon Fomena and Collewet, 2011a], we recall that the state vector is estimated by

$$\widehat{\mathbf{x}}(t) = \mathbf{x}(t) + \frac{1}{N_x}\mathbf{e}(t), \tag{C.13}$$

where N_x is the number of pixels of the camera in the streamwise direction of the flow and $\mathbf{e}(t)$ is related to the measurements noise ([Tatsambon Fomena and Collewet, 2011a]). Therefore, (C.12) becomes

$$\mathbf{u}(t) = \frac{1}{\mu}\left(\mathbf{x}(t) + \frac{1}{N_x}\mathbf{e}(t)\right). \tag{C.14}$$

By plugging this control law into (C.1) and taking into account (C.10), the state evolution equation becomes

$$\begin{aligned}
\mathbf{L}\dot{\mathbf{x}}(t) &= \mathbf{A}\mathbf{x}(t) + \mathbf{B}\mathbf{u}(t) + \mathbf{E}\dot{\mathbf{u}}(t) \\
\mathbf{L}\dot{\mathbf{x}}(t) &= \mathbf{A}\mathbf{x}(t) + \frac{\lambda\mathbf{E} - \mu(\lambda\mathbf{L} + \mathbf{A})}{\mu}\widehat{\mathbf{x}}(t) + \frac{\mathbf{E}}{\mu}\dot{\widehat{\mathbf{x}}}(t) \\
(\mathbf{L} - \frac{\mathbf{E}}{\mu})\dot{\mathbf{x}}(t) &= -\lambda(\mathbf{L} - \frac{\mathbf{E}}{\mu})\mathbf{x}(t) + \frac{\lambda\mathbf{E} - \mu(\lambda\mathbf{L} + \mathbf{A})}{\mu N_x}\mathbf{e}(t) \\
&+ \frac{\mathbf{E}}{\mu N_x}\dot{\mathbf{e}}(t).
\end{aligned} \tag{C.15}$$

If $\mathbf{L} - \dfrac{\mathbf{E}}{\mu}$ is a regular matrix, we obtain

$$\dot{\mathbf{x}}(t) = -\lambda\mathbf{x}(t) + \frac{\mathbf{a}}{\mu N_x}\mathbf{e}(t) + \frac{\mathbf{b}}{\mu N_x}\dot{\mathbf{e}}(t), \tag{C.16}$$

with

$$\begin{cases} \mathbf{a} = (\mathbf{L} - \dfrac{\mathbf{E}}{\mu})^{-1}\,(\lambda\mathbf{E} - \mu(\lambda\mathbf{L} + \mathbf{A})) \\ \mathbf{b} = (\mathbf{L} - \dfrac{\mathbf{E}}{\mu})^{-1}\mathbf{E} \end{cases} \tag{C.17}$$

Since in practice N_x is a large value, the term $\dfrac{\mathbf{a}}{\mu N_x}\mathbf{e}(t)$ is also in practice small. However, due to $\dot{\mathbf{e}}(t)$, $\dfrac{\mathbf{b}}{\mu N_x}\dot{\mathbf{e}}(t)$ may be potentially high. Therefore, to ensure that this term remains small whatever $\dot{\mathbf{e}}(t)$, we set $\mathbf{E} = 0$ from a suitable choice of the $\mathbf{F}_m(y_i)$ vectors as will be shown in section C.4. Consequently, (C.16) becomes

$$\dot{\mathbf{x}}(t) = -\lambda\mathbf{x}(t) - \frac{\lambda\mathbf{I} + \mathbf{L}^{-1}\mathbf{A}}{N_x}\mathbf{e}(t) \tag{C.18}$$

leading to

$$\dot{\mathbf{x}}(t) \approx -\lambda\mathbf{x}(t). \tag{C.19}$$

Therefore, our approach is again very robust to measurement noise.

The next section describes the way to proceed to ensure both $\mathbf{B} = -\mu(\lambda\mathbf{L} + \mathbf{A})$ and $\mathbf{E} = 0$.

C.4 Use of Hermite interpolation to ensure $\mathbf{B} = -\mu(\lambda\mathbf{L}+\mathbf{A})$ and $\mathbf{E} = 0$

It is well known that the Lagrange interpolation is a technique that allows to compute coefficients of a polynomial according to constraints on the function we want to interpolate at a set of points. The Hermite interpolation extends the Lagrange interpolation by taking into account additional constraints on the derivatives of the function.

The Hermite interpolation is here constructed to not only ensure the condition $\mathbf{B} = -\mu(\lambda\mathbf{L} + \mathbf{A})$ and $\mathbf{E} = 0$ but also reduce the influence of the control signals on the kinetic energy density and the skin friction drag.

In our case, we are looking for the constraints that the functions $f_{v,l,n}(y)$, $f_{v,u,n}(y)$, $f_{\eta,l,n}(y)$ and $f_{\eta,u,n}(y)$ have to satisfy. We denote $f_{\phi,\psi,n}(y)$ where $\phi = v$ or $\phi = \eta$ and $\psi = l$ or $\psi = u$.

Note that the dimension of the state matrices $\mathbf{L}$ and $\mathbf{A}$ are reduced (see the section 5.3.4) only from the collocation point y_1 to the collocation point y_{N-1} for the Combined method 2 and from the collocation point y_2 to the collocation point y_{N-2} for the Combined method 1. For our convenience in writing, we use the Combined method 2, from the collocation point y_1 to the collocation point y_{N-1}.

C.4.1 2D plane Poiseuille flow

The state and input matrices are

$$\begin{cases} \mathbf{L} & = j(-\alpha^2\mathbf{D}0_{DN}(\Xi) + \mathbf{D}2_{DN}(\Xi)) \\ \mathbf{A} & = (-\alpha^3\overline{U} - \alpha\overline{U}'' - \dfrac{\alpha^4\mathbf{I}}{jR})\mathbf{D}0_{DN}(\Xi) + (\alpha\overline{U} + \dfrac{2\alpha^2\mathbf{I}}{jR})\mathbf{D}2_{DN}(\Xi) - \dfrac{1}{jR}\mathbf{D}4_{DN}(\Xi) \end{cases} \tag{C.20}$$

and

$$\begin{cases} \mathbf{E} & = j(\alpha^2\mathbf{D}0_{DN}(\mathbf{F}_v) - \mathbf{D}2_{DN}(\mathbf{F}_v)) \\ \mathbf{B} & = (-\alpha^3\overline{U} - \alpha\overline{U}'' - \dfrac{\alpha^4\mathbf{I}}{jR})\mathbf{D}0_{DN}(\mathbf{F}_v) + (\alpha\overline{U} + \dfrac{2\alpha^2\mathbf{I}}{jR})\mathbf{D}2_{DN}(\mathbf{F}_v) - \dfrac{1}{jR}\mathbf{D}4_{DN}(\mathbf{F}_v). \end{cases} \tag{C.21}$$

According to (C.21) and to the definitions of the matrices involved in these equations, the constraints to ensure $\mathbf{B} = -\mu(\lambda\mathbf{L} + \mathbf{A})$ are straightforward

$$\begin{aligned} &(-\alpha^3\overline{U} - \alpha\overline{U}'' - \frac{\alpha^4\mathbf{I}}{jR})\mathbf{D}0_{DN}(\mathbf{F}_v) + (\alpha\overline{U} + \frac{2\alpha^2\mathbf{I}}{jR})\mathbf{D}2_{DN}(\mathbf{F}_v) - \frac{\mathbf{D}4_{DN}(\mathbf{F}_v)}{jR} \\ &= -\mu\left[(-j\lambda\alpha^2\mathbf{I} - \alpha^3\overline{U} - \alpha\overline{U}'' - \frac{\alpha^4\mathbf{I}}{jR})\mathbf{D}0_{DN}(\Xi) + (j\lambda\mathbf{I} + \alpha\overline{U} + \frac{2\alpha^2\mathbf{I}}{jR})\mathbf{D}2_{DN}(\Xi) - \frac{\mathbf{D}4_{DN}(\Xi)}{jR}\right]. \end{aligned} \tag{C.22}$$

According to (C.21) and to the definitions of the matrices involved in these equations, the constraints to ensure $\mathbf{E} = 0$ are straightforward

$$\alpha^2\mathbf{D}0_{DN}(\mathbf{F}_v) - \mathbf{D}2_{DN}(\mathbf{F}_v) = 0. \tag{C.23}$$

Concerning $\mathbf{B} = -\mu(\lambda\mathbf{L} + \mathbf{A})$ the constraints are given by (C.22) that can be rewritten as follows

$$\begin{aligned} &(-\alpha^3\overline{U}(y_i) - 2\alpha\overline{U}''(y_i) - \frac{\alpha^4}{jR})f_{v,\psi,n}(y_i) + (\alpha\overline{U}(y_i) + \frac{2\alpha^2}{jR})f''_{v,\psi,n}(y_i) \\ &-\frac{1}{jR}f''''_{v,\psi,n}(y_i) = -\mu\left[(-j\lambda\alpha^2 - \alpha^3\overline{U}(y_i) - 2\alpha\overline{U}''(y_i) - \frac{\alpha^4}{jR})\Xi_n(y_i)\right. \\ &\left.+(j\lambda + \alpha\overline{U}(y_i) + \frac{2\alpha^2}{jR})\Xi''_n(y_i) - \frac{1}{jR}\Xi''''_n(y_i)\right], \end{aligned} \tag{C.24}$$

which must hold also for $i = 1 \ldots N-1$ and $n = 2 \ldots N$.

Concerning $\mathbf{E} = 0$ the constraints are given by (C.23) that can be rewritten as follows

$$\alpha^2 f_{v,\psi,n}(y_i) - f''_{v,\psi,n}(y_i) = 0, \tag{C.25}$$

which must hold for $i = 1 \ldots N-1$ and $n = 2 \ldots N$.

In order to reduce the influence of the control signals on the kinetic energy density, we give the condition for $f_{v,\psi,n}(y_i)$ and $f'_{v,\psi,n}(y_i)$. Remark that the kinetic energy density is calculated by

$$\varepsilon(t) = \mathbf{x}^\top(t)\mathbf{Q_{11}}\mathbf{x}(t) + \mathbf{x}^\top(t)\mathbf{Q_{12}}\mathbf{u}(t) + \mathbf{u}^\top(t)\mathbf{Q_{21}}\mathbf{x}(t) + \mathbf{u}^\top(t)\mathbf{Q_{22}}\mathbf{u}(t) \tag{C.26}$$

where

$$\begin{cases} \mathbf{Q_{11}} &= \frac{1}{8k^2}(\mathbf{T}_{a_v}^\top \mathbf{Q}\mathbf{T}_{a_v} + (\partial\mathbf{T}_{a_v}/\partial y)^\top \mathbf{Q}(\partial\mathbf{T}_{a_v}/\partial y)) \\ \mathbf{Q_{12}} &= \frac{1}{8k^2}(\mathbf{T}_{a_v}^\top \mathbf{Q}\mathbf{T}_{q_v} + (\partial\mathbf{T}_{a_v}/\partial y)^\top \mathbf{Q}(\partial\mathbf{T}_{q_v}/\partial y)) \\ \mathbf{Q_{21}} &= \frac{1}{8k^2}(\mathbf{T}_{q_v}^\top \mathbf{Q}\mathbf{T}_{a_v} + (\partial\mathbf{T}_{q_v}/\partial y)^\top \mathbf{Q}(\partial\mathbf{T}_{a_v}/\partial y)) \\ \mathbf{Q_{22}} &= \frac{1}{8k^2}(\mathbf{T}_{a_v}^\top \mathbf{Q}\mathbf{T}_{a_v} + (\partial\mathbf{T}_{a_v}/\partial y)^\top \mathbf{Q}(\partial\mathbf{T}_{a_v}/\partial y)). \end{cases} \tag{C.27}$$

We want to set $(\partial\mathbf{T}_{q_v}/\partial y) = 0$, this condition is straightforward by setting

$$f'_{v,\psi,n}(y_i) = 0, \tag{C.28}$$

which holds for $i = 0 \dots N$ and $n = 2 \dots N$. Note that we can set $f'_{v,\psi,n}(y_i) = 0$ at the collocation points y_0 and y_N due to the homogeneous Neumann boundary condition. Therefore, we have

$$\begin{cases} \mathbf{Q_{11}} &= \frac{1}{8k^2}\mathbf{T}_{a_v}^\top \mathbf{Q}\mathbf{T}_{a_v} + (\partial\mathbf{T}_{a_v}/\partial y)^\top \mathbf{Q}(\partial\mathbf{T}_{a_v}/\partial y) \\ \mathbf{Q_{12}} &= \frac{1}{8k^2}\mathbf{T}_{a_v}^\top \mathbf{Q}\mathbf{T}_{q_v}, \mathbf{Q_{21}} = \frac{1}{8k^2}\mathbf{T}_{q_v}^\top \mathbf{Q}\mathbf{T}_{a_v}, \mathbf{Q_{22}} = \frac{1}{8k^2}\mathbf{T}_{q_v}^\top \mathbf{Q}\mathbf{T}_{q_v}. \end{cases} \tag{C.29}$$

Furthermore, the influence of the control signals on the kinetic energy density still may be reduced more by setting $\mathbf{T}_{q_v}(y_i) = 0$ which holds for $i = 1 \dots N-1$, except at the collocation points y_0 and y_N due to the inhomogeneous Dirichlet boundary condition. This condition is straightforward by setting

$$f_{v,\psi,n}(y_i) = 0, \tag{C.30}$$

which hold for $i = 1 \dots N-1$ and $n = 2 \dots N$.

Therefore, by plugging (C.30) into (C.25) and (C.24), the conditions on $f_{v,\psi,n}(y)$ at the collocation points from y_1 to y_{N-1} can be chosen by setting

$$\begin{cases} f_{v,\psi,n}(y_i) &= 0 \\ f''_{v,\psi,n}(y_i) &= 0 \\ f''''_{v,\psi,n}(y_i) &= j\mu R\left[(-j\lambda\alpha^2 - \alpha^3\overline{U}(y_i) - 2\alpha\overline{U}''(y_i) - \frac{\alpha^4}{jR})\Xi_n(y_i)\right. \\ &\quad \left. +(j\lambda + \alpha\overline{U}(y_i) + \frac{2\alpha^2}{jR})\Xi''_n(y_i) - \frac{1}{jR}\Xi''''_n(y_i)\right]. \end{cases} \tag{C.31}$$

And for our convenience, we propose $f'''_{v,\psi,n}(y_i) = 0$ for $i = 1 \dots N-1$ and $n = 2 \dots N$. This condition is condition to which we can assign any value that we want.

Next, we have to determine the condition at the collocation points $y_0 = -1$ and $y_N = +1$. These conditions are given by the inhomogeneous Dirichlet boundary condition and the homogeneous Neumann boundary condition

$$\begin{cases} f_{v,\psi=l,n}(y_0) & = 1,\ f_{v,\psi=u,n}(y_0) = 0 \\ f_{v,\psi=l,n}(y_N) & = 0,\ f_{v,\psi=u,n}(y_N) = 1 \\ f'_{v,\psi,n}(y_0) & = 0 \\ f'_{v,\psi,n}(y_N) & = 0 \\ n & = 2 \dots N. \end{cases} \tag{C.32}$$

In order to reduce the influence of the control signals on the skin friction drag, we give the condition for $f''_{v,\psi,n}(y_0)$ and $f''_{v,\psi,n}(y_N)$. Remark that the skin friction drag is calculated by

$$\mathbf{d}(t) = \mathbf{D}_1\mathbf{x}(t) + \mathbf{D}_2\mathbf{u}(t), \tag{C.33}$$

where $\mathbf{D}_2 = \begin{bmatrix} -1 & +1 \end{bmatrix} \mathbf{S}_2$ and the shear stress from the control signals is given by

$$\mathbf{S}_2 = +\frac{j\alpha}{k^2 R} \begin{bmatrix} \mathbf{F}''_{v,2}(y=+1) & \dots & \mathbf{F}''_{v,N}(y=+1) \\ \mathbf{F}''_{v,2}(y=-1) & \dots & \mathbf{F}''_{v,N}(y=-1) \end{bmatrix}. \tag{C.34}$$

The influence of the control signals on the skin friction drag is reduced by setting $\mathbf{D}_2 = 0$, furthermore $\mathbf{S}_2 = 0$. This condition is straightforward by setting

$$\begin{cases} f''_{v,\psi,n}(y_0) & = 0 \\ f''_{v,\psi,n}(y_N) & = 0. \end{cases} \tag{C.35}$$

And for our convenience, we propose $f^{(i)}_{v,\psi,n}(y_0) = f^{(i)}_{v,\psi,n}(y_N) = 0$ for $i = 3 \dots 4$, $n = 2 \dots N$.

Finally, the conditions on $f_{v,\psi,n}(y)$ at the collocation points from y_1 to y_{N-1} are chosen by setting

$$\begin{cases} f_{v,\psi,n}(y_i) & = 0 \\ f'_{v,\psi,n}(y_i) & = 0 \\ f''_{v,\psi,n}(y_i) & = 0 \\ f'''_{v,\psi,n}(y_i) & = 0 \\ f''''_{v,\psi,n}(y_i) & = j\mu R \Big[(-j\lambda\alpha^2 - \alpha^3\overline{U}(y_i) - 2\alpha\overline{U}''(y_i) - \dfrac{\alpha^4}{jR})\Xi_n(y_i) \\ & \quad + (j\lambda + \alpha\overline{U}(y_i) + \dfrac{2\alpha^2}{jR})\Xi''_n(y_i) - \dfrac{1}{jR}\Xi''''_n(y_i) \Big] \\ i & = 1 \dots N-1 \\ n & = 2 \dots N, \end{cases} \tag{C.36}$$

and at the collocation points from y_0 to y_N are chosen by setting

$$\begin{cases} f_{v,\psi=l,n}(y_0) & = 1,\ f_{v,\psi=u,n}(y_0) = 0 \\ f'_{v,\psi,n}(y_0) & = f''_{v,\psi,n}(y_0) = f'''_{v,\psi,n}(y_0) = f''''_{v,\psi,n}(y_0) = 0 \\ f_{v,\psi=l,n}(y_N) & = 0,\ f_{v,\psi=u,n}(y_N) = 1 \\ f'_{v,\psi,n}(y_N) & = f''_{v,\psi,n}(y_N) = f'''_{v,\psi,n}(y_N) = f''''_{v,\psi,n}(y_N) = 0 \\ n & = 2 \dots N. \end{cases} \tag{C.37}$$

We can thus construct the function $f_{\phi,\psi,n}(y)$ (with $\phi = v$) from the condition $f^{(j)}_{\phi,\psi,n}(y)$ in (C.36) and (C.37) based on the Hermite interpolating polynomials ($P = 4$ for $\phi = v$)

$$f_{\phi,\psi,n}(y) = \sum_{i=0}^{N}\sum_{j=0}^{P} f^{(j)}_{\phi,\psi,n}(y_i) H_{\phi,ij}(y), \tag{C.38}$$

where the polynomials $H_{\phi,ij}(y)$ are given by (see e.g. [Berezin and Zhidkov, 1973])

$$H_{\phi,ij}(y) = \frac{1}{j!}\sum_{k=0}^{P-j}\frac{1}{k!}\left(\frac{(y-y_i)^{P+1}}{\Omega_\phi(y)}\right)^{(k)}_{y=y_i}\frac{\Omega_\phi(y)}{(y-y_i)^{P+1-j-k}}, \tag{C.39}$$

with $\Omega_\phi(y) = \prod_{i=0}^{N}(y-y_i)^{P+1}$.

C.4.2 3D plane Poiseuille flow

The state and input matrices are

$$\begin{cases}
\mathbf{L}_{11} &= j(-k^2\mathbf{D}0_{DN}(\Xi) + \mathbf{D}2_{DN}(\Xi)) \\
\mathbf{L}_{12} &= [0] \\
\mathbf{L}_{21} &= [0] \\
\mathbf{L}_{22} &= j\mathbf{D}0_D(\Theta) \\
\mathbf{A}_{11} &= (-\alpha\overline{U}k^2 - \alpha\overline{U}'' - \frac{k^4\mathbf{I}}{jR})\mathbf{D}0_{DN}(\Xi) + (\alpha\overline{U} + \frac{2k^2\mathbf{I}}{jR})\mathbf{D}2_{DN}(\Xi) - \frac{1}{jR}\mathbf{D}4_{DN}(\Xi) \\
\mathbf{A}_{12} &= [0] \\
\mathbf{A}_{21} &= \beta\overline{U}'\mathbf{D}0_{DN}(\Xi) \\
\mathbf{A}_{22} &= (\alpha\overline{U} + \frac{k^2\mathbf{I}}{jR})\mathbf{D}0_D(\Theta) - \frac{1}{jR}\mathbf{D}2_D(\Theta).
\end{cases} \tag{C.40}$$

and

$$\begin{cases}
\mathbf{E}_{11} &= j(k^2\mathbf{D}0_{DN}(\mathbf{F}_v) - \mathbf{D}2_{DN}(\mathbf{F}_v)) \\
\mathbf{E}_{12} &= [0] \\
\mathbf{E}_{21} &= [0] \\
\mathbf{E}_{22} &= -j\mathbf{D}0_D(\mathbf{F}_\eta) \\
\mathbf{B}_{11} &= (-\alpha\overline{U}k^2 - \alpha\overline{U}'' - \frac{k^4\mathbf{I}}{jR})\mathbf{D}0_{DN}(\mathbf{F}_v) + (\alpha\overline{U} + \frac{2k^2\mathbf{I}}{jR})\mathbf{D}2_{DN}(\mathbf{F}_v) - \frac{1}{jR}\mathbf{D}4_{DN}(\mathbf{F}_v) \\
\mathbf{B}_{12} &= [0] \\
\mathbf{B}_{21} &= \beta\overline{U}'\mathbf{D}0_{DN}(\mathbf{F}_v) \\
\mathbf{B}_{22} &= (\alpha\overline{U} + \frac{k^2\mathbf{I}}{jR})\mathbf{D}0_D(\mathbf{F}_\eta) - \frac{1}{jR}\mathbf{D}2_D(\mathbf{F}_\eta).
\end{cases} \tag{C.41}$$

According to (C.41) and to the definitions of the matrices involved in these equations, the constraints to ensure $\mathbf{B} = -\mu(\lambda\mathbf{L} + \mathbf{A})$ are straightforward

$$\begin{cases} \beta\overline{U}^{'}\mathbf{D}0_{DN}(\mathbf{F}_v) = -\mu\beta\overline{U}^{'}\mathbf{D}0_{DN}(\Xi) \\ (-\alpha k^2\overline{U} - \alpha\overline{U}^{''} - \dfrac{k^4\mathbf{I}}{jR})\mathbf{D}0_{DN}(\mathbf{F}_v) + (\alpha\overline{U} + \dfrac{2k^2\mathbf{I}}{jR})\mathbf{D}2_{DN}(\mathbf{F}_v) - \dfrac{\mathbf{D}4_{DN}(\mathbf{F}_v)}{jR} \\ = -\mu\left[(-j\lambda k^2\mathbf{I} - \alpha k^2\overline{U} - \alpha\overline{U}^{''} - \dfrac{k^4\mathbf{I}}{jR})\mathbf{D}0_{DN}(\Xi) + (j\lambda\mathbf{I} + \alpha\overline{U} + \dfrac{2k^2\mathbf{I}}{jR})\mathbf{D}2_{DN}(\Xi) - \dfrac{\mathbf{D}4_{DN}(\Xi)}{jR}\right] \\ (\alpha\overline{U} + \dfrac{k^2\mathbf{I}}{jR})\mathbf{D}0_D(\mathbf{F}_\eta) - \dfrac{1}{jR}D2_D(\mathbf{F}_\eta) = -\mu\left[(j\lambda\mathbf{I} + \alpha\overline{U} + \dfrac{k^2\mathbf{I}}{jR})\mathbf{D}0_D(\Theta) - \dfrac{1}{jR}\mathbf{D}2_D(\Theta)\right], \end{cases} \tag{C.42}$$

Concerning $\mathbf{B} = -\mu(\lambda\mathbf{L} + \mathbf{A})$ the constraints are given by (C.42) that can be rewritten as follows (C.43)

$$\begin{cases} f_{v,\psi,n}(y_i) = -\mu\Xi_n(y_i) \\ (-\alpha k^2\overline{U}(y_i) + 2\alpha\overline{U}^{''}(y_i) - \dfrac{k^4}{jR})f_{v,\psi,n}(y_i) + (\alpha\overline{U}(y_i) + \dfrac{2k^2}{jR})f^{''}_{v,\psi,n}(y_i) - \dfrac{1}{jR}f^{(4)}_{v,\psi,n}(y_i) \\ = -\mu\left[(-j\lambda k^2 - \alpha k^2\overline{U}(y_i) - 2\alpha\overline{U}^{''}(y_i) - \dfrac{k^4}{jR})\Xi_n(y_i) + (j\lambda + \alpha\overline{U}(y_i) + \dfrac{2k^2}{jR})\Xi^{''}_n(y_i) - \dfrac{1}{jR}\Xi^{''''}_n(y_i)\right] \\ (\alpha\overline{U}(y_i) + \dfrac{k^2}{jR})f_{\eta,\psi,n}(y_i) - \dfrac{1}{jR}f^{''}_{\eta,\psi,n}(y_i) = -\mu\left[(j\lambda + \alpha\overline{U}(y_i) + \dfrac{k^2}{jR})\Theta_n(y_i) - \dfrac{1}{jR}\Theta^{''}_n(y_i)\right]. \end{cases} \tag{C.43}$$

which must hold also for $i = 1 \ldots N-1$ and $n = 2 \ldots N$.

According to (C.41) and to the definitions of the matrices involved in these equations, the constraints to ensure $\mathbf{E} = 0$ are straightforward

$$\begin{cases} k^2 f_{v,\psi,n}(y_i) - f^{''}_{v,\psi,n}(y_i) & = 0 \\ f_{\eta,\psi,n}(y_i) & = 0, \end{cases} \tag{C.44}$$

which must hold for $i = 1 \ldots N-1$ and $n = 2 \ldots N$.

Therefore, based on (C.44) and (C.43), the conditions on $f_{v,\psi,n}(y)$ and $f_{\eta,\psi,n}(y)$ at the collocation points from y_1 to y_{N-1} can be chosen by setting

$$\begin{cases} f_{v,\psi,n}(y_i) & = -\mu\Xi_n(y_i) \\ f^{''}_{v,\psi,n}(y_i) & = -\mu k^2\Xi_n(y_i) \\ f^{''''}_{v,\psi,n}(y_i) & = j\mu R\left[(-j\lambda k^2 - \alpha k^2\overline{U}(y_i) - \dfrac{2k^4}{jR})\Xi_n(y_i)\right. \\ & \left. +(j\lambda + \alpha\overline{U}(y_i) + \dfrac{2k^2}{jR})\Xi^{''}_n(y_i) - \dfrac{1}{jR}\Xi^{''''}_n(y_i)\right] \\ f_{\eta,\psi,n}(y_i) & = 0 \\ f^{''}_{\eta,\psi,n}(y_i) & = \mu jR(j\lambda + \alpha\overline{U}(y_i) + \dfrac{k^2}{jR})\Theta_n(y_i) - \mu\Theta^{''}_n(y_i). \end{cases} \tag{C.45}$$

In order to reduce the influence of the control signals on the kinetic energy density, we give the condition for $f^{'}_{v,\psi,n}(y_i)$. Remark that the kinetic energy density is calculated by

$$\varepsilon(t) = \mathbf{x}^\top(t)\mathbf{Q_{11}}\mathbf{x}(t) + \mathbf{x}^\top(t)\mathbf{Q_{12}}\mathbf{u}(t) + \mathbf{u}^\top(t)\mathbf{Q_{21}}\mathbf{x}(t) + \mathbf{u}^\top(t)\mathbf{Q_{22}}\mathbf{u}(t), \tag{C.46}$$

where

$$\begin{cases} \mathbf{Q_{11}} &= \frac{1}{8k^2}(\mathbf{T}_{a_v}^\top \mathbf{Q}\mathbf{T}_{a_v} + (\partial\mathbf{T}_{a_v}/\partial y)^\top \mathbf{Q}(\partial\mathbf{T}_{a_v}/\partial y) + \mathbf{T}_{a_\eta}^\top \mathbf{Q}\mathbf{T}_{a_\eta}) \\ \mathbf{Q_{12}} &= \frac{1}{8k^2}(\mathbf{T}_{a_v}^\top \mathbf{Q}\mathbf{T}_{q_v} + (\partial\mathbf{T}_{a_v}/\partial y)^\top \mathbf{Q}(\partial\mathbf{T}_{q_v}/\partial y) + \mathbf{T}_{a_\eta}^\top \mathbf{Q}\mathbf{T}_{q_\eta}) \\ \mathbf{Q_{21}} &= \frac{1}{8k^2}(\mathbf{T}_{q_v}^\top \mathbf{Q}\mathbf{T}_{a_v} + (\partial\mathbf{T}_{q_v}/\partial y)^\top \mathbf{Q}(\partial\mathbf{T}_{a_v}/\partial y) + \mathbf{T}_{q_\eta}^\top \mathbf{Q}\mathbf{T}_{a_\eta}) \\ \mathbf{Q_{22}} &= \frac{1}{8k^2}(\mathbf{T}_{q_v}^\top \mathbf{Q}\mathbf{T}_{q_v} + (\partial\mathbf{T}_{q_v}/\partial y)^\top \mathbf{Q}(\partial\mathbf{T}_{q_v}/\partial y) + \mathbf{T}_{q_\eta}^\top \mathbf{Q}\mathbf{T}_{q_\eta}). \end{cases} \tag{C.47}$$

We want to set $(\partial\mathbf{T}_{q_v}/\partial y) = 0$. This condition is straightforward by setting

$$f'_{v,\psi,n}(y_i) = 0, \tag{C.48}$$

which holds for $i = 0 \dots N$ and $n = 2 \dots N$. Note that we can set $f'_{v,\psi,n}(y_i) = 0$ at the collocation points y_0 and y_N due to the homogeneous Neumann boundary condition. Therefore, we have

$$\begin{cases} \mathbf{Q_{11}} &= \frac{1}{8k^2}(\mathbf{T}_{a_v}^\top \mathbf{Q}\mathbf{T}_{a_v} + (\partial\mathbf{T}_{a_v}/\partial y)^\top \mathbf{Q}(\partial\mathbf{T}_{a_v}/\partial y) + \mathbf{T}_{a_\eta}^\top \mathbf{Q}\mathbf{T}_{a_\eta}) \\ \mathbf{Q_{12}} &= \frac{1}{8k^2}(\mathbf{T}_{a_v}^\top \mathbf{Q}\mathbf{T}_{q_v} + \mathbf{T}_{a_\eta}^\top \mathbf{Q}\mathbf{T}_{q_\eta}), \mathbf{Q_{21}} = \frac{1}{8k^2}(\mathbf{T}_{q_v}^\top \mathbf{Q}\mathbf{T}_{a_v} + \mathbf{T}_{q_\eta}^\top \mathbf{Q}\mathbf{T}_{a_\eta}) \\ \mathbf{Q_{22}} &= \frac{1}{8k^2}(\mathbf{T}_{q_v}^\top \mathbf{Q}\mathbf{T}_{q_v} + \mathbf{T}_{q_\eta}^\top \mathbf{Q}\mathbf{T}_{q_\eta}), \end{cases} \tag{C.49}$$

And for our convenience, we propose $f'''_{v,\psi,n}(y_i) = f'_{\eta,\psi,n}(y_i) = 0$ for $i = 1 \cdots N-1$ and $n = 2 \cdots N$. These conditions are condition to which we can assign any value that we want.

Next, we have to determine the conditions $f_{v,\psi,n}(y_i)$ and $f_{\eta,\psi,n}(y_i)$ at the collocation points $y_0 = -1$ and $y_N = +1$. These conditions are given by the inhomogeneous boundary condition and the Neumann boundary condition

$$\begin{cases} f_{v,\psi=l,n}(y_0) &= 1,\ f_{v,\psi=u,n}(y_0) = 0 \\ f_{v,\psi=l,n}(y_N) &= 0,\ f_{v,\psi=u,n}(y_N) = 1 \\ f'_{v,\psi,n}(y_0) &= 0 \\ f'_{v,\psi,n}(y_N) &= 0 \\ f_{\eta,\psi=l,n}(y_0) &= 1,\ f_{\eta,\psi=u,n}(y_0) = 0 \\ f_{\eta,\psi=l,n}(y_N) &= 0,\ f_{\eta,\psi=u,n}(y_N) = 0 \\ n &= 2 \dots N \end{cases} \tag{C.50}$$

In order to reduce the effect of the control signals on the skin friction drag, we give the condition for $f''_{v,\psi,n}(y_i)$ and $f''_{\eta,\psi,n}(y_i)$ at the collocation points y_0 and y_N. Remark that the skin friction drag is calculated by

$$\mathbf{d}(t) = \mathbf{D}_1\mathbf{x}(t) + \mathbf{D}_2\mathbf{u}(t), \tag{C.51}$$

where $\mathbf{D}_2 = \left[\begin{array}{cccc} -1 & +1 & 0 & 0 \end{array} \right] \mathbf{S}_2$ and the shear stress from the control signals is given by

$$\left\{ \begin{array}{ll} \mathbf{S}_{2,11} & = +\dfrac{j\alpha}{k^2 R} \left[\begin{array}{ccc} \mathbf{F}_{v,2}^{''}(y=+1) & \ldots & \mathbf{F}_{v,N}^{''}(y=+1) \\ \mathbf{F}_{v,2}^{''}(y=-1) & \ldots & \mathbf{F}_{v,N}^{''}(y=-1) \end{array} \right] \\ \mathbf{S}_{2,21} & = +\dfrac{j\beta}{k^2 R} \left[\begin{array}{ccc} \mathbf{F}_{v,2}^{''}(y=+1) & \ldots & \mathbf{F}_{v,N}^{''}(y=+1) \\ \mathbf{F}_{v,2}^{''}(y=-1) & \ldots & \mathbf{F}_{v,N}^{''}(y=-1) \end{array} \right] \\ \mathbf{S}_{2,12} & = -\dfrac{j\beta}{k^2 R} \left[\begin{array}{ccc} \mathbf{F}_{\eta,2}^{'}(y=+1) & \ldots & \mathbf{F}_{\eta,N}^{'}(y=+1) \\ \mathbf{F}_{\eta,2}^{'}(y=-1) & \ldots & \mathbf{F}_{\eta,N}^{'}(y=-1) \end{array} \right] \\ \mathbf{S}_{2,22} & = +\dfrac{j\alpha}{k^2 R} \left[\begin{array}{ccc} \mathbf{F}_{\eta,2}^{'}(y=+1) & \ldots & \mathbf{F}_{\eta,N}^{'}(y=+1) \\ \mathbf{F}_{\eta,2}^{''}(y=-1) & \ldots & \mathbf{F}_{\eta,N}^{''}(y=-1) \end{array} \right]. \end{array} \right. \tag{C.52}$$

The influence of the control signals on the skin friction drag is reduced by setting $\mathbf{D}_2 = 0$, furthermore $\mathbf{S}_2 = 0$. This condition is straightforward by setting

$$\left\{ \begin{array}{l} f_{v,\psi,n}^{''}(y_0) = f_{v,\psi,n}^{''}(y_N) = 0 \\ f_{\eta,\psi,n}^{''}(y_0) = f_{\eta,\psi,n}^{''}(y_N) = 0. \end{array} \right. \tag{C.53}$$

And for our convenience, we propose $f_{v,\psi,n}^{(i)}(y_0) = f_{v,\psi,n}^{(i)}(y_N) = 0$ for $i = 3 \ldots 4$ and $f_{\eta,\psi,n}^{'}(y_0) = f_{\eta,\psi,n}^{'}(y_0) = 0$ and $n = 2 \ldots N$. These conditions are condition to which we can assign any value that we want.

Finally, the conditions on $f_{v,\psi,n}(y)$ and $f_{\eta,\psi,n}(y)$ at the collocation points from y_1 to y_{N-1} can be chosen by setting

$$\left\{ \begin{array}{ll} f_{v,\psi,n}(y_i) & = -\mu \Xi_n(y_i) \\ f_{v,\psi,n}^{'}(y_i) & = 0 \\ f_{v,\psi,n}^{''}(y_i) & = -\mu k^2 \Xi_n(y_i) \\ f_{v,\psi,n}^{'''}(y_i) & = 0 \\ f_{v,\psi,n}^{''''}(y_i) & = j\mu R \left[(-j\lambda k^2 - \alpha k^2 \overline{U}(y_i) - \dfrac{2k^4}{jR}) \Xi_n(y_i) \right. \\ & \left. + (j\lambda + \alpha \overline{U}(y_i) + \dfrac{2k^2}{jR}) \Xi_n^{''}(y_i) - \dfrac{1}{jR} \Xi_n^{''''}(y_i) \right] \\ f_{\eta,\psi,n}(y_i) & = 0 \\ f_{\eta,\psi,n}^{'}(y_i) & = 0 \\ f_{\eta,\psi,n}^{''}(y_i) & = \mu j R (j\lambda + \alpha \overline{U}(y_i) + \dfrac{k^2}{jR}) \Theta_n(y_i) - \mu \Theta_n^{''}(y_i) \\ i & = 1 \ldots N-1 \\ n & = 2 \ldots N \end{array} \right. \tag{C.54}$$

and at the collocation points y_0 and y_N can be chosen by setting

$$\begin{cases} f_{v,\psi=l,n}(y_0) & = 1,\ f_{v,\psi=u,n}(y_0) = 0 \\ f'_{v,\psi,n}(y_0) & = f''_{v,\psi,n}(y_0) = f'''_{v,\psi,n}(y_0) = f''''_{v,\psi,n}(y_0) = 0 \\ f_{v,\psi=l,n}(y_N) & = 0,\ f_{v,\psi=u,n}(y_N) = 1 \\ f'_{v,\psi,n}(y_N) & = f''_{v,\psi,n}(y_N) = f'''_{v,\psi,n}(y_N) = f''''_{v,\psi,n}(y_N)0 \\ f_{\eta,\psi=l,n}(y_0) & = 1,\ f_{\eta,\psi=u,n}(y_0) = 0 \\ f'_{\eta,\psi,n}(y_0) & = f''_{\eta,\psi,n}(y_0) = 0 \\ f_{\eta,\psi=l,n}(y_N) & = 0,\ f_{\eta,\psi=u,n}(y_N) = 1 \\ f'_{\eta,\psi,n}(y_N) & = f''_{\eta,\psi,n}(y_N) = 0 \\ n & = 2 \cdots N \end{cases} \tag{C.55}$$

We can thus construct the functions $f_{\phi,\psi,n}(y)$ (with $\phi = v$ or $\phi = \eta$) from the conditions $f^{(j)}_{\phi,\psi,n}(y)$ in (C.54) and (C.55) based on the Hermite interpolating polynomials ($P = 4$ for $\phi = v$ and $P = 2$ for $\phi = \eta$)

$$f_{\phi,\psi,n}(y) = \sum_{i=0}^{N} \sum_{j=0}^{P} f^{(j)}_{\phi,\psi,n}(y_i) H_{\phi,ij}(y), \tag{C.56}$$

where the polynomials $H_{\phi,ij}(y)$ are given by (see e.g. [Berezin and Zhidkov, 1973])

$$H_{\phi,ij}(y) = \frac{1}{j!} \sum_{k=0}^{P-j} \frac{1}{k!} \left(\frac{(y - y_i)^{P+1}}{\Omega_\phi(y)} \right)^{(k)}_{y=y_i} \frac{\Omega_\phi(y)}{(y - y_i)^{P+1-j-k}}, \tag{C.57}$$

with $\Omega_\phi(y) = \prod_{i=0}^{N} (y - y_i)^{P+1}$.

C.5 Simulation results

C.5.1 Case I: 2D plane Poiseuille flow

We set $\alpha = 1$, $\beta = 0$ and $R = 10\ 000$ (see section 5.6). We set $N = 100$. We choose $\lambda = 0.25$ and $\mu = 1$. We simulate the behavior of the closed loop system with and without measurement noise.

The behavior of the state vector versus time is shown in Figure C.1. The state vector is of course an exponential decoupled decrease in Figure C.1(a). In the presence of measurement noise appears and using the optical flow, the behavior of the state vector is very robust to measurement noise as observed from Figure C.1(b) to Figure C.1(d). Results for the kinetic energy density and the skin friction drag are depicted in Figure C.2 and Figure C.3, respectively. Note that the proposed approach allows us to ensure that the exponential decoupled decreases of the state vector, the skin friction drag and the velocity component are $-\lambda t$ while for the kinetic energy density it is $-2\lambda t$.

The behavior of velocity component is given in Figure C.4. The kinetic energy density, the velocity profile and the velocity field are also given. As shown from Figure

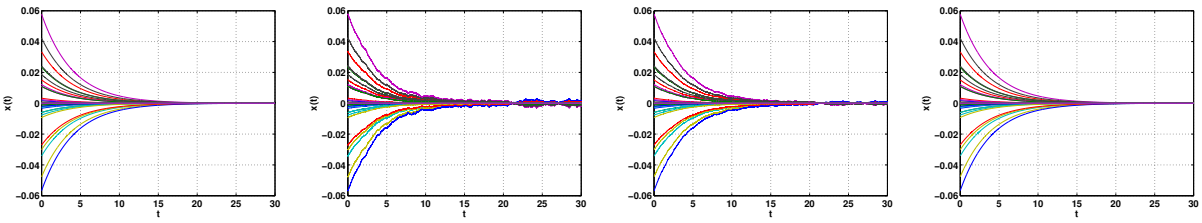

(a) (b) $N_x = 2$ (c) $N_x = 4$ (d) $N_x = 256$

Figure C.1: Behavior of the state vector versus time.

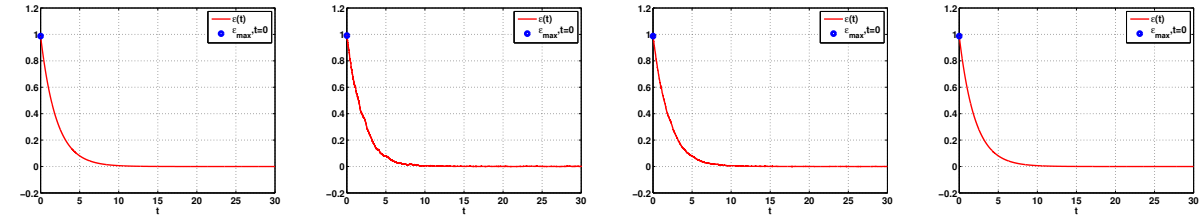

(a) (b) $N_x = 2$ (c) $N_x = 4$ (d) $N_x = 256$

Figure C.2: Behavior of kinetic energy density versus time.

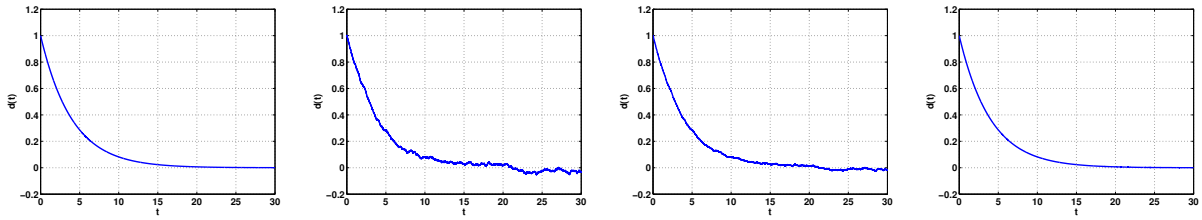

(a) (b) $N_x = 2$ (c) $N_x = 4$ (d) $N_x = 256$

Figure C.3: Behavior of the skin friction drag versus time.

C.4(a) to Figure C.4(d), the evolution of the controlled flow is versus time. The proposed control law leads the velocity component to an exponential decoupled decrease, this is very nice result. By applying the control, the velocity component becomes the steady solution $(1 - y^2, 0)$ by an exponential decoupled decrease.

C.5.2 Case II: 3D plane Poiseuille flow

C.5.2.1 3D plane Poiseuille flow, the stream vortex, $\alpha = 0$ and $\beta = 2.044$

The uncontrolled flow of this case is interesting, the transient energy density has a maximal value with respect the other cases.

We set $\alpha = 0$, $\beta = 2.044$ and $R = 5\ 000$ (see section 5.6). And we set $N = 50$. We choose $\lambda = 0.25$ and $\mu = 1$. Similar results like the 2D plane Poiseuille flow are reported

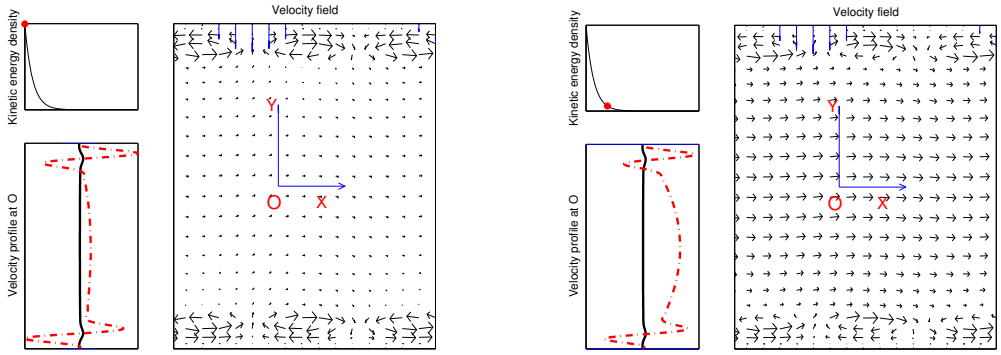

(a) $t = 0$ (b) $t = 0.2\ t_{end}$

(c) $t = 0.6\ t_{end}$ (d) $t = t_{end}$

Figure C.4: Shape of the flow perturbation with measurement noise, $N_x = 256$

in Figure C.5, Figure C.6 and Figure C.7 for the state vector, the kinetic energy density and the skin friction drag, respectively.

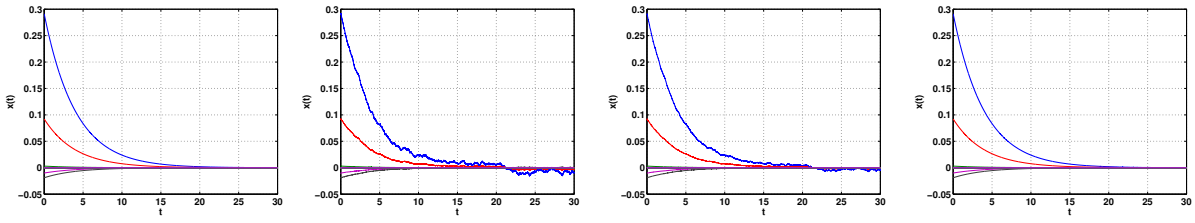

(a) (b) $N_x = 2$ (c) $N_x = 4$ (d) $N_x = 256$

Figure C.5: Behavior of the state vector versus time.

The behavior of the kinetic energy density, the velocity profile and the velocity field are given in Figure C.8. As shown from Figure C.8(a) to Figure C.8(a), the evolution of the controlled flow is versus time. In contrast to the uncontrolled flow or the **LQR**

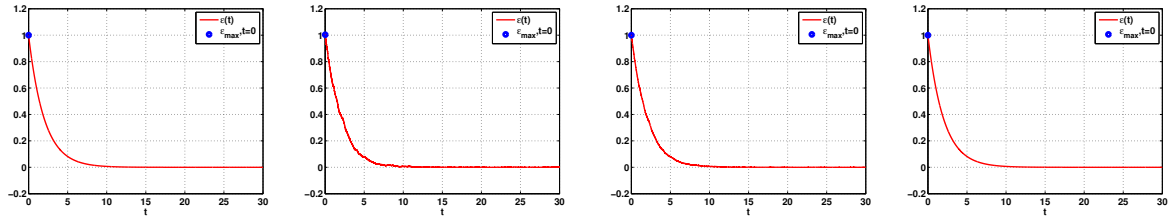

(a) (b) $N_x = 2$ (c) $N_x = 4$ (d) $N_x = 256$

Figure C.6: Behavior of the kinetic energy density versus time.

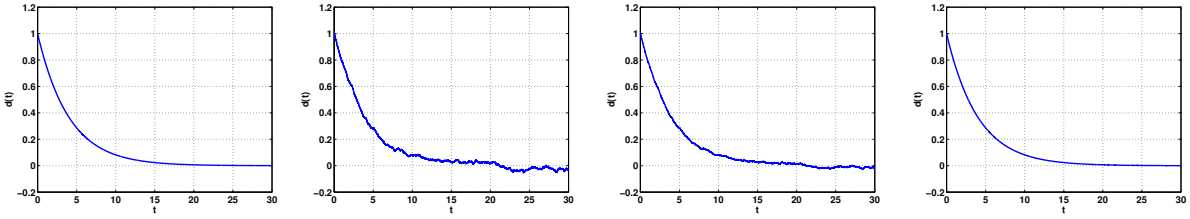

(a) (b) $N_x = 2$ (c) $N_x = 4$ (d) $N_x = 256$

Figure C.7: Behavior of the skin friction drag versus time.

control, an exponential decoupled decrease achieves a very small value of contours, the level contours are only from 0 to 1, the maximal value is 1, while 150 for the uncontrolled flow and 80 for the **LQR** control (note that the levels of contour at $t = 0$ are from 0 to 1). The way that the flow becomes laminar is not turbulent. The velocity component becomes the steady solution $(1 - y^2, 0, 0)$ by an exponential decoupled decrease.

C.5.2.2 3D plane Poiseuille flow, the oblique wave, $\alpha = 1$ and $\beta = 1$

We also consider the oblique wave system. We set $\alpha = 1$, $\beta = 1$, $R = 5\,000$ and $N = 50$. We choose $\lambda = 0.25$ and $\mu = 1$. The results are reported in Figure C.9. Again, we have a nice result of the controlled flow.

C.6 Conclusion

In this chapter, we use the Hermite interpolating polynomials to design a controller which achieves an exponential decoupled decrease without inverting a matrix. Using this method, the state vector, the kinetic energy density, the skin friction drag and the velocity component have also an exponential decoupled decrease. So, not only does the proposed method solve the non-normality but it also solves the bad condition number issue. The way of setting the Hermite interpolating polynomials is not only such that an exponential decoupled decrease of state vector is ensured but also such that influence of the control signals on the skin friction drag and the kinetic energy density is reduced.

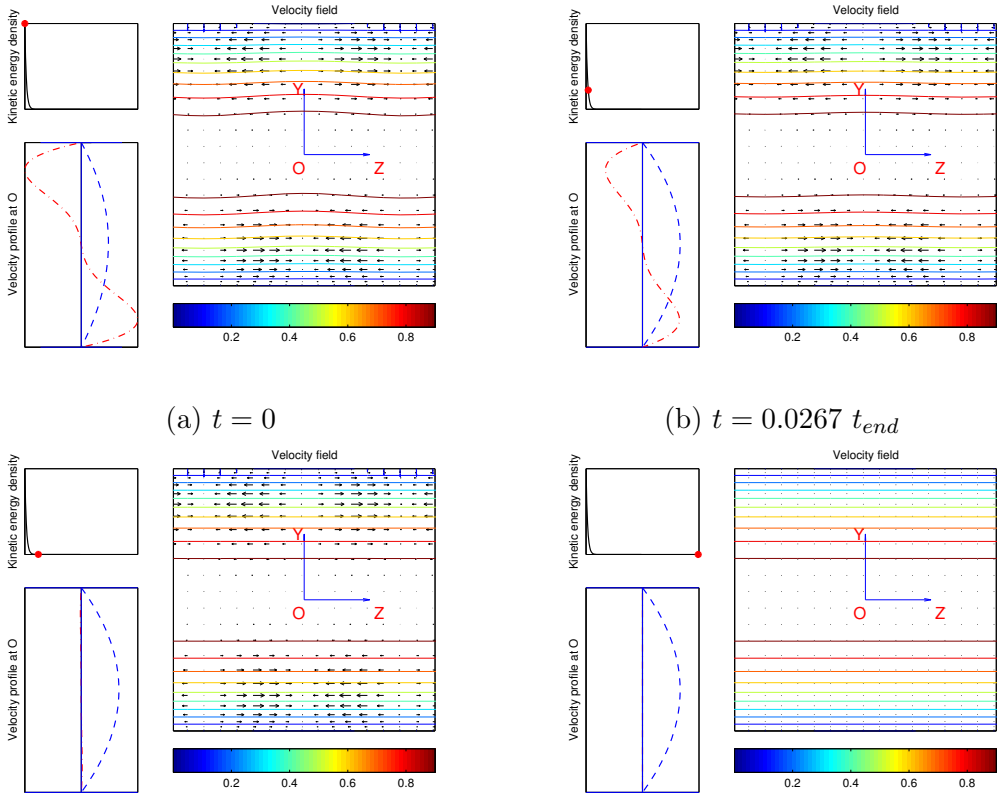

(a) $t = 0$ (b) $t = 0.0267\ t_{end}$

(c) $t = 0.1267\ t_{end}$ (d) $t = t_{end}$

Figure C.8: Shape of the flow perturbation with measurement noise, $N_x = 256$

Concerning the measurement noise, by using the optical flow to estimate the state vector, the proposed control is very robust to measurement noise.

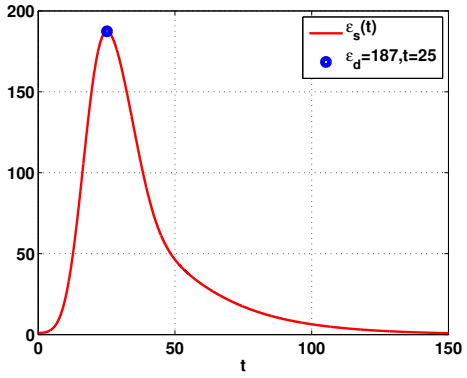

(a) kinetic energy density versus time

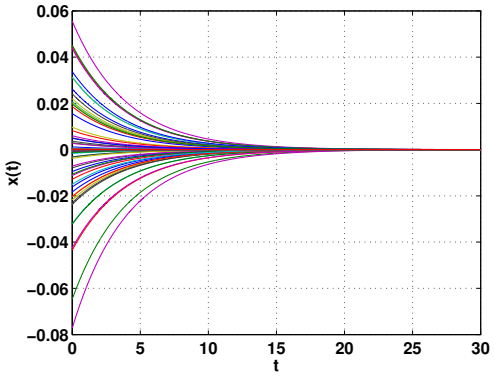

(b) state vector versus time

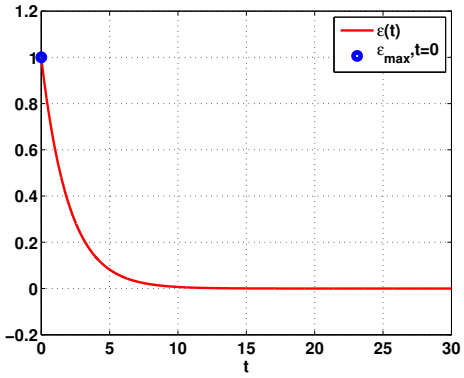

(c) kinetic energy density versus time

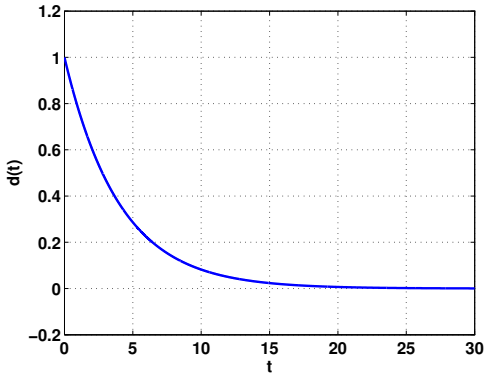

(d) skin friction drag versus time

Figure C.9: Behavior of the oblique wave system: (a) uncontrolled flow, (b)-(d) controlled flow.

Appendix D

Model reduction, r is large enough

D.1 2D plane Poiseuille flow

Once again, we talk about the advantage of increasing **DOF** in the next results. We try to use the visual servoing control based on the model reduction (9.18). Indeed, we increase **DOF** to ensure that we can use the visual servoing control $\mathbf{u}(t) = \mathbf{K}_r\mathbf{z}_r(t)$ which guarantees $\dot{\mathbf{z}}_r(t) = -\lambda\mathbf{z}_r(t) \rightarrow \dot{\varepsilon}_r(t) = -2\lambda\varepsilon_r(t)$. Note that the way of increasing **DOF** has been given in Chapter 7.

The initial condition is chosen as the worst initial condition of each closed loop system (9.28). The behavior of the system (9.28) is given in Figure D.1 in the case of $r = 50 < n = 94$. Note that $\dot{\mathbf{z}}_r(t) = -\lambda\mathbf{z}_r(t)$, therefore $\mathbf{u}(t) = \mathbf{K}_r\mathbf{z}_r(t)$ always has an exponential decrease. However, we still have $\dot{\mathbf{z}}_{n-r}(t) = \mathbf{B}_{n-r,m}\mathbf{K}_r\mathbf{z}_r(t) + \Lambda_{n-r}\mathbf{z}_{n-r}(t)$, therefore the state vector has not an exponential decrease. Although the control law is designed based on the model reduction, the behavior of the synchronic transient energy growth and the skin friction drag are very good. This result allows us to see that even $\dot{\mathbf{z}}(t) \neq -\lambda\mathbf{z}(t)$ but $\dot{\varepsilon}(t) \approx -2\lambda\varepsilon(t)$ when the important modes are remained.

The behavior of the synchronic transient energy growth $\varepsilon_s(t)$ is depicted in Figure D.2 versus the variation of r with $\lambda = 0.25$. We choose the model reduction (9.18) with $r = 20$, $r = 30$, $r = 40$ and $r = 50$. We also obtain a good result for the synchronic transient energy growth $\varepsilon_s(t)$ even in the case of $r = 20$, the model reduction only contains 20% of the full state vector. When r is large enough, the behavior of the model reduction is equivalent to the full system.

In the case of $r = 40$, the influence of the parameter λ is on the behavior of the system (9.28) is depicted in Figure D.3. We can choose parameter λ to have a good result.

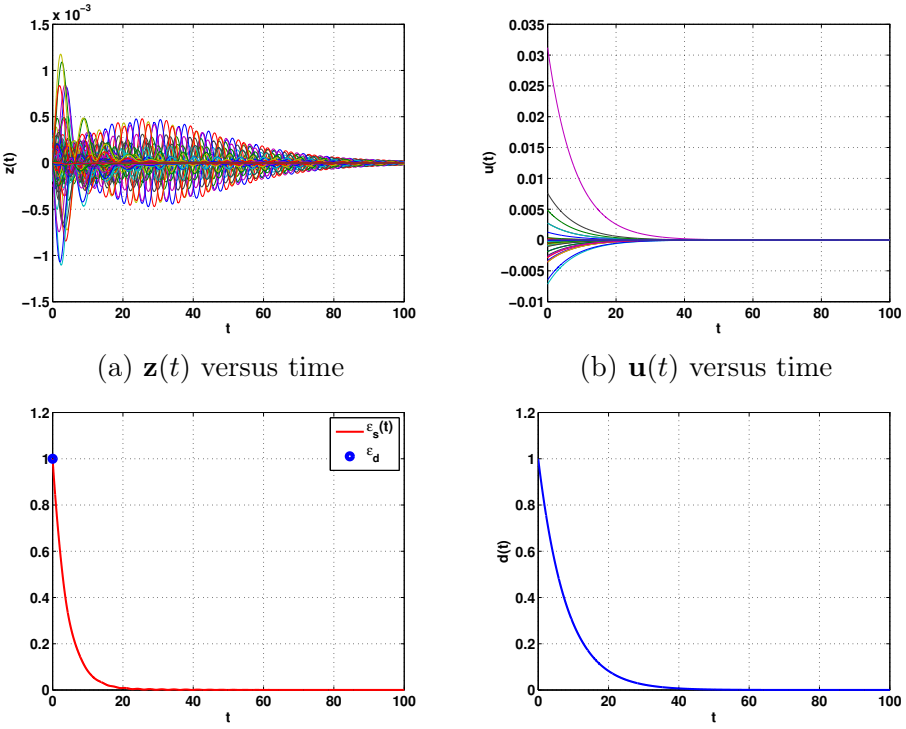

(a) $\mathbf{z}(t)$ versus time (b) $\mathbf{u}(t)$ versus time

(c) $\varepsilon_s(t)$ versus time (d) $\mathbf{d}(t)$ versus time

Figure D.1: Behavior of the closed loop system ($n = 94$, $r = 50, \lambda = 0.125$).

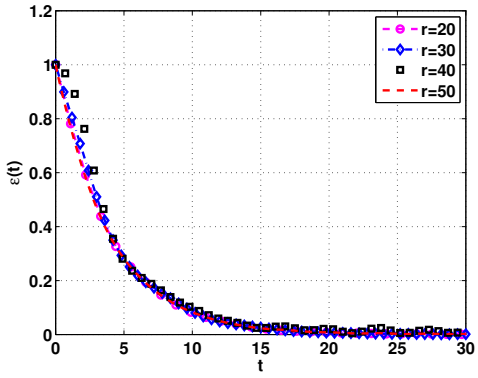

Figure D.2: Behavior of the synchronic transient energy growth versus time with the visual servoing control law designed on the model reduction (n=94) for various values of r.

D.2 3D plane Poiseuille flow

The behavior of the state vector, the control signal, the synchronic transient energy growth and the skin friction drag are depicted in Figure D.4, respectively. As in the 2D

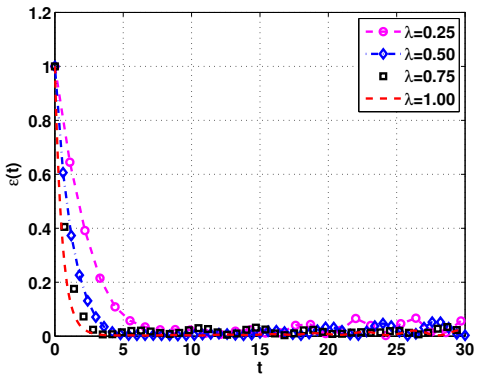

Figure D.3: Behavior of the synchronic transient energy growth versus time with the visual servoing control law designed on the model reduction ($r = 40$) for various values of λ.

plane Poiseuille flow, we have a good result for the synchronic transient energy growth even all state vectors have not an exponential decrease.

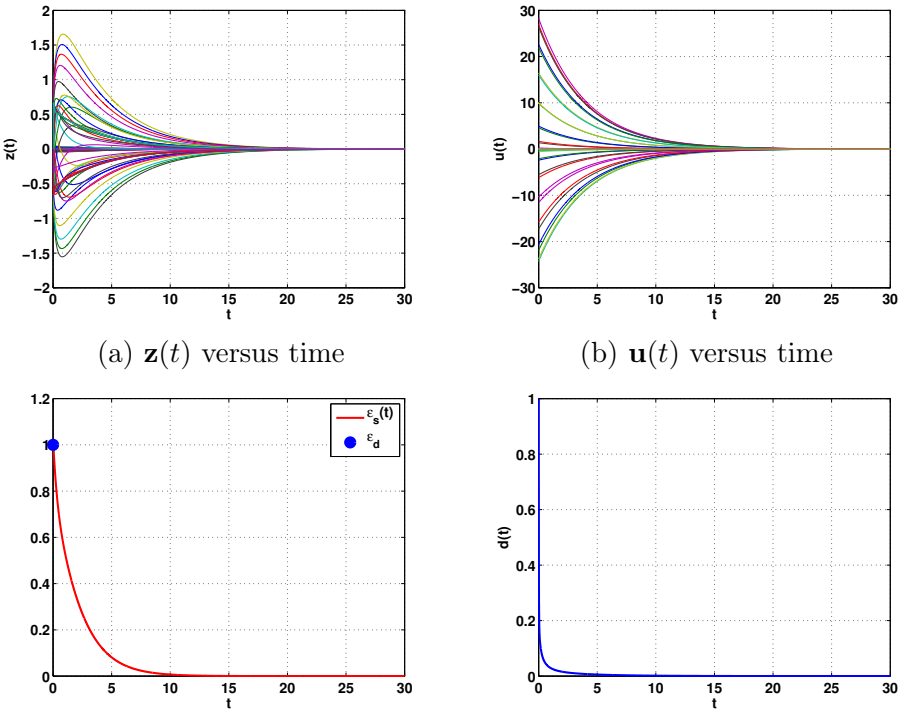

(a) $\mathbf{z}(t)$ versus time (b) $\mathbf{u}(t)$ versus time

(c) $\varepsilon_s(t)$ versus time (d) $\mathbf{d}(t)$ versus time

Figure D.4: Behavior of the closed loop system ($n = 96$, $r = 62$, $\lambda = 0.25$).

Because we only use the visual servoing control based on the model reduction, there-

fore one question is that we still have good result in the case of $\varepsilon(t) \approx \mathbf{z}^\top(t)\mathbf{Q}_z\mathbf{z}(t)$? Figure D.5 provides a good result of minimizing the synchronic transient energy growth. Indeed, $r = 64$ is large enough, we always can have a good result even $\varepsilon(t) \approx \mathbf{z}^\top(t)\mathbf{Q}_z\mathbf{z}(t)$. However, we must give a lot of control signal energy $\mathbf{u}^\top(t)\mathbf{R}_z\mathbf{u}(t) < \mathbf{z}^\top(t)\mathbf{Q}_z\mathbf{z}(t) << \mathbf{u}^\top(t)\mathbf{u}(t)$. Therefore, we need to use another functions $f_{v,l,i}(y)$, $f_{v,u,i}(y)$, $f_{\eta,u,i}(y)$ and $f_{\eta,l,i}(y)$.

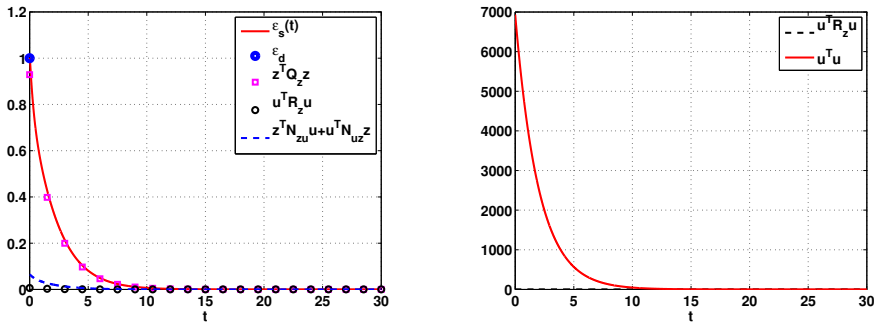

Figure D.5: Behavior of the synchronic transient energy growth and components versus time ($\alpha = 0$, $\beta = 2.044$, $R = 5\ 000$, $n = 96$, $r = 62$, $\lambda = 0.25$).

In order to obtain a better result. We find the new functions $f_{new,v,l,i}(y)$, $f_{new,v,u,i}(y)$, $f_{new,\eta,u,i}(y)$ and $f_{new,\eta,l,i}(y)$. We assume that the new functions are $100f_{v,l,i}(y)$, $100f_{v,u,i}(y)$, $100f_{\eta,u,i}(y)$ and $100f_{\eta,l,i}(y)$. The result in Figure D.6 is better than the result in Figure D.5 when $\mathbf{u}^\top(t)\mathbf{u}(t) < \mathbf{u}^\top(t)\mathbf{R}_z\mathbf{u}(t)$.

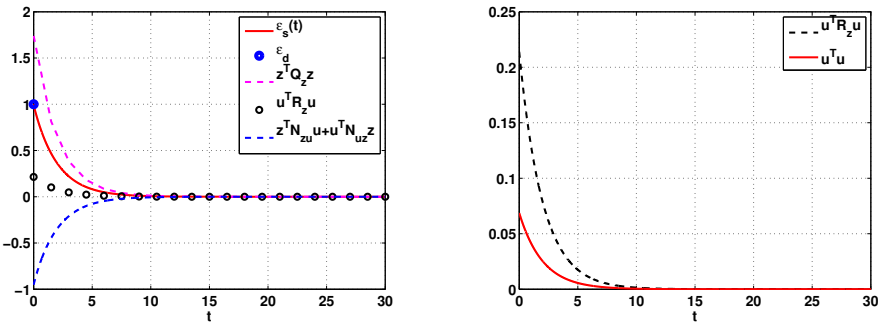

Figure D.6: Behavior of the synchronic transient energy growth and its components versus time ($\alpha = 0$, $\beta = 2.044$, $R = 5\ 000$, $n = 96$, $r = 62$, $\lambda = 0.25$).

Appendix E

Uncertain Plane Poiseuille Flow

In this chapter, we consider an uncertain system for the plane Poiseuille flow. The flow may be not known exactly or it parameter is varying in evolution of this flow. Furthermore, we approximate the flow by a reduced linear model. Therefore, an uncertain model is necessary in [Farrell and Ioannou, 2002a], [Farrell and Ioannou, 2002b], [Farrell and Ioannou, 2002c] and usually known as an uncertain operator. An uncertain model of the plane Poiseuille flow was proposed in [Schmid, 2007]. On the other hand, the uncertain system of the plane Poiseuille flow is also interesting in the control based on reduced order system.

Because we consider a linear model of the plane Poiseuille flow, we need to know that an uncertain system could be reduced to a model reduction. Fortunately, in [Beck and Bendotti, 1997], [Beck et al., 1996], there exist a control law to apply to the reduced uncertain order model instead of the full uncertain system.

In the next section, we consider the uncertain Reynolds number R and its effect on the transient energy growth. Of course, there are also other uncertain parameters in a flow which should be take into account.

E.1 Uncertain Reynolds number

In this section, we consider the effect of the uncertain Reynolds number R on the transient energy growth. The behavior of the transient energy growth versus the uncertain Reynolds number is a very interesting problem. Furthermore, we also consider the effect of the uncertain Reynolds number R and the variation of the wavenumbers α, β on the transient energy growth. For the plane Poiseuille flow, the Reynolds number R is considered as a parameter uncertainty in [Joshi et al., 1997]. From a practical point of view, the Reynolds number R may not be known exactly or may change frequently as in the flight of an airplane.

Talking into account the uncertain Reynolds number, we first determine the diachronic transient energy growth versus the Reynolds number at time $t = \tau$

$$\begin{cases} \varepsilon_d &= P_{\varepsilon,p}(R) \\ \tau &= P_{\tau,p}(R). \end{cases} \tag{E.1}$$

We then propose the functions $P_{\varepsilon,p}(R)$ and $P_{\tau,p}(R)$ which are approximated by

$$\begin{cases} P_{\varepsilon,p}(R) &= \sum_{i=0}^{p} a_i R^{i/2} \\ P_{\tau,p}(R) &= \sum_{i=0}^{p} b_i R^{i/2}, \end{cases} \tag{E.2}$$

where p is the degree of the polynomial. We use the function **polyfit** in **Matlab** to compute the coefficients a_i and b_i.

E.1.1 Case I: 2D plane Poiseuille flow

Due to the critical Reynolds number $R_T \approx 5772$, when the Reynolds number $R > 5772$, the transient energy growth is unbounded. In order to examine the diachronic transient energy growth, we only consider $R < 5\,000$. We set $\alpha = 1$, $\beta = 0$, $150 \leq R \leq 5\,000$ and $N = 100$.

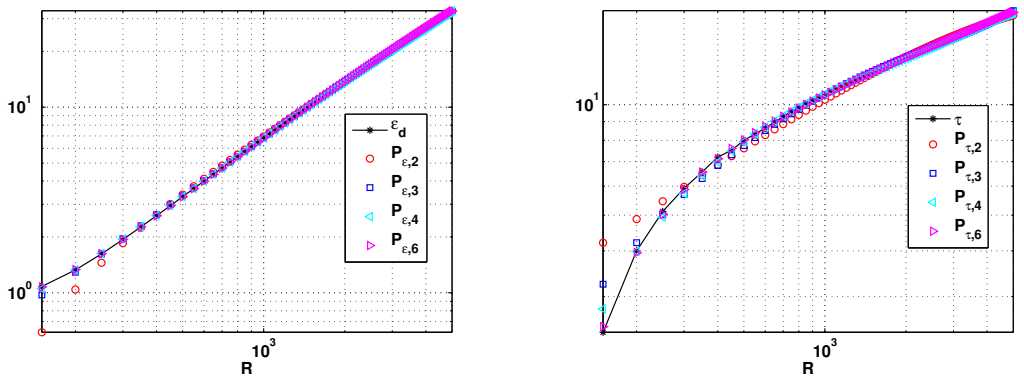

(a) ε_d (b) τ

Figure E.1: Diachronic transient energy growth ε_d at time τ versus the Reynolds number.

We use the data $R = 150 : 50 : 5\,000$. The behavior of the diachronic transient energy growth ε_d for various choices of the Reynolds number R is depicted in Figure E.1(a) while the time τ is depicted in Figure E.1(b). The diachronic transient energy growth ε_d is an increasing function of the Reynolds number R, the same is valid for the time τ. We want to determine the degree of this function. We use these polynomials $P_{\varepsilon,p}(R)$ and $P_{\tau,p}(R)$ to do it. We use the approximation polynomials $P_{\varepsilon,p}(R)$ and $P_{\tau,p}(R)$ from (E.2) and we choose $p = 2, 3, 4, 6$. The comparison between ε_d, τ and their approximations are given in Figure E.1. As can be seen in this figure, the approximation is very good for $P_{\varepsilon,p}(R)$ with $p \geq 3$, while for $P_{\tau,p}(R)$ with $p \geq 4$. The corresponding coefficients of the approximations for $P_{\varepsilon,p}(R)$ and $P_{\tau,p}(R)$ are given in Table E.1 and Table E.2, respectively. As shown in Table E.1, these results allow us to ensure that

the diachronic transient energy growth ε_d grows approximately as $O(R)$, as can be seen from $p = 3, a_3 \approx 0$. While as shown in Table E.2, the diachronic transient energy growth ε_d is achieved at time $O(R^{3/2})$, as can be seen from $p = 4, b_4 \approx 0$.

Table E.1: Polynomial $P_{\varepsilon,p}(R) = a_0 + a_1\sqrt{R} + a_2 R + a_3 R\sqrt{R} + a_4 R^2 + a_5 R^2\sqrt{R} + a_6 R^3$

p	a_0	a_1	a_2	a_3	a_4	a_5	a_6
2	-1.1412	0.0719	**0.0058**				
3	0.3954	-0.0618	**0.0092**	≈ 0			
4	1.1330	-0.1526	**0.0130**	-0.0001	≈ 0		
6	1.8151	-0.2704	**0.0206**	-0.0003	≈ 0	≈ 0	≈ 0

Table E.2: Polynomial $P_{\tau,p}(R) = b_0 + b_1\sqrt{R} + b_2 R + b_3 R\sqrt{R} + b_4 R^2 + b_5 R^2\sqrt{R} + b_6 R^3$

p	b_0	b_1	b_2	b_3	b_4	b_5	b_6
2	-0.5293	0.4142	-0.0022				
3	-4.6380	0.7715	-0.0113	**0.0001**			
4	-8.9791	1.3062	-0.0333	**0.0004**	≈ 0		
6	-18.3136	2.9532	-0.1435	**0.0041**	-0.0001	≈ 0	≈ 0

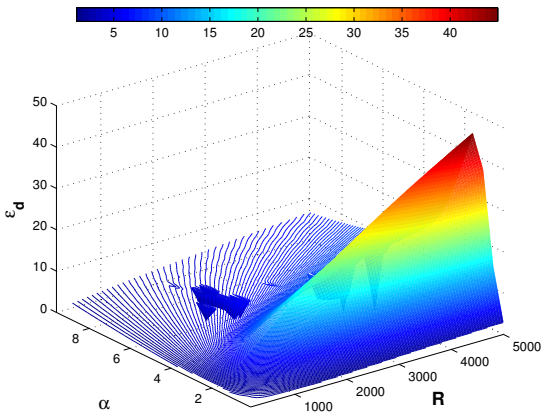

Figure E.2: Diachronic transient energy growth ε_d versus the Reynolds number R and the wavenumber α.

Next we analyze the behavior of the diachronic transient energy growth ε_d versus the Reynolds number R and the wavenumber α. We use the data $\alpha = 0.1 : 0.5 : 10$ and $R = 150 : 50 : 5\,000$. The diachronic transient energy growth ε_d is depicted as a function of the Reynolds number R and the wavenumber α in Figure E.2. The result

allows us to observe that the diachronic transient energy growth ε_d firstly increases, then achieves the maximum value and after that decreases when the wavenumber α increases. We want to determine the zone of the transient energy growth ε_d and also the value of Reynolds number R and the wavenumber α where the diachronic transient energy growth ε_d achieves the maximum value. The contours of the diachronic transient energy growth ε_d are depicted versus the Reynolds number R and the wavenumber α in Figure E.3. With the selected data, the diachronic transient energy growth ε_d obtains the maximum value at the wavenumber $\alpha \approx 1.6$ in the case of $500 < R \leq 5\,000$ ($\alpha \approx 2.1$ in the case of $150 \leq R \leq 500$).

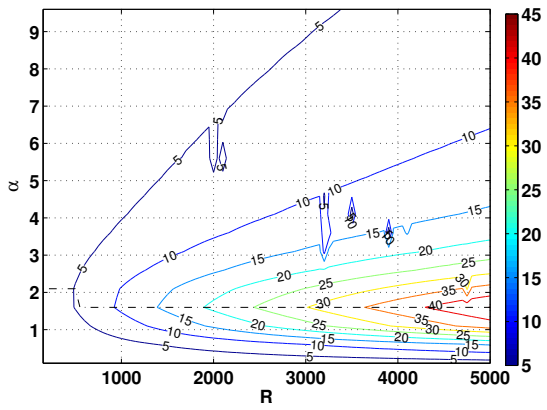

Figure E.3: Contours of diachronic transient energy growth ε_d versus the Reynolds number R and the wavenumber α. Dashed-line represents the value of wavenumber α where the diachronic transient energy growth obtains the maximum value.

E.1.2 Case II: 3D plane Poiseuille flow

- We consider the streamwise vortex and set $\alpha = 0$, $\beta = 2.044$, $100 \leq R \leq 20\,000$ and $N = 50$.

We use the data $R = 100 : 500 : 20\,000$. The behavior of the diachronic transient energy growth ε_d for various choices of the Reynolds number R is depicted in Figure E.4(a) while the time τ is depicted in Figure E.4(b). The comparison between ε_d, τ and their approximations are given in Figure E.4. As can be seen in this figure, the approximation is very good for $P_{\varepsilon,p}(R)$ with $p \geq 4$ while for $P_{\tau,p}(R)$ with $p \geq 2$. The corresponding coefficients of the approximations for $P_{\varepsilon,p}(R)$ and $P_{\tau,p}(R)$ are given in Table E.3 and Table E.4. As shown in Table E.3, these results allow us to ensure that the diachronic transient energy growth grows approximately as $O(R^2)$, as can be seen from $p = 6, a_5 \approx 0$. While as shown in Table E.4, the diachronic transient energy growth is achieved at time $O(R)$, as can be seen from $p = 3, b_3 \approx 0$. This result corresponds to the one presented in [Butler and Farrell, 1992] and [Trefethen et al., 1993].

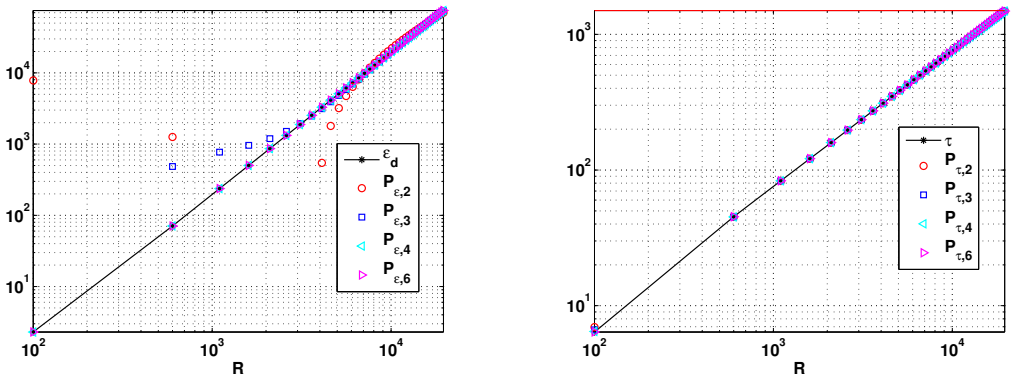

(a) ε_d (b) τ

Figure E.4: Diachronic transient energy growth ε_d at time τ versus the Reynolds number R.

Table E.3: Polynomial $P_{\varepsilon,p}(R) = a_0 + a_1\sqrt{R} + a_2 R + a_3 R\sqrt{R} + a_4 R^2 + a_5 R^2\sqrt{R} + a_6 R^3$

p	a_0	a_1	a_2	a_3	a_4	a_5	a_6
2	1.4359 10^4	-732.3934	8.0686				
3	-2.5717 10^3	241.6969	-6.2544	0.0605			
4	0.3670	-0.0034	0.0001	≈ 0	**0.0002**		
6	0.4075	-0.0093	0.0003	≈ 0	**0.0002**	≈ 0	≈ 0

Table E.4: Polynomial $P_{\tau,p}(R) = b_0 + b_1\sqrt{R} + b_2 R + b_3 R\sqrt{R} + b_4 R^2 + b_5 R^2\sqrt{R} + b_6 R^3$

p	b_0	b_1	b_2	b_3	b_4	b_5	b_6
2	-0.7970	0.0180	**0.0757**				
3	-1.4306	0.0544	**0.0752**	≈ 0			
4	-2.0473	0.1124	**0.0737**	≈ 0	≈ 0		
6	-2.6339	0.1961	**0.0700**	0.0001	≈ 0	≈ 0	≈ 0

We use the data $\beta = 0.044 : 0.5 : 12.044$ and $R = 100 : 500 : 20\ 000$. We give the behavior of the diachronic energy density ε_d versus the Reynolds number R and the wavenumber β. The diachronic transient energy growth ε_d is depicted as a function of the Reynolds number R and the wavenumber β in Figure E.5. The contours of the diachronic transient energy growth ε_d versus the Reynolds number R and the wavenumber β are depicted in Figure E.6. As can be seen in this figure, we can determine the level of transient energy growth versus the Reynolds number R and the wavenumber β, e.g. the level diachronic transient energy growth $\varepsilon_d \leq 1\ 000$ is associated to the left

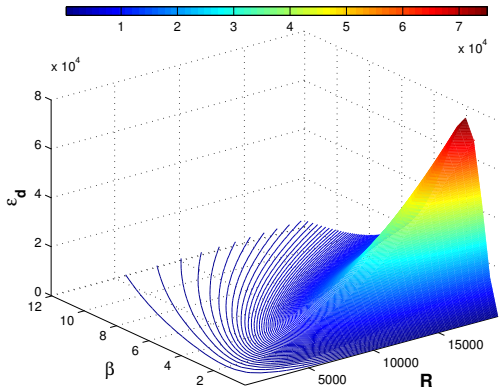

Figure E.5: Diachronic transient energy growth ε_d versus the Reynolds number R and the wavenumber β.

zone of the line 1 000 and the diachronic transient energy growth $\varepsilon_d = 4897 \approx 5\ 000$ at $R = 5\ 000$ and $\beta = 2.044$, see the line 5 000. With the selected data, the diachronic transient energy growth obtains the maximum value at the wavenumber $\beta = 2.044$ for all the Reynolds numbers $100 \leq R \leq 20\ 000$. The wavenumber $\beta = 2.044$ is again a very important wavenumber.

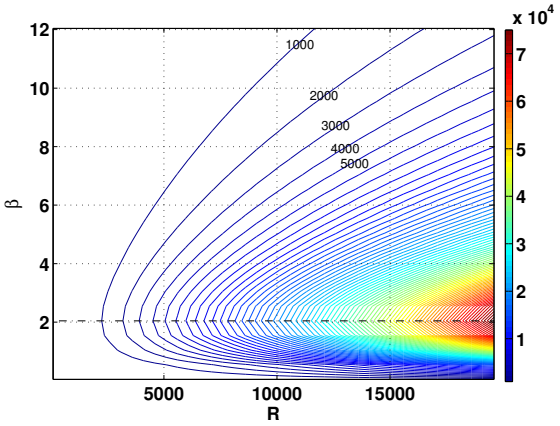

Figure E.6: Contours of diachronic transient energy growth ε_d versus the Reynolds number R and the wavenumber β. Dashed-line represents the value of the wavenumber β where the diachronic transient energy growth obtains the maximum value.

- We consider the oblique wave and set $\alpha = 1$, $\beta = 1$, $150 \leq R \leq 5\ 000$ and $N = 50$.

We consider the oblique wavenumber $\alpha = 1$ and $\beta = 1$. We use the data $R = 150 : 50 : 5\ 000$. The analysis is done as in the previous two cases. The behavior of the diachronic transient energy growth ε_d for various choices of the Reynolds number

R is depicted in Figure E.7(a) while the time τ is depicted in Figure E.7(b). The

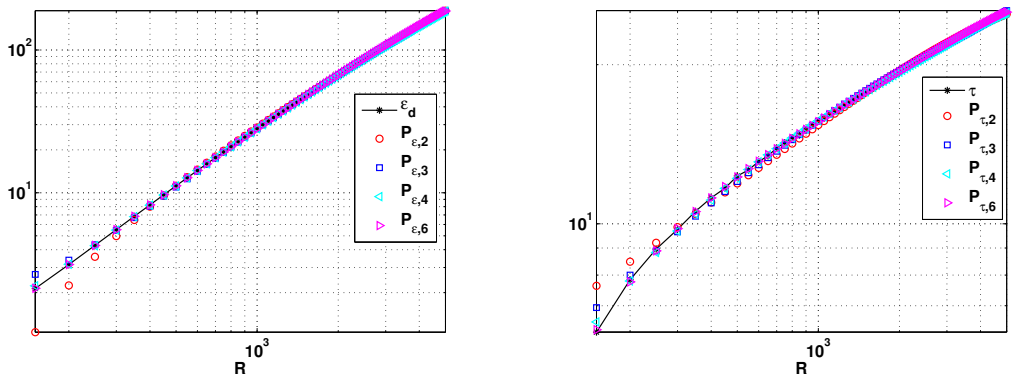

(a) ε_d (b) τ

Figure E.7: Diachronic transient energy growth ε_d at time τ versus the Reynolds number R.

comparison between ε_d, τ and their approximations are given in Figure E.7. As can be seen in this figure, the approximation is very good for $P_{\varepsilon,p}(R)$ with $p \geq 4$ while for $P_{\tau,p}(R)$ with $p \geq 4$. As shown in Table E.5, these results allow us to ensure that the diachronic transient energy growth ε_d grows approximately as $O(R^{3/2})$, as can be seen from $p = 4, a_4 \approx 0$. This result corresponds to the results in [Farrell and Ioannou, 1993]. While as shown in Table E.6, the diachronic transient energy growth ε_d is achieved at time $O(R^{3/2})$, as can be seen from $p = 4, b_4 \approx 0$.

Table E.5: Polynomial $P_{\varepsilon,p}(R) = a_0 + a_1\sqrt{R} + a_2 R + a_3 R\sqrt{R} + a_4 R^2 + a_5 R^2\sqrt{R} + a_6 R^3$

p	a_0	a_1	a_2	a_3	a_4	a_5	a_6
2	1.2567	-0.5742	0.0456				
3	8.1934	-1.1775	0.0609	-0.0001			
4	3.9866	-0.6594	0.0395	**0.0002**	≈ 0		
6	1.9340	-0.3289	0.0201	**0.0008**	≈ 0	≈ 0	≈ 0

Since the effect of the Reynolds number R on the transient energy growth is investigated, finding an appropriate uncertain model of the system is discussed in the next section.

Table E.6: Polynomial $P_{\tau,p}(R) = b_0 + b_1\sqrt{R} + b_2 R + b_3 R\sqrt{R} + b_4 R^2 + b_5 R^2\sqrt{R} + b_6 R^3$

p	b_0	b_1	b_2	b_3	b_4	b_5	b_6
2	1.7121	0.5162	-0.0027				
3	-1.2353	0.7725	-0.0092	0.0001			
4	-5.1676	1.2568	-0.0291	**0.0004**	≈ 0		
6	-11.5329	2.3578	-0.1009	**0.0027**	≈ 0	≈ 0	≈ 0

E.2 Uncertain model

The plane Poiseulle flow is considered as an uncertain system

$$\begin{cases} \dot{\mathbf{z}}(t) &= \mathbf{A}_z(t)\mathbf{z}(t) + \mathbf{B}_z(t)\mathbf{u}(t) \\ \varepsilon(t) &= \mathbf{z}^\top(t)\mathbf{Q}_z(t)\mathbf{z}(t) + \mathbf{z}^\top(t)\mathbf{N}_{zu}(t)\mathbf{u}(t) + \mathbf{u}^\top(t)\mathbf{N}_{uz}(t)\mathbf{z}(t) + \mathbf{u}^\top(t)\mathbf{R}_z(t)\mathbf{u}(t) \\ \mathbf{d}(t) &= \mathbf{D}_{z1}(t)\mathbf{z}(t) + \mathbf{D}_{z2}(t)\mathbf{u}(t) \\ \mathbf{z}(0) &= \mathbf{z}_0 \end{cases} \tag{E.3}$$

The underlying system matrix should hence be modeled as a stochastic matrix operator, as proposed by Schmid in [Schmid, 2007]

$$\mathbf{A}_z(t) = \mathbf{A}_z + \varsigma\mu(t)\mathbf{S}_1, \tag{E.4}$$

where $\mathbf{A}_z$ denotes the statistically steady part of $\mathbf{A}_z(t)$, and $\mathbf{S}_1$ the matrix containing the terms influenced by uncertainty. The stochastic process is $\mu(t)$ and the amplitude of the stochastic perturbations is ς (see [Schmid, 2007] for more details).

In [Khargonekar et al., 1990], [Zhou et al., 1996], an internal uncertainty can be imposed using a standard uncertainty

$$\begin{cases} \Delta\mathbf{A}_z = \varsigma\mu(t)\mathbf{S}_1 = \Pi\Sigma(\theta(t))\Omega \\ \Delta\mathbf{B}_z = \varsigma\mu(t)\mathbf{S}_2 = \Pi\Sigma(\theta(t))\Phi, \end{cases} \tag{E.5}$$

where $\Sigma(\theta(t))$ is an uncertain matrix, $\|\Sigma(\theta(t))\|$ is assumed to be bounded and Π, Φ and Ω are well known matrices. Therefore, the uncertain model becomes

$$\dot{\mathbf{z}}(t) = (\mathbf{A}_z + \Delta\mathbf{A}_z)\mathbf{z}(t) + (\mathbf{B}_z + \Delta\mathbf{B}_z)\mathbf{u}(t), \tag{E.6}$$

this is a standard uncertainty form.

However, the uncertain system may be a polytopic uncertain system. The ideal is to design one controller for all wavenumber pairs by considering all subsystems which are in a polytopic uncertain system. In this case, the uncertain system is given by

$$\dot{\mathbf{z}}(t) = \mathbf{A}_z(t)\mathbf{z}(t) + \mathbf{B}_z(t)\mathbf{u}(t), \begin{cases} \mathbf{A}_z(t) \in Co\{\mathbf{A}_{z1}, \mathbf{A}_{z2}, \cdots, \mathbf{A}_{zN_{st}N_{sp}}\} \\ \mathbf{B}_z(t) \in Co\{\mathbf{B}_{z1}, \mathbf{B}_{z2}, \cdots, \mathbf{B}_{zN_{st}N_{sp}}\}. \end{cases} \tag{E.7}$$

Note that, each subsystem $(\mathbf{A}_{zi}, \mathbf{B}_{zi})$ corresponds to one wavenumber pair (α_i, β_i).

E.3 $\mathbf{H}_\infty$ control theory

We design a control law $\mathbf{u}(t) = \mathbf{K}\mathbf{z}(t)$ which stabilize the uncertain system (E.6). By using the $\mathbf{H}_\infty$ control theory in [Khargonekar et al., 1990], as shown that it exists a control law for the system (E.6).

We suppose that $rank(\Phi) = i_o \leq j_o$. Define $\Sigma_2 \in \Re^{i_o \times m_o}$ such that $rank(\Sigma_2) = i_o$, and $\Phi^\top \Phi = \Sigma_2^\top \Sigma_2$. Let $\Psi \in \Re^{m_o - i_o \times m_o}$ be chosen such that

$$\begin{cases} \Psi \Sigma_2^\top = 0 \\ \Psi \Psi^\top = \mathbf{I}, \end{cases} \tag{E.8}$$

or, if $i_o = m_o$

$$\begin{cases} \Psi \Sigma_2^\top = 0 \\ \Psi = 0. \end{cases} \tag{E.9}$$

Let $\Upsilon = \Sigma_2^\top (\Sigma_2 \Sigma_2^\top)^{-2} \Sigma_2$. Note, if $\Phi = 0$, then $\Sigma_2 = 0$, $\Psi = 0$, and $\Upsilon = 0$. Also, note that if $rank(\Phi) = m_o$, the Σ_2 is square and nonsingular, and $\Upsilon = (\Sigma_2^\top \Sigma_2)^{-1} = (\Phi^\top \Phi)^{-1}$ and $\Psi = 0$.

The theorem E.3.1 is taken from [Khargonekar et al., 1990] (see theorem 2.3 in [Khargonekar et al., 1990]).

Theorem E.3.1 *The uncertain system (E.6) is quadratically stabilizable via linear control if there exists $\rho > 0$ such that the following Algebraic Riccati Equation*

$$\begin{aligned} \left(\mathbf{A}_z - \mathbf{B}_z \Upsilon \Phi^\top \Omega\right)^\top \mathbf{P} + \mathbf{P}\left(\mathbf{A}_z - \mathbf{B}_z \Upsilon \Phi^\top \Omega\right) + \mathbf{P}\left(\Pi\Pi^\top - \mathbf{B}_z \Xi \mathbf{B}_z^\top - \frac{1}{\rho}\mathbf{B}_z \Psi^\top \Psi \mathbf{B}_z^\top\right)\mathbf{P} \\ + \Omega^\top \left(\mathbf{I} - \Pi \Xi \Pi^\top\right)\Omega + \rho \mathbf{I} = 0, \end{aligned} \tag{E.10}$$

has a positive definite symmetric solution $\mathbf{P}$. In this case, a stabilizing state-feedback control law is given by

$$\mathbf{K} = -\left[\left(\frac{1}{2\epsilon}\Psi^\top \Psi + \Upsilon\right)\mathbf{B}_z^\top \mathbf{P} + \Upsilon \Phi^\top \Omega\right]. \tag{E.11}$$

Conversely, if the uncertain system (E.6) is quadratically stabilizable via linear control, then exists $\rho^* > 0$ such that for all ρ in $(0, \rho^*)$, the Riccati equation (E.10) admits a symmetric solution $\mathbf{P_0}$ such that $\left(\mathbf{A}_z - \mathbf{B}_z \Upsilon \Phi^\top \Omega\right) + \left(\Pi\Pi^\top - \mathbf{B}_z \Upsilon \mathbf{B}_z^\top - \frac{1}{\rho}\mathbf{B}_z \Psi^\top \Psi \mathbf{B}_z^\top\right)\mathbf{P_0}$ is asymptotically stable and this solution $\mathbf{P_0}$ is positive definite.

E.4 LMI control theory

By using the **LMI** control for the uncertain system (E.6), the control law $\mathbf{u}(t) = \mathbf{K}\mathbf{z}(t)$ is designed based on

$$\mathbf{K} = \mathbf{Y}\mathbf{P}^{-1}. \tag{E.12}$$

E.4.1 Standard form

If the uncertain system is in a standard form, we use the theorem E.4.1 which is taken from the result of Lam et al. in [Lam and Xu, 2006] (see the Corollary 4.3, p.62 proposed in [Lam and Xu, 2006]).

Theorem E.4.1 *The uncertain system (E.6) is quadratically stabilizable via linear control if and only if there exists matrices* $\mathbf{P} = \mathbf{P}^\top > 0$, $\mathbf{Y}$ *and a scalar* $\rho > 0$ *such that the* ***LMI*** *hold*

$$\begin{bmatrix} \mathbf{P}\mathbf{A}_z^\top + \mathbf{A}_z\mathbf{P} + \mathbf{B}_z\mathbf{Y} + \mathbf{Y}^\top\mathbf{B}_z^\top + \epsilon\Pi\Pi^\top & \mathbf{P}\Omega^\top + \mathbf{Y}^\top\Phi^\top \\ \Omega\mathbf{P} + \Phi\mathbf{Y} & -\rho\mathbf{I} \end{bmatrix} < 0 \tag{E.13}$$

E.4.2 Polytopic form

If the uncertain system is in a polytopic uncertain system, we use the following theorems E.4.2 and E.4.2 which are taken from Boyd in [Boyd et al., 1994] (see the LMI synthesis was given in [Boyd et al., 1994], p.100 - p.104, eq.(7.5), eq.(7.12) and eq.(7.16)).

Theorem E.4.2 *The uncertain system (E.7) is quadratically stabilizable via linear control if and only if there exists* $\mathbf{P} = \mathbf{P}^T > 0$ *and* $\mathbf{Y}$ *such that the* ***LMIs*** *hold*

$$\mathbf{A}_{zi}\mathbf{P} + \mathbf{P}\mathbf{A}_{zi}^\top + \mathbf{B}_{zi}\mathbf{Y} + \mathbf{Y}^\top\mathbf{B}_{zi}^\top < 0, i = 1,\ 2\cdots, N_{st}N_{sp}. \tag{E.14}$$

For a practical design of a controller, it is necessary to limit the expenditure of the control effort, we have:

Theorem E.4.3 *The uncertain system (E.7) is quadratically stabilizable and the control effort is limited via linear control if and only if there exists* $\mathbf{P} = \mathbf{P}^\top > 0$ *and* $\mathbf{Y}$ *such that the* ***LMIs*** *hold*

$$\begin{cases} \mathbf{A}_{zi}\mathbf{P} + \mathbf{P}\mathbf{A}_{zi}^\top + \mathbf{B}_{zi}\mathbf{Y} + \mathbf{Y}^\top\mathbf{B}_{zi}^\top & < 0, i = 1,\ 2\cdots,\ N_{st}N_{sp} \\ \mathbf{P} & \geq \mathbf{I} \\ \begin{bmatrix} \mathbf{P} & \mathbf{Y}^\top \\ \mathbf{Y} & \mu^2\mathbf{I} \end{bmatrix} & \geq 0 \end{cases} \tag{E.15}$$

where μ *is the constraint of the control effort* $\|\mathbf{u}(t)\|_{t\geq 0} \leq \mu$.

We want to minimize $\|\mathbf{z}(t)\|$, we use the theorems E.4.4 and E.4.5 which are based on the combination of the results in [Boyd et al., 1994] and [Whidborne and McKernan, 2007], [Whidborne et al., 2008].

Theorem E.4.4 *The uncertain system (E.7) is quadratically stabilizable, the control effort is limited and the upper bound of the transient energy density is minimized via*

linear control if and only if there exists $\mathbf{P} = \mathbf{P}^\top > 0$ *and* $\mathbf{Y}$ *such that the* ***LMIs*** *hold*

$$\textit{min } \gamma \textit{ subject to } \begin{cases} \mathbf{A}_{zi}\mathbf{P} + \mathbf{P}\mathbf{A}_{zi}^\top + \mathbf{B}_{zi}\mathbf{Y} + \mathbf{Y}^T\mathbf{B}_{zi}^\top & < 0, i = 1, 2 \cdots, N_{st}N_{sp} \\ \mathbf{I} \leq \mathbf{P} & \leq \gamma\mathbf{I} \\ \begin{bmatrix} \mathbf{P} & \mathbf{Y}^\top \\ \mathbf{Y} & \mu^2\mathbf{I} \end{bmatrix} & \geq 0 \end{cases} \tag{E.16}$$

Or we want to minimize the kinetic energy density $\mathbf{z}^\top(t)\mathbf{Q}\mathbf{z}(t)$, we have:

Theorem E.4.5 *The uncertain system (E.7) is quadratically stabilizable, the control effort is limited and the upper bound of the kinetic energy density is minimized via linear control if and only if there exists* $\mathbf{P} = \mathbf{P}^\top > 0$ *and* $\mathbf{Y}$ *such that the* ***LMIs*** *hold*

$$\begin{cases} \begin{bmatrix} \mathbf{A}_{zi}\mathbf{P} + \mathbf{P}\mathbf{A}_{zi}^\top + \mathbf{B}_{zi}\mathbf{Y} + \mathbf{Y}^\top\mathbf{B}_{zi}^\top & \mathbf{P}\mathbf{C}^\top \\ \mathbf{C}\mathbf{P} & \mu^2\mathbf{I} \end{bmatrix} & \leq 0, i = 1,\ 2 \cdots,\ N_{st}N_{sp} \\ \mathbf{P} & \geq \mathbf{I} \\ \begin{bmatrix} \mathbf{P} & \mathbf{Y}^\top \\ \mathbf{Y} & \mu^2\mathbf{I} \end{bmatrix} & \geq 0 \end{cases} \tag{E.17}$$

where the weight matrix of kinetic energy density is decomposed by $\mathbf{Q} = \mathbf{C}^\top\mathbf{C}$.

The kinetic energy density is limited by the upper value $\mathbf{z}_0^\top\mathbf{P}^{-1}\mathbf{z}_0$.

E.5 Simulation results

Based on the above results, we consider the Reynolds number as a parameter uncertainty. Note that this is similar case where we consider the multiple wavenumber pairs (α_i, β_i). The uncertain system can be given as follows

$$\{\mathbf{A}_z(R), \mathbf{B}_z(R)\} = \begin{cases} (\mathbf{A}_{z1}, \mathbf{B}_{z1}) & R = 10\ 000, \\ (\mathbf{A}_{z2}, \mathbf{B}_{z2}) & R = 7\ 500, \\ (\mathbf{A}_{z3}, \mathbf{B}_{z3}) & R = 12\ 500. \end{cases} \tag{E.18}$$

and we have three subsystems. We must design a robust controller like **LMI** for the uncertain system. Note that in previous works, we need three **LQR** controllers with respect to one **LMI** controller.

For the simulation result, we set $\alpha = 1$, $\beta = 0$ and $N = 50$. Although one **LMI** controller is used but it stabilizes the uncertain system where all poles are stabilized in Figure E.8. The behavior of the closed loop uncertain system is given in Figure E.9 where the kinetic energy density is minimized.

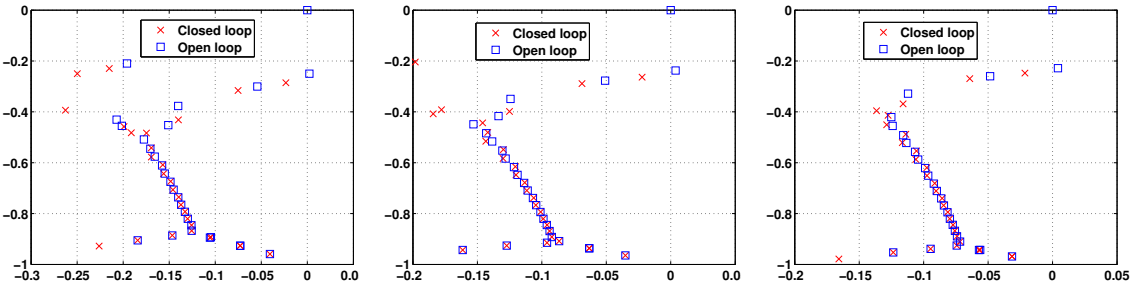

(a) $R = 7\ 500$ (b) $R = 10\ 000$ (c) $R = 12\ 500$

Figure E.8: Uncertain system: poles map for $R = 7\ 500$, $R = 10\ 000$ and $R = 12\ 500$

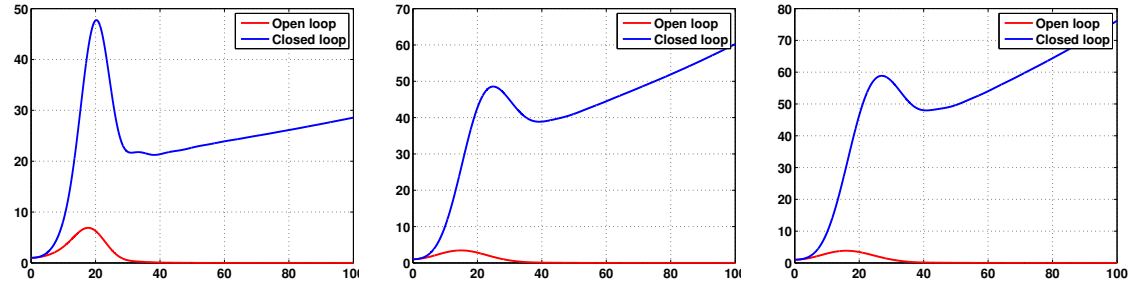

(a) $R = 7\ 500$ (b) $R = 10\ 000$ (c) $R = 12\ 500$

Figure E.9: Uncertain system: kinetic energy density versus time for $R = 7\ 500$, $R = 10\ 000$ and $R = 12\ 500$

E.6 Conclusion

When the flow changes the state, the parameter is unknown or varying. In addition, we want to consider a control law for the multiple wavenumber. Therefore the uncertain model is required for the flow control. We have given an example where the uncertain model of the plane Poiseuille flow with uncertain parameter given by the Reynolds number was considered. It effects on the transient energy growth was given. We have chosen the Reynolds number due to its role in transient to turbulence. In the case of the wavenumber pairs $\alpha = 1$ and $\beta = 0$, for $R > 5772$, the transient energy growth is unbounded and insignificant. However, for $R < 5772$, the transient energy growth is bounded, and it has been concluded that it grows as $O(R)$ over the time $O(R^{3/2})$. In the case of the wavenumber pairs $\alpha = 0$ and $\beta = 2.044$, the diachronic transient energy growth grows as $O(R^2)$ over the time $O(R)$. In the case of the wavenumber pairs $\alpha = 1$ and $\beta = 1$, the diachronic transient energy growth grows as $O(R^{3/2})$ over the time $O(R^{3/2})$. In conclusion, we also have proposed an robust control for the uncertain model of the plane Poiseuille flow. The robust control is proposed such as $\mathbf{H}_2/\mathbf{H}_\infty$ or **LMI** control.

Bibliography

[Aamo, 2002] Aamo, O. (2002). *Modeling and Control of Flow and Marine Structures*. PhD thesis, Depertment of Engineering Cybertics, Norwegian University of Science and Technology.

[Aamo et al., 2003] Aamo, O., Krstic, M., and Bewley, T. (2003). Control of mixing by boundary feedback in 2d channel flow. *Automatica*, 39(9):1597–1606.

[Amitay et al., 1997] Amitay, M., Honohan, A., Trautman, M., and Glezer, A. (1997). Modification of the aerodynamic characteristics off bluff bodies using fluidic actuators. In *AIAA, paper 2004*.

[Amitay et al., 1999] Amitay, M., Kibens, V., Parekh, D., and Glezer, A. (1999). Flow reattachment dynamics over a thick airfoil controlled by synthetic jet actuators. In *37th AIAA Aerospace Sciences Meeting*.

[Amitay et al., 2001] Amitay, M., Smith, D., Kibens, V., Parekh, D., and Glezer, A. (2001). Aerodynamic flow control over an unconventional airfoil using synthetic jet actuators. *AIAA journal*, 39(3):361–370.

[Balogh et al., 1999] Balogh, A., Liu, W.-J., and Krstic, M. (1999). Stability enhancement by boundary control in 2-d channel flow - part i: Regularity of solution. In *Proc. 38th Conference on Decision and Control*, pages 2869–2874.

[Balogh et al., 2000] Balogh, A., Liu, W.-J., and Krstic, M. (2000). Stability enhancement by boundary control in 2-d channel flow - part ii: Numerical implementation and stability. In *Proc. 2000 American Control Conference*, pages 4259–4263.

[Balogh et al., 2001] Balogh, A., Liu, W.-J., and Krstic, M. (2001). Stability enhancement by boundary control in 2-d channel flow. *IEEE Transactions on Automatic Control*, 46(11):1696–1711.

[Bamieh and Dahleh, 1999] Bamieh, B. and Dahleh, M. (1999). Disturbance energy amplification in three dimensional channel flows. In *Proc. 1999 American Control Conference*, pages 4532–4537.

[Bamieh and Dahleh, 2001] Bamieh, B. and Dahleh, M. (2001). Energy amplification in channel flows with stochastic excitation. *Physic of Fluids*, 13(11):3258–3269.

[Beck and Bendotti, 1997] Beck, C. and Bendotti, P. (1997). Model reduction method for unstable uncertain systems. In *Conference on Decision and Control*, pages 3298–3303, San Diego, California.

[Beck et al., 1996] Beck, C., Doyle, J., and Glover, K. (1996). Model reduction of multidimensional and uncertain systems. *IEEE Transactions on Automatic control*, 41(10):1466–1477.

[Berezin and Zhidkov, 1973] Berezin, I. and Zhidkov, N. (1973). *Computing methods.* Pergamon Press.

[Bergmann and Brancher, 2005] Bergmann, M. Cordier, L. and Brancher, J. (2005). Optimal rotary control of the cylinder wake using proper ortogonal decomposition reduced-order model. *Physic of Fluids*, 17(9):097101–097122.

[Berkooz et al., 1993] Berkooz, G., Holmes, P., and Lumley, J. (1993). The proper orthogonal decomposition in the analysis of turbulent flows. *Annual Review of Fluid Mechanics*, 25(1):539–575.

[Bewley, 1999] Bewley, T. (1999). New frontiers for control in fluid mechanics: A renaissance approach. In *Proc. of 3rd ASMS/JSME Joint Fluids Engineering Conference.*

[Bewley et al., 1993] Bewley, T., Choi, H., Temam, T., and Moin, P. (1993). Optimal feedback control of turbulent channel flow. Annual research briefs.

[Bewley and Liu, 1998] Bewley, T. and Liu, S. (1998). Optimal and robust control and estimation of linear paths to transition. *Journal of Fluid Mechanics*, 365:305–349.

[Bewley and Protas, 2004] Bewley, T. and Protas, B. (2004). Skin friction and pressure: The 'footprints' of turbulence. *Physica D*, 196:28–44.

[Bewley, 2001] Bewley, T. R. (2001). Flow control: New challenges for a new renaissance. *Progress in Aerospace Sciences*, 37(1):21–58.

[Bird et al., 1960] Bird, R. B., Stewart, W. E., and Lightfoot, E. N. (1960). *Transport Phenomena.* John Wiley & Sons, inc.

[Bonin-Font et al., 2008] Bonin-Font, F., Ortiz, A., and Oliver, G. (2008). Visual navigation for mobile robots: a survey. *Journal of Intelligent and Robotic Systems*, 53(3):263–296.

[Boyd, 2001] Boyd, J. P. (2001). *Chebyshev and Fourier Spectral Methods.* Second edition, Dover, Mineola, New York.

[Boyd et al., 1994] Boyd, S., Ghaoui, L., Feron, F., and Balakrishman, V. (1994). *Linear Matrix Inequalities in Systems and Control Theory.* SIAM.

[Bushnell and Hef, 1990] Bushnell, D. and Hef, J. (1990). Viscous drag reduction in boundary layers. *Progress in Aeronautics and Astronautics, AIAA*, 123.

[Butler and Farrell, 1992] Butler, K. and Farrell, B. (1992). Three-dimensional optimal perturbations in viscous shear flow. *Physic of Fluids A*, 4(8):1637–1650.

[Canuto et al., 2007] Canuto, C., Hussaini, M., and Quarteroni, A. (2007). *Spectral Methods Evolution to Complex Geometries and Applications to Fluid Dynamics*. Springer.

[Caraballo et al., 2008] Caraballo, E., Kasnakoglu, C., Serrani, A., and Samimy, M. (2008). Control input separation methods for reduced order model based feedback control. *AIAA journal*, 46(9):2306–2322.

[Cattafesta et al., 2003] Cattafesta, L., Williams, D., Rowley, C., and Alvi, F. (2003). Review of active control flow included cavity resonance. In *AIAA*, volume 3567.

[Cattafesta III and Sheplak, 2011] Cattafesta III, L. and Sheplak, M. (2011). Actuators for active flow control. *Annual Review of Fluid Mechanics*, 43(1):247–272.

[Chatto, 2006] Chatto, J. (2006). Low speed design and analysis of wing/winglet combinations including viscous effects. *Journal of Aicraft*, 43(2):386–389.

[Chaumette and Hutchinson, 2006] Chaumette, F. and Hutchinson, S. (2006). Visual servo control, part i: Basic approaches. *IEEE Robotics and Automation Magazine*, 13(4):82–90.

[Chen, 1999] Chen, Y. (1999). *Model order reduction for nonlinear system*. PhD thesis, Massachusetts Institute of Technology.

[Chevalier et al., 2006] Chevalier, M., Hoepffner, J., Bewley, T., and Henningson, D. (2006). State estimation in wall-bounded flows systems. part 2. turbulent flows. *Journal of Fluid Mechanics*, 552:167–187.

[Choi et al., 2008] Choi, H., Jeon, W., and Kim, J. (2008). Control of flow over a bluff body. *Annual Review of Fluid Mechanics*, 40:113–139.

[Choi et al., 1993a] Choi, H., Moin, P., and Kim, J. (1993a). Direct numerical simulation of turbulent flow over riblets. *Journal of Fluid Mechanics*, 255:503–539.

[Choi et al., 1994] Choi, H., Moin, P., and Kim, J. (1994). Active turbulence control for reduction in wall-bouned flows. *Journal of Fluid Mechanics*, 262:77–110.

[Choi et al., 1993b] Choi, H., Teman, H., Moin, P., and Kim, J. (1993b). Feedback control for unsteady flow and its application to stochastic burgers equation. *Journal of Fluid Mechanics*, 253(509).

[Chughtai and Werner, 2010] Chughtai, S. and Werner, H. (2010). Transient energy analysis of a spatially interconnected model for 3d poiseuille flow. In *Proc. 2010 American Control Conference*.

[Collis et al., 2004] Collis, S., Joslin, R., Seifert, A., and Theofilis, V. (2004). Issues in active flow control: theory, control, simulation, and experiment. *Progress in Aerospace Sciences*, 40:237–289.

[Comte-Bellot, 1976] Comte-Bellot, G. (1976). Hot-wire anemometry. *Annual Review of Fluid Mechanics*, 8(1):209–231.

[Cortelezzi et al., 1998a] Cortelezzi, L., Lee, K., Kim, J., and Speyer, J. (1998a). Skin-friction drag reduction via robust reduced-order linear feedback control. *International Journal of Computational Fluid Dynamics*, 11:79–92.

[Cortelezzi and Speyer, 1998] Cortelezzi, L. and Speyer, J. (1998). Robust reduced-order controller of laminar boundary layer transitions. *Physical Review E*, 58(2):1906–1910.

[Cortelezzi et al., 1998b] Cortelezzi, L., Speyer, J., Lee, K., and Kim, J. (1998b). Robust reduced-order control of turbulent channel flows via distributed sensors and actuators. In *37th Conference on Decision and Control*, Tampa, Florida.

[Dao and Collewet, 2012] Dao, X.-Q. and Collewet, C. (2012). Drag reduction of the plane poiseuille flow by partitioned visual servo control. In *Proc. 2012 American Control Conference*, pages 4084–4089.

[Drazin and Reid, 1981] Drazin, P. and Reid, W. (1981). *Hydrodynamic stability*. Cambridge University Express.

[Durst, 2008] Durst, F. (2008). *Unstable Flows and Laminar-Turbulent Transition*, pages 495–522. Springer Berlin Heidelberg.

[Espiau et al., 1992] Espiau, B., Chaumette, F., and Rives, P. (1992). A new approach to visual servoing in robotics. *EEE Trans. on Robotics and Automation*, 8(3):313–326.

[Fan et al., 1993] Fan, X., Hofmann, L., and Herbert, T. (1993). Active flow control with neural networks. In *AIAA Shear Flow Conference*.

[Farrell and Ioannou, 1993] Farrell, B. and Ioannou, P. (1993). Stochastic forcing of the linearized navier-stokes equations. *Physic of Fluids A*, 5:2600–2609.

[Farrell and Ioannou, 2002a] Farrell, B. and Ioannou, P. (2002a). Optimal perturbation of uncertain systems. *Stochastics and Dynamics*, 2(3):395–402.

[Farrell and Ioannou, 2002b] Farrell, B. and Ioannou, P. (2002b). Perturbation growth and structure in uncertain flows. part i. *Journal of Atmospheric Sciences*, 59(18):2629–2646.

[Farrell and Ioannou, 2002c] Farrell, B. and Ioannou, P. (2002c). Perturbation growth and structure in uncertain flows. part ii. *Journal of Atmospheric Sciences*, 59(18):2647–2664.

[Flaig, 2008] Flaig, A. (2008). Eco-efficient by design. In *Challenges for aerodynamics engineer for future aircraft design, 8th World Congress on Computational Mechanics*, Venic, Italy.

[Gad-el Hak, 1996] Gad-el Hak, M. (1996). Modern developments in flow control. *Applied Mechanics Review*, 49(7):365–379.

[Gad-el Hak, 2000] Gad-el Hak, M. (2000). *Flow Control Passive, Active, and Reactive Flow Management*. Cambridge University Express, Cambridge, UK.

[Gad-el Hak, 2010a] Gad-el Hak, M. (2010a). *The MEMS handbock*. CRC press.

[Gad-el Hak, 2010b] Gad-el Hak, M. (2010b). *MEMS: introduction and fundamentals*. CRC press.

[Gad-el Hak and Blackwelder, 1989] Gad-el Hak, M. and Blackwelder, R. (1989). Selective suction for controlling bursting events in a boundary layer. *AIAA journal*, 27(4):308–314.

[Gad-el Hak et al., 1998] Gad-el Hak, M., Pollard, A., and Bonnet, J. (1998). *Flow control: fundamentals and pratices*. Springer lecture notes in plysics, Springer-Verlag, Berlin.

[Garcia-Mayoral and Jimenez, 2011] Garcia-Mayoral, R. and Jimenez, J. (2011). Drag reduction by riblets. *Philosophical Transactions of the Royal Society A: Mathematical, Physical and Engineering Sciences*, 369(1940):1412–1427.

[Glezer and Amitay, 2002] Glezer, A. and Amitay, M. (2002). Synthetic jets. *Annual Review of Fluid Mechanics*, 1(503):529.

[Glover, 1984] Glover, K. (1984). All optimal hankel-norm approximation of linear multivariable systems and their l-error bounds. *International Journal of Control*, 39(6):1115–1193.

[Gustavsson, 1991] Gustavsson, L. H. (1991). Energy growth of the three-dimensional disturbances in plane poiseuille flow. *Journal of Fluid Mechanics*, 224:241–260.

[Hammond et al., 1998] Hammond, E., Bewley, T., and Moin, P. (1998). Observed mechanisms for turbulence attenuation and enhancement in opposition-controlled wall-bounded flows. *Physic of Fluids*, 10(9):2421–2423.

[Heinrichs, 1989] Heinrichs, W. (1989). Improved condition number for spectral methods. *Mathematics of Computation*, 53(187):103–119.

[Heinrichs, 1991] Heinrichs, W. (1991). A stabilized treatment of the biharmonic operator with spectral methods. *SIAM Journal on Scientific and Statistical Computing*, 12(5):1162–1172.

[Heitz et al., 2010] Heitz, D., Menin, E., and Schorr, C. (2010). Variational fluid flow measurements from image sequences: synopsis and perspectives. *Exp. Fluids*, 48(3):369–393.

[Henningson, 1991] Henningson, D. (1991). An eigenfunction expansion of localized disturbances. In *Advances in Turbulence 3*, pages 162–169.

[Henningson et al., 1993] Henningson, D., Lundbladh, A., and Johansson, A. (1993). A mechanism for bypass transition from localized disturbalces in wall-bounded shear flows. *Journal of Fluid Mechanics*, 250:169–207.

[Ho and Tai, 1996] Ho, C. and Tai, Y. (1996). Review - mems and its applications for flow control. *J. Fluids Eng. Trans. AMSE*, pages 118– 437.

[Ho and Tai, 1998] Ho, C. and Tai, Y. (1998). Micro-electro-mechanical-system (mems) and fluid flows. *Annual Review of Fluid Mechanics*, 30(579-612).

[Hoepffner et al., 2005] Hoepffner, J., Chevalier, M., Bewley, T., and Henningson, D. (2005). State estimation in wall-bounded flows systems. part 1. perturbed laminar flows. *Journal of Fluid Mechanics*, 534:363–294.

[Högberg and Bewley, 2000] Högberg, M. and Bewley, T. (2000). Spatially localized convolution kernels for feedback control of transition flows. In *Proc. 39th IEEE Conference on Decision and Control*, pages 3278–3283.

[Högberg et al., 2001] Högberg, M., Bewley, T., and Henningson, D. (2001). Optimal control of transition initiated by obtique waves in channel flow. In *Proc. 2nd INternational Symposium on Turbulence and Shear Flow Phenomena.*

[Högberg et al., 2003] Högberg, M., Bewley, T., and Henningson, D. (2003). Linear feedback control and estimation of transition in plane channel flow. *Journal of Fluid Mechanics*, 481:149–175.

[Högberg and Henningson, 2002] Högberg, M. and Henningson, D. (2002). Linear optimal control applied to instabilities in spatially developing boundary layers. *Journal of Fluid Mechanics*, 470:151–179.

[Joseph and Carmi, 1969] Joseph, D. D. and Carmi, S. (1969). Stability of poiseuille flow in pipes, annuli and channels. *Quarterly of Applied Mathematics*, 26:575–599.

[Joshep, 1976] Joshep, D. (1976). *Stability of Fluid Motions.* Springer-Verlag.

[Joshi, 1996] Joshi, S. (1996). *A systems Theory Approach to the Control of Plane Poiseuille Flow.* PhD thesis, University of California, Los Angeles, CA.

[Joshi et al., 1995] Joshi, S., Speyer, J., and Kim, J. (1995). Modeling and control of two dimensional poiseuille flow. In *Proc. 34th IEEE Conference on Decision and Control*, pages 921–927, Los Angeles, CA.

[Joshi et al., 1997] Joshi, S., Speyer, J., and Kim, J. (1997). A systems theory approach to the feedback stabilization of infinitesimal and finite-amplitude disturbances in plane poiseuille flow. *Journal of Fluid Mechanics*, 332:157–184.

[Joshi et al., 1999] Joshi, S., Speyer, J., and Kim, J. (1999). Finite dimensional optimal control of poiseuille flow. *AIAA Journal of Guidance, Control, and Dynamics*, 22(2):340–348.

[Kang et al., 1999] Kang, S., Ryder, V., Cortelezzi, L., and Speyer, J. (1999). State-space formulation and control design for three-dimensional channel flows. In *American Control Conferenc*, San Diego, California.

[Kato, 1976] Kato, T. (1976). *Perturbation Theory for Linear Operators*. Springer-Verlag, New York.

[Kautsky et al., 1985] Kautsky, J., Nichols, N., and Van Dooren, P. (1985). Robust pole assignment in linear state feedback. *International Journal of Control*, 41(5):1129–1155.

[Khargonekar et al., 1990] Khargonekar, P., Petersen, I., and Zhou, K. (1990). Robust stabilization of uncertain linear systems: Quadratic stabilizability and h_∞ control theory. *IEEE Transactions on Automatic control*, 35(3):356–361.

[Kim, 2003] Kim, J. (2003). Control of turbulent boundary layers. *Physic of Fluids*, 15(5):1093–1105.

[Kim, 2011] Kim, J. (2011). Physics and control of wall turbulence for drag reduction. *Philosophical Transactions of the Royal Society A*, 369:1396–1411.

[Kim and Bewley, 2007] Kim, J. and Bewley, T. (2007). A linear system approach to flow control. *Annual Review of Fluid Mechanics*, 39:383–417.

[Kim and Lim, 2000] Kim, J. and Lim, J. (2000). A linear process in wall-bounded turbulent shear flows. *Physic of Fluids*, 12(8):1885–1888.

[Kim et al., 1987] Kim, J., Moin, P., and Moser, R. (1987). Turbulence statistics in fully developed channel flow at low reynolds number. *Journal of Fluid Mechanics*, 177:133.

[Kim et al., 2008] Kim, K., Debiasi, M., Schultz, R., Serrani, A., and Samimy, M. (2008). Dynamic compensation of a synthetic jetlike actuator for closed loop cavity flow control. *AIAA journal*, 46(1):232–240.

[Kim et al., 2009] Kim, K., Kasnakoglu, C., Serrani, A., and Samimy, M. (2009). Extermum seeking control of subsonic cavity flow. *AIAA journal*, 47(1):195–205.

[Kokotovic, 1992] Kokotovic, P. (1992). The joy of feedback: nonlinear and adaptive. *IEEE Control System Magazine*, 12(3):7–17.

[Kral, 2000] Kral, L. D. (2000). Active flow control technology. Technical report, ASME Fluids Engineering Technical Brief.

[Lam and Xu, 2006] Lam, J. and Xu, S. (2006). *Robust control and filtering of singular systems*. Springer Berlin Heidelberg.

[Lanczos, 1950] Lanczos, C. (1950). An iteration method for the solution of the eigenvalue problem of linear differential and integral operators. *Journal of Research of the National Bureau of Standards*, 45(4):255–282.

[Lauga and Bewley, 2002] Lauga, E. and Bewley, T. (2002). The decay of stabilizability with reynolds number in a linear model of spatially developing flow. In *Proc. Royal Society London A*, volume 459, pages 2077–2095.

[Lee et al., 1997] Lee, C., Kim, J., Badcook, D., and Goodman, R. (1997). Application of neural networks to turbulence control for drag reduction. *Physic of Fluids*, 9(1740).

[Lee et al., 2001] Lee, K., Cortelezzi, L., Kim, J., and Speyer, J. (2001). Application of robust reduced-order controller to turbulent flows for drag reduction. *Physics of Fluids*, 13(5):1321–1330.

[Lim, 2003] Lim, J. (2003). *A linear control in turbulent boundary layers*. PhD thesis, University of California, Los Angeles.

[Lundbladh and Johansson, 1991] Lundbladh, A. and Johansson, A. V. (1991). Direc simulation of the turbulent spots in plane couette flow. *Journal of Fluid Mechanics*, 229:499–516.

[Martinelli et al., 2009] Martinelli, F., Quadrio, M., McKernan, J., and Whidborne, J. (2009). Feedback control of transient energy growth in subcritical plane poiseuille flow. In *Seventh IUTAM Symposium on Laminar-Turbulent Transition*. Stockholm, Sweden.

[Martinelli et al., 2011] Martinelli, F., Quadrio, M., McKernan, J., and Whidborne, J. (2011). Linear feedback control of transient energy growth and control performance limitations in subcritical plane poiseuille flow. *Physics of Fluids*.

[McKernan, 2006] McKernan, J. (2006). *Control of Plane Poiseuille Flow: A Theoretical and Computational Investigation*. PhD thesis, School of Engineering, Cranfield University.

[McKernan et al., 2007] McKernan, J., Whidborne, J., and Papadakis, G. (2007). Linear quadratic control of plane poiseuille flow the transient behaviour. *International Journal of Control*, 80(12):1912–1930.

[Min and Choi, 1999] Min, C. and Choi, H. (1999). Suboptimal feedback control of vortex shedding at low reynolds number. *Journal of Fluid Mechanics*, 401:123–156.

[Moin and Bewley, 1994] Moin, P. and Bewley, T. (1994). Feedback control of turbulence. *Applied Mechanics Review*, 47(6):3–13.

[Moin and Mahesh, 1998] Moin, P. and Mahesh, K. (1998). Direct numerical simulation: A tool in turbulence research. *Annual Review of Fluid Mechanics*, 30(1):539–578.

[Monsma et al., 1995] Monsma, D., Lodder, J.C. Popma, T., and Dieny, B. (1995). Perpendicular hot electron spin-value effect in a new magnetic field sensor: the spin-value transistor. *Physical Review Letter*, 74(26):5260–5263.

[Moore, 1981] Moore, B. (1981). Principal component analysis in linear systems: controllability, observability, and model reduction. *IEEE transactions on Automatic Control*, 26:17–32.

[Morkovin et al., 1994] Morkovin, M., Reshotko, E., and Herbert, T. (1994). Transition in open flow systems-a reassessment. *Bulletin of the American Physical Society*, 39(1882):9.

[Orszag, 1971] Orszag, S. (1971). Accurate solution of the orr-sommerfeld stability equation. *Journal of Fluid Mechanics*, 50(4):689–703.

[Patel and Head, 1969] Patel, V. and Head, M. (1969). Some observation on skin friction and velocity profiles in fully developed pipe and channel flows. *Journal of Fluid Mechanics*, 38:181–121.

[Pinarbasi and Liakopoulos, 1995] Pinarbasi, A. and Liakopoulos, A. (1995). The role of variable viscosity in the stability of channel flow. *International communications in heat and mass transfer*, 22(6):837–847.

[Reddy and Henningson, 1993] Reddy, S. and Henningson, D. (1993). Energy growth in viscous channel flows. *Journal of Fluid Mechanics*, 252:209–238.

[Reddy et al., 1993] Reddy, S., Schmid, P., and Henningson, D. (1993). Pseudospectra of the orr-sommerfeld operator. *SIAM Journal on Applied Mathematics*, 53(1):15–47.

[Reshotko, 2001] Reshotko, E. (2001). Transient growth : A factor in bypass transition. *Physic of Fluids*, 13(5):1067–1075.

[Reshotko et al., 2006] Reshotko, E., Tumin, A., Meier, G., Sreenivasan, K., Heinemann, H. J., and Gladwell, G. M. L. (2006). *Application of Transient Growth Theory to Bypass Transition*, volume 129, pages 83–93. Springer Netherlands.

[Rowley, 2005] Rowley, C. (2005). Model reduction for fluids, using balanced proper orthogonal decomposition. *International Journal of Bifurcation and Chaos*, 15(3):997–1013.

[Rowley and Williams, 2006] Rowley, C. and Williams, D. (2006). Dynamics and control of high-reynolds-number flow over open cavities. *Annual Review of Fluid Mechanics*, 38:251–276.

[Samimy et al., 2007] Samimy, M., Debiasi, M., Caraballo, E., Serrani, A., Yuan, X., Little, J., and Myatt, J. (2007). Feedback control of subsonic cavity flows using reduced order models. *Journal of Fluid Mechanics*.

[Sastry and Bodson, 1989] Sastry, S. and Bodson, M. (1989). *Adaptive control: stability, convergence, and robustness*. Prentice-Hall, Inc. Upper Saddle River, NJ, USA.

[Schlichting and Gersten, 2000] Schlichting, H. and Gersten, K. (2000). *Boundary-Layer Theory*. Springer.

[Schmid, 2007] Schmid, P. (2007). Nonmodal stability theory. *Annual Review of Fluid Mechanics*, 39:129–162.

[Schmid and Henningson, 2001] Schmid, P. and Henningson, D. (2001). *Stability and Transition in Shear Flows*. Springer-Verlag, New York.

[Schrauf and Golling, 2006] Schrauf, Gand Wood, N. and Golling, B. (2006). Key aerodynamic technologies for aircraft performance improvement. 5th Community Aeronautics Days.

[Skogestad and Postlenthwaite, 2007] Skogestad, S. and Postlenthwaite, I. (2007). *Multivariable Feedback Control: Analysis and Design*. Wiley.

[Smith and Glezer, 1998] Smith, B. and Glezer, A. (1998). The formation and evolution of synthetics jets. *Physic of Fluids*, 10(9):2281–2297.

[Tatsambon Fomena and Collewet, 2011a] Tatsambon Fomena, R. and Collewet, C. (2011a). Fluid flow control: a vision-based approach. *International Journal of Flow Control*, 3(2).

[Tatsambon Fomena and Collewet, 2011b] Tatsambon Fomena, R. and Collewet, C. (2011b). Fluid flows control using visual servoing. In *IFAC World Congress*, Milan, Italy.

[Trefethen, 1992] Trefethen, L. (1992). Pseudospectra of matrices. In *Numerical analysis 1991: proceedings of 14th Dundee Conference*, volume 260.

[Trefethen and Embree, 2005] Trefethen, L. and Embree, M. (2005). *Spectra and Pseudospectra: The behavior of Nonnormal Matrices and Operators*. Princeton: Princeton Univ. Press.

[Trefethen et al., 1993] Trefethen, L., Trefethen, A., Reddy, S., and Driscoli, T. (1993). Hydrodynamic stability without eigenvalues. *Science*, 261:578–584.

[Tsao et al., 1997] Tsao, T., Jiang, F., Miller, R., Tai, Y.C. Gupta, B., Goodman, R. Tung, S., and Ho, C. (1997). An integrated mems system for turbulent boundary layer control. In *Proc. of the 1997 International Conference on Solid State Sensors and Actuators*, Chicago.

[Vazquez et al., 2009] Vazquez, R., Schuster, E., and Kristic, M. (2009). A closed form full state feedback controller for stabilization of 3d magnetohydrodynamic channel flow. *Journal of Dynamic Systems, Measurement, and Control*, 131:41001–41010.

[Whidborne and McKernan, 2007] Whidborne, J. and McKernan, J. (2007). On the minimization of maximum transient energy growth. *IEEE transactions on automatic control*, 52(9).

[Whidborne et al., 2008] Whidborne, J., McKernan, J., and Papadakis, G. (2008). Minimizing transient energy growth in plane poiseuille flow. *Proceedings of the Institution of Mechanical Engineers, Part I, Journal of Systems and Control Engineering*, 222(15):323–331.

[Willcox and Peraire, 2002] Willcox, K. and Peraire, J. (2002). Balanced model reduction via the proper orthogonal decomposition. *AIAA journal*, 40(11):2323–2330.

[Wygnanski, 1997] Wygnanski, I. (1997). Boundary layer flow control by periodic addition of momentum. In *4th AIAA Shear Flow Control Conference*, USA.

[Xu et al., 2008] Xu, C., Schuster, E., Vazquez, R., and Kristic, M. (2008). Stabilization of linearized 2d magnetohydrodynamic channel flow by backstepping boundary control. *System & Control Letters*, 57(10):805–812.

[Xu et al., 2003] Xu, Y., Tai, Y., Huang, A., and Ho, C. (2003). Ic-integrated flexible shear-stress sensor skin. *Microelectromechanical Systems*, 12(5):740–747.

[Yan et al., 2004] Yan, P., Debiasi, M., Yuan, X., Caraballo, E., Efe, M., Ozbay, H., Samimy, M., DeBonis, J., Camphouse, R., Myatt, J., Serrani, A., and Malone, J. (2004). Controller design for active closed loop control of cavity flows. In *4th AIAA Aerospace Science Meeting*.

[Yan et al., 2006] Yan, P., Debiasi, M., Yuan, X., Little, J., Ozbay, H., and Samimy, M. (2006). Experimental study of linear closed loop control of subsonic cavity flows. *AIAA journal*, 44(5):929–938.

[Yuan et al., 2005] Yuan, X., Caraballo, E., Yan, P., Serrani, A., DeBonis, J., Myatt, J., and Samimy, M. (2005). ntal study of linear closed loop control of subsonic cavity flow. In *43th AIAA Aerospace Sicences Meeting and Exhibit*.

[Zhou et al., 1996] Zhou, K., Doyle, J., and Glover, K. (1996). *Robust and Optimal Control*. Prentice Hall, New Jersey.